Investigation of Microstructure and Corrosion in Al-Cu and Al-Mg alloys with and without Li additions

By

David Matthew Carrick

Doctoral Thesis

Submitted in partial fulfilment of the requirements for the award of

Doctor of Philosophy of Loughborough University

September 2015

Abstract

The corrosion performance of Al-Cu and Al-Mg alloys with and without Li additions have been investigated. These include; AA2024-T3, AA2099-T8E77 (coarse and fine grain structure), AA5083-T351, spray formed Al-Mg-Li and spray formed Al-Mg-Li-Cu-Zn alloy. Atmospheric corrosion was investigated for up to 12 months of exposure in a rural-urban environment, prolonged immersion testing in 3.5 wt.% NaCl for up to 96 hr's and potentiodynamic polarisation in 3.5 wt.% NaCl were examined. This was to answer whether Li additions, spray forming and grain size impacted on the corrosion resistance. Atmospheric exposure showed $Al_2(CO_3)_3$, NO_x, SO_x and NaCl compounds being deposited. Cathodic intermetallic compounds (Fe, Si, Mn and Cu rich) were shown to be associated with pitting corrosion, whereas anodic intermetallic compounds (Mg rich) offered sacrificial protection to the matrix. The Al-Cu alloys showed more corrosion compared to the Al-Mg alloys in all three corrosion investigations. The Al-Cu alloys showed pitting corrosion and intergranular corrosion, compared to primarily pitting corrosion on the Al-Mg alloys. AA2024-T3 developed a weakened, friable layer on the surface, consisting of a network of intergranular corrosion and numerous shallow pits. The Al-Cu-Li alloys also showed intergranular corrosion and pitting corrosion, but also developed selective grain dissolution, leading to extensive sub-surface cavities. This showed that Li additions in the Al-Cu alloys was detrimental and was primarily associated with the T type phases likely to be; T_1 phase (Al_2CuLi). Li additions in the Al-Mg alloys did not show any measurable improvement or reduction in corrosion resistance. Spray forming also did not appear to improve the corrosion resistance. Grain size in turn was shown to impact on corrosion resistance, with the general consensus being that finer grains offer increased corrosion resistances. Al-Cu alloys showed fine grain structures developed easy path propagation for intergranular corrosion, whereas fine grain structures on Al-Mg alloys promoted increased corrosion resistance.

Acknowledgements

I would like to offer my utmost thanks to my supervisors Dr Geoffrey Wilcox and Dr Simon Hogg for their kind support, valuable discussion, patience and guidance throughout this project.

I would like to thank all members of the Loughborough Materials Characterisation Centre for their training, guidance and friendship throughout this project. I would also like to thank Mr Trevor Atkinson, Mr Mac Callendar, Mr David Insley and Mr Mike Kemp for their assistance in the preparation of my material for this project, their assistance was invaluable.

Thanks to all of my colleagues working in the Materials Degradation Centre and all my friends past and present in Loughborough.

Thanks to the Loughborough Graduate Research School for funding my project and thanks to my supervisors for their financial contributions towards my career especially for allowing me to present at international conferences on an annual basis.

I would like to thank my family for their guidance and encouragement throughout this project. Special thanks to my girlfriend, Miss Emma Townend for her patience, love and support throughout my studies.

Finally I would like to dedicate this thesis to a close friend, Mr Keith Padgett who sadly could not be here to see the completion of this work but will always be remembered.

Table of contents

Glossary of terms

f.c.c	Face-centred-cubic
IMC	Intermetallic Compound
Epit	Pitting Potential
IGC	Intergranular Corrosion
OCP	Open Circuit Potential
SCC	Stress Corrosion Cracking
θ'	Al_2Cu
δ'	Al_3Li
SSSS	Super Saturated Solid Solution
GP	Guinier-Preston
S	Al_2CuMg
T_1	Al_2CuLi
PFZ	Precipitate Free Zone
GB	Grain boundaries
β	Al_3Mg_2
SAXS	Small Angle X-ray Scattering
V_f	Volume Fraction
T_2	Al_6CuLi_3
XRD	X-ray Diffraction
δ	AlLi
T	Al_2MgLi
η'	$MgZn_2$
R	Al_5CuLi_3
SCE	Saturated Calomel Electrode
EDS	Energy Dispersive X-ray Spectroscopy
IMFP	Inelastic Mean Free Path
SMAT	Surface Mechanical Attrition
ECAP	Equal Channel Angular Pressing
i_{corr}	Corrosion current
i_{pass}	Passivation current
TEM	Transmission Electron Microscope
E_{corr}	Corrosion Potential
R_p	Polarisation Resistance
ITT	Isothermal Time Transformation
α	Aluminium

RH	Relative Humidity
TOW	Time of Wetness
FEGSEM	Field Emission Gun Scanning Electron Microscopy
EBSD	Electron Backscatter Diffraction
BSD	Backscatter Detection
SiC	Silicon Carbide
SDD	Silicon Drift Detector
FEGTEM	Field Emission Gun Transmission Electron Microscopy
HAADF	High Angle Annular Dark Field
XPS	X-ray Photoelectron Spectroscopy
Cu1	AA2024-T3
Cu2	AA2099-T8E77 extrusion
Cu3	AA2099-T8E77 plate
Mg1	AA5083-T3510
SF1	Spray formed Al-Mg-Li alloy
SF2	Spray formed Al-Mg-Li-Cu-Zn alloy
SF	Spray formed
BE	Binding Energies
HT	Heat treated
NHT	Non-heat treated

List of figures

CHAPTER 1: LITERATURE REVIEW

CHAPTER 2: EXPERIMENTAL PROCEDURES

CHAPTER 3: MATERIALS CHARACTERISATION

CHAPTER 4: ATMOSPHERIC CORROSION

CHAPTER 5: IMMERSION TESTING

CHAPTER 6: POTENTIODYNAMIC POLARISATION

List of tables

CHAPTER 1: LITERATURE REVIEW

CHAPTER 2: EXPERIMENTAL PROCEDURES

CHAPTER 3: MATERIALS CHARACTERISATION

CHAPTER 4: ATMOSPHERIC CORROSION

CHAPTER 5: IMMERSION TESTING

CHAPTER 6: POTENTIODYNAMIC POLARISATION

Introduction

Williams and Starke [1] stated that in the 21st century the key characteristics of successful automotive and aerospace products were customer value and minimal environmental impact. Recently value has been achieved by incorporating improved structural materials that benefit from new manufacturing technologies. Light weighting in particular has become a universal requirement, by improving the overall performance of a material, whilst also reducing its environmental impact. One area of importance for light weighting is to optimise the Al alloys that are used. Recently there has been a change in the consideration of which Al alloy series are used, primarily relating to improved performance, whilst also offering increased corrosion response. Among the Al alloy groups of critical importance, especially to the aerospace industry, are Al-Li alloys.

Development of these as commercial alloys began in the late 1950s with AA2020 [2]. In the 1980s Alcoa's AA2090 and other second generation Al-Li alloys, such as AA8090, were developed. These, however, never received widespread industrial use due to their poor anisotropy, low fracture toughness, poor corrosion resistance and, often, manufacturing issues.

Third generation Al-Li alloys, however, have addressed some of the limiting factors behind Li additions. This has been achieved by effectively managing a number of factors, including the control of impurity elements, such as H, Na, K and P that are present during the preparation of Li-containing alloys. Grain refining elements such as Mn, Zr and Zn have also been used, which aid in precipitating Li phases away from the grain boundaries (GB), helping to alleviate issues associated with intergranular corrosion (IGC) and poor fracture toughness. Reducing the amount of Li and improved casting abilities have also played a significant role in improving fracture toughness and corrosion resistance of Li containing alloys [3]. More recently, however, optimisation of heat treatments has allowed for substantial control of Li phases within the matrix. *Henon et al.* [4] has shown that by altering the artificial aging conditions and the subsequent microstructure of Al-Cu-Li alloys, the susceptibility to IGC can be reduced.

Li is, however, a highly reactive metal which poses concerns for Al alloy corrosion resistance [5]. The main driver behind their use, however, is that Li additions offer the advantages of significantly reducing weight as well as improving specific modulus and strength, provided the Li stays within solid solution and does not precipitate out [6].

For these reasons the impact of Li has been evaluated in this thesis with regards to its impact on corrosion resistance. Other areas will also be investigated as secondary objectives, including the impact of grain size and a relatively new forming technology, termed spray forming.

This thesis will be broken into six chapters. Chapter 1 will examine current literature within the scientific community and summarise what the current knowledge and theories are relating to aluminium alloys, their corrosion resistances, lithium additions, types of corrosion and the spray forming technique.

Chapter 2 will explain the experimental procedures that have been undertaken to answer some of the questions raised following the literature review as well as the aims and objectives of the thesis. Chapter 3 will characterise each of the aluminium alloys in question with regards to particle distribution, chemistry and grain structure. Chapter 4 will examine the atmospheric corrosion resistances of each of the aluminium alloys following a 12 month exposure to a rural/urban environment. Chapter 5 will examine the open circuit potential response for up to 96 hrs of immersion in a conductive solution. Chapter 6 will examine the potentiodynamic polarisation response including estimations of corrosion resistances.

Chapter 1: Literature Review

This chapter will give a background to the materials examined in this thesis and discuss any relevant published literature relating to them.

1.1 Al and Al Alloys

Aluminium (Al) is one of the most abundant elements found in the earth's crust. It has a face-centred-cubic (f.c.c) crystal structure and a density of 2700 kgm^{-3} which makes it one of the lightest metallic elements, found in the Earth's crust. Its Young's modulus (70.5 GPa) is approximately one third of that of steel, which means that Al can be sensitive to deformation, however due to its substantial strength to weight ratio makes it an interesting engineering material [7]. Al also has a high natural resistance to corrosion, due to its high affinity for oxygen (O) on a fresh surface. A thin oxidised surface forms protecting the substrate from any further attack. Alloying Al can significantly improve the strength to weight ratio and as such the alloys can be used in a range of structural applications where both characteristics are critical, for example in the automotive sector, where keeping mass low is critical but maintaining a high level of strength for the likes of crash safety. Unfortunately higher strength alloys typically have a reduced corrosion resistance, due to the formation of electrochemically active phases, they can also be susceptible to fatigue[8].

Al alloys are typically divided into 8 series with each series corresponding to a specific alloying element. The main alloying elements are Mg, Cu, Si, Zn and Mn, as represented in Table 1-1. Other elements are, however, alloyed such as Ni, Ti, Ca and so on, all giving the Al alloys very unique properties [9]. These 8 series can be divided into sub-series; cast and wrought semi-finished products. Wrought alloys are typically flat rolled, extruded or forged and cast Al alloys are those that have undergone die, mould or sand casting. Both sets can be further divided into heat-treatable and non-heat-treatable grades. Heat-treatable Al alloys (2XXX, 6XXX and 7XXX) undergo specifically designed tempering to strengthen the alloy. Non-heat-treatable Al alloys (1XXX, 3XXX and 5XXX) are primarily strengthened via cold working or by annealing to soften the structure of which Table 1-2 shows the most common tempering treatments applied to Al alloys.

Table 1-1: Most common Al alloy series and their main alloying elements [10], [11].

Series	Main alloying element (s)
1XXX	Pure (> 99%) Aluminium
2XXX	Copper
3XXX	Manganese
4XXX	Silicon
5XXX	Magnesium
6XXX	Magnesium + Silicon
7XXX	Zinc + Magnesium + Copper
8XXX	Others

Table 1-2: Definition of metallurgical tempers for heat treatable Al alloys according to the standard EN 515:1993 [12].

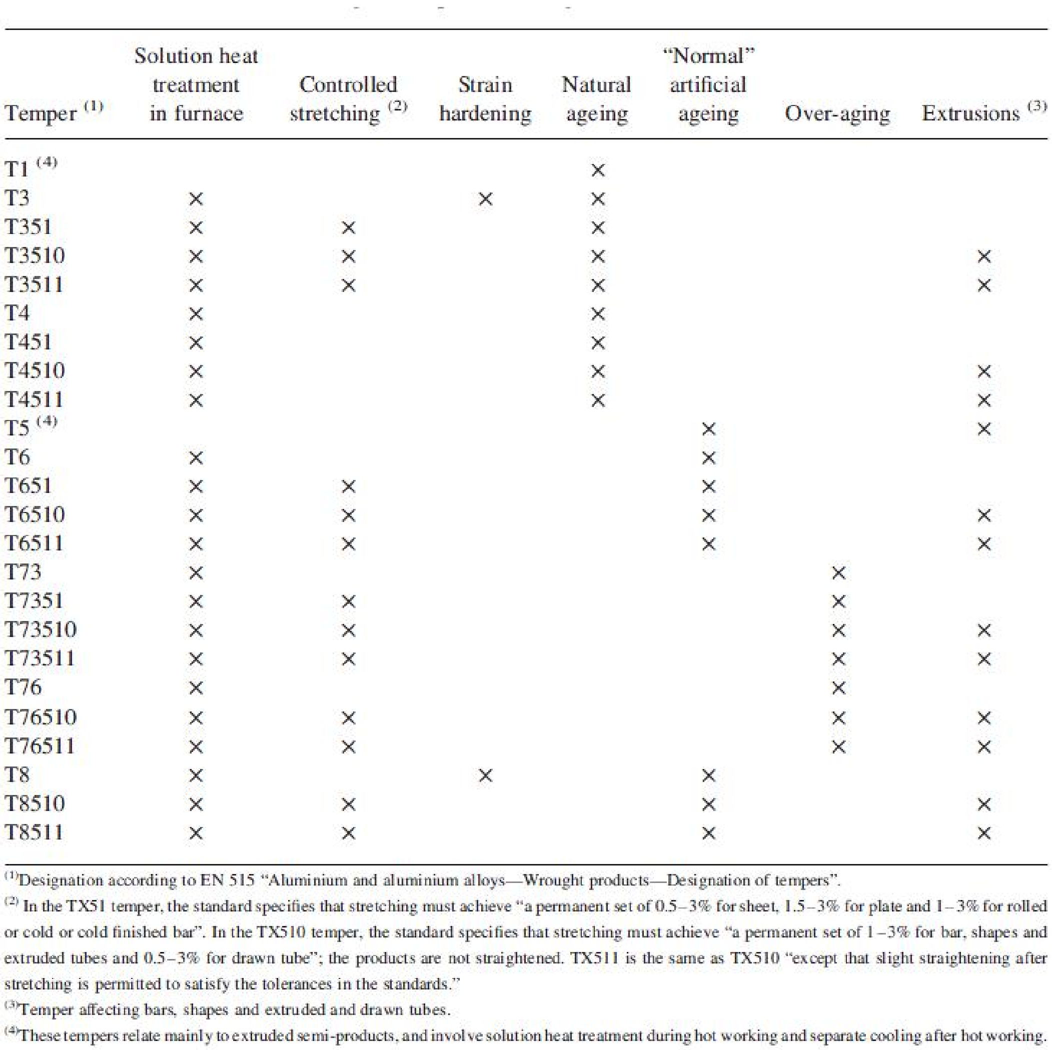

Temper (1)	Solution heat treatment in furnace	Controlled stretching (2)	Strain hardening	Natural ageing	"Normal" artificial ageing	Over-aging	Extrusions (3)
T1 (4)				×			
T3	×		×	×			
T351	×	×		×			
T3510	×	×		×			×
T3511	×	×		×			×
T4	×			×			
T451	×			×			
T4510	×			×			×
T4511	×			×			×
T5 (4)					×		×
T6	×				×		
T651	×	×			×		
T6510	×	×			×		×
T6511	×	×			×		×
T73	×					×	
T7351	×	×				×	
T73510	×	×				×	×
T73511	×	×				×	×
T76	×					×	
T76510	×	×				×	×
T76511	×	×				×	×
T8	×		×		×		
T8510	×	×			×		×
T8511	×	×			×		×

(1)Designation according to EN 515 "Aluminium and aluminium alloys—Wrought products—Designation of tempers".

(2) In the TX51 temper, the standard specifies that stretching must achieve "a permanent set of 0.5–3% for sheet, 1.5–3% for plate and 1–3% for rolled or cold or cold finished bar". In the TX510 temper, the standard specifies that stretching must achieve "a permanent set of 1–3% for bar, shapes and extruded tubes and 0.5–3% for drawn tube"; the products are not straightened. TX511 is the same as TX510 "except that slight straightening after stretching is permitted to satisfy the tolerances in the standards."

(3)Temper affecting bars, shapes and extruded and drawn tubes.

(4)These tempers relate mainly to extruded semi-products, and involve solution heat treatment during hot working and separate cooling after hot working.

Typical Al alloys used within the aerospace industry include 2XXX, 7XXX and 8XXX series. 8XXX series Al alloys typically include some experimental grades containing lithium additions such as AA8090. An example of an Al alloy used currently in the aerospace industry is AA2024[1] which is used as the under surface skin of aircraft wings to provide high tensile strength [13], [14]. More recently, however, some Al-Cu-Li based alloys have started to be introduced, primarily as structural components within the fuselage.

---

[1] AA is the standard derivation of the Aluminium Association, which register Al alloy compositions.

At present 5XXX and 6XXX series Al alloys are used primarily in the automotive industry on a range of products, including structural components and inner/outer panels. The industry is moving more towards Al alloy usage, which has led to the Body-in-White structure of some automotive manufacturers being comprised primarily of Al alloys. This is due to the demand for lighter vehicles, to help reduce CO_2 emissions and fuel consumption to meet global CO_2 targets by 2020, whilst also offering higher performance [15].

For the basis of this thesis a number of Al alloys have been investigated from various series, including 2XXX and 5XXX as well as Li containing variations of these Al alloy systems.

1.2 Alloying Elements, phases and intermetallic particles

Alloying content and microstructural control are the key areas for improving Al alloy performance [16]. Extensive alloying and heat treatments are required to obtain precipitation strengthening via second phase IMC (Intermetallic Compound), however, these can increase the susceptibility to localised corrosion [17], [18].

The addition of almost any alloying element to Al will result in change to the pitting potential (E_{pit}). Depending on whether the alloying element is more noble or less noble than Al will determine whether the E_{pit} increases or decreases [19]. An example being Mg and Zn, which are less noble than Al, which means that when a galvanic cell forms between the Al and the alloying elements, the Mg / Zn becomes the anode (positively charged) acting in a sacrificial manner to the Al matrix. In comparison Cu is more noble than Al and as such is more cathodic (negatively charged) causing the Al to be dissolved. This is ultimately why 5XXX series Al alloys have a higher corrosion resistance than the 2XXX series.

Figure 1-1 shows the effect of some alloying elements on the open circuit potential (OCP) of Al alloys, as detailed by *Vargel* [12]. For reference the OCP of a pure Al alloy is ~ -0.85 V based on Figure 1-1. OCP is the rest potential of a system in which there is no current flowing and can be significantly altered depending on chemical composition [12], as demonstrated by Figure 1-1.

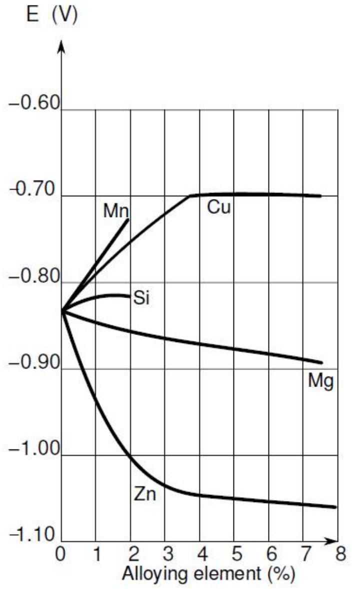

Figure 1-1: Influence of alloying elements on the OCP of Al alloys [12].

An Al alloy is a system with a balance of anodic and cathodic regions, during OCP these regions are in equilibrium. The anodic and cathodic phases have their own half-cell electrode potentials where electrons are released at the anode and absorbed at the cathode. By applying a current to the system, a polarisation curve can be generated, from which the Butler-Volmer equation can be used to determine the anodic and cathodic potentials. This can then be plotted against log of current density and termed an Evans diagram, as shown in Figure 1-2. These Evans diagrams can then be used to get an understanding of the electrochemical behaviour of a system.

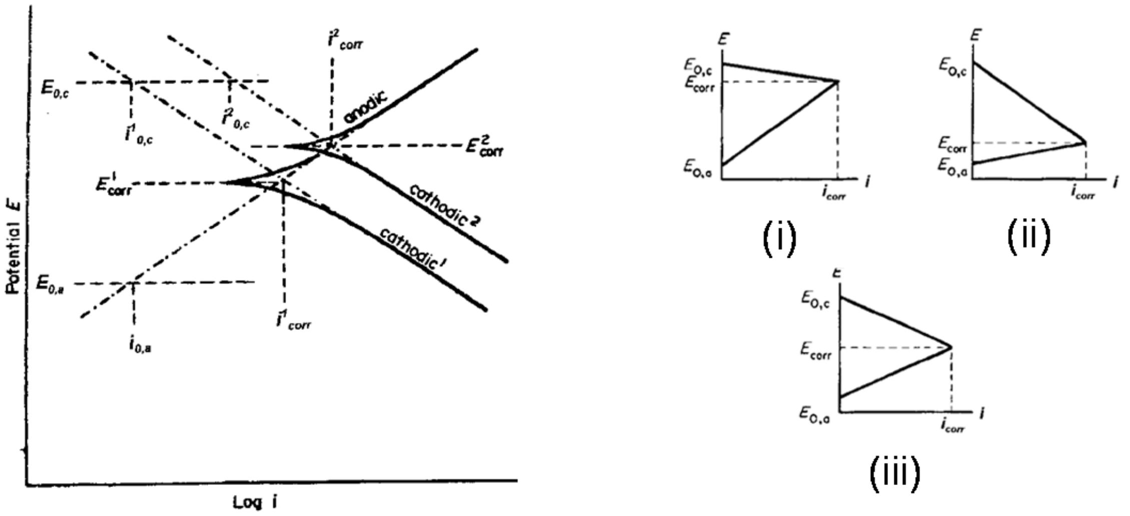

Figure 1-2: a) Plot showing the potential against logarithm of the current density for a metallic system b) Extrapolation of the anodic and cathodic plots shown in Figure 1-2 a form an Evans diagram, i is anodically controlled, ii is cathodically controlled and iii is controlled by both reactions [20].

Alloying elements can be classified into 4 categories; major, minor, microstructure modifiers and impurities [21]:

- *Major*; typically includes Si, Cu, Zn and Mg

- *Minor*; includes Ni and Sn
- *Microstructure modifiers*; includes Li, Ti, B, Sr, P, Be and Mn
- *Impurities*; includes Fe and Cr

Alloy microstructure and phase selection is largely determined by the alloying elements utilised. As such this section will discuss the primary alloy additions within the stated alloys under investigation and discuss the phases and IMCs developed through such additions, as well as their impact on alloy performance.

1.2.1 Copper

Cu has one of the greatest impacts of all the alloying elements on the strength and hardness of Al alloys, as well as increasing the machinability. Cu does, however, reduce the corrosion resistance and in some Al alloy variations promotes Stress Corrosion Cracking (SCC) [21]. Cu additions can also lead to improved creep resistance, however, electrical conductivity is reduced and welding is made more difficult.

In Al-Cu-Li alloys the high strength mechanics arise from the co-precipitation of θ' [2] (Al_2Cu) and δ' (Al_3Li) phases. The θ' phase is the main strengthening phase and δ' phases increase the elastic modulus [5]. Clustering of Cu IMCs have also been observed to increase the hardness of Cu containing Al alloys, however, they can also be associated with increased susceptibility to corrosion [13], [22].

The precipitation sequence in binary Al-Cu systems has been widely accepted to be:

Supersaturated solid solution (SSSS) --> GP (I) zone --> GP (II) zone or θ'' --> θ' --> θ [23]

Cu atoms are also noted to aggregate along the $\{001\}$ plane forming small coherent Cu-rich disk shaped regions, termed Guinier-Preston (GP) zones [23]. Aging of an Al-Cu will lead to the formation of GP (II) / θ'' which lie parallel to {001} and are a few atoms thick, whereas GP (I) zones have a single atom thickness. GP (II) zones are fully coherent with the lattice, thus offering the highest strengthening mechanisms but also increased brittleness. Growth of GP (II) zones ultimately leads to θ' formation, which co-exist with θ'' phases offering the highest level of strengthening from Cu-rich phases [23]. The θ type phases, do, however, segregate at the grain boundary (GB) in the form of fine precipitates which due to their potential difference with the surrounding Al matrix can promote intergranular corrosion (IGC).

In AA2024-T3, the primary phase that is present is the S phase (Al_2CuMg). This S phase has been shown by *Buchheit et al.* [24] to contain 14 at.% Cu and 16 at.% Mg. The S phase is prone to corrosion, due to the inhomogeneous Cu distribution [24–26]. During corrosion, de-alloying of the Mg takes place and pitting has been seen to occur around the remnant particles [24].

---

[2] Partially coherent tetragonal Al_2Cu structure in the aluminium matrix, lattice parameter = 0.404 nm [23].

Cu is more noble than Al and as such higher concentrations will cause an anodic shift in the OCP and E_{pit} [27]. Fe and Cu aggregates can affect the OCP, generating electrochemically active phases [27]. θ and T type phases are examples of Cu containing phases that form in Al-Cu-Li alloys which are known to be detrimental to the corrosion resistance [19], [28]. Localised galvanic cells develop between Cu rich IMCs and Cu depleted matrix regions. *Ren et al.* [25] observed a change in the OCP of the S phase, related to the preferential dissolution of the Mg and enrichment of the Cu on the surface of a solid S phase specimen galvanically coupled to pure Al. *Lacroix* [29] measured the change in OCP for the S phase and θ phase which can be seen in Figure 1-3. It shows that over the initial 100 minutes of immersion the θ phase is more anodic than the S phase; however, after this the S phase becomes more anodic. This relates to the selective dissolution of the Mg within the S phase. *Lacroix* [29] also measured a difference in the current densities at the S phase particles to be higher than the θ phase, which is associated with the higher Cu concentration within the S phase. A similar mechanism was also seen to take place with regards to the T_1 phase (Al_2CuLi) in Al-Cu-Li alloys, where the Li was active and Cu became more noble [23–25].

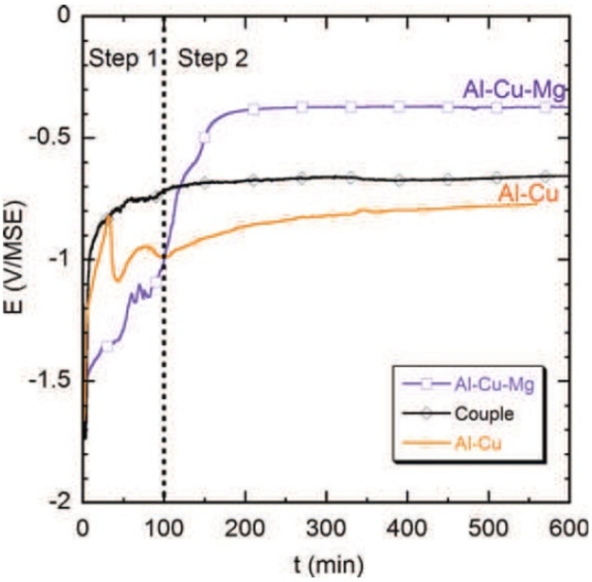

Figure 1-3: OCP measurements of the galvanic couple between Al-Cu-Mg and Al-Cu systems, as well as their individual potentials [29].

Micro-segregation of Cu and Fe impurities have been shown to increase the tendency of pit formation at OCP [19]. *Gu et al.* [33] also suggested Cu and Zn containing phases were detrimental to the corrosion resistance of an Al-Zn-Li-Mg-Cu alloy investigated.

Cu is an element frequently alloyed in 6XXX series Al alloys to improve their high strength capabilities through solid solution hardening, however, a suitable low concentration that improves the high strength but does not lower the corrosion resistance, has yet to be established. It was theorised that a Cu content as low as 0.4% was required before an increase in the susceptibility to IGC and pitting corrosion was observed, however, later reports have suggested values as low as 0.12 wt.% can be detrimental [34], [35].

A similar impact was observed on 7XXX by *Meng et al.* where the Cu additions were investigated [36] and showed that the age hardening ability made the Al alloy more susceptible to corrosion. Cu was seen to be distributed in a range of sizes, from nanometre sized precipitates to micron sized IMCs. *Meng et al.* [36] showed that the addition of Cu formed PFZ (Precipitate Free Zones) and GB precipitates in a range of 7XXX series Al alloys that were examined. Breakdown potentials of the Al alloys were also observed to become more anodic in nature with the addition of up to 2 wt.% Cu, showing the effect of reduced corrosion resistance.

1.2.2 Magnesium

Mg can be used to increase the strength and harden Al alloys; however, this is purely based on the Mg concentration [21]. Systems containing < 4 wt.% Mg will offer enhanced corrosion resistance, good machinability and attractive appearance upon anodising [37]. However, with increasing Mg content, Al-Mg systems are more susceptible to SCC due to the super saturation of solid solution and increased tendency to precipitate the β phase (Al_3Mg_2) at the GB [38]. Additions of 4.25 wt.% Mg have been shown to develop a high level of strain hardening; however, continuous intergranular β phase will be present. These regions are anodic compared to the matrix, as such, increasing the susceptibility to localised corrosion such as IGC [25], [39].

Mg levels of 4.8 wt.% within an Al-Li alloy has been shown to create an anodic shift in the breakdown potential with regards to aging time. However, in general the increase in Mg content above 4.8 wt.% appears to have no effect on the corrosion resistance [5]. *Du et al.* [40] showed that the β phase precipitates were flat and ellipsoidal in shape via Small Angle X-ray Scattering (SAXS). Cu and Mg additions have been recorded to form this β phase in AA2020[3] and AA8090[4] Al alloys.

Mg has also been noted to reduce the solubility of Li in Al, thus promoting a large volume fraction (V_f) of δ' precipitates. However, as the concentration of Mg and Li increase within an Al alloy, heterogeneous precipitation of insoluble Al_3MgLi occurs. *Niskanen et al.* [5] showed that Al specimens alloyed with Mg consisted of equiaxed recrystallised grains.

1.2.3 Lithium

Li offers attractive possibilities to the aerospace industry in particular. One reason for this is that Li is one of a small number of elements, that when alloyed with Al, simultaneously increases its strength and elastic modulus, alongside offering a significant reduction in density, provided that the Li stays within solid solution [2], [5], [6], [41–44]. For a 1 wt.% Li addition, the elastic modulus can increase by 3 GPa alongside a density reduction of ~ 80 kg m^{-3} [14], [37]. *Liu and Williams* [43] even stated that weight savings > 15 % could be achieved with Li additions, resulting in significant economic savings, reduced CO_2 emissions and the potential for increased aircraft payloads. Figure 1-4 demonstrates the potential

---

[3] Primary additions of Cu, Li, Mn and Cd [166], [167].

[4] Primary additions of Cu and Li [167].

weight saving opportunities for utilising Li additions within 2XXX series alloys for lower wing regions. Tensile strength is also seen to increase linearly with Li content [45].

Al-Li based systems have high specific strength, enabling significant strength to weight ratios. However, binary Al-Li systems have not found commercial use primarily due to the reduction in fracture toughness and high manufacturing cost. Li is a highly reactive metal which poses concerns for corrosion resistance [5], [45]. The metastable δ′ strengthening phase is the reason for the enhanced mechanical properties. δ′ causes significant planar slip, as such Zr additions are typically made to disperse the slip through shear resistant Al_3Zr dispersoids. These help by pinning GBs by providing a strong obstacle to dislocation movements during thermal and mechanical processing of the Al alloy [46].

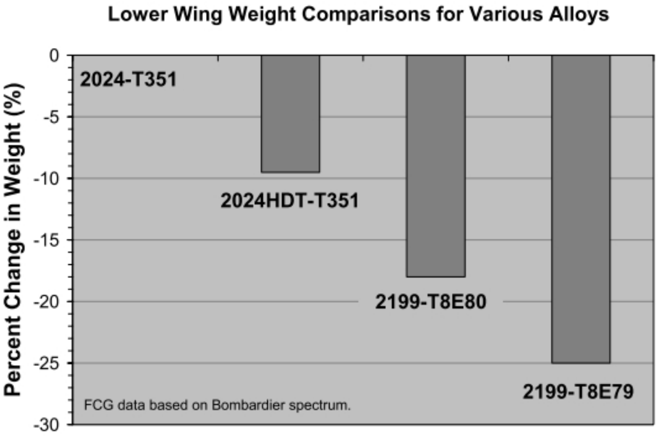

Figure 1-4: Weight saving potential for utilising Al-Cu-Li alloys over conventional Al-Cu systems in Lower Wing regions for the aerospace industry [2].

Recent development of Al-Li alloys, have addressed some of the limiting factors behind Li incorporation in Al alloys. This has been achieved by effectively managing a number of factors, including the control of impurity elements, such as H, Na, K and P that are present during the preparation of Li-containing alloys. Grain refining elements such as Mn, Zr and Zn, which aid in precipitating Li phases away from GB locations, have been used to alleviate issues associated with IGC and poor fracture toughness. Reducing the amount of Li and improved casting abilities have also played a significant role in improving fracture toughness and corrosion resistance of Li containing alloys [3].

Elements for alloying with Al-Li systems include Mg and / or Cu and have been deemed suitable for special applications in military aircraft, automotive and aerospace industries. This is primarily as they offer the formation of major strengthening phases [47]. *Niskanen et al.* [5] stated that small changes to Li content and heat treatment profiles can have dramatic impacts on corrosion resistance. The addition of Li to Al alloys is documented in literature [2], [4], [44], [48] to be detrimental to the corrosion resistance, however, as the understanding of how Li affects Al alloys has advanced, tempering methods have been introduced that appear to improve the corrosion resistant nature of Al-Li alloys. Lithium rich precipitates nucleate and grow preferentially at the GB during ageing which can lead to PFZ, inducing an area of weakness for potential IGC to initiate [44], [48].

Tempering methods have been devised to try to improve the corrosion resistance of the most common Al-Li alloys, which are those with Cu additions. These tempers precipitate the detrimental phases away from the GB thus alleviating the potential for IGC. *Henon et al.* [4] demonstrated that by altering the aging condition of Al-Li alloys the degree of IGC susceptibility can also be altered. This can, however, mean that these detrimental phases are now incorporated into the matrix instead of being at the GB, potentially increasing the susceptibility to pitting corrosion. However, the main aim would be to incorporate the Li into solid solution. The argument can therefore be said that Li does alter the corrosion resistance of Al alloys [2].

Cu is alloyed with Al-Li systems to form strengthening phases in the form of T_1, T_2 (Al_6CuLi_3 or Al_5CuLi_3), and θ' [2], [14], [30–32]. These precipitates, however, are also known for their detrimental impact on the localised corrosion behaviour of Al-Cu-Li alloys. T_1 is the main strengthening phase within Al-Cu-Li alloys such as 2090[5] and 2195[6] forming on the $\{111\}$ plane. The T_1 phase naturally precipitates at dislocation sites, sub-grains and GBs, making it an ideal nucleation site for corrosion. Within Al-Cu-Li alloys the T_1 phase co-exists with the S' and θ' phase [14]. During its precipitation, however, a Cu and Li depleted PFZ is formed as well as the T_2 equilibrium phase along the sub-grain and GB [30], [31]. Figure 1-5 shows the typical precipitates and dispersoids that form in Al-Cu-Li base Al alloys and their corresponding positions and profiles with relation to the alloy microstructure.

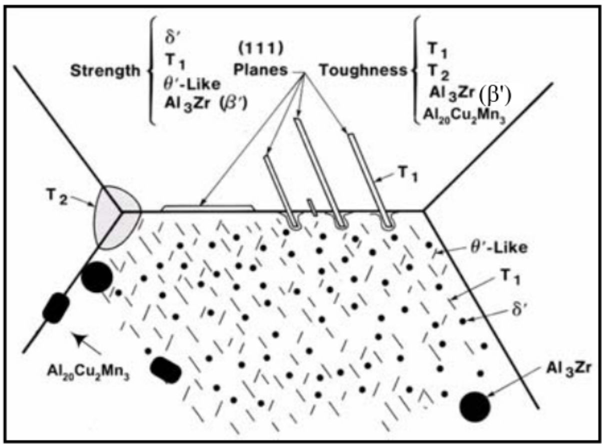

Figure 1-5: Precipitates and dispersoids that form and contribute to the strength and toughness in a typical Al-Cu-Li system [2].

Examples of some commercial Al-Li alloys include 1420 (Al-Mg-Li) which was a Russian Al-Li alloy that was used on military aircraft and 2195 (Al-Cu-Li) which was used for the external tank on the American space shuttles [14], [30]. More recently, however, Constellium have developed the next generation of Al-Cu-Li alloys, which have been approved for use on commercial airliners. This new generation is being termed AIRWARE, an example being 2050 Al alloy.

---

[5] Nominal composition: 1.9-2.6 Li, 2.4-3.0 Cu, 0.25 Mg, 0.1 Si, 0.12 Fe, 0.05 Mn, 0.1 Zn, 0.08-0.15 Zr, Al bal [159]

[6] Nominal composition: 1.0 Li, 4.0 Cu, 0.4 Mg, 0.14 Zr, 0.4 Ag, Al bal [30], [116]

Al forms a eutectic point at 602^{o}C with the intermetallic Al-Li phase at 9.9 wt.%. This Al-Li phase melts at 718^{o}C and has an extensive homogeneity range [49]. *Niskanen et al.* [5] stated that Al alloys containing 1 wt.% Li would be in a solid solution state, whereas those containing 3 wt.% would be precipitation hardened. The precipitation sequence of Al-Li systems has been shown, via X-ray diffraction (XRD) techniques, to be:

SSSS ----> δ' ----> δ (AlLi) [23], [47]

Metastable δ' phases develop in Al-Li based alloys by homogeneous decomposition upon quenching from the solution heat treatment temperature, in alloys containing > 1.7 wt.% Li. Microstructural analysis of 1 wt.% and 3 wt.% Li Al alloys showed a coarse, recrystallised grain structure. *Liu and Williams* [43] stated that the primary reason behind the improved mechanical properties of Li containing alloys is due to the δ' phase. In alloy 1420, *Meng et al.* [50], showed that the δ' phase precipitates transform into the T_1 phase (Al_2CuLi) which can be found on the GB.

Any changes to the microstructure which promote the formation of the δ' phase increase the susceptibility of Al-Li alloys to localised attack when immersed in a 3.5 wt.% NaCl solution. An anodic shift in the corrosion behaviour is seen when the δ' phase becomes a dominant microstructural feature as it is highly susceptible to corrosion [5].

A Li content of 1.3 wt.% is the maximum recommended in non-heat treatable grade Al alloys [51]. A Li level of 1.0 wt.% shows a fine dispersion of precipitates in Al-Li-Mg-Cu alloys. If the Li content is < 1.0 wt.% η' phase ($MgZn_2$) will be produced generating a reduction in density and increased strength [16].

Li discourages lattice diffusion with Al alloys, which decreases precipitation growth, making it difficult for coarse η' phases to form and as such the formation of fine η' phases can take place [33]. Li alters the precipitation behaviour of Al-Zn-Mg-Cu alloys, thus the diffusion of Zn and Mg atoms are suppressed, affecting nucleation and subsequent precipitation processes [52]. The detrimental effect the Li has on the precipitation leaves large concentrations of alloying elements such as Zn and Mg in solid solution [53]. The addition of Li to Al-Zn-Mg-Cu alloys has been seen to cause Zn-rich phases to preferentially precipitate on the GB and form large particles, which can lead to IGC [52]. IGC, is however, more common in Al-Li alloys that contain > 2 wt.% Li, but also elongated grain structures have been observed to increase the susceptibility to IGC [44].

Li possesses a higher vacancy binding energy (~ 0.25 - 0.26 eV) than both Zn and Mg (~ 0.02 eV and ~ 0.01 - 0.05 eV respective [54]), therefore reducing the overall number of free vacancies available for transportation of Zn and Mg [6], [33], [40], [42]. This enables GP (II) zones to become coarse and subsequently suppress the η' phase. The higher binding energy (BE) does, however, cause precipitation of the δ' and η' phases.

1.2.4 Zinc

Zn additions assist in the homogeneous distribution of the S phase in Al-Cu systems; as such Al alloys containing high levels of Zn will have a higher homogeneity than those with lower levels of Zn. The S phase has been seen to develop in Zn modified 5XXX series Al alloys also, at Cu levels near 0.15 wt.% [55]. The addition of Zn to Al-Li alloys can be detrimental as by increasing the Zn-Li ratio the ductility of an alloy will be improved but the strength will be reduced, due to the reduction in the V_f of the δ' phase.

An increase in the V_f of the S phase was seen by *Dinsdale et al.* [56] to reduce the ductility of an Al-Li alloy with test direction. Zn is typically added to try to improve the corrosion resistance of Al alloys, but since it is never observed in the precipitated state, it is assumed to be present in solid solution [2]. Additions of Zn to Al-Li systems have, however, been observed to stimulate the precipitation of the δ’ phase, similarly Zn alloyed to Al-Li-Cu systems has been suggested to lower the stacking-fault energies via nucleation [23]. It has also been shown that the T_1 phase will form on GBs when Zn is incorporated into an Al-Li-Cu alloy, increasing the tendency for IGC [30–32]. *Buchheit et al.* [57] investigated an Al-Cu-Li alloy in the T3 condition, along with artificial aging at 150°C and found that the aging treatments led to the precipitation of the δ', β', T_2 and R (Al_5CuLi_3) phases, the latter was found on the GB, promoting IGC.

Carroll et al. [58] investigated the effect of Zn additions at 1 - 2 wt.% on the impact of SCC for modified 5XXX series alloys. It was found that additions at this level increased the SCC resistance, due to the formation of stable ternary Al-Mg-Zn particles along with a refined grain structure [58]. Small additions of 0.68 - 0.70 wt.% Zn can form this τ phase, which was found to be less susceptible to anodic dissolution at the GB than the β phase [58]. The τ phase that forms when Cu is alloyed to a Zn modified 5XXX series alloy, leads to elevated levels of Cu on the GB even in samples with as little as 0.075 wt.% Cu, showing that Cu and Zn act in a similar manner [55].

Kobe et al. [59] modified a typical 5XXX series Al alloy with Cu and Zn, along with thermal processing to increase the corrosion resistance. The addition of Cu and Zn was suggested to delay or eliminate the precipitation of the β phase at the GB and as such strengthen them. Another alloying element capable of this is Mn, as it provides alternate precipitation sites for the Mg. A number of phases were identified, most being beneficial, however, the S phase which developed promoted IGC [59]. Increased Cu and Zn levels were found to resist IGC and it was observed that no precipitates formed on the GB.

1.2.5 Iron

Another problematic element with regards to corrosion of Al alloys is Fe, which is classed as an impurity element. Due to its low solid solubility in the Al matrix, second phase IMCs are readily formed [60]. Under equilibrium conditions Fe will be present in the form of the Al_3Fe phase; however, if equilibrium is not reached it may be present in a supersaturated state, or in the form of non-equilibrium intermetallic phases.

Ambat et al. [60] and other authors [61–64] have shown that Fe containing IMCs are detrimental to the corrosion resistance of Al alloys. Fe IMCs act as catalytic sites for cathodic reactions, and as such form nearby pit initiation sites, in fact low concentrations of Fe in Al generate a more noble potential due to the formation of cathodically active Al_3Fe phases. Since Fe is a noble element compared to Al it will affect the anodic dissolution characteristics of the Al alloys. *Ambat et al.* [60] showed that the number of Al_3Fe IMCs increases, when a binary Al-Fe alloy was annealed, promoting cathodic reactions on the surface.

High Fe concentrations will lead to a redox[7] reaction taking place, leading to a local increase in pH as high as 11. This local alkalisation results in the dissolution of the Al matrix, surrounding any Al_3Fe inclusion. *Ambat et al.* [60] found that a potential of -1.2 V vs. SCE (saturated calomel electrode) was necessary to remove these particles and that a dilute (0.01 - 0.1 M) NaCl solution resulted in the greatest dissolution around the Al_3Fe inclusions. The redox reactions, shown in Equation ***1-1*** and Equation ***1-2***, assist in breaking down the oxide layer near cathodic particles such as Fe containing IMCs [63]. This process is cathodic in nature, causing the reduction of O state, leading to a localised increase in pH.

$$\boldsymbol{O_2 + 2H_2O + 4e^- \rightarrow 4OH^-} \qquad \textit{\textbf{Equation 1-1}}$$

Anodic dissolution of the Al matrix can be described by Equation ***1-2*** shown below [63]:

$$\boldsymbol{Al \rightarrow Al^{3+} + \ 3e^-} \qquad \textit{\textbf{Equation 1-2}}$$

Yasakau et al. [63] conducted immersion tests on an AA5083 alloy from which dissolution of the matrix material surrounding Fe containing particles took place. It was found that both the Al-(Fe, Mn, Cr, Si) and Al_6 (Fe, Mn) IMCs appear to corrode in a similar manner; however, a compositional analysis was unable to identify the mechanism of corrosion taking place.

Ambat et al. [60] showed that an Al alloy containing 0.04 wt.% Fe increased the susceptibility of corrosion as the Fe phases act as cathodic sites, causing the Al to become anodic and thus actively dissolve [40], [60]. Electrochemical tests were carried out, which showed that anodic attack lead to crystallographic pit structures. Each pit was shown to be a network of faceted cavities, on the $\{100\}$ plane, similar to that of tunnelling. Any crevices that form between the particles and the matrix, acted as pit initiation sites [60].

Relationships between IMCs and the OCP of Al alloy phases suggest that the Al_6 (Fe, Mn) phases are more noble than the matrix and as such redox reactions are responsible for the localised corrosion [60–64].

---

[7] A reaction that takes place in an aqueous solution where electrons are transferred between two species. One species will lose / donate electrons and the other species will gain / receive electrons [168].

1.2.6 Manganese

Mn is a dispersoid forming elements that are used extensively during thermo-mechanical processing to control grain size and restrict recrystallisation [23]. Mn and Cr are typically alloyed with 5XXX series alloys to control SCC initiation, by reducing the GB electrochemical potentials. They have also been suggested to increase the strength at the expense of formability and ductility [49]. Mn and Cr cause a beneficial change to the morphology of Fe containing phases and in some cases Mn is used as an alternative to Fe [21]. An increase in Mn levels from 0.32 wt.% to 1.26 wt.% leads to a fine recrystallised grain structure being formed [5], as shown in Figure 1-6. Mn in Al-Cu-Li systems will typically form $Al_{20}Cu_2Mn_3$ dispersoids, which help to homogenise the slip, thus improving the fracture toughness and fatigue resistance.

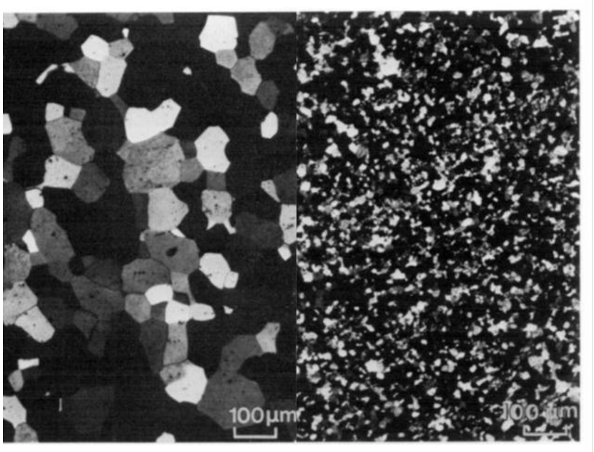

Figure 1-6: Impact on the microstructure from altering the Mn level from 0.32 wt.% to 1.26 wt.% in an AA5083 Al alloy [5].

1.2.7 Zirconium

New generations of aerospace Al alloys require very good mechanical properties. Zr is an element that can be used to increase certain mechanical properties, like fatigue resistance as similar to Mn, Zr is also a dispersoid forming. Many studies have been conducted looking at the impact of Zr additions to Al alloys. Zr forms spherical tri-aluminides (Al_3Zr) with a low solubility and low diffusion coefficient assisting in the control of the microstructure [65]. The Al_3Zr precipitates develop a large coarsening resistance in the matrix in addition to offering a high thermal stability. The ordered cubic $L1_2$ particles provide strength and stabilise the microstructure over a range of temperatures by slowing the recrystallisation kinetics. Al_3Zr particles are also very stable against coarsening and re-dissolution, which causes a more uniform distribution of dislocations at the GBs [47], [65].

Ning et al. [66] reported the addition of 0.16 wt.% Zr, alongside the formation of Al_3Zr precipitates (Ø = 50 - 100 nm) enhanced the thermal stability of an Al-Mg-Mn based Al alloy, along with grain size refinement and improved strength but a reduction in elongation. The average grain size was reduced from 2.2 µm to 0.6 µm, which is due to the GB pinning behaviour of the Al_3Zr precipitates. Figure 1-7 a shows Al_3Zr precipitates pinning the GB of an Al-Mg-Mn base Al alloy and Figure 1-7 b shows the corresponding Energy Dispersive Spectroscopy (EDS) spectrum.

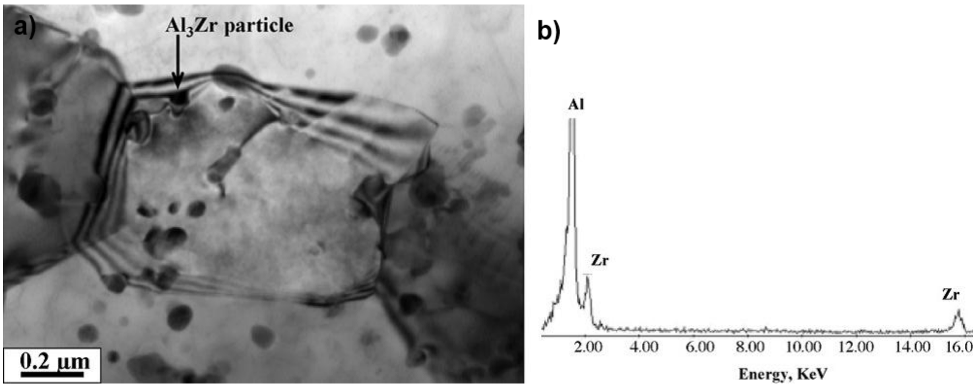

Figure 1-7 a) Micrograph detailing the GB pinning of Al_3Zr precipitates in an Al-Mg-Mn base alloys b) EDS plot of the particles highlighting the presence of Zr [66].

1.3 Localised corrosion in Al and its alloys

Corrosion is defined as the destruction of materials by chemical or electrochemical action, that cannot be prevented only managed and reduced [67]. As such, corrosion resistance is a critical area of investigation within the aerospace and automotive industries and as such some of the most critical forms have been analysed in this literature survey. A number of types of localised corrosion can take place on Al alloys including; pitting, IGC, crevice, SCC and galvanic. Of these pitting, IGC and galvanic corrosion will be discussed alongside relevant literature indicating how they form and affect Al alloys.

1.3.1 Passive Oxide Film

Al and its alloys have a natural resistance to corrosion via a thin, non-coherent, non-uniform passive oxide film that grows on their surface. On pure 99.9 % Al the oxide thickness is supposedly ~ 2 - 3 nm, however, heating will increase the oxide thickness [68]. The structure of this oxide is believed to be similar to that of $\gamma\text{-}Al_2O_3$. The outermost layers of the oxide layer are typically hydrated and have a pseudo-boehmite structure (AlO(OH)). Mill finished samples will also have a thin carbonaceous layer which is deposited from the environment and can be typically around 10 - 20 Å thick [69].

The oxide layer is under compressive stress due to the molecular volume of the oxide layer being ~ 1.5 times greater than that of the substrate. This allows for some deformation to take place without rupturing, as such the oxide film offers favourable mechanical properties and the unusual chemical stability offers enhanced corrosion protective properties. The oxide will also affect the surface wettability and adhesion performance [69].

When a substrate has a thin oxide layer (< 75-85 Å) XPS can reveal the oxide (and / or hydroxide [OH^-]) peak and the metallic substrate in the high resolution Al 2p and Al 2s spectra. It is difficult, however, to differentiate between the oxide and OH^- peaks using the Al 2p peak. The higher BE component is characteristic of the OH^- peak as shown in Figure 1-8.

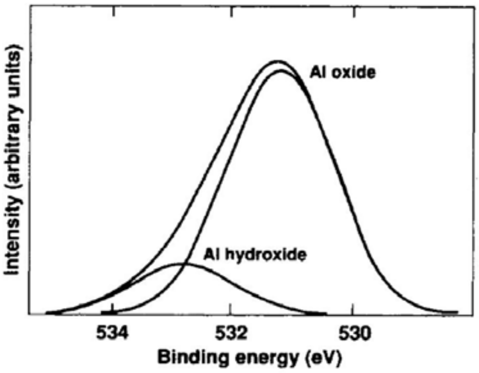

Figure 1-8: XPS spectra from an Al 1145 alloy foil showing the respective hydroxide (532.8 eV) and oxide components (531.3 eV) [69].

Comparison of the Al 2p peak intensities allows for the oxide thickness to be determined [69] shown in Equation ***1-3***:

$$d = \lambda_o \sin\theta \, \ln\left[\frac{N_m\lambda_m}{N_o\lambda_o}\frac{I_o}{I_m} + 1\right] \qquad \textit{Equation 1-3}$$

Where d - oxide thickness in Å, I_m, I_o - photoelectron peak intensities of the metal and oxide respective. N_m, N_o - volume densities of metallic ions in the metal and oxide respective. λ_m, λ_o - inelastic mean free path (IMFP) of the metal and oxide respective, measured in Å. θ - electron take off angle.

Equation ***1-3*** can be simplified depending on the X-ray source to either Equation ***1-4*** for a Mg Kα source or Equation ***1-5*** for an Al Kα source [69]. The typical accuracy of these equations is ~ ±2 Å.

$$d\,(\text{Å}) = 24 \, \ln\left(1.4\,\frac{I_o}{I_m} + 1\right) \qquad \textit{Equation 1-4}$$

$$d\,(\text{Å}) = 28 \, \ln\left(1.4\,\frac{I_o}{I_m} + 1\right) \qquad \textit{Equation 1-5}$$

The passive oxide film present on Al alloys is different for each alloy as it is dependent on the composition and structure of the alloy [61], [70]. Passive films are also affected by the physical and chemical environment, from which a different structure, thickness and composition will form [19].

1.3.2 Effect of microstructure on localised corrosion

GBs have distinct properties relative to the bulk material in terms of atomic coordination, reactivity and diffusion rates. The proportions of atoms that lie at inter-crystalline regions as a total of the surface area are significant as the grain size decreases. It is therefore not unreasonable to expect regions with high GB densities to exhibit different electrochemical responses to those with lower GB densities. Figure 1-9 a, b and c shows the relationship between corrosion current, pitting potential and passivation current and average grain size. Typically improvements to the corrosion resistance are made through bulk alloying or via the use of various coatings. Few efforts, however, have been made to improve corrosion resistance through grain size adjustments. One issue with using cladding[8], coatings and bulk alloying, is that they are prone to defects and as such using grain size alterations, could offer improved corrosion resistance without major changes to the underlying bulk material [71], [72].

Relating grain size to corrosion is inherently difficult with Al alloys, simply because specific alloying elements can impact grain refining properties, but they can also induce different electrochemical responses. Thermo-mechanical processing can also affect the electrochemical behaviour by altering the mechanical and physical properties such as; internal stresses, texture formation and alloy segregation [72]. Literature suggests that with reduced grain size, the corrosion rate is seen to decrease but the results are not readily explained. Of the results shown in Figure 1-10, the results from *Ralston* [71] examined 99.9% pure Al in a 0.1 M NaCl solution and as such is the most relevant to this study, for which it is seen that fine grain sizes < 1 µm^2 have a high resistance to corrosion, by showing a low corrosion current density [72]. *Mahmoud* examined a 6XXX series Al alloy in 1M HCl and showed the opposite to that of *Ralston*. However, *Mahmoud* used a highly acidic electrolyte on an Al-Mg-Si alloy and as such a difference may be expected.

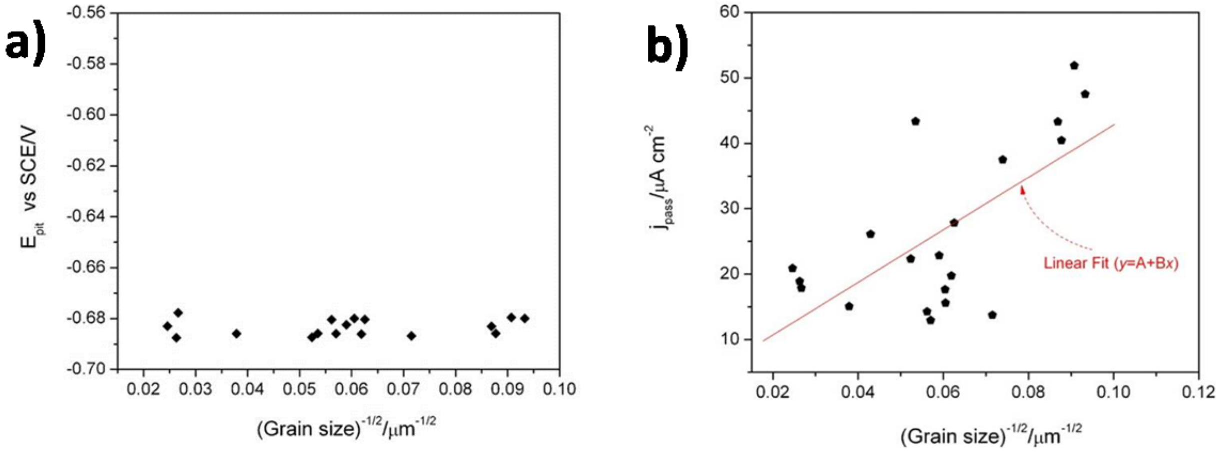

Figure 1-9 a) Plot showing that grain size does not appear to impact on E_{pit} c) Plot showing a comparison between average grain size and passivation current [71].

Ralston and Birbilis [72], [73] suggested that depending on the ability of the surface to passivate, materials could experience either an increase or decrease in the corrosion resistance with grain refinement. They showed that in an active system grain refinement can lead to a decrease in the corrosion resistance. Those environments that encourage passivation showed that a reduction in grain size could encourage more uniform corrosion and less localised attack. *Gollapudi* [74] examined a pure Mg alloy, with grain sizes of 75 and 1150 µm^2 for which an increase in corrosion resistance was noted to the higher density of GBs. Figure 1-11 shows a schematic demonstrating that nano-crystalline microstructures show that fine grain structure has a relatively uniform oxide but coarse grains have a relatively open passive layer [74].

---

[8] Typically known as the bonding of dissimilar materials. Main use is joining of a pure Al system on top of an Al alloy to offer increased corrosion protection [71].

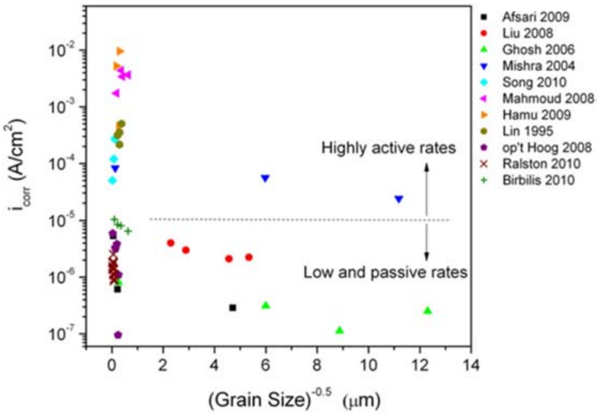

Figure 1-10: The effect of grain size on corrosion rate (expressed in A cm^{-2}) for different materials and environments. Afshari examined Fe in NaOH, Liu examined Ni$_{50.5}$Al$_{49.5}$ in NaCl, Ghosh examined Ni-Cu in deaerated NaCl, Mishra examined Ni in H$_2$SO$_4$, Song examined Mg in NaCl, Mahmoud examined AA6063 in HCl, Hamu examined AZ31 Mg in NaCl, Lin examined alloy 600 in boiling ferritic sulfate, op't Hogg examined Mg in NaCl, ralston examined Al in NaCl and Birbilis examined Mg in NaCl [72].

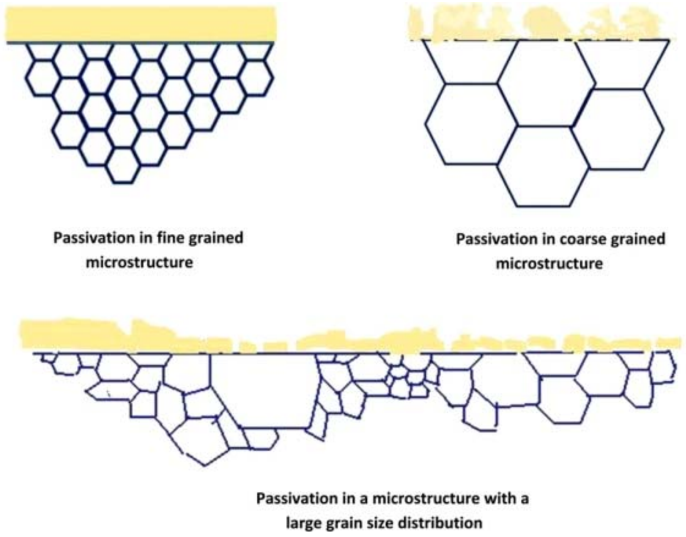

Figure 1-11: Schmetic showing how different sized grains can alter the passivation kinetics of metallic alloys, in particular this example demonstrates the effect on a Mg alloy [74].

Research has been conducted examining the change in grain size and its subsequent impact on corrosion resistance, unfortunately there are contrasting views. Some believe that as grain size decreases the corrosion resistance improves, but others think the contrary. Related to this is the densities of atoms at the GB themselves, in that high density boundaries have a higher resistance to corrosion due to their inherent nature to passivate more readily [71].

The type of GB has also been suggested to play a role on the susceptibility to corrosion, high energy GBs, which are those with a large mis-orientation angle, have been shown to have reduced levels of corrosion resistance in some metals. The reason for this is due to the termination of grain lattices at the boundary regions with a high level of defects [13], [75]. This high level of defects allows easier transport of corrosive electrolytes, reducing the corrosion resistance. *Davenport et al.* [76], found that GBs with < 20° mis-orientation in an AA5182 Al alloy resulted in a high IGC resistance. However, a lack of β phase precipitating in the GB regions could have been the reason for the high IGC resistance. *Luo et al.* [13],

[75], however, showed that grain mis-orientation did not correlate to IGC in an AA2024-T3 alloy. They did, however, show that grains with a high level of stored energy were susceptible to IGC and subsequently, since high stored energy typically reflects a high dislocation density that grains with a high number of dislocations were susceptible to IGC.

Lillard [77] investigated the relationship between crystal orientation and pitting corrosion, where it was shown that single crystal f.c.c Al had a reduced pitting potential in the order of $\{001\} > \{011\} > \{111\}$. Simultaneously it was seen that the rate of dissolution increased in the order of $\{001\} < \{011\} < \{111\}$. Interestingly the work showed that there was no relation between the movement of dislocations in the matrix and pit geometry and that the most common explanation of pit geometry was surface energy.

Ralston et al. [71] examined the impact of grain size on the corrosion response of a high purity Al system via different thermo-mechanical treatments. They revealed that processing techniques can alter the fundamental corrosion characteristics of a material. They showed that for a technique, termed SMAT (surface mechanical attrition) some alloying elements were seen to segregate to the surface layers, reducing the corrosion resistance. A technique termed ECAP (equal channel angular pressing) showed a very high resistance to anodic polarisation techniques, in that potentials as high as 2 V could be passed before any significant corrosion was observed. *Ralston et al.* [71] also showed with decreasing grain size an increase in corrosion current (i_{corr}) was observed.

Unfortunately, the data could only be related to their experiments and there was no control over the residual stresses or microstructural textures. Interestingly, however, when the E_{pit} was examined no difference was observed with regards to altering the grain size with a spread of only 0.015 V vs. SCE between several different processing routes. However, the passivation current (i_{pass}) values were seen to increase rather significantly with reducing grain size [71].

Brunner et al. [73] investigated a conventional AA2024 Al alloy with respect to the corrosion behaviour changes through ultra-fine grain structure development. ECAP processing was used to refine the grain structure, with elongated textured grains and ultra-fine grains (< 200 nm) being generated. EBSD analysis showed that a high level of stored energy was present at the GB due to the high density of dislocations. It was shown that with increasing ECAP processing, the corrosion mechanisms shifted more in the favour of pitting over IGC. This is due to the desensitisation of the GB and redistribution of Cu over the surface of the samples. As such they showed that ultrafine grains on AA2024 via ECAP processing did not affect the IGC behaviour.

Handel et al. [78] also examined a commercially extruded AA6082 alloy in a peak-aged temper condition. Analysis of the specimen showed that it consisted of a substantial recrystallised region on the outer surface, where the average grain size was > 500 µm and the inner regions had an average grain size of < 10 µm. Corrosion analysis showed that in the outer regions pitting corrosion was seen to progress to a depth of ~ 22 µm, whereas in the inner region, the average pit depth was only 5 µm, showing that grain size can have a large impact on corrosion resistance of Al alloys.

1.4 Role of intermetallic particles and phases on localised corrosion

In wrought Al alloys the resistance to localised corrosion, in particular pitting corrosion, is found to be in the following order; 1XXX, 5XXX, 3XXX, 6XXX, 7XXX and 2XXX [12]. Intermetallic character and morphology play a key role in determining this order. Depending on their composition and location, IMCs can act as anodic, cathodic or even neutral sites.

The corrosion behaviour of Al alloys is governed by the density of the heterogeneously distributed cathodic precipitates, for example Al_6 (Mn, Fe, and Cr). This distribution can be either by design or as impurities. The distribution of inclusions or IMCs develops the differential anodic and cathodic zones. Anodic zones tend to be pit initiation sites that are dissolved via dissolution and cathodic zones are generally protected, surrounding these anodic regions. The size, shape and chemical composition of the IMCs, however, is governed by the processing routes, in regards to heat treatments and forming [79]. An example being the formation of shell-shaped particles in AA2024 following a long quench delay time , as shown in Figure 1-12 [79].

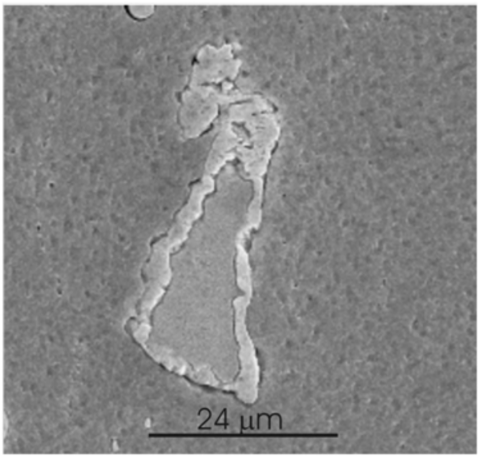

Figure 1-12: Shell-shaped particle within AA2024 as shown by Campestrini et al. [79]

These shell-shaped IMCs were seen to reduce the resistance to pitting corrosion. IMCs can, however, be divided into the following categories [26]:

- *Precipitates* grow following the nucleation and growth mechanisms of a SSSS during a natural or low temperature aging cycle. These are typically Angstroms (Å) to fractions of a micrometre (µm) in size. They can be spherical, needle shaped, laths and / or plate shape. When they are homogeneously dispersed, their impact on localised corrosion is negligible, however, when they are concentrated near / on a GB, alloys can be susceptible to IGC and SCC. Typical examples of these include, β phase, θ phase, η' phase, $Al_{32}Zn_{49}$ and the T_1 phase.
- *Constituent particles* or *second phase particles* are irregular in shape and can range up to 10 µm in size. They are typically formed during alloy solidification and subsequent thermo-mechanical

processing does not dissolve them. Rolling and extrusion of alloys tends to break up and align constituent particles into bands. Typically these particles are rich in alloying elements, meaning their electrochemical activity is entirely different to the surrounding matrix. Examples include Al_3Fe and Al_7CuFe.

- *Dispersoids* are small particles, ranging in the size of 0.05 to 0.5 µm that are insoluble in Al. Typical dispersoids forming elements are Cr, Ti, Zr and Mn. They form at high temperatures and are used to control grain size and recrystallisation behaviour. Examples include Al_3Ti, Al_6Mn, $Al_{20}Cu_2Mn_3$ and Al_3Zr.

Numerous investigations have been undertaken to examine the impact of particles on the corrosion resistant nature of Al alloys. *Aballe et al.* [80] showed that hemispherical pits developed over the surface of an AA5083 alloy immersed in an aerated 3.5 wt.% NaCl solution. Cathodic zones were observed and EDS analysis showed these zones contained Al_6 (Mn, Fe, Cr) particles. The cathodic character of these particles leads to a redox reaction taking place, leading to the formation of OH^- groups. The oxide layer above the precipitates is then subsequently dissolved, after which localised attack takes place, caused by the alkalisation of the interfaces between the matrix and particles resulting in hemispherical pits [39].

Aballe et al. [80] examined the OCP of AA5083, demonstrating how from specimen to specimen there was a difference in OCP, however, values tended to converge after prolonged immersion. OCP values were seen to converge after ~ 5000 sec, as shown in Figure 1-13. *Aballe et al.* [80] described this as the demand from the cathodic IMCs for a current, however, this is more likely to be the anodic and cathodic phases coming to equilibrium. Between samples there will be a difference in the concentration of IMCs at the surface causing a slight change in the initial OCP, which helps to explain why the starting OCP shown in Figure 1-13 are different. Polarisation sweeps shown in Figure 1-14 also help to demonstrate this theory, by showing the change in E_{corr} of each specimen with the E_{pit} staying the same at -720 mV.

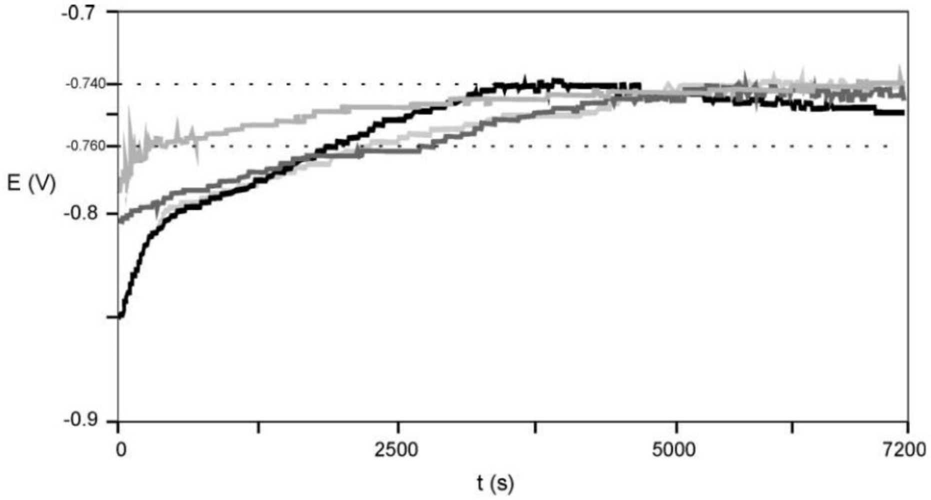

Figure 1-13: OCP of AA5083 specimens showing the impact on the potential behaviour with regards to IMC distribution [80].

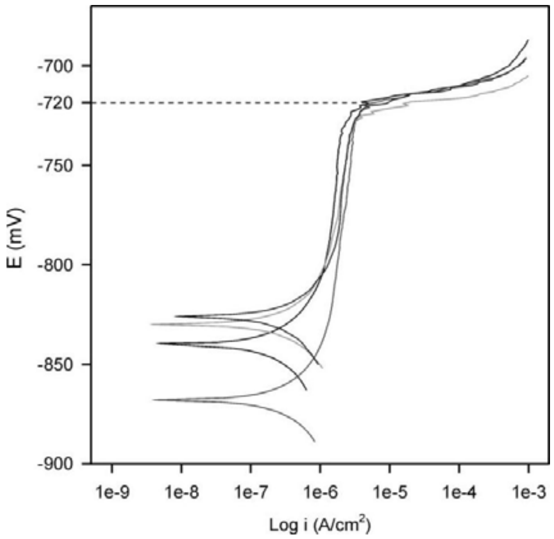

Figure 1-14: Impact of IMC distribution on anodic polarisation of AA5083 Al alloy with respect to changing E_{corr} value [80].

A comparison of the E_{corr}, (initial potential of corrosion), E_{pit} and R_p (polarisation resistance) values showed that for a 1 cm^2 target area the E_{pit} values were relatively uniform. *Aballe et al.* [80], however, did find that to reduce the error in E_{corr} values and subsequent R_p values, a larger target area in the region of 25.5 cm^2 would be required on AA5083 due to the heterogeneous distribution of IMCs. Table 1-3 shows a comparison of the standard deviations and errors achieved.

Table 1-3: Comparison of E_{corr}, E_{pit} and R_p for a 25.5 cm^2 target area on an AA5083 following anodic polarisation [80].

	Standard deviation (mV)	**Error (mV)**
E_{corr}	33.75	8.71
E_{pit}	2.13	0.55
R_p	13.33	3.44

Birbilis and Buchheit [26] conducted an investigation into the E_{pit} and E_{corr} values of IMCs that are commonly found in 7XXX series alloys. They also examined the change in the E_{pit} and E_{corr} values with varying NaCl concentration. Table 1-4 a and b shows a comparison of the E_{pit} and E_{corr} values for different IMCs over a range of NaCl concentrations. This information can be used to highlight the type of corrosion that can take place, in that corrosion associated with IMCs can be initiated by 2 methods; dissolution of the matrix surrounding an IMCs or via selective dissolution of the IMC itself. Pits of the second type typically are very deep and contain remnants of the IMC. Whereas the first type, the matrix surrounding the IMC is dissolved into solution. Cu bearing alloys typically undergo this second type of dissolution [26]. *Birbilis and Buchheit* [26] made a few conclusions from their work related to IMCs, from which the following can be noted:

- Noble particles with high electrochemical activity (E_{corr} of the IMC is greater than the E_{corr} of the matrix) such as Al_2Cu and Al_7Cu_2Fe, that have the ability to sustain large cathodic currents are associated with pitting.

- Noble particles with low electrochemical activity such as Al_3Zr, that cannot sustain large cathodic currents are too small to adversely impact on corrosion.
- Active particles with a high dissolution rate such as $MgZn_2$ have the ability to undergo anodic dissolution.

In particular *Birbilis and Buchheit* [26] observed a distinct breakdown in the β phase (Al_3Mg_2) at values below -0.8 V vs. SCE indicating it has a window of passivity when immersed in a NaCl solution. The β phase is therefore classed as being active and that with the E_{pit} value is generally below that of the alloy system from which the β phase is found can improve the likelihood of corrosion.

Table 1-4 a) Comparison of E_{corr} values for a range of IMCs and alloying elements in NaCl solutions b) Comparison of E_{pit} values for a range of IMCs and alloying elements in NaCl solutions [26].

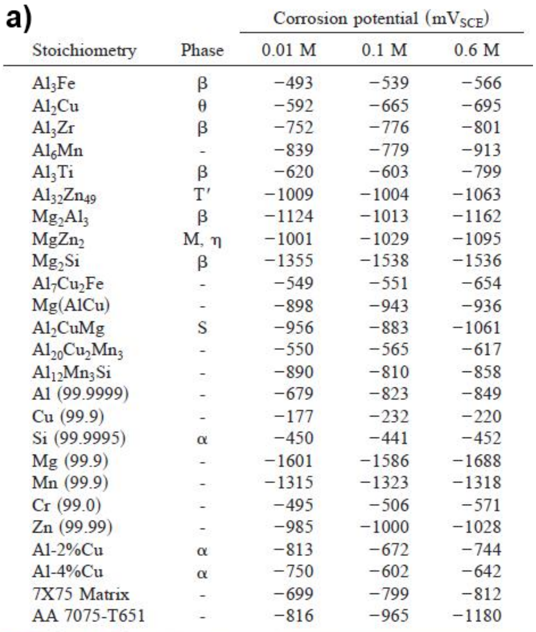

a)

Stoichiometry	Phase	Corrosion potential (mV_{SCE}) 0.01 M	0.1 M	0.6 M
Al_3Fe	β	−493	−539	−566
Al_2Cu	θ	−592	−665	−695
Al_3Zr	β	−752	−776	−801
Al_6Mn	-	−839	−779	−913
Al_3Ti	β	−620	−603	−799
$Al_{32}Zn_{49}$	T′	−1009	−1004	−1063
Mg_2Al_3	β	−1124	−1013	−1162
$MgZn_2$	M, η	−1001	−1029	−1095
Mg_2Si	β	−1355	−1538	−1536
Al_7Cu_2Fe	-	−549	−551	−654
Mg(AlCu)	-	−898	−943	−936
Al_2CuMg	S	−956	−883	−1061
$Al_{20}Cu_2Mn_3$	-	−550	−565	−617
$Al_{12}Mn_3Si$	-	−890	−810	−858
Al (99.9999)	-	−679	−823	−849
Cu (99.9)	-	−177	−232	−220
Si (99.9995)	α	−450	−441	−452
Mg (99.9)	-	−1601	−1586	−1688
Mn (99.9)	-	−1315	−1323	−1318
Cr (99.0)	-	−495	−506	−571
Zn (99.99)	-	−985	−1000	−1028
Al-2%Cu	α	−813	−672	−744
Al-4%Cu	α	−750	−602	−642
7X75 Matrix	-	−699	−799	−812
AA 7075-T651	-	−816	−965	−1180

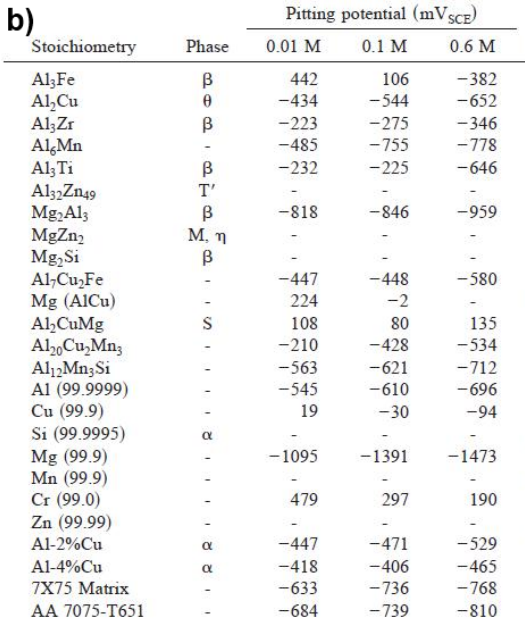

b)

Stoichiometry	Phase	Pitting potential (mV_{SCE}) 0.01 M	0.1 M	0.6 M
Al_3Fe	β	442	106	−382
Al_2Cu	θ	−434	−544	−652
Al_3Zr	β	−223	−275	−346
Al_6Mn	-	−485	−755	−778
Al_3Ti	β	−232	−225	−646
$Al_{32}Zn_{49}$	T′	-	-	-
Mg_2Al_3	β	−818	−846	−959
$MgZn_2$	M, η	-	-	-
Mg_2Si	β	-	-	-
Al_7Cu_2Fe	-	−447	−448	−580
Mg (AlCu)	-	224	−2	-
Al_2CuMg	S	108	80	135
$Al_{20}Cu_2Mn_3$	-	−210	−428	−534
$Al_{12}Mn_3Si$	-	−563	−621	−712
Al (99.9999)	-	−545	−610	−696
Cu (99.9)	-	19	−30	−94
Si (99.9995)	α	-	-	-
Mg (99.9)	-	−1095	−1391	−1473
Mn (99.9)	-	-	-	-
Cr (99.0)	-	479	297	190
Zn (99.99)	-	-	-	-
Al-2%Cu	α	−447	−471	−529
Al-4%Cu	α	−418	−406	−465
7X75 Matrix	-	−633	−736	−768
AA 7075-T651	-	−684	−739	−810

Literature has shown that the levels of Cu and the positioning of Cu containing phases within the microstructure are the most common initiation mechanisms behind corrosion within 2XXX series Al alloys [24], [29], [81], [82]. Typical IMCs that can be found in most 2XXX series Al alloys, are Al-Cu-Mg, Al-Cu-Mn-Fe and Al-Cu-Mg-Fe-Si [83]. *Campestrini et al.* [79] showed that the Al-Cu-Mg IMC had a lower potential difference (100 mV compared to 130 mV vs. SCE) to that of the Al matrix, suggesting that it was more resistant to corrosion. The Al-Cu-Mg rich IMC act in a similar manner to the S phase precipitates, in that the Mg is selectively dissolved, resulting in a subsequential pit trench around the particle, once the Mg has been dissolved [84]. Cu-rich phases are noted to sit along the GB generating micro-galvanic cell regions, which subsequently can lead to IGC. PFZ zones can also lead to IGC within 2XXX series Al alloys, however, in the case of AA2024-T3, no evidence has been shown to suggest the formation of PFZ at the GB. Artificial aging has, however, been shown to lead to Cu depleted zones at the GB, resulting in the formation of PFZ. *Frankel et al.* [85] showed that following anodic polarisation a double breakdown potential was established, relating to breakdown of the GB and the matrix respectively. Figure 1-15 shows this double breakdown phenomenon, with the more noble breakdown at E2 representing the pitting corrosion of the matrix and E1 the breakdown of the GB. *Meng et al.* [36] also observed this double breakdown potential taking place on 7XXX series Al alloys that had additions of Cu.

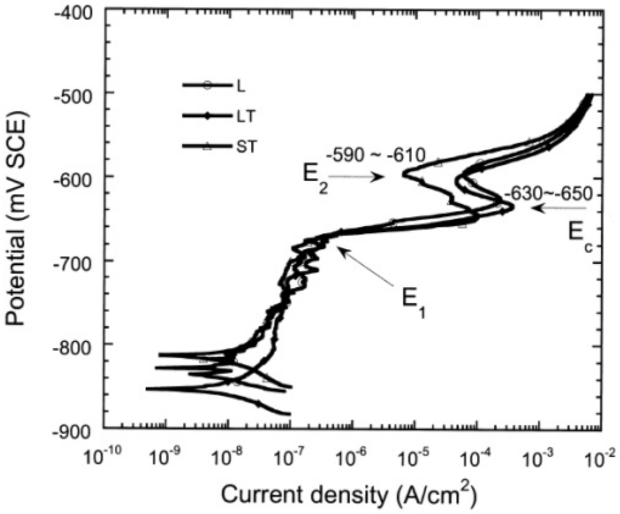

Figure 1-15: Anodic polarization curves for AA2024-T3 in Ar-deaerated 1 M NaCl at a scan rate of 0.1 mVs^{-1} [85].

1.5 Corrosion morphology

1.5.1 Pitting Corrosion

Pitting corrosion will only take place in the presence of aggressive anionic species, generally in the form of chlorides [19], [70], [86]. Pitting will propagate in the presence of an electrolyte with a pH value between 4.5 - 8.5 and tends to increase with temperature, ion concentration and agitation. Excessive agitation can also lead to erosion-corrosion. 2XXX series alloys show the lowest pitting corrosion resistance compared to other alloy series [39].

Al alloys, as described previously have a natural oxide passivation layer. Transport of anions through this passive film leads to aggressive dissolution due to their strong acidic nature. Anions are relatively small, however, they promote a very high dissolution rate and as such interfere with passivation [70]. If Cl$^-$ ions get into a passive film, at a critical concentration the passive film will start to breakdown and form pit initiation sites, as shown in Figure 1-16.

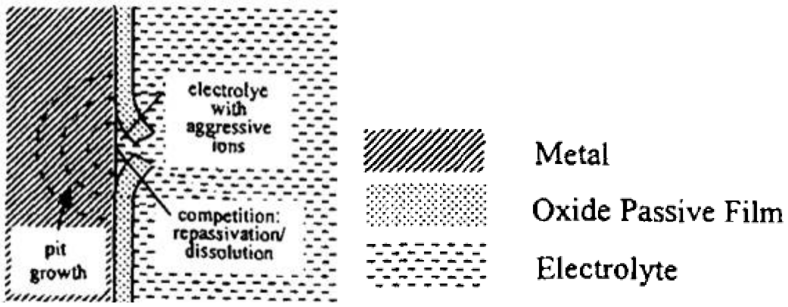

Figure 1-16: Film breakdown mechanics for pitting corrosion [70].

Any imperfections on the surface of a sample can absorb Cl^- ions and can subsequently lead to pit nucleation [62]. In terms of electrochemistry, once the passive region has been removed the β phase (Al_3Mg_2) [9] will drop to the nucleation pitting potential, leading to subsequent crystallographic corrosion. Crystallographic corrosion is where the crystal structure of the material can be clearly seen following active dissolution, it can be clearly identified as cubic structures. Changes in OCP have also been linked to the difference in the number of cathodic precipitates present on the surface of the sample creating a demand for current, accelerating the corrosion [86]. However, on a pure Al system no cathodic particles are present as such a reduction in OCP is related to the grain structure.

Cl^- rich environments are the most common for analysis of the corrosion of Al and its alloys. The movement of Cl^- ions into flaws in the passive film reduces the re-passivation rate[10], subsequently decreasing the corrosion resistance [61]. Typically Cl^- rich media will dissolve the passive film and attack the underlying Al matrix, which is linked to the formation and re-passivation of micro-size pits (Ø = ~ 10 µm) known as metastable pits [61]. Metastable pits form due to oscillations of current at a constant potential that takes place below the pitting potential in Cl^- solutions and the rate and volume of metastable pits that form is dependent on Cl^- concentration and potential applied [61], [87].

Oxidising agents in a Cl^- rich environment will also add to the rate of corrosion that takes place, having a detrimental effect on the localised corrosion. Active-passive cells stimulate attack on the anodic regions within a sample and as such accelerate the rate of corrosion [19].

Pitting is considered to be autocatalytic, where once a pit starts to grow, the conditions lead to subsequent pit formations [70]. Stable pits only form at potentials around 30 mV greater than that of re-passivation [88]. This re-passivation provides information on the stable growth criteria for pits [70]. Some metastable pits do not re-passivate and form stable pits, from which analysis can be conducted [61]. The growth of pits is, however, controlled by the presence of a salt film at the base of the pit with a high dissolution rate [88].

Broli and Holtan [89] found that at specific potentials[11] there was a sudden increase in current density, related to the breakdown of the passive layer. *Pourbaix* [90] stated that pits can propagate at potentials below those needed for pit initiation, and that pitting potentials can be affected by temperature.

Natishan et al. [91] found that the rate of pitting corrosion was linked to the adsorption of Cl^- ions at the alloy surface. XPS and SIMS techniques were used to analyse Cl^- adsorption on passive films at OCP and at applied anodic potentials. Adsorption took place on a local scale, and varied from site to site, due to the heterogeneous structure of pure Al, however, only a minority of these sites were active pits. Pitting can therefore take place when the oxide film becomes positively charged allowing Cl^- ions to be

---

[9] The OCP is determined by the demand for current imposed by the cathodic processes [80].
[10] Rate of the re-growth of the passive layer of the Al alloy [105].
[11] Dependant on alloy system and alloying elements.

adsorbed [91]. *Aballe et al.* [70], showed that pitting corrosion will only progress if specific current densities are surpassed in that a current density > 0.5 μA cm^{-2} can lead to pitting.

Adsorption of the Cl^- was also found to increase linearly with an increase in potential [88]. However, for pits to form the conditions within the pits must be highly acidic [91]. Enhanced passivity is achieved via oxidised solutes that can make the passive film more resistant to Cl^- attack due to an electrostatic repulsion being generated or by the modification to the oxide structure [91].

Applying an increasing potential to an AA2024-T3 sample after exposure to an OCP will increase the number and size of pit initiation sites. If the potential is too low for continuous stable pit growth, tunnelling occurs [86]. Tunnelling has been described as the alternative to pit re-passivation when the potential is below that required for re-passivation [92]. Increasing the potential subsequently increases the tunnel width and rate of tunnelling, however, if the potential is reduced slightly the surface of the sample must either re-passivate or split into active and passive regions [92]. Tunnels adopt a width that allows the minimum possible amount of current to form a stable transition. Pitting generally propagates via this tunnelling process, from which only the tunnel tip is active [86]. After tunnel nucleation has taken place the current will be insufficient to keep the pits stable and over a period of time they will become diluted and re-passivate. It could be argued that this tunnelling action of pitting corrosion is the same process as filiform corrosion, where thin worm-like structures progress across the surface. Their appearance is formed through the growth of corrosion product beneath the surface, which appears to link in well with this tunnelling phenomenon.

Tunnel structures are hard to examine as generally the morphology of the tunnel is hidden beneath the Al matrix. *Moore et al.* [93] utilised resin replicas[12] to examine these structures. Figure 1-17 a and b show micrographs taken from the resin replicas.

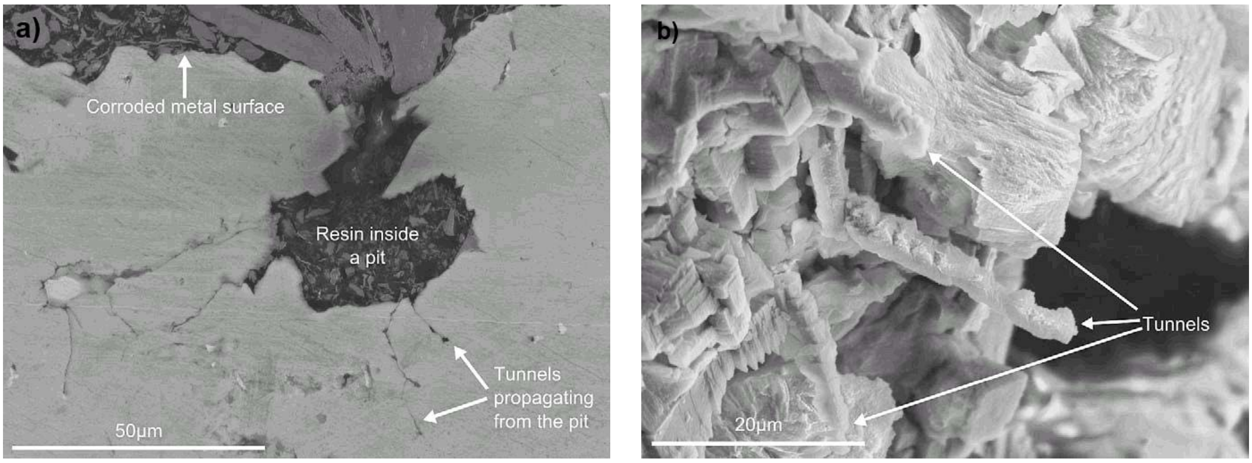

Figure 1-17 a) SEM micrograph of pitting tunnel structure in AA5083 following anodic polarisation b) SEM micrograph showing the resin replica system, detailing a tunnel network [94].

---

[12] Conductive phenolic resin was used as the mounting agent, where the sample was positioned, so that the resin flowed into the corroded region.

The number of exposed cathodic particles per sample will alter and change the OCP value [28]. Pitting corrosion has been linked with pH, temperature, the presence of anions in the solution and the physical-chemical characteristics of the passive layer or particles. At high anodic potentials, the pH in the galvanic cell decreases, but the oxides of the alloying elements remain stable and as such result in an enhanced pitting resistance [91]. Al is not an active-passive metal and as such shows a continuous increase in dissolution with a decreasing pH at all potentials [92].

As Al alloys dissolve, hydrolysis takes place, reducing the pH of the pit, making oxide formation unfavourable, as from this point forward a pit can no longer passivate and as such forms a stable pit [61], [70]. Literature shows that Al_6 (Fe, Mn, Cr) particles have a more noble potential than that of an Al matrix and can therefore be attributed to the formation of pits in the surrounding matrix [66]. The cathodic component of a redox reaction produces hydroxyl anions, which assist in the dissolution of the oxide layer near cathodic particles such as Cu / Fe-containing. Equation ***1-6*** represents this hydrolysis reaction (*Me* represents noble metallic electrons):

$$\boldsymbol{Me^{2+} + 2H_2O = Me(OH)^+ + H^+ + H_2O = Me(OH)_2 + 2H^+} \text{ [19]} \qquad \textbf{\textit{Equation 1-6}}$$

Solubility of oxides has been directly linked to the determination of the pitting potential. Anodic particles form pit nucleation sites, whereas cathodic particles form localised alkaline corrosion sites [86].

One of the most common Al alloys utilised in the aerospace industry is AA2024-T3, which is a heat treated (HT) grade [13], [14], [95]. HT systems are more prone to corrosion, therefore aging cycles are critical to ensure suitable corrosion protection [49]. *Battocchi et al.* [95] investigated the pitting corrosion of AA2024-T3 by observing the OCP measured within 5 min's of immersion. An issue with this format is that some Al alloys can take up to 2 hr’s to achieve a stable OCP and others will start to corrode immediately upon immersion. *Liao and Wei* [96] suggested that all particles within AA2024 behave in a cathodic nature relative to the surrounding matrix. Irrespective of whether the particles are anodic or cathodic in nature, they will all eventually lead to preferential dissolution sites for pitting corrosion to initiate.

Battocchi et al. [95] noted that Cu re-distributes over the alloy surface, which subsequently leads to changes in the surface electrochemical activity, promoting redox reactions to take place. *Williams et al.* [97] stated that galvanic interactions between Cu-rich particles and the Al matrix increase the susceptibility of Al-alloys such as AA2024-T3 to pit under aqueous Cl^- conditions. The vast majority of particles present within AA2024-T3 (ca. 60%) are the S phase and the second most abundant can be identified as Al-Cu-Fe-Mn [24]. These Al-Cu-Fe-Mn IMCs are prime regions for pit initiation, with *Boag et al.* [84] demonstrating that after 30 min's of immersion in a 0.1 M NaCl, stable trench sites had formed surrounding these particles. *Boag et al.* [84] divided the IMCs that were present in AA2024 into 2 groups; $(Al,Cu)_x(Fe,Mn)_ySi$ and those that were Al, Cu, Mn and Fe containing. The division was due to a difference in the Cu / Fe ratio, with the first group having a low ratio of ~ 0.5 and the second a ratio >

2.5. They showed that the S phase particles were the most active, followed by the high Cu / Fe ratio particles then the low Cu / Fe ratio particles.

Ezuber et al. [39] showed that the IMCs present in AA5083 were primarily Al-Mg, Al (Si, Mg), Al-Mg-Cr and Al_6 (Fe, Mn, Cr). Electrochemical polarisation results compared to those of *Aballe et al.* [80] showed the higher pitting corrosion resistance of an AA1100 alloy was attributable to the lower density of cathodic IMCs. Figure 1-18 shows an anodic polarisation plot for the 2 alloys at 23°C and 60°C.

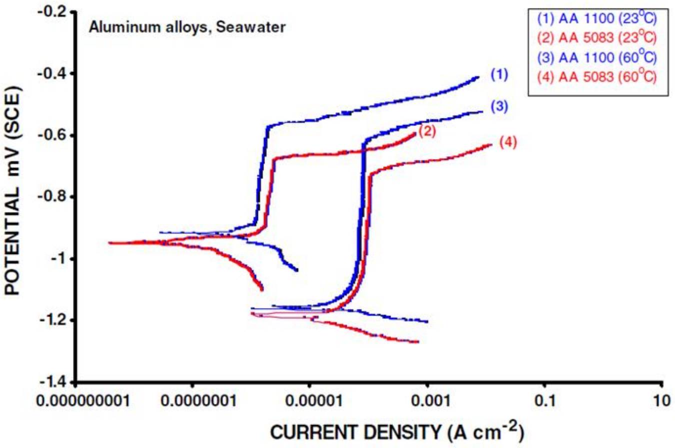

Figure 1-18: Comparison of anodic polarisation sweeps for an AA1100 and AA5083 alloy at 23°C and 60°C [39].

Al_6Fe, Al_3Fe and $Al_{12}Fe_3Si_2$ particles are also known to be cathodic in nature. The oxide layer above these particles will be dissolved as galvanic cells are introduced, promoting pitting initiation and growth. Redox reactions will take place, resulting in a cathodic reaction generating hydroxyl ions, increasing the pH and dissolution of the matrix surrounding the particles forming circular pits [39].

An increase in electrolyte temperature was noted by *Ezuber et al.* [39] to shift the OCP potential of AA5083 in a more negative direction, subsequently reducing the pitting potential value whereas the passive current density increased. This suggests that at increased temperatures the corrosion resistance is reduced. The increased temperature will facilitate O diffusion to the surface of the alloys creating a higher concentration of corrosion cells. The change in E_{pit} was related to the change in the hydration of the oxide film, with samples examined below 60°C having an $Al(OH)_3$ and $Al_2O_3 \cdot 3H_2O$ structure. However, samples examined above 60°C showed an AlO(OH) and $Al_2O_3 \cdot 3H_2O$ structure. The reduction in pitting potential was also linked to the chemisorption of Cl^- ions on the alloy surface resulting in an easier breakdown of the oxide [39]. See Table 1-5.

Table 1-5: Comparison of an AA1100 and AA5083 alloy with regards to temperatures effects on E_{corr} and E_{pit} [39].

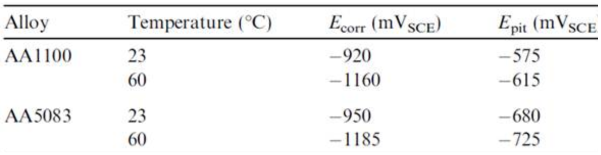

Alloy	Temperature (°C)	E_{corr} (mV$_{\mathrm{SCE}}$)	E_{pit} (mV$_{\mathrm{SCE}}$
AA1100	23	−920	−575
	60	−1160	−615
AA5083	23	−950	−680
	60	−1185	−725

The degree of polishing has also been noted by *Aballe et al.* [98] to impact on the pitting response of AA5083. Figure 1-19 a and b show the comparison of different SiC surfaces finishes on an AA5083 alloy anodically polarised. *Aballe et al.* [98] showed that by reducing the surface roughness, the OCP reduced. They showed that a difference of ~ 100 mV was noted between an 80 grit and 1200 grit surface finish. The E_{pit} value for the alloys, however, does not appear to be affected with each having an E_{pit} value of ~ -720 mV. Analysis of the OCP showed that the smaller the SiC grit number the more noise that was generated, showing the impact of surface roughness on the OCP signal, as shown in Figure 1-19 b.

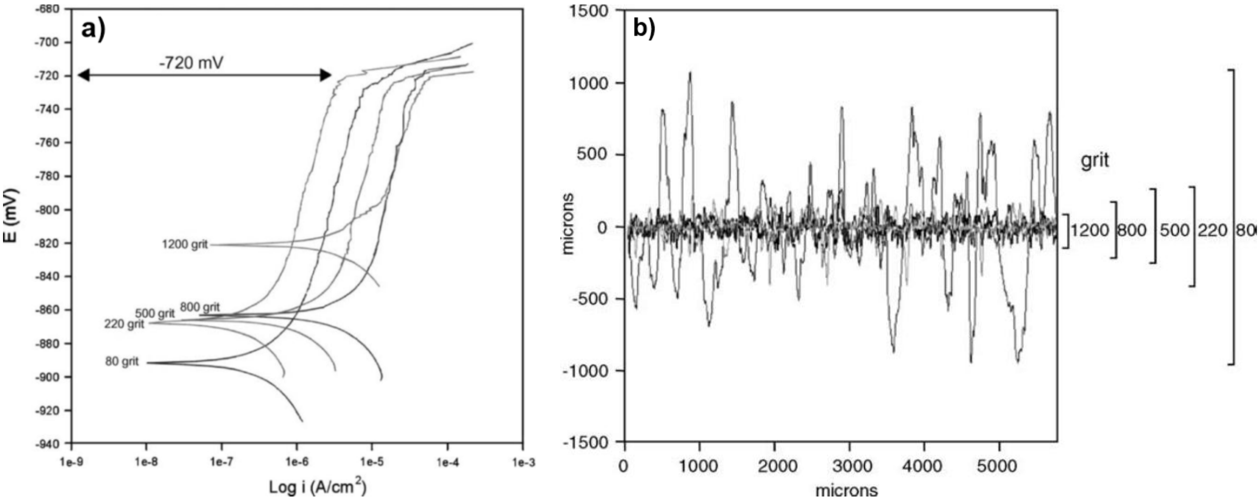

Figure 1-19 a) Anodic Polarisation curve for an AA5083 alloy, showing the impact of surface finish with regards to SiC grit numbers b) Change in surface rugosity with changing SiC levels [98].

1.5.2 Galvanic Corrosion

Galvanic corrosion takes place when two dissimilar metallic systems are in physical contact. One of the metals will corrode preferentially, while the other is protected [28]. The electrolyte provides a conductive connection so that metallic ions can be released from the anodic material [99]. One of the systems will act as the anode, where dissolution will take place and the other will act as the cathode where a redox reaction will take place [28]. The system with the more negative E_{corr} value will undergo galvanic attack, provided the conditions are favourable. *Vargel* [12] stated that galvanic corrosion will only take place if there is a difference in potential of ~ 100 mV. Unlike pitting corrosion, galvanic corrosion is highly localised to the zones of direct connection between the 2 materials. This theory relates to micro-galvanic cells that form on the surface of Al alloys, where interactions between alloying elements and the matrix form galvanic cells, leading to subsequent corrosion.

Vargel [12] stated that 3 items are required before galvanic corrosion can take place; 2 dissimilar metals, conducting electrolyte and electrical continuity. If one of these conditions are not met then galvanic corrosion will not take place.

The galvanic series shown in Figure 1-20 could be used to investigate which of the 2 metallic systems under examination will act as an anode or cathode. It highlights that Al alloys are highly anodic in nature, along with other potential alloying elements such as Mg, which means they are more likely to corrode preferentially when coupled with more noble based materials. Mg in particular can be very problematic as it is very susceptible to galvanic corrosion when coupled with either Al or steel [100].

In a galvanic cell the cathodic reactions depends on the electrolyte used;

Acidic

$$O_2 + 4H^+ + 4e^- \rightarrow 2H_2O \text{ or } 2H^+ + 2e^- \rightarrow H_2$$

Alkaline

$$O_2 + 2H_2O + 4e^- \rightarrow 4OH^-$$

Since galvanic corrosion acts in a similar manner to a battery system, Faraday's law can be used to determine the metal loss at the anode. Equation ***1-7*** shows Faradays law:

$$m = \frac{1}{96500} \cdot \frac{A}{n} It \qquad \textbf{\textit{Equation 1-7}}$$

Where *m* - mass (kg), *A* - atomic mass of the metal (kg m^{-3}), *n* - valency, *I* - current (amperes) and *t* - time (seconds).

Vargel [12] also showed that temperature and physical distance between anode and cathode can impact on the galvanic corrosion taking place.

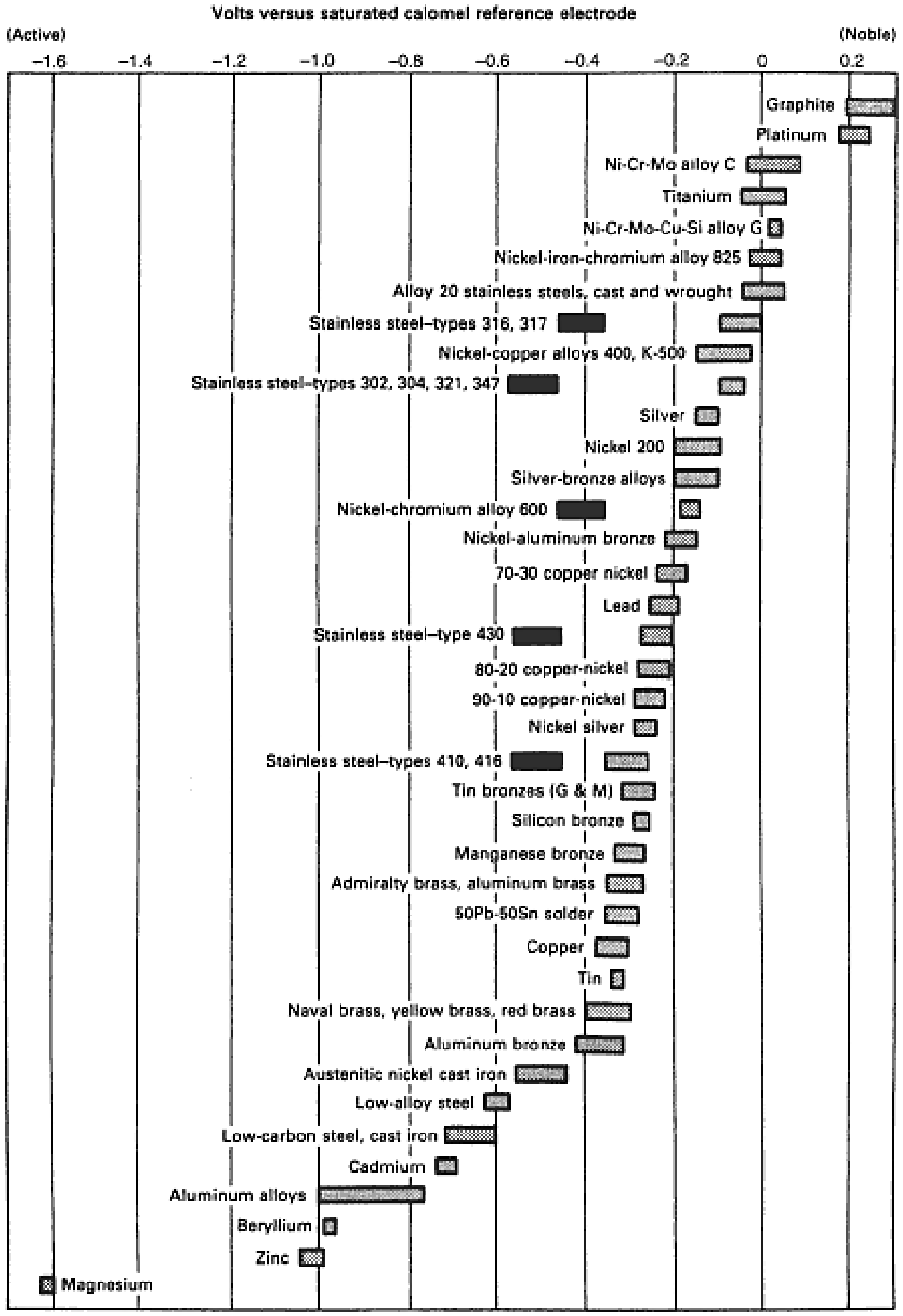

Figure 1-20: Galvanic series detailing the likely anodic and cathodic alloys when immersed in seawater [101].

1.5.3 Intergranular Corrosion

IGC is the selective attack of the GB regions with no appreciable attack of the grain body or matrix [102]. IGC arises due to a potential difference between the grain and GBs, where the difference typically arises from cathodic or anodic precipitates at the GB locations [34], [35], [103]. PFZ can, however, also act in a similar manner in that the PFZ will be either highly anodic or cathodic in comparison to the grain body. Figure 1-21 shows schematically how IGC attack can be formed within Al alloys. Figure 1-22 demonstrates how the type of corrosion can change depending on the aging conditions under which the Al alloy has been manufactured.

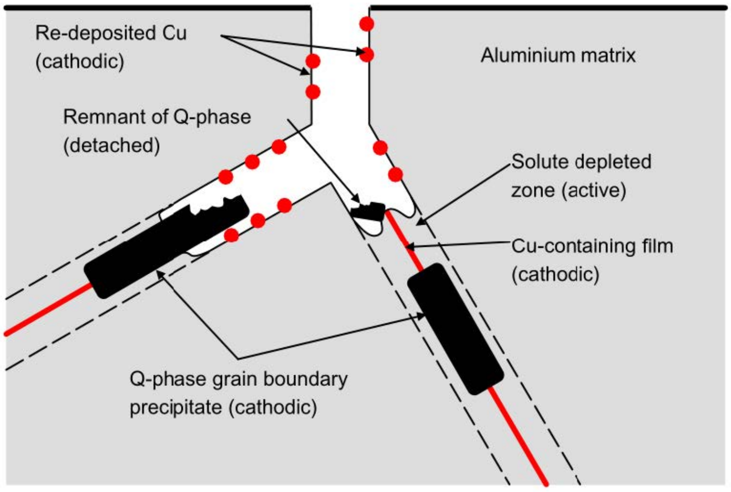

Figure 1-21: Schematic detailing potential routes in which IGC can take place. Example is for a 6XXX series Al alloy [35].

Al alloys by nature are prone to IGC, but the propagation is dependent on the corrosive environment, alloy structure and composition. Solution HT systems are more resistant to IGC, due to the removal of precipitates; however, in reducing the number of precipitates the alloy properties can be restricted. Some phases that act as anodic regions are the β phase, μ' phase and Al_xZn_xMg, whereas the θ phase and S phase are cathodic. As such, using heat treatments or alloys that form precipitates within the grain body instead of the boundaries are preferable, but IGC can occur randomly, based on differences in precipitate compositions across the grains [102]. One issue with this, as demonstrated by Figure 1-22, is that by repositioning the phases and particles away from the GB, the alloy itself could become more susceptible to pitting corrosion. IGC also has a limiting factor in that, even though it penetrates more rapidly than pitting it has a self-limiting depth. The reason for this is that the transport of O and corrosion product to the corrosion path is restricted.

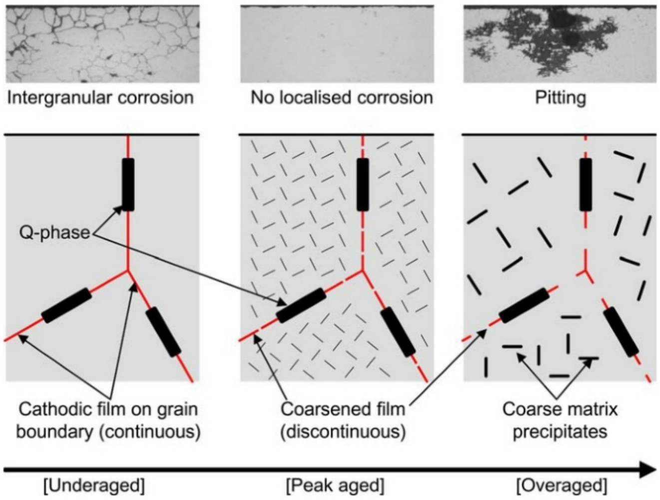

Figure 1-22: Schematic showing the change in precipitation behaviour within a 6XXX series Al alloy, demonstrating how changing the aging conditions can affect the type of corrosion that can take place [35].

In 2XXX series alloys selected heat treatments will cause preferential GB precipitation and as such they are susceptible to IGC. 2XXX series alloys containing > 4 wt.% Cu have been studied, showing that if the

Cu remains in solid solution then IGC can be avoided. Generally the Cu is in solid solution at ~480^{o}C but is not entirely soluble at room temperature. As such, heat treatments are used to dissolve the Cu into the Al matrix. Systems are then quenched to hold the Cu within the solid Al system. If 2XXX series are aged at room temperature the θ phase will precipitate out, leading to Cu depleted zones [102].

In 5XXX series alloys that contain < 3 wt.% Mg, the effect of IGC is deemed negligible. However, systems containing > 3 wt.% Mg are susceptible, due to the preferential attack of the β phase. In 5XXX series, susceptibility is increased with Mg content, temperature, cold working, time at temperatures > 27^{o}C [104], [105]. *Tan and Allen* [106] examined AA5083 in regards to IGC by examination of the precipitates that form on GBs such as the β phase. They showed that alloys containing > 3 wt.% Mg were more likely to initiate IGC sites, especially when the sensitisation effect between 80^{o}C and 250^{o}C was considered. *Jain et al.* [107] examined the sensitisation impact on an Al-Mg alloy with regards to IGC formation. They showed that Mg segregates to the GB after exposure to elevated temperatures (50 to 200^{o}C), thus promoting the precipitation of the β phase at the GB. This β phase is seen to form preferentially near to Al_6Mn IMCs after short temperature exposures; however, over longer exposures the β phase will coarsen and become more closely packed along the GB. *Jain et al.* [107] observed that the β phase dimensions were ~ 50 to 190 nm in width and 100 to 1000 nm in length. *Jain et al.* [107] also showed that low angle GB systems (< 20^{o}) were less susceptible to β phase formation than high angle boundaries, they also showed that the β phase has a breakdown potential of ~ 200 mV less than the OCP of the Al-Mg alloy examined.

When Cu or increased levels of Si are introduced to Al alloys, they tend to diffuse to the GB. This subsequently weakens the GB and makes them susceptible to breakdown; of the 2 elements, Cu is deemed the most detrimental. In comparison, Si has been observed to be related to severe cases of IGC especially when the Mg-Si ratio exceeds 1.73 [34], [35], [108], [109].

Impurity elements, such as Fe and Mn, can be used, to control the effect of Si on IGC formation. Fe rich phases such as Al_3Fe and Al_6Fe on their own will increase a tendency to form pitting corrosion, however, when Mn is also alloyed, AlMnFe phases can combine. These preferentially attract Si, which forms a new IMC that can reduce their impact on corrosion. In Al alloys, pitting corrosion is heavily associated with IMCs. These form due to a low solubility of the alloying element within the Al [35].

Mg within solid solution has been noted to have a negligible impact on the corrosion resistance of Al alloys. The β phase, however, is anodic to the surrounding matrix and as such is an active site for corrosion. In this case though the phase becomes depleted in Mg as it will be preferentially dissolved into the Al matrix, as such the impact of the β phase can be said to be negligible [35].

Svenningsen et al. [34], [110–112] developed an isothermal time transformation (ITT) diagram for a 6XXX series alloy containing 0.13 wt.% Cu and observed the effect of corrosion with different aging periods, as shown in Figure 1-23. They showed that in the under aged condition IGC was observed, however, in the peak aged condition no localised corrosion developed. They also showed that changing the method for cooling after artificial aging; air cooled or water quenched, played a big role in the susceptibility to localised corrosion, with water quenching being more detrimental to the corrosion response in the under and peak aged condition. Interestingly, however, when the rate of cooling is observed following artificial aging, air cooled samples showed higher levels of IGC than those water quenched, which was related to the precipitation of the Q and β phases to the GB.

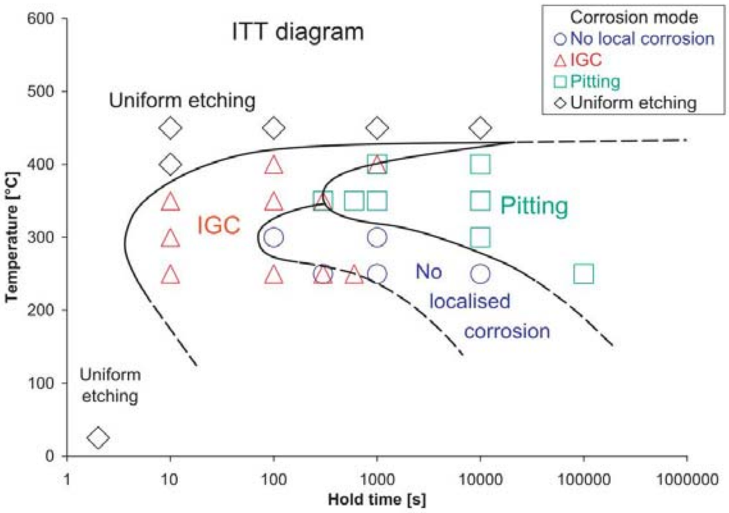

Figure 1-23: ITT diagram for a 6XXX series alloy containing 0.13 wt.% Cu observing the effect of corrosion with different gaining period [34], [110–112].

It is still unknown as to whether the anodic dissolution of the T_1 phase at GB or preferential dissolution of the PFZ at the GB causes a susceptibility to IGC in Al-Cu-Li alloys [30–32]. *Li et al.* [32] showed that the T_1 phase was similar to the S phase and Mg_2Si particles, in that one of the elements is preferentially dissolved, enriching the other. In the T_1 phase the Li is dissolved, enriching the level of Cu present. For the S phase and Mg_2Si, the Mg is more active and is preferentially dissolved, enriching the levels of Cu and Si respectively. Figure 1-24 shows the electrochemical nature of pure α (Al) compared to the T_1 phase, showing that the α (Al) is more noble and thus more corrosion resistant, prior to the enrichment of Cu on the surface.

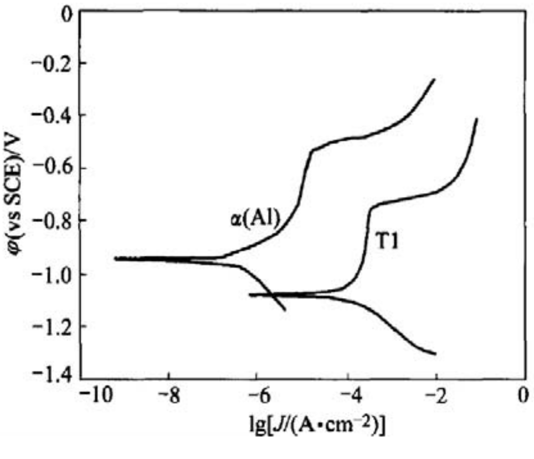

Figure 1-24: Potentiodynamic polarisation of α (Al) and T_1 phase in 3.5 wt.% NaCl [32].

Li et al. [31] examined T_1 and T_2 phases and following anodic polarisation compared their electrochemical nature to that of pure α (Al). The curves shown in Figure 1-25, show that pure α (Al) is more noble than both T phase specimens, which indicates that in an active galvanic cell the T phase materials would undergo preferential dissolution. Of the T phases, T_1 is more noble, this is related to the reduced concentration of Li within the phase compared to T_2 [30–32].

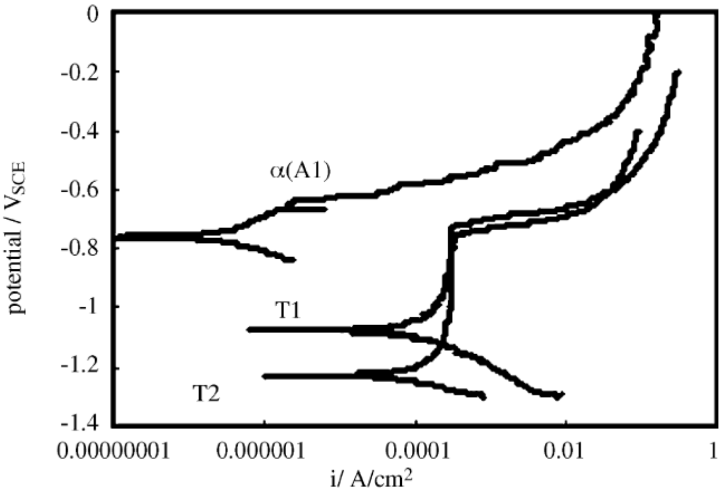

Figure 1-25: Comparison of anodic polarisation for pure α (Al) versus T_1 and T_2 phases [31].

A number of authors [31], [32], [46], [113], [114] have examined T_1 phase nucleation and found that it nucleates preferentially on dislocation sites and sub-GBs; however, its relationship to corrosion behaviour at present still has not been established. *Proton et al.* [115] showed that non-heat treated (NHT) samples of AA2050 alloy formed IGC, but the average depth stabilised after 1 day of immersion in a 0.7 M NaCl electrolyte, whilst its maximum depth seemed to increase. The NHT specimens showed a maximum depth of 80 µm after 7 days, whereas the HT specimens showed a maximum depth of 45 µm after the same time period. Using information from *Li et al.* [32], they showed that the corrosion potential of the T_1 phase is -1.076 mV vs. SCE in 4% NaCl, whereas the Al matrix was -0.855 mV. Due to the large potential difference between the T_1 phase rich grains and the matrix, the former can undergo selective grain corrosion by forcing the grains to become sacrificial anodes. The conclusion showed that the evolution of corrosion in AA2050 can be linked to the location of T_1 phase whether it was at GB or with the grain.

Xu et al. [116] showed by increasing the temperatures for aging treatments on a AA2195 Al alloy, the susceptibility to IGC was increased. This was related to the increased concentration of T_1 phases that precipitated at the GB as well as the presence of PFZ and θ' phases. *Xu et al.* [116] showed that at lower temperature aging treatments the T_1 phase would precipitate away from the GB, thus alleviating the tendency to form IGC; IGC was, however, still observed on both high and low temperatures aging cycles, but the low temperature cycle showed the lowest IGC penetration depth. As, however, previously stated, precipitating the phases away from the GB will transfer them into the grain, which could increase the susceptibility to pitting corrosion and lead to potential selective grain dissolution. Figure 1-26 shows the increase in size and number of T type phase with increasing aging times and Table 1-6 shows a comparison between the multi-stage tempers utilised.

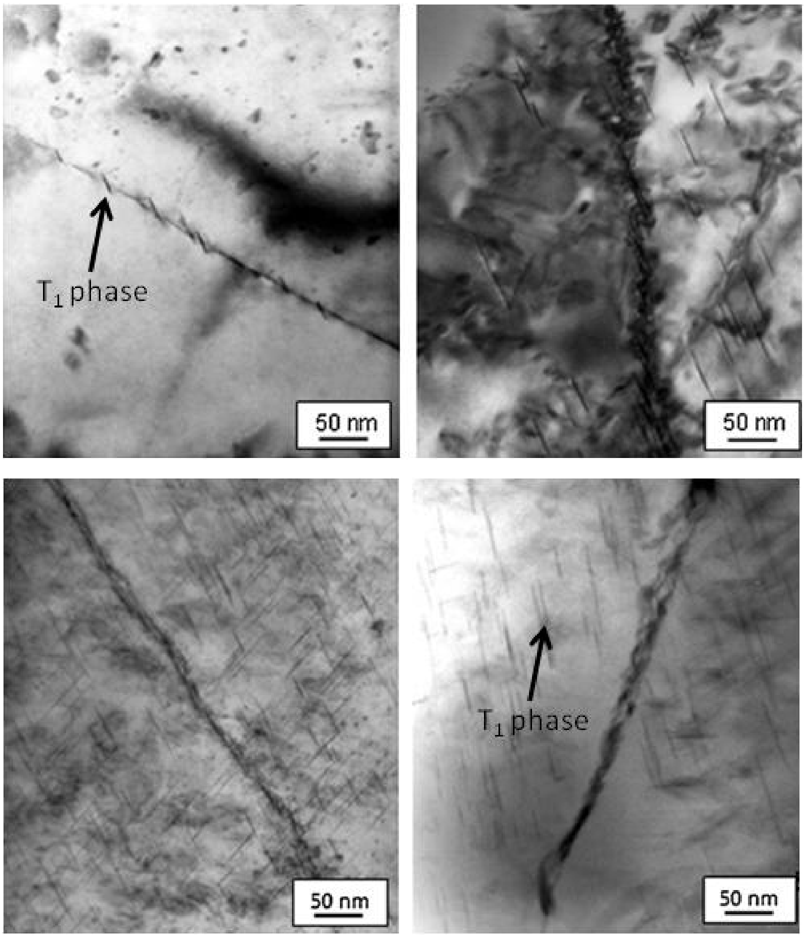

Figure 1-26 a) NHT 2050 Al alloy showing the presence of plate like T_1 phase aligned on the grain boundary b) 2050 Al alloy aged at 150^{o}C for 3 hr's showing precipitation of the T_1 phase away from the grain boundary c) 2050 Al alloy aged at 150^{o}C for 3 hr's showing precipitation of the T_1 phase away from the grain boundary d) HT 2050 Al alloy, which shows the change in precipitation kinetics of the T_1 phase now that they are absent from the grain boundary but present in the bulk [115].

Table 1-6: Comparison of high and low temperature aging cycles conducted on Al alloy AA2195 [116].

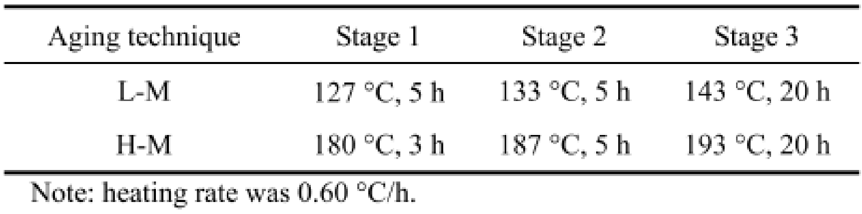

Aging technique	Stage 1	Stage 2	Stage 3
L-M	127 °C, 5 h	133 °C, 5 h	143 °C, 20 h
H-M	180 °C, 3 h	187 °C, 5 h	193 °C, 20 h

Note: heating rate was 0.60 °C/h.

Following immersion testing, where a pure α (Al) matrix is coupled with either a T_1 or T_2 phase in a 3.5 wt.% NaCl, *Li et al.* [31], showed that the α (Al) matrix at the beginning of immersion is cathodically protected, however, following immersion for 10 days, the anodic nature of the T_1 phase changes and the matrix becomes subsequently anodic and attacked. A similar phenomenon is observed for the T_2 phase, however, as time advances the system appears to fluctuate between the α (Al) and the T_2 phase being the active anodic site. *Li et al.* [31] suggested that the reason for this fluctuation was associated with the preferential dissolution of the Li and subsequent enrichment of the Cu.

Luo et al. [13], [75] has examined GB stored energy and its potential impacts on IGC for AA2024-T3. They showed that the common precipitates within AA2024-T3 that precipitate towards the GB allow for a depletion of alloying elements within the grain itself, which tends towards IGC susceptibility. Relations between the high and low angle GB and the corrosion resistance were noted. It was also noted that only around 15% of the GB examined showed any sign of precipitates being present on them, indicating that the precipitates are not continuous films at the GB. Interestingly, one of the conclusions was that having precipitates on the GB can lead to IGC and that the composition alone does not play any role in determining the IGC resistance. They also demonstrated that GB mis-orientation does not correlate to IGC susceptibility, however, GB stored energy does, in that grains with high levels of stored energy were seen to be prone to IGC attack.

1.5.4 Atmospheric Corrosion

Atmospheric corrosion is a global concern for its impact on the service life of components and within industry is the main cost contributor. The main factors that affect atmospheric corrosion include temperature, moisture, rainfall, solar, wind, weathering and relative humidity (RH). Air pollutants such as SO_4^{2-}, oxides, chlorides and NOx also affect the rate of atmospheric attack. Therefore atmospheric corrosion is distinctly difficult to predict [67].

It can be split into 3 categories: dry, wet and damp. Dry oxidation takes place when a surface has a negative free energy of oxide formation. Damp films are created at certain critical humidity levels (adsorption of water molecules). Wet films are associated with dew, rain, ocean spray etc. Atmospheric environments can also be split into 3 categories: Rural, Urban and Marine [67].

- *Rural* - free of aggressive agents - mainly moisture, SOx and CO_2. Ammonia from farm fertilisers and their decompositions may also be present. At specific RHs corrosion will initiate (typically around 70%) and these sites are generally the least corrosive.
- *Urban* - similar to rural, SOx and NOx varieties from motor vehicles and fuel emissions combined with dew and water cause aggressive thin films to form (RH of 60%).
- *Marine* – highly dependent on topography of the shoreline, i.e. effect of winds, sprays etc. Storms, however, can carry Cl^- ions as far as 15 km inland (RH of 55%) and is the most corrosive environment.

Liu [117] showed the difference between rural and coastal corrosion on a pure Al system after 12 months of exposure, highlighting the impact of Cl^- ions on the corrosion rate. High Cl^- concentrations lead to higher corrosion rates. Figure 1-27 a, b, c and d shows the difference in surface corrosion and cross-sectional information from the pure Al systems after 12 months of exposure. *Liu* [117] also measured the change in OCP with exposure time for the different atmospheric environments and these are shown in Figure 1-28. The OCP data highlighted that the unexposed system had the most electronegative potential at -0.9 V vs. SCE. With increased exposure time, the OCP shifts in the anodic direction due to the formation of a native oxide on the surface offering an increased level of corrosion protection. However, from 6 to 12 months the trend for both environments is a shift in the cathodic direction. After 12 months the coastal specimens had OCP values of ~ -0.68 V vs. SCE compared to ~ -0.64 V vs. SCE for the rural location samples [117].

The influence of atmospheric exposure can be characterised in terms of the RH, time of wetness and exposure time. Wind conditions have also to be considered as they can cause marine environments in urban and rural location through the distribution of Cl^- ions. As such this can make experimental standards such as ISO 9223[13] invalid in that predictions are in most cases different to the actual measured values [118].

The effect of pollutants on the surface is dependent on the formation of a humid layer on the surface of the metallic system, thus greater times of wetness (TOW) lead to greater attack and a concentration of pollutants. Na favours higher pH values at the cathodic sites which causes the dissolution of the passivation Al_2O_3 film [117], [118].

Mendoza et al. [119] showed that thick layers of water act as a sink for SO_2 but act as barriers for NO_2. Thick layers of water can therefore, in some cases, be detrimental, as it has been shown that on some metallic systems such as Al, NO_2 can actually act as a corrosion inhibitor. Washing of the surface can remove the corrosion products, thus reducing the overall amount of attack that takes place as it also removes the corrosion stimulators, and as such pits are always seen to be deeper on surfaces which are sheltered from the weather.

---

[13] Corrosion of metals and alloys -- Corrosivity of atmospheres -- Classification, determination and estimation [169]

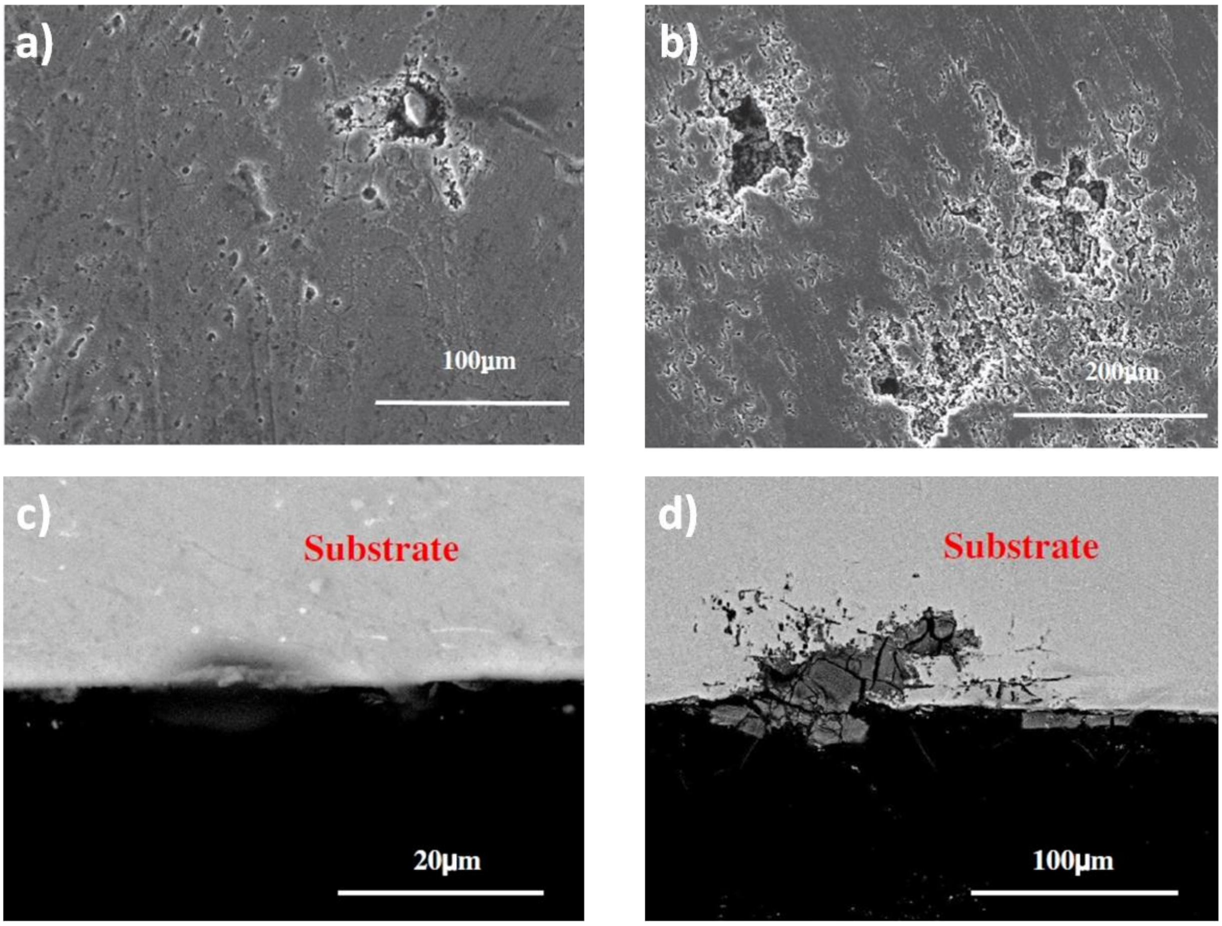

Figure 1-27: SEM micrographs showing the surface of pure Al following 12 months exposure in a) rural and b) coastal locations and their corresponding cross sections, c) rural cross section and d) coastal cross section [117].

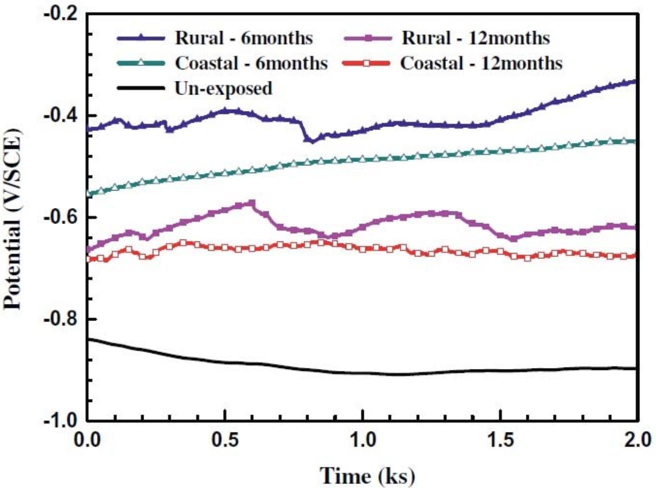

Figure 1-28: OCP measurements in 0.1 mol/L Na_2SO_4 *solution, showing the differences for pure Al in the un-exposed condition and following 6 and 12 months exposure in rural and coastal locations* [117].

It should be noted that with sheltered conditions dust particles can play a big role in the corrosion mechanics as they are not washed away by the rain. Dust can absorb moisture and sulphur compounds producing an acid medium on the surface of the specimens. NH_3 and SO_4^{2-} ions are also the most abundant in dust particles commonly found in urban environments [67], [119]. As such, under these conditions, the oxide films produced are not very stable and do not offer any residual protection to the substrate Al. The same, however, can be said about other pollutants in that if they were to form concentrated regions they would alter the corrosion mechanics in their own way [119].

Hernandez et al. [118] stated that over time, with the increase of corrosion product at the anodic sites, corrosion will start to initiate at the borders of pits thus forming a series of shallow pits across the surface of the specimen. They also showed that when Cl^- ions are the only pollutant present, the formation of large pit sites occur, however, in contrast when SO_4^{2-}ions are only present, the pit site frequency and size are seen to reduce.

Thin film electrolytes form on metallic surfaces at specific RH levels. When a thin film is present, a balance between the anodic and cathodic regions is created, causing anodic dissolution and cathodic reduction of O to take place. O is readily supplied to these thin films but also from anodic dissolution, the concentration of O in the films can increase with reaction time [67]. Composition of the thin film electrolyte is fundamentally what determines the rate of attack.

Passive films are different to corrosion products as they are more adherent and as such provide a higher resistance to attack; passive films thus tend to allow localised attack such as pitting to take place. The most common oxides that can form are: Al_2O_3 and bayerite ($Al_2O_3.3H_2O$) as well as $Al(OH)_{3,}$ [67].

Al when exposed to humid atmospheric conditions will stain. The colour will be either a greyish to black colour and the colour is dependent on the rate of O diffusion. This stained region is bayerite. Al-Mg alloys are the most prone to staining due to the formation of Mg oxide films [67].

Al corrodes slowly in atmospheric conditions due to the formation of the insulating amorphous oxide film. Typically the corrosion products that form are rich in $Al_2(SO_4)_3$ and $Al_2(SO_4)_3$ hydrate [67].

Atmospheric air is a mixture of dry air and water vapour; gases such as SO_2, Cl^-, H_2S and NaCl particulates are also present. The main contaminants in air that lead to corrosion, however, are SOx, NOx, chlorides, CO_2, H_2O_2, HCL, O_3, O, H_2S and organic acids, of which S and Cl^- compounds are the most common and the main contributors towards atmospheric corrosion [117], [120].

SO_2 is a product of combustion, it has a high solubility in water (2600 times more soluble in water than O, therefore reduces at cathodic sites more readily), thus forming H_2SO_4 in the presence of surface moisture. It has also been shown to be a cathodic depolariser as SO_2 can be reduced to sulphide. H_2SO_4 has also been noted to turn the passive film into Al hydroxyl SO_4^{2-}, increasing the rate of corrosion [117], [120]. The chemical equation below demonstrates how SO_2 can become H_2SO_4.

$$\mathbf{SO_2 + O_2 + 2e^- = SO_4^{2-}}$$

High levels of SO_2 can cause dissolution of protective layers and the formation of soluble corrosion product.

N compounds from road and energy production, of which most are emitted as NO in the combustion process; where in the atmosphere oxidation takes place to form NO_2 as per the following:

$$\mathbf{2NO + O_2 = 2NO_2}$$

As the NO_2 move further away from its combustion source it becomes further oxidised by ozone:

$$\mathbf{NO+O_3 = NO_2 + O_2}$$

However, given enough NO can become HNO_3, as per the following:

$$\mathbf{2NO + H_2O + 3/2\ O_2 = 2HNO_3}$$

Cl^- are the most aggressive of all atmospheric contaminants as they are the most water soluble, thus causing accelerating dissolution of protective passive layers [120]. Examples are NaCl and $MgCl_2$.

CO_2 forms the likes of $Al_2(CO_3)_3$ on the surface. *Blucher* [120] showed that CO_2 reduced the rate of attack on Al alloys unless the system was exposed to NaCl; without the presence of NaCl the corrosion was negligible. It was noted that high pH regions formed due to cathodic reactions, destabilising the passive layer. *Blucher* [120] observed that with increasing temperature the corrosion rate of Al alloys increased, however, when CO_2 was deposited onto the surface the corrosion rate reduced due to the CO_2 neutralising the $Al(OH)_3$ formation.

Hydrogen peroxide, if a surface passivates the impact of the H_2O_2 is dramatically reduced [67].

O_3 promotes the oxidation of SO_2 to $SO_4^{2-}$and NO to NO_2 [67] .

O aids in the oxidation of surfaces through its adsorption onto a metal surface.

Al and its alloys are used extensively in outdoor applications. Typically they are coated in a range of protective layers to help resist corrosion. These applications range from use in transport, electrical engineering, building and even marine applications. Atmospheric exposure, unlike any electrochemical testing method, is not a controlled system, meaning it can change from day to day even from hour to hour [121].

Al and its alloys resistance to corrosion comes from the formation of a highly adherent hydrated alumina film ($Al_2O_3.3H_2O$) through atmospheric exposure. These films are strongly passivating and insoluble in water, prevent attack from corrosive agents. Pollutants such as Cl^- and SO_2, however, affect the corrosion kinetics forming less compact more soluble corrosion products. Atmospheric corrosion almost always means that the highest proportions of localised attack are found in areas with longest time of wetness. Atmospheric pollutants also promote different salt concentrations changing the corrosion reactions for which the type and concentrations of dissolved pollutants causes changes to the intensity of the attack [122].

Typically to understand the corrosion mechanisms of Al alloys, electrochemical testing is used. This typically involves potentiodynamic testing and OCP measurements. In these electrochemical cells the constituent elements within the experiment are controlled, whereas in reality a car body panel or an aircraft wing skin would not be in such a controlled environment. An understanding of how Al alloys performed when exposed to atmospheric conditions is therefore required. Some institutions worldwide look at exposing Al alloys to atmospheric conditions, by placing them at coastline regions for long periods, ranging from months to years of exposure. This offers a substantial difference in time to examine an Al alloy, however, it could offer a more realistic understanding.

Most of the field tests that are conducted to examine atmospheric corrosion are performed in regions of high contamination (primarily Cl^- and SO_2) with relatively high humidity (> 80 %). *Wang et al.* [121] noticed that few studies had been conducted in arid, salt rich environments with low humidity < 50% and as such examined atmospheric corrosion on AA2024 at a salt lake location in China. The difference between salt lakes and seawater is that salt lakes typically have higher concentrations of Mg ions. Studies with regards to the impacts of NaCl on corrosion have been studied in abundance, however, investigations on Mg^{2+} ions are rather scarce. *Wang et al.* [121] found that Mg ions played a significant role in the corrosion of the AA2024 in the form of a reactant.

Ganesh et al. [123] stated that with its natural susceptibility to corrosion, Al is more vulnerable to microbial attack than anticipated. Microbial attack can take place in two forms; via the production of water soluble acids from bacteria or via the formation of differential aeration cells on the surface of the sample. The localised regions of bacteria can cause localised changes to pH, ion concentration, solution conductivity on a local scale and could generate the conditions for redox reactions to take place. One item to note is that these attacks will be much smaller than a typical precipitate phase undergoing dissolution; as such a significant number of regions of attack would have to take place for any real characterisation to be undertaken.

Knight et al. [124] investigated AA2024, with respect to atmospheric conditions for corrosion behaviours. Atmospheric conditions have been highlighted as the leading cause of most structural damage that takes place on aircraft and as such must be controlled. Examinations into the effect of RH on the corrosion nature of AA2024, showed that with increasing humidity the corrosion depth increased. Figure 1-29 shows the impact of 95 % RH on AA2024 and AA7050, when exposed to 3.5 % NaCl solution over time.

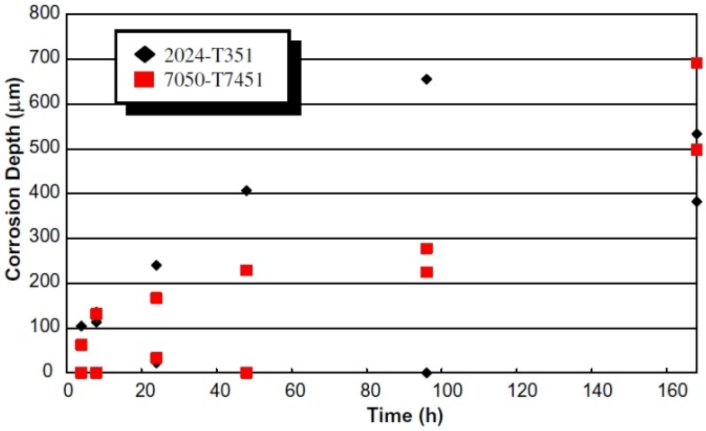

Figure 1-29: Change in Intergranular corrosion depth with respect to time for AA2024-T351 and AA7050-T7451 Al alloy specimens exposed to 3.5 % NaCl at 95 % relative humidity [124].

Knight et al. [124] showed that after 96 hr's of exposure, the corrosion, specifically IGC, reached a limiting depth and progressed no further (up to 168 hr's of exposure were investigated). Interestingly the volume of corrosion product continued to increase beyond the 96 hr's of exposure, signifying that corrosion sites were still active. *Knight et al.* [124] also concluded that the higher dissolved O content, the higher the level of corrosion observed [124].

Cheng et al. [82] investigated the impact of electrolyte thickness on the corrosion rate of an AA2024-T3 Al alloy. It was found that electrolyte thickness can directly affect mass transport of dissolved O, accumulation of corrosion product and hydration of dissolved ions. Following cathodic polarisation 3 regions formed; a weak polarisation region close to that of OCP, a diffusion controlling range for the rate of O reduction and where H^+ evolution caused an increase in current density. Figure 1-30 shows the cathodic polarisation curves produced by *Cheng et al.* [82]. In regions I and II the main reaction on the electrode was Al hydroxide ($Al(OH)_3$) formation which could block redox sites on the surface, reducing the area in which electrode diffusion could take place. As such when the electrolyte layers are > 200 µm there is less $Al(OH)_3$ and as such the OH^- ions are not restricted as much in their diffusion. This showed that when the electrolyte thickness was > 200 µm the oxygen reduction current was similar to that of a bulk solution. However, when the layers are thin, the OH^- ions are restricted causing a reduction in the current densities [82].

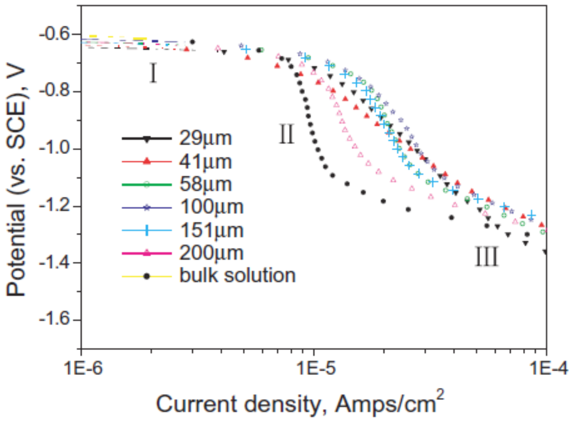

Figure 1-30: Cathodic polarisation curves, showing the impact via electrolyte thickness on AA2024-T3 [82].

The thickness of the electrolyte can therefore directly impact the corrosion rate, with a thin layer of electrolyte offering significant restriction to oxidation processes, thus once the corrosion products start to form the rate of corrosion will reduce. With thicker films, however, the rate of corrosion only slows once the amount of corrosion product reaches a point as to where reactions can no longer take place with the bare sample being exposed [82].

Vera et al. [122] examined the effect of atmospheric pollutants on the corrosion of pure Al and a 6XXX series Al alloy. They examined marine and marine-industrial locations for 24 months and showed, using XRD (see Table 1-7) that different corrosion products formed between the 2 test locations. EDS of the surface regions after 4 and 11 months showed changes to the surface compositions (see Table 1-8), with time on the pure Al sample. They concluded that Cl^- ions promote nucleation and attack, whereas SO_2 ions caused pit propagation. The presence of Na, Mg, Si, Fe and Ca was found to come from the soil which could fill cracks and voids, thus causing a barrier to corrosion. This layer of soil, could, however, cause an increase in corrosion, depending on the moisture content.

Table 1-7: X-ray diffraction of the corrosion products formed on Al and on the AA6201 alloy in the marine and marine-industrial test sites after different exposure times [122].

Aluminium		AA6260 alloy	
Marine sites	Marine-indust. sites	Marine sites	Marine-indust. sites
Quartz (SiO_2) Sodium chloride ($NaCl$)	Albite ($NaAlSi_3O_8$) Aluminium oxichloride ($AlOCl$)	Quartz (SiO_2) Sodium chloride ($NaCl$)	Albite ($NaAlSi_3O_8$) Aluminium oxichloride ($AlOCl$)
Albite ($NaAlSi_3O_8$) Aluminium oxide (Al_2O_3) Iron–silicon hydrated oxide ($Fe_2O_{3.90}SiO_2H_2O$) Aluminium–hydrogen silicate ($H–Al_2O_3–SiO_2$)	Quartz (SiO_2)	Albite ($NaAlSi_3O_8$) Iron chloride ($FeCl_2$)	Quartz (SiO_2)

Table 1-8: Table of EDS spectra showing the change in surface chemistry with time on the pure Al samples exposed to marine environments [122].

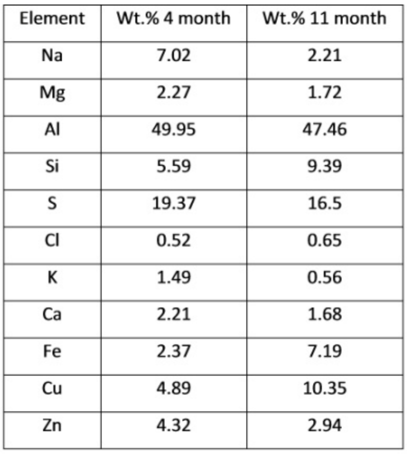

Element	Wt.% 4 month	Wt.% 11 month
Na	7.02	2.21
Mg	2.27	1.72
Al	49.95	47.46
Si	5.59	9.39
S	19.37	16.5
Cl	0.52	0.65
K	1.49	0.56
Ca	2.21	1.68
Fe	2.37	7.19
Cu	4.89	10.35
Zn	4.32	2.94

Dan et al. [125] used ASTM G85-A5[14] and SAE J2334[15] standards to examine the response of AA1100 and AA6061 under cyclic corrosion tests and constant humidity tests to simulate atmospheric corrosion. *Dan et al.* [125] showed that the corrosion products that formed were very porous and cracked readily. Chemical analysis of the corrosion products showed that the main constituents were Al, Na, S, C, Cl and O. *Dan et al.* [125] did, however, show that atmospheric corrosion is highly unpredictable as from each time frame of analysis different elements were observed, so unlike electrochemical testing where elements increase in concentration, atmospheric corrosion showed a lot of fluctuations with time.

Sun et al. [126] demonstrated that atmospheric corrosion rates are significantly affected by geographic location. Three sites were examined in this study; urban, coastal and industrial. They saw that industrial locations had higher SO_2 levels in the rain and a higher average humidity of ~ 81%. Coastal locations showed higher Cl^- concentrations in the rain and a high humidity of ~ 86%. The urban location, however, showed a humidity of ~ 57% and low precipitation, which showed that weight loss in urban sites was minimal in comparison to the other sites. It should also be noted that the critical humidity for which corrosion of metals takes place is 70% [127]. The types of corrosion observed also appeared to be affected by the location with samples at urban sites showing only signs of pitting corrosion, whereas those at coastal sites showed extensive exfoliation corrosion. Figure 1-31 shows the impact of atmospheric location on the corrosion of an AA2024 alloy after 20 years of exposure. XRD showed the surfaces were all composed of $Al(OH)_3$ and $Al_2O_3.3H_2O$ [126].

---

[14] Dilute electrolyte cyclic fog / dry test [170]

[15] Laboratory cyclic corrosion test [171]

Figure 1-31: Different types of atmospheric corrosion on AA2024 which are dependant on location a) urban, b) coastal c) industrial [126].

Urban locations showed a dense and compact corrosion layer formed containing Ca, Na and Si, which were attributed to the dust particles in the air. At the coastal locations, S and Cl were seen as well as those elements seen in urban locations [126]. A relatively thick corrosion product of ~ 150 to 200 µm had formed. The corrosion product at coastal sites was different to urban in that it was very porous and contained a lot of cracks. The Cl^- from the rain water can penetrate into these defective regions and replace the OH^- to form soluble $AlCl_3$, slowly dissolving the protective oxide film [126]. The industrial site showed similar elements, but high levels of C were also observed. It was believed that the S levels came from either SO_2 or SO_4^{-2} from acidic rain [126].

SO_2 can be selectively absorbed on Al surfaces. Under humid conditions the metal oxide surface can catalyse the SO_2 into SO_3 promoting the formation of H_2SO_4. The H_2SO_4 can then react with the $Al(OH)_3$ forming hydrated $Al_2(SO_4)_3$. C can also come from carbonaceous pollutants from smoke and car fumes. These have also been shown to have an effect on the corrosion rate of Al alloys [126].

Yao et al. [128] showed, via XPS, that the main pollutant being deposited on atmospheric samples was S, primarily from SO_2 but also from SO_4^{2-}. The oxide layers that formed were seen over time to rupture into plates. Anodic polarisation of samples after immersion showed a trend of corrosion potential in the anodic direction with increasing time; a similar effect was seen with regards to the E_{corr} also. Figure 1-32 shows the impact on anodic polarisation resistance, via increased immersion time in the 0.006 mol/L NaCl solution. The cathodic process was also shown to be promoted by the evolution of H. This shows that the formation of the corrosion products suppresses the anodic reaction. In this form of simulated atmospheric attack no Cl^- peaks were observed via XPS and the main corrosion driver was found to be $Al_2(SO_4)_3$ [128].

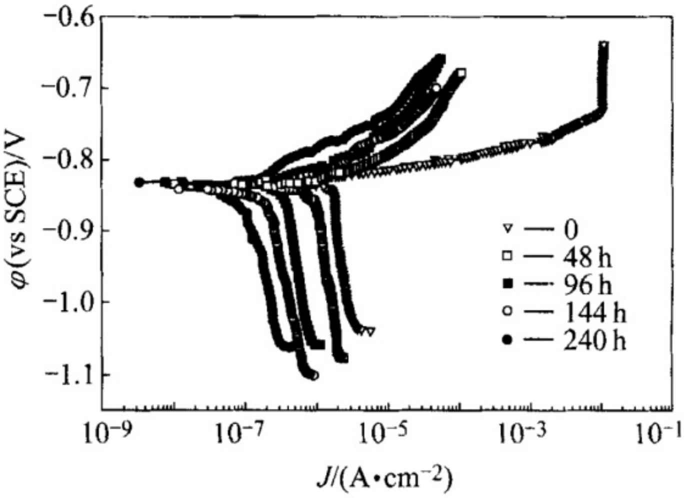

Figure 1-32: Anodic polarisation curve, demonstrating the impact on polarisation resistance following increasing immersion time in a 0.006 mol/L NaCl solution, with increased time immersion showing a reduction in current density [128].

With atmospheric corrosion, highly localised regions of attack form as the entire sample surface will not be under the same conditions as the surface is not totally immersed in an electrolyte. *Vilche et al.* [129] stated that electrochemical testing of the corrosion products was important to see whether the corrosion product acted as a passive layer and thus protected the surface. They examined pure Al over a 4 year period at 3 locations; marine, urban and rural. It was seen that the current density of the samples with increasing exposure was seen to reduce, thus increasing the corrosion resistance of the surface in electrochemical tests. Alongside this the corrosion product morphology was also seen to change with increasing exposure time, demonstrating a change in the oxide kinetics. The corrosion products that formed had poor cohesion, compactness and adherence to the surface, which meant that they could easily be removed by H_2O. Urban and rural locations showed less attack, showing that those sites rich in Cl^- ions would generate the most attack. Those aggressive environments however formed thicker, more stable oxide films. One of the main issues with atmospheric corrosion is that it cannot be controlled and *Vilche et al.* [129] showed that even on replicated samples uneven pollutant deposits caused discrepancies in their findings.

1.6 Spray Forming

Spray forming is the process by which inert gas atomisation of a liquid metal stream takes place [130], [131]. It combines spray atomisation, chemical reactions and deposition of a material into a single process. This, thereby, promotes a refined microstructure with a dispersion of fine particles (strengtheners or secondary phases) [132]. The process consists of 3 sequential steps; atomisation of the liquid metal stream, control of the resulting droplet spray and deposition of the droplets on a substrate [131–133].

Spray forming starts by charging an alloy in a crucible, under an inert or air atmosphere to a temperature above the alloy's liquidus temperature. When a pre-determined temperature is reached (50 - 200^{o}C above liquidus) the high pressure inert gas flow is initiated.

Spray forming can then be conducted via 2 processes; spray atomisation and rotating disc. A schematic of both can be seen in Figure 1-33 a and b. The first being where a stream of molten droplets are produced and propelled away from the region of atomisation by the fast flowing atomising gas [130], [131]. In most commercial spray forming apparatus, a twin-fluid atomiser is used. This breaks down the continuous melt stream into a discrete droplet spray. The cylindrical liquid stream exits a melt-delivery nozzle and enters a gas flow. Small perturbations at the gas / liquid interface form waves that eventually break up the continuous liquid stream into droplets [130], [133].

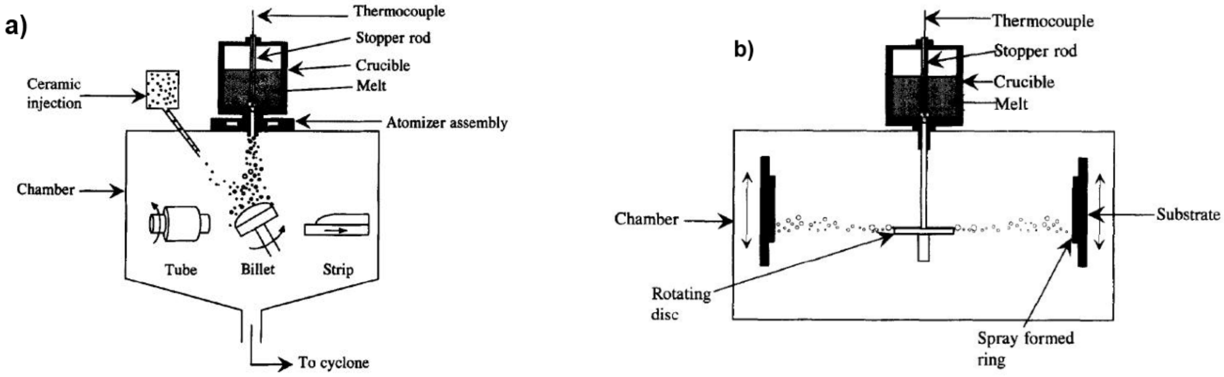

Figure 1-33 a) Gas atomisation spray forming process b) Centrifugal spray forming process [130].

Spray forming can also take place by pouring the liquid metal onto a rotating disc, where atomisation takes place under centrifugal forces on the surface of the disc [130]. This process acts in a different manner in that a block of feedstock is heated in a tundish to the desired temperature and is then poured into a reservoir above the atomiser [130].

The kinetic energy of an impinging high velocity gas jet disintegrates the metal flow into droplets for deposition. Inert gases (N_2, Ar, He) are used to avoid excessive oxidation. The melt falls into a region where the atomisation occurs, the gas then atomises the metal on exit from the entry nozzle as seen in Figure 1-34 a and b, this is known as an open atomiser. A closed atomiser is used for low melting point materials, as the delivery nozzle is chilled and as such the metal may freeze before atomisation. Typical powder diameters for this process are 20 - 200 µm [130].

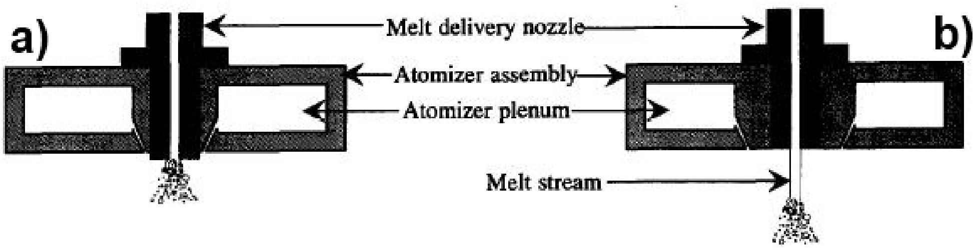

Figure 1-34: Schematic showing the two atomiser systems for spray forming apparatus a) Open atomiser system b) Closed atomiser system [130].

The spray of droplets can be a variety of sizes and their trajectories can be random. The stream is, however, directed at a substrate which collects and solidifies the droplets into a coherent preform. The continuous movement of the substrate allows for a large preform to be generated.

Droplets that interact with the preform can be fully liquid, solid or mushy, and therefore so can the preform. However, it is the balance between heat input and heat output that determines the spray cast microstructure. Table 1-9 shows details of interaction between substances.

Table 1-9: Re-drawn comparison of droplet and substrate condition with regards to the impact on the spray form process [58].

		Spray condition		
		Solid	**Mushy**	**Liquid**
Preform condition	**Solid**	bounce off	partial sticking	good sticking (layered)
	Mushy	partial sticking	good sticking	good sticking
	Liquid	surface ejected and whipped up	surface ejected and whipped up	surface ejected and whipped up

The advantages of using spray forming are that a refined (10 – 100 µm), equiaxed grain structure can be achieved. This microstructure also typically has low levels of internal solute partitioning along with refined intermetallic dispersoids, secondary precipitates and eutectic phases. As-sprayed alloys frequently exhibit solid solubility or metastable phases, as such subsequent thermo-mechanical and / or heat treatments can be used to allow the control of fine scale matrix precipitation. Spray forming also allows for large near net shape forms to be produced with fine grain structures, directly from the melt. This offers significant economic benefits in comparison to both ingot and powder metallurgy [130]. Spray forming can also allow for the manufacturing of a wide range of materials that can be difficult to produce by other methods, including Al, Cu, Mg, Ni, Ti and steels.

Spray forms will, however, always contain some porosity. Additional heat treatments and / or forgings are therefore required to optimise the microstructure and mechanical properties. This can, however, lead to grain coarsening and texture development. Materials losses are also common from; overspray[16], bounce off[17] and preform rejection[18].

Another issue with spray forming is that segregation has been shown to form in SF Al billets. This occurs by an inverse mechanism whereby solute-rich liquid is drawn back through a solid network of inter-dendritic channels by solidification shrinkage [134]. Liquid flow outwards is, however, enhanced by the centrifugal forces produced by the rotation of the spray form. This outward liquid is continuously enriched in solute, resulting in solute depletion in the centre of the spray form. As such elements that may normally form dispersoids will not be able as they will be locked into the solid network [134]. Segregation is determined by the liquid fraction and other solidification conditions present in this process [134]. The liquid fraction usually needs to be in the range of 10 - 30 % for a reasonable quality microstructure to form.

---

[16] Droplets that do not impact with the substrate.
[17] Droplets that 'bounce' off the substrate.
[18] Quality or metallurgical issues.

Hogg et al. [51] investigated a high quality Al-Mg-Li-Zr system produced via spray casting. The system had an original grain size of ~ 10 µm. It was found that the Zr distribution was non-uniform, with denuded regions being located adjacent to coarse L1$_2$ Al$_3$Zr precipitates at GB. Heat treatments at 400^{o}C for 4 hr's showed a slight grain size coarsening. The findings suggested that spray casting, combined with simple thermo-mechanical processing can provide an attractive and potentially cheaper method for producing fine grain size and high dispersoid containing alloys than conventional alloying.

Dai et al. [132] noted that an as-sprayed AA5083 exhibited a uniform, fine and equiaxed microstructure, where the average grain size was 40 µm. Transmission Electron Microscopy (TEM) observations noted Al$_6$Mn particles distributed throughout the grain and at the GB. Annealing of these spray forms at 530^{o}C lead to a rapid increase in grain size, where after 24 hr's at temperature the grain size had increased to 66 µm. Figure 1-35 a and b show a comparison between the two grain structures [132]. Such a high temperature is used to ensure super plasticity of the material.

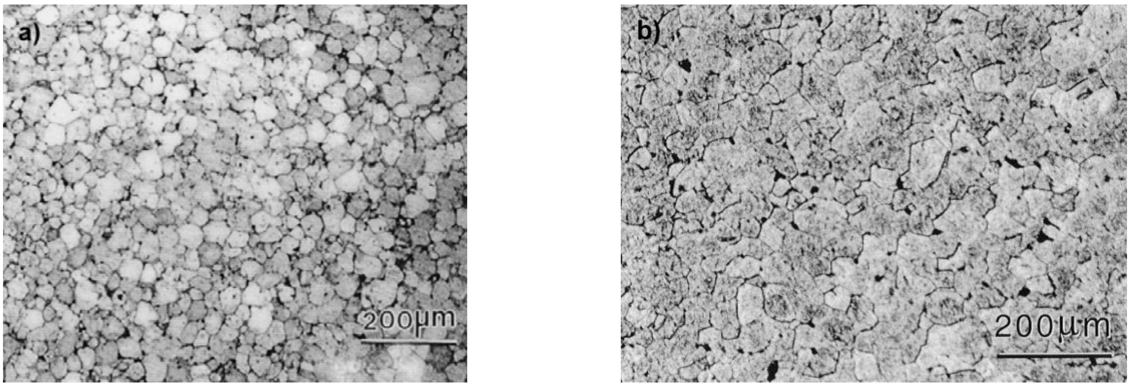

Figure 1-35 a) Optical micrograph of a SF AA5083 b) Optical Micrograph of a SF AA5083 annealed for 24 hr's at 530^{o}C [132].

Authors [28], [93], [130], [131], [135] have found that spray casting of Al has a significant impact on the corrosion resistance, by increasing the potential at which pitting occurs, to the extent where only a few at.% of specific alloying elements can increase the E_{pit} value by ~ 200 mV [136]. Surface oxidation is minimised along with other deleterious surface reactions, primarily via heat treatment [17]. The average grain size for a spray cast material is ~ 25 µm. Low levels of segregation allow for reduced or lack of heat treatments, for optimising mechanical properties [33]. Financial benefits include reduced processing, and with powder handling being removed, chances of contamination or combustion are also reduced.

Moore et al. [28] examined 2 spray formed (SF) Al alloys, one being an Al-Mg-Li-Zr Al alloy with 1.34 wt.% Li and 0.4 wt.% Zr and the other being an Al-Cu-Mg-Li-Zr Al alloy with 1 wt.% Li, 0.3 wt,% Zr and 0.5 wt.% Ag. They showed that essentially the 2XXX series alloy had an E_{pit} value the same as its E_{corr}, which has been noted in the literature as a typical phenomenon of 2XXX series Al alloys. The Zr was added as a grain refiner and as such has no impact on the corrosion response. The results, however, showed that the SF material did not show any improvement to the corrosion response. Care has to be taken, however, in the understanding of these results, as the Al alloys all contained different alloying elements, some of which are known to reduce the pitting corrosion resistance of Al alloys.

1.7 Literature Review Summary

This literature survey has identified that 2XXX series Al alloys are prone to corrosion, primarily through the addition of more noble elements to the Al matrix such as Cu and Fe. Cu in particular is detrimental as it has a tendency to form precipitates at the GBs. With it being more noble than Al this forms a galvanic cell with the Al being anodic and thus dissolved compared to the Cu being cathodic and subsequently protected. This typically means that 2XXX series Al alloys have poor corrosion resistance due to IGC and pitting corrosion. 5XXX series Al alloys are, however, more corrosion resistance and this is due to the Al matrix now being more noble than the Mg, this means that the Mg undergoes sacrificial corrosion thus limiting the amount of corrosion of the matrix to take place. These 5XXX series Al alloys can be prone to IGC also, however, under specific alloy compositions and heat treatments.

Heat treatments have been shown to both be detrimental and beneficial for corrosion; with in some cases forming precipitates that can sit at GB sites but also dissolve these precipitates back in solid solution. An example of this is related to Li additions into 2XXX series which typically form Al-Cu-Li phases at GBs thus sensitising the system to IGC, heat treatments have been shown to dissolve these phases into solid solution thus removing the sensitivity to IGC. Li is highly noble compared to an Al matrix, thus will undergo sacrificial dissolution this does however mean that lots of defective sites are then left within the matrix where corrosion can initiate. Li is however highly advantageous when coupled with Al systems as it has the opportunity to reduce the overall weight of the system whilst also offering increased mechanical properties, provided that it remains within solid solution. For this reason further research into Al-Li alloys will be undertaken in this work.

This literature survey has identified a number of areas of research that should be undertaken to further advance the understanding of Al-Li alloys. Research has been conducted investigating 2XXX and 5XXX series Al alloys with and without Li additions, however, none to limited research has been undertaken / reported that looks at atmospheric exposure, prolonged immersion testing or potentiodynamic polarisation. Further to this detailed information relating to the impact of grain size on the corrosion resistance could be further understood of which a relatively new technique termed spray forming will be examined for both the effect of grain size and whether it alone can improve corrosion resistance. For this reason the following aims and objectives have been devised.

1.8 Aims and Objectives

A number of factors have to be considered and examined when using the information found in this literature review with the work to be conducted in this thesis. It has been found that alloying elements play a significant role in the development and growth of localised corrosion within Al alloys. They also govern the type of corrosion that initiates. It is not, however, just the alloying elements that control the corrosion, with microstructure, texture development, grain stored energy, mis-orientation angle and so on all affecting the corrosion rates and mechanisms in some form or other.

This literature review has therefore highlighted a number of areas that further or new research is required. Utilising the Al alloys that are available for this thesis the following aims and objectives have been devised:

- To investigate the impact of grain size on the corrosion mechanisms and rate of corrosion.
- Further research the impact of Li additions on the corrosion response of Al-Cu-Li Al alloys.
- Investigate the impact of spray forming on corrosion response of 5XXX series Al alloys.
- Investigate Li additions into SF 5XXX series Al alloys and its potential impact on corrosion resistance.
- Investigate the atmospheric corrosion response of the Al alloys examined in this thesis with regards to corrosion product, corrosion type, depth and rate of evolution.
- Compare traditional electrochemical corrosion tests to the results observed for atmospherically corroded specimens.

Chapter 2: Experimental Procedures

This chapter will describe the experimental procedures utilised throughout this thesis to explore the corrosion resistance of a range of Al alloys. Prior to corrosion analysis, material characterisation was conducted for which details of the specific equipment utilised and experimental parameters are outlined.

A range of material directions have been examined throughout this thesis, from which all can be identified from Figure 2-1. This was to allow a detailed characterisation of the materials before and after corrosion analysis in a three dimensional format.

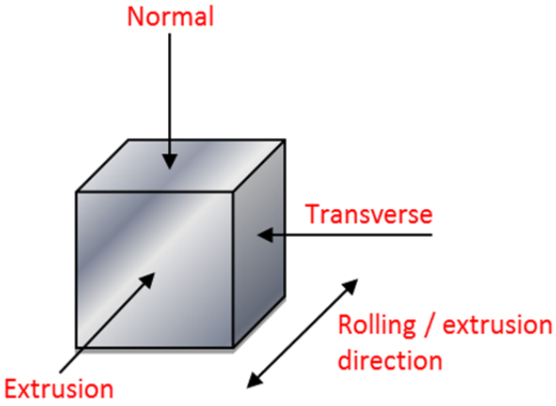

Figure 2-1: Schematic detailing the directions from which analysis was taken on all Al alloys.

Samples for analysis were mounted in different resins depending on the type of analysis. For FEGSEM, EBSD and immersion testing analysis, samples were mounted in a Conducto-Mount 2 conductive phenolic mounting resin black supplied by MetPrep [137]. For EBSD analysis some specimens were mounted in woods metal (these were very few due to problems associated with solidification rates). To ensure no electrical connection could be made between samples undergoing corrosion tests and the conductive mounting resin, lacomit varnish from Agar Scientific Ltd [138] was used to mark out a select area on the specimen to be tested.

2.1 Materials

This thesis has examined a range of Al alloys that are used or have the potential to be used within the aerospace industry. Of these, two Al alloy series have been investigated; 2XXX and 5XXX. For both of these Al alloys series the impact of Li additions on the corrosion and microstructural response have been investigated and a commercial Li free alloy alternate for each has been used as a comparison. AA2024-T3 (Cu1) was commercial sheet material, AA2099-T8E77 (Cu2 and Cu3) were extruded T profile and plate stock material respectively. All of the 5XXX series alloys were extruded material; however, Al-Mg-Li (SF1) and Al-Mg-Li-Cu-Zn (SF2) was also SF. Table 2-1 shows the nominal compositions of each of the Al alloys investigated in this thesis.

Table 2-1: Nominal composition of Al-Cu [139], [140] *and Al-Mg* [28], [93] *alloys under investigation in this thesis.*

Alloy designation	Al wt.%	Cu wt.%	Mg wt.%	Fe wt.%	Mn wt.%	Li wt.%	Zr wt.%	Zn wt.%
AA2024-T3	Bal.	3.8 - 4.9	1.2 – 1.8	Max 0.5	0.3 - 0.9	/	/	Max 0.25
AA2099-T8E77	Bal.	2.4 – 3.0	0.1 – 0.5	0.07	0.1 – 0.5	1.6 – 2.0	0.05 – 0.12	0.40 – 1.0
AA5083-T3510	Bal.	/	4.61	0.05	/	/	/	/
SF Al-Li-Mg	Bal.	/	5.24	0.03	/	1.4	0.41	/
SF Al-Li-Mg-Cu-Zn	Bal.	0.57	4.18	0.03	/	1.98	0.2	1.01

2.1 Corrosion testing

Three corrosion tests have been examined; corrosion via atmospheric exposure, immersion testing and potentiodynamic polarisation. This section will discuss the parameters used for each of these different tests. Preparation of all corrosion experiment surfaces was via a mechanical polish using SiC paper from MetPrep from 240 through to 1200 grit sequentially.

2.1.1 Corrosion via atmospheric exposure

Following mechanical polishing to 1200 grit using SiC, samples were rinsed in de-ionised H_2O then immersed in an ultrasonic bath of de-ionised H_2O for 15 min's. Samples were then attached using double sided tape to a polyvinylchloride mounting board. The edges of the specimens were then coated in lacomit varnish from Agar Scientific Ltd [138] to ensure that only the normal direction was exposed.

Atmospheric corrosion tests have an inherent lack of control, and are typically conducted close to large sources of either Cl^- (coastal) or SO_2 (urban). Neither of these was readily available and as such a more rural-urban investigation was conducted. Samples were placed on the roof of the Department of Materials, Loughborough University, LE11 3TU and were held at 45 degrees in an open air environment to ensure adequate weathering could take place. Specimens were exposed for 12 months from July 2013 to July 2014. Samples were removed from the weathering environment and examined at 1, 2, 3, 6 and 12 months from which 1 specimen ~ 2.5 cm^2 per Al alloy was examined per time period.

2.1.2 Immersion testing

Samples were mounted in Conducto-Mount 2 conductive phenolic mounting resin black and mechanically ground to 1200 grit using SiC Paper. Prior to immersion and after mechanical polishing, samples were rinsed with methanol and de-ionised H_2O before being ultrasonically cleaned in de-ionised H_2O for 5 min's. A 1 cm^2 target region was marked out using lacomit varnish and once dry, samples were fixed into a specifically designed mounting rig as shown in Figure 2-2 and attached to Cu tape using Ag paint to ensure an electrical connection was made.

A 3.5 wt.% NaCl solution with a conductivity of ~ 77.7 Ms cm^{-1} was used as the electrolyte for all immersion testing. The normal surface on all Al alloys was examined, see Figure 2-1. These mounting rigs were then filled with 100 ml of electrolyte and the OCP was measured using an Ag / AgCl reference electrode supplied by BASI [141]. The rigs were naturally aerated and examined at room temperature (~ 20 ^{o}C) under quiescent conditions. OCP measurements were recorded every min for 96 hrs. A minimum of 10 samples per Al alloy were examined for each of the set time periods; 24, 48, 72 and 96 hrs. An ACM Instruments B.O.B 8 system connected to a PicoTech High Resolution Data Logger was utilised to measure the OCP of the samples.

After immersion samples were rinsed with methanol and then ultrasonically cleaned with deionised H_2O for 10 min's. The de-ionised H_2O stopped the corrosion process and the ultrasonic cleaning helped to remove any residual NaCl remnant on the surface. Any samples that generated large amounts of corrosion product were immersed in 1M $HNO_3$for 30 min's prior to rinsing to help reveal the underlying corrosion. They then underwent ultrasonic cleaning in de-ionised H_2O for 10 min's and then cold air stream dried.

Corrosion topography and chemistry was examined using FEGSEM and EDS, after which cross sections were taken of the specimens and once again FEGSEM and EDS were utilised.

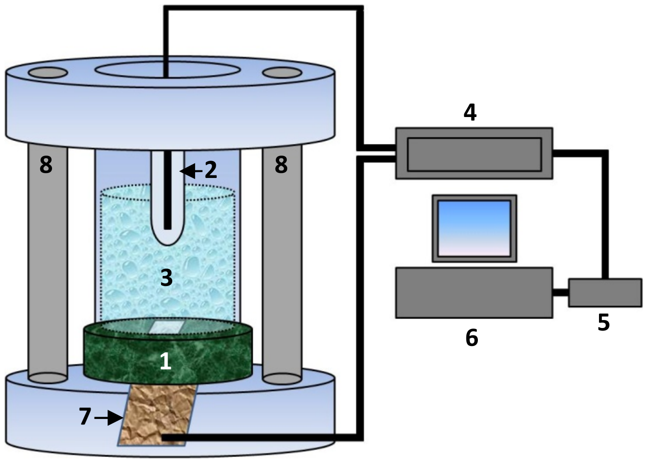

1. Working electrode
2. Ag / AgCl Reference electrode
3. 3.5 wt.% NaCl electrolyte
4. ACM Instruments B.O.B 8
5. PicoTech datalogger
6. PC running PicoTech data logging software
7. Cu wire *(to allow an electrical connection between the specimen and datalogger)*
8. Stainless steel threaded rods *(nuts either end of the rods ensure the system is kept closed stopping any leaks)*

Figure 2-2: Schematic showing the components of the testing rig used for immersion corrosion testing of the Al alloys.

2.1.3 Potentiodynamic polarisation

Samples were examined in both the as-received (degreased) condition and mechanically ground to 1200 grit using SiC. All samples were ultrasonically cleaned in methanol for 5 min's and then rinsed with deionised H_2O and cold air stream dried. All samples had 3M chemically resistant polyester tape applied so that a 1 cm^2 target area was visible. The normal direction on all Al alloys was examined for all polarisation experiments (see Figure 2-1) and a 3.5 wt.% NaCl solution was utilised as the conducting medium for potentiodynamic polarisation.

Information that was obtained from the polarisation plots was pitting potentials (E_{pit}), open circuit potentials (E_{corr}) and a measure of how much charge had passed over the experiment. Charge was used to give an indication of the amount of current that had passed over the experiment, for which the final total charge passed was recorded. Pitting potential and open circuit potentials (OCP) were used to give an indication of how corrosion resistant each Al alloy was to allow for comparison. By taking the E_{corr} from the E_{pit} a measure of corrosion resistance could be obtained, in that the larger the difference the higher the corrosion resistance. Figure 2-3 shows typical locations for where E_{pit} and E_{corr} are recorded. Typically E_{corr} is taken at the point where there is no current, thus when the system is in equilibrium and E_{pit} is recorded at the point where there is a sudden, dramatic increase in current.

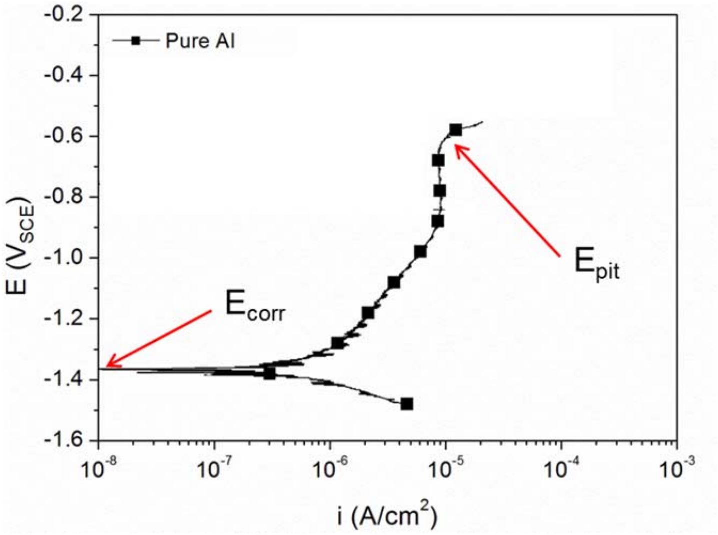

Figure 2-3: Re-drawn graph showing a polarisation curve of a pure Al system, labelled to show where E_{corr} and E_{pit} values are typically taken from on a polarisation plot [142].

A Solartron ECI 1286 potentiostat connected to a computer running CorrWare software was used to monitor the polarisation potentials and an EG&G potentiostat model 263A running Powersuit software was also used to validate the results. This experiment utilised a typical 3 electrode cell; working electrode (specimen to be tested), counter electrode (platinised titanium mesh) and reference electrode (vs. Ag / AgCl). A schematic of the 3 electrode cell is shown in Figure 2-4. Samples were examined at room temperature (~ 20 ^{o}C) under quiescent conditions.

To try to eliminate any major fluctuations in OCP that could affect the potentiodynamic polarisation output, a 5 min immersion time, similar to that used by *Proton et al.* [115], was introduced prior to potentiodynamic polarisation to allow the cell to come to a stable potential. Following this immersion period samples were then swept anodically from 100 mV below the OCP recorded, up to their corresponding OCP then swept for 500 mV in the anodic direction, as utilised by *Ezuber et al.* [39]. The rate of analysis for these investigations was chosen to be 30 mV/min.

Corrosion topography and chemistry were examined using FEGSEM and EDS, after which cross-sections were taken of the specimens and once again FEGSEM and EDS were utilised.

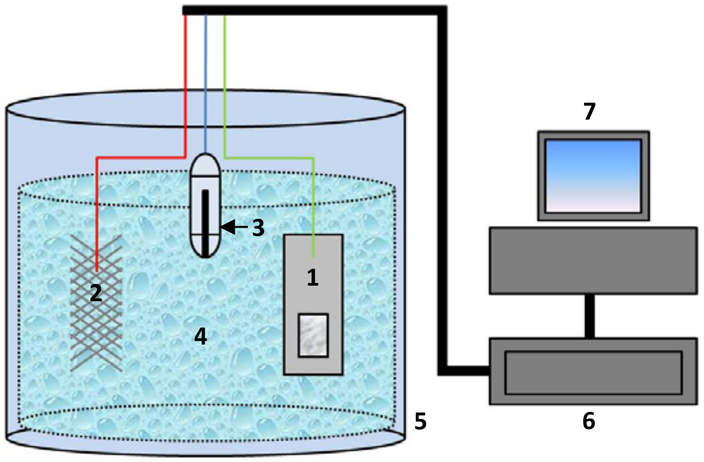

1. Working electrode
2. Reference electrode (Ag / AgCl)
3. Counter electrode (platinised titanium mesh)
4. 3.5 wt.% electrolyte
5. Glass beaker
6. Potentiostat (Solartron / EG&G)
7. CorrWare / Powersuit software

Figure 2-4: Schematic showing the three electrode cell used for potentiodynamic polarisation of the Al alloys.

2.2 Material Characterisation techniques

2.2.1 Field Emission Gun Scanning Electron Microscopy (FEGSEM)

For characterisation methods, samples were mechanically ground using silicon carbide (SiC) abrasive paper from MetPrep from 240 through to 1200 grit sequentially, followed by subsequent polishing stages through 6, 3 and 1 µm using diamond lubricants. The polishing cloths used were MD-Dac and MD-Floc for the 6 and 3 µm stages where DiaDuo-2 suspensions were used from Struers Ltd [143]. For the 1 µm polishing stage a Leco [144] final stage Imperial polishing cloth and DiaDuo-2 diamond suspension were used [143]. A final 0.25 µm colloidal silica polish was also conducted using an MD-Chem cloth. After polishing, samples were rinsed using tap H_2O and wiped using cotton wool, followed by rinsing with methanol and de-ionised H_2O to remove any excess lubricant. After cleaning samples were ultrasonically cleaned in de-ionised H_2O for 2 min's after which samples were cold air stream dried.

A Carl Zeiss Leo 530-VP FEGSEM fitted with EBSD (Electron Backscatter Detection) software, BSD (Backscatter detection) and EDS facilities were utilised.

Secondary electrons are used to generate images, based on topographical features and are what are used to generate the micrographs in this work. Backscattered electrons are used to determine areas of different atomic mass, by changing contrasts. This means that particles with a high atomic number will show up differently to those with a low atomic number allowing IMCs to be easily identified within the matrix [145]. BSD micrographs were therefore generated at specific magnifications to capture the size and distribution of the IMCs for each of the Al alloys examined. Image J software was utilised to threshold these IMCs from the micrographs to allow for a size information to be extracted. EDS using an Oxford Instruments X-max 80 mm^2 windowless Silicon Drift Detector (SDD) running Aztec microanalysis software was used for chemical analysis of corrosion products and IMCs. EDS works on the basis that the incident high energy electrons onto the surface cause interactions within the atomic structure of the elements. This interaction subsequently causes a release of an X-ray which is picked up by the SDD. Each element has a specific X-ray energy which when detected can be used to identify the presence of specific elemental compounds. The higher the incoming energy of the electrons the greater the interaction with the substrate, in that the electrons are able to progress to a higher penetration depth, see Figure 2-5 and Figure 2-6.

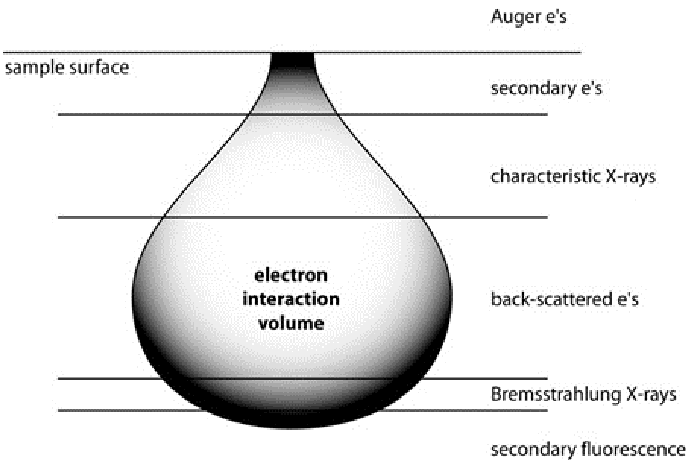

Figure 2-5: Schematic showing the interaction volumes of incident electrons onto the surface of a material [146].

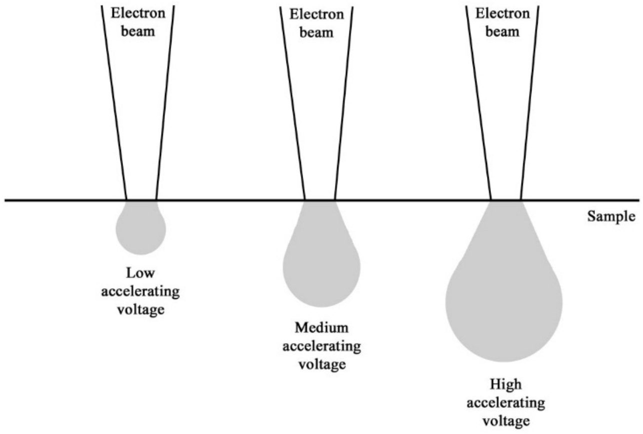

Figure 2-6: Schematic showing the interaction volumes of incident electrons depending on the incoming accelerating voltage of the electrons [147].

EBSD was accomplished using an HKL Nordlys F high speed camera running Aztec microanalysis software. This was utilised to observe the underlying microstructure of the Al alloys to allow for further information to be extracted. For this thesis, EBSD was used to give an indication of grain size and any specific rolling or extrusion features. EBSD software maps the crystal orientations of a grain by looking at the collection of closely packed pixels. These pixels can have what is termed as a mis-orientation which must be less than a specific angle (5 degrees) which allows the user to identify where grain boundaries fit. This is based around the principle that any pixels that have a mis-orientation greater than the specified angle are classed as different grains [148].

FEGSEM was utilised to examine visible surface corrosion and corrosion products following all corrosion tests, EDS was also used on all samples to examine the change in IMC composition with time as well as corrosion product chemistry. FEGSEM and EDS were also used to characterise each of the Al alloys prior to corrosion to ensure a benchmark was available for comparison. Samples were mechanically sectioned to allow for cross sectional information to be obtained from the longest atmospherically exposed sample, after 24 and 96 hrs following immersion and after being swept 500 mV for anodic polarisation. Corrosion depth was measured along with EDS mapping of corrosion products. For this samples were sectioned to allow for examination of the extrusion / rolling direction as well as the transverse direction and mounted in Conducto-Mount 2 conductive phenolic mounting resin black.

2.2.2 Transmission Electron Microscopy (TEM)

Samples for all TEM work were mechanically ground using SiC paper to a thickness of ~ 100 µm, after which 3.0 mm discs were mechanically punched from the sample. Following this each 3.0 mm disc was mechanically ground with 1200 grit SiC paper to ensure the samples were as flat as possible. Samples were then electro-polished to make them electron transparent. A TenuPol 5 system was used with and a HNO_3 and methanol electrolyte with a 7:3 mix ratio respectively to electro-polish the specimens. Electro-polishing requires very low temperatures to operate effectively, as such liquid nitrogen was used to reduce the temperature of the electrolyte to -30 ^{o}C prior to and during electro-polishing and a current of 20 V was applied to the sample. Samples were typically electro-polished for 1 to 2 min's depending on how thick the disc was. After electro-polishing samples were rinsed in methanol and de-ionised H_2O before air drying.

A JEOL 2000 FX TEM fitted with EDS facilities was used to assess the quality of the TEM discs prior to use in the FEGTEM. A TEM has a light source that emits a beam of electrons from the top of the vacuum column. This beam of electrons is focussed into a thin beam onto a sample by using electromagnetic lenses. This incident beam then passes through the sample of interest, from which most of the incident electrons can pass through the sample and interact with a fluorescent screen that is studied by the user. Not all electrons can pass through the material and a lot can be scattered away, depending on the density of the material and wavelength of the incident electrons, governed by the accelerating voltage [149].

A Gatan Erlangshen ES500W CCD camera with Gatan digital micrograph software was used to obtain micrographs at an accelerating voltage of 200 kV and an Oxford Instruments, 30 mm^2 Si-Li drift detector with polymer window EDS system running Aztec microanalysis software was used for chemical analysis.

2.2.3 Field Emission Gun Transmission Electron Microscopy (FEGTEM)

An FEI Tecnai F20 FEGTEM with high angle annular dark field (HAADF) and EDS mapping facilities was used to examine the fine scale particles, dispersoids and precipitates that are present with the grain structure and GB locations. High resolution micrographs alongside EDS mapping were acquired to reinforce the results obtained from the JEOL 2000 FX TEM system. Prior to analysis samples were plasma cleaned using a Fischione 1020 bench top plasma cleaner that operates at < 12 eV using a 25% oxygen and 75% argon gas mix for 5 min's. This ensured that any organic materials could be removed prior to analysis and as such did not impact on imaging and chemical mapping.

A Gatan Multiscan CCD camera with Gatan digital micrograph software was used to obtain micrographs at an accelerating voltage of 200 kV and an Oxford Instruments X-max 80 mm^2 windowless SDD running Aztec microanalysis software was used for chemical analysis.

2.2.4 X-ray Photoelectron Spectroscopy (XPS)

Samples for characterisation were mechanically ground to a 1200 grit using SiC and cleaned with methanol, de-ionised H_2O and a 2 min ultrasonic clean in de-ionised H_2O before cold air stream drying. All specimens were then placed onto a Cu plate that was inserted into the XPS chamber for analysis. Samples were held in place using double sided cello tape and an electrical connection was made using metallic pins.

A Thermo Scientific K-Alpha XPS system was utilised to examine the chemical composition of the Al alloys examined in this thesis. Samples are placed under a high vacuum to allow for high energy X-rays to be directed onto a surface. These incident X-rays excite photoemissions from the core levels of the atoms present at the surface of the specimen. The interaction with the surface causes photo-electrons to be released. Each photo-electron released has its own unique binding energy which can be associated with specific elements; this allows the user to be able to identify which elements are present on the surface. The larger the number of photo-electrons detected the higher the concentration [150].

Multiple surface spectra were collected to ensure validity of results. Each survey scan comprised of 10 scans, from which a 400 µm area was examined per spectra and a further 5 high resolution spectra were collected to examine oxidation states. For the high resolution spectra, multiple elements were collected including Al, O, C, Si, S and so on. For this work however, only the Al and O peaks were examined in detail. Please see the Appendix for additional data relating to the chemical composition change over the 12 months of exposure for each Al alloy.

XPS was used as a surface sensitive technique to ensure that signals from the base metal were kept to a minimum. XPS was therefore used to survey the corrosion products that formed on the atmospherically corroded samples that had developed on the surface of the specimens for which a comparison over time was produced. For each specimen examined 10 sites were examined and three line scans made up of 15 data points were collected to allow for a detailed analysis of chemical change over the surface of the specimens.

Chapter 3: Materials Characterisation

As described in Section 2.1 a range of 2XXX and 5XXX series Al alloys have been examined with and without the addition of Li. 5XXX series are high corrosion resistant Al alloys and offers a good comparison to the poor corrosion resistant 2XXX series Al alloys.

Prior to corrosion testing detailed characterisation of the as-received Al alloys was conducted. This characterisation examined the specimens from the macro to nano scale, with respect to their particle chemistry, morphology and V_f as well as the general alloy grain structure.

The chapter is divided into 2 sections; characterisation of Al-Cu alloys and characterisation of Al-Mg alloys.

To investigate coarse and fine scale particles, FEGSEM has been utilised to identify the second phase particles and FEGTEM has been utilised to examine the fine scale precipitates and dispersoids that reside in and around the GBs. Second phase particles are classed as those that are > 1 µm, whereas precipitates and dispersoids are those that are seen to be typically < 1 µm.

3.1 Material Characterisation of Al-Cu alloys

The 2XXX series Al alloys investigated were; AA2024-T3 (Al-Cu) and AA2099-T8E77 (Al-Cu-Li). 2 different AA2099-T8E77 alloys were received for analysis, the first being a non-commercial plate stock material and the second a commercial T-joint extrusion. For convenience the Al alloys are referred to as Cu1 (AA2024-T3), Cu2 (AA2099-T8E77 extrusion) and Cu3 (AA2099-T8E77 plate) throughout this work. The nominal compositional data for each 2XXX series Al alloy examined are shown in Table 2-1.

Table 3-1: Nominal composition of Al-Cu alloys under investigation [139], [140].

Alloy designation	Al wt.%	Cu wt.%	Mg wt.%	Fe wt.%	Mn wt.%	Li wt.%	Zr wt.%	Zn wt.%
AA2024-T3	Bal.	3.8 - 4.9	1.2 – 1.8	Max 0.5	0.3 - 0.9	/	/	Max 0.25
AA2099-T8E77	Bal.	2.4 – 3.0	0.1 – 0.5	0.07	0.1 – 0.5	1.6 – 2.0	0.05 – 0.12	0.40 – 1.0

3.1.1 AA2024-T3 (Cu1)

Cu1 was commercial grade sheet material. Figure 3-1 a, b and c show micrographs of the 3 directions. It is evident that there is a large V_f of coarse second phase IMCs and data analysis via Image J helps to demonstrate this. All directions show ~ 70 % of the IMCs being < 3 µm^2, however, ~ 10 % of the IMCs were > 20 µm^2 and some were > 100 µm^2 (< 1 %) with the largest IMC observed on the normal direction being ~ 430 µm^2. In comparison to the normal direction, the largest IMC observed on the transverse and extrusion directions were ~ 100 µm^2 and ~ 140 µm^2 respective. Image J analysis also assisted in showing that the IMCs were elongated in the extrusion direction.

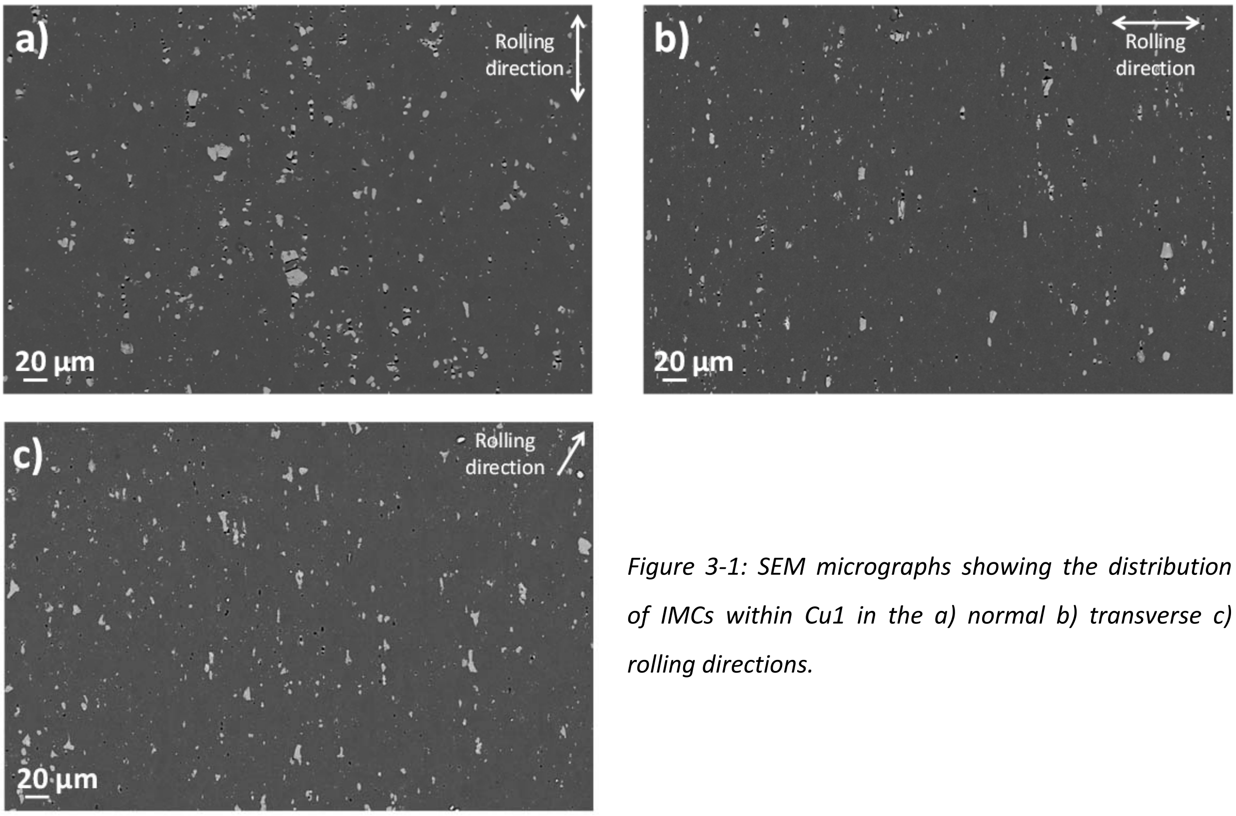

Figure 3-1: SEM micrographs showing the distribution of IMCs within Cu1 in the a) normal b) transverse c) rolling directions.

EDS showed that there were 4 main IMC types within Cu1; Al-Cu-Fe-Mn (Cu-rich and Cu-depleted), Al-Cu-Mg and Al-Cu-Mg-Fe-Mn particles, which agrees with literature [24], [84]. *Buchheit et al.* [24] showed that the S phase contained 14 at.% Cu and 16 at.% Mg, similar to what was observed in the Al-Cu-Mg IMCs in this thesis, see Table 3-2. The majority of the IMCs contain high levels of Cu, Mg, Mn and Fe and as such ~ 80 % of the particles identified contained levels of Al, Cu, Mg, Fe and Mn. Figure 3-2 shows example EDS maps of some IMCs examined within Cu1 and Table 3-2 shows the typical chemistries of the four IMCs examined. The IMCs were irregular in shape and had no specific morphology, however, alignment with the extrusion direction could be observed which is not unexpected [26].

Table 3-2: Measured EDS compositions of coarse IMCs, identified via SEM, fine scale precipitates and dispersoids identified by FEGTEM; in Cu1 (at.%).

Particle Type	Phase	Al at.%	Cu at.%	Fe at.%	Mn at.%	Mg at.%
Coarse Intermetallic Compounds	Al-Cu-Fe-Mn (Cu rich)	65±1	21±4	7±1	6±2	/
	Al-Cu-Fe-Mn	85±2	10±1	3±1	3±1	/
	Al-Cu-Mg	48±3	30±2	<1	<1	19±2
	Al-Cu-Mg-Fe-Mn	62±1	28±1	2±3	2±2	4±2
Fine scale Precipitates and dispersoids	Al-Cu (θ type phase)	94±1	5±1	/	1	1
	Al-Cu (θ type phase) at GB	88±4	5±2	/	1	1
	Al-Cu-Mn	91±3	3	/	2±1	1
	Al-Cu-Mg (S type phase)	86	8	/	/	5
	Al-Cu-Fe-Mn	92	3	2	2	1

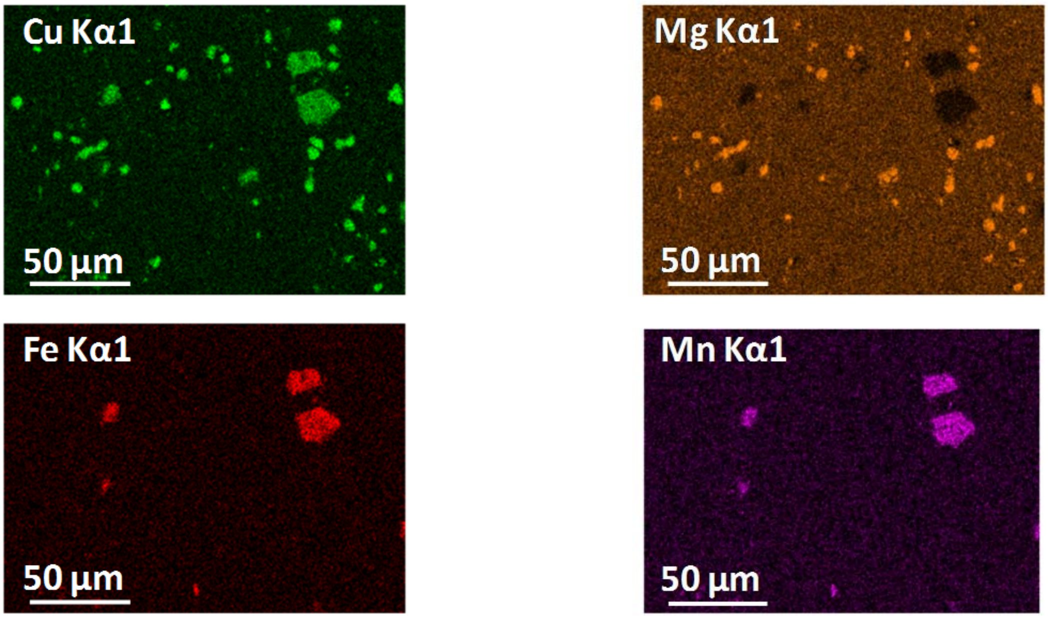

Figure 3-2: EDS maps from Cu1 showing the main elemental constituents within the IMCs.

FEGTEM analysis of Cu1 showed a large V_f of fine scale particles within the matrix. Although all grains showed a high V_f of particles, some showed a higher density than others. They had a wide range of morphologies with some being rectangular, some spherical and some rod-like. Examples of these can be seen in Figure 3-3 a, b and c. Examination of their morphologies shows that they are fine scale precipitates that have formed via the heat treatment cycle [26]. The size of the particles were all < 500 nm in size, but no specific type showed a distinct set of dimensions. EDS showed that there was a range of precipitates within Cu1; Al-Cu-Fe-Mn, Al-Cu-Mg, Al-Cu-Mn and Al-Cu for which the compositions of each can be seen in Table 3-2. Of these, Al-Cu precipitates were found, both within the matrix and on the GBs and can be identified as the θ type phase likely Al_2Cu, which are typical of any 2XXX series alloy [19], [26], [49], some examples can be seen in Figure 3-3 b and c. Examination of the GBs showed particles in the form of fine spherical θ type precipitates. The other precipitates identified were, however, only located within the matrix. Mg was found primarily in one precipitate type, identified as characteristic S type phase likely Al_2CuMg [24]. Of all the precipitates investigated, the main ones within the matrix were Al-Cu-Mn and Al-Cu. Figure 3-4 shows EDS maps of Figure 3-3 c which is a GB region showing evidence of θ type phase on the GB, as well as Al-Cu-Fe-Mn and Al-Cu-Mn within the matrix, which agrees with literature with regards to the typical phases present within Cu1 [24], [83], [84].

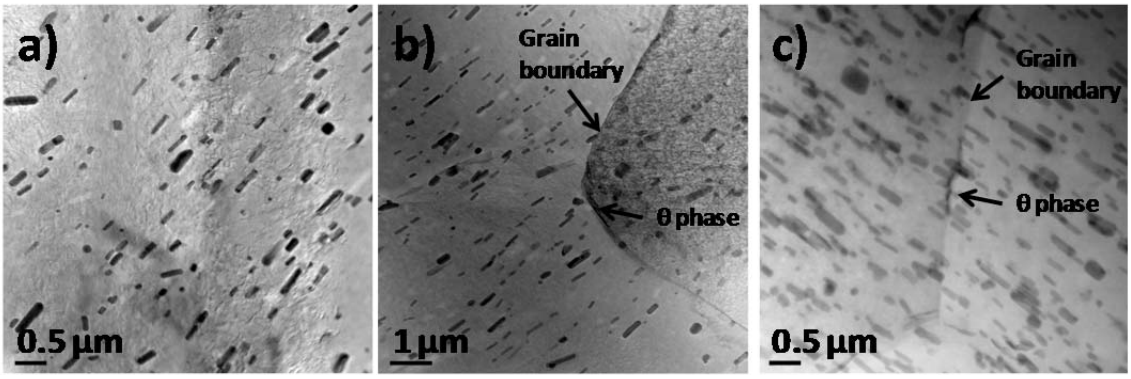

Figure 3-3: FEGTEM micrographs of Cu1 detailing the a) distribution of precipitates and dispersoids within the matrix. b) GB particles. c) high density of precipitates and GB particles.

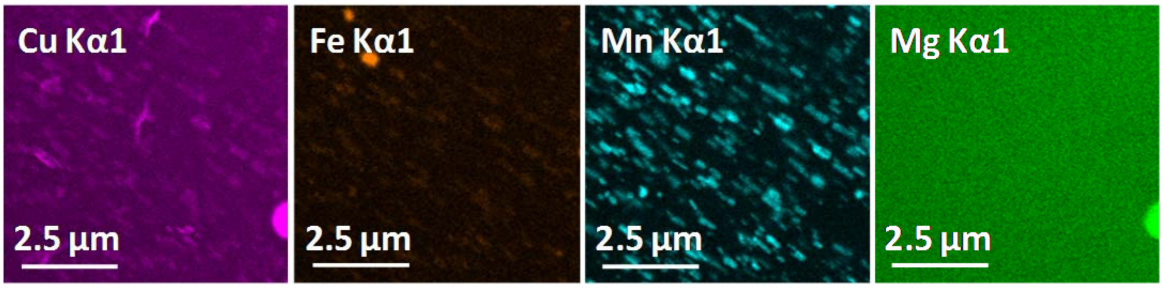

Figure 3-4: EDS maps of a site within Cu1 (Figure 3-3c) showing the main elemental constituents of the precipitates and Cu segregation on the GBs.

EBSD showed that Cu1 has a fine, equiaxed grain structure. Figure 3-5 a indicates that the normal direction is made up of different sized grains, with some being < 5 µm^2 and others > 1000 µm^2. Figure 3-5 b was obtained from the transverse direction, which in comparison to the normal, has a much more elongated grain structure. The grains in the transverse direction are also finer with 85 % of all grains being < 100 µm^2 compared to 70 % on the normal direction. Figure 3-5 c shows the extrusion direction demonstrating evidence of a ~ 50 µm, coarse recrystallised grain layer at the specimen surface. The recrystallised grains were not that much bigger than the grains within the bulk of Cu1, but a coarsening can be seen. Figure 3-5 d shows the extrusion direction which also demonstrates a similar trend to that of the transverse direction with ~ 80 % of all grains being < 100 µm^2. Elongation of the grains in the extrusion direction can also be seen.

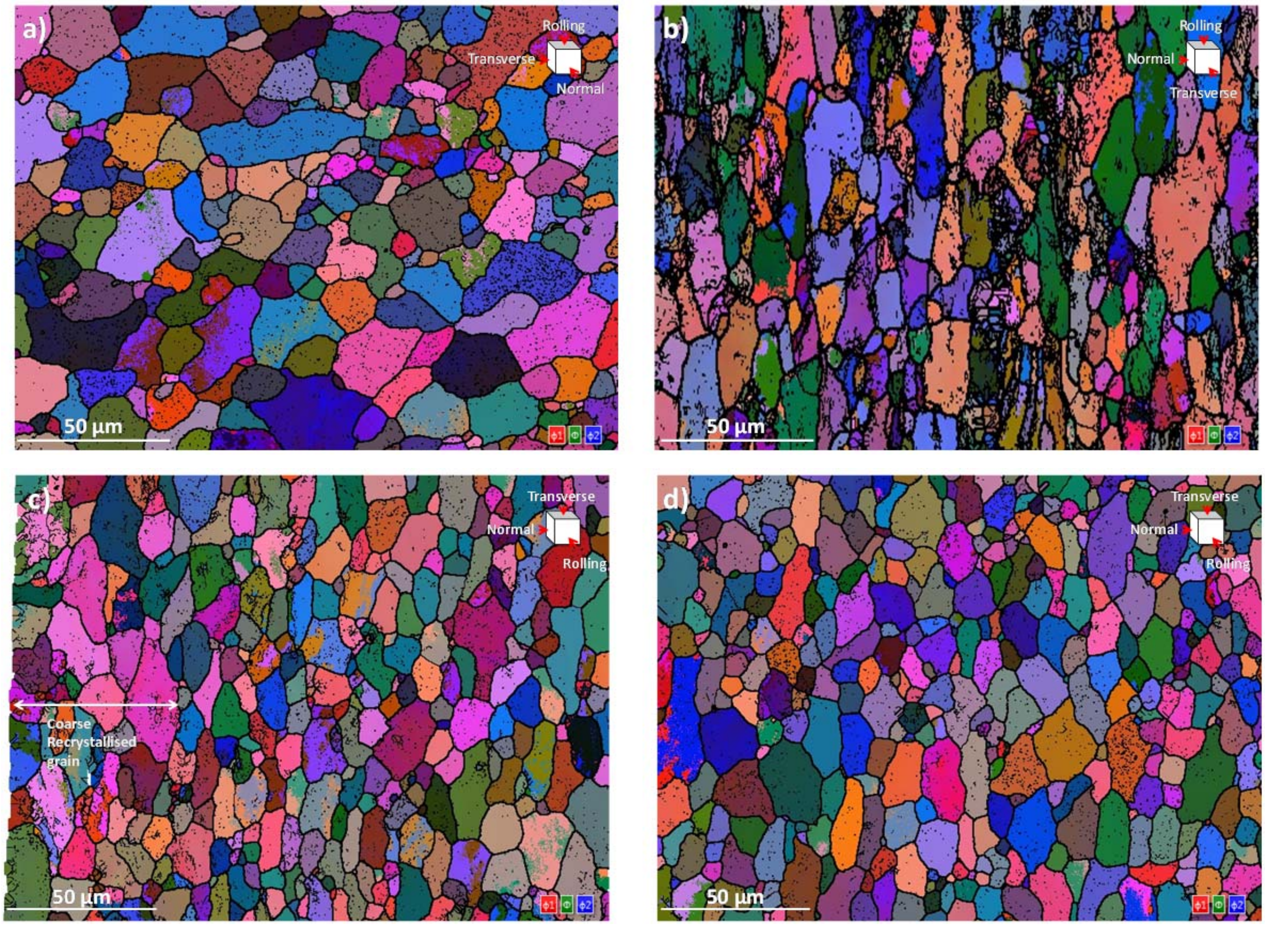

Figure 3-5: EBSD maps of Cu1 showing the a) normal direction. b) transverse direction. c) rolling direction demonstrating a coarse recrystallised grain surface layer of < 50 µm. d) rolling direction.

3.1.2 AA2099-T8E77 extrusion (Cu2)

Cu2 was an extruded commercial grade T-joint. Figure 3-6 a, b and c show micrographs of the 3 directions examined on Cu2. It can be seen from Figure 3-6 a, b and c that Cu2 has a fine grain structure. A low V_f of IMCs was observed and Image J showed that the largest IMC was on the normal direction at 33 μm^2, where in comparison the largest IMCs seen on the transverse and extrusion directions were ~ 22 μm^2 and ~ 31 μm^2 respectively. ~ 90 % of all the IMCs recorded were < 5 μm^2 and only ~ 4 % were > 10 μm^2. The Al-Cu-Fe-Mn IMCs were also dominant with ~ 85 % of all the IMCs recorded being of this designation.

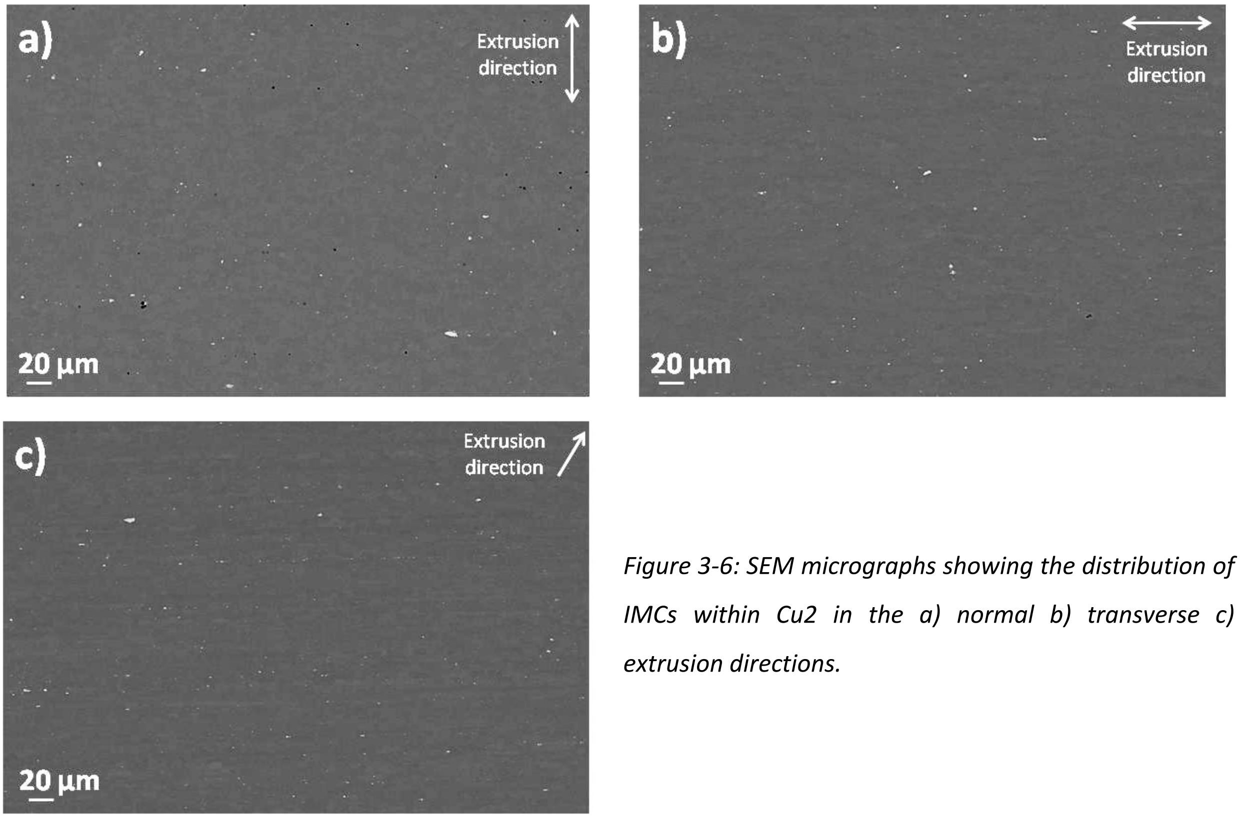

Figure 3-6: SEM micrographs showing the distribution of IMCs within Cu2 in the a) normal b) transverse c) extrusion directions.

Of these IMCs, EDS showed that there were 2 main types; Al-Cu-Fe-Mn and Al-Cu-Mn particles which agrees with literature with regards to the typical phases present within Al-Cu-Li alloys [2], [5], [14], [31], [83]. Figure 3-7 shows example EDS maps of an IMC within Cu2 and Table 3-3 shows the typical chemistries of the IMCs. Observations showed that the IMCs were well dispersed throughout the matrix and this resulted in a low V_f. The IMCs were also irregular in shape and had no regular morphological characteristics, however, alignment of the IMCs with the extrusion direction could be observed [26].

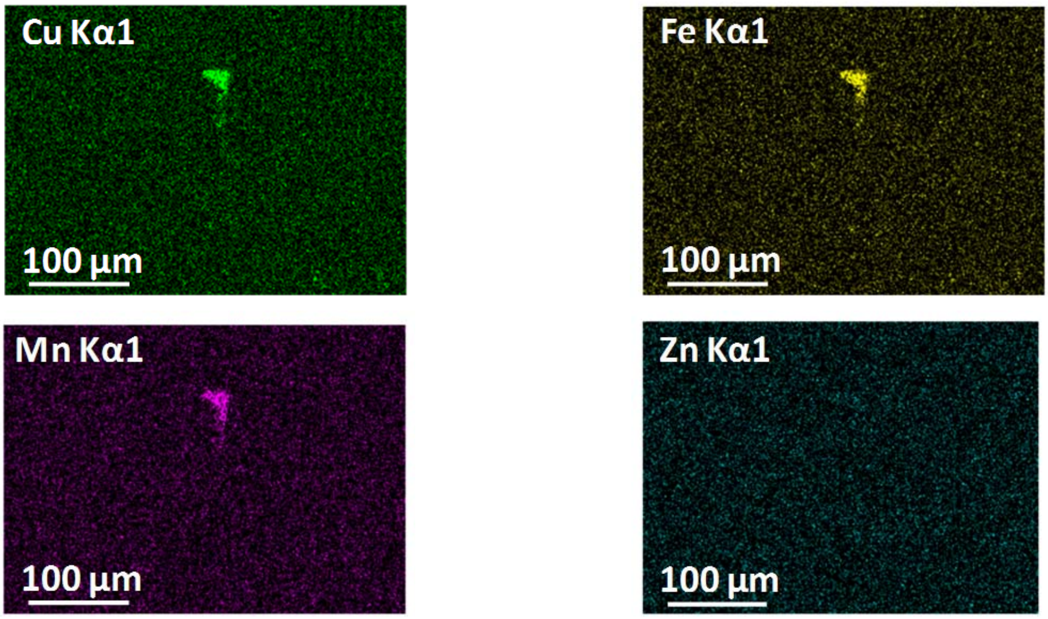

Figure 3-7: EDS maps of Cu2 showing the main elemental constituents within the IMCs.

Table 3-3: Measured EDS compositions of coarse IMCs, identified via SEM, fine scale precipitates and dispersoids identified by FEGTEM; in Cu2 (at.%).

Particle Type	Phase	Al at.%	Cu at.%	Fe at.%	Mn at.%	Zr at.%
Intermetallic Compounds	Al-Cu-Fe-Mn	87±10	6±4	4±3	3±2	/
	Al-Cu-Mn	96±2	2±1	/	<1	/
Precipitates and dispersoids	Al-Cu-Zr	90±8	5±3	/	/	<1
	Al-Mn-Cu-Fe-Zr	75±9	10±3	2±1	10±4	<1

FEGTEM analysis of Cu2 shows a relatively small number of spherical precipitates, as seen in Figure 3-8 a. EDS showed two types; Al-Cu-Zr and Al-Mn-Cu-Fe-Zr, however, a further two precipitates were also identified by their morphologies; T type phase, likely T_1 phase (Al_2CuLi) and θ type phase likely to be Al_2Cu, which have been shown in literature to be typical phases within Al-Cu-Li alloys [2], [5], [31], [32]. EDS is unable to identified Li due to its atomic number, which means all Li containing phases were identified using morphological data from literature. The distribution of these precipitates was not very homogenous and banding of precipitates could also be seen, no chemical information was gathered for these precipitates. A high V_f of T type phases were seen within the grains and on GBs, as shown by Figure 3-8 b and c. The T type phases are long plate like precipitates, with the vast majority of those seen within the grains being between 50 and 100 nm in length. The T type phases precipitated on the GB, however, tended to be > 100 nm, some were a similar size to that seen within the grains but most were ~ 200 nm, as shown in Figure 3-8 c. Evidence of Cu in the form of θ type phase on GBs has been identified via EDS, as shown in Figure 3-9, however, the number of these occurrences was limited. Large amounts of Zr containing particles were also seen to be distributed throughout the matrix, which is suggested to be Al_3Zr, some of which have been highlighted in Figure. These help by assisting in pinning GBs by providing a strong obstacle to dislocation movements during thermal and mechanical processing of the Al alloy [3], [46], [47], [65], [66].

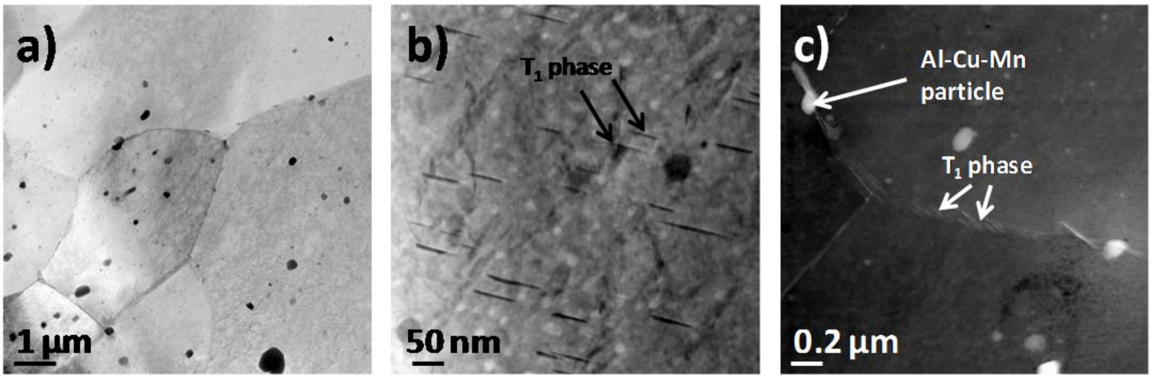

Figure 3-8: FEGTEM micrographs of Cu2 detailing the a) distribution of precipitates and dispersoids within the matrix. b) T type phase distribution within the matrix. c) T type phase particles on GB locations using HAADF.

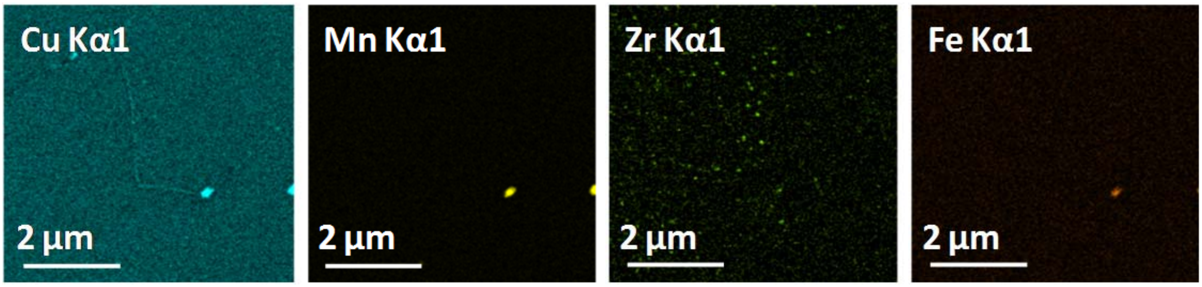

Figure 3-9: EDS maps of a site within Cu2 showing the main elemental constituents within the precipitates and Cu segregation on the GBs.

EBSD shows that Cu2 has a fine, equiaxed grain structure in all 3 directions which may be expected with the high concentration of grain refiners utilised in Al-Cu-Li alloys such as Mn, Zn and Zr [3], [23]. Figure 3-10 a shows grain banding in the normal direction and Figure 3-10 b and c show the transverse and extrusion directions of Cu2 respectively. A lower magnification EBSD map of the transverse direction showed a < 100 µm coarse recrystallised grain structure at the surface of the specimens. Figure 3-10 c shows the extrusion direction with no banding or alignment as observed in Figure 3-10 a and b, suggesting it may be associated with coarse surface recrystallised grains. EBSD showed that ~ 70 % of all grains were < 50 μm^2 and ~ 15 % of grains were > 100 μm^2. Fluctuations in the coarse structure on the surface of the specimens is shown in Figure 3-10 c. Figure 3-10 d shows an EBSD map taken from the main bulk of the extrusion direction, below the coarse recrystallised region, showing that the grain size beneath the coarse structure is very fine and equiaxed.

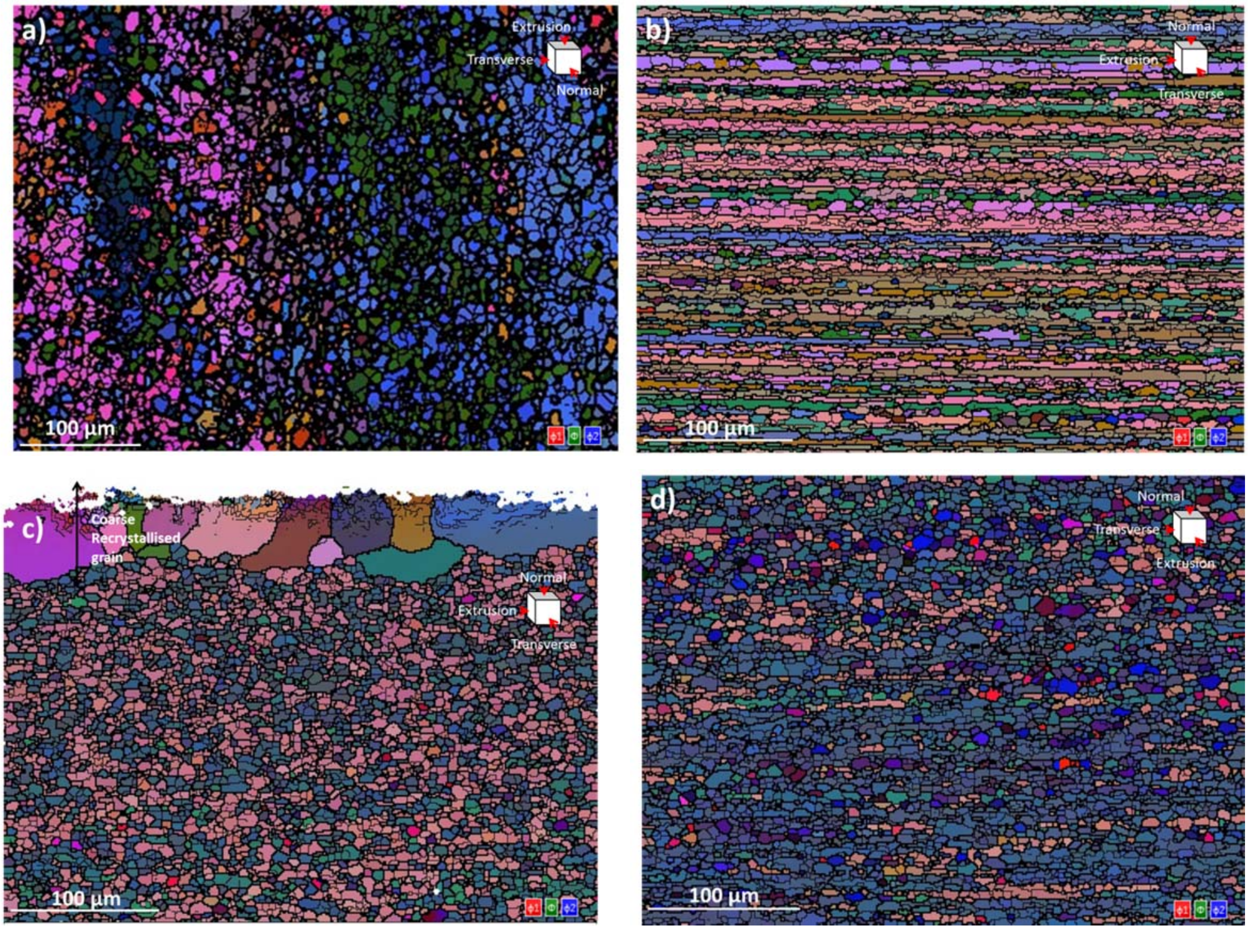

Figure 3-10: EBSD maps of Cu2 showing the a) normal direction demonstrating grain bands. b) transverse direction. c) transverse direction demonstrating a coarse recrystallised surface grain layer of < 100 µm. d) extrusion direction.

3.1.3 AA2099-T8E77 plate (Cu3)

Cu3 was a non-commercial grade plate stock material. Figure 3-11 a, b and c show micrographs of the 3 directions examined on Cu3. There was a low V_f of IMCs, which is reinforced by Image J analysis. The size of the IMCs was fine, with ~ 85 % of all IMCs from the three directions being < 3 μm^2 and only 2 % of all IMCs recorded being > 10 μm^2. The largest IMC recorded was on the normal direction and was 97 μm^2, however, in comparison the largest IMCs seen on the transverse and extrusion directions were 77 μm^2 and 22 μm^2 respectively. The IMCs were also irregular in shape and had no regular morphology, however, alignment with the extrusion direction could be observed [26].

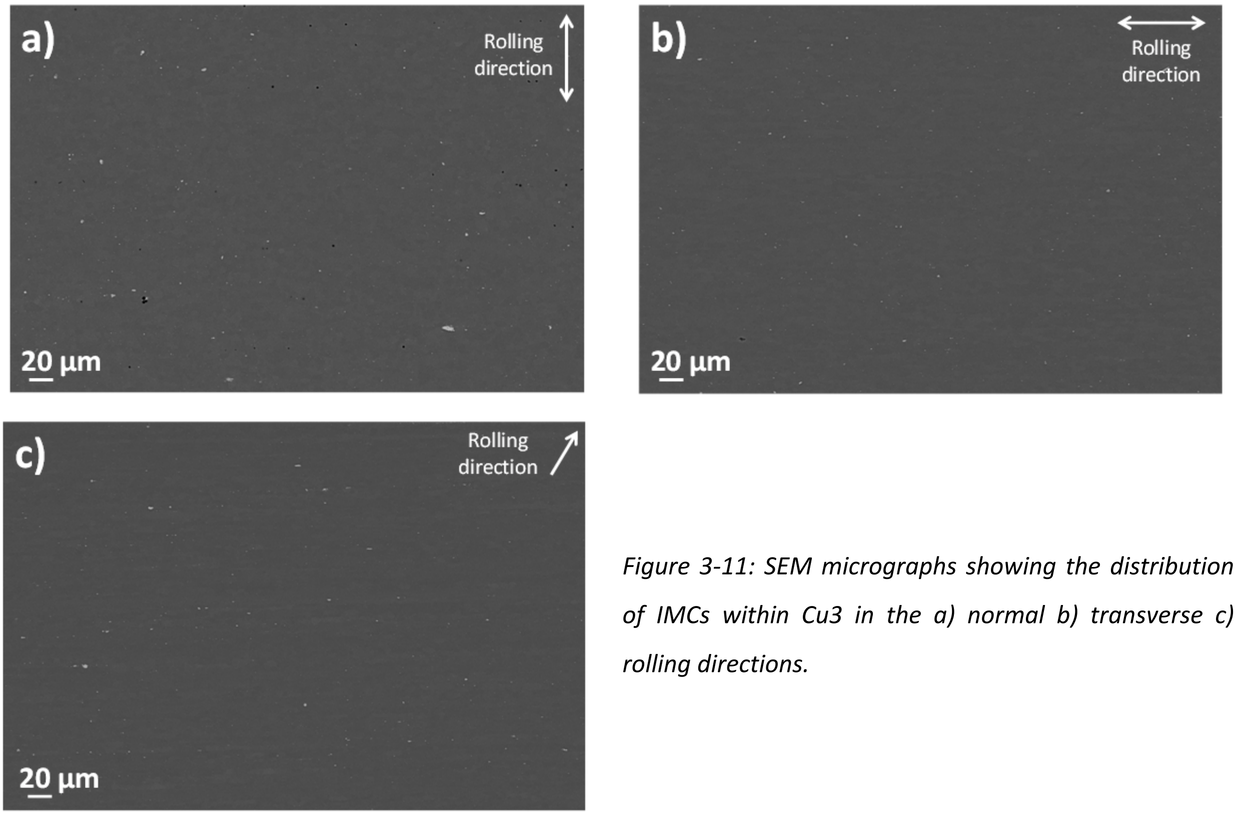

Figure 3-11: SEM micrographs showing the distribution of IMCs within Cu3 in the a) normal b) transverse c) rolling directions.

Of the IMCs, EDS showed that there were 2 main types; Al-Cu-Mn-Fe and Al-Fe-Mn-Cu particles which agrees with literature [24], [83], [84]. Figure 3-12 shows example EDS maps of IMCs within Cu3 from which the typical chemistries can be seen in Table 3-4. Neither of the IMC types identified showed a higher V_f over the other and due to the similar chemistry it would not be unexpected if these two IMC types were actually within the composition range of a single IMC composition. Observations showed that the IMCs were well dispersed throughout the matrix and as such demonstrated a low V_f of IMC within Cu3.

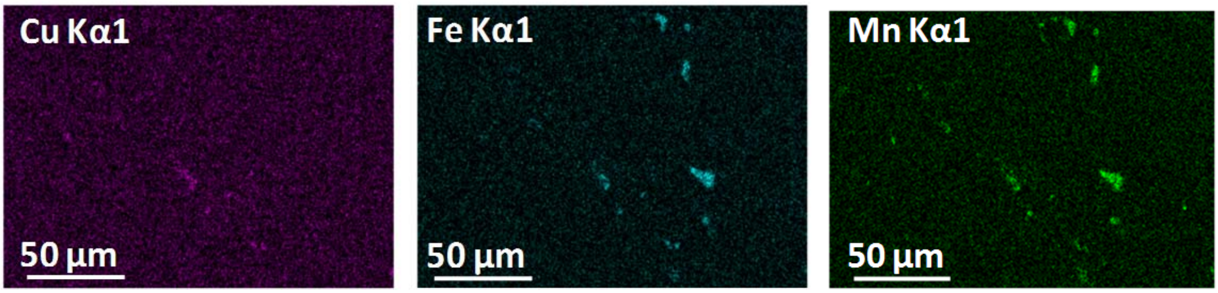

Figure 3-12: EDS maps of Cu3 showing the main elemental constituents within the IMCs.

Table 3-4: Measured EDS compositions of coarse IMCs, identified via SEM, fine scale precipitates and dispersoids identified by FEGTEM; in Cu3 (at.%).

Particle Type	Phase	Al at.%	Cu at.%	Fe at.%	Mn at.%	Zr at.%
Coarse Intermetallic Compounds	Al-Cu-Mn-Fe	85±2	5±1	5±1	5±1	<1
	Al-Fe-Mn-Cu	90±3	1±1	5±2	5±1	<1
Fine scale Precipitates and dispersoids	Al-Cu-Zr	94±8	5±2	/	/	<1
	Al-Cu-Mn-Fe-Zr	75±9	10±3	2±1	10±4	<1

FEGTEM of Cu3 showed the presence of T type phases within the grains, however, no evidence of these were seen on the GB as demonstrated in Figure 3-13 a. The T type phases were < 100 nm in length. Cu particles on GBs was extensive, with FEGTEM revealing that these regions contained closely packed, < 50 nm, spherical θ type particles, see Figure 3-13 b. The presence of the T type and θ type phase particles in Cu3 agrees with literature with regards to typical phases within Al-Cu-Li alloys [2], [21], [31], [32]. The main precipitates were: Al-Cu-Zr and Al-Cu-Mn-Fe-Zr, see Table 3-4. The Al-Cu-Zr particles were relatively small (Ø = 100 nm) and spherical in morphology. The Al-Cu-Mn-Fe-Zr particles were also spherical (Ø = 500 nm) in the main, but some were rectangular in morphology. These rectangular particles differed in size, with some being around 500 nm in length but others being close to 2 μm. Figure 3-14 shows the corresponding EDS maps for Figure 3-13 c, detailing the distribution of elements in some fine scale precipitates and those associated with GBs. Zr rich dispersoids were also observed, which are believed to be Al_3Zr [26].

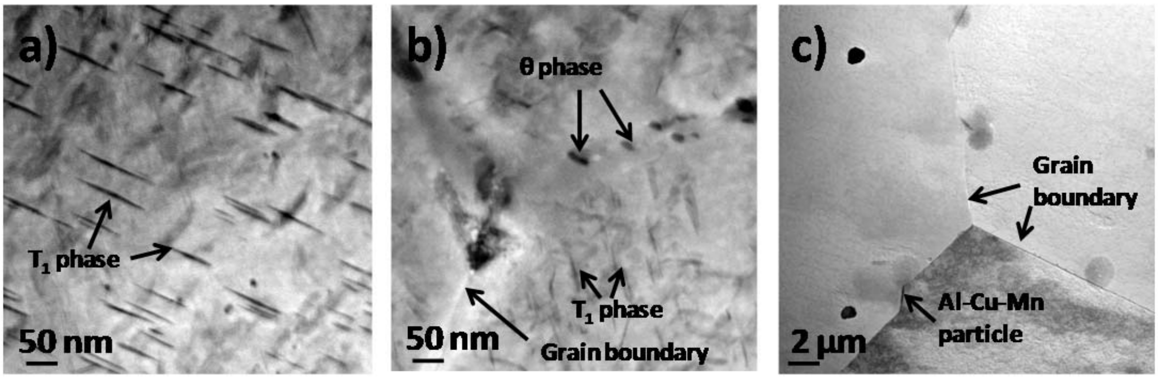

Figure 3-13: FEGTEM micrographs of Cu3 detailing the a) distribution of T type phase particles within the matrix. b) GB particles. c) low V_f of precipitates and GB particles.

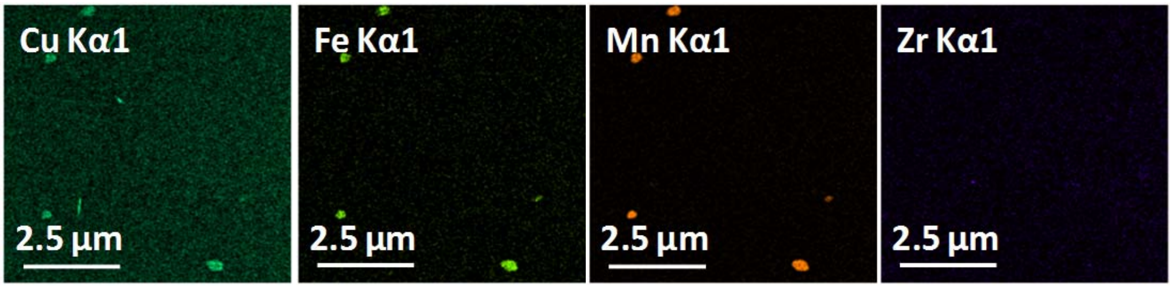

Figure 3-14: EDS maps of a site within Cu3 showing the main elemental constituents within the precipitates and Cu segregation on the GBs.

EBSD shows that Cu3 has a coarse recrystallised grain structure in all three directions. Figure 3-15 a shows very coarse grains, but also some regions showing a fine grain formation. Figure 3-15 b shows the transverse direction of the Cu3 alloy, showing the alignment of the coarse grains in the extrusion direction, with ~10 % > 1000 μm^2. Figure 3-15 c shows the extrusion direction close to the surface highlighting the formation of recrystallised grains. The number of grains identified at these regions was around 30 % less than that taken within the bulk of the specimen. A much larger proportion of the grains had areas greater than 100 μm^2 (~ 30%) and 20 % had areas > 1000 μm^2. The reason for the difference in the number of grains is because of the amount of fine grains observed in the bulk of the specimen. Examination of the surface recrystallised grain structure shows that it was ~ 150 μm deep, with grains beyond this region having a higher level of elongation in the extrusion direction. All of the grains seen at the surface were coarse in structure, but their overall size was less than that seen in the bulk; grains or regions of fine scale were also not observed in this 150 µm region. Figure 3-15 d also shows the grain structure in the extrusion direction, once again highlighting the elongated coarse grain structure of Cu3.

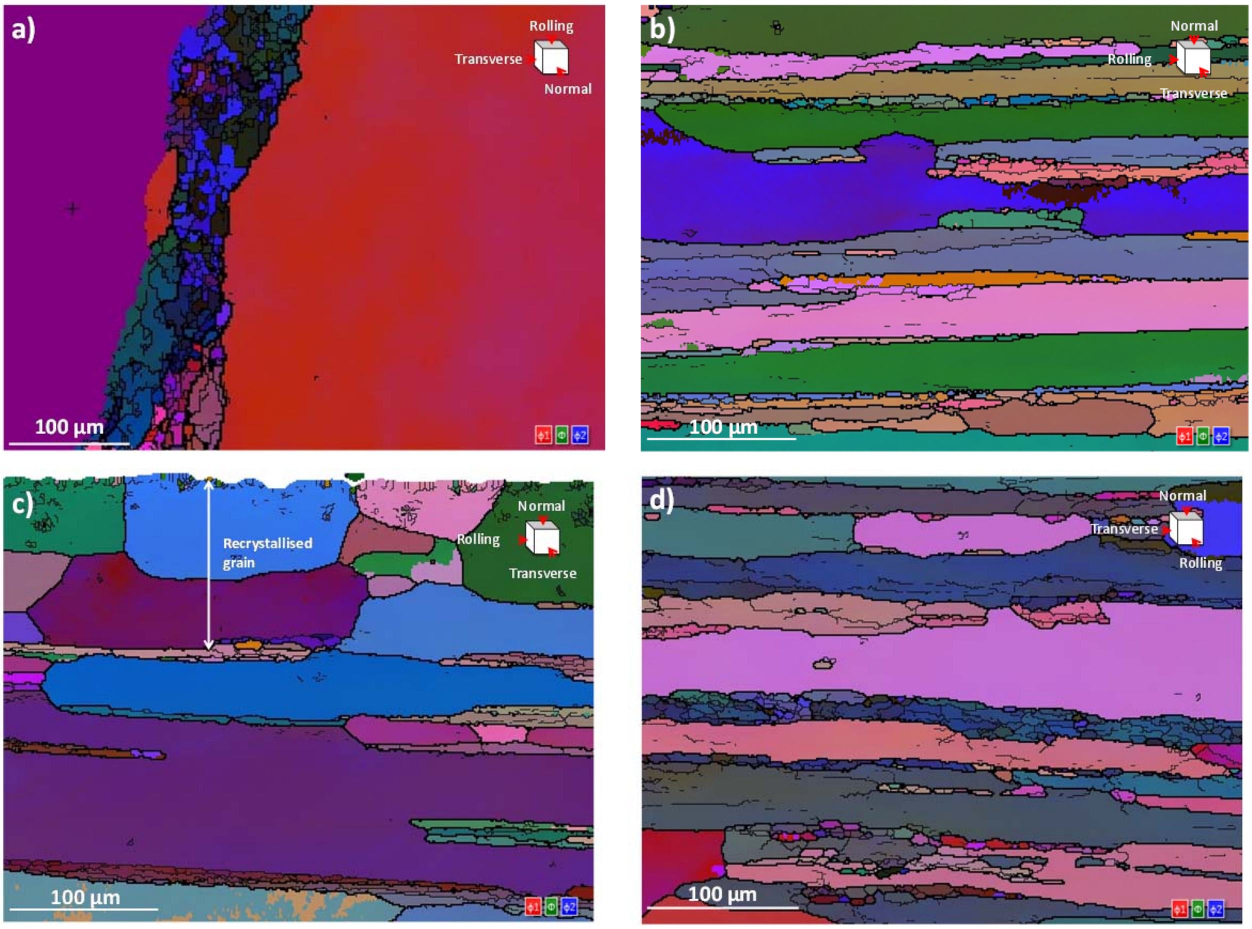

Figure 3-15: EBSD maps of Cu3 showing the a) normal direction. b) transverse direction. c) transverse direction demonstrating a coarse recrystallised surface grain layer of ~ 150 µm. d) rolling direction.

3.2 Material Characterisation of Al-Mg alloys

Of the 5XXX series Al alloys a commercial AA5083-T3510 (Al-Mg) Al alloy was compared against two SF Al alloys; termed SF1 (Al-Mg-Li) and SF2 (Al-Mg-Li-Cu-Zn). The two SF Al alloys were experimental variants, thus the impact of spray forming on corrosion resistance could also be evaluated. The nominal compositional data for each 2XXX series Al alloy examined is shown in Table 3-5.

Table 3-5: Nominal composition of Al-Mg alloys under investigation [28], [93].

Alloy designation	**Al wt.%**	**Mg wt.%**	**Li wt.%**	**Zr wt.%**	**Fe wt.%**	**Cu wt.%**	**Zn wt.%**	**Mn wt.%**
AA5083-T3510	Bal.	4.61	/	/	0.05	/	/	/
SF Al-Li-Mg	Bal.	5.24	1.4	0.41	0.03	/	/	/
SF Al-Li-Mg-Cu-Zn	Bal.	4.18	1.98	0.2	0.03	0.57	1.01	/

3.2.1 AA5083-T3510 (Mg1)

Mg1 was extruded commercial grade material. Figure 3-16 a, b and c show the distribution of IMCs throughout the matrix for each of the observed directions. It can be seen that some of the IMCs are much larger than others. Image J analysis showed that ~ 90 % of the IMCs were < 10 µm^2 but some were seen to be > 80 µm^2. The largest IMC observed was seen on the transverse direction and was 104 µm^2. Clustering of some IMCs has also been observed, but the size and distribution of the IMCs are relatively homogenous. Elongation of the IMCs was also observed in the extrusion direction. Some IMCs were seen to be blocky with others long and thin, however, this could be associated to different grain directions or the breaking up of IMCs during processing [26].

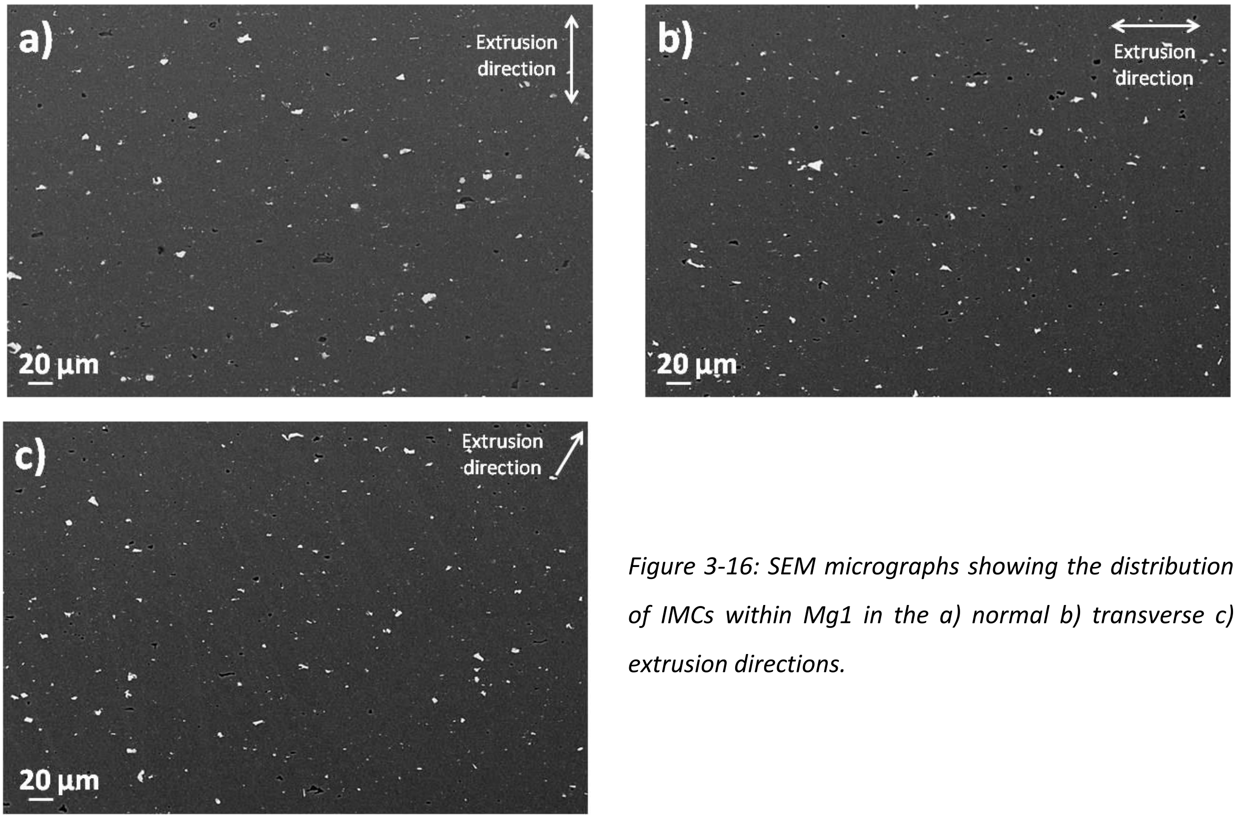

Figure 3-16: SEM micrographs showing the distribution of IMCs within Mg1 in the a) normal b) transverse c) extrusion directions.

Table 3-6 demonstrates that 3 distinct types of IMC can be identified; Al-Mn-Si, Al-Mg-Si and Al-Fe-Mn-Mg-Si. From all of the IMCs examined ~ 60 % of them were Al-Fe-Mn-Mg-Si, ~ 35 % were Al-Mg-Si and the remainder were Al-Mn-Si. There was, however, no observed correlation between IMC morphology and EDS data. *Ezuber et al.* [39] showed that the main IMCs present in a Mg1 alloy were primarily Al-Mg, Al (Si, Mg), Al-Mg-Cr and Al_6 (Fe, Mn, Cr), which is similar to what has been observed in this thesis, however, the Cr concentration in Mg1 were < 1 at.%. Figure 3-17 shows EDS maps of Mg1 highlighting the distribution of the elements within the IMCs.

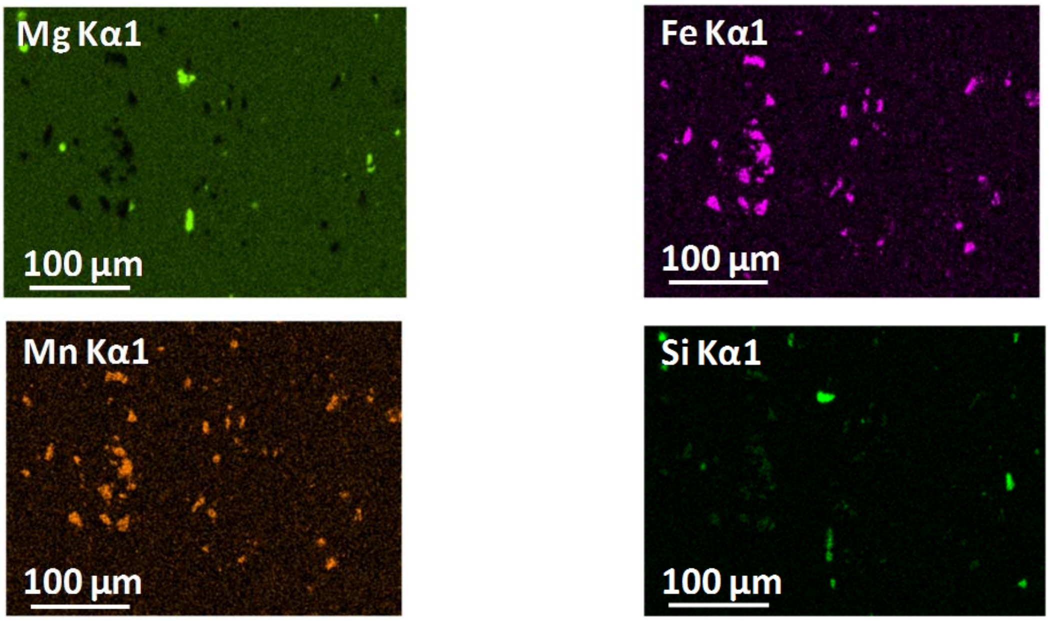

Figure 3-17: EDS maps of Mg1 showing the main elemental constituents within the IMCs.

Table 3-6: Measured EDS compositions of coarse IMCs, identified via SEM, fine scale precipitates and dispersoids identified by FEGTEM; in Mg1 (at.%).

Particle Type	Phase	Al at.%	Mg at.%	Fe at.%	Mn at.%	Cr at.%	Si at.%	Ti at.%
Coarse Intermetallic Compounds	Al-Mg-Si	38±22	36±12	/	/	/	30±18	/
	Al-Mn-Si	81	<1	/	10	<1	2	/
	Al-Fe-Mn-Si-Mg	80±3	1±2	10±2	6±2	<1	3±1	/
Fine scale Precipitates and dispersoids	Al-Mg-Mn-Fe-Cr-Ti	86±6	5±2	1±1	5±5	1±1	/	1±1

FEGTEM revealed a large distribution of precipitates within Mg1. This distribution was in some cases homogenous but some regions showed distinct clustering of precipitates as shown in Figure 3-18 a. These precipitates showed a large variety of morphologies and sizes as shown in Figure 3-18 a, b and c, with some being blocky in nature but some being rod-like. EDS, however, shows that there was only really a single type of precipitate; Al-Mg-Mn-Fe-Cr-Ti for which the chemical composition is shown in Table 3-6. These Al-Mg-Mn-Fe-Cr-Ti precipitates appear relatively complex, however, EDS shows that the primary constituents are Al, Mg and Mn, with the remaining elements comprising < 3 at.% on average. Looking at the differences in V_f between the blocky and rod-like precipitates shows that there are a lot more blocky precipitates than rod-like. EDS as shown, however, cannot distinguish any chemical difference between them. Figure 3-19 shows typical EDS maps within Mg1 showing the distribution of specific elements; Ti, Mn, Fe and Mg.

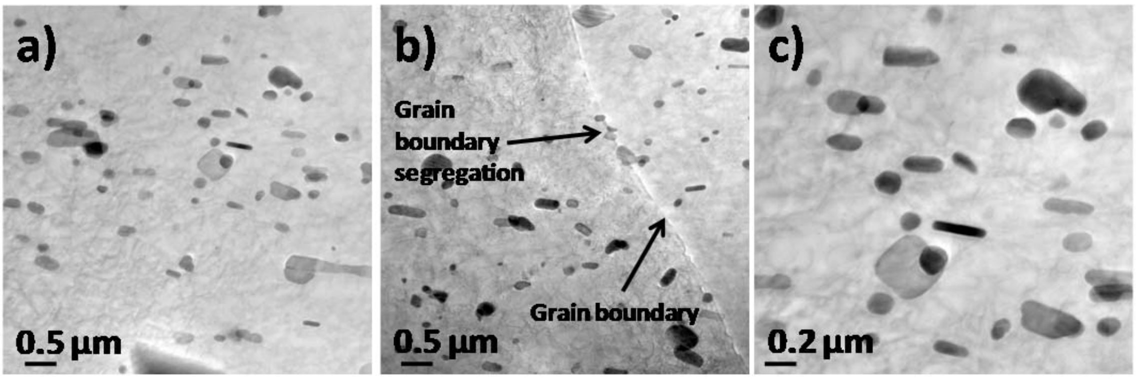

Figure 3-18: FEGTEM micrographs of Mg1 showing a) high densities of precipitates within the matrix. b) GB location. c) the different particle morphologies.

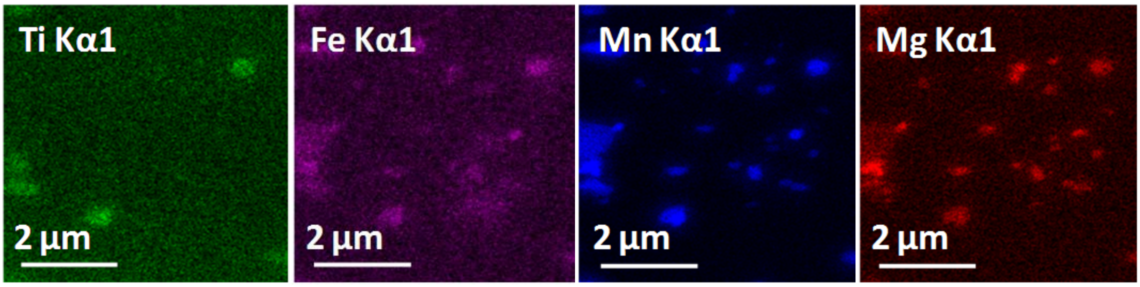

Figure 3-19: EDS analysis of a site within Mg1 showing the main elemental constituents of the precipitates.

EBSD examination shows that Mg1 comprises of a coarse recrystallised grains. Figure 3-20 a shows the normal direction with some regions of fine grains. Similarly, Figure 3-20 b shows the transverse direction highlighting a fine grain region within Mg1. These fine grain regions were distributed throughout the matrix. A distinct elongation of the grain structure along the transverse direction was also observed. Similarly observation of the extrusion direction shows elongated grains as indicated in Figure 3-20 c. The fine grain regions affected some of the data regarding grain size values, however, 70 to 80 % of all the grains were < 100 µm^2. Data also shows that between 10 and 20% of the grains were > 1000 µm^2 as such the influence of fine grain regions has a large impact on the average grain dimensions. Figure 3-20 d shows a lower magnification EBSD micrograph of the transverse direction that highlights the large recrystallised grains at the surface of Mg1, which are ~ 200 µm deep.

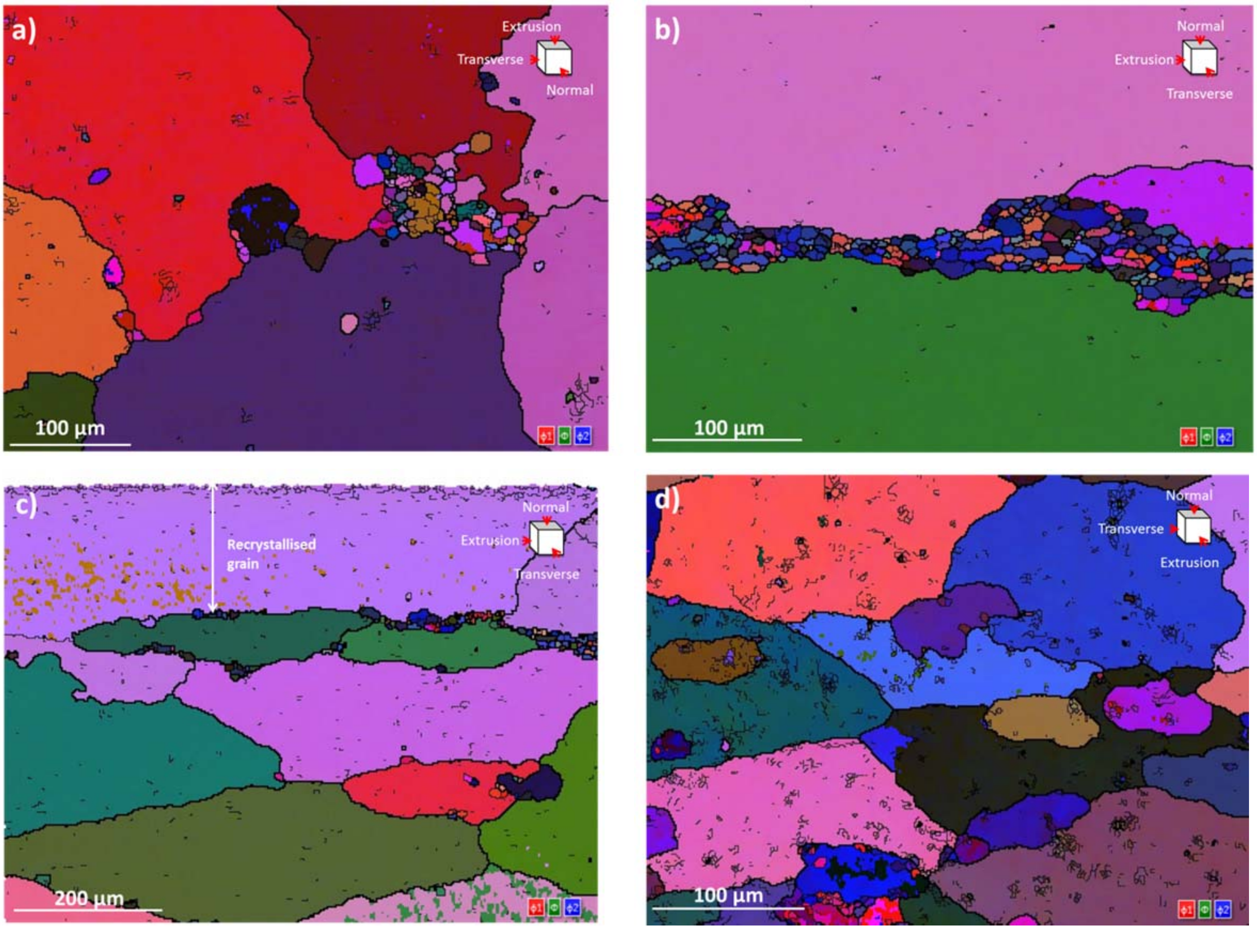

Figure 3-20: EBSD maps of Mg1 showing the a) normal direction. b) transverse direction. c) transverse direction showing a coarse recrystallised surface grain layer of ~ 200 µm. d) extrusion direction.

3.2.2 Spray formed Al-Mg-Li (SF1)

SF1 was extruded SF, non-commercial grade material and as such has undergone microstructural refinement. Microscopy showed a fine distribution of IMCs throughout the matrix, identified by BSD analysis shown in Figure 3-21 a, b and c. Initial observations show a very low V_f of IMCs, but this was to be expected due to the refining nature of the spray forming technique. The size of the IMCs was also very fine, with ~ 95 % of all IMCs from the 3 directions being < 3 µm^2 and < 1 % were > 5 µm^2. The largest IMC recorded was 23 µm^2 on the transverse direction, however, in comparison the largest IMCs seen on the normal and extrusion directions were 11 µm^2 and 10 µm^2 respective. Once again elongation of the IMCs was observed. The dark spots shown in Figure 3-21 a, b and c are porosity, which is typical of SF Al alloys [134].

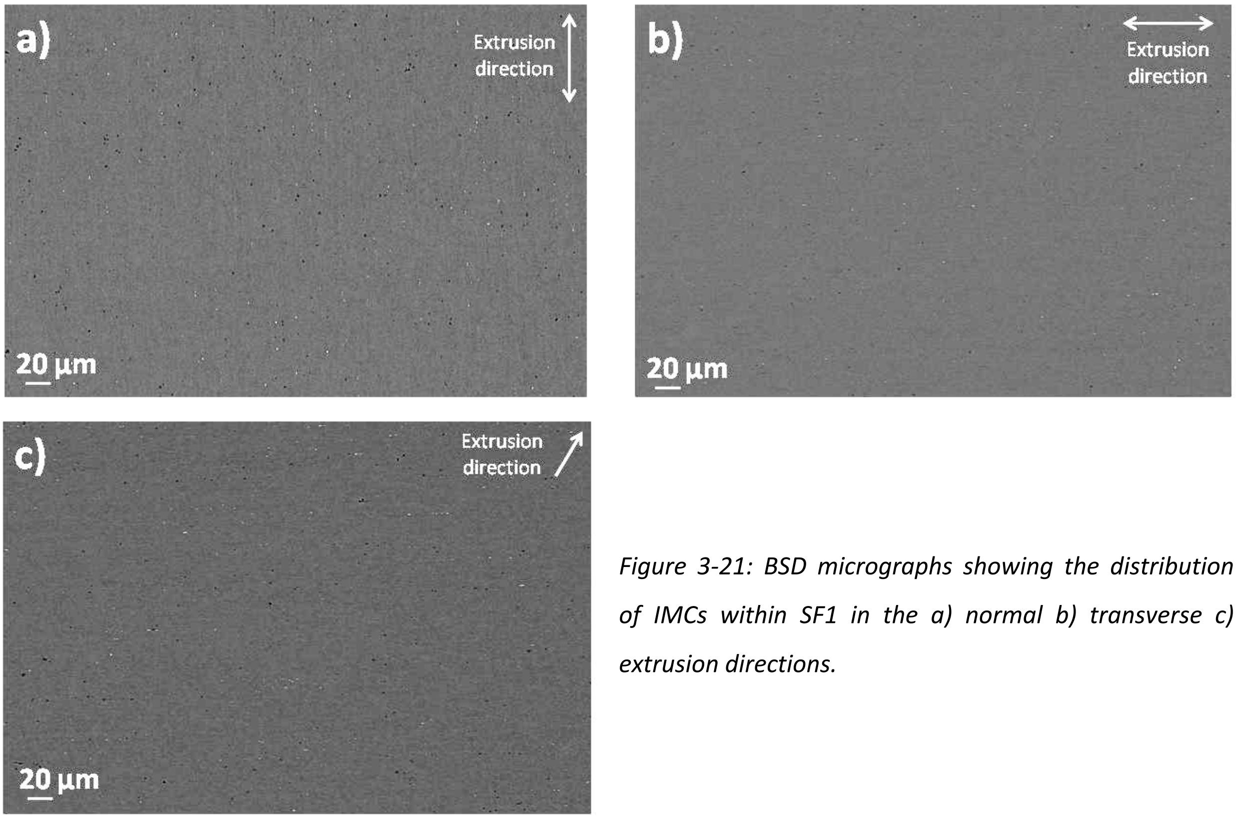

Figure 3-21: BSD micrographs showing the distribution of IMCs within SF1 in the a) normal b) transverse c) extrusion directions.

Example EDS maps are shown in Figure 3-22, showing the distribution of elements within the IMCs in SF1. 2 main types of IMC were identified; Al-Mg-Si and Al-Mg-Si-Fe of which there chemistries can be seen in Table 3-7. The ratio of each IMC was relatively uniform with no distinct IMC type having a higher concentration.

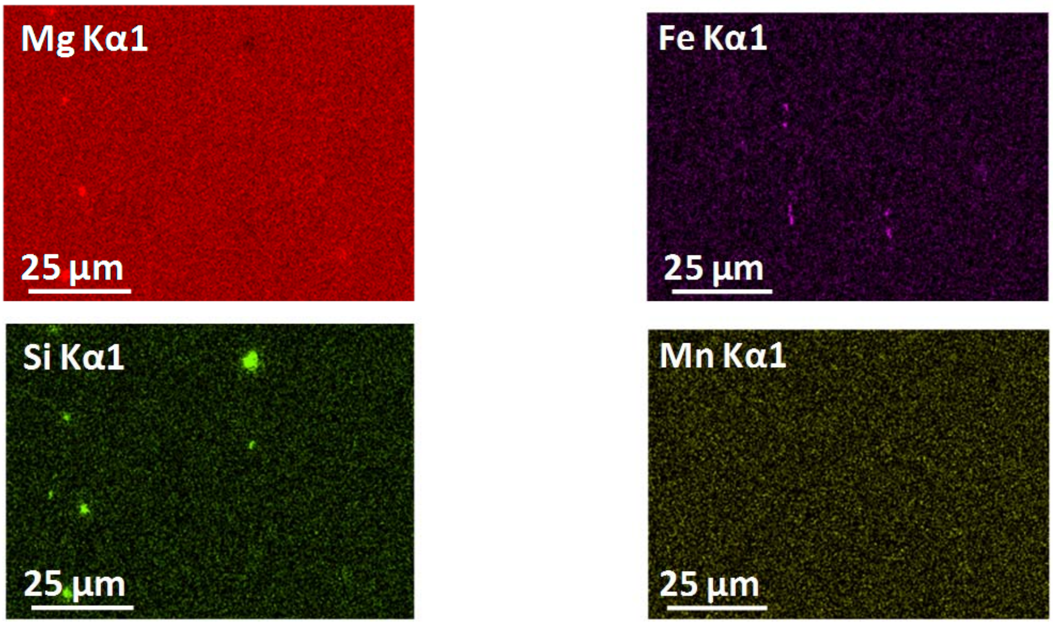

Figure 3-22: EDS maps of SF1 showing the main elemental constituents of the IMCs.

Table 3-7: Measured EDS compositions of coarse IMCs, identified via SEM; in SF1 (at.%).

Particle Type	Phase	Al at.%	Mg at.%	Fe at.%	Mn at.%	Cr at.%	Si at.%
Coarse Intermetallic Compounds	Al-Mg-Si	77±4	14±4	/	/	/	7±2
	Al-Mg-Si-Fe	81±6	12±4	3±2	/	/	5±1

With SF1 being a SF alloy a very fine equiaxed grain structure was expected [130]. EBSD reveals that in all three directions this was the case. Figure 3-23 a, b and c show the 3 directions examined from which it can be seen that over 80 % of all grains measured were < 4 µm^2. EBSD maps were taken from the transverse direction at the specimen surface to see if any coarse recrystallised grain structures could be observed and from Figure 3-23 d it can be seen that none were observed. From the data analysis a trend was seen in that the grains closer to the surface were smaller than those in the bulk of the material, as the average grain size from the bulk was ~ 4 µm^2 compared to ~ 2 µm^2 near the surface.

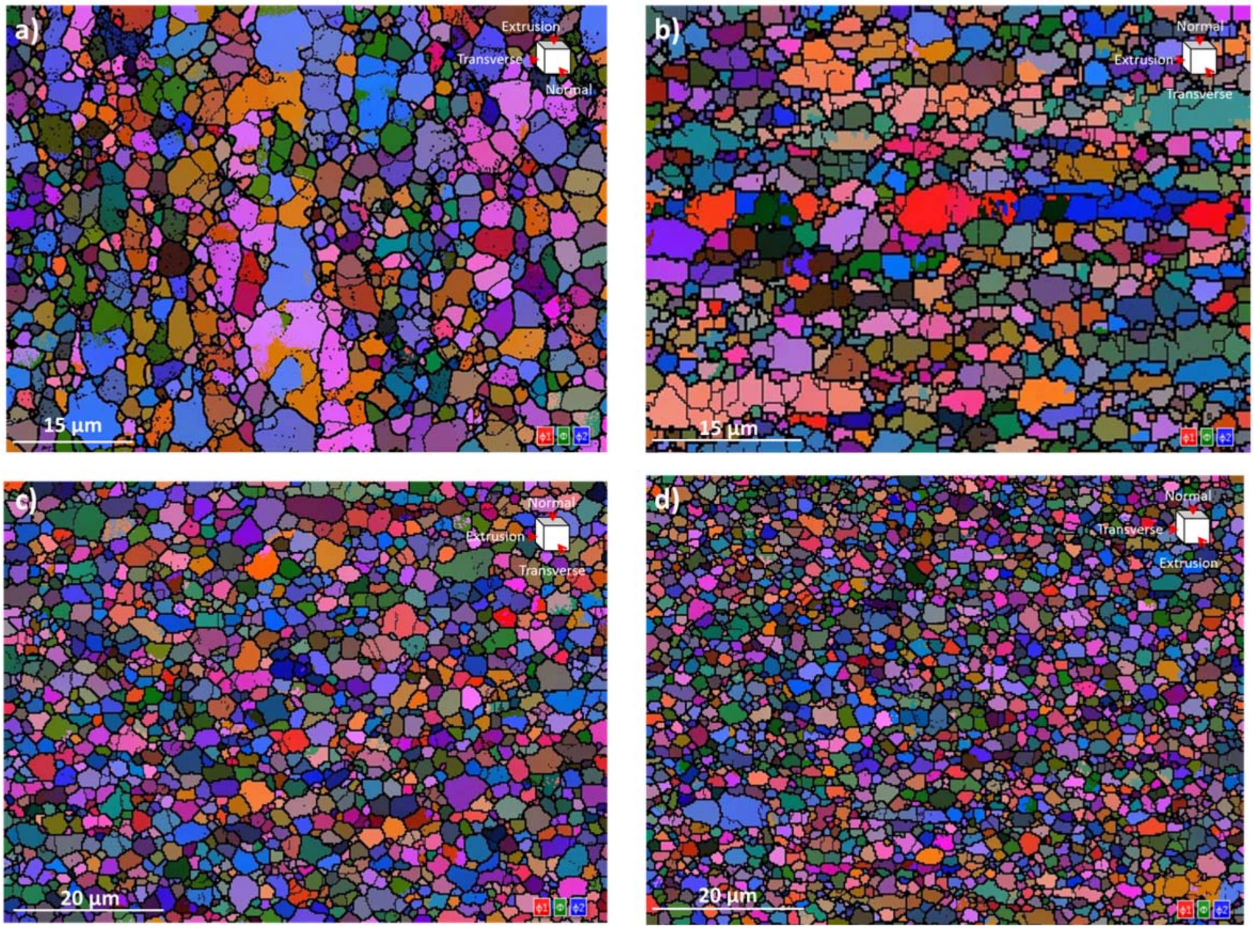

Figure 3-23: EBSD maps of SF1 showing the a) normal direction. b) transverse direction. c) extrusion direction at the surface. d) extrusion direction.

3.2.3 Spray formed Al-Mg-Li-Cu-Zn (SF2)

Microscopy shows a fine distribution of IMCs through the matrix (see Figure 3-24 a, b and c). BSD analysis shows that the IMCs appeared to cluster together but these clusters are well dispersed throughout the matrix. BSD also revealed a banded / weld structure which ran through the centre of the specimen, as shown in Figure 3-24 a. This banded structure is likely to be a weld zone generated from the extrusion process of the material, where the 2 sides of the hollow component re-join. Observations in the extrusion and transverse direction also revealed this weld structure on both the surface edges of the specimen. A very low V_f of IMCs was observed, which was reinforced by Image J analysis. The size of the IMCs were also seen to be on average < 3 µm^2 and < 1 % of all IMCs recorded were > 5 µm^2. The largest IMC recorded was on the extrusion direction and was 7 µm^2, however, in comparison the largest IMC seen on the normal and transverse directions were 6 µm^2. This shows that no significant change in

IMC morphology can be noted between the 3 directions for SF2, however, a slight elongation of the IMCs was observed using Image J analysis. The banded region showed similar sized IMCs, however, the V_f of these was much more substantial. The dark spots that can be seen are porosity within the matrix, which is typical of SF Al alloys [134].

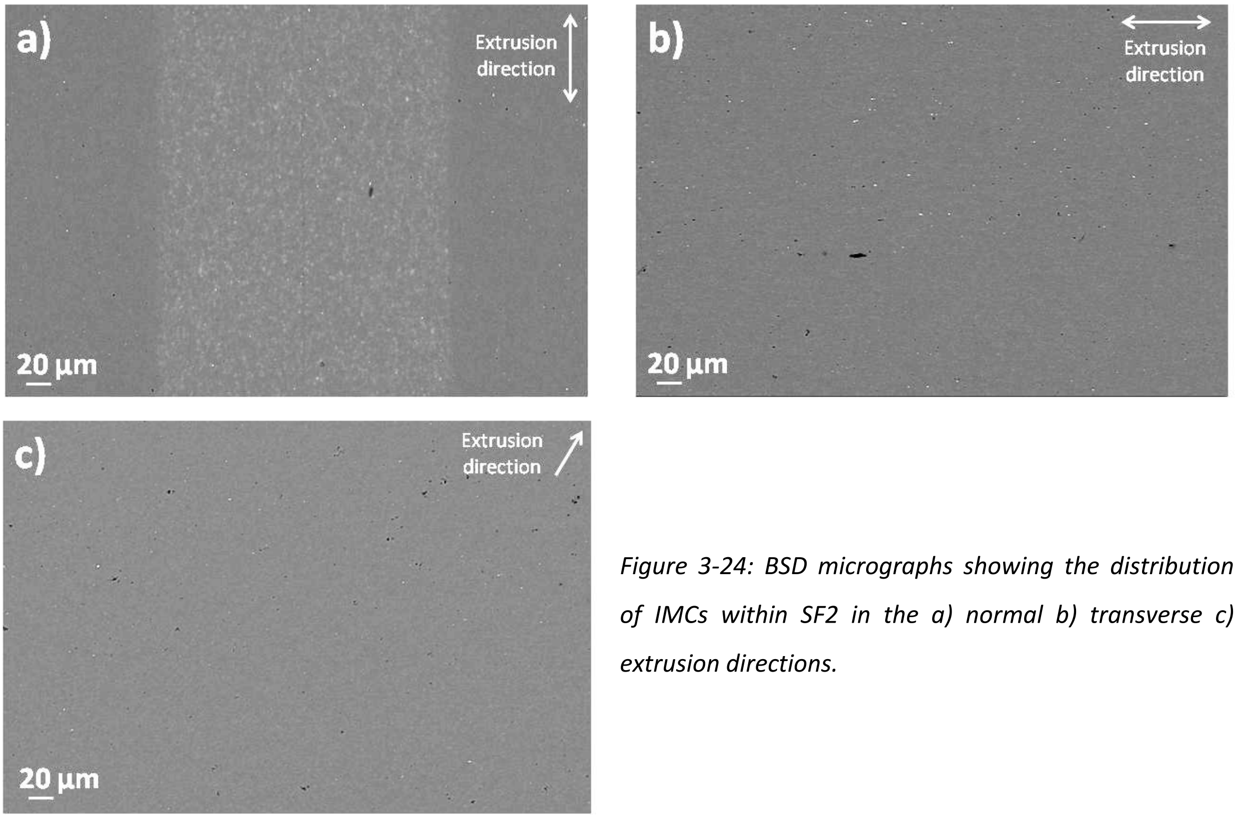

Figure 3-24: BSD micrographs showing the distribution of IMCs within SF2 in the a) normal b) transverse c) extrusion directions.

With the weld region only being visible via BSD, this showed that there was a chemical difference for these regions. EDS of the weld region, illustrated in Figure 3-24 a, shows that this region had evidence of Cu (0.27 at.%) and Zn (0.47 at.%), whereas the region around the band does not show any measurable Cu or Zn. The band also had a lower Mg level at 4 at.% compared to a general concentration of 6 at.%. This weld region shall therefore be termed the Cu and Zn rich region and the non-weld region shall be classed as the denuded region, to signify the absence of Cu and Zn. Figure 3-25 shows EDS maps demonstrating the difference in Mg, Cu and Zn levels between the two regions and a BSD micrograph taken from the extrusion direction, showing the morphology of the band. This suggests that the Cu and Zn rich region could be some form of weld joint formed through the extrusion process. This Cu and Zn rich region, at the surface, suggests that significant levels of heating have taken place during the process causing the Cu, Zn to segregate in turn forcing some Mg to segregate in the opposite direction.

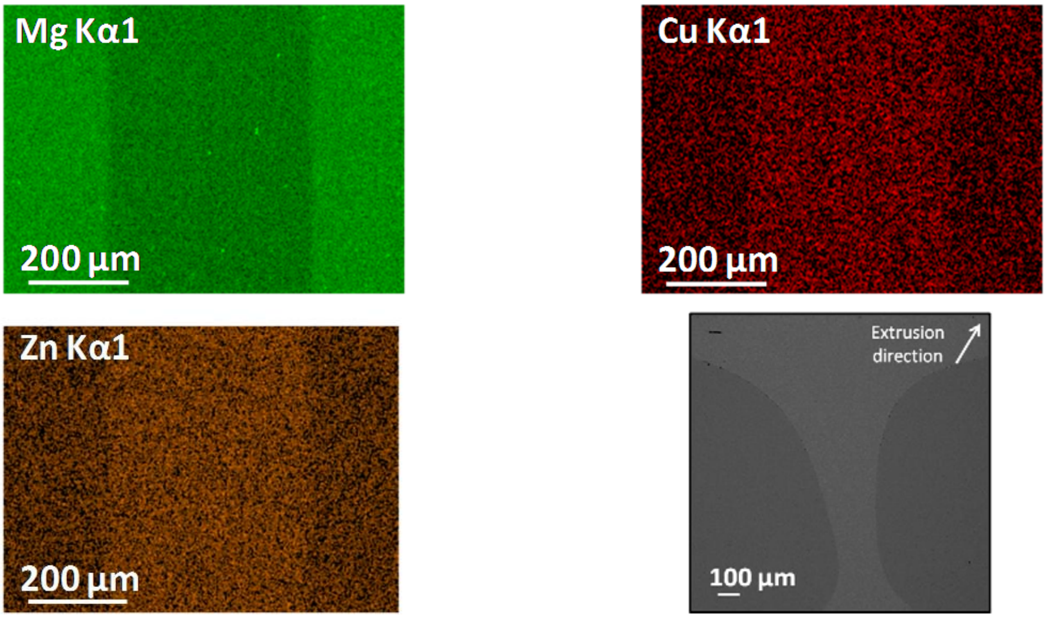

Figure 3-25: EDS maps of SF2 showing the main elemental constituents of the Cu and Zn rich region and a micrograph from the extrusion direction showing the Cu and Zn rich region.

EDS maps are shown in Figure 3-26, illustrating the distribution of elements within the IMCs in SF2. 2 main types of IMC were identified; Al-Mg-Si and Al-Mg-Fe-Si and their respective chemistries are shown in Table 3-8. The ratio of each IMC was relatively uniform with neither type having a higher concentration. Interestingly, no IMCs were seen to contain Cu suggesting that the Cu had been dissolved into solid solution from the processing. Spray forming has been shown in literature [134] to cause segregation and as such may be what has taken place with this specimen.

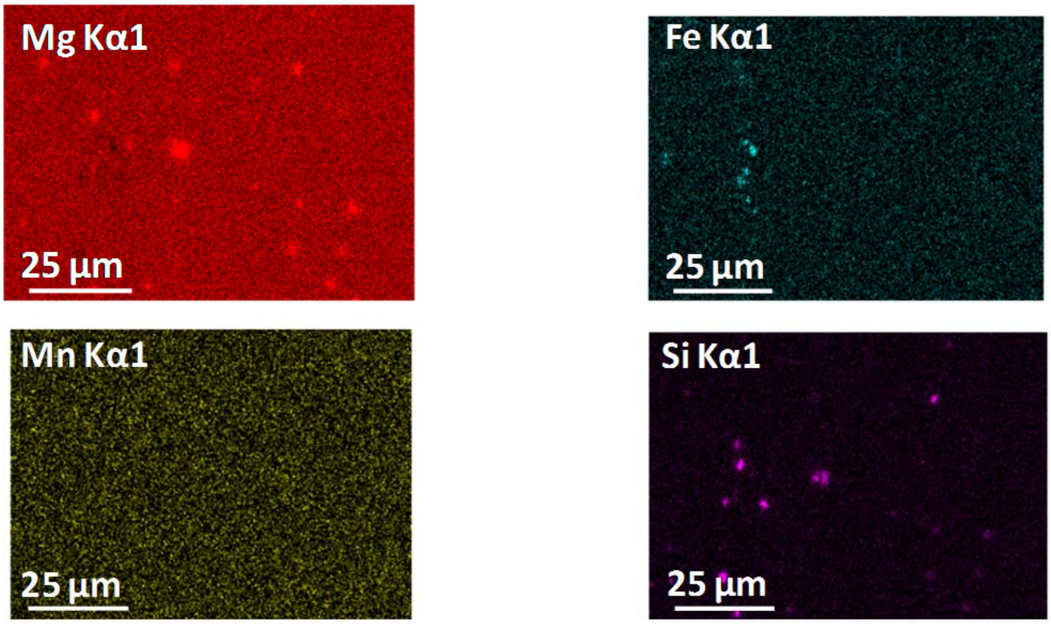

Figure 3-26: EDS maps of SF2 showing the main elemental constituents of the IMCs.

Table 3-8: Measured EDS compositions of coarse IMCs, identified via SEM; in SF2 (at.%).

Particle Type	Phase	Al at.%	Mg at.%	Fe at.%	Mn at.%	Cr at.%	Si at.%
Coarse Intermetallic Compounds	Al-Mg-Si	77±4	14±4	/	/	/	7±2
	Al-Mg-Fe-Si	80±6	12±4	3±3	/	/	<1

Figure 3-27 a and b show an overview of the Cu and Zn rich region and the surrounding material to show that no difference in grain structure was present from the extrusion and normal direction respectively (highlighted region is the Cu and Zn rich region).

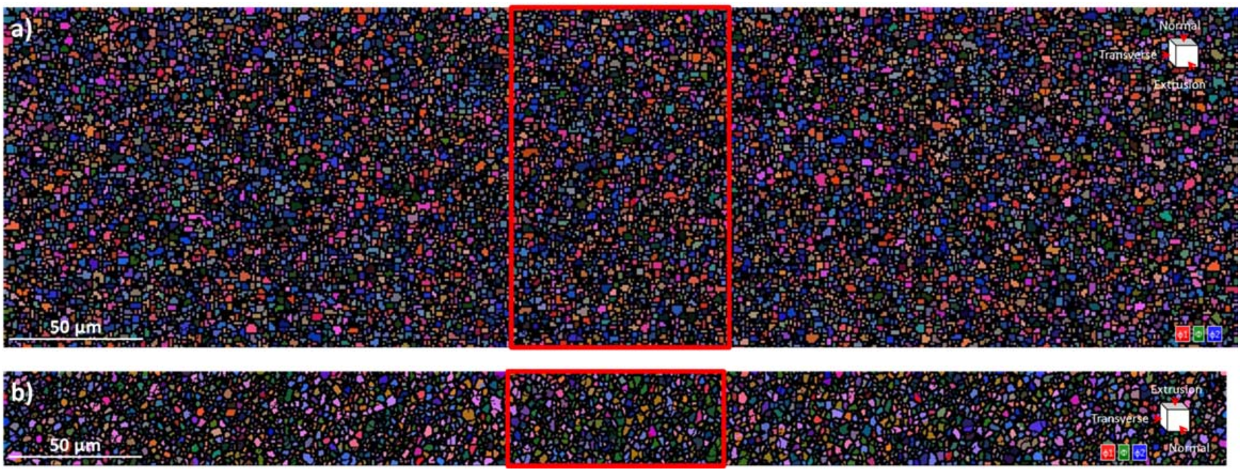

Figure 3-27: EBSD maps of SF2 showing the a) extrusion direction, showing no distinct change in grain structure over the Cu and Zn rich region highlighted. b) normal direction showing no distinct change in grain structure over the Cu and Zn rich region highlighted.

EBSD shows that SF2 had a very fine grain structure. Figure 3-28 a shows the grain structure in the normal direction taken from the Cu and Zn rich region, whereas Figure 3-28 b shows an EBSD map taken from a region to the side of the Cu and Zn rich region in the normal direction. Visually there was no strong correlation to say that there was any difference in the grain structure, however, as highlighted in Figure 3-25 there was a difference in chemical composition of the Cu and Zn rich region. 75 % of the grains in the normal direction were ~ 3 μm^2. Some were seen to be larger than this, with some having areas of ~ 20 μm^2, however, these were rare instances and in fact are likely to be multiple grains close together where the HKL software cannot determine a GB. Examination of the transverse direction, as seen in Figure 3-28 c, once again shows a very fine grain structure from which data show a slightly smaller overall grain size of ~ 2 μm^2. The extrusion direction showed that no real difference can be identified between the Cu and Zn rich structure shown in Figure 3-28 d and the denuded regions, shown in Figure 3-28 e. Figure 3-28 f highlights the surface zone taken from the extrusion direction and highlights the region where the Cu and Zn rich structure was located. This EBSD map tends to suggest a finer grain structure at the periphery of the Cu and Zn rich region, but this was not observed in all locations. Towards the surface zone, no coarse recrystallised grains were observed, but this was to be expected from the spray forming technique.

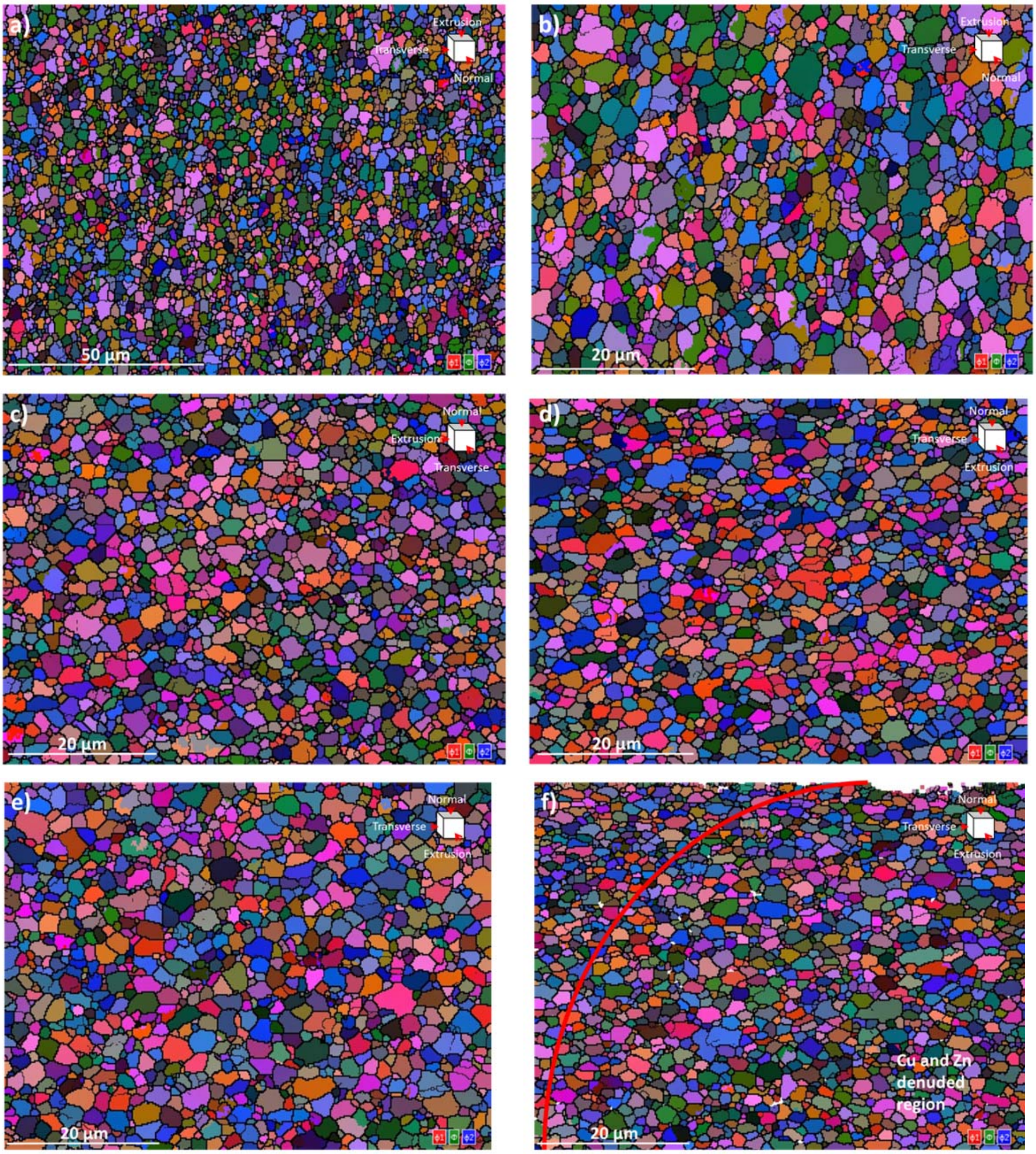

Figure 3-28: EBSD maps of SF2 showing the a) normal direction looking at the Cu and Zn rich structure. b) normal direction looking at the regions either side of the weld. c) transverse direction. d) extrusion direction looking at the Cu and Zn rich structure. e) extrusion direction looking at the regions either side of the weld. f) extrusion direction looking at the surface locations, highlighting the Cu and Zn rich region.

3.3 Summary

This section will offer a theoretical examination of how this authors predicts each alloy will perform with regards to corrosion resistance.

3.3.1 Al-Cu alloys

The Al-Cu alloys showed significant difference between each of the Al alloys to be examined. Noticeable differences in IMC V_f, IMC size and grain size were recorded. Similar IMC types were, however, observed. The Al-Cu-Li alloys did show evidence of T type phases throughout the matrix as well as at the GBs in Cu2. With reference to literature [30–32], this characterisation suggests that all 3 of these Al-Cu alloys will be susceptible to IGC, due to the high V_f of particles at the GBs primarily in the form of the θ type phase, however, Cu2 showed evidence of T type phase segregation at the GB also. It is also suggested that in Cu1 and Cu3 large numbers of galvanic cells will form around the IMCs, however, in Cu2 the IMCs are much finer and are at a much lower V_f and as such may not pose as much of an issue with regards to corrosion. However, it has been shown that most of the elements present within the typical IMCs and precipitates within all three Al-Cu alloys are cathodic in nature, however, the Li and Mg containing particles will be more anodic to the Al matrix. Literature suggests that Cu2 and Cu3 may be subject to selective grain dissolution due to the presence of the T type phases within the grain matrix [30–32], [46], [113–115]. The presence of Al-Cu-Mg IMCs within Cu1 shows that Cu1 will be highly active due to the high V_f of cathodic IMCs and precipitates within the matrix and on the GBs [24–26], [29–32]. It is thought that Cu1 may have the worst corrosion resistance out of the 3 Al-Cu alloys, however, an understanding of how detrimental the Li additions are on Al-Cu will decide the findings. Finer grain structures have been shown in literature [71], [72], [74] to show a higher resistance to corrosion and the current investigations will be able to directly compare the impact of a coarse grain structure versus a fine grain structure. *Pasang et al.* [44], however, stated that elongated grain structures had increased susceptibility to IGC and as such Cu3 may be highly sensitive to IGC. The impact of surface recrystallised grain structures will also be examined since all of the Al-Cu alloys show evidence of differing thickness of coarse grain structures at their surface regions. Cu2 also shows a very coarse recrystallised region on top of a very fine grain structure, so a direct comparison on the same Al alloy can take place.

3.3.2 Al-Mg alloys

The Al-Mg alloys showed significant difference between each of the Al alloys to be examined. Noticeable differences in IMC V_f, IMC size and grain size were recorded. Similar IMC types were, however, observed. The SF alloys showed a very low V_f of Al-Mg-Si and Al-Mg-Si-Fe IMCs, compared to Mg1 which showed a much larger V_f of coarse IMCs. Mg1 showed Al-Fe-Mn-Mg-Si, Al-Mg-Si and Al-Mn-Si. FEGTEM was only conducted on Mg1, for which no evidence of GB particles was observed, so no IGC should be observed on Mg1. However, SF1 and SF2 could form IGC, especially SF2 with the presence of Cu within its Cu and Zn rich region [19], [28]. There is also the likelihood of β phase and Al_3MgLi formation in these alloys, especially since Mg and Si appear to be the main constituent elements within the IMCs [5], [32], [38].

The presence of cathodic elements within the IMCs does, however, show that all of the Al-Mg alloys will be susceptible to pitting corrosion and galvanic corrosion surrounding the IMCs. Since the V_f of IMCs is much less and the IMCs are much finer in the SF alloys, they could show higher corrosion resistances which agrees with what literature suggests for SF alloys [28], [93], [130], [131], [135]. Finer grain structures have also been shown in literature [71], [72], [74] to show a higher resistance to corrosion and the current investigations have been able to directly compare the impact of a coarse grain structure (Mg1) versus a fine grain structure (SF1 and SF2).

Atmospheric corrosion is based around thin film electrolytes and as such can offer a comparison to corrosion morphologies of those experiments utilising immersed samples. This study will allow the Al alloys under investigation to corrode at a rate governed by the Al alloy constituents and atmospheric pollutants, not laboratory grade electrolytes. One note that must be made is that studying atmospheric corrosion is difficult as there are a lot of uncontrolled parameters including pollutant deposition rates. Rain can also wash away corrosion products and pollutants at different rates, which means that each new batch of samples at a different exposure time could be classed as independent studies.

As stated in Chapter 2, samples were exposed for 12 months in a rural / urban environment in Loughborough, United Kingdom. Loughborough's proximity to major transport links; motor vehicles (< 1 mile) and aircraft (< 7 mile) as well as a coal fired power station (< 10 mile) will be considered in this analysis. For thoroughness, information from Loughborough University, Department of Geography's meteorological office allowed a timeline showing the average weather conditions between January 2013 and December 2014 to be collated (see Figure 4-1).

This chapter will therefore discuss each Al alloy investigated and the change in the corrosion mechanisms and structure over 12 months of exposure. The structure of this chapter will be broken down into two sections; atmospheric corrosion on Al-Cu series Al alloys, atmospheric corrosion on Al-Mg series Al alloys which both include comparative discussions. The Appendix shows additional data relating to the change in chemical composition over the 12 month exposure period for each Al alloys.

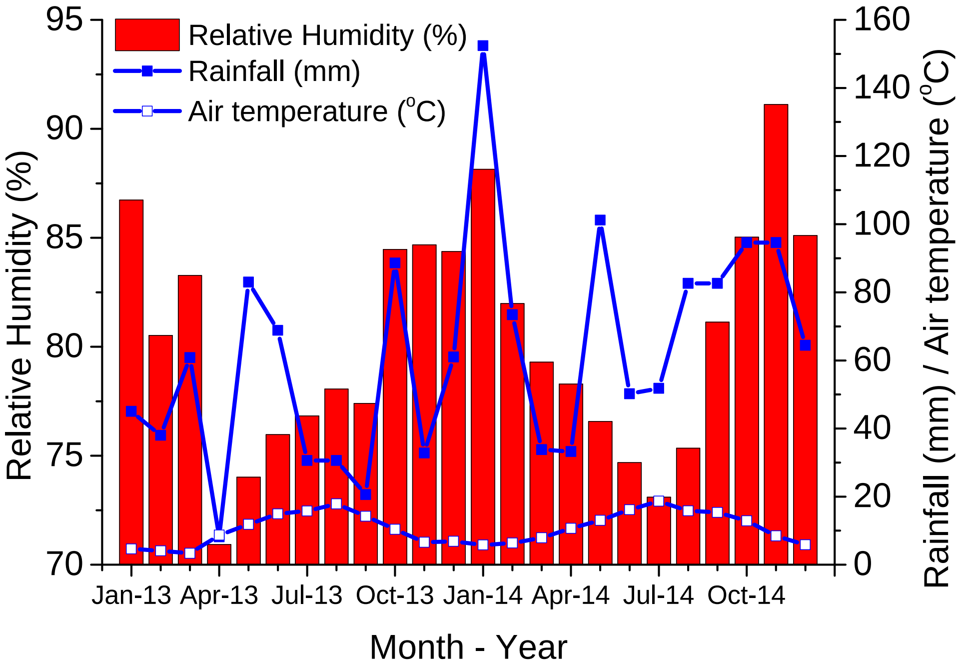

Figure 4-1: Meteorological data for Loughborough University showing a comparison between average relative humidity, air temperature and total rainfall between January 2013 and December 2014 [151].

4.1 Atmospheric corrosion of Al-Cu alloys

4.1.1 AA2024-T3 (Cu1)

Figure 4-2 a, b, c and d show an visual increase in the amount of corrosion products seen on the surface of Cu1 following 1, 3, 6 and 12 months respectively. These micrographs along with others in this thesis were used to give a visual indication of how much corrosion product had formed, in that the higher the volume the greater the amount of dissolution and corrosion that had taken place. With increasing time, outlines from where a thin H_2O film had initiated corrosion can be seen, as shown by Figure 4-2 c. When surface H_2O is present it allows the transfer of electrons and ions. Oxygen is readily supplied from the atmosphere to these thin films of H_2O. This process can initiate pitting corrosion, by nucleating around a defective site such as an IMC, which causes galvanic cells to form allowing free Al electrons to be released into the solution. The H_2O reacts with these free Al electrons generated from the dissolution of the Al anode, forming $Al(OH)_3$ / AlO(OH) corrosion products. When H_2O is split, the H^+ flows into a pit, creating a highly acidic region over time, which can draw in other pollutant elements in, such as Cl^- and at a certain pH, H_2 evolution will take place [19].

Other pollutants such as SO_x, O_x and NO_x can also be absorbed into the thin film of H_2O [67]. Literature has also shown that in the presence of these thin films certain compounds will develop, an example being the formation of H_2SO_4, from the breakdown of SO_2 within the H_2O [12], [126]. As such highly acidic or alkaline solutions can be made, which accelerate the rate of corrosion. Figure 4-2 d shows as time increased the corrosion products started to form plate-like structures, showing the formation of a thick corrosion product starting to crack from residual stresses [128].

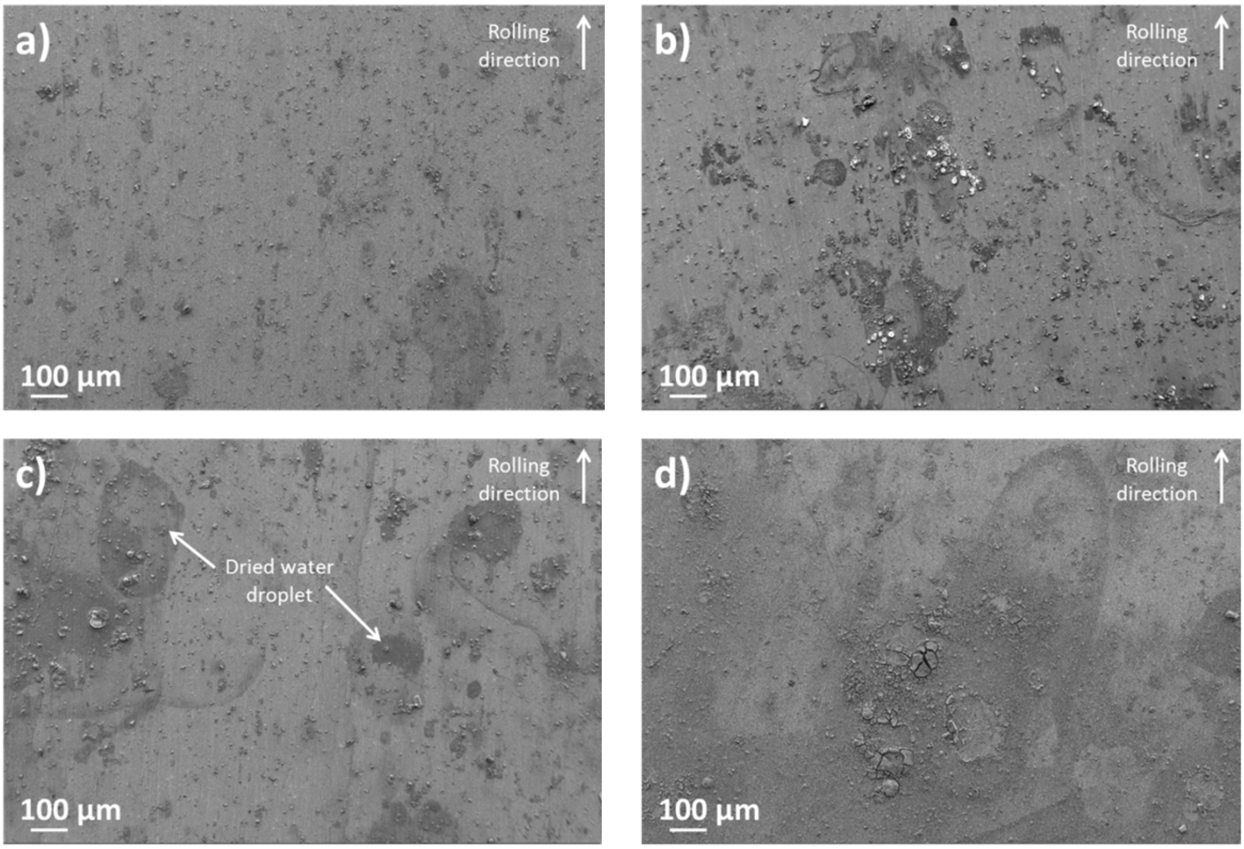

Figure 4-2: SEM micrograph of Cu1 showing the build-up of corrosion products and pollutants after a) 1 month b) 3 months c) 6 months and d) 12 months of atmospheric exposure.

High volumes of corrosion products were observed, alongside evidence of galvanic corrosion surrounding IMCs as well as IGC and pit initiation, as shown in Figure 4-3 a. Figure 4-3 b shows the formation of circular corrosion products, formed from where a thin film of H_2O has initiated corrosion, leading to the likely formation of $Al(OH)_3$ / $AlO(OH)$ [19]. The IMCs within the thin film underwent redox reactions which EDS showed an increase in O content at ~ 20 at.% compared to ~ 8 at.% outside of the thin H_2O film region. Figure 4-3 b shows evidence of pit and IGC initiation forming from where a thin film was situated. Pitting corrosion was observed outside of these thin H_2O film regions, primarily from where H_2O had initiated corrosion but, due to atmospheric conditions, the electrolyte was removed, stopping / reducing the rate of corrosion. TOW therefore shows a direct impact on corrosion with a reduced TOW showing limited corrosion developing [67]. As time increased the number of circular corrosion product sites also increased and it can be concluded that the reason for this is due to a higher surface roughness and surface energy from the corrosion products that restricted H_2O run-off. Figure 4-3 c shows a cathodic IMC where a mossy / needle like corrosion product has formed. Cross-sections of the specimens showed that after 6 months of exposure IGC and pitting corrosion can be seen and the pit depth, as shown in Figure 4-3 d was < 10 µm.

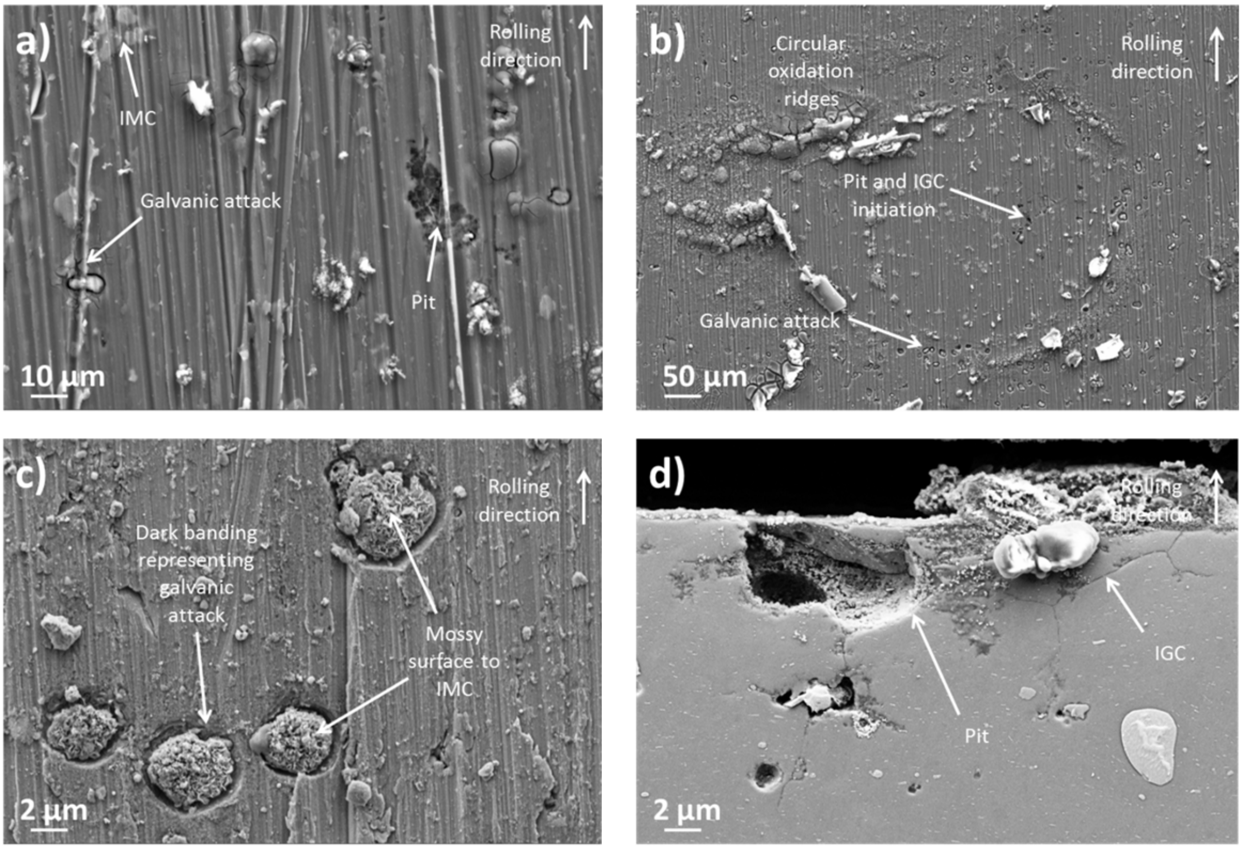

Figure 4-3: SEM micrographs of Cu1 after a) 1 month of atmospheric exposure, showing pit initiation sites and galvanic corrosion surrounding IMCs. b) 3 months of atmospheric exposure, showing galvanic corrosion of IMCs outside of a circular corrosion product region, whereas IGC and pitting corrosion are within the circular corrosion region. c) 3 months of atmospheric exposure, showing galvanic corrosion surrounding IMCs and a mossy corrosion on surface of IMCs. d) Cross-sectional micrograph showing pitting and IGC after 6 months of atmospheric exposure.

Figure 4-4 a and b show cross-sectional micrographs in the extrusion direction and Figure 4-4 c and d show cross-sectional micrographs in the transverse direction following 12 months of atmospheric exposure on Cu1. The progression of corrosion from 6 to 12 months has accelerated with most pits being > 10 µm and some ~ 20 µm. IGC, however, appears to have progressed much further than pitting corrosion with some regions showing IGC at ~ 45 µm depth. *Knight et al.* [124] observed AA2024 under atmospheric conditions and also showed that the IGC progressed further into the specimens than pitting corrosion. Figure 4-4 a and b demonstrate how IMCs are heavily associated with pitting corrosion and IGC. Due to the susceptibility of Cu1 to IGC it can also be concluded that the θ type phase on the GBs, as shown in Section 3.1.1 are detrimental to corrosion and that the fine equiaxed grain structure allows for easy path propagation of IGC [18], [24–26], [60], [63], [80]. Figure 4-2 a, b, c and d, did not suggest a high corrosion depth, however, Figure 4-4 shows that corrosion can progress very deep into a sample from a very small pit opening (most being < 5 µm and the maximum seen at 10 µm). Most of the corrosion was seen to develop from IGC, progressing from the surface, generating sub-surface corrosion. This shows that systems prone to IGC have a reduced corrosion resistance due to the transfer of electrolyte into the matrix, that can develop sub-surface corrosion [13], [75].

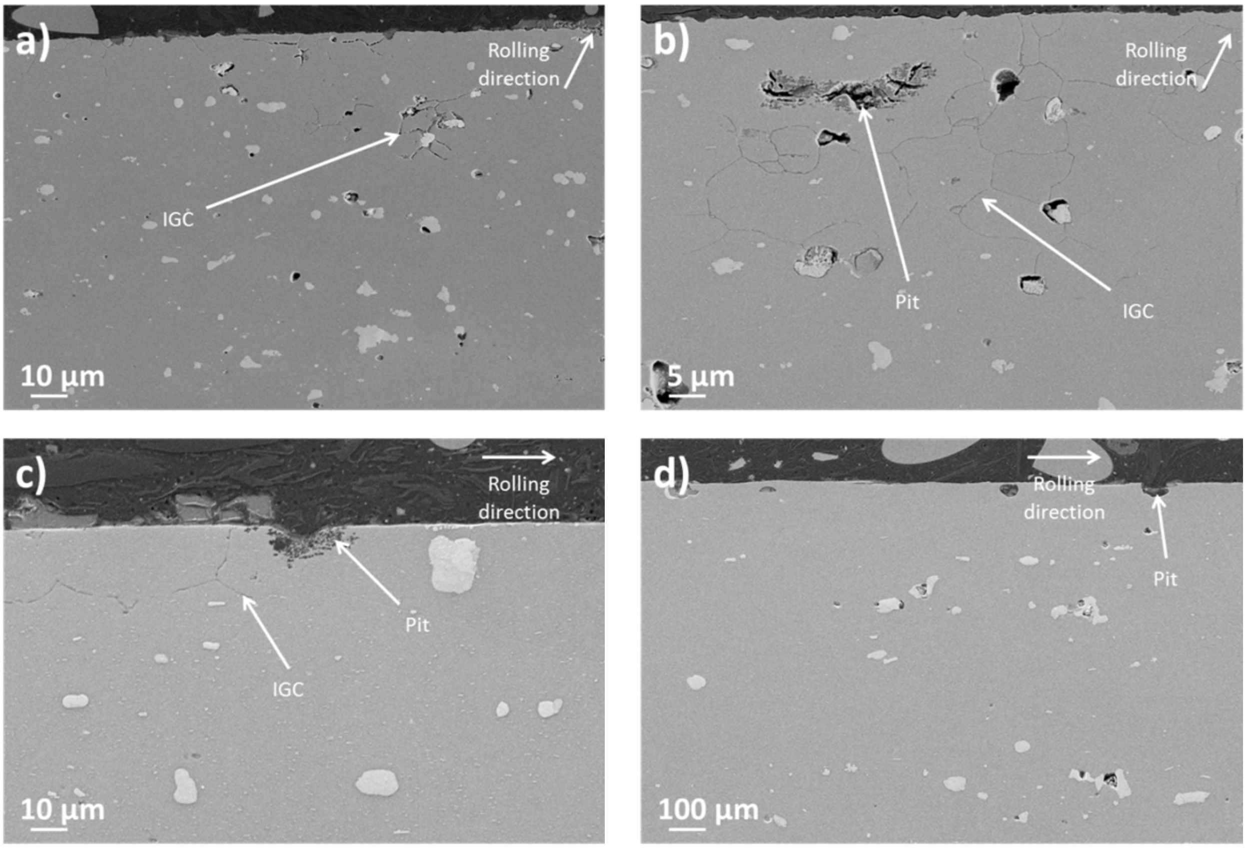

Figure 4-4: Cross-sectional SEM micrographs of Cu1 after 12 months of atmospheric exposure showing evidence a) IGC surrounding IMCs b) IGC and sub-surface pitting corrosion c) IGC and pitting corrosion and d) shallow pitting corrosion.

EDS showed that, with increasing time, the amount of O present on the surface increased from ~ 10 at.% to ~ 25 at.% between 1 and 12 months respectively. Figure 4-5 shows EDS maps of the O distribution over the surface of Cu1 after 1 and 12 months respectively. The rate of increase was relatively steady between 1 and 6 months at ~ 6 at.% and between 6 and 12 months the increase was ~ 9 at.%. Alongside this increase in O was a respective reduction in Al content from ~ 70 at.% to ~ 65 at.% for 1 and 12 months respectively, which is expected with the dissolution of Al into the electrolyte and its formation of oxide and OH^-based corrosion products. The Al:O ratios changed from ~ 6:1 to ~ 3:1 after 12 months. Other elements such as Cu, Mg, Mn and Fe stayed at similar values over the 12 month period with < 1 at.% reduction for each. Approximately 10 at.% of the surface chemistry was associated with pollutants after 12 months, with the remainder being Al and O.

EDS was used to examine the change in corrosion product chemistry over time for which an increase in O content was seen with reducing Al concentration. After 1 month 46 at.% O and 43 at.% Al were observed, compared to 68 at.% O and 22 at.% Al after 12 months. Within this time period the amount of Cu and Mg observed within the corrosion product also reduced. Mg dissolution has been shown in literature to combine with O to form MgO [67] and it is assumed the reduction in Cu content was in relation to the density of the corrosion products. Throughout exposure the concentration of C fluctuated but there was always a presence of S (maximum of 5 at.%) and Cl^- (maximum of 0.5 at.%)

within corrosion sites, suggesting the adsorption of SO_2 and NaCl species, which can accelerate the rate of corrosion [117], [120].

Knight et al. [124] investigated AA2024 and concluded that Cl^- ions promoted pit nucleation, however, the pit propagation was heavily associated with the presence of SO_2 ions. SO_2 ions are primarily found in urban environments and arise from combustion sources, which makes their examination important in this study [67]. The main pollutants said to be present in an urban environments atmosphere are varieties of C, SO_x and NO_x from motor vehicles and fuel emissions combined with dew and H_2O causing aggressive thin films to form [67]. NO_X have been shown to form HNO_3 and SO_X can form H_2SO_4, which creates a reduced pH within the thin films of moisture, accelerating the corrosion [12]. C typically comes from carbonaceous pollutants such as car fumes and have been shown to have an effect on the corrosion rate of Al alloys [126] as it forms carbonaceous Al products .

Figure 4-5: EDS maps showing the increase in O concentration with increasing atmospheric exposure time on Cu1.

Examination of the IMCs revealed that some showed greater dissolution than others. EDS identified that the main IMC types within Cu1 are; Al-Cu-Fe-Mn (Cu-rich and Cu-depleted), Al-Cu-Mg and Al-Cu-Mg-Fe-Mn [26], [60], [80]. Throughout exposure it seems that different IMCs become active with time, in particular, only the Al-Cu-Mg IMCs showed galvanic corrosion after 1 month. Figure 4-3 a shows IMCs which have undergone galvanic corrosion and some that have not. EDS showed that the IMCs that generated galvanic corrosion were more noble and it was also seen that they had an reduced concentration of Mg. Mg rich IMCs, like the Al-Cu-Mg IMCs, show selective dissolution of the less noble Mg compared to the more noble Al and Cu [24], [29], [152]. Fe is also more noble than Al and as such acts in a similar manner to that of Cu, in that it creates cathodic IMCs [60], [63]. Figure 4-6 shows EDS maps demonstrating the distribution of Mg, Fe, Mn and Cu within IMCs in Cu1.

Once the Mg in the Al-Cu-Mg IMCs was dissolved, a highly cathodic Cu rich region is formed, causing accelerated dissolution of the anodic Al matrix, through micro-galvanic cell formation [26]. *Buchheit and Birbilis* [26] showed that phases with a dual polarity, i.e. those than contain anodic and cathodic phases, such as the S and T type phases, undergo selective dissolution. So for the Al-Cu-Mg particles, the Mg is dissolved as it is anodic, this ultimately causes a polarity reversal to take place, with the phase, with time becoming more noble. This has been shown to cause accelerated corrosion around the remnant cathodic particles [24]. The Al-Cu-Fe-Mn (Cu rich) IMCs also showed a high rate of dissolution of the surrounding matrix, due to the presence of highly cathodic Cu, Fe and Mn [26], [60], [80]. The most problematic IMCs were; Al-Cu-Mg and Al-Cu-Fe-Mn (Cu rich), whereas the Al-Cu-Fe-Mn and Al-Cu-Mg-Fe-Mn IMC types showed a higher corrosion resistance (in that less matrix was seen to be dissolved or they dissolved themselves). Literature [24–26] also shows that Al-Cu-Mg IMCs within Cu1 and more noble elements are known to accelerate corrosion.

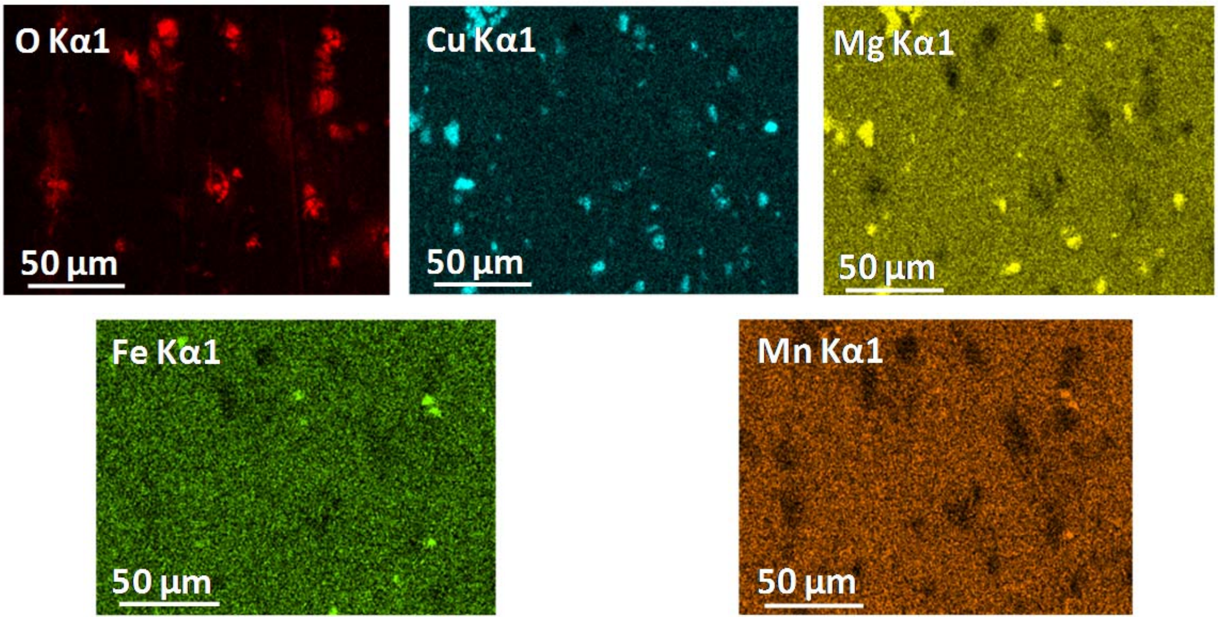

Figure 4-6: EDS maps of IMCs, showing the distribution of IMC elements within Cu1.

Figure 4-7 shows XPS survey spectra taken from each sample after each time interval and shows that overall there are minimal changes in the elemental compositions after exposure. Prior to exposure, high concentrations of Cu (5 at.%), Mg (6 at.%), Al (46 at.%) and O (34 at.%) were observed but no evidence of any other elements. The deposition of so called contaminant elements such as C, Si, S, Na and Cl^- was shown to be irregular, with some months showing evidence of specific compounds and the other months showing no trace. The surveys also showed gradual increases in Na, Cl^-, S, Si and C content with increasing time, alongside reductions in Cu, O and Al. Trace elements of F were measured, however, they were < 1 at.% as such could be deemed to be in error. If they are present then likely they have come from atmospheric emissions associated with the nearby traffic and / or chemical extraction hoods from the department. The total amount of pollutants present after 12 months on Cu1, was seen to be ~ 37 at.%, which is a 10 at.% increase from the first month. The sum of Al and O goes from 81 at.% pre-exposure to 64 at.% after 12 months, with the ratio of Al:O going from ~ 4:3 to ~ 1:3, demonstrating the formation of voluminous corrosion products and increasing deposition of pollutants. Examination of the individual binding energies (BE) also showed that the Al peak is associated to Al_2O_3 pre-exposure at 532 eV, however, after 1 month this changes to ~ 535 eV which is associated with $Al(OH)_3$ / AlO(OH).

The presence of Na, Si and Ca were found by *Knight et al.* [124] to come from airborne soil pollution, once again highlighting the unpredictable nature of atmospheric corrosion. The concern with Na is that it can form NaCl if Cl^- is present, but also Na favours higher pH values at the cathodic sites which causes the dissolution of the passivating alumina film [118].

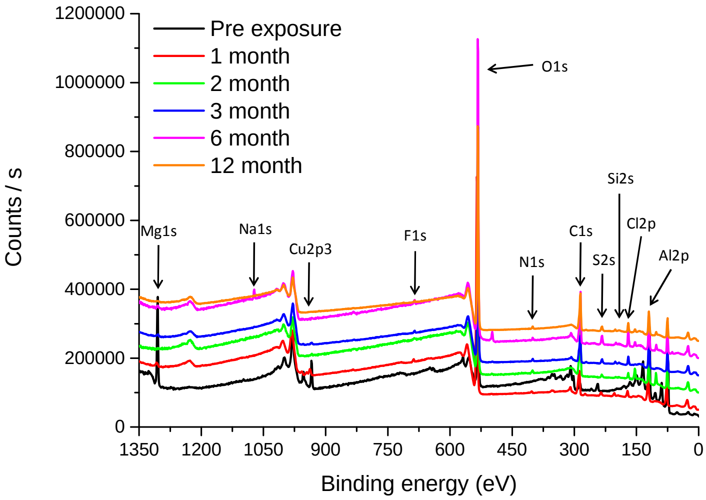

Figure 4-7: XPS survey spectra of Cu1 over a 12 month atmospheric exposure, showing changes in elemental constituents with time.

High resolution analysis of the Al peak showed that after 1 month, ~ 3 at.% Al metal (m) could be identified with 19 at.% Al oxide (ox), as shown in Figure 4-8. After 3 months no Al (m) could be identified and only Al (ox) was present. This is to be expected as the metallic Al is dissolved to become part of the corrosion products. Interestingly as time increased, the O content on the surface seemed to remain stable, but the amount of Al (ox) reduced. This was due to a higher concentration of other pollutants such as C, F, N, Si, S, Na and Cl^-. The reduction in Al (ox) was associated with an increase in C from 16 to 24 at.% from 1 to 12 months respective, which is likely to be from the formation of carbonaceous Al products. High resolution XPS also showed that S, Si, and Cl^- concentrations showed minimal increases with time with the maximum of each being seen at 3.1 at.%, 1.5 at.% and 1.2 at.% respective. Even though Na was seen this was only on the 2 and 6 month samples. Na and Cl are most likely a compound in the form of NaCl which will accelerate the rate of corrosion and likely to have been deposited by road salts. Since S was not present in any of the characterised IMCs within Cu1 it has to be assumed it was deposited from an atmospheric source, most likely SO_2 and or SO_4^{2-} from combustion sources. Approximately 6 at.% of the surface after 12 months was surface pollutants, excluding 24 at.% C and 51 at.% O, thus 81 at.% of the surface elements were from corrosion products.

Vera et al. [122] stated that Cl^- also affected the corrosion products by making them less compact and more H_2O soluble. Typically the corrosion products that form have been seen by authors rupture into plates over time [128] and in most cases this is what was seen to take place on all of the Al alloys investigated in this thesis. Those environments rich in Cl^- ions generate the most corrosion and form thicker, more stable corrosion products, highlighting a difference in the corrosion nature of a specimen exposed to marine and industrial environments.

SO_2 ions are highly soluble in H_2O and as such reduce at cathodic sites, increasing the potential between anodic and cathodic zones. This in turn accelerates the rate of anodic dissolution. SO_2 is a specific ion that can be selectively absorbed on Al surfaces and under humid conditions the metal oxide surface can catalyse the SO_2 into SO_3 promoting the formation of H_2SO_4. The H_2SO_4 can then react with the $Al(OH)_3$ / AlO(OH) forming hydrated $Al_2(SO_4)_3$ [126]. As such regions with high levels of SO_2 are highly acidic and can lead to high levels of corrosion, mainly through the quick breakdown of passive layers but also forming soluble corrosion products [117], [120].

Yao et al. [128] showed via XPS that the main pollutant being deposited on atmospheric samples of Al was S, primarily from SO_2 but also from SO^{2-}_4 and *Syed et al.* [67] also stated that the typical corrosion products that form in urban environments were rich in $Al_2(SO_4)_3$ and hydrated $Al_2(SO_4)_3$. From XPS analysis of this work it could be said that these compounds also formed on the specimens investigated at Loughborough, with SO_4^{2-}, Al_2O_3, carbonaceous Al products and OH^- all being identified.

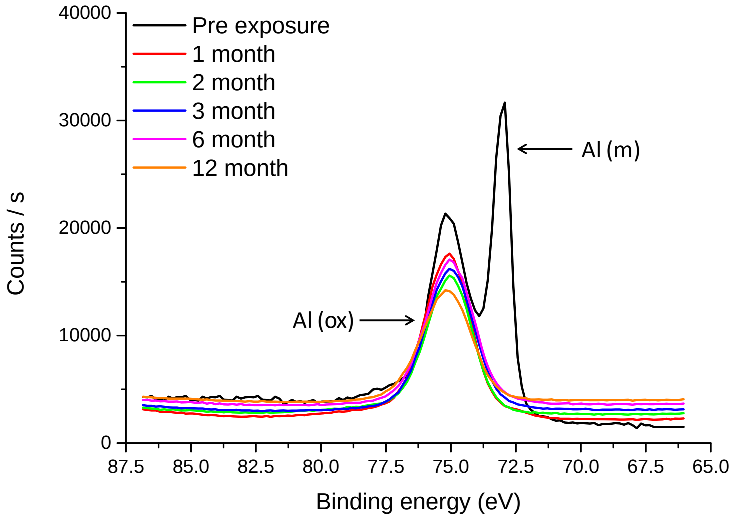

Figure 4-8: XPS spectra showing the Al2p metal and oxide peaks over a 12 month atmospheric exposure of Cu1, highlighting the rate of change from Al (m) to Al (ox).

4.1.2 AA2099-T8E77 extrusion (Cu2)

Visual observations of Cu2 following atmospheric exposure showed that, with increasing time, a higher concentration of corrosion products formed, however, the volume observed was not very substantial. No 12 month samples were examined for Cu2. Figure 4-9 a, b and c demonstrate the amount of pollutants and corrosion products seen on Cu2 following 1, 3 and 6 months respectively. Regions where thin H_2O films have initiated corrosion can also be observed, as detailed in Figure 4-9 c. The corrosion products observed also started to form plate like structures [128] and with the low volume of corrosion products it is expected that large amounts of H_2O run-off could occur, reducing the concentration of electrolytes and potentially the volume of corrosion products [119]. This washing action not only removes any loose corrosion product, but it also dilutes any acidic or alkaline regions on the specimens, reducing or neutralising the corrosion.

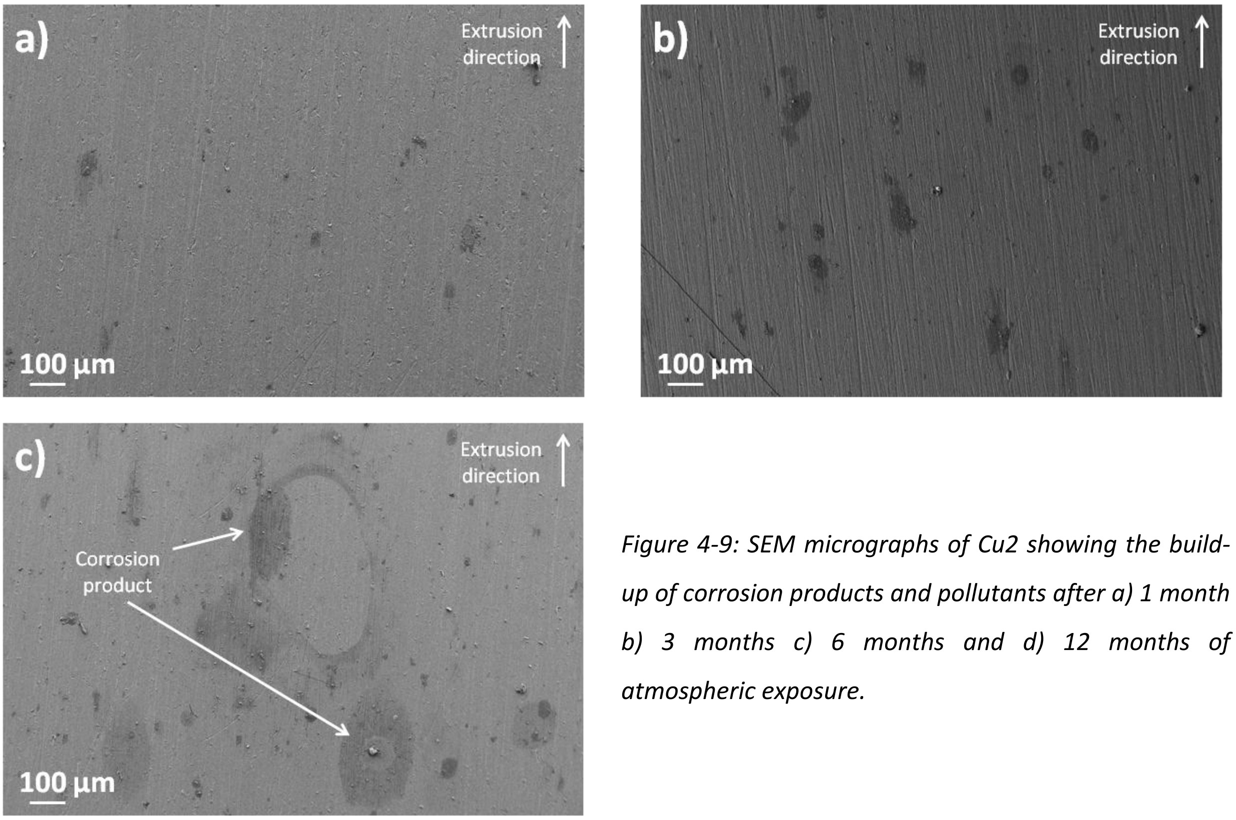

Figure 4-9: SEM micrographs of Cu2 showing the build-up of corrosion products and pollutants after a) 1 month b) 3 months c) 6 months and d) 12 months of atmospheric exposure.

Evidence of galvanic corrosion surrounding IMCs was seen after 1 month of exposure, as shown in Figure 4-10 a. This shows that the IMCs are cathodic in nature [26], [60], [80], however, no pit initiation or IGC sites were seen to develop within a close proximity, which suggests that a large V_f of IMCs are required to generate large scale pitting corrosion. Figure 4-10 b and c show the formation of circular corrosion products, which appeared on samples after 3 months of exposure, however, little evidence of corrosion propagation, was observed. This shows that it took 3 months for enough corrosion product to develop to allow H_2O to become trapped on the surface, suggesting a slow rate of corrosion. Some fine scale pits were seen in Figure 4-10 b, which were < 10 µm wide. This suggests that Cu2 has a very high resistance to corrosion, with very little corrosion being observed even after 6 months of exposure.

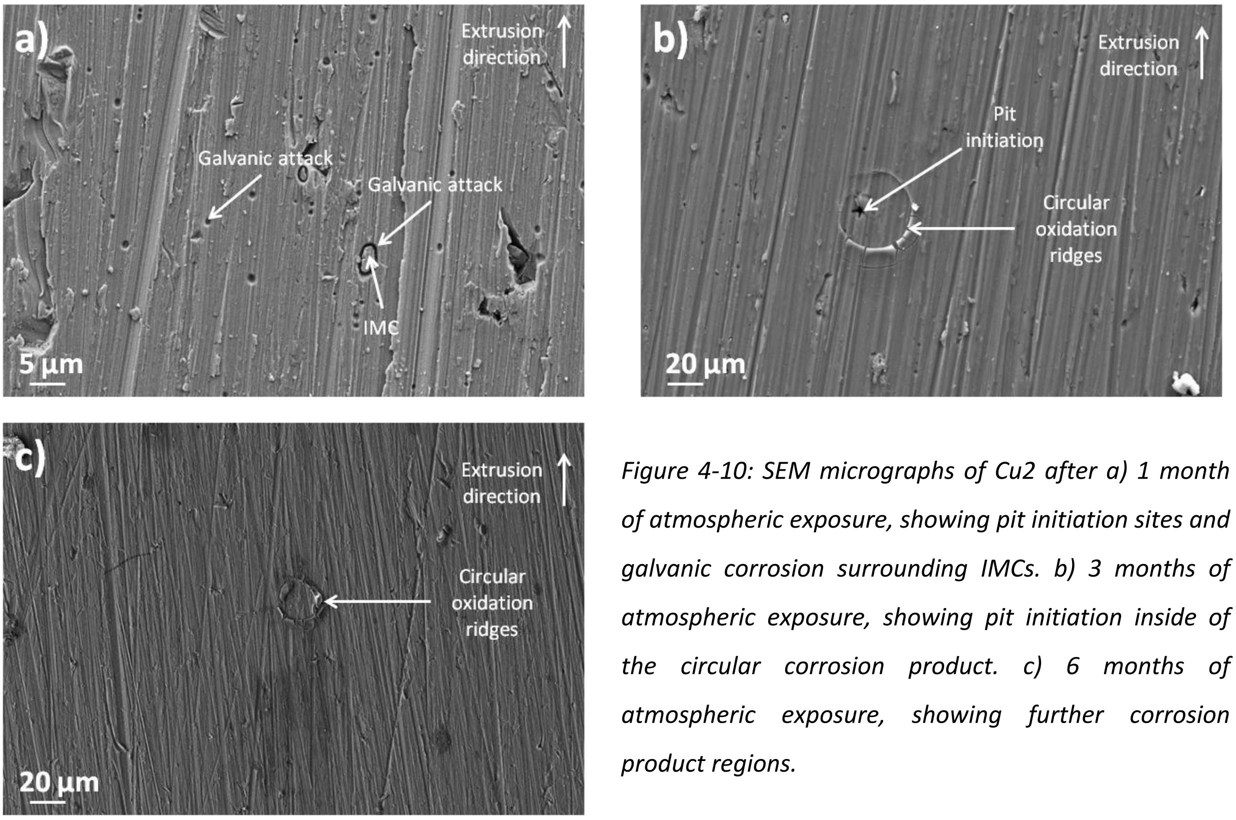

Figure 4-10: SEM micrographs of Cu2 after a) 1 month of atmospheric exposure, showing pit initiation sites and galvanic corrosion surrounding IMCs. b) 3 months of atmospheric exposure, showing pit initiation inside of the circular corrosion product. c) 6 months of atmospheric exposure, showing further corrosion product regions.

Figure 4-11 a and b show cross-sectional micrographs of the extrusion direction and Figure 4-11 c and d show cross-sectional micrographs of the transverse direction in Cu2. It can be seen that they all show evidence of pitting, selective grain dissolution and IGC after 6 months of exposure. Figure 4-11 a shows evidence of multiple fine scale pits and IGC within the matrix. The pit depths as shown in Figure 4-11 b and c are between 20 and 30 µm. Figure 4-11 d shows IGC, demonstrating that Cu2 is prone to IGC but it does not appear that Cu2 is as susceptible to IGC as it is to pitting corrosion. This was interesting as FEGTEM showed evidence of θ and T type phases around the GBs, which are noted in literature to reduce the corrosion resistance [31], [32], [46], [113–116]. The θ type phase is more noble, thus cathodic to the Al matrix, whereas the T type phase is less noble, thus anodic.

Buchheit and Birbilis [26] showed that phases with a dual polarity, i.e. those than contain anodic and cathodic elements, undergo selective dissolution. The T type phase has been shown to act in the same manner as the Al-Cu-Mg IMCs, in that the Li is dissolved as it is anodic, causing a polarity reversal. This has been shown to cause accelerated corrosion around the remnant cathodic particles [24], [29], [31], [32], [152]. The presence of both highly anodic and cathodic elements at the GBs may be the reason for the reduced propagation. This offers an inherent level of corrosion resistance, however, with time once the Li is dissolved, highly cathodic Cu rich regions are formed, accelerating the corrosion of the surrounding matrix.

Some of the corrosion observed was in the form of selective grain dissolution, with Figure 4-11 b showing the corrosion encapsulates an entire grain but does not appear to progress across the GB. This selective grain dissolution has been noted in literature to form on Al-Cu-Li alloys and has been shown to be associated with the concentration of the T type phase within specific grains [31], [32], [46], [113–116]. T type phases also has a tendency to precipitate to the GB, however, heat treatments have been able to re-position these back into the grain, but this then alters the potential of the grain instead of the GB, which ultimately leads to one grain being more anodic / cathodic than one of its neighbours and selective grain dissolution occurs [4]. This allows the corrosion to be extensive, with the corrosion seen on Figure 4-11 b being ~ 30 µm deep at its maximum but over 100 µm wide. Cu2 was shown to have a > 100 µm coarse recrystallised grain structure and the size of the grain corroding in Figure 4-11 b would suggest this is such a region. Most of the pitting corrosion observed, however, was closer to that seen in Figure 4-11 c and d, where the pit depth and width were relatively shallow. These smaller pits are related to the fine grain structure regions, whereas the selective grain dissolution is more associated with coarse grain structures, suggesting a fine grain structure has a higher corrosion resistance [71], [72], [74]. The main concern is that these large selectively dissolved grains are not present on the surface and observations suggest that most of the corrosion is taking place sub-surface.

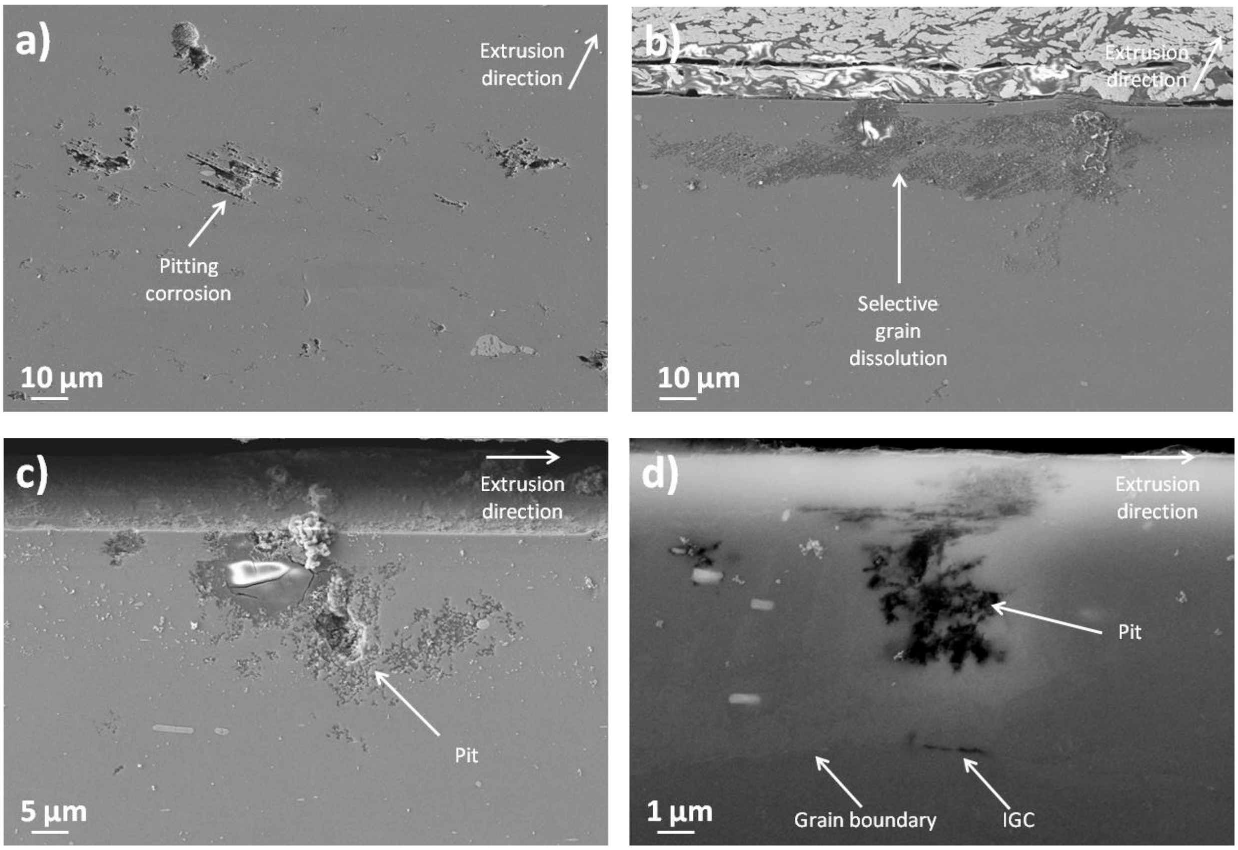

Figure 4-11: Cross-sectional SEM micrographs of Cu2 after 6 months of atmospheric exposure showing evidence of a) pitting corrosion and selective grain dissolution. b) selective grain dissolution in the form of selective grain corrosion. c) pitting corrosion. d) pitting and IGC along a recrystallised GB.

EDS analysis showed that with increasing exposure time the amount of O present on the surface increased from ~ 2 to ~ 4 at.% between 1 and 6 months. Figure 4-12 shows EDS maps demonstrating the distribution of O content on the surface after 1 and 6 months respectively. A high concentration of O was seen after 2 month at 11 at.%, however, this was seen to reduce to 4 at.% a month later. This shows the impact that the atmosphere can have, in that the corrosion products were removed from the surface, most likely by washing. This suggests that the corrosion products were highly soluble, since they were removed so easily and it has been shown that some elements, mainly S and Cl^-, can increase the solubility of corrosion products [117], [120]. The rate the O increased was very slow and lower than expected, likely due to the expected poor corrosion resistance of Al-Cu-Li alloys [2], [4], [44], [48]. This could be related to the selective dissolution of the Li containing phases, reducing the amount of Al oxides being produced. The Al:O ratios were seen to go from ~ 20:1 to ~ 17:1 after 6 months, highlighting the slow formation of corrosion products. This meant that ~ 25 at.% of the surface chemistry was attributable to surface pollutants, which was comprised of primarily C. This increase in pollutants can cause localised acidic / alkaline electrolytes that can accelerate corrosion [19], [39], [63], [86].

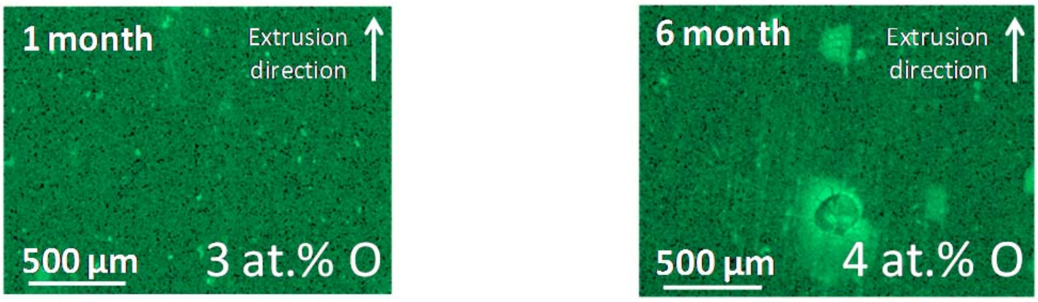

Figure 4-12: EDS maps showing the increase in O concentration with increasing atmospheric exposure time on Cu2.

EDS of the corrosion products showed no trace of C on the 1 and 2 month samples, however, for the 3 and 6 month samples C was observed at 78 and 43 at.% respectively, showing considerable formation of carbonaceous Al products. This suggests that some form of considerable pollution of the surface has taken place, most likely associated with the TOW that causes the increased level of measured pollutants. The corrosion product chemistries from 1 and 6 months show a reduction in Al (25 and 16 at.% respectively) and O (71 at.% to 38 at.% respectively) with increasing pollutant concentrations, however, the values of data taken from 2 and 3 months do not fit any trend due to large pollutant anomalies. Other elements identified to be present within the corrosion product were Si, S and Cl^- and can be seen in the EDS maps of Figure 4-13 [67].

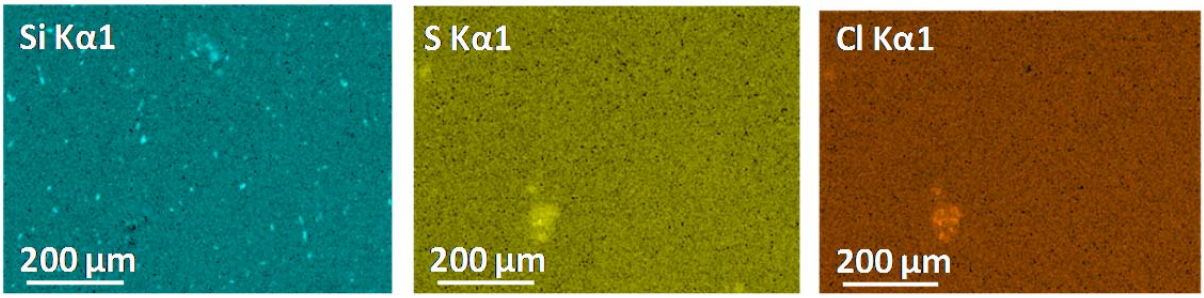

Figure 4-13: EDS maps showing the concentration of Si, S and Cl^- on corrosion products present on the surface of Cu2 after 6 months of atmospheric exposure.

The main IMC types in Cu2 are; Al-Cu-Fe-Mn and Al-Cu-Mn. The main IMCs of concern are Al-Cu-Fe-Mn, which shows higher dissolution of the matrix compared to the Al-Cu-Mn particles [18], [24–26], [60], [63], [80]. Theory states that Cu and Fe in particular are detrimental to the corrosion resistance of Al alloys [19], [27], [60], [63] because they are more noble. These elements force the surrounding Al matrix to be anodic, accelerating the galvanic corrosion effect and increasing the localised pH. EDS shows that from prior to 6 months of exposure, the Al, Cu, Fe and Mn content of each of these particles reduces alongside an increase in O, which is expected through the formation of a corrosion product at the IMCs.

Figure 4-14 demonstrated that there was not a considerable increase in the number of pollutants with time. Most were present from the first month, however, some were seen to increase substantially after 6 months, mainly S1s and Na1s peaks. This increase after 6 months showed that TOW impacts on atmospheric corrosion. The Al and O contents reduced with increasing time; however, C, Na, S, Si and Cl^- were all seen to increase, demonstrating an increase in Al (ox) and surface pollutants deposited with time. The sum of Al and O went from 92 at.% to 56 at.% after 6 months, with the ratio of Al:O changing from ~ 2:1 to ~ 1:3 after 6 months, demonstrating the formation of corrosion products. Examination showed that the Al peak shifted, demonstrating the hydration of the Al. The concentration of pollutants within the corrosion products was measured to be ~ 44 at.% of which 29 at.% was C and 15 at.% was SO_x, NO_x and NaCl compounds.

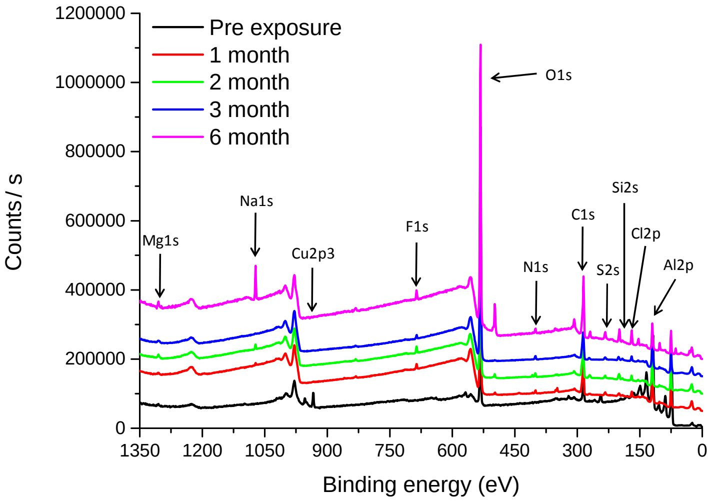

Figure 4-14: XPS survey spectra of Cu2 over a 6 month atmospheric exposure, showing changes in elemental constituents with time.

High resolution analysis of the Al peak showed that over the 6 month period an Al (m) peak could be identified at each time interval. After 6 months, however, the Al (m) peak had a concentration of < 0.5 at.%, so it could be argued that no Al (m) was observed after 6 months of atmospheric exposure. After 3 months the Al (m) content was seen to be ~ 3 at.% alongside 22 at.% Al (ox). Figure 4-15 shows the rate of change from Al (m) to Al (ox) for Cu2. The Al (m) content showed a 1 at.% reduction from 1 to 3 months, however, the Al (ox) showed a significant increase from 9 to 22 at.%. This agrees with the XPS survey spectra and EDS, highlighting the transformation of metallic Al to Al based corrosion products.

XPS also revealed that there was a trend between the reduction in Al and O, with increasing pollutants. The Al (ox) content reduced after 3 months, corresponding to a reduction in O content (55 to 44 at.% between 1 and 6 months respectively). These reductions do, however, correspond to an increase in pollutant concentrations, especially C, which increased as the Al (ox) reduced. One item of concern was with the increasing concentration of Si, N, S, Na and Cl^- concentrations. Increasing the number of pollutants in a thin H_2O film will increase the amount of elements using O to form compounds, which may explain the reduction in Al (ox) concentration via masking. Thus NaCl, SO_4^{2-}, NO_{3-}, NO_x and / or SO_x are being adsorbed onto the surface of Cu2 [125]. Approximately 85 at.% of the surface elements were from corrosion products, of which 45 at.% was O.

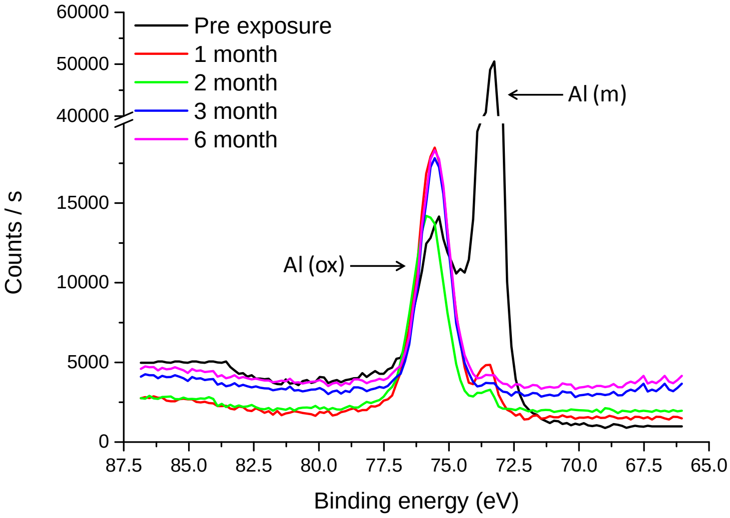

Figure 4-15: XPS spectra showing Al2p metal and oxide peaks over a 6 month atmospheric exposure of Cu2, highlighting the rate of change from Al (m) to Al (ox).

4.1.3 AA2099-T8E77 plate (Cu3)

Figure 4-16 a, b, c and d show the amount of corrosion products seen on Cu3 following 1, 3, 6 and 12 months respectively. Regions where thin H_2O films have initiated corrosion were seen, but primarily only on samples after 12 months as detailed in Figure 4-16 d. Figure 4-16 shows that the amount of corrosion products on the surface was minimal, as typically corrosion products increase the surface roughness, inhibiting H_2O runoff, suggesting a high corrosion resistance. Figure 4-16 c is a good example of how atmospheric corrosion cannot be predicted, in that contaminants from the atmosphere can deposit onto the surface in a very un-controlled manner. Figure 4-16 c in particular shows deposition of some foreign material, which would not happen in controlled electrochemical testing.

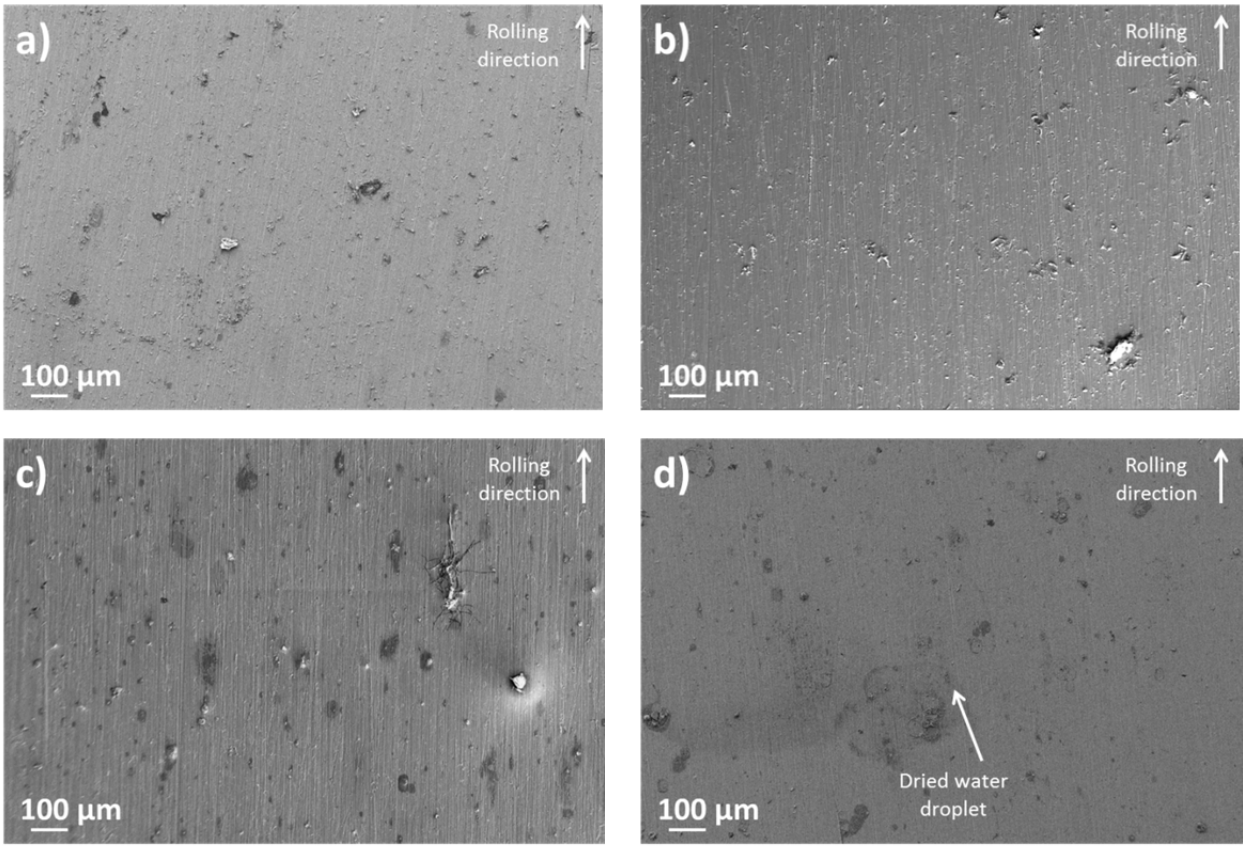

Figure 4-16: SEM micrographs of Cu3 showing the build-up of corrosion products and pollutants after a) 1 month b) 3 months c) 6 months and d) 12 months of atmospheric exposure.

Cu3 showed that after 2 months, pit initiation could be identified, as shown in Figure 4-17 a. After 1 month ruptured plate-like corrosion products were observed, however, no pitting corrosion could be located beneath them [128]. The progression of the corrosion did not increase as expected with time, in that after 12 months similar surface features could be seen as those after 1 month, suggesting a higher corrosion resistance. Cross-sectioning after 6 months revealed that corrosion can initiate at defective surface sites, with Figure 4-17 b showing progression of IGC and pitting corrosion, in some cases the IGC was seen to progress to a depth of ~ 70 µm after only 6 months. Even though the corrosion initiated at a surface defect, it shows that the corrosion is progressing in depth more than width, as demonstrated by the < 5 µm pit openings. The size of the pits was also relatively small, as shown in Figure 4-17 c and d, with Figure 4-17 c showing a circular corrosion product forming, where H_2O has created a thin film, from the redox reaction that has taken place [19] and Figure 4-17 d shows the correlation between pitting corrosion and cathodic IMCs [24–26], [60], [63], [80]. At this stage there is nothing to suggest that Li additions have had a negative impact on corrosion [2], [4], [5], [23], [44], [47], [48], with surface observations showing a very limited amount and progression of corrosion.

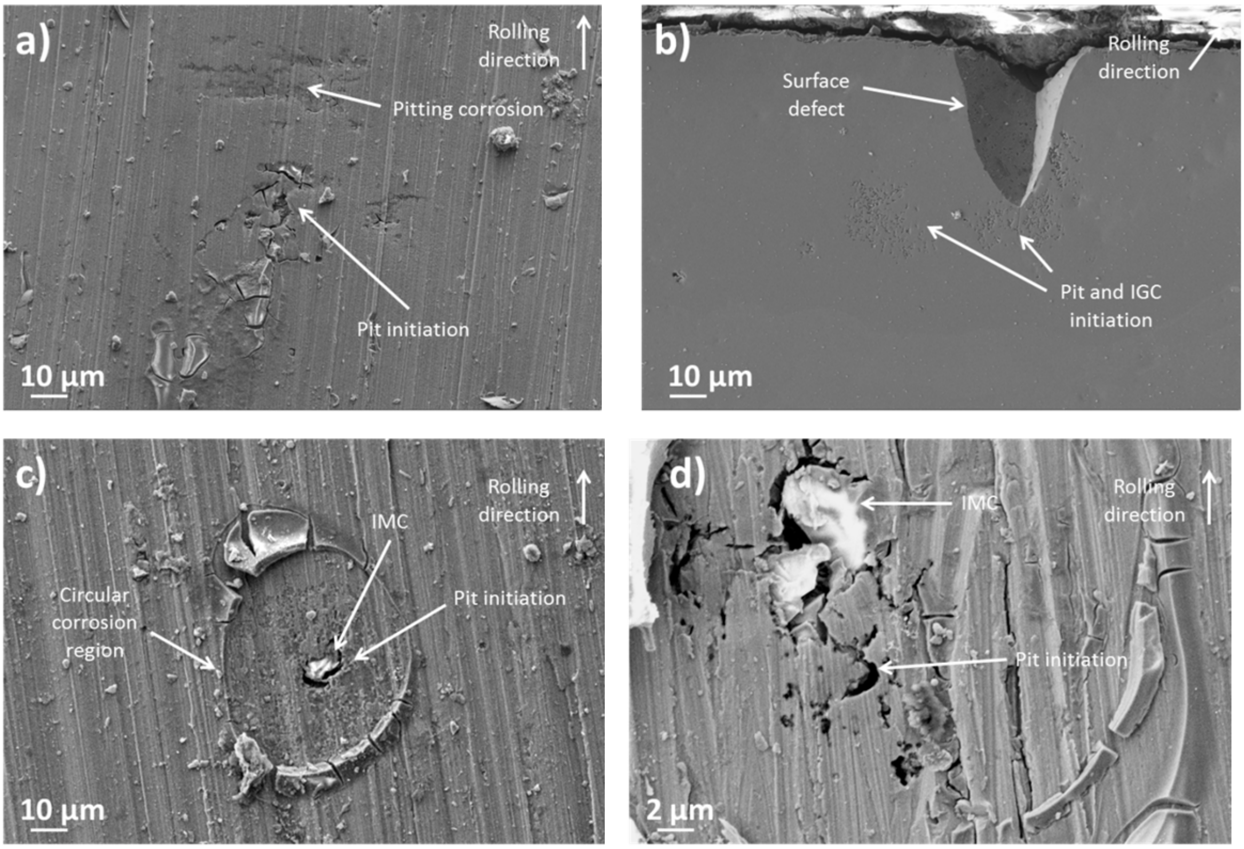

Figure 4-17: SEM micrographs of Cu3 showing a) galvanic corrosion of IMCs inside of a circular corrosion product region after 6 months of atmospheric exposure. b) pitting corrosion and IGC at a surface defect after 6 months of atmospheric exposure. c) galvanic corrosion surrounding IMCs within a galvanic circular corrosion product after 12 months of atmospheric exposure. d) pitting corrosion around IMCs after 12 months of atmospheric exposure.

Figure 4-18 a and b show cross-sectional micrographs of the extrusion direction and Figure 4-18 c and d show cross-sectional micrographs of the transverse direction after 12 months of exposure of Cu3. Figure 4-18 a and b show evidence of pitting corrosion which progresses to ~ 10 µm but Figure 4-18 a shows two pits that have progressed to a depth of ~ 70 µm. The reason for the low evidence of IGC is related to the coarse grain size of Cu3. IGC was shown to be related to the θ type phase that was observed to have a high V_f at the GBs within Cu3 [24–26], [60], [63], [80], [84]. Figure 4-18 c and d show evidence of selective grain dissolution, which is where corrosion envelopes the entire grain before progressing to a neighbouring grain [32], [115]. As previously mentioned this selective grain dissolution has been noted in Al-Cu-Li alloys by several authors [31], [32], [46], [113–116] and has been related to the T type phase, in particular the T_1 phase.

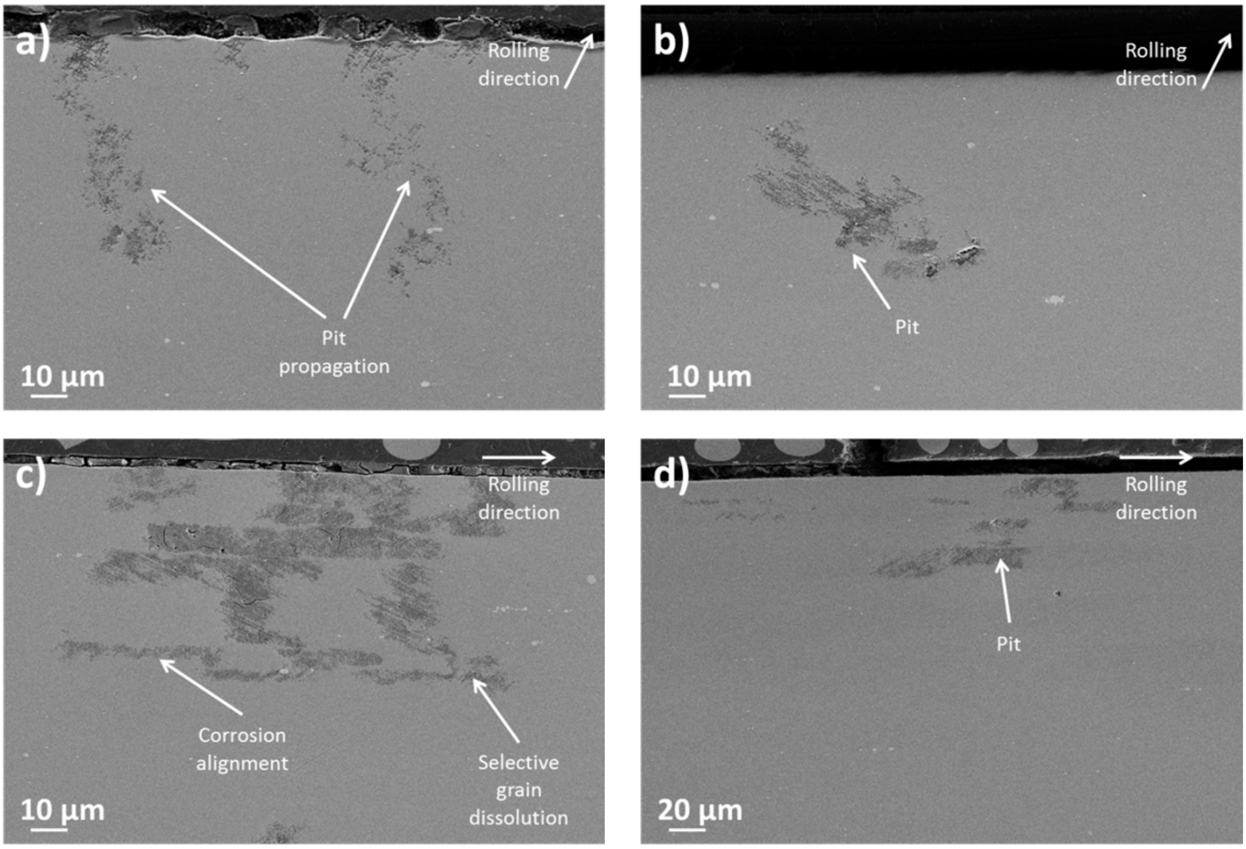

Figure 4-18: Cross-sectional SEM micrographs of Cu3 after 12 months of atmospheric exposure showing evidence of a) pitting corrosion. b) pitting corrosion. c) selective grain dissolution d) selective grain dissolution of T enriched grains.

EDS analysis showed that with increasing time the amount of O increased from ~ 4 to ~ 7 at.% between 1 and 12 months. The rate of increase was expected to be greater than observed, due to the reported highly active corrosion nature of Al-Cu-Li alloys [2], [4], [44], [48]. This data, however, suggests that Cu3 may have a high resistance to corrosion. This could be related to the selective dissolution of the Li containing phases reducing the amount of Al oxides being produced. With increasing time the concentration of Al reduced, from ~ 84 to ~ 77 at.% between 1 and 12 months. This reinforces the theory that Cu3 may have a high corrosion resistance due to the lack of corrosion products being measured, especially with the Al:O ratios being seen to reduce from ~ 14:1 to ~ 11:1 after 12 months. Figure 4-19 shows EDS maps, demonstrating the distribution of O content of the 1 and 12 month specimens respectively. The sum of the pollutants after 12 months was < 8 at.% of which 7 at.% was C. Interestingly, the 6 month specimen showed much higher concentrations of pollutants, totalling 47 at.%. This demonstrates that the TOW may have an influence on the corrosion resistance or the specimens were contaminated by a large pollution source and that the main corrosion product was carbonaceous Al products. *Blucher et al.* [120], however, stated that the impact of C on corrosion was negligible without the presence of NaCl.

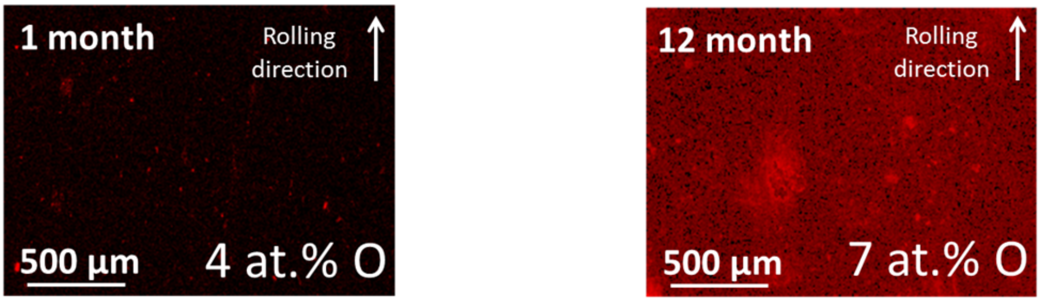

Figure 4-19: EDS maps showing the increase in O concentration with increasing atmospheric exposure time on Cu3.

EDS of the corrosion product showed an increase in O content with reducing Al. After 1 month 52 at.% O and 35 at.% Al were observed, compared to 63 at.% O and 32 at.% Al after 12 months. This highlights the slow corrosion resistance of Cu3 to atmospheric conditions, once again reinforcing some theories that Li promotes an increase in corrosion resistance [3], [5]. Cu, Fe, Mn and Mg concentrations were all seen to reduce with time as the corrosion product thickened. Other elements, like Si, S, Cl^- and C were seen to increase, for which Figure 4-20 shows the presence of Cu, Si, Cl^- and S within the corrosion product. After 12 months ~ 1 at.% Si, 4 at.% S, 0.5 at.% Cl^- and 5 at.% C were present within the corrosion products, which all can combine with O to form corrosive compounds, such as H_2SO_4, carbonaceous Al products and NaCl.

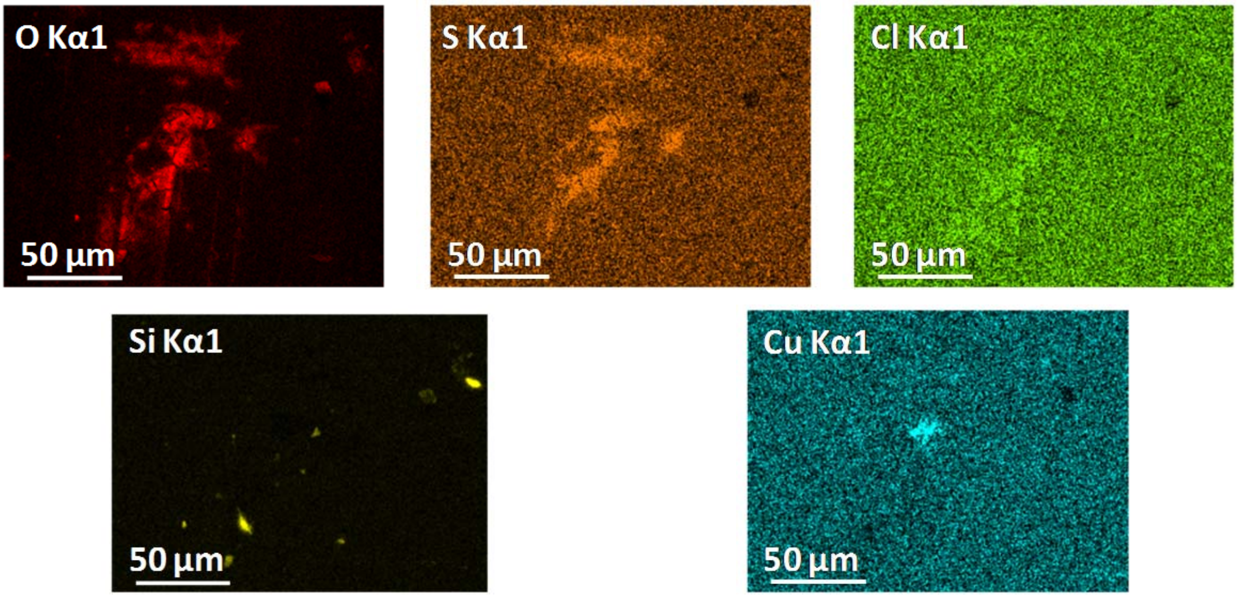

Figure 4-20: EDS maps showing the presence of Si, Cu, Cl^- and S at surface corrosion product sites on Cu3 after 2 months of atmospheric exposure.

The main IMC types in Cu3 are; Al-Cu-Mn-Fe and Al-Fe-Mn-Cu. Analysis of micrographs demonstrating galvanic corrosion around IMCs alongside EDS showed that the main concern was Al-Cu-Mn-Fe, due to the highly cathodic nature of the Cu and Fe [29], [34], [60], [80], [97]. Over time these IMCs were shown to reduce in Cu content, alongside an increase in O. The Al-Fe-Mn-Cu IMCs were not seen to be as active, which is believed to be associated with the low concentration of Cu present (< 2 at.%), compared to the Al-Cu-Mn-Fe IMCs. Their individual electrochemical potentials are closer to that of Al, as such the rate of corrosion around these particles will be reduced compared to the high Cu containing IMCs.

Figure 4-21 shows the XPS survey spectra of Cu3 over the 12 month exposure time and reveals that there are minimal changes in the elemental compositions. A gradual increase in C, S and Si alongside reductions in Al (22 at.% to 12 at.% for 1 to 12 months respectively) and O (46 at.% to 39 at.% for 1 to 12 months respectively). N and Ca were also observed throughout the exposure time with maximum values of 2 at.% and 1 at.% respective after 12 months of exposure. Cl^- concentrations reduced from 1 to ~ 0.4 at.% after 12 months. Na was observed, however, it was only seen on the 2 month samples, suggesting it had been washed off on other samples. It was shown that 49 at.% of the surface after 12 months was attributable to pollutants such as C, S, Si, Cl^- and Na. The sum of Al and O was seen to go from 92 at.% to 51 at.% after 12 months, with the ratio of Al:O going from ~ 2:1 to ~ 1:3 after 12 months, highlighting the formation of large amounts of corrosion products over time. Examination showed that the Al peak shifted, demonstrating the hydration of the Al.

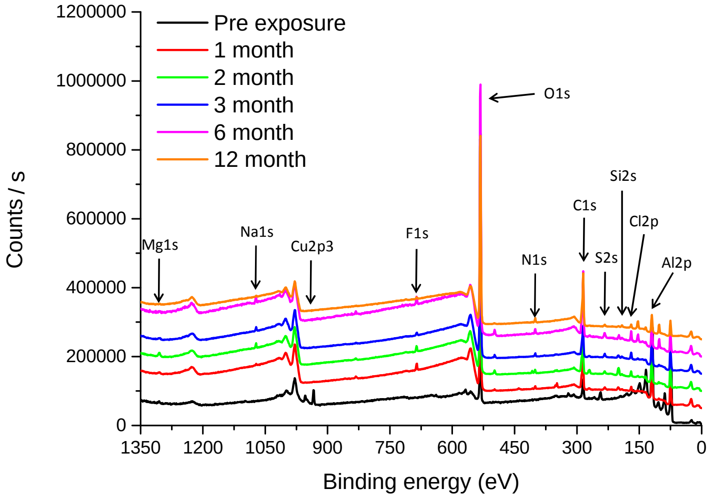

Figure 4-21: XPS survey spectra of Cu3 over a 12 month atmospheric exposure, showing changes in elemental constituents with time.

High resolution analysis of the Al peak showed that Al (m) was still identified in small measures after 6 months, as shown by Figure 4-22. The amount of Al (ox) reduced with time, showing after 1 month 22 at.% compared to 12 at.% after 12 months. This reduction coincides with a direct increase in C content which increased from 20 to 34 at.% between 1 and 12 months respectively which tends to agree with the results seen using EDS. The reduction can therefore be attributed to the demand from other pollutant sources for the O reducing the overall Al (ox) concentration within a given area. With the increase in C it can be assumed that large amounts of carbonaceous Al products build-up on the surface. XPS also demonstrated that an increase in Na, Cl^-, Si and S concentrations. XPS also revealed concentrations of N present on all of the specimens throughout exposure. The maximum N value was seen to be 0.7 at.% after 12 months. Approximately 85 at.% of the surface elements were from corrosion products, likely being carbonaceous Al products, NO_x, SO_x and NaCl in composition. XPS also revealed a change in pollutant concentrations after 6 months; however, like the EDS which showed the concentrations then reduced from 6 to 12 months, XPS showed that they stayed at similar values. This shows that the TOW does have a significant impact on the rate of corrosion that develops [67].

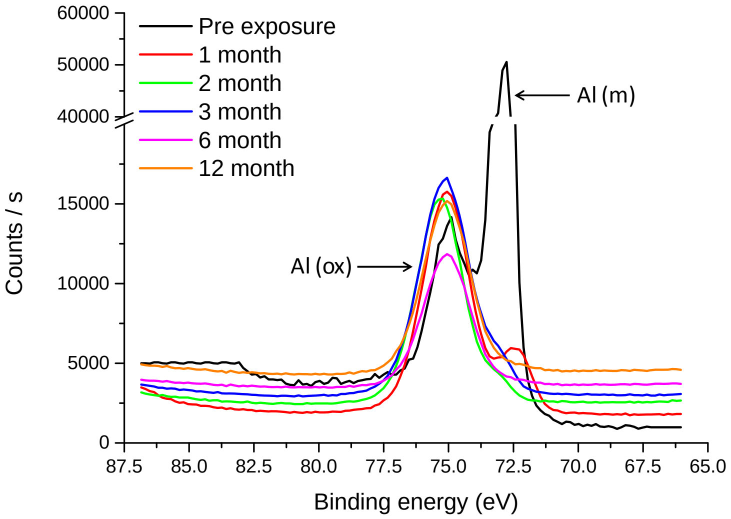

Figure 4-22: XPS spectra showing the Al2p metal and oxide peaks over a 12 month atmospheric exposure of Cu3, highlighting the rate of change from Al (m) to Al (ox).

4.1.4 Discussion of Al-Cu atmospheric exposure resistance

Analysis has shown that both of the Al-Cu-Li (Cu2 and Cu3) alloys perform in a similar manner. The Al-Cu alloy (Cu1), however, is a non-Li containing Al-Cu series Al alloy and as such offers a large number of fundamental differences. Details of these differences can be observed in Section 3.1. Initial observations show that over 12 months of exposure large amounts of corrosion product form on Cu1. Overall Cu1 showed a much higher concentration of O on the surface, from the first to 12 month of exposure as shown in Table 4-1. Due to the limitations in the EDS technique, it can be argued how valid these results are, however, there are distinct differences in chemical values recorded for each Al-Cu alloy, which can be used to give an indication of corrosion response. This is associated with the higher V_f of IMCs on Cu1 compared to Cu2 and Cu3, demonstrating the association of IMCs and accelerated corrosion [17], [18]. After 12 months the O content on Cu3 was 7 at.%, which is less than after 1 month of exposure for Cu1. This was lower than expected with literature [2], [4], [44], [48] suggesting a poor corrosion resistance of Al-Cu-Li systems, however, the difference in these results could be associated with the majority of the corrosion on the Al-Cu-Li alloys appearing to develop sub-surface. This would mean that there would be limited O to measure on the surface if it is all contained within the pits themselves. It can also be argued that the Li, being less noble than Al could offer a level of increased corrosion resistance. This shows that Cu1 has a very high corrosion rate from the amount of corrosion product that forms and corrodes at a higher rate compared to the Al-Cu-Li systems. EDS showed that after 1 month the Al content of Cu1 was less than that of the Al-Cu-Li systems, showing that more of the metallic Al had formed corrosion products. This trend continues throughout the exposure period, with a uniform difference between Cu1 and the Al-Cu-Li systems. Even without EDS analysis, visual densification of corrosion products can be seen on Cu1 compared to that of Cu2 and Cu3.

Table 4-1: Changes in Al and O concentration on the surface of samples measured by EDS on Cu1, Cu2 and Cu3 after 1 and 12 month exposure period.

At.%	O after 12/6 months of exposure	O within the corrosion product after 12/6 months of exposure	Al after 1 month	Al + O after 1 month of exposure	Al after 12/6 months	Al + O after 12/6 month of exposure
Cu1	25	68	69	80	64	89
Cu2	4	38	79	83	68	72
Cu3	7	63	84	90	78	85

Due to the large V_f of IMCs within Cu1, there was a distinct high volume of galvanic corrosion taking place. This large V_f of IMCs meant that when they became active, hydroxyl anions were produced and the size of the corrosion products became more voluminous than those seen on the Al-Cu-Li systems [66]. An example of corrosion on Cu1 was seen to be Ø = ~ 400 µm, compared to those seen on the Al-Cu-Li systems at Ø = ~ 50 µm. The reason for the size difference could be related to surface roughness, with more corrosion product being able to accumulate H_2O in localised regions, accelerating the corrosion for those localised sites. Due to the high V_f of IMCs it was also seen that more IMCs became active at any one time. Literature [117], [122] has shown that the effect of pollutants on corrosion is dependent on the formation of a humid layer on the surface of the metallic system, the greater TOW leads to more corrosion and concentration of pollutants [67]. The IMCs were also associated with pitting corrosion on each Al-Cu alloy and a relation to IGC was also observed, especially on Cu1.

EDS showed that there were more IMC types in Cu1 compared to both Cu2 and Cu3. It was shown that on Cu1 different IMCs became active at different time intervals. After 1 month Al-Cu-Mg particles showed galvanic corrosion, whilst others showed no corrosion. Al-Cu-Mg particles have been shown by literature to be the main IMCs within Cu1 developing accelerated corrosion [24–26]. EDS in this work has also demonstrated the poor corrosion resistance of the Al-Cu-Mg IMC's, however, has also demonstrated that some IMCs that were absent / had reduced levels of Mg within them were also highly active. This is because Mg is less noble to the Al matrix and as such undergoes selective dissolution over the Al and Cu [19], [27], [60], [63], [64]. On Cu2 and Cu3 the main problematic IMCs were Al-Cu-Fe-Mn [26], [60], [63], [80], [84], [153]. So in comparison, it has been shown that different IMCs are responsible for corrosion initiation, however, there are a number of similarities in that the Cu and Fe rich IMCs are most susceptible to form galvanic corrosion. But due to the higher V_f of IMCs within Cu1, it can be said that there will be more corrosion sites and that is what is observed. The concentration of Cu within the corrosion products on each Al-Cu alloys was seen to reduce, showing that Cu is re-distributed into the corrosion product [24], [26], [36], [95].

Cross-sectioning of Cu1 after 6 months shows extensive IGC and pitting corrosion sub-surface. The depth of corrosion was not as deep as that of Cu2 and Cu3, however, the number of individual corrosion sites had increased. Pitting corrosion was seen on Cu1 in a large number of locations, however, the maximum pit depth was < 10 µm, which was generally the minimum pit depth seen on the Al-Cu-Li systems. IGC was seen to progress to depths of ~ 70 µm on Cu3 after 6 months, however, Cu2 showed very minimal amounts of IGC and the IGC that was seen did not progress any further than the pitting corrosion. It was also seen that any pit sites that were visible on the surface of all three Al-Cu alloys were similar in opening size, with all being mainly < 5 µm. Comparing that to Cu1, the maximum IGC depth observed was ~ 50 µm, but even though this depth may be less than seen on Cu1, the volume of IGC seen was greater. Due to the small grain structure of Cu1, it meant that IGC progressed a lot further than that seen on either of Cu2 and Cu3. A question can therefore be asked, which relates directly to Cu1 in comparison to Cu2 and Cu3;

Which offers a higher corrosion resistance, lots of small corrosion sites or a few large corrosion sites?

This question relates purely to the case that Cu1 developed a weakened friable layer across its entire surface, with lots of small pits and IGC being observed. Whereas Cu2 and Cu3 showed less corrosion sites but those that were observed, were more substantial in size, through selective grain dissolution. All Al-Cu alloys investigated also showed evidence of sub-surface corrosion. It therefore has to be concluded that the Al-Cu-Li alloys had the poorer corrosion resistance.

EDS showed that the amount of O present on the surface of Cu1 was much higher than either of Cu2 or Cu3. EDS also showed that after 6 months the O content was double the combined O content of the Al-Cu-Li systems, highlighting the significant difference in corrosion rate. After 6 months, however, similar levels of Al were seen on Cu1 as that of Cu2 and Cu3, there was, however, a distinct reduction in C seen on the Cu1 specimen. Since both Cu2 and Cu3, did not contain Mg, a difference between the Al-Cu and Al-Cu-Li systems will be the impact of the less noble Mg. XPS showed that with time Mg content within Cu1 reduced, due to the selective anodic dissolution of Mg within the IMCs [24], [63], [152]. This ultimately created an enriched cathodic region, once the Mg was removed. Li acts in a similar manner and it can be said that the T type phase in the Al-Cu-Li alloys undergoes the same dissolution, leaving an enriched Cu region once the less noble Li is dissolved. Examination of the Al:O ratios show that on Cu1, pre-exposure the ratio was ~ 4:3 compared to ~ 2:1 seen on Cu2 and Cu3 and after 6 months the ratios between Cu1 and the Al-Cu-Li systems were actually similar at ~ 1:3.

EDS of the corrosion products showed that Cu1 had a similar trend to the Al-Cu-Li systems in that the Al concentration reduced, with increasing O content. The results in Table 4-1 show that after 12 months both Cu1 and the Al-Cu-Li systems showed very similar corrosion product chemistries. This suggests that the Al-Cu-Li systems actually produce Al oxide quicker even though there were fewer initiation sites. This could be related to the high V_f of fine scale precipitates within the matrix, especially the highly anodic T type phases, which have been shown in literature to be detrimental to corrosion [31], [32], [46], [113–116]. The volume of corrosion product on Cu1 was higher than that seen on either Cu2 or Cu3. In fact it could be said that more corrosion product was seen on Cu1 after 1 month than what was seen on Cu2 or Cu3 after 6 and 12 months respectively. Other similarities lay with the pollutants, with S and Cl^- being ever present on Cu1 specimens. Many authors have shown that S and Cl^- are the main atmospheric elements that are deposited onto samples examined under urban environments, showing a strong correlation with literature [117], [120].

High resolution XPS showed that after the first month, similar amounts of Al (m) could be seen on Cu1, Cu2 and Cu3. However, by 3 months no evidence of Al (m) could be seen on Cu1, whereas ~ 3 to 4 at.% Al (m) was seen on Cu2 and Cu3, once again reaffirming the higher, apparent corrosion resistant nature of the Al-Cu-Li systems, however, this could be purely associated with fewer initiation sites and not that less corrosion is taking place. Figure 4-23 shows the XPS comparison of Cu1, Cu2 and Cu3 over the 12 month exposure. Alongside this Al (m) reduction was an increase in Al (ox) which was 8 at.% higher for Cu1 than those of Cu2 and Cu3 after 6 months. The O content was also seen to be ~ 11 at.% higher at the same time, showing that there must have been a higher proportion of the surface exposed to a thin film for which O could react [67]. Overall on all Al-Cu alloys examined the EDS and XPS showed similar trends with regards to chemical distribution of elements, one note that was made, was that a clear difference in interaction volume was observed with the EDS being able to measure more of the substrate elements whereas the XPS was able to identify more the corrosion products being a surface sensitive technique.

Overall EDS and XPS have shown that the main pollutants from urban conditions are N, S, Si, C, O, Na and Cl^-. Changes in the binding energies of the system have identified that N was organic matrix material (400 eV), S and O were in the form of a SO_4^{2-} (169 eV and 532 eV respective), C was in the form of carbonaceous pollutants and could have formed $Al_2(CO_3)_3$ (285 eV). O had formed numerous compounds as SO_4^{2-}, Al_2O_3, OH^- and in some locations PO_4^{3-} (532 eV). Of these elements the most problematic were O, C and S, suggesting that carbonaceous products and SO_4^{2-}species are the main corrosion products that form in the urban area investigated in this work, agreeing with literature [122], [125].

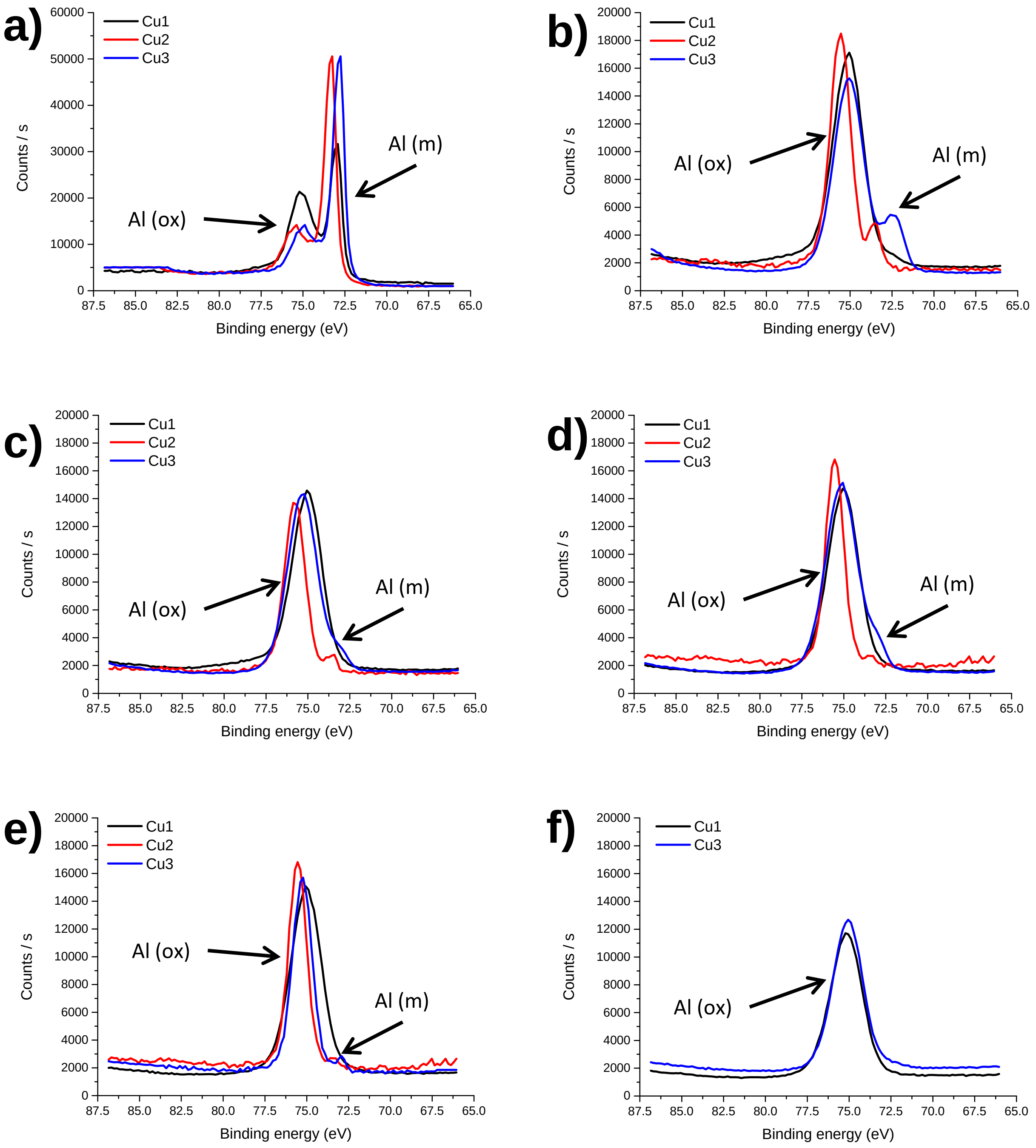

Figure 4-23: XPS spectra showing the comparison between Cu1, Cu2 and Cu3 a) pre-atmospheric exposure b) 1 month b) 2 months c) 3 months d) 6 months e) 12 months.

4.2 Atmospheric corrosion of Al-Mg alloys

4.2.1 AA5083-T3510 (Mg1)

Mg1 showed evidence of an increase in the amount of corrosion product with increasing time. Figure 4-24 a, b, c and d show micrographs of the amount of pollutant and corrosion products seen on the surface of Mg1 following 1, 3, 6 and 12 months exposure respectively. Corrosion product and pollutants were observed on the surface during the first 3 months of analysis, however, these sites were highly localised. After 6 months, more corrosion product was seen and after 12 months evidence of where thin films of H_2O had initiated corrosion were also seen. These results show that there was not enough pollutant or corrosion product to restrict the flow of H_2O off the surface, as such the rate of corrosion could be reduced since electrolytes could easily run off samples, however, thin film corrosion via adsorption of H_2O could still initiate.

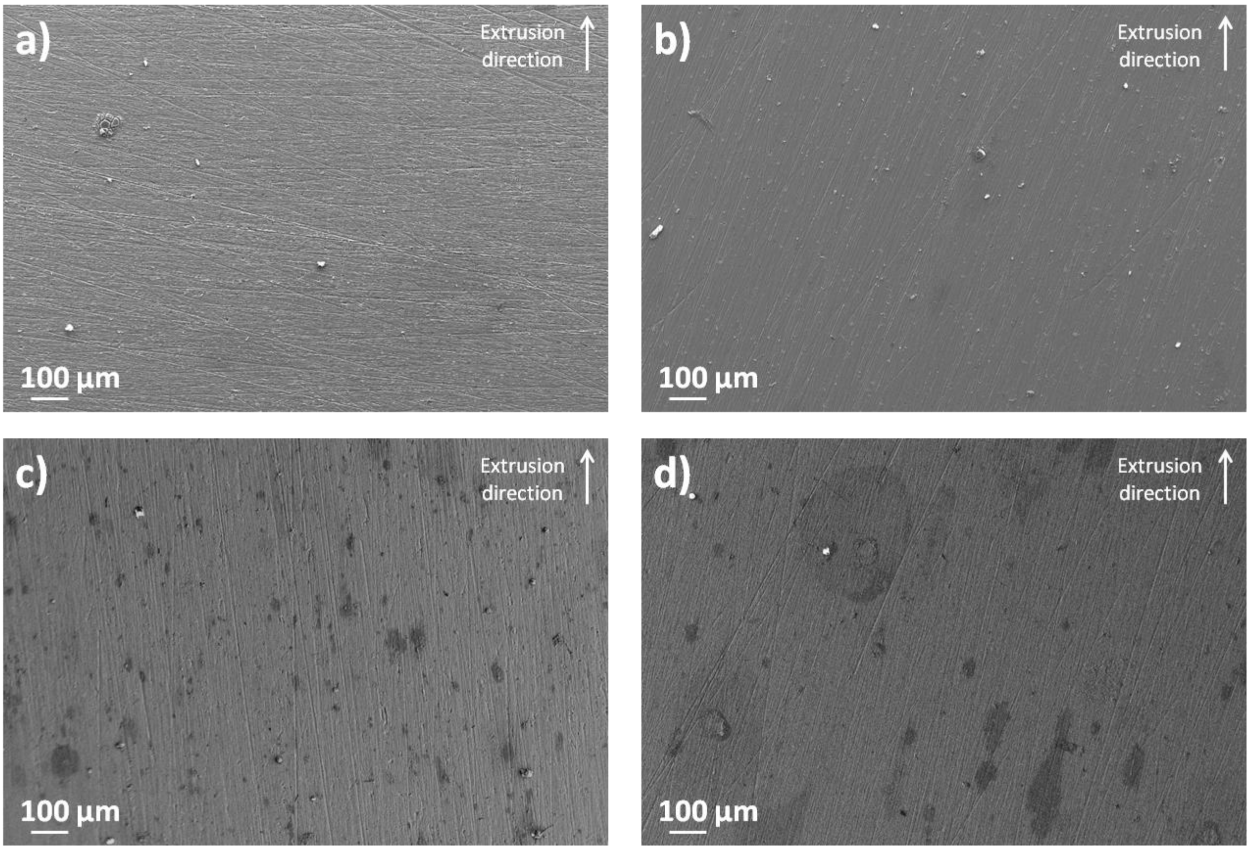

Figure 4-24: SEM micrographs of Mg1 showing the build-up of corrosion products and pollutants after a) 1 month b) 3 months c) 6 months and d) 12 months of atmospheric exposure.

Very little corrosion was seen on Mg1 in the first 6 months of exposure. Some small corrosion product sites and sites where thin films of H_2O had initiated corrosion were observed, however, examination of the IMCs showed that no significant galvanic corrosion had taken place. This shows that the IMCs are anodic to the Al matrix or that no corrosion has been initiated due to the lack of TOW. EDS showed that Mg rich IMCs were present within the matrix which will undergo selective dissolution before the matrix dissolves. Fe rich IMCs were, however, also observed, which suggests that they corrode at different potentials but also that the TOW had not been great enough to cause galvanic cells to form. After 12 months faceted pitting corrosion was seen and the pitting corrosion in Figure 4-25 a was linear but did not appear to have any substantial depth. Not all corrosion types were linear, most were spherical in shape. After 12 months regions of corrosion product were observed, as seen in Figure 4-25 b, these corrosion products ruptured, which could be associated with the vacuum of the FEGSEM or XPS. Since both systems require high vacuums to operate it is likely that the corrosion product could have been dehydrated during the vacuum process, causing the corrosion product to crack, like shown in Figure 4-25 c revealing pitting corrosion beneath them, like that seen in Figure 4-24 a and Figure 4-25 d. After 12 months the pit openings were larger in size, but still gave the impression of shallow progression. Some corrosion products form plate like structures, however, others which show a mossy-like structure, were also observed [128]. The likelihood is that these different corrosion products, relate to both anodic and cathodic IMC respectively; Mg rich and Fe rich.

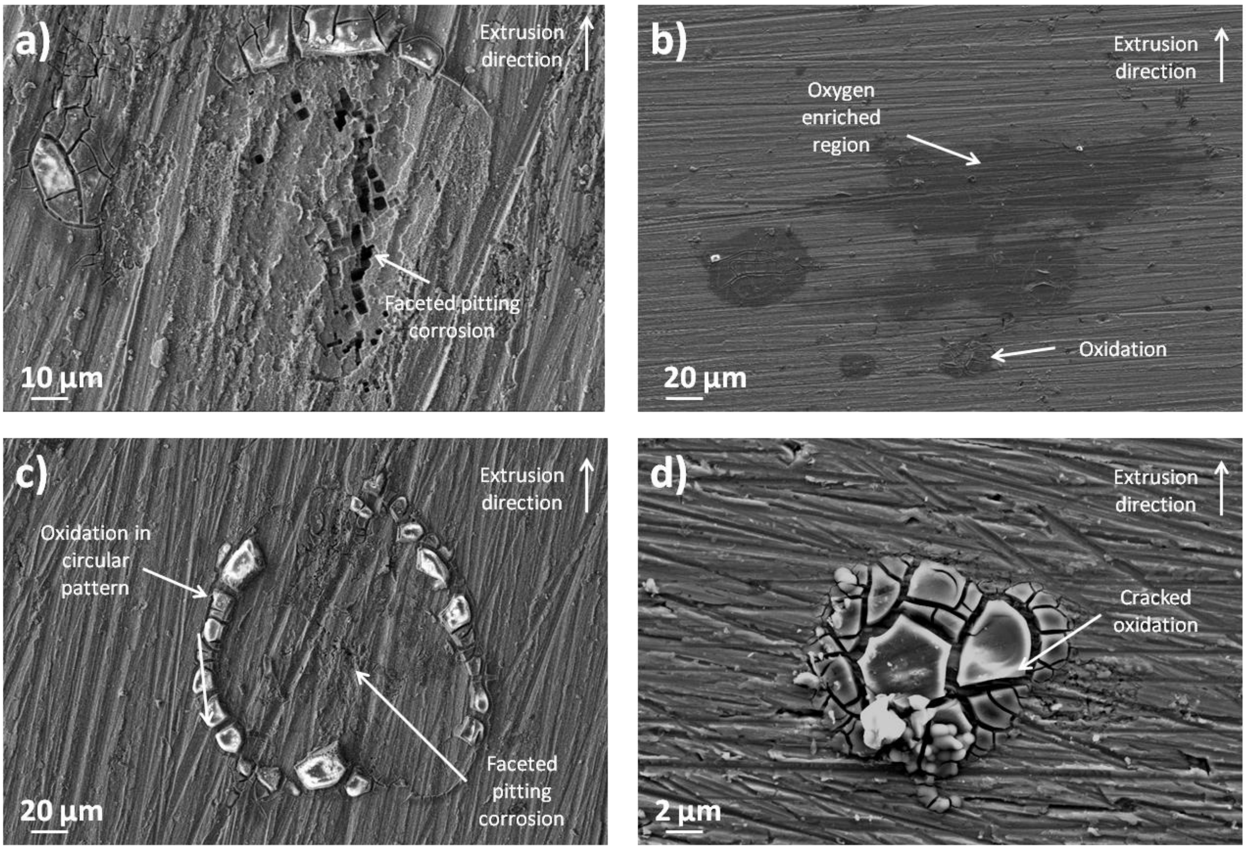

Figure 4-25: SEM micrographs of Mg1 after 12 months of atmospheric exposure showing a) faceted pitting corrosion. b) surface corrosion product and surface oxide patches. c) pitting corrosion within a corrosion product ring. d) ruptured corrosion product regions typically associated with pitting corrosion.

Figure 4-26 a and b show cross-sectional micrographs of the extrusion direction and Figure 4-26 c and d show cross-sectional micrographs of the transverse direction after 12 months of exposure on Mg1. Figure 4-26 a, c and d show evidence of faceted pitting corrosion taking place and the pitting corrosion seen in Figure 4-26 a is ~ 70 µm deep. The majority of the pits, however, did not progress as far with most being ~ 10 µm deep with pit openings being very narrow in most cases < 10 µm. Evidence of sub-surface corrosion can, however, be seen in Figure 4-26 c and d. This highlights that the tip of corrosion is highly acidic, since most of the corrosion takes place sub-surface. Figure 4-26 b shows that even though there were some regions of substantial corrosion, most of the specimen surface were absent of corrosion products and pitting. Figure 4-26 d shows dissolution along a GB, however, following FEGTEM characterisation no particles were seen on any GBs, thus the likelihood that this is IGC is low and more likely it is a cross-section view through some pitting corrosion.

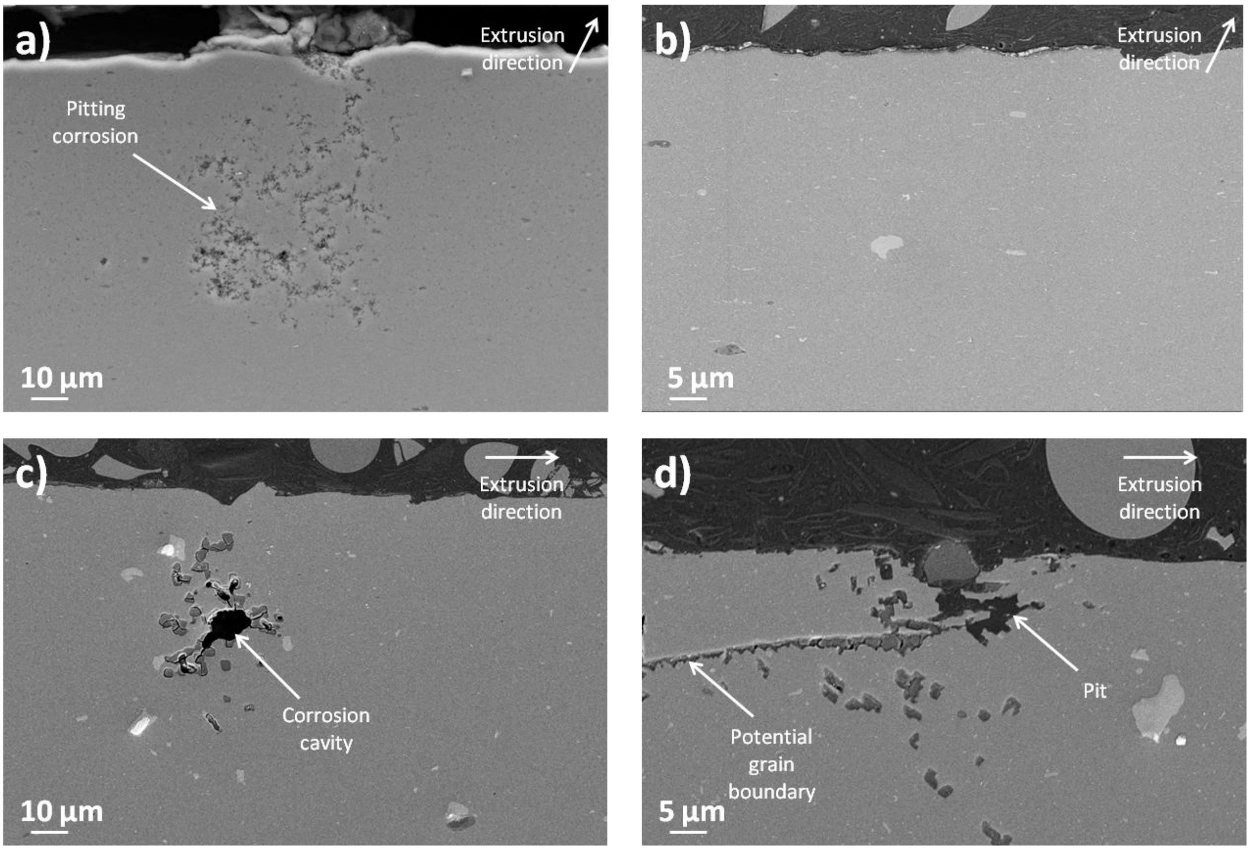

Figure 4-26: Cross-sectional SEM micrographs of Mg1 after 12 months of atmospheric exposure showing evidence of a) pitting corrosion with a small pit opening. b) a site with no evidence of corrosion. c) sub-surface faceted pitting corrosion. d) faceted pitting corrosion and potential GB dissolution after 12 months of atmospheric exposure.

EDS analysis showed that, with increasing time, the amount of O present on the surface increased from ~ 6 at.% to ~ 8 at.% after 12 months. This rate of increase was expected due to the highly corrosion resistant nature of Al-Mg alloys, however, as previously mentioned this change is likely to be incorporated into the error of the EDS system, as such shows very limited change. This high corrosion resistance is due to the Mg IMCs undergoing selective anodic dissolution so that the Al matrix is forced to be cathodically protected [19], [27], [60], [63], [64]. This could create a MgO corrosion product, which offers increased corrosion resistance through the formation of this passive layer. As time increased the concentration of Al reduced from ~ 76 to 65 at.% between 1 and 12 months respectively, showing that eventually the Al becomes anodic, most likely once the Mg concentration has reduced to a critical concentration. The Al:O ratios were seen to go from ~ 13:1 to ~ 8:1 after 12 months, showing the slow corrosion rate of Mg1 with the total Al and O concentration after 12 months being 73 at.%. Figure 4-27 shows EDS maps, demonstrating the distribution of O content on the surface of the 1 and 12 months specimens respectively. Reductions in Mg were seen with increasing time, however, after 12 months the Mg content had only reduced by ~ 1 at.% from 4 at.%. Other elements were observed on the surface, such as Si and S, however, they showed combined concentrations of < 2 at.% over the entire period of exposure. The main pollutant seen was C, which increased from 1 to 21 at.% over the 12 months of atmospheric exposure. Overall ~ 27 at.% of the surface chemistry after 12 months was associated with the corrosion products of which the highest concentration was deemed to be carbonaceous Al products.

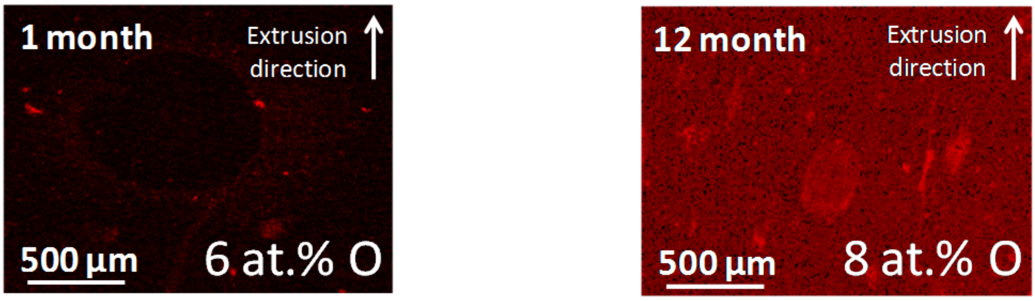

Figure 4-27: EDS maps showing the increase in O concentration with increasing atmospheric exposure time on Mg1.

EDS examination of the corrosion products showed an increase in O content alongside a reduction in Al. After 1 month 59 at.% O and 35 at.% Al were observed, compared to 62 at.% O and 25 at.% Al after 12 months. Small increases in O content are seen, however, a larger reduction in Al is observed. This coincides with an increase in the amount of C, Si, S and Cl^- measured within the corrosion products. After 12 months ~ 0.5 at.% Si, 3 at.% S, 0.5 at.% Cl^- and 5 at.% C were present within the corrosion products and Figure 4-28 shows the presence of S and the absence of Mg within corrosion products on Mg1 after 12 months of atmospheric exposure. It is assumed that the Cl^- could not be seen using the EDS map due to the very low atomic percentages present. *Syed et al.* [67] stated that Al-Mg alloys following atmospheric exposure showed a higher degree of staining compared to other Al alloys, through the formation of MgO films, however, no staining was observed on Mg1. Theory dictates that MgO could develop, therefore it has to be assumed that the specimens simply were not exposed to atmospheric conditions long enough for staining to form.

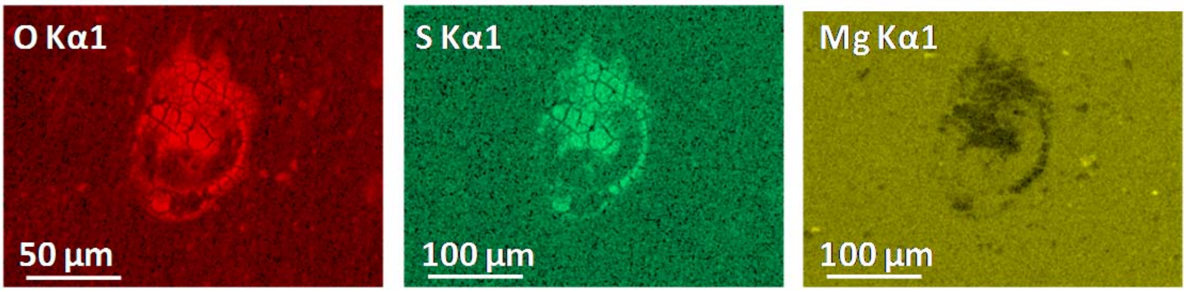

Figure 4-28: EDS maps showing the presence of Si and an absence of Mg at surface corrosion product sites on Mg1 after 12 months of atmospheric exposure.

The main IMC types within Mg1 are; Al-Mg-Si, Al-Mn-Si and Al-Fe-Mn-Si-Mg. Of these IMCs, the Al-Mg-Si and Al-Mn-Si showed very good resistance to corrosion, in that they did not form galvanic corrosion. This is due to them having similar and less noble electrochemical potential compared to that of the Al matrix [60]. Over time it was, however, observed that the Mg content reduced through sacrificial, anodic dissolution. As expected with the reduction in these elements an increase in the amount of O was seen. Si reduced, however, this can be attributed to masking by the C content. The Al-Fe-Mn-Si-Mg

IMCs, however, showed evidence of pit initiation and galvanic corrosion, due to the potential difference of the Fe compared to the Al matrix [60]. With time the Fe, Mn, Si and Mg contents were all reduced. No Mg could be seen on these IMCs after 12 months of exposure, suggesting it had all been anodically dissolved, leaving a Fe, Mn and Si rich region.

Figure 4-29 shows XPS survey spectra taken from each sample of Mg1 over the 12 months exposure. The XPS surveys show substantial increases in C and Si alongside reductions in Al (62 at.% to 13 at.% for 1 to 12 months respective) and increases in O (23 at.% to 42 at.% for 1 to 12 months respective). Mg and Cl^- concentrations were also seen to reduce with no Mg being observed after 6 months of exposure and only very small concentrations of Cl^- at < 0.5 at.% were seen after 12 months. S, N and Na concentrations remained relatively stable over the entire time period (~ 2 at.%, ~ 2 at.% and ~ 0.5 at.% respective). The sum value of Al and O concentration changed from 85 at.% to 55 at.% after 12 months exposure, with the ratio of Al:O progressing from ~ 3:1 to ~ 1:3 after 12 months. This shows that after 12 months ~ 45 at.% of the surface is pollutants. An increase in pollutants was seen between 3 and 6 months, which tends to suggest the TOW can affect the corrosion, with the 6 months samples being those exposed to winter climates and those with high moisture levels. Examination showed that the Al peak shifted, demonstrating the hydration of the Al.

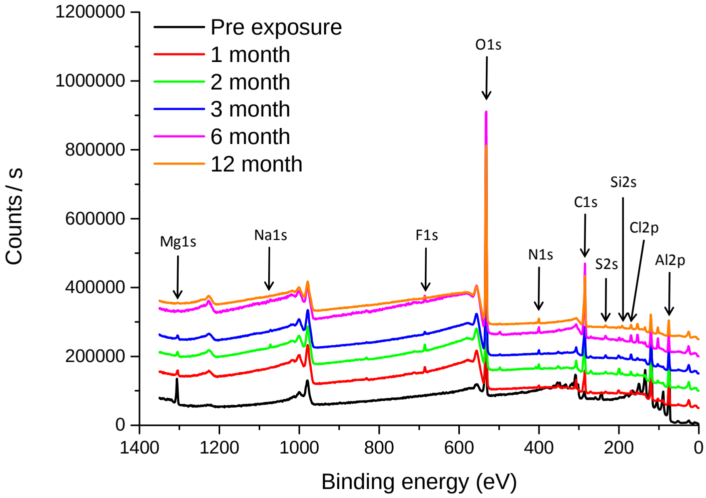

Figure 4-29: XPS survey spectra of Mg1 over a 12 month atmospheric exposure, showing changes in elemental constituents with time.

High resolution analysis of the Al peak showed that prior to exposure, substantial Al (m) could be observed at a concentration of 38 at.% alongside an 18 at.% Al (ox) peak. With time the Al (m) peak reduced but was still identified in small quantities after 6 months of exposure as shown by Figure 4-30. The Al concentration was seen to reduce from 22 at.% after 1 month to 15 at.% after 12 months. The rate of reduction coinciding with an increase in the C content on the surface with the C concentrations going from 21 at.% to 34 at.% after 12 months, which can be attributed to the formation of carbonaceous Al products. The O content also reduced with time, which suggested a high demand for O from pollutant sources like C, S and N. XPS revealed concentrations of N present on all of the specimens throughout exposure, with the maximum value seen to be 1.5 at.% after 12 months. It was also observed that ~ 42 at.% of the surface after 6 months was pollutants, including 33 at.% C and 44 at.% O, thus 86 at.% of the surface was from corrosion products. Once again an increase in C was seen on specimens after 6 months, showing that TOW has a large impact on deposited pollutants.

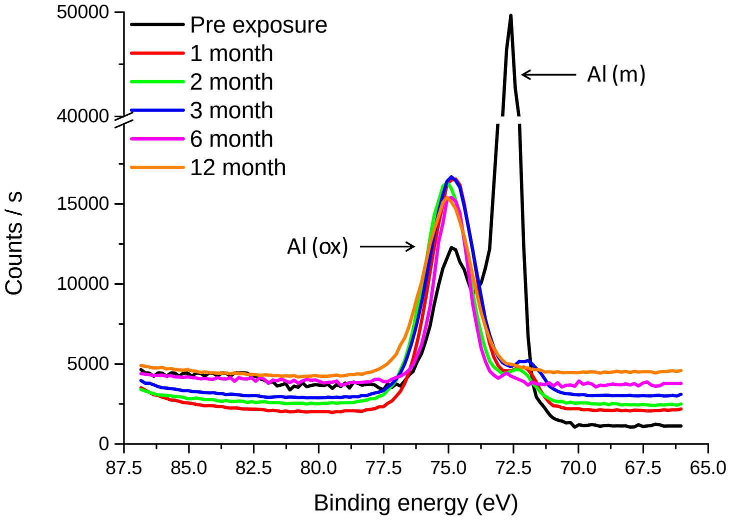

Figure 4-30: XPS spectra showing the Al2p metal and oxide peaks over a 12 month atmospheric exposure of Mg1, highlighting the rate of change from Al (m) to Al (ox).

4.2.2 Spray formed Al-Mg-Li (SF1)

SF1 following atmospheric exposure showed that with increasing time the amount of corrosion products increased, however, the 6 months specimen showed the highest volume of corrosion products. Figure 4-31 a, b, c and d show micrographs of the amount of pollutants and corrosion product seen on the surface of SF1 following 1, 3, 6 and 12 months respectively. Thin films of H_2O caused the most corrosion, with only these locations establishing corrosion products. After ~ 3 months these sites started to develop corrosion with most micrographs showing very little evidence prior to this. This gives the impression that SF1 has a good corrosion resistance. A number of authors [28], [93], [130], [131], [135] have shown that spray forming can improve the corrosion resistance of Al alloys as such these initial results tend to agree with this theory.

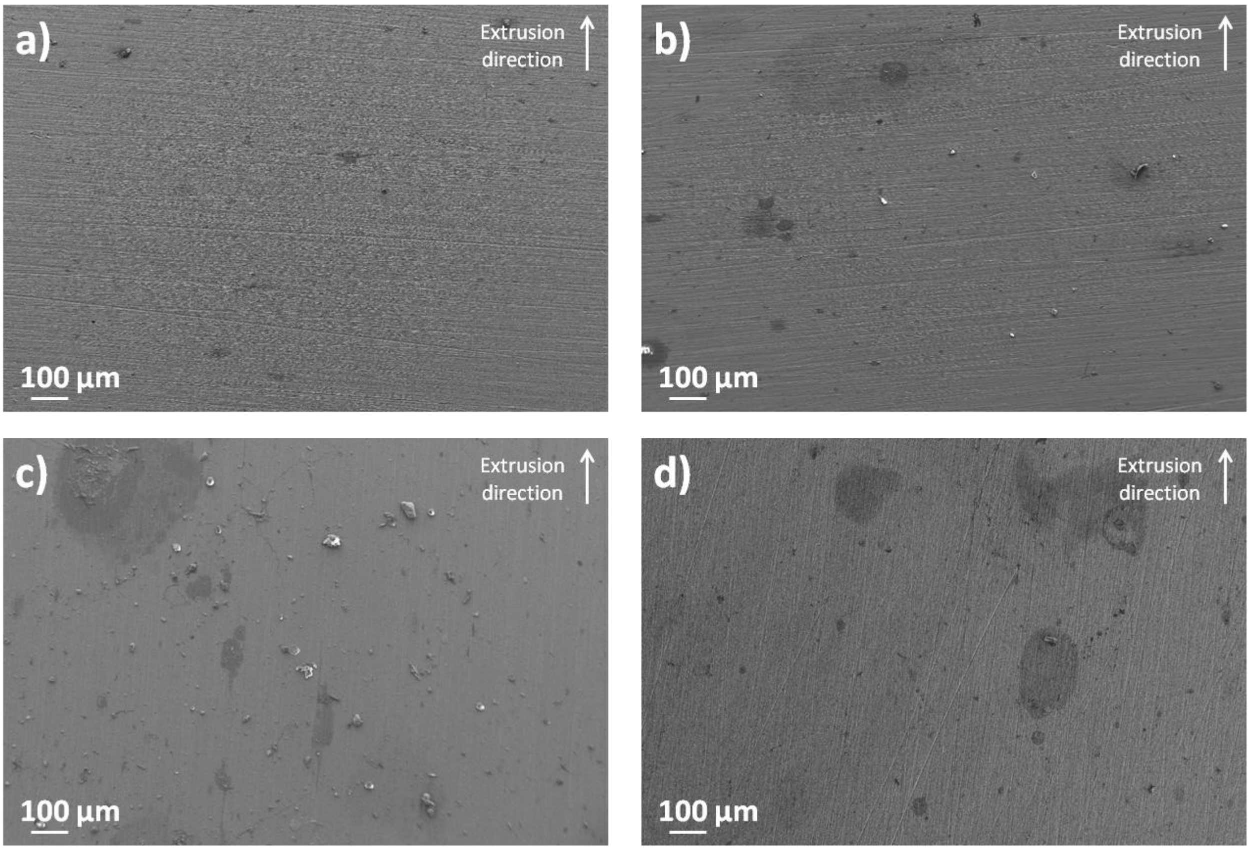

Figure 4-31: SEM micrographs of SF2 showing the build-up of corrosion products and pollutants after a) 1 month b) 3 months c) 6 months and d) 12 months of atmospheric exposure.

After 1 month of exposure galvanic corrosion was taking place around IMCs, as shown in Figure 4-32 a. Little evidence of corrosion had taken place on SF1, however, Figure 4-32 b shows a region after 2 months of exposure demonstrating faceted, pitting corrosion forming beneath a ruptured corrosion product [128]. This shows that SF1 is corroding; however, the depth of corrosion is unknown at this stage. Visually it does suggest that the corrosion has not progressed very far into the specimens, once again agreeing with theory that SF alloys have an increased corrosion resistance [28], [93], [130], [131], [135]. The number of corrosion sites was low, however, with time they increased and the progression of the pitting accelerated as shown in Figure 4-32 c and d. Even with these pitting sites identified, with the number of established pit sites being very small it can be said that SF1 showed a relatively high corrosion resistance.

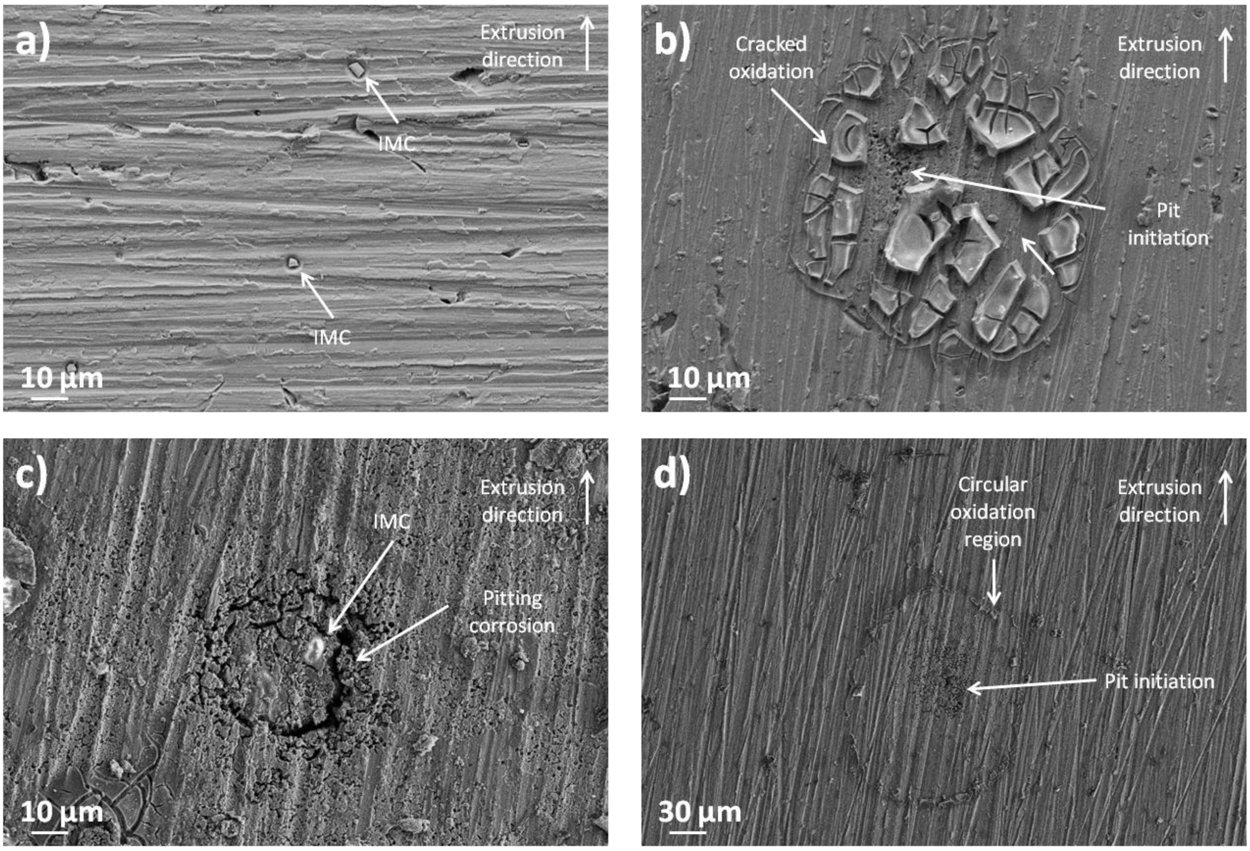

Figure 4-32: SEM micrographs of SF1 after a) 1 month of atmospheric exposure, showing galvanic corrosion surrounding IMCs. b) 3 months of atmospheric exposure, showing pit initiation beneath a ruptured corrosion product site. c) 12 months of atmospheric exposure, showing galvanic corrosion surrounding IMCs and pitting corrosion nucleation. d) 12 months showing evidence of pitting corrosion.

Figure 4-33 a and b show cross-sectional micrographs of the transverse direction and after 12 months of exposure on SF1. No evidence of corrosion was seen on the extrusion direction, but this will probably be related to the cross-sectioning location not that no corrosion propagated. It also gives a good indication of the high corrosion resistant nature of SF1. In Figure 4-33 a and b evidence of pitting corrosion and potential IGC were seen. The pit seen in Figure 4-33 a progressed to a depth of < 10 µm but the IGC progressed to a depth of ~ 30 µm. Figure 4-33 b shows a more substantial pit depth, progressing to a depth of ~ 60 µm. The pit openings visible on the surface were also shown to be < 10 µm. IGC was not expected to be seen on SF1, however, Figure 4-33 a shows evidence of GB breakdown, and the size of the corrosion sites agree with the average grain size identified through EBSD. This apparent IGC could, however, be a cross-section through a pitting corrosion site. Segregation is, however, possible within SF alloys and with SF1 containing Li, which has a natural tendency to precipitate to the GBs it would not be unexpected if δ, δ', Al_3MgLi phases or even β phase were seen on the GB of SF1. These alter the corrosion resistance because they are highly anodic thus they dissolve themselves, instead of the matrix [17], [18], [24–26], [60], [63], [80], [84].

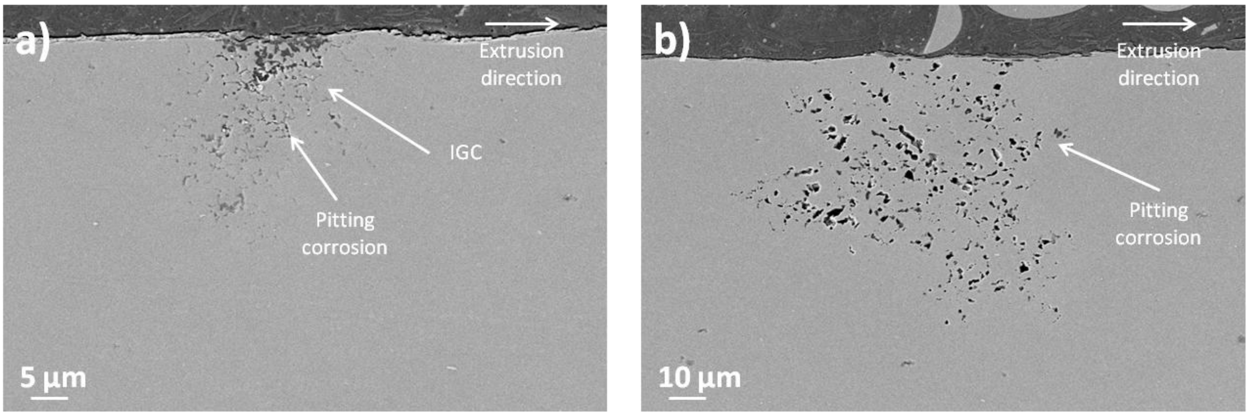

Figure 4-33: Cross-sectional SEM micrographs of SF1 after 12 months of atmospheric exposure showing a) pitting and potential IGC. b) porous pitting corrosion.

EDS showed that with increasing time the amount of O present on the surface increased from ~ 2 at.% to ~ 6 at.% after 12 months. Figure 4-34 shows EDS maps, demonstrating the distribution of O content on the surface of the 1 and 12 months specimens respectively. This highlights a very slow build-up of corrosion products and as such would suggest a finite concentration of corrosion taking place. The Al content reduced by 4 at.% over the 12 months of exposure, highlighting the absence of any substantial corrosion products. The Al:O ratios changed from ~ 40:1 to ~ 13:1 after 12 months, showing the very low level of corrosion product formation. C concentrations increased to ~ 10 at.% after 12 months, but due to the lack of O and thin films of H_2O for C and other pollutants to combine with, no other elements were observed at concentrations > 0.5 at.%. In total ~ 15 at.% of the surface was attributed to pollutants (C, Si, S etc.) after 12 months, which was the same after 1 month, once again highlighting the corrosion resistant nature of SF1. The Mg content, however, reduced with time, demonstrating the anodic nature of the Mg as it selectively dissolves [19], [27], [60–64].

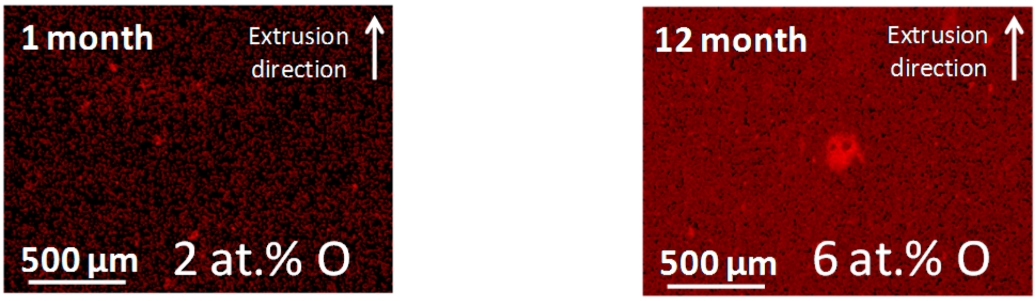

Figure 4-34: EDS maps showing the increase in O concentration with increasing atmospheric exposure time on SF1.

EDS of the corrosion product showed that with increasing time the O content reduced with an increase in Al being observed. After 1 month 73 at.% O was seen, compared to 37 at.% after 12 months, showing that O is now being used by other pollutants. Mg content was seen to reduce to < 1 at.% after 12 months, reinforcing theory that Mg is selectively dissolved [19], [27], [60–64]. S was also seen to increase from 1 at.% to ~ 3 at.% after 12 months. C increased with time to a maximum of 25 at.% after 6 months, however, this dropped to 10 at.% on the 12 months sample, showing the unpredictable nature of atmospheric exposure. Combined with the reduced level of O in the corrosion products it would be safe to conclude that carbonaceous Al products and H_2SO_4 are forming. This shows that the TOW can have an impact on corrosion, with the winter months having a higher period of wetness, large amounts of pollutants can combine with any surface H_2O and corrosion products will form [67]. Figure 4-35 shows evidence of O, S and C forming corrosion products, most likely $Al_2(SO_4)_3$ and carbonaceous Al products such as $Al_2(CO_3)_3$.

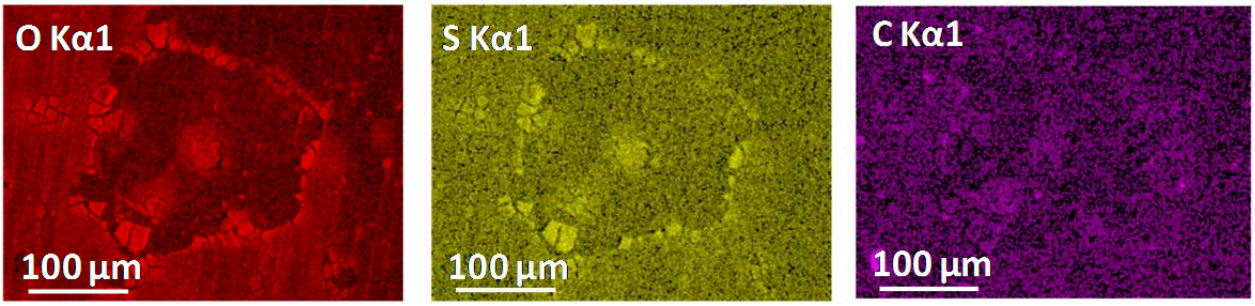

Figure 4-35: EDS maps showing the presence of O, S and C within corrosion products on SF1 after 6 months of atmospheric exposure.

The main IMC types in SF1 are; Al-Mg-Si and Al-Mg-Si-Fe. As time increased both IMCs showed increased concentrations of O and C, however, the Al content of the Al-Mg-Si-Fe IMCs reduced to ~ 20 at.% after 12 months, suggesting the IMCs are highly cathodic in nature [25], [26], [60], [80]. This can be suggested as Al-Mg-Si, showed an increase in Al content, as the Mg and Si concentrations reduced with time. Both showed similar levels of corrosion taking place around them which shows that they are both slow corroding IMCs, however, in theory cathodic IMCs are more likely to be detrimental [19], [27], [60–64].

Figure 4-36 shows the XPS survey spectra taken from each sample after each time interval, they show that overall there are very small changes in the elemental compositions after exposure, but a trend can still be observed. As time increases the amount of Al reduced, whereas the C, S, Si, N, Cl^- and Na values all increased [125]. The Al content reduced from 36 at.% to 12 at.% after 12 months, the O content, however, stayed at ~ 44 at.% over the entire exposure period. This demonstrates that there is likely to be a constant influx of O from the atmosphere into the thin films of moisture and that the Al is constantly being attacked. After 12 months there was a combined 47 at.% of pollutants on the surface, with C corresponding to 38 at.% of that, most likely as carbonaceous Al products such as $Al_2(CO_3)_3$. However, after 6 months the C concentration was 45 at.%, which shows that TOW can affect atmospheric corrosion [67]. The 6 months sample coincided with winter and thus wet months, causing a higher saturation of adsorbed pollutants into the thin films of H_2O. The sum value of Al and O concentration changed from 76 at.% to 51 at.% after 12 months exposure, with the ratio of Al:O going from ~ 1:1 to ~ 1:3 after 12 months, demonstrating the formation of small amounts of corrosion products. Examination showed that the Al peak shifted, demonstrating the hydration of the Al.

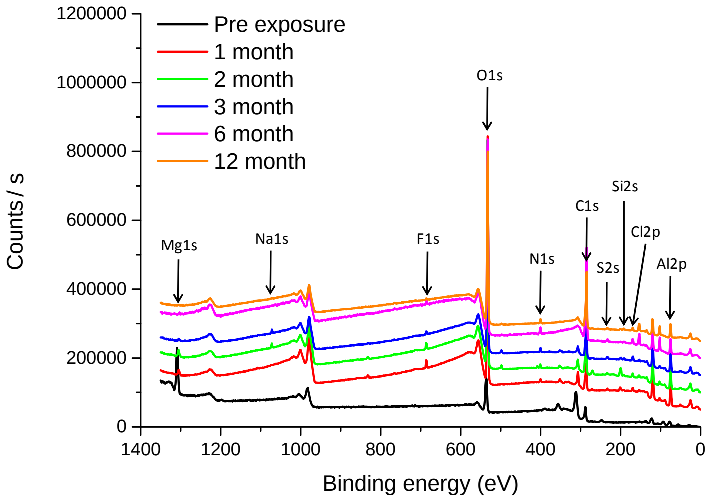

Figure 4-36: XPS survey spectra of SF1 over a 12 month atmospheric exposure, showing changes in elemental constituents with time.

High resolution analysis of the Al peak showed, prior to exposure, Al (m) and Al (ox) could be identified, as shown in Figure 4-37. Al (m) can be seen on specimens after 6 months of exposure, however, the concentration is < 0.5 at.%. The Al and O contents reduced with increasing time. The main driving force for this Al (ox) reduction was an increase in C and Si concentrations from 22 to 30 at.% and <1 to 6 at.% respective from 1 to 12 months. XPS showed the presence of N, S, Si, Na and Cl^- on the surface, however, of these only Si and N had concentrations that exceeded 1 at.%, with the maximum for each being 5 at.% and 2 at.% respectively. Na and Cl^- were observed at 2 at.% each on 2 and 3 months samples only, suggesting they had been washed off in the following months. S concentrations also fluctuated with time implying that S is readily absorbed into the corrosion product. Overall the total concentration of pollutants increased from 27 at.% to 46 at.% from 1 to 12 months of exposure. From this information it suggests that the most common compounds found on the surface are C, N and S rich [67].

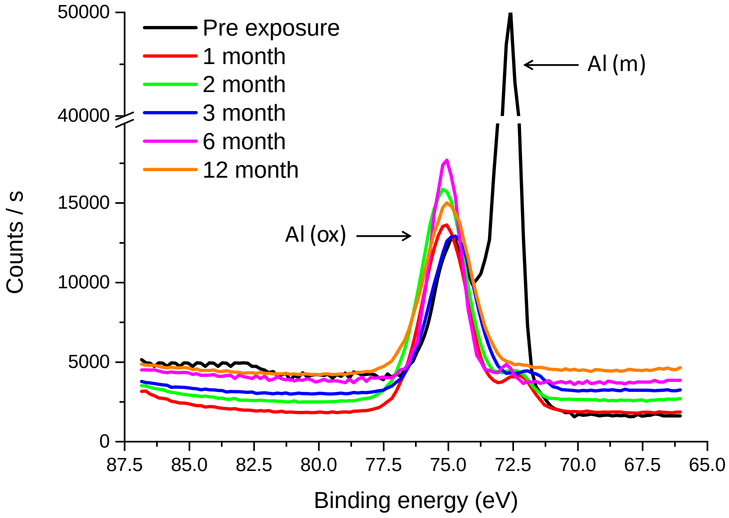

Figure 4-37: XPS spectra showing the Al2p metal and oxide peaks over a 12 month atmospheric exposure of SF1, highlighting the rate of change from Al (m) to Al (ox).

4.2.3 Spray formed Al-Mg-Li-Cu-Zn (SF2)

SF2 following atmospheric exposure showed very little change in the amount of pollutants and corrosion products with increased time. The greatest amount of corrosion product and pollutants was seen on the 6 months specimen, but pollutants were removed by 12 months. This spike in pollutants has been a common occurrence on all of the Al alloys in this thesis and tends to show that the TOW affects the rate of corrosion [67]. It also suggests that the corrosion products are highly soluble, since they have been removed by 12 months of exposure. Figure 4-38 a, b, c and d show the amount of pollutants seen on the surface of SF2 following 1, 3, 6 and 12 months respectively. Some ruptured corrosion product sites were observed, however, they do tend to suggest a very low concentration of corrosion taking place after 12 months of exposure. Even after this period, there were very few sites where thin films of H_2O had established any corrosion suggesting a very high corrosion resistance to SF2. This was surprising as the Cu and Zn rich region that was observed following EBSD was expected to reveal galvanic corrosion.

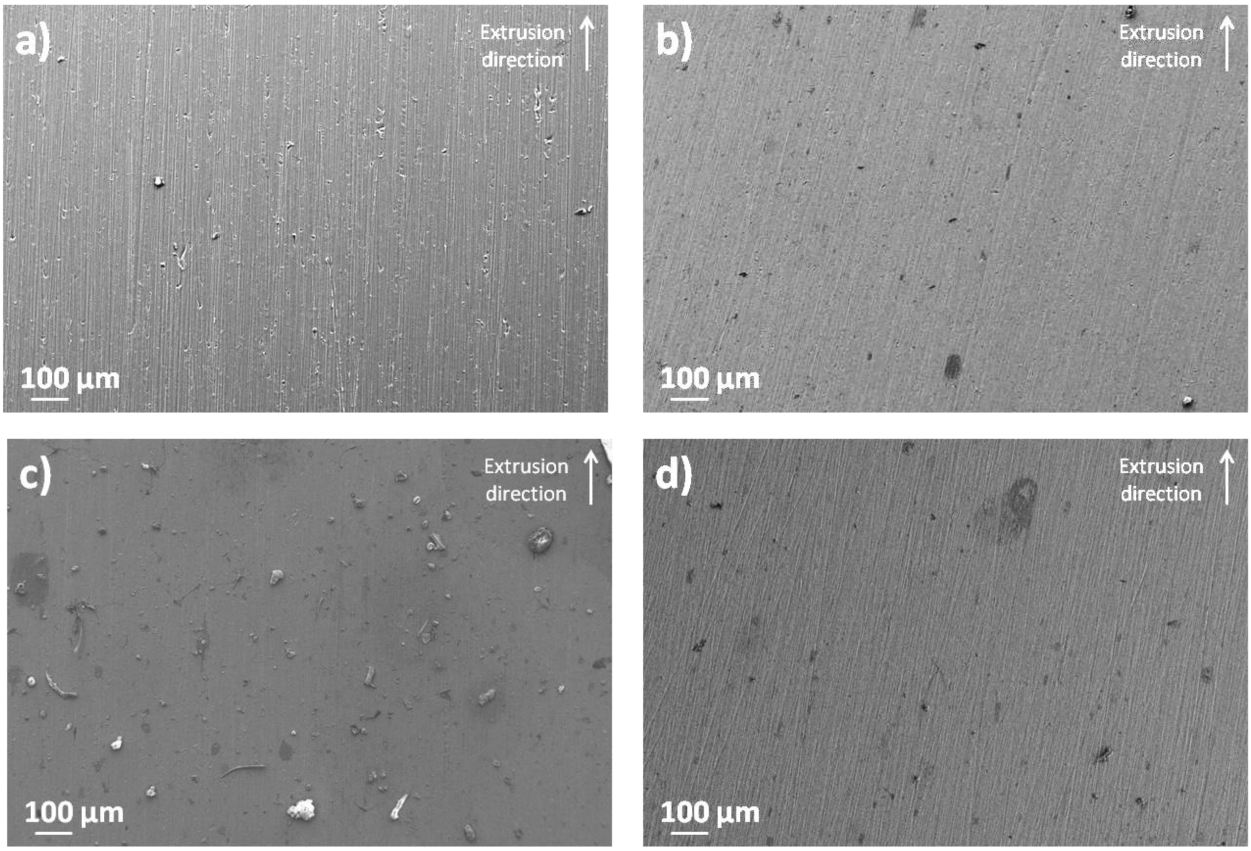

Figure 4-38: SEM micrographs of SF2 showing the build-up of corrosion products and pollutants after a) 1 month b) 3 months c) 6 months and d) 12 months of atmospheric exposure.

Figure 4-39 a shows that after 1 month galvanic corrosion around IMCs took place and Figure 4-39 b shows a ruptured corrosion product after 2 months of exposure above a pitting corrosion site. This shows that the surface is active during exposure, but examination of the surface revealed no established pitting corrosion, however, it is known that pitting corrosion can develop beneath corrosion products. A large number of corrosion product sites, similar to that seen in Figure 4-39 b were observed, but none of them had fractured to reveal any underlying pitting corrosion. Even though the number of corrosion product sites was high, their actual size was relatively small. The link between the low V_f of IMCs within

SF2 and the low volume of pitting corrosion, which in theory is a logical assumption, with IMCs being directly associated to pitting corrosion [17], [18].

Figure 4-39 c shows a cross-section taken after 6 months of exposure, revealing IGC and galvanic corrosion around IMCs. No evidence of pitting corrosion, suggesting that any pit initiation sites had very small openings and propagation. Analysis of the GBs using FEGTEM has not been conducted on SF2 and as such it is difficult to conclude whether the corrosion is IGC or a cross-section through an established pit. IGC has the possibility to progress of SF alloys due to a susceptibility to GB segregation; SF2 also has Li additions which have a tendency to segregate to GBs [115]. Figure 4-39 d shows evidence of more corrosion product on the surface of SF2, after 12 months of atmospheric exposure, showing that, over time, thin films of H_2O started to initiate corrosion.

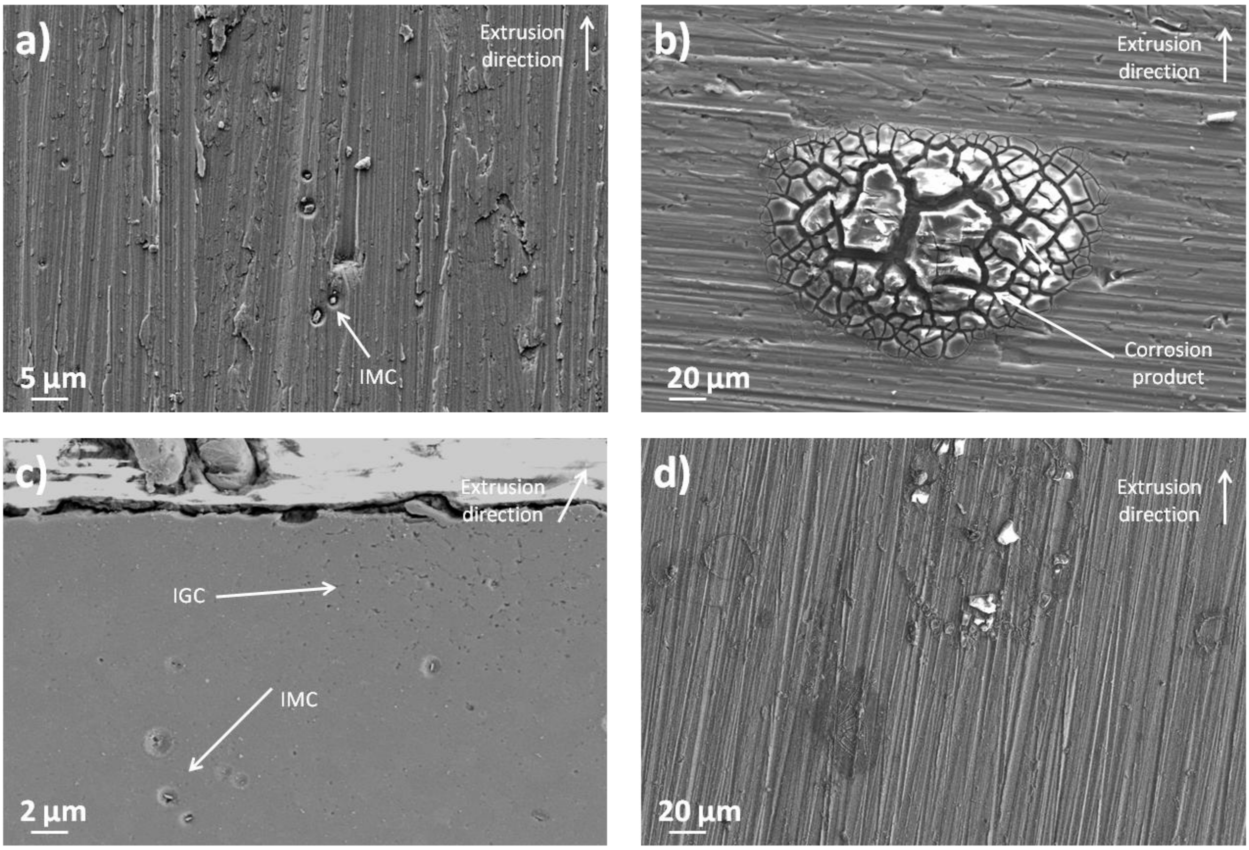

Figure 4-39: SEM micrographs of SF2 after a) 1 month of atmospheric exposure, showing galvanic corrosion surrounding IMCs. b) 2 months of atmospheric exposure, corrosion product in the form of surface ruptured corrosion product. c) 6 months of atmospheric exposure, showing evidence of IGC in the cross-section. d) 12 months showing evidence of surface corrosion product sites.

Figure 4-40 a and b show cross-sectional micrographs of the extrusion direction after 12 months of exposure in SF2 from which no corrosion was observed in the transverse direction. Figure 4-40 a and b show evidence of pitting corrosion and IGC on the extrusion direction. The pit opening was < 5 µm, however, it progressed to a depth of ~ 30 µm in Figure 4-40 a and ~ 20 µm in Figure 4-40 b. Figure 4-40 b shows that the pit opening is very small and suggests that the main form of corrosion on SF2 is IGC. The IGC seen in Figure 4-40 b, however, is seen to progress further into the specimen than the pit at a depth of ~ 30 µm. Due to the presence of Cu within SF2 the potential for IGC is increased due to the nature of Cu to segregate at GB regions [29], [34], [80], [83], [84], [97], [154]. EDS revealed that Cu and Zn could only be identified in the weld zone region, which theoretically explains why the IGC was only observed in this location, hence Figure 4-40 b was observing the weld region and Figure 4-40 a the regions either side of the weld. IGC is associated with an electrochemical difference in potential at the GB from which cathodic elements are typically the main culprit. This shows that in atmospheric conditions the Cu-containing region formed a galvanic cell with the surrounding Cu denuded regions, accelerating the IGC susceptibility. Interestingly no pitting corrosion was observed on the Cu denuded regions, but this could be related to the location of the cross-section.

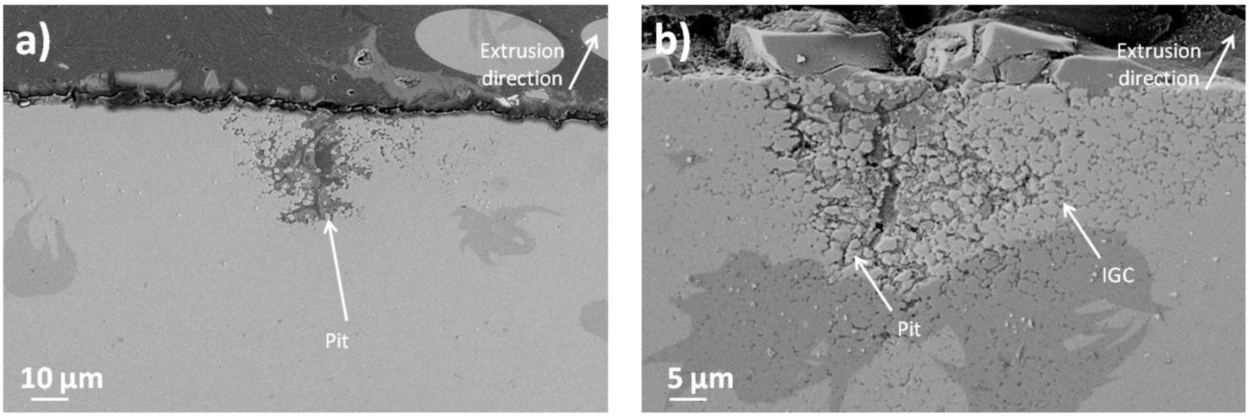

Figure 4-40: Cross-sectional SEM micrographs of SF2 after 12 months of atmospheric exposure showing evidence of a) pitting corrosion. b) pitting and IGC.

EDS showed that with increasing time the amount of O present on the surface increased from ~ 2 at.% after 1 month to ~ 4 at.% after 12 months. This highlights a very slow rate of corrosion and growth of corrosion products. The Al content dropped by 3 at.% over the 12 months of exposure, supporting the SEM micrographs in Figure 4-38 showing a low volume of corrosion products over time. The Al:O ratio changed from ~ 27:1 to ~ 20:1 after 12 months, but the total Al and O concentrations were similar at 84 at.% on the 1 and 12 months samples. Figure 4-41 shows evidence of Si, C and Cl^- deposition over the surface of SF2 following 3 months of atmospheric exposure. C concentrations were seen to increase to ~ 10 at.% after 12 months, but due to the lack of thin films and subsequent O for C and other pollutants to combine with, no other elements were observed at concentrations > 0.5 at.%. The total amount of pollutants on SF2 after 12 months was ~ 15 at.%. The Mg content was, however, seen to reduce with time, highlighting the anodic nature of the Mg [19], [27], [60–64].

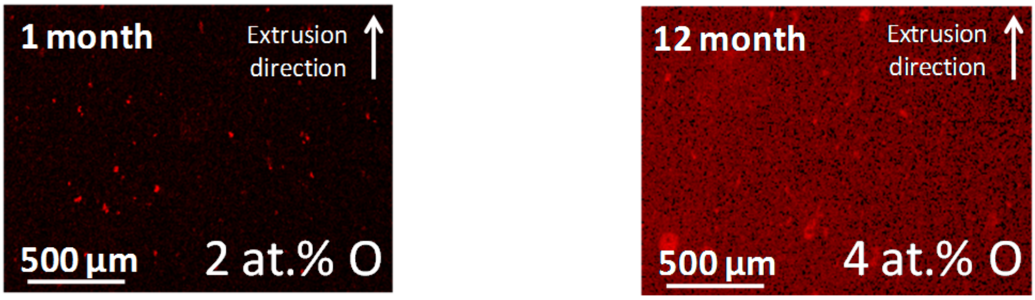

Figure 4-41: EDS maps showing the increase in O concentration with increasing atmospheric exposure time on SF2.

EDS of the corrosion products did not show any significant trends as time increased. The C content after 1 month was ~ 28 at.% but after 3 and 6 months it was seen to be 9 and 44 at.% respectively. This affected any trends that could have been seen with regards to changes in O and Al concentrations. O concentrations increased from 25 at.% to 46 at.% between 1 and 12 months, however, in this time period the Al had been recorded at 26 at.%, 42 and 36 at.% for 2, 3 and 6 months respectively. Figure 4-42 shows that S, Si and Cl^- were observed in the corrosion products from the first month of exposure [122], [125]. There concentrations fluctuated over time but they remained present throughout the entire 12 month exposure period. This highlights the issues associated with atmospheric conditions in that trends can sometimes be masked by fluctuating weather conditions and pollutant deposits.

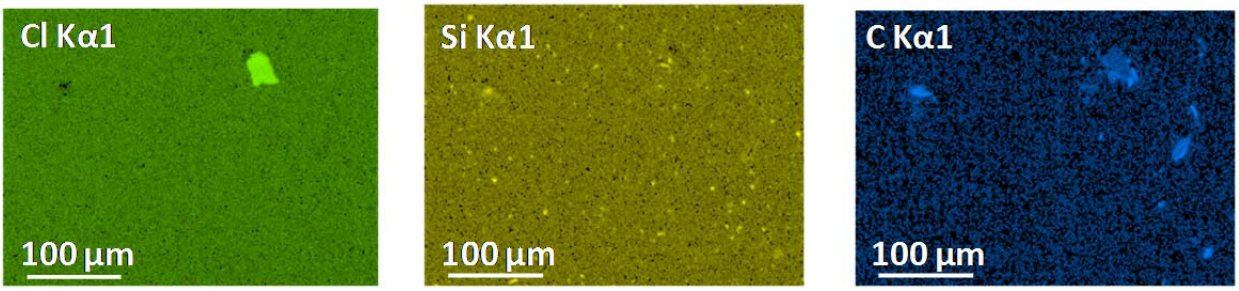

Figure 4-42: EDS maps showing the presence of Si, Cl^- and C on the surface of SF2 after 3 months of atmospheric exposure.

The main IMC types on SF2 are; Al-Mg-Si and Al-Mg-Si-Fe. As time increased both IMCs showed increased concentrations of O and C, however, the Al content of the Al-Mg-Si-Fe IMCs reduced to ~ 25 at.% after 12 months. Al-Mg-Si IMCs, showed a reduction in Al content, as the Mg and Si concentrations reduced with time, alongside an increase in the O content. Neither showed any preference towards corrosion, however, the Al-Mg-Si-Fe IMCs in theory are more likely to be detrimental [24–26].

Figure 4-43 shows the XPS survey spectra taken from each sample after each time interval, they show that overall there are very minimal changes in the elemental compositions. XPS surveys do, however, show that C, S and Si concentrations increase with exposure time. The maximum values of each were recorded after 12 months of exposure at 35 at.%, 2 at.% and 5 at.% respectively. The O content was seen to reduce with time alongside the Al content, which is due to the increase in surface pollutants. The sum value of Al and O concentrations goes from 79 at.% to 57 at.% after 12 months exposure, with the ratio of Al:O going from ~ 1:1 to ~ 1:3 after 12 months. Examination showed that the Al peak shifted, demonstrating the hydration of the Al. N concentrations are stable around 1-2 at.% over the exposure time, but these results show that it was increasing with time.

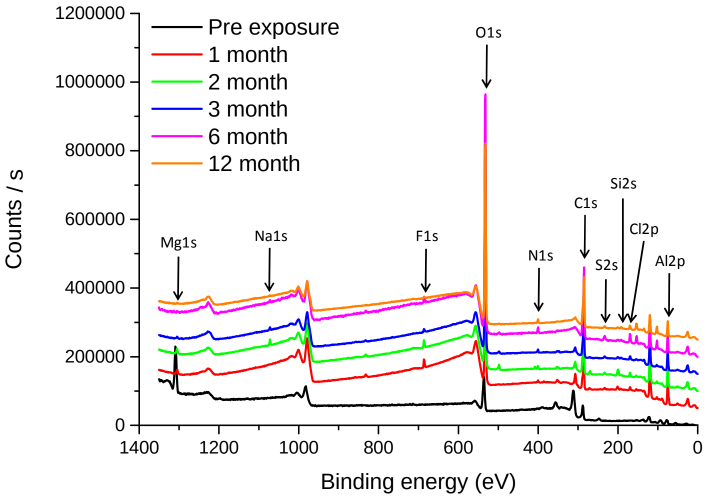

Figure 4-43: XPS survey spectra of SF2 over a 12 month atmospheric exposure, showing changes in elemental constituents with time.

High resolution analysis of the Al peak shows that pre-exposure Al (ox) and Al (m) can be observed, with a 24 at.% Al (m) and 7 at.% Al (ox) content. Al (m) can be seen on SF2 after 6 months of exposure, however, the value is < 0.5 at.%. After 3 months the Al (m) content was 4 at.%, so between 3 and 6 months large amounts of corrosion products and pollutants are deposited onto the surface reducing the Al (m) content. Figure 4-44 shows the Al peak highlighting the change in Al (m) content with increasing exposure time. XPS showed an increase in the S, Si, and N concentrations with time with the maximum of each being seen at 2 at.%, 4 at.% and 1.4 at.% respectively after 12 months of exposure. Cl^- and Na were observed in very small concentrations throughout the 12 month exposure period with the maximum being 2 at.% combined. The total amount of pollutants was seen to be 41 at.% after 12 months, which was double that after 1 month.

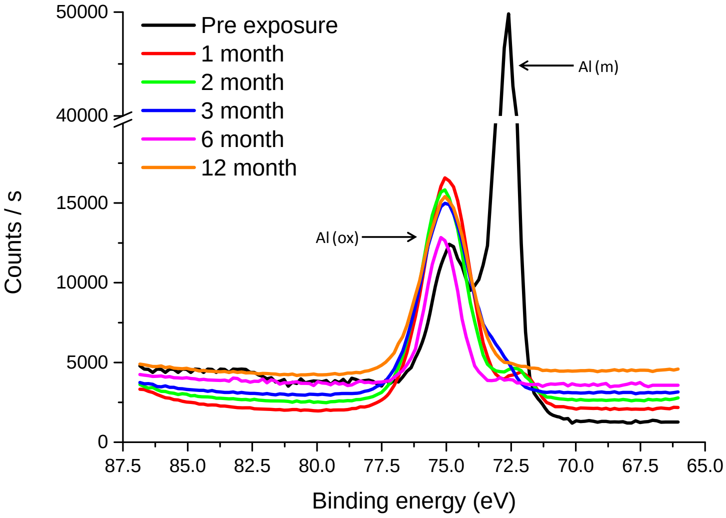

Figure 4-44: XPS spectra showing the Al2p metal and oxide peaks over a 12 month atmospheric exposure of SF2, highlighting the rate of change from Al (m) to Al (ox).

4.2.4 Discussion of Al-Mg atmospheric exposure resistance

Mg1, SF1 and SF2, all show very similar densities of corrosion products and pollutant deposited over 12 months of exposure. After 12 months all three showed evidence of thin H_2O films, where circular corrosion products formed. Table 4-2 suggests a higher level of corrosion on Mg1 than either of the SF alloys due to the increased O concentration. However, this increase in corrosion product could be related to the high V_f of IMCs within Mg1 compared to both SF alloys. Mg1 and SF2 showed only a 2 at.% increase in O concentration over 12 months, however, SF1 showed a 4 at.% increase. EDS suggests that SF1 has shown the most corrosion product being formed suggesting the lowest corrosion resistance. However, due to the limitations of the EDS technique it can be argued that all Al-Mg alloys performed in a very similar manner. Similar to the Al-Cu alloys, an increase in pollutant concentrations was observed after 6 months of exposure showing that TOW does have an impact on corrosion [67].

Table 4-2: Changes in Al and O concentration on the surface of samples measured by EDS on Mg1, SF1 and SF2 after 1 and 12 month exposure period.

At.%	O after 12 months of exposure	O within the corrosion product after 12 months of exposure	Al after 1 month	Al + O after 1 month of exposure	Al after 12 months	Al + O after 12 month of exposure
Mg1	8	62	76	85	65	55
SF1	6	37	82	77	78	52
SF2	4	47	81	74	78	57

Mg1 showed very little corrosion over the first 6 months of exposure, however, both SF1 and SF2 showed galvanic corrosion of the matrix surrounding IMCs after 1 month [13], [22], [63]. Even though the V_f of the IMCs within the SF alloys was lower than those in Mg1, it was evident they were more cathodic. This is likely to be associated with the large amounts of Mg containing IMCs on Mg1 undergoing selective dissolution, whereas the IMCs on SF1 and SF2 had less Mg within them. Once pitting corrosion developed on each, it was faceted in morphology. Most of the surface showed evidence of corrosion product formation as plates, which with increasing exposure time fractured and revealed underlying pitting [126]. Mg1 showed evidence of fractured, plate-like corrosion products on top of what can be assumed to be anodic sites, and mossy structures were seen to develop on cathodic regions [126].

Cross-sectioning of Mg1 revealed that the number of localised pitting corrosion sites was very limited. On average the pits did not progress far into the specimens, however, there were some pits that were seen to be 70 µm deep but most were ~ 10 µm deep with pit openings being < 10 µm. Mg1 also showed that sub-surface corrosion developed, with corrosion cavities being observed. In comparison SF1 and SF2 in addition to pitting showed evidence of IGC and the number of pits observed on SF1 and SF2 was higher than Mg1. The presence of IGC suggests that there may be segregation at the GBs on both SF1 and SF2. In SF2 it has been shown that Cu is present, therefore it can be predicted that Cu rich phases may be present at the GBs [24], [26], [36], [80], [95]. However, in SF1 the likelihood is that either the β phase and / or Li containing phases such as Al_3MgLi, δ and δ' could be present [2], [4], [44], [48]. As discussed the maximum pit depth on SF1 was ~ 60 µm and SF2 was ~ 30 µm, but most were closer to 20 µm. IGC, however, was seen to progress to a maximum depth of ~ 30 µm on SF1 and SF2. Overall it can be concluded that SF2 cannot be used as a comparison due to the large galvanic Cu and Zn rich region. As such a comparison between Mg1 and SF1, shows that Mg1 visually has the superior corrosion resistance and following cross sectioning shows a similar corrosion depth.

EDS showed that both SF1 and SF2 had very similar surface chemistries over the 12 months of exposure. In comparison Mg1 showed a higher O concentration after only 1 month compared to the 12 months SF alloy values. However, the O content after 12 months was seen to be 8 at.% so there was no significant difference in O concentration between the Al-Mg alloys. The Al content of Mg1 was also seen to reduce by ~ 10 at.% compared to 4 at.% of the SF alloys, showing a higher formation of corrosion products. The Al:O ratios for Mg1 changed from ~ 13:1 to ~ 8:1 after 12 months, which is similar to that of the SF alloys. Mg concentrations on the Al-Mg alloys were seen to reduce with time, demonstrating the anodic nature of the Mg as it selectively corrodes [19], [27], [60–64]. Overall with the lack of thin H_2O films a low volume of corrosion products developed, clearly demonstrating a correlation between corrosion and TOW [67].

Comparisons of the corrosion products show that after 12 months of exposure, SF1 had the lowest combined Al and O concentration, suggesting large amounts of pollutants were deposited. Table 4-2 shows that Mg1 had the highest O content suggesting SF1 had the lowest amount of corrosion taking place, thus had the highest corrosion resistance. Similar to the surface, EDS analysis showed that C, Si, S and Cl^- were the main pollutants observed on the surfaces of the Al-Mg alloys.

SF1 and SF2 had similar IMC types being; Al-Mg-Si and Al-Mg-Si-Fe particles, however, Mg1 showed in addition; Al-Mn-Si and Al-Fe-Mn-Si-Mg IMCs. EDS identified that the Fe containing IMCs were of concern in Mg1, SF1 and SF2 because they developed galvanic corrosion surrounding them [24–26]. The Al-Mg-Si IMCs were shown to have potentials less noble to that of the Al-Mg matrix and showed reduced corrosion resistances [19], [27], [60–64]. Over time they showed selective dissolution, but remained anodic to the cathodic matrix. The Fe rich IMCs, however, once the Mg concentrations were removed left highly cathodic zones, that accelerated corrosion [24–26].

After 1 month of exposure there was a higher concentration of Al on Mg1, compared to both SF1 and SF2, as shown in Table 4-2. Table 4-2 also shows that the combined Al and O concentration was higher on Mg1 than SF1 and SF2 respectively. After 12 months, however, the total Al and O concentrations were very similar at ~ 55 at.%, showing that they all had very similar amounts of corrosion products and pollutants deposited. The Al:O ratios, however, were different with Mg1 having a ~ 3:1 ratio pre-exposure compared to ~ 1:1 of the SF alloys, whereas after 12 months all Al-Mg alloys had a ~ 1:3 ratio. This shows that with time all Al-Mg alloys, with regards to surface chemistry corroded at a similar rate and examination of the Al peaks showed that the Al (m) was seen to be < 0.5 at.% after 6 months on each. TOW has been shown to impact surface chemistry [67], and this may be why no Al (m) can be seen on any of the Al-Mg alloys after 6 months, with high levels of pollutants being recorded. Figure 4-45 shows the change in Al (m) and Al (ox) content with increasing exposure time on Mg1, SF1 and SF2. As previously mentioned the trends between XPS and EDS were similar, however, a distinct difference in interaction volume was observed with more substrate elements such as Mg being recorded on all specimens after 12 months, whereas for XPS this was not seen after 1 month of exposure.

XPS showed that a reduction in Mg content was seen on Mg1, which accompanied with the increase in O could suggest the formation of a MgO corrosion product, which has been noted in literature [67] to cause staining on the surface, however, no staining was observed. This could be due to the low volume of corrosion products, suggesting that Al-Mg alloys needed longer exposure times to reveal this staining phenomenon. Similar to SF1 and SF2; C, N, S, Si, Na and Cl^- were observed on the surface of Mg1, showing that pollutant deposits are constant and once again shows that carbonaceous Al products, NO_x, SO_x and NaCl compounds are ever present [125]. It must, however, be noted that it could not be identified how much of the O was attributed to the carbonaceous Al products, OH^-, NO_x, SO_x and Al_2O_3 and any other compounds that may have formed.

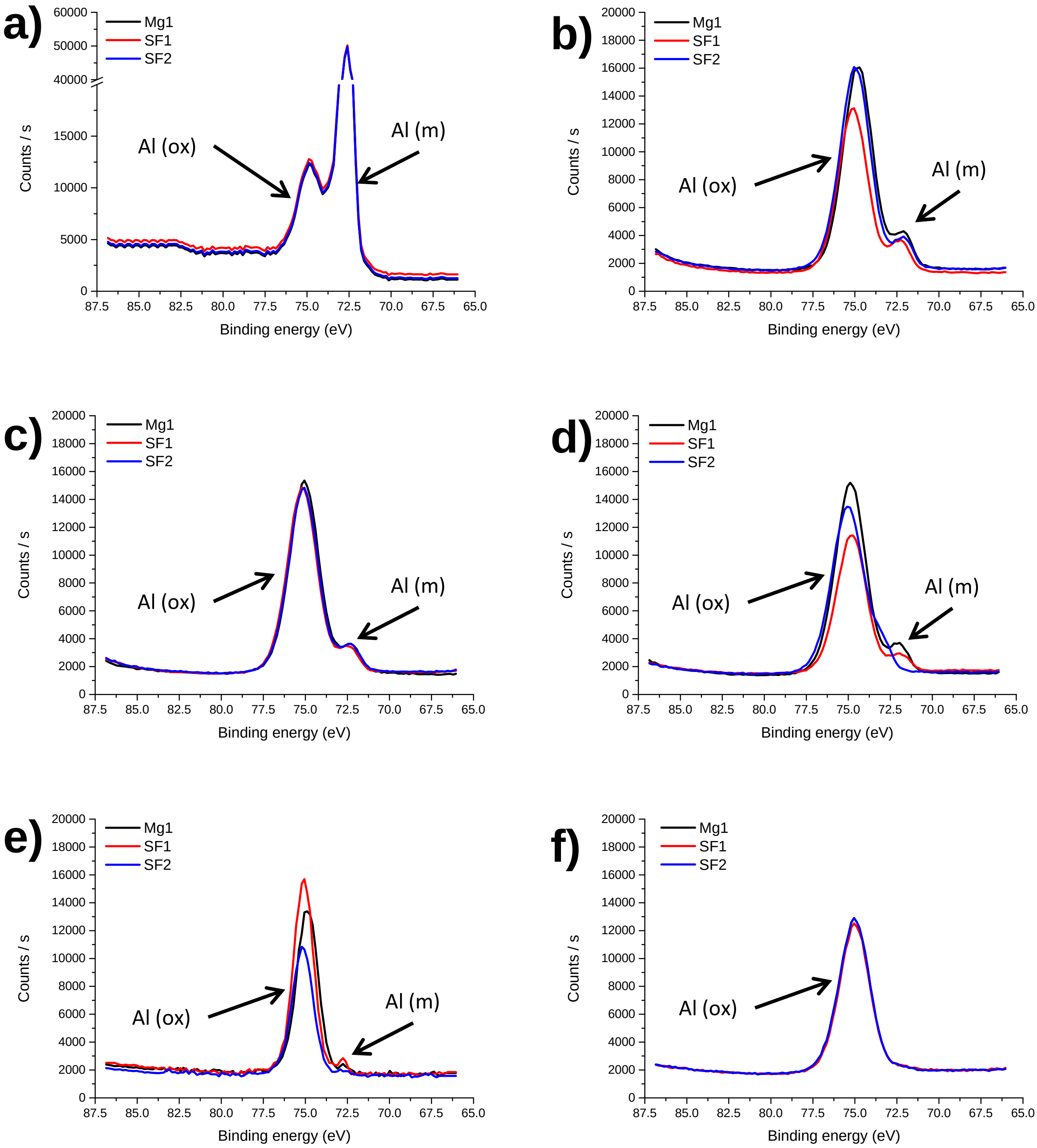

Figure 4-45: XPS spectra showing the comparison between Mg1, SF1 and SF2 a) pre-atmospheric exposure b) 1 month c) 2 months d) 3 months e) 6 months f) 12 months.

Chapter 5: Immersion testing

Prolonged immersion testing in a 3.5 wt.% NaCl solution has been conducted to get an understanding of the corrosion mechanisms of a range of Al alloys. All samples have been mechanically ground as explained in Chapter 2. OCP has been plotted against time, to show how it changed as immersion time increased. The analysis will also be able to give an understanding of how the microstructure, particle distributions and chemistry influence the resulting corrosion performance.

5.1 Immersion testing of Al-Cu alloys

5.1.1 AA2024-T3 (Cu1)

OCP measurements show that over 96 hrs of immersion on Cu1 a reduction in potential is seen with increasing time. Figure 5-1 a and b show the OCP over the initial 6 hrs of immersion and 96 hour immersion period respectively. The starting potential of Cu1 was seen to fluctuate substantially, however, after 20 min's reduced to within 15 mV, as highlighted by Figure 5-1 a. Figure 5-1 b shows that the overall trend for Cu1, is a reduction of ~ 136 mV, as highlighted by Table 5-1. Overall Cu1 shows a relatively reproducible OCP trend, with, as stated an average standard deviation of 32mV. *Vargel* [12] stated that a reduction in potential signifies corrosion taking place, as such it can be assumed that Cu1 shows a poor corrosion resistance. This is primarily associated with Cu being more noble than Al causing anodic dissolution of the Al matrix [26], [63], [80], [84], [154], [155].

Table 5-1: OCP of Cu1 over the 96 hour immersion period in 3.5 wt.% NaCl.

Time (hrs)	**0**	**24**	**48**	**72**	**96**
OCP (mV)	-610±57	-630±35	-668±36	-733±31	-746±34

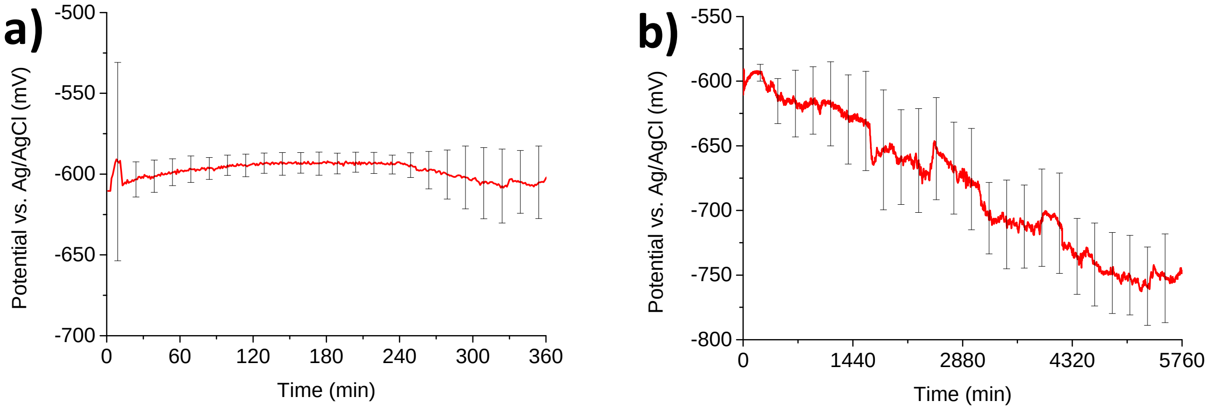

Figure 5-1: Graph showing the OCP of Cu1 following immersion in 3.5 wt.% NaCl for a) 6 hrs. b) 96 hrs.

Figure 5-2 a, b, c and d show the surface after 24, 48, 72 and 96 hrs of immersion respectively, from which a visual increase in the amount of corrosion product can be observed. It can also be identified that IMCs are highly susceptible to corrosion. Figure 5-2 a and b show dimpling of the surface where corrosion has taken place surrounding the cathodic Cu, Fe and Mn rich IMCs which causes the Al matrix to undergo anodic dissolution, leading to particle drop out [26], [35], [39], [60], [63]. This process is a typical redox reaction that leads to local alkalisation of the cathodic regions and acidification of the anodic regions [19], [39], [63], [86], [91]. Formation of corrosion domes identified in Figure 5-2 a and d is suggests the formation of H_2 bubbles [19]. These corrosion domes are formed from the corrosion that takes place between cathodic IMCs and the anodic Al matrix and with increasing immersion time the number of these domes increases but their respective size did not (Ø = ~ 100 µm). Through dissolution of the Al matrix and the resultant reaction with H_2O, a H_2 bubble can form on the surface, which becomes encapsulated within a corrosion product as dissolution takes place. Since the H_2 bubble is then enclosed within the corrosion product, this causes a reduction in pH beneath the corrosion dome as the concentration of the corrosive medium, now enclosed becomes more acidic. This causes accelerated corrosion to take place, thus allowing the corrosion to propagate deep into the specimens [19], [39], [63], [86], [91]. EDS revealed that the darker patches of corrosion product on Figure 5-2 a, b, c and d were those rich in O.

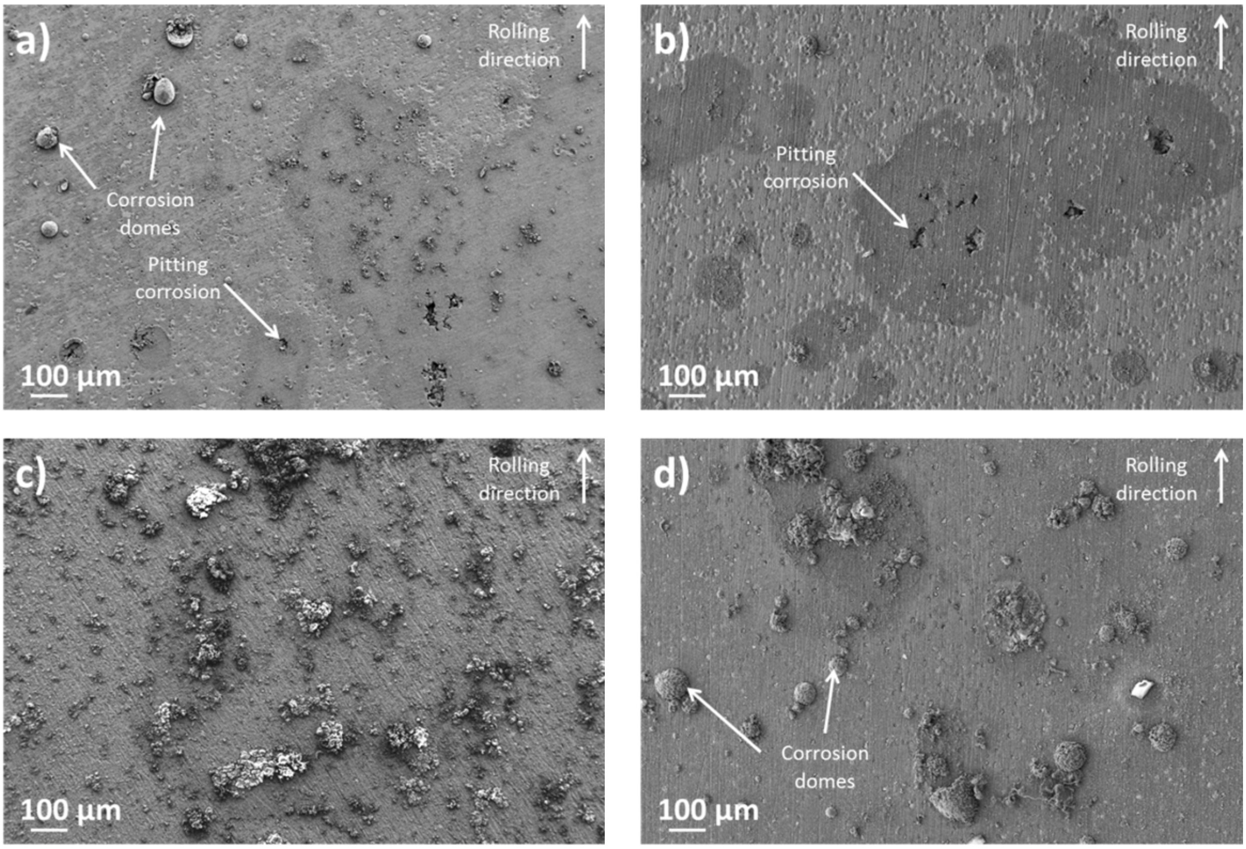

Figure 5-2: SEM micrographs of Cu1 immersed in 3.5 wt.% NaCl for a) 24 hrs. b) 48 hrs. c) 72 hrs. d) 96 hrs.

Figure 5-3 a and b show micrographs of the corrosion domes, for which Figure 5-3 b shows an intact corrosion dome and one that has ruptured. Beneath the corrosion domes, pitting corrosion can be seen, confirming the highly acidic nature of the pits. Rupturing of the corrosion domes could have taken place via agitation, however, this is not likely as the corrosion product is typically insoluble in H_2O. The most likely outcome is that the localised change in pH has eventually dissolved the corrosion product, thus allowing the H_2 bubble to detach from the surface. Figure 5-3 c shows corrosion of individual grains, following dissolution around IMCs and precipitates within the grain structures [26], [35], [39], [60], [63].

All of the IMCs and precipitates within Cu1 were Cu, Fe and Mn containing and as such all were more noble than the matrix forming galvanic cells [26], [60], [63], [80], [84], [154], [155]. Figure 5-3 d provides evidence of a correlation between IMCs and pitting corrosion sites.

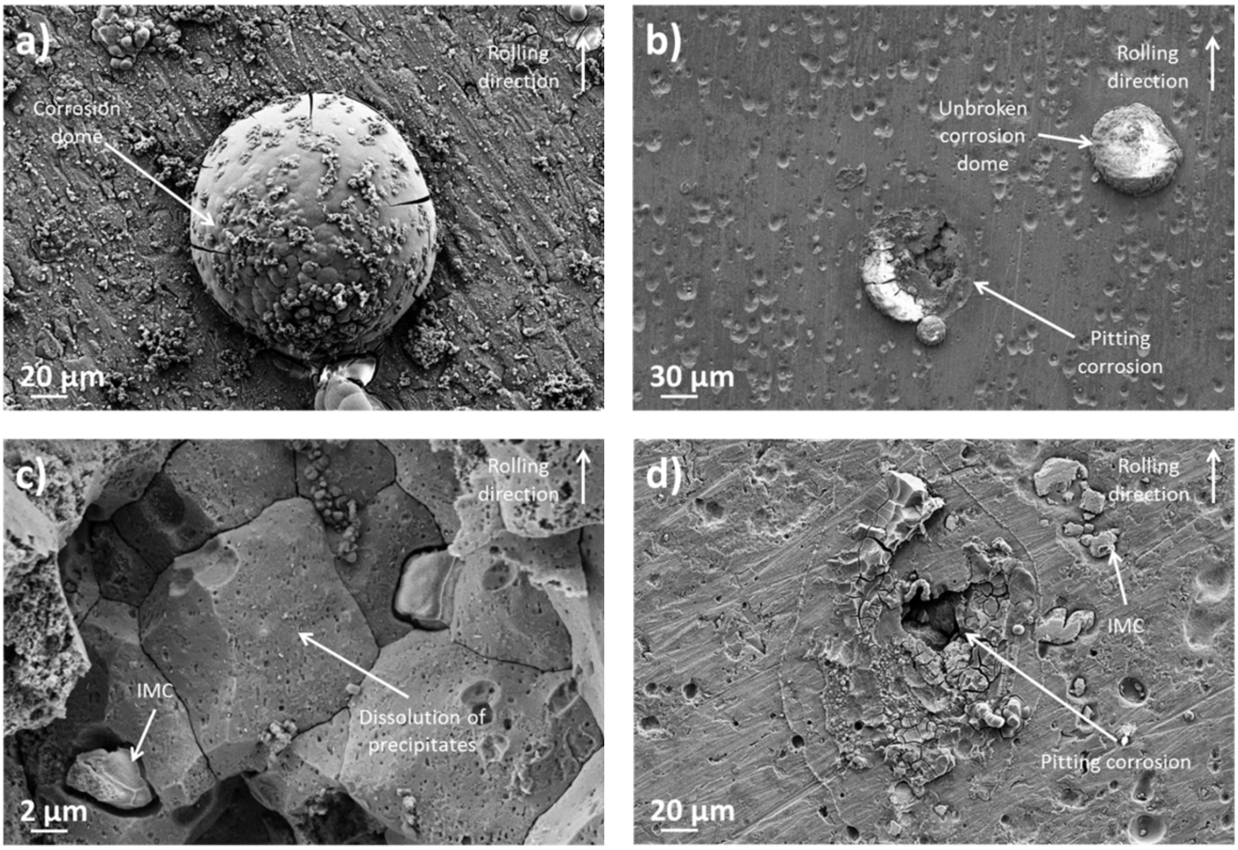

Figure 5-3: SEM micrographs of Cu1 showing a) corrosion dome formed through the generation of H_2 bubbles. b) ruptured and intact corrosion domes formed through the generation of H_2 bubbles, highlighting pitting corrosion developing beneath. c) galvanic dissolution of the Al matrix surrounding IMCs and precipitates. d) dissolution around IMCs and pitting corrosion.

Figure 5-4 shows an increase in O on the surface of Cu1. The corrosion product, O concentration increased from 24 to 47 at.% over the 96 hour immersion period, which also meant that the Al:O ratio changed from ~ 5:1 to ~ 7:4 after 96 hrs of immersion. The concentration of O was similar between 24 and 48 hrs at 24 at.%, suggesting limited corrosion had taken place or some of the corrosion product had been removed either through dissolution or had been washed off during agitation. OCP data suggests that additional O should have been observed on the surface after 48 hrs due to the reduction in potential, thus it can be assumed that some of the corrosion product has been removed. After 48 hrs the O increased by ~ 10 at.% per additional 24 hrs of immersion, as such the final Al and O concentrations were measured to be 49 at.% and 47 at.% respectively. Cu concentration remained stable throughout immersion, however, the level of Cl^- was seen to increase on the surface, which is to be expected as Cl^- starts to become incorporated into the corrosion product.

Figure 5-4: EDS maps showing the increase in O concentration with increasing immersion time on Cu1.

With increasing immersion time the concentration of O increased whilst a reduction in Al was observed within the corrosion product, whereas the only other elements that increased in concentration were Mg and Cl^-, although at very small concentrations (< 1 at.%). It can be assumed that the increase in Mg is through sacrificial dissolution, with it being less noble than Al [67] and the Cl^- increase from the breakdown of NaCl solution. The Al:O ratio changed from 1:2 to 1:4 after 96 hrs, with the final Al and O concentrations being 20 at.% and 79 at.% respectively. The Mg and Cl^- concentrations increased to 0.8 at.% and 1.2 at.% respectively. Cu concentrations did not change, which tends to agree with literature that Cu can be redistributed over the surface when corrosion initiates [24], [26], [36], [95].

Figure 5-5 shows example EDS maps of the IMCs within Cu1. IMCs within the corrosion product domes showed O at 21 at.% and Al at 76 at.%, whereas IMCs outside showed O at 17 at.% and Al at 79 at.%, which shows evidence of redox reactions taking place. EDS identified Al-Cu-Mg IMCs after 96 hrs of immersion and showed lower O concentrations compared to the Al-Cu-Fe-Mn IMCs at 4 at.% compared to 33 at.%. This highlights the sacrificial nature of the Mg within the Al-Cu-Mg IMCs and identifies the cathodic nature of the Al-Cu-Fe-Mn IMCs [24], [26], [29], [60], [80], [84], [152]. The Al-Cu-Mg IMCs showed a reduction in Mg from ~ 19 at.% to 5 at.% after 96 hrs of immersion [19], [27], [60–64]. The Al-Cu-Fe-Mn IMCs showed reductions in Fe, Mn and Cu which can be associated with the increase in O concentration present. Overall, all of the IMCs within Cu1 are active whether they are acting as anodes or cathodes. Literature has shown that on Cu1 the Al-Cu-Fe-Mn and Al-Cu-Mg particles are the most detrimental to corrosion and EDS has assisted in demonstrating this [24], [26], [29], [60], [80], [84], [152]. This also confirms that IMCs in general are detrimental to the corrosion resistance of Al alloys [26], [35], [39], [60], [63].

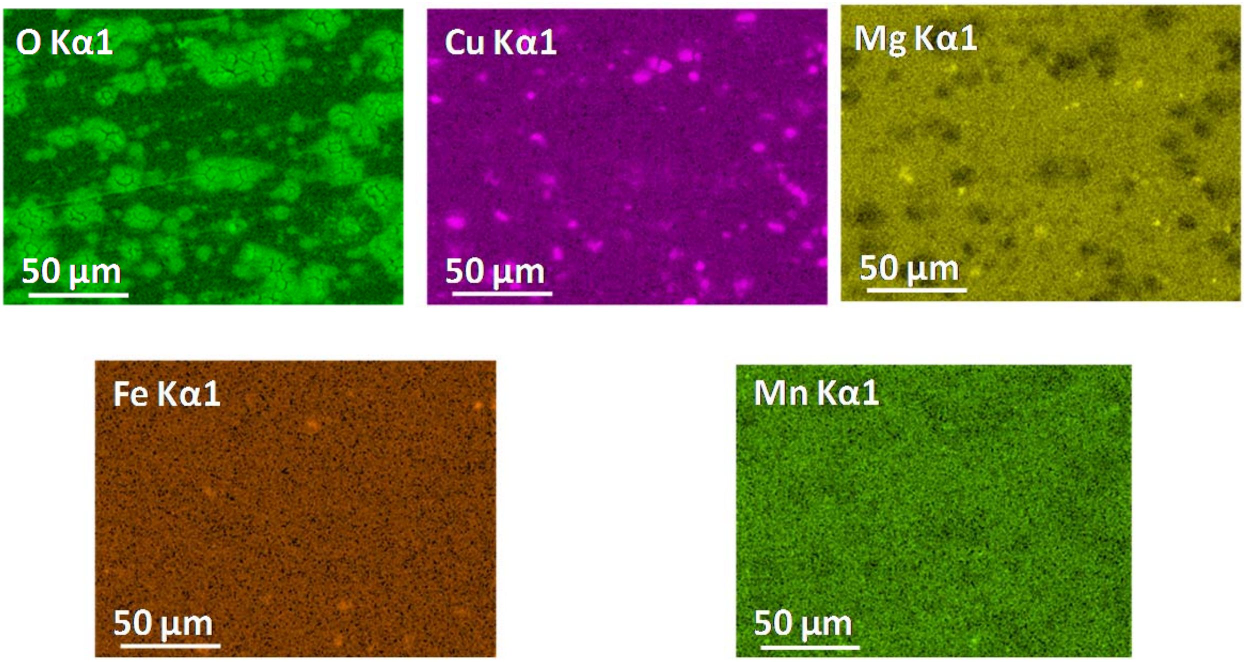

Figure 5-5: EDS maps highlighting the increased O concentration at the Cu, Fe and Mn rich IMC locations in Cu1.

Figure 5-6 a and b show the extrusion direction and Figure 5-6 c and d show the traverse direction after 24 hrs of immersion, from which evidence of pitting and IGC can be seen. *Birbilis and Buchheit* [26] showed that the E_{pit} of the θ phase is -652 mV vs. SCE and as such it can be concluded that the θ type phases will have been active within 24 hrs of immersion as per Figure 5-1. FEGTEM revealed Cu particles at the GBs, which appeared as closely packed, θ type phases. In this case dissolution of the Al matrix around the θ type phases takes place, hence the thick nature to the IGC, as shown in Figure 5-6 a, b and d. When pitting corrosion was observed, in most cases IGC was also seen, for which the IGC propagated deeper. *Knight et al.* [124] observed AA2024 and also stated that the IGC progressed further than pitting corrosion. Figure 5-6 b, c and d show pitting corrosion and IGC for which in all cases IMCs are in close proximity to the corrosion [26], [35], [39], [60], [63]. Figure 5-6 b shows the furthest propagation of IGC at a depth of ~ 40 µm, however, on average most of the IGC was between 10 and 20 µm. Pitting corrosion was seen to be shallower at a maximum depth of ~ 15 µm and the size of the pit openings ranged from 10 to 20 µm in width. The pitting corrosion depth was difficult to distinguish due to large amounts of IGC also being observed, as seen in Figure 5-6 c and d. Figure 5-6 c also shows the formation of a sub-surface corrosion cavity, where the corrosion progressed more substantially sub-surface to that of the surface.

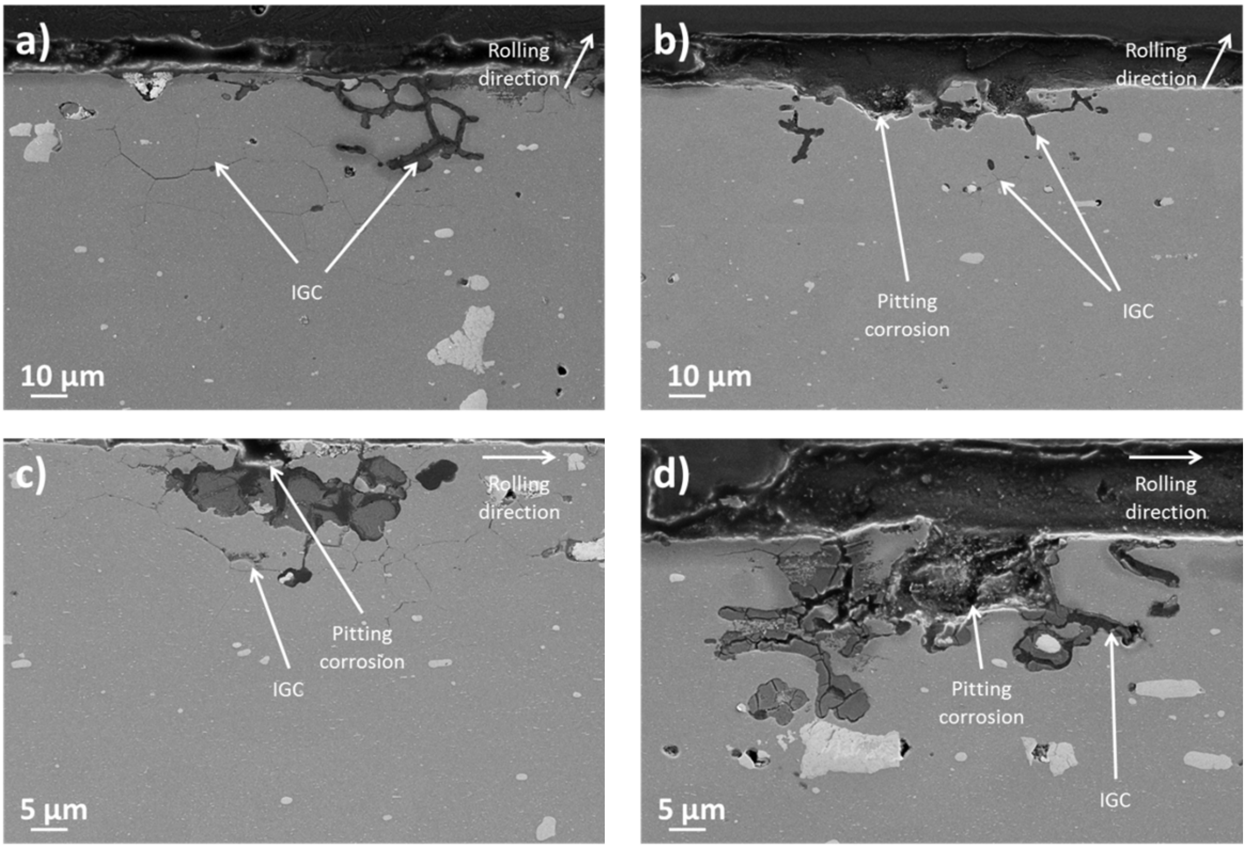

Figure 5-6: Cross-sectional SEM micrographs of Cu1 after 24 hrs of immersion in 3.5 wt.% NaCl showing evidence of a) IGC penetration. b) shallow pitting and IGC. c) sub-surface cavity formation from pitting corrosion and IGC and d) pitting and IGC around IMCs.

Figure 5-7 a and b show micrographs of the extrusion direction and Figure 5-7 c and d show the traverse direction after 96 hrs of immersion. The depth of corrosion was not notably different as to what was expected with the average IGC depth increasing to ~ 40 µm, however, the pitting corrosion depth was not seen to change. The number of pits and IGC sites, however, did increase. This formed a friable weakened layer on the surface of Cu1 with a large number of pit openings and a large network of IGC sub-surface. With electrolytes being able to travel along the GBs to a point of weakness, typically particle segregation, this meant that cavities could form sub-surface from the dissolution of the Al matrix surrounding them [26]. The amount of sub-surface corrosion also increased with time, however, this was to be expected.

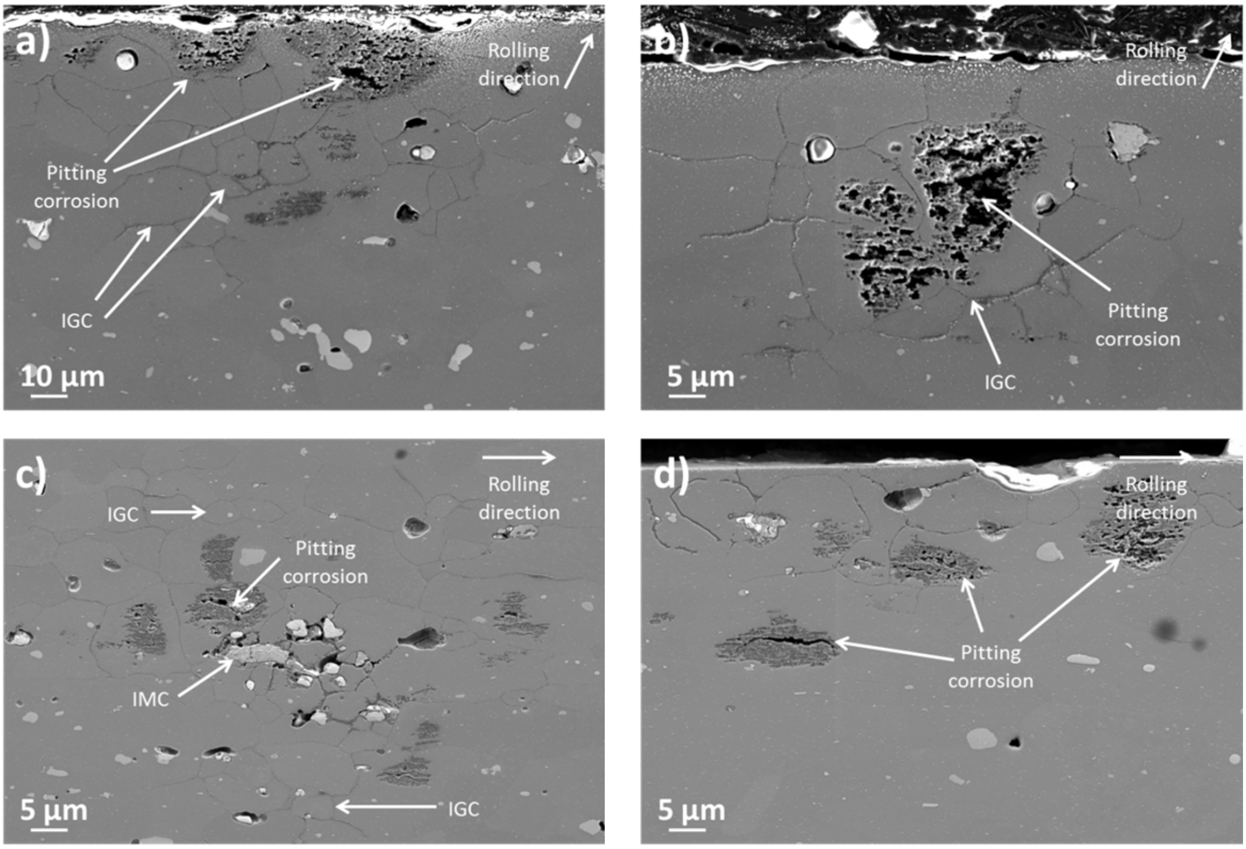

Figure 5-7: Cross-sectional SEM micrographs of Cu1 after 96 hrs of immersion in 3.5 wt.% NaCl showing evidence of a) IGC penetrating deeper into specimens than pitting corrosion. b) cross section through some pitting corrosion and IGC. c) sub-surface pitting corrosion and IGC around IMCs and d) sub-surface corrosion.

5.1.2 AA2099-T8E77 extrusion (Cu2)

Figure 5-8 a and b show the OCP over the initial 6 hrs of immersion and 96 hour immersion period respectively. Figure 5-8 a shows that over the initial hour of immersion the OCP reduces significantly, whereas after this the OCP remains relatively stable, as highlighted by Table 5-2. Even though the standard deviation can be seen to fluctuate over the immersion period, the trend in OCP is relatively constant. The fluctuations in standard deviation averaged at 8 mV, however, the maximum deviation was 28 mV. From immersion to when the specimens were removed the OCP for Cu2 was seen to reduce by 30 mV suggesting a high resistance to corrosion. *Proton et al.* [115] examined the OCP of a HT / NHT Al-Cu-Li alloy and showed that it had an OCP of -730 mV vs. SCE compared to ~ -620 mV vs. SCE after 168 hrs of immersion in a 0.7 M NaCl. This demonstrates that the OCP values obtained in this work are similar to those of literature [115].

Table 5-2: OCP of Cu2 over the 96 hour immersion period in 3.5 wt.% NaCl.

Time (hrs)	0	24	48	72	96
OCP (mV)	-640±12	-665±8	-664±11	-665±8	-670±9

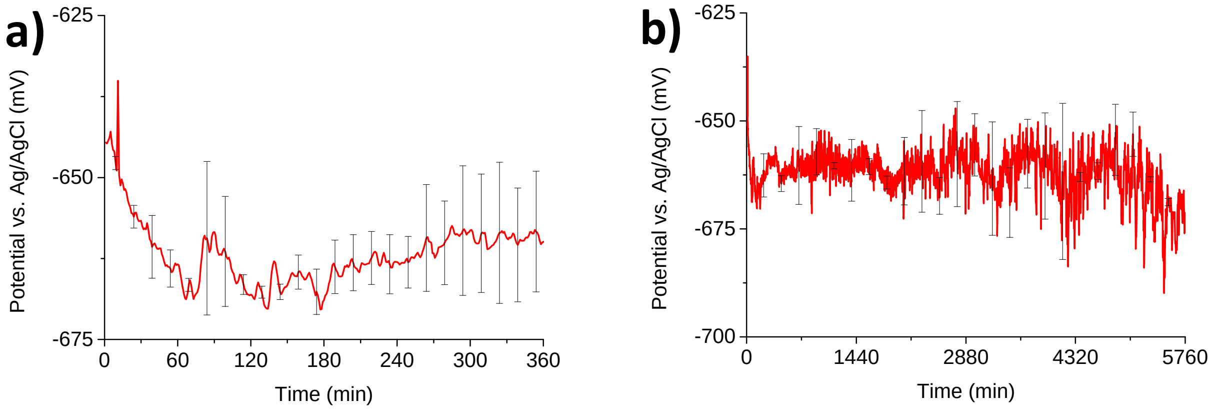

Figure 5-8: Graph showing the OCP of Cu2 following immersion in 3.5 wt.% NaCl for a) 6 hrs. b) 96 hrs.

Figure 5-9 a, b, c and d show the surface after 24, 48, 72 and 96 hrs of immersion respectively. Substantial corrosion can be seen after 24 hrs of immersion, with the corrosion seen in Figure 5-9 a being > 100 μm in length and ~ 80 μm in width. As immersion time increased, the size of these corrosion sites also increased, but primarily in length not width and the size of the corrosion site in Figure 5-9 d was > 500 μm in length and at its maximum was ~ 150 μm in width. This suggests that the corrosion is following specific grains, with EBSD revealing ~ 100 μm wide bands of different grain orientations in the normal direction. This suggests that select grain orientations were prone to selective grain dissolution. This phenomena has been mentioned in literature to take place on Al-Cu-Li alloys and is primarily associated with the T_1 phase but can also be related to grain stored energy and grain mis-orientation [13], [31], [32], [46], [75], [113–116]. Li is less noble than Al and *Li et al.* [32] showed that the T_1 phase had a potential of -1076 mV vs. SCE compared to -855 mV vs. SCE of Al. High concentrations of T_1 phase within the matrix and at GBs allows galvanic corrosion at the GB to form IGC or galvanic corrosion within the grains forming selective grain dissolution.

As immersion time increased, the number of pitting corrosion sites increased, however, the number of selective grain dissolution sites like those seen in Figure 5-9 a, b, c and d stayed similar. No evidence of IGC was seen after 24 hrs, however, it was theorised that corrosion was progressing more sub-surface, especially with the T_1 and θ type phases being present on the GBs in Cu2, as shown in Figure 3-8. Evidence of circular corrosion products can be identified from Figure 5-9 a, b, c and d, showing that the initiation of these pitting corrosion sites was through the formation of H_2 bubbles, which subsequently caused a localised reduction in pH [19]. There was a substantial increase in selective grain dissolution size from 24 to 48 hrs, but after this there growth rate reduced. The largest corrosion site was ~ 1.2 mm in length and was seen on a specimen immersed for 72 hrs, but most were ~ 800 μm. All of the pits were, however, ~ 100 to 150 μm in width, reinforcing the theory of certain grain structures being more susceptible [71], [72], [78]. Comparison of the OCP data suggests that both the OCP and visual corrosion can be strongly correlated in that the OCP trend shows the greatest change over the initial 24 hrs and the same can be said about the corrosion observed on the normal direction.

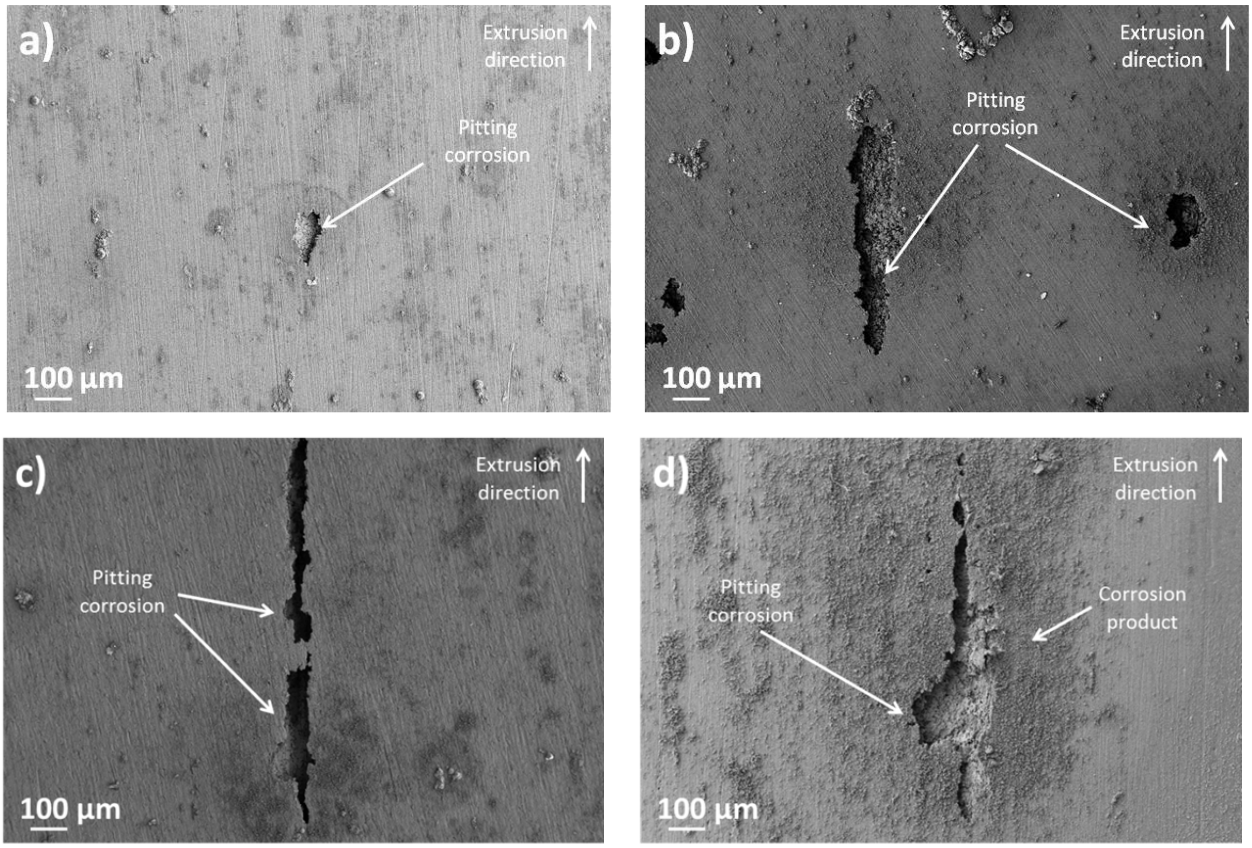

Figure 5-9: SEM micrographs of Cu2 immersed in 3.5 wt.% NaCl for a) 24 hrs. b) 48 hrs. c) 72 hrs. d) 96 hrs.

Corrosion on Cu2 was primarily seen in the form of linear cavities, however, IGC was also observed as shown in Figure 5-10 a and b. Figure 5-10 a shows surface IGC around an IMC, highlighting the cathodic nature of the IMC leading to corrosion [26], [35], [39], [60], [63]. IMCs are typically associated with pitting corrosion, however, in this case IGC is seen to develop prior to pitting and due to the fine grain nature of Cu2 it is anticipated that the IGC will progress rapidly due to the easy path for it to follow. Figure 5-10 b shows IGC within a corrosion site, highlighting that IGC and pitting corrosion tend to form in a similar locations on Cu2. The amount of IGC is rather substantial but this was expected due to the large concentration of anodic and cathodic phases at the GBs. The T type phases will undergo selective dissolution, leaving remnant Cu at the GB. When this occurs the remnant Cu plus the θ type phases create a highly cathodic region causing accelerated dissolution of the Al matrix [26]. The number of corrosion sites did increase with time, but the number of large cavities did not. Figure 5-10 c and d show evidence of both linear and circular corrosion products. These linear sites were made up of lots of circular corrosion sites, forming a linear pattern. Some circular corrosion products seen had an Ø = 100 µm, whereas those seen in Figure 5-10 c have an Ø = 200 µm. Figure 5-10 d highlights the oxidation behaviour of the specific grains that undergo redox reactions. This suggests a higher nobility of these bands, however, EDS did not reveal any significant chemistry difference.

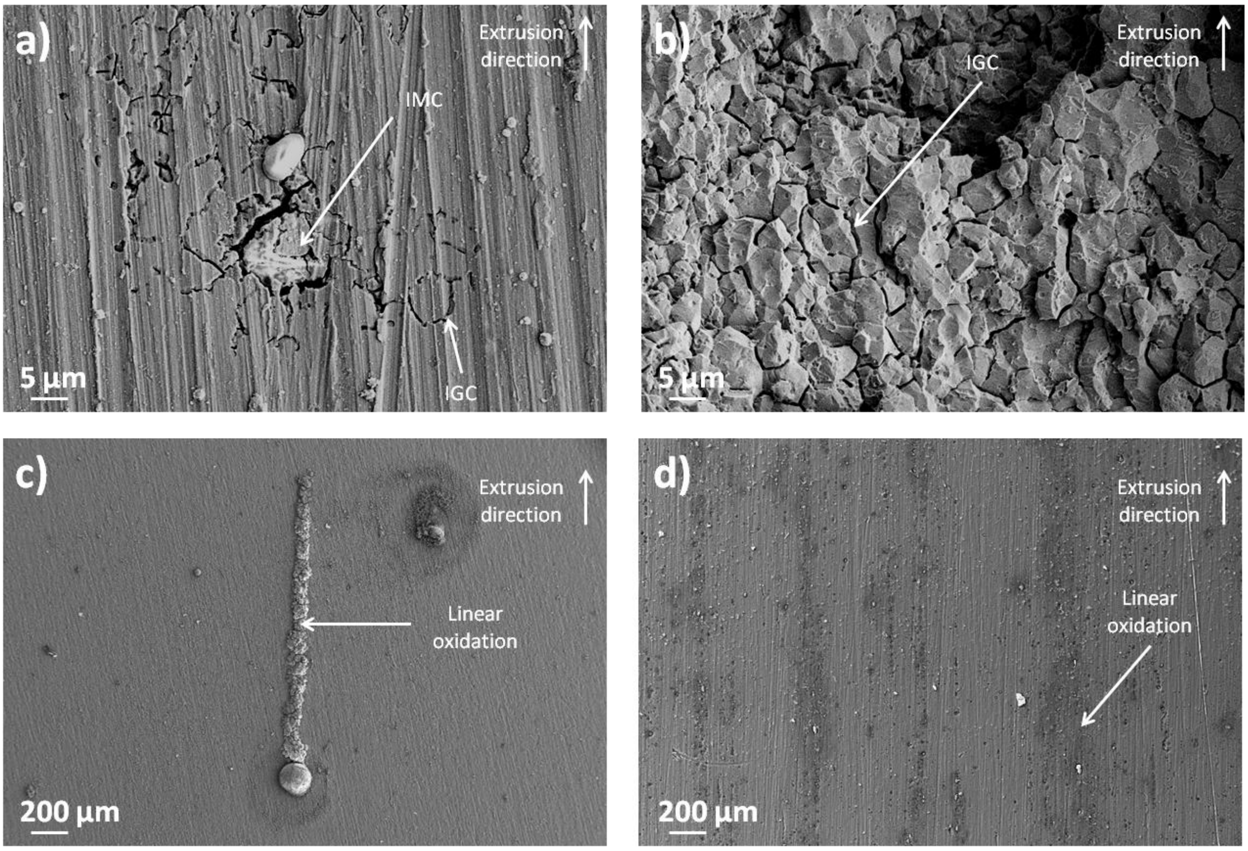

Figure 5-10: SEM micrographs of Cu2 showing evidence of a) IGC surrounding an IMCs that has undergone cathodic protection after 24 hrs of immersion. b) IGC within pitting corrosion sites after 24 hrs of immersion. c) linear and circular corrosion products after 96 hrs of immersion. d) linear oxidation banding, showing selective grain dissolution.

Figure 5-11 shows an increase in the O concentration from ~ 21 at.% to 52 at.% after 96 hrs of immersion. EDS showed an increase in the surface O concentration within the corrosion products and Figure 5-9 a, b, c and d show a visual densification in the amount of corrosion products with increasing immersion time. EDS showed an increased O content on one of the grain orientations and as such identifies that certain grains may have a lower corrosion resistance, in that they are more likely to dissolve. The bands which show elevated O had an Al concentration of ~ 38 at.% and 42 at.% O whereas the regions absent of oxidation showed ~ 54 at.% Al and 26 at.% O. As well as linear oxidation, circular regions were observed which can be attributed to the formation of H_2 bubbles [19]. EDS demonstrated that the chemical constituents of the circular corrosion products were similar to that of the linear oxidation bands.

The surface ratio of Al:O changed from ~ 4:1 to ~ 9:10 after 96 hrs of immersion and the final Al and O concentrations were measured to be 46 at.% and 52 at.% respectively. The concentration of both Al and O were seen to reduce by ~ 10 at.% per 24 hrs of immersion. The O content and the amount of corrosion products were seen to be directly related and when compared to the OCP, tend to follow a similar trend, in that both show uniform oxidation growth. Cu, Fe and Mn concentrations were all seen to reduce with increasing immersion time, which was to be expected with the increased coverage of corrosion product.

The reduction in Cu was unexpected as literature [24], [26], [36], [95] mentions that Cu can be re-distributed over the surface.

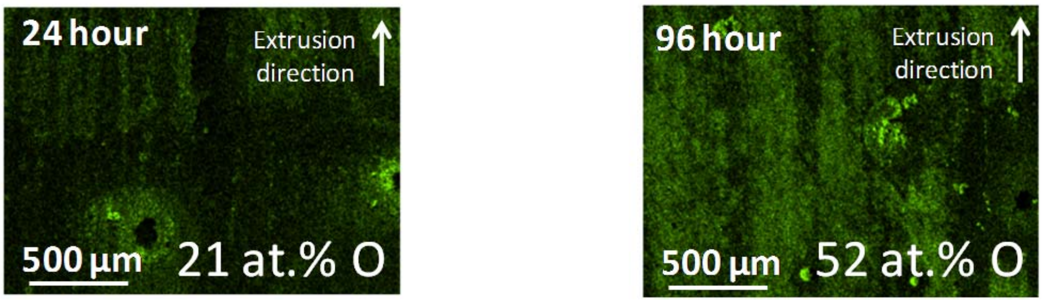

Figure 5-11: EDS maps showing the increase in O concentration with increasing immersion time on Cu2.

With increasing immersion time the concentration of O increased whilst a reduction in Al was observed within the corrosion product. EDS showed that the corrosion products around the corrosion sites and on the linear bands had similar compositions. The only other element that showed an increase with immersion time was Cl^-, which had a maximum at 2.7 at.%. Figure 5-12 highlights the presence of Cl^- within the corrosion product. The ratio of Al:O changed from ~ 3:1 to ~ 1:3 after 96 hrs of immersion with the final Al and O concentrations being 24 at.% and 72 at.% respectively. As immersion time increased, the concentration of Cu was also seen to reduce from 1 at.% to negligible values after 48 hrs of immersion. Fe and Mn concentrations were also seen to reduce to negligible values after only 24 hrs of immersion.

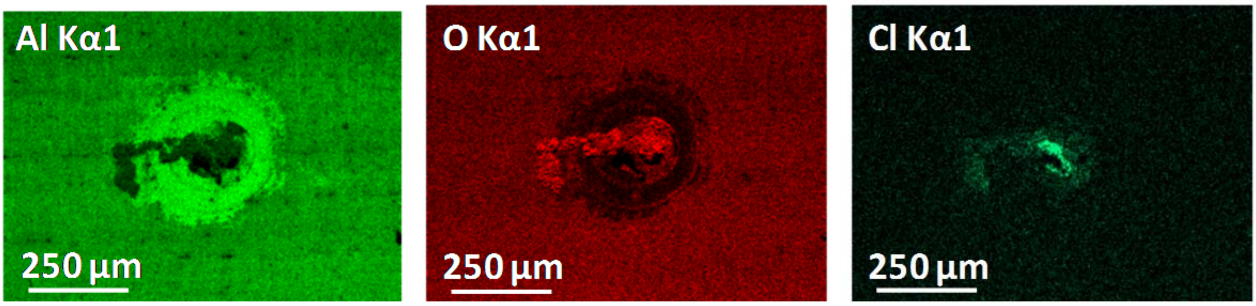

Figure 5-12: EDS maps highlighting the concentration increase of Cl within the corrosion product on Cu2.

Figure 5-13 shows example EDS maps of IMCs within Cu2. EDS showed that Cu2 had 2 IMC types; Al-Cu-Fe-Mn and Al-Cu-Mn of which both have been noted in literature to be detrimental to corrosion [24], [26], [60], [80], [84], [152]. EDS showed that both formed active galvanic cells from within 24 hrs of immersion with O concentrations increasing significantly with time. After 96 hrs 48 at.% O was present on the Al-Cu-Fe-Mn IMCs compared to 33 at.% on the Al-Cu-Mn IMCs. This may be expected due to Fe being more noble than Al and shows that the Al-Cu-Fe-Mn IMCs were the most problematic and caused the highest amount of anodic dissolution, once again agreeing with literature [24], [84].

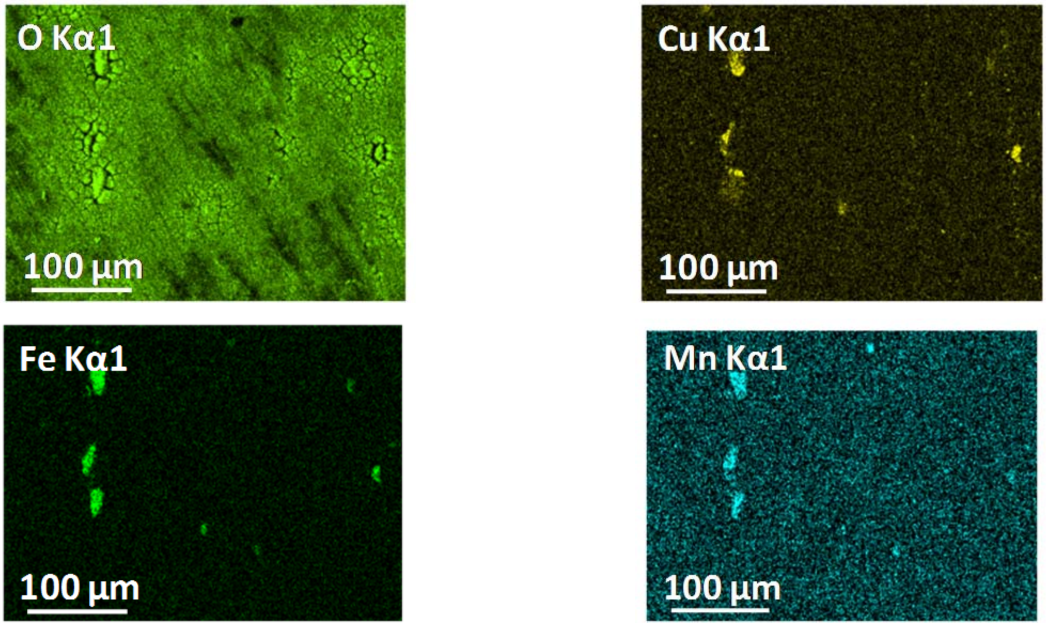

Figure 5-13: EDS maps highlighting the increased O concentration at the Cu, Fe and Mn rich IMCs locations on Cu2.

Figure 5-14 a and b show cross sections of Cu2 after 24 hrs of immersion. Even though the corrosion sites were substantial in size in the normal direction, there V_f was low which made it difficult to locate corrosion sites following cross sectioning. Pitting corrosion and sub-surface corrosion propagation were still, however, observed. Their size did not directly relate to the corrosion sites in Figure 5-9 and Figure 5-10. Corrosion was seen to progress to a depth of ~ 20 µm, however, no IGC was observed. This shows that even though extensive corrosion was seen on the surface, a conclusive understanding of corrosion depth is limited. Further analysis is therefore required to fully understand the corrosion propagation on Cu2 following immersion testing.

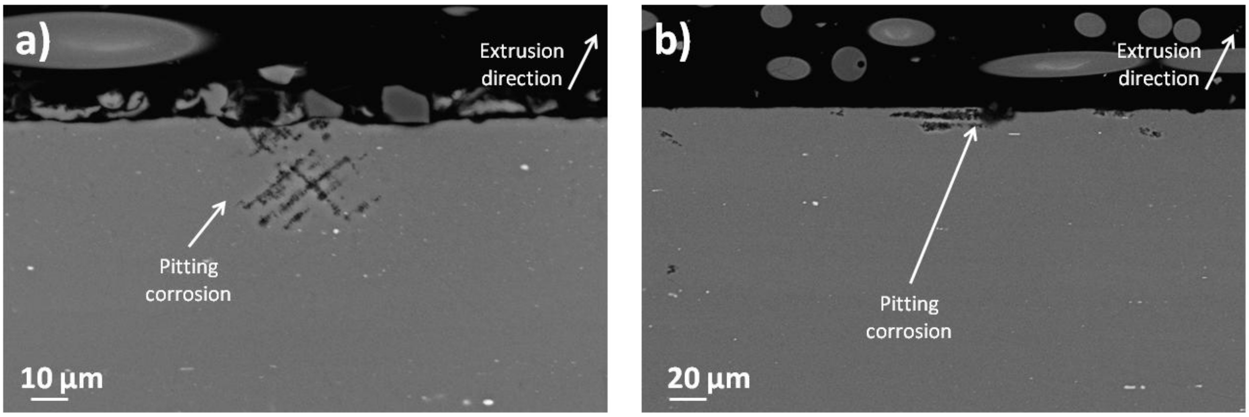

Figure 5-14: Cross-sectional SEM micrographs of Cu2 after 24 hrs of immersion in 3.5 wt.% NaCl showing evidence of a) pitting corrosion. b) Pitting corrosion and sub-surface corrosion.

Figure 5-15 a and b show cross sections of Cu2 after 96 hrs of immersion. Figure 5-15 a shows selective grain dissolution taking place. Figure 5-15 a also shows evidence of selective grain dissolution being associated with IMCs and that sub-surface corrosion developed. Figure 5-15 b shows IGC progressing to a depth of ~ 20 µm, which was the maximum recorded for Cu2. However, it has already been observed that IGC forms within pits and as such it can be assumed that IGC does progress to depths similar to that seen in Figure 5-15 a, where the pit is ~ 48 µm deep. The width of the pit in Figure 5-15 a was 161 µm, which agrees with Figure 5-9 and Figure 5-10 with regards to the width of the linear banded regions.

Proton et al. [115] examined an Al-Cu-Li (AA2050) alloy for 168 hrs in 0.7 M NaCl and observed that the average depth of corrosion stayed very similar over immersion time, but the maximum depths increased. With increasing time the depth of corrosion increased. *Proton et al.* [115] showed that the NHT variant had corrosion progress to a depth of 80 µm whereas the HT specimen progressed to 45 µm. This shows that the corrosion on Cu2 is similar to those results seen in literature with the maximum pit depth recorded at 48 µm.

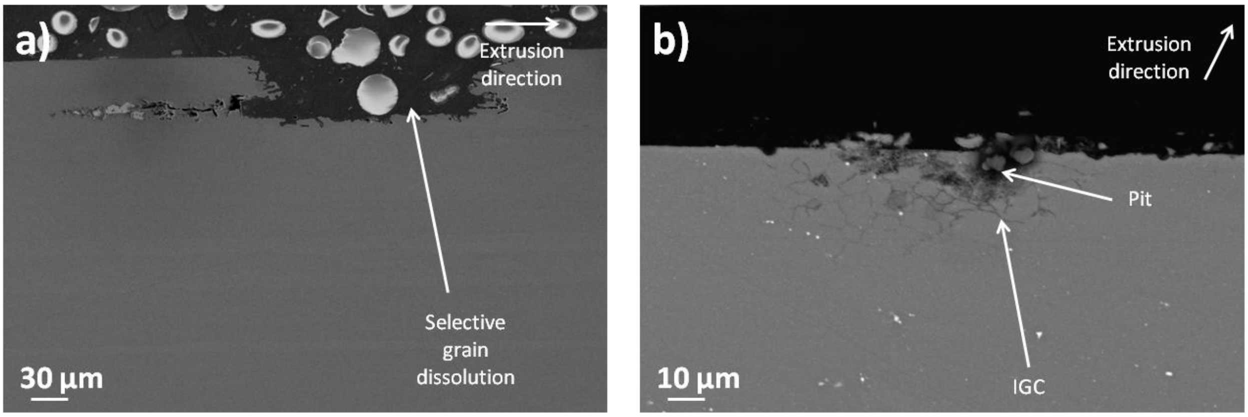

Figure 5-15: Cross-sectional SEM micrographs of Cu2 after 96 hrs of immersion in 3.5 wt.% NaCl showing evidence of a) selective grain dissolution and sub-surface corrosion. b) Pitting corrosion and IGC progression.

5.1.3 AA2099-T8E77 plate (Cu3)

Figure 5-16 a and b show the OCP over the initial 6 hrs of immersion and 96 hour immersion period respectively. Figure 5-16 a shows that over the initial 30 min's the OCP reduced significantly, after which it remains relatively stable. Figure 5-16 b shows that the overall trend was a reduction of ~ 30 mV, suggesting a rather high corrosion resistance. The fluctuations in standard deviation average at 11 mV, however, the maximum deviation was 48 mV and as can be seen in Figure 5-16 b is that the standard deviation increased with immersion time. Similar to Cu2, these results relate well to the work by *Proton et al.* [115].

Table 5-3: OCP of Cu3 over the 96 hour immersion period in 3.5 wt.% NaCl.

Time (hrs)	**0**	**24**	**48**	**72**	**96**
OCP (mV)	-652±13	-681±7	-685±11	-682±15	-682±22

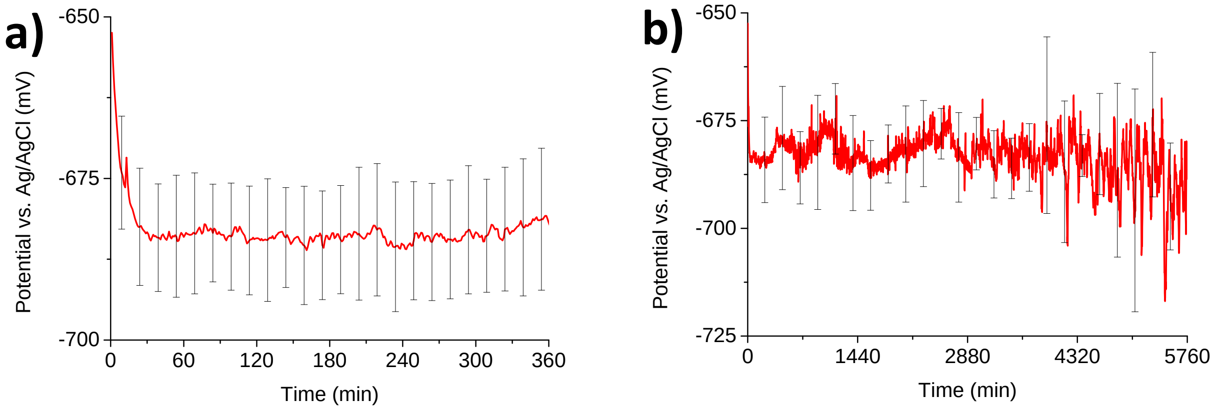

Figure 5-16: Graph showing the OCP of Cu3 following immersion in 3.5 wt.% NaCl for a) 6 hrs. b) 96 hrs.

Figure 5-17 a, b, c and d show the surface of Cu3 after 24, 48, 72 and 96 hrs of immersion respectively and they all show substantial evidence of selective grain dissolution, however, no evidence of IGC was observed. The corrosion site seen in Figure 5-17 a after 24 hrs of immersion was > 200 µm wide and > 400 µm in length. In most cases less than 10 corrosion sites were seen on a specimen surface (1 cm^2), however, due to their size this accounts for a large corroded area. With increasing immersion time the size of the corrosion sites did not appear to increase. As mentioned in Cu2 analysis, selective grain dissolution has been shown primarily in literature to be associated with the T_1 phase [13], [31], [32], [46], [75], [113–116]. It has also been noted in literature to be a potential issue associated with stored energy / grain mis-orientation and as such further investigation has been suggested [13], [75]. Figure 5-17 d is an example of the size some sites became, but the largest site observed on Cu3 was ~ 2 mm in length and ~ 500 µm wide. Analysis of the surface does tend to relate to the OCP data, in that over the initial 24 hrs substantial levels of attack take place but after that the corrosion proceeds at a relatively steady state.

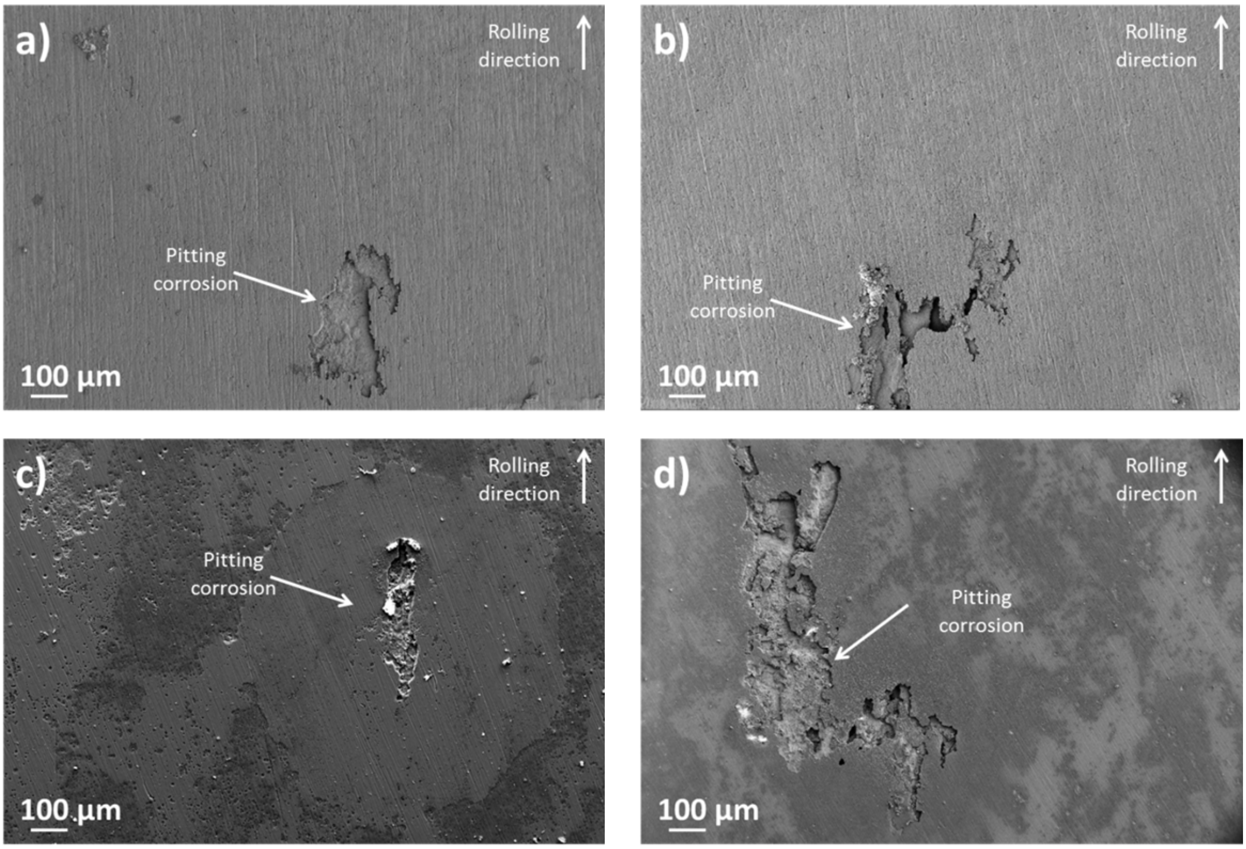

Figure 5-17: SEM micrographs of Cu3 immersed in 3.5 wt.% NaCl for a) 24 hrs. b) 48 hrs. c) 72 hrs. d) 96 hrs.

The corrosion morphology gives evidence of directionality, suggesting that the grains that have been attacked had a specific grain orientation, as shown in Figure 5-18 a. Figure 5-18 b shows that the corrosion is a form of pitting corrosion, hemispherical in particular [39], [80]. Hemispherical pitting corrosion has been noted in the literature to be associated with localised alkalisation of the surface and thus is a product of the redox reaction at cathodic IMCs [39], [80]. Figure 5-18 c showed cathodic protection of the IMCs and anodic dissolution of the Al matrix [24], [26], [60], [80], [84], [152] and Figure 5-18 d shows the extent of some of the corrosion sites that were observed on Cu3 after 96 hrs. The maximum pit size was ~ 2.2 mm in length and was seen on the 96 hour specimens, however, there were some pits seen after 24, 48 and 72 hrs that were of a similar size at 2.1, 1.8 and 1.9 mm respectively. Some of the corrosion sites were more linear than broad but this could be related to the processing route as EBSD analysis showed that the grains within Cu3 were substantial in width and length. Limited corrosion product can be observed, therefore it could be concluded that it has been removed during the cleaning process of the specimens prior to examination.

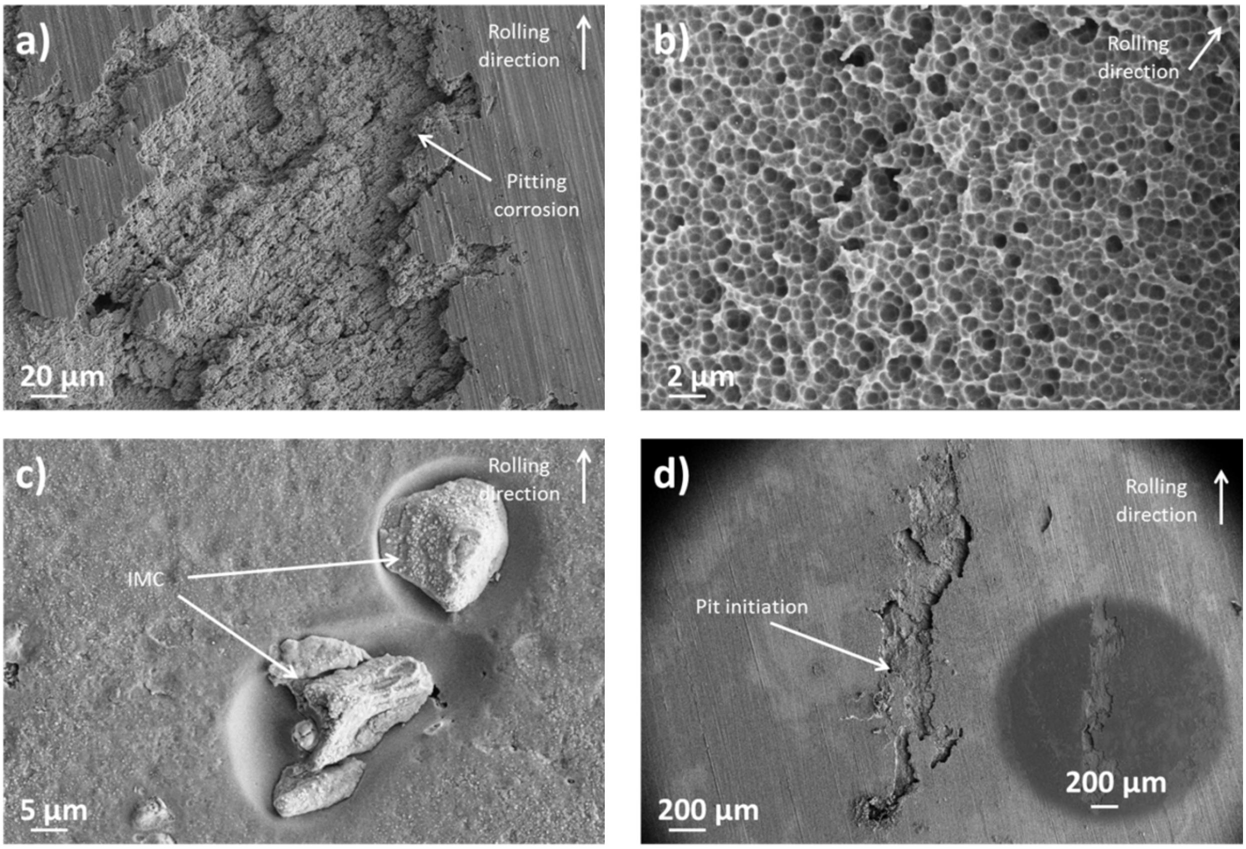

Figure 5-18: SEM micrographs of Cu3 showing evidence of a) directionality within the pitting corrosion after 24 hrs of immersion. b) hemispherical pitting corrosion after 24 hrs of immersion. c) the cathodic nature of the IMCs to the Al matrix after 24 hrs of immersion. d) expansive linear selective grain dissolution after 96 hrs of immersion.

Figure 5-19 shows an increase in O from ~ 21 at.% to 45 at.% after 96 hrs of immersion. The number of corrosion sites does not increase with immersion time, however, those sites that become active upon immersion continued to grow. With increasing immersion time the amount of O on the surface increased and the Al concentration decreased. The ratio of Al:O changed from ~ 3:1 to ~ 10:9 after 96 hrs of immersion, with the final Al and O concentrations being 51 at.% and 43 at.% respectively. The increase in corrosion product volume showed that with increasing immersion time both Al and O concentrations reduced and increased respectively by 15, 8 and 3 at. % between 48 and 72 hrs and 72 hrs and 96 hrs respectively. This shows that the rate of corrosion slowed after 48 hrs directly relating to the steady state OCP data. Cu, Fe and Mn concentrations were all seen to reduce with increasing immersion time, which was to be expected with the increased coverage of corrosion product.

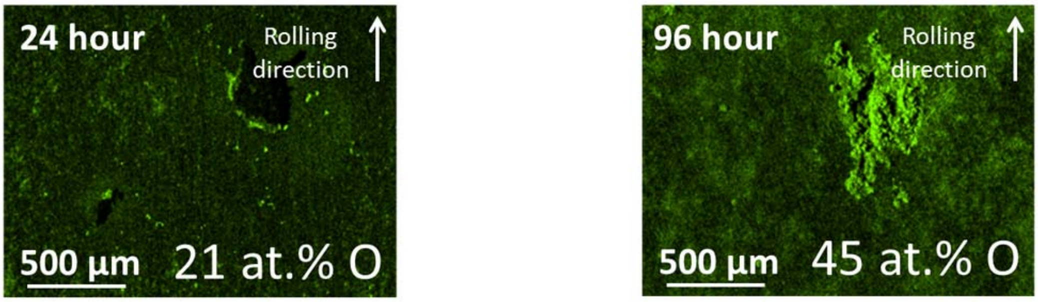

Figure 5-19: EDS maps showing the increase in O concentration with increasing immersion time on Cu3.

With increasing immersion time the concentration of O increased whilst a reduction in Al was observed within the corrosion products. Corrosion products formed in a circular pattern around corrosion sites due to the formation of H_2 bubbles [19]. Similar to the surface EDS the rate of corrosion product growth slowed with increasing immersion time. After 48 hrs the O content was 73 at.% and after 96 hrs the O content had increased by 7 at.%, compared to the 15 at.% increase from 24 to 48 hrs. The ratio of Al:O also changed from ~ 2:3 to ~ 1:4 after 96 hrs of immersion, with the final Al and O concentrations being 20 at.% and 80 at.% respectively. Cu, Fe and Mn concentrations were seen to reduce, similar to that seen through the overview EDS maps.

Figure 5-20 shows example EDS maps of IMCs within Cu3. The 2 IMC types within Cu3 were; Al-Cu-Fe-Mn and Al-Fe-Mn-Cu of which both have been noted in literature to be detrimental to corrosion [24], [26], [60], [80], [84], [152]. Both were seen to be active from within 24 hrs of immersion with the O concentration increasing significantly with time [19], [39], [63], [86], [91]. After 96 hrs both showed similar O concentrations at 42 and 45 at.% for Al-Cu-Fe-Mn and Al-Fe-Mn-Cu respectively. This shows that both were highly active and unlike Cu1 and Cu2 neither appeared to form a higher acceleration factor on corrosion than the other.

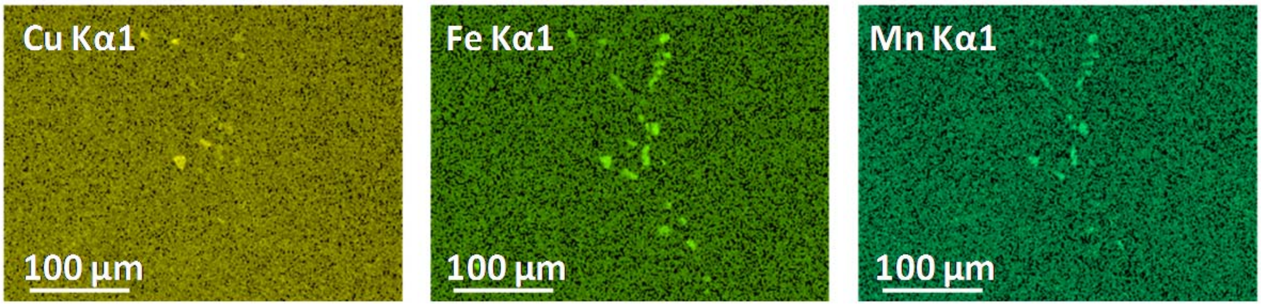

Figure 5-20: EDS maps showing the cathodic nature of the Cu, Fe and Mn rich IMCs in Cu3.

Figure 5-21 a and b show the extrusion direction and Figure 5-21 c and d show the traverse direction after 24 hrs of immersion. IGC, pitting corrosion and selective grain dissolution can be seen. Pitting corrosion in most cases was seen to have substantial openings, with the pit seen in Figure 5-21 a having a pit opening of ~ 100 µm. The corrosion progressed deep into the specimens at a depth of 84 µm as seen in Figure 5-21 b.

As previously mentioned *Proton et al.* [115] examined an Al-Cu-Li (AA2050) alloy and observed that the NHT variant had pitting corrosion progress to a depth of 80 µm whereas the HT specimen progressed to

45 µm. This shows that the corrosion on Cu3 is far in excess of the results seen in literature with after only 24 hrs in immersion. This could be primarily related to the difference in heat treatments for Cu3 compared to those of *Proton et al.* [115]. Especially since heat treatments have been shown in literature to control and in some cases mitigate corrosion in Al-Cu-Li alloys [4].

Figure 5-21 b also shows the relation between IGC and pitting corrosion. The grain structure of Cu3 is very coarse as shown in Section 3.1.3, however, some finer grain structures were seen and the corrosion seen in Figure 5-21 b and d show evidence of smaller grain regions. In some cases pitting corrosion is associated with selective grain dissolution as observed in Figure 5-21 c. This selective grain dissolution dissolves an entire grain before moving onto another and due to the large grain structure of Cu3 this means large areas will be attacked [31], [32], [115], [116]. Figure 5-21 d shows that the IGC is not continuous and appears as a dotted line across the GB, demonstrating that the cathodic θ type phases that resides on the GB within Cu3 are associated with the IGC [26].

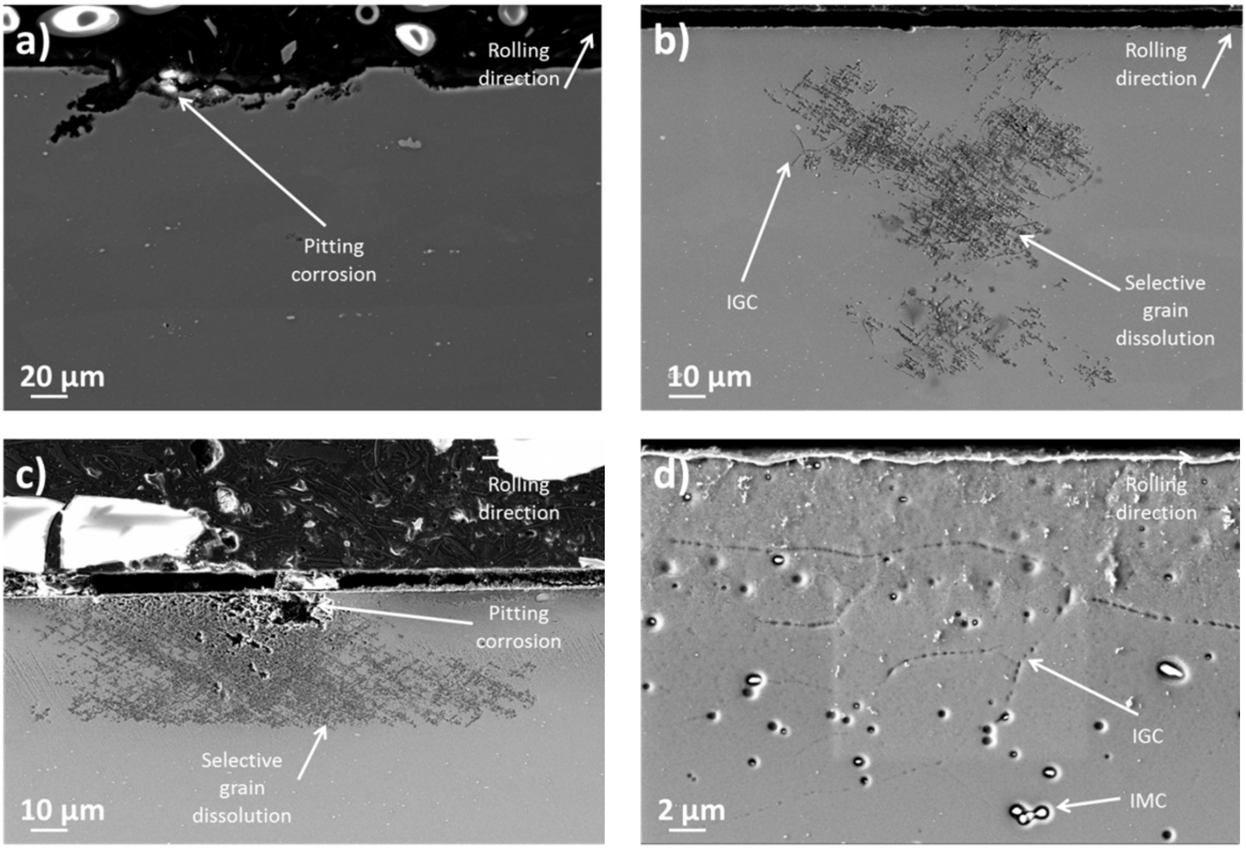

Figure 5-21: Cross-sectional SEM micrographs of Cu3 after 24 hrs of immersion in 3.5 wt.% NaCl showing evidence of a) surface pitting corrosion. b) sub-surface selective grain dissolution and IGC. c) selective surface grain dissolution and pitting corrosion. d) IGC and galvanic corrosion around fine scale IMCs.

Figure 5-22 a and b show micrographs of the extrusion direction and Figure 5-22 c and d show the traverse direction after 96 hrs of immersion. Propagation of corrosion between 24 and 96 hrs was less than expected, with evidence of pitting, IGC and selective grain dissolution still being observed, relating well with the OCP data and surface observations. Figure 5-22 a shows that the propagation of the pitting corrosion is not uniform and Figure 5-22 b, once again shows the relationship between pitting corrosion and IGC. Cross sectioning revealed that some of the pits from the surface show relatively small pit openings, however, Figure 5-22 c shows that the corrosion progresses much further into (36 µm) and wider sub-surface (200 µm). Therefore examination of the surface alone cannot be used to understand the corrosion resistance of Cu3. This confirms that the increased activity of the OCP with increasing time is related to the corrosion taking place sub-surface. The selective grain dissolution, as shown in Figure 5-22 c and d has progressed further after 96 hrs. The corrosion in Figure 5-22 d is shown to be ~ 50 µm beneath the surface and is > 50 µm in length. Overall this highlights the poor corrosion resistance of Cu3 with regards to the amount of corrosion progressing sub-surface. With the selective grain dissolution being associated with Li additions, primarily in the form of the T type phases such as T_1; the Li could be causing a reduction in corrosion resistance through the formation of sub-surface and surface selective grain dissolution [31], [32], [115], [116].

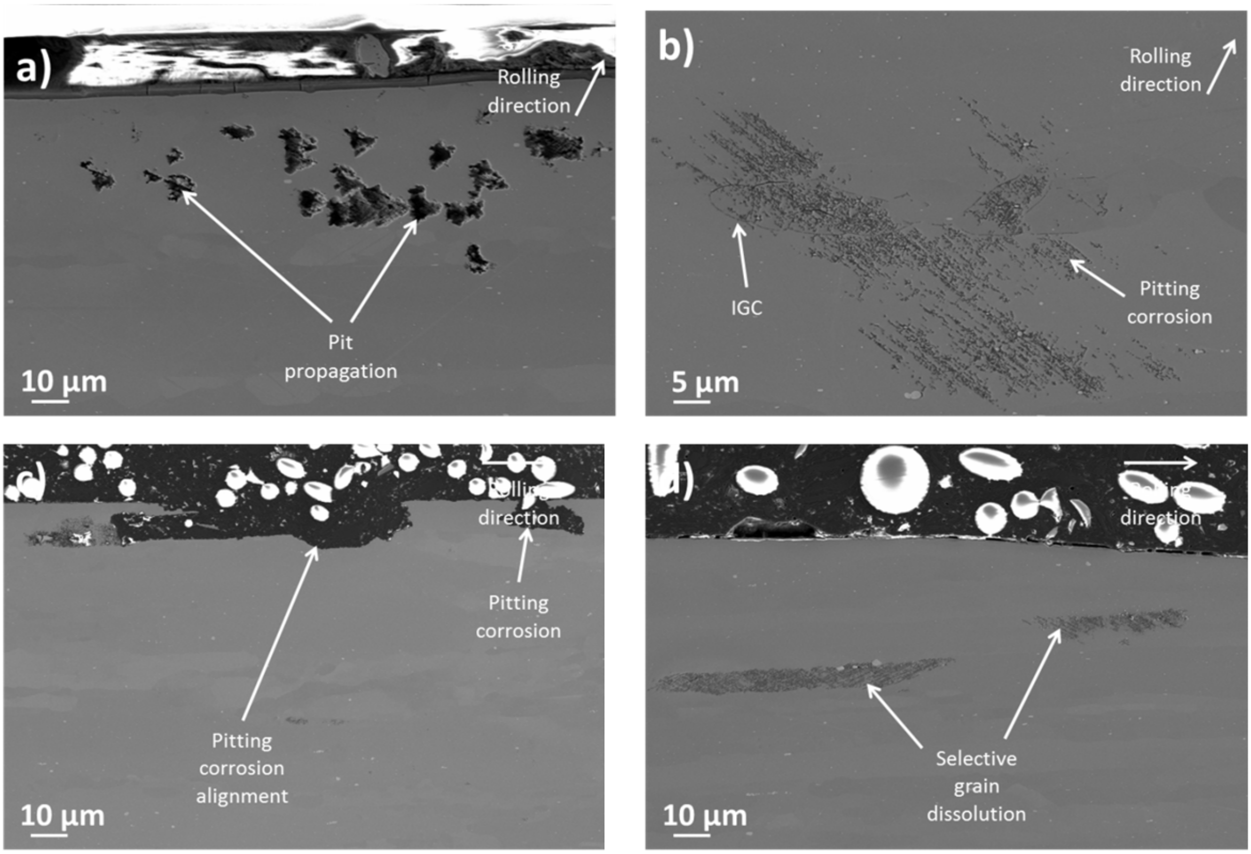

Figure 5-22: Cross-sectional SEM micrographs of Cu3 after 96 hrs of immersion in 3.5 wt.% NaCl showing evidence of a) sub-surface pitting corrosion. b) selective grain dissolution sub-surface and IGC. c) selective surface grain dissolution. d) selective sub-surface grain dissolution.

5.1.4 Comparison of Al-Cu alloys following immersion testing

Figure 5-23 shows a comparison of the OCPs for Cu1, Cu2 and Cu3 and it can be seen that Cu1 (Al-Cu) has a different profile compared to Cu2 and Cu3 (both Al-Cu-Li). Cu2 and Cu3 had a very similar response to immersion as each other, which is not unexpected. The major difference between Cu2 and Cu3 was primarily the size of the grain structure with Cu2 having a fine grain structure and Cu3 being a coarse grain structure as shown in Sections 3.1.2 and 3.1.3 respective. The difference is that Cu2 is more noble than Cu3 which suggested that Cu2 has the higher corrosion resistance [12], [156–158] which agrees with theory that a fine grain structure typically has a higher corrosion resistance [71], [72], [74].

Table 5-4 shows the change in OCP for each of the Al-Cu alloys from the initial OCP through to after 96 hrs of immersion.

Cu2 and Cu3 show a reduction in OCP over the initial 60 min's of ~ 25 mV each. After this the OCP was relatively stable, but as immersion time increased the standard deviation also increased, which may be a sign of corrosion taking place. Table 5-4 and Figure 5-23 show that Cu2 and Cu3 had total reductions in potential of 30 mV respectively, suggesting a good corrosion resistance. In comparison Cu1 had a more noble starting OCP but showed a higher reduction in OCP with immersion time. After ~ 48 hrs Cu1 had a similar potential to Cu2 and Cu3, however, after 96 hrs the OCP had reduced by 136 mV. *Vargel* [12] stated that reductions in OCP signify corrosion taking place, which suggests that Cu1 is undergoing more corrosion than Cu2 and Cu3 and thus has a lower corrosion resistance. After 48 hrs, Cu2 and Cu3 were more noble than Cu1 and according to literature, had a higher corrosion resistance [12], [156–158].

Table 5-4: OCP of Cu1, Cu2 and Cu3 over the 96 hour immersion period in 3.5 wt.% NaCl.

Time (hrs) / Alloy OCP (mV)	0	24	48	72	96
Cu1	-610±57	-630±35	-668±36	-733±31	-746±34
Cu2	-640±12	-665±8	-664±11	-665±8	-670±9
Cu3	-652±13	-681±7	-685±11	-682±15	-682±22

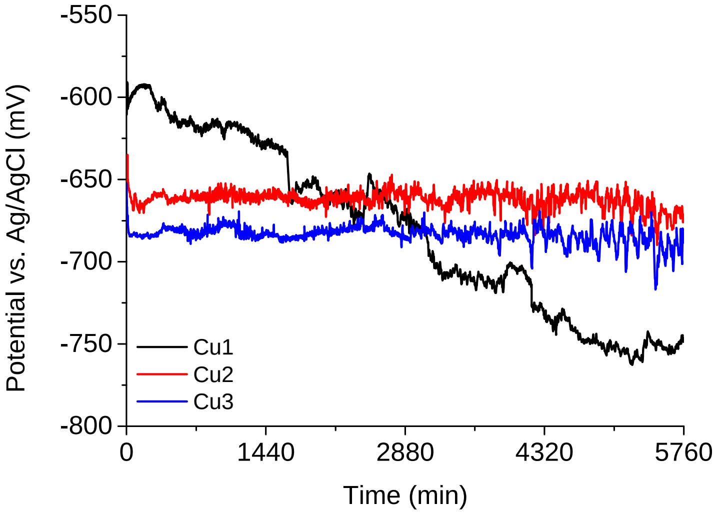

Figure 5-23: Graph showing the OCP of Cu1, Cu2 and Cu3 over a 96 hour immersion in 3.5 wt.% NaCl.

All of the Al-Cu alloys showed substantial amounts of corrosion taking place, with all demonstrating faceted pitting corrosion and IGC. Cu1 formed numerous corrosion domes (Ø = 100 µm) across the surface, with pitting corrosion beneath them. As the immersion time increased the number of these corrosion domes increased but their size remained the same. In comparison Cu2 and Cu3 showed a smaller number of corrosion sites (selective grain dissolution), however, they were bigger in size. The largest corrosion site on Cu2 was 1.2 mm in length and ~ 100 to 150 µm wide, whereas on Cu3 the largest was 2 mm in length and ~ 500 µm wide. This suggests that more matrix was dissolved for the Al-Cu-Li alloys compared to Cu1. The corrosion on Cu2 was highly linear and following EBSD analysis of the grain structure, suggested that specific grains had a higher sensitivity to corrosion than others. The corrosion sites were expected to be bigger on Cu3 as the corrosion was based on the philosophy of selective grain dissolution. This theory was reinforced on Cu2 which showed specific bands of grains being selectively dissolved. One point to note is that on each Al-Cu alloy the size of the pits did not increase with immersion time. In most cases their frequency did, but they all appeared to have limiting factors controlling their size. The V_f of θ type phases could account for why Cu2 showed a more noble OCP compared to Cu3. Cu1 had a higher Cu addition overall as such it was expected to show the more noble OCP of all the Al-Cu alloys.

EDS of the surface and corrosion products showed that with increasing immersion time the Al and O concentrations reduced and increased respectively on all of the Al-Cu alloys. Table 5-5 shows the Al and O concentrations after 96 hrs of immersion on the surface of Cu1, Cu2 and Cu3. The concentration of O increased with immersion time on Cu1, however, for Cu2 and Cu3 it was relatively steady, suggesting steady state corrosion, which is similar to what the OCP suggests. It was evident that more corrosion product formed on Cu1, however, associated with the larger V_f of cathodic IMCs that cause corrosion products to form, thus creating a higher O concentration. The main difference between the Al-Cu alloys was on Cu2, which showed oxidation bands which related to specific grains, but showed that the bands had increased O concentrations to the surrounding matrix, suggesting selective grain dissolution in Al-Cu-Li alloys [31], [32], [115], [116].

Table 5-5: Change in Al and O concentration for Cu1, Cu2 and Cu3 on the surface and in the corrosion product over the 96 hour immersion period in 3.5 wt.% NaCl.

at.%	Surface				Corrosion Product			
	24 hrs		96 hrs		24 hrs		96 hrs	
	Al	O	Al	O	Al	O	Al	O
Cu1	73	24	49	47	30	70	20	79
Cu2	78	21	46	52	74	24	24	72
Cu3	76	21	51	45	41	58	20	80

Table 5-5 shows the change in Al and O concentrations within the corrosion product after 96 hrs of immersion, which suggests that Cu2 had the highest corrosion resistance as less Al has been dissolved and combined into corrosion product. This also suggested that each Al-Cu alloy had similar corrosion products. The only other element that was seen in the corrosion product was Cl^-, which is present from the NaCl.

Examination of the IMCs showed that the Al-Cu-Fe-Mn systems in all Al-Cu alloys formed galvanic corrosion cells with the surrounding matrix, accelerating the corrosion [24], [84]. These IMCs are detrimental to Al-Cu alloys and as such agrees with the results in this thesis. In Cu1 the Al-Cu-Mg IMCs were also seen to be detrimental but only once the Mg had been selectively dissolved leaving a highly cathodic remnant Cu IMC [24], [29], [84], [152]. Overall it can be said that any Cu, Fe and Mn containing particles are cathodic to Al, thus cause galvanic corrosion and anodic dissolution of the Al matrix. Mg containing IMCs will offer sacrificial protection for a limited period by being less noble than Al [19], [27], [60–64].

Cross sectioning, following 24 hrs in immersion showed evidence of IGC on Cu1 and Cu3, however, no IGC was observed on Cu2. The IGC progressed to 40 µm deep on Cu1 following the fine network of GBs. The IGC on Cu3 was not seen to progress far into the specimen but this was associated with the coarse grain structure. This shows that overall Cu1 had a higher sensitivity to IGC than Cu2 or Cu3. All Al-Cu alloys showed pitting corrosion, with maximum pit depths being recorded at 15, 20 and 84 µm for Cu1, Cu2 and Cu3 respectively suggesting that fine grain structures have a higher resistance to pitting corrosion [71], [72], [74]. All showed evidence of sub-surface corrosion; however Cu1 showed the most extensive cavities. Cross sectioning also revealed that the pit openings on Cu1 were < 20 µm in width. IMCs were also observed to be associated with the IGC and pitting corrosion on Cu1, however, due to the reduced V_f of IMCs within Cu2 and Cu3, this correlation was not as apparent [26], [35], [39], [60], [63].

After 96 hrs, however, IGC was now observed on all of the Al-Cu alloys. On Cu1 the depth of attack did not change much with the maximum IGC depth being ~ 40 µm and the maximum pit depth being ~ 20 µm. The average corrosion depths and number of corrosion sites did, however, increase, forming a weakened friable layer. Cu2 and Cu3 showed strong evidence towards selective grain dissolution and the maximum pit depths were seen to be 48 µm and 36 µm respectively. This shows that on Cu3 the depth of pits is not uniform. However, Cu3 did show evidence of selective grain dissolution ~ 50 µm below the surface which would eventually create sub-surface cavities. Overall the results from Cu2 and Cu3 relate well to literature [115] in most cases, however, it can be said that Cu3 is highly active and has the reduced corrosion resistance compared to Cu2.

Overall all Al-Cu alloys formed pitting and IGC, however, the main differences were that Cu1 developed a friable weakened layer with lots of small corrosion sites. The Al-Cu-Li alloys developed selective grain dissolution that removed large amounts of matrix material in a single area which also progressed further into the specimens. Even though both Al-Cu-Li alloys suggested higher corrosion resistances following analysis of the OCP data this author believes that it is difficult to distinguish which system offered the higher corrosion resistance. However, if it is assumed that more material was removed from the Al-Cu-Li alloys through selective grain dissolution thus Cu1 offered the higher corrosion resistance.

5.2 Immersion testing of Al-Mg alloys

5.2.1 AA5083-T3510 (Mg1)

Figure 5-24 a and b show the OCP over the initial 6 hrs of immersion and 96 hour immersion period respectively. The starting OCP as shown in Figure 5-24 a was -714±1 mV and after 6 hrs had increased to -707±2 mV. Figure 5-24 b shows that the overall trend for Mg1, was a reduction of 14 mV suggesting a high corrosion resistance, as highlighted by Table 5-6. The standard deviation was 5 mV over the 96 hour immersion period; however, the maximum was 20 mV. As immersion time increased the level of standard deviation was also seen to increase, however, this is to be expected with fluctuations in OCP typically signifying metastable pitting corrosion [98]. Literature [28], [70], [80], [93], [98] has shown that AA5083 has a varying OCP. *Moore et al.* [28], [93] showed that AA5083 had an OCP of - 842 mV and -887 mV vs. SCE, whereas *Aballe et al.* [70], [80], [98] showed AA5083 to have an OCP of -740 mV and -760 mV vs. SCE. When converted to Ag/AgCl the results by *Aballe et al.* [70], [80], [98] are closer to those in this thesis, however, it also demonstrates the large variability in AA5083 OCP reproducibility. *Aballe et al.* [70], [80], [98] did, however, show that specimen size influences the OCP.

Table 5-6: OCP of Mg1 over the 96 hour immersion period in 3.5 wt.% NaCl.

Time (hrs)	**0**	**24**	**48**	**72**	**96**
OCP (mV)	-714±1	-708±5	-711±8	-716±6	-728±1

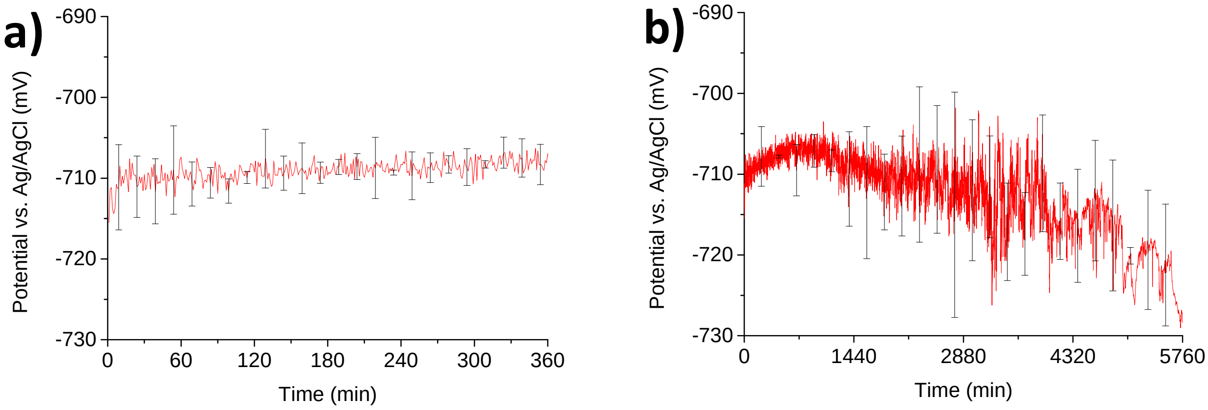

Figure 5-24: Graph showing the OCP of Mg1 following immersion in 3.5 wt.% NaCl for a) 6 hrs. b) 96 hrs.

Figure 5-25 a, b, c and d show the surface after 24, 48, 72 and 96 hrs of immersion. After 24 hrs in immersion, large regions (some > 200 µm in length and width), have undergone pitting corrosion, however, progression into the sample was not very deep [28], [60], [70], [80], [86], [93]. As immersion time increased the number of regions that had undergone pitting corrosion also increased. The maximum corrosion site seen on Mg1 was > 500 µm in length and > 300 µm in width. This shows that large amounts of pitting corrosion takes place on Mg1, to the point that most of the surface becomes an active corrosion site, however, even after 96 hrs the progression of corrosion into the sample was still very shallow. A number of authors [28], [60], [70], [80], [86], [93] have also observed pitting corrosion behaviour on AA5083.

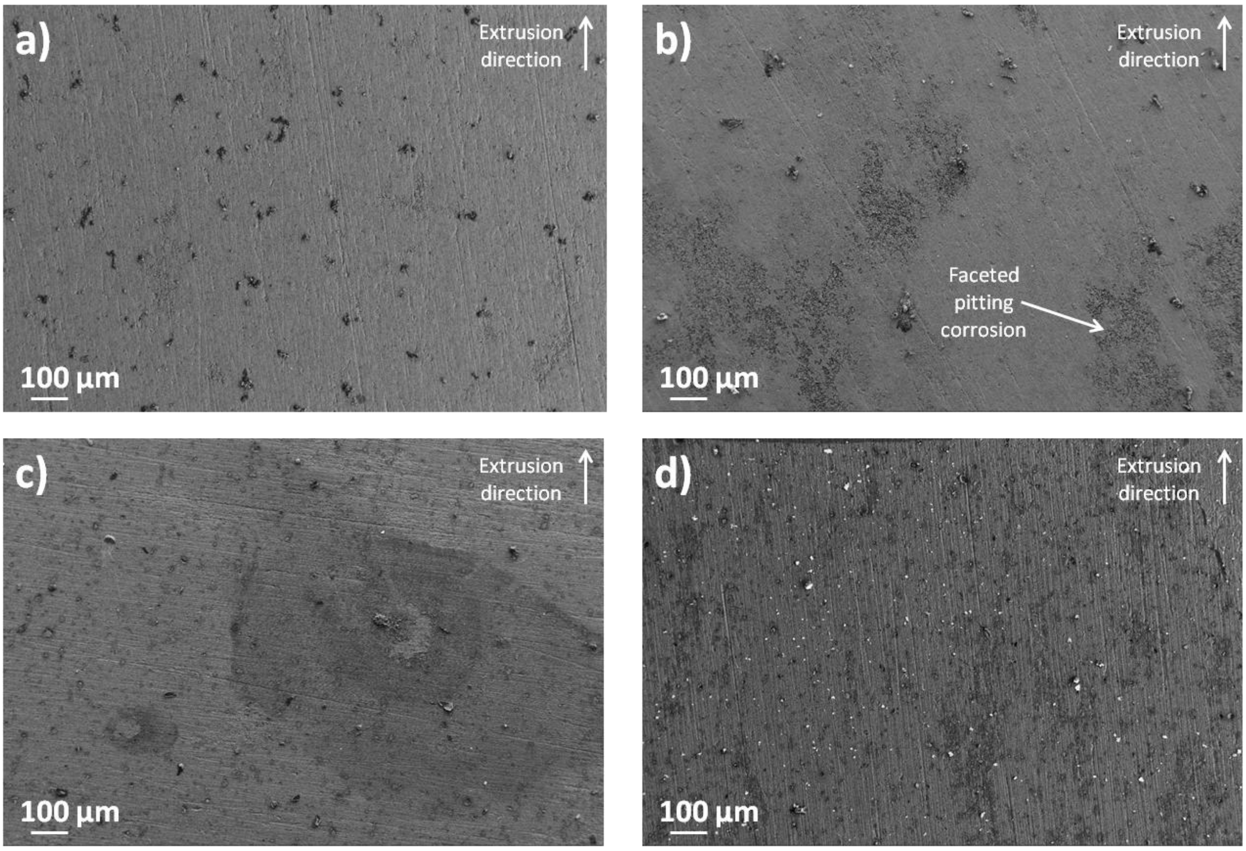

Figure 5-25: SEM micrographs of Mg1 immersed in 3.5 wt.% NaCl for a) 24 hrs. b) 48 hrs. c) 72 hrs. d) 96 hrs.

Figure 5-26 a show evidence of galvanic corrosion surrounding cathodic IMCs, in that dissolution of the Al matrix takes place but the IMC remains. Figure 5-26 a also shows how IMC fall out can take place. Figure 5-26 b shows the pitting corrosion after 96 hrs of immersion, highlighting how much of the surface has been corroded, but also that there is no significant depth to the corrosion. Figure 5-26 b also demonstrates the correlation between IMCs and pitting corrosion, in this case a cathodic IMC within the matrix. EDS showed that all of the IMCs contained some form of cathodic element, primarily in the form of Fe, Mn and Si. These will cause galvanic corrosion since they are more noble than the Al matrix [26], [60], [63], [64]. Figure 5-26 c shows evidence of faceted pitting corrosion, Figure 5-26 d, however shows evidence of both hemispherical and faceted pitting corrosion. *Aballe et al.* [80] and *Ezuber et al.* [39] also observed hemispherical pitting corrosion taking place on AA5083 specimens. They showed that the reason for its morphology is associated with the redox reaction creating localised alkalisation between cathodic IMCs and the anodic matrix. As such hemispherical pitting forms around sites that are undergoing redox reactions and faceted pitting corrosion around those undergoing anodic dissolution.

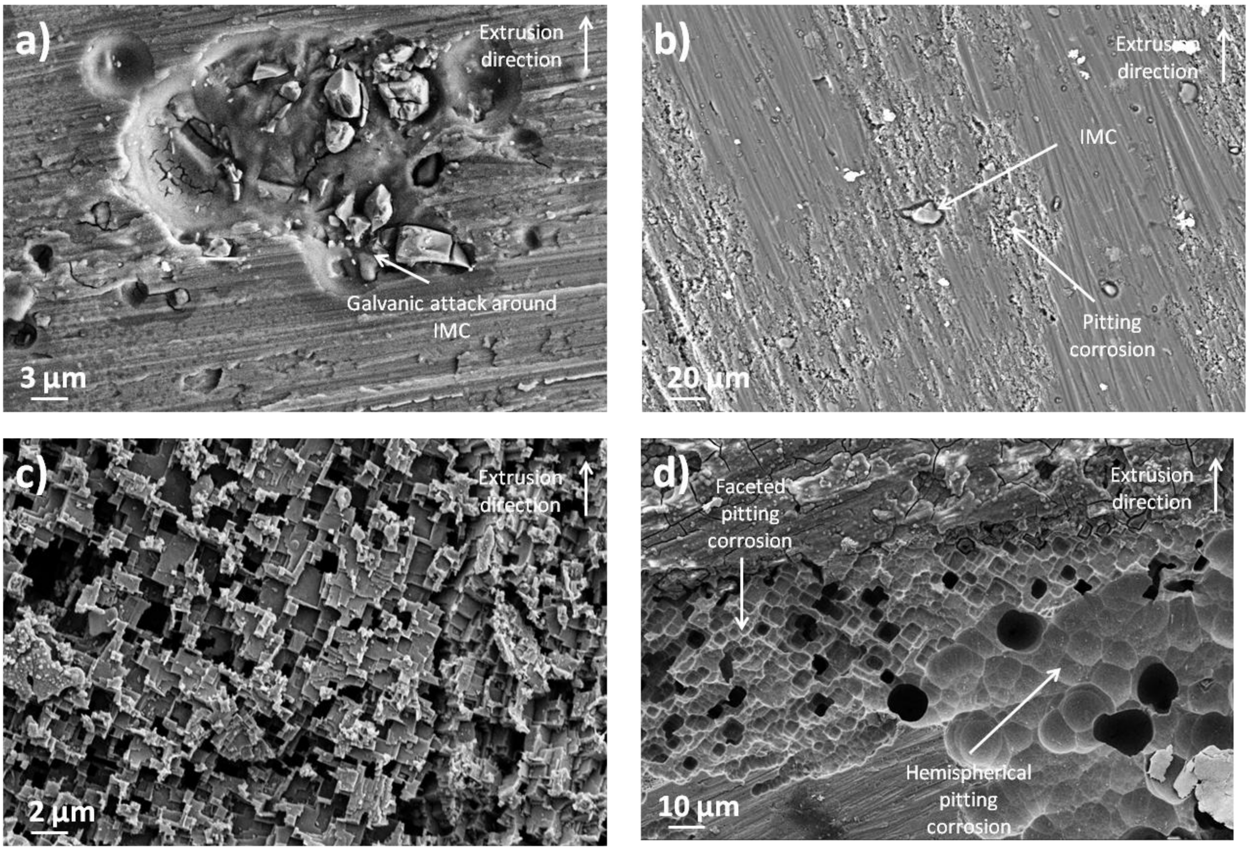

Figure 5-26: SEM micrographs of Mg1 immersed in 3.5 wt.% NaCl showing evidence of a) galvanic corrosion around IMCs after 24 hrs. b) the relationship between IMCs and pitting corrosion after 96 hrs. c) faceted pitting corrosion after 96 hrs. d) hemispherical and faceted pitting corrosion after 96 hrs.

Figure 5-27 shows an increase in surface O and thus corrosion products from ~ 18 at.% to 24 at.% after 96 hrs, however, the increase in O content is not very significant and suggests a high corrosion resistance [12]. Even though an increase in O concentration has been observed, limited evidence of corrosion products can be seen. With Mg being less noble than Al, the likelihood is that MgO corrosion products will form [67]. Comparison of the OCP to the visual observations tends to suggest that they follow a similar trend in that since the OCP is very stable, little corrosion is expected. Large amounts of corrosion were, however, expected since Mg is the anode when joined to Al in an electrochemical cell, as such the Mg is the element that corrodes not the Al matrix observed in the Al-Cu alloys [19], [27], [60–64].

With increasing immersion time, the amount of O increased and the Al concentration decreased on the surface. The ratio of Al:O changed from ~ 4:1 to ~ 3:2 after 96 hrs of immersion. The concentration of both Al and O were seen to reduce by ~ 3 at.% per 24 hrs of immersion with the final Al and O concentrations measured at 62 at.% and 24 at.% respectively. Mg concentrations were seen to reduce also from 3 at.% after 24 hrs to 2 at.% after 96 hrs. This is to be expected with the sacrificial nature of Mg, but also because the Mg is now being associated with the corrosion products.

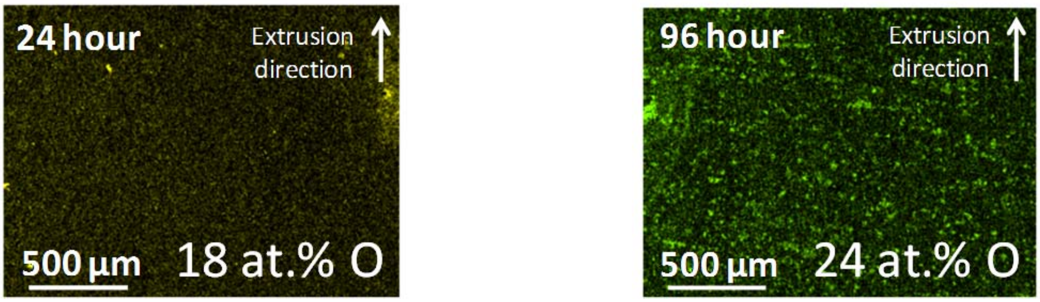

Figure 5-27: EDS maps showing the increase in O concentration with increasing immersion time on Mg1.

EDS of the corrosion product showed with increasing immersion time the concentration of O increased whilst a reduction in Al was observed. The corrosion products had no distinct morphology and there was no evidence of circular oxide that would signify H_2 bubble formation. The ratio of Al:O content changed from ~ 1:2 to ~ 1:4 after 96 hrs, with the final Al and O concentrations being 19 at.% and 78 at.% respectively. Mg concentrations reduced to negligible values, which suggest that MgO corrosion products are not forming and that the vast majority of Mg is being dissolved into solution.

Figure 5-28 shows example EDS maps of IMCs within Mg1. Mg1 contains 3 types of IMC; Al-Mg-Si, Al-Mn-Si and Al-Fe-Mn-Si-Mg. EDS showed that the Al-Mg-Si IMCs show selective dissolution of the Mg concentration with increasing immersion time [26], [60], [63], [80]. The Al-Fe-Mn-Si-Mg IMCs showed higher O concentrations than either of the Al-Mg-Si or Al-Mn-Si IMCs due to the highly cathodic nature of Al-Fe-Mn-Si-Mg IMCs [25], [26], [60], [63], [80]. This therefore showed that the Fe, Si and Mn acted as cathodic sites and the Mg acted as the anode. This meant that some IMCs were active whilst others were not, which is what was observed.

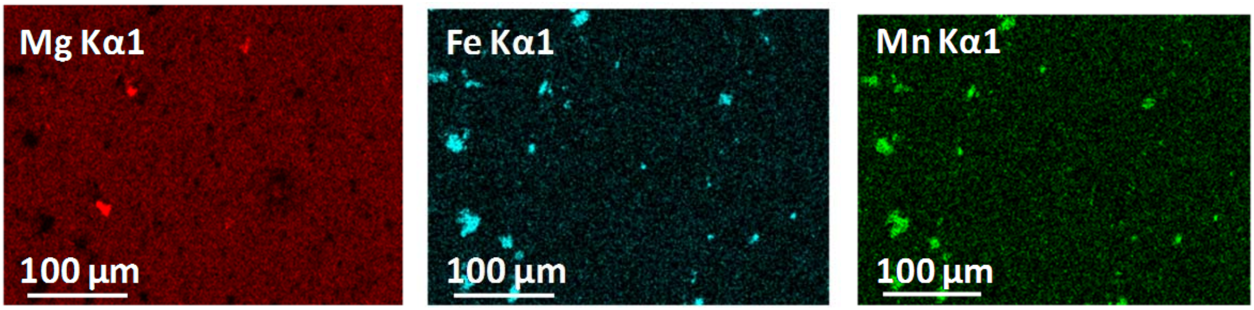

Figure 5-28: EDS maps showing the cathodic nature of the Fe and Mn rich IMCs and the anodic nature of the Mg IMCs with Mg1.

Figure 5-29 a and b show micrographs of the extrusion and traverse direction respectively after 24 hrs of immersion. IMCs were associated with pitting corrosion but not all were seen to be active. This coincides with what was observed using EDS, which showed that the Mg rich IMCs underwent selective dissolution, thus no galvanic corrosion was observed on these IMCs [26], [60], [63], [80]. However, the Fe, Mn and Si rich IMCs generated galvanic corrosion and became initiation points for pitting corrosion [26], [60], [63], [64], [80], [84]. Cross sections showed that in most cases the depth of corrosion was not very substantial (< 5 µm) showing a very high corrosion resistance but all of the corrosion was observed to be faceted in morphology. There were some sites of established pitting, as shown in Figure 5-29 a and

b. Most of the established pit sites had narrow openings, mainly < 5 µm and the depth was at a maximum of 30 µm. Most of the pits seen, however, did not progress any further than ~ 20 µm.

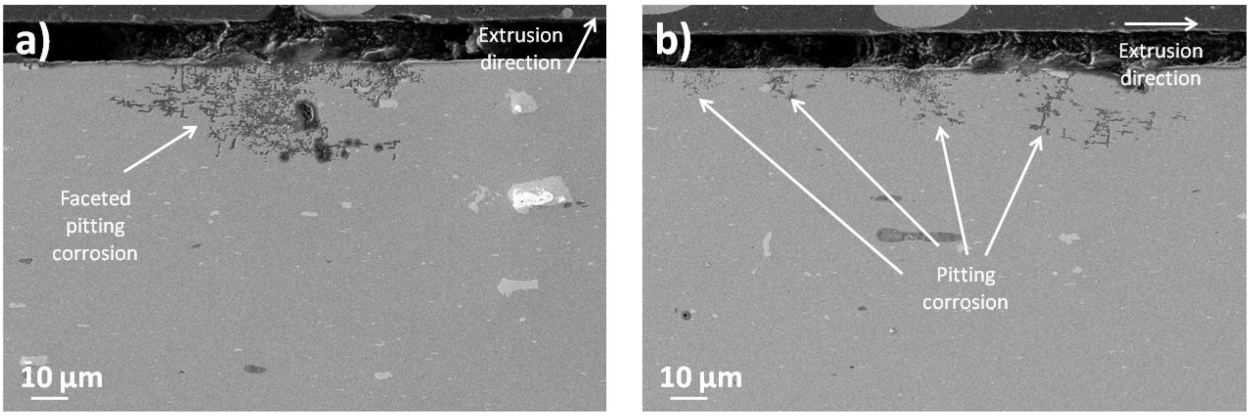

Figure 5-29: Cross-sectional SEM micrographs of Mg1 after 24 hrs of immersion in 3.5 wt.% NaCl showing evidence of a) shallow faceted pitting corrosion. b) shallow faceted pitting corrosion.

Figure 5-30 a and b show the extrusion and traverse direction respectively after 96 hrs of immersion. The difference in the amount of corrosion between 24 and 96 hrs was not very noticeable with the major difference being in the number of established pit sites. The depth of the corrosion was, however, very similar to that after 24 hrs of immersion at maximum depths of ~ 30 µm. Pit openings were wider after 96 hrs at ~ 10 µm. It can be said that the sacrificial anodic nature of the Mg has improved the corrosion resistance of the Al alloy, which would explain the low rate of corrosion taking place over 96 hrs of immersion.

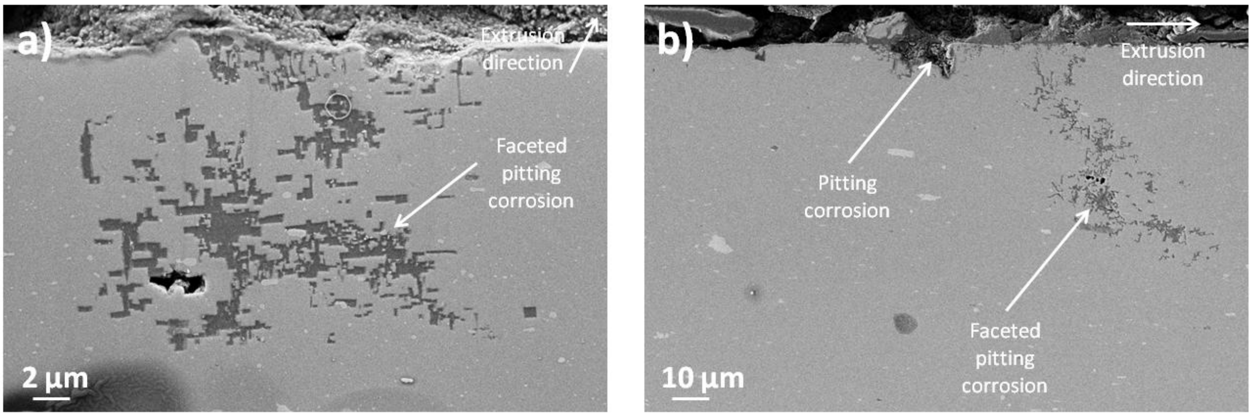

Figure 5-30: Cross-sectional SEM micrographs of Mg1 after 96 hrs of immersion in 3.5 wt.% NaCl showing evidence of a) shallow faceted pitting corrosion. b) shallow and deep faceted pitting corrosion.

5.2.2 Spray formed Al-Mg-Li (SF1)

Figure 5-31 a and b show the OCP over the initial 6 hrs and 96 hour immersion period respectively. The OCP showed a significant reduction from -758±5 mV to -886±19 mV after 6 hrs of immersion. Figure 5-31 b and Table 5-7 shows that after 6 hrs the trend continues to reduce till around 48 hrs where it stabilises. This shows that SF1 had an ~ 290 mV reduction over the 96 hour immersion time, suggesting a poor corrosion resistance [12]. *Moore et al.* [28], [93] showed that the OCP of SF1 was -838±72 mV vs. SCE after a 2 hour immersion which agree with those seen in this thesis.

Table 5-7: OCP of SF1 over the 96 hour immersion period in 3.5 wt.% NaCl.

Time (hrs)	**0**	**24**	**48**	**72**	**96**
OCP (mV)	-758±5	-924±66	-1057±16	-1055±24	-1049±1

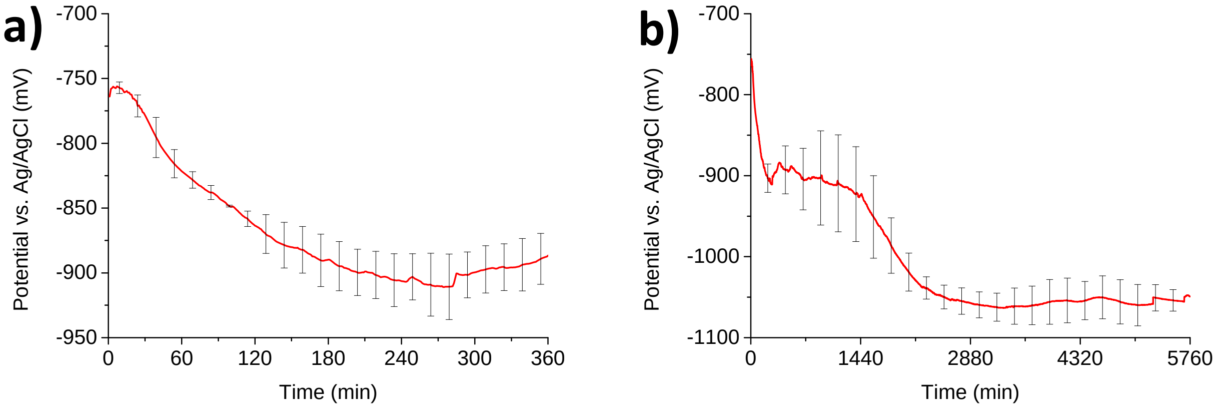

Figure 5-31: Graphs showing the OCP of SF1 following immersion in 3.5 wt.% NaCl for a) 6 hrs. b) 96 hrs.

Figure 5-32 a, b, c and d show the surface after 24, 48, 72 and 96 hrs of immersion respectively. SF1 had a limited amount of corrosion on the specimens up to 72 hrs of immersion. This was, however, expected with SF1 being an Al-Mg base alloy, which literature states have a high corrosion resistance [28], [93], [130], [131], [135]. SF1 also has Li additions which are less noble than Al and could result in increased corrosion resistance [5], [31], [114], [159]. Li additions, have also been associated with reduced corrosion resistances due to their highly anodic behaviour [5], [23], [31], [115], [159]. SF1 is also SF, which could promote a high corrosion resistance [71], [72], [74]. Factoring all of this information, should suggest that SF1 had potentially a very high corrosion resistance, which does not necessarily agree with the OCP plot.

Pitting corrosion was seen on samples immersed for 24 hrs with an average Ø of ~ 50 µm. After 48 hrs, pitting corrosion was observed, however, the number of pits did not appear to have increased. After 72 hrs, large amounts of corrosion product was observed, evidence of pitting corrosion, however, could not be seen, but this is likely to be the corrosion product covering the underlying pitting corrosion. After 96 hrs, there were more established pits and they showed circular corrosion products due to the formation of H_2 bubbles [19]. Beneath some of the corrosion products, showed pitting corrosion to an apparently extensive depth. The largest pits observed had a Ø of 120 µm. OCP data suggested that a significant level of corrosion took place on SF1, however, observations of the surface do not replicate this. This could be due to corrosion taking place sub-surface.

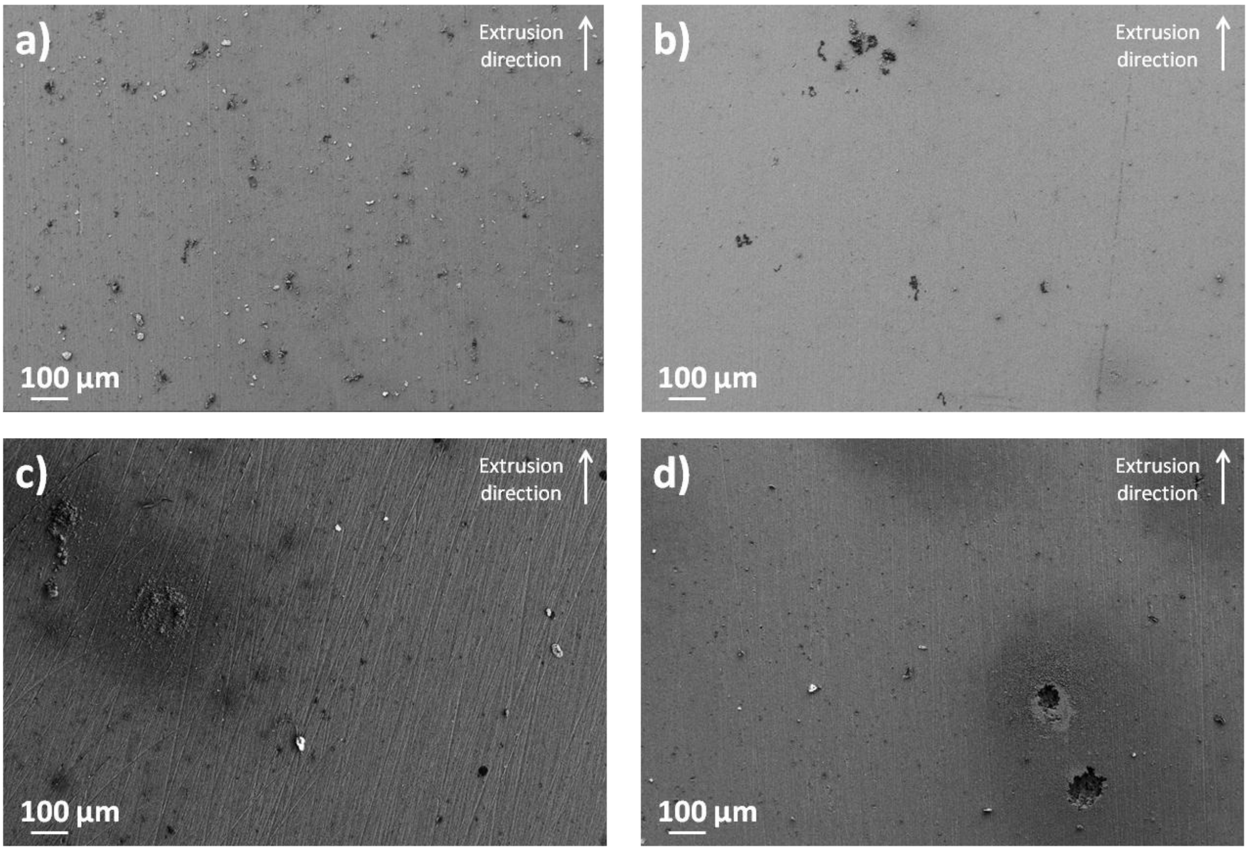

Figure 5-32: SEM micrographs of SF1 immersed in 3.5 wt.% NaCl for a) 24 hrs. b) 48 hrs. c) 72 hrs. d) 96 hrs.

Figure 5-33 a shows galvanic corrosion around Fe and Si rich IMCs after 24 hrs of immersion, which can lead to pitting corrosion [26], [60], [63], [80]. Figure 5-33 b shows some of the pitting corrosion that formed after 48 hrs of immersion and were ~ 200 µm in length and < 100 µm wide. Figure 5-33 b also shows a surface region that is collapsing in, suggesting sub-surface corrosion has taken place. This possible sub-surface corrosion is consistent with the trends in the OCP. Examination of the pitting corrosion shows that it has a hemispherical morphology, which can be seen in Figure 5-33 c. Figure 5-33 d, however, shows evidence of faceted pitting corrosion. This shows that both anodic and cathodic corrosion, since both faceted and hemispherical corrosion develop. Corrosion product on the surface, especially those with a cracked appearance were shown to have pitting corrosion beneath them, but also the pitting corrosion is a similar size to the corrosion product.

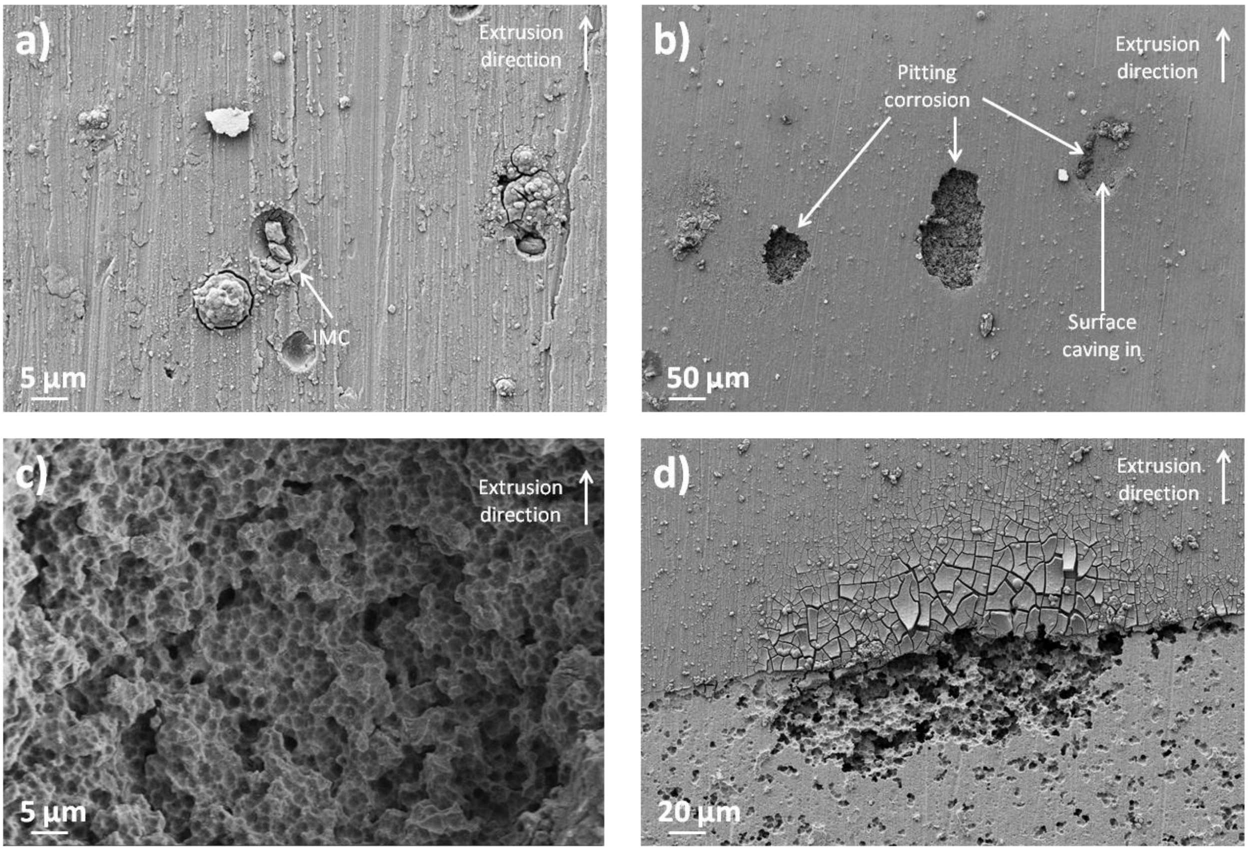

Figure 5-33: SEM micrographs of SF1 showing evidence of a) galvanic corrosion around cathodic IMCs. b) pitting corrosion and regions where sub-surface caverns have formed. c) hemispherical pitting corrosion. d) faceted pitting corrosion beneath a cracked corrosion product.

Figure 5-34 shows an increase in surface O from ~ 16 at.% to 23 at.% after 96 hrs, however, the increase in O content is not very significant [28], [93], [130], [131], [135]. The corrosion products formed in 2 morphologies; cracked and mossy, which are related to anodic (faceted) and cathodic (hemispherical) corrosion respectively. The O concentrations suggest that SF1 has a high corrosion resistance, with very minimal changed between 24 and 96 hrs of immersion with the O concentrations being 16 at.% and 23 at.% for 24 and 96 hrs respectively. The ratio of Al:O changed from ~ 5:1 to ~ 3:1 after 96 hrs of immersion. The concentration of Al and O does not change much over the 96 hrs of immersion with the average Al and O content being 75 at.% and 18 at.% respectively. The Mg content does not reduce with time at ~ 5 at.% and the same can be said about the Fe and Si concentrations. This suggests that there are more cathodic reactions taking place than anodic, as with anodic dissolution the Mg concentration would be expected to reduce [26], [60], [63], [80]. Analysis of the O and Al concentrations does not agree with the results seen by OCP in that over the initial 48 hrs of immersion the visual and chemical analysis suggests a low level of corrosion, however, the OCP shows that a large reduction takes place over this same time period.

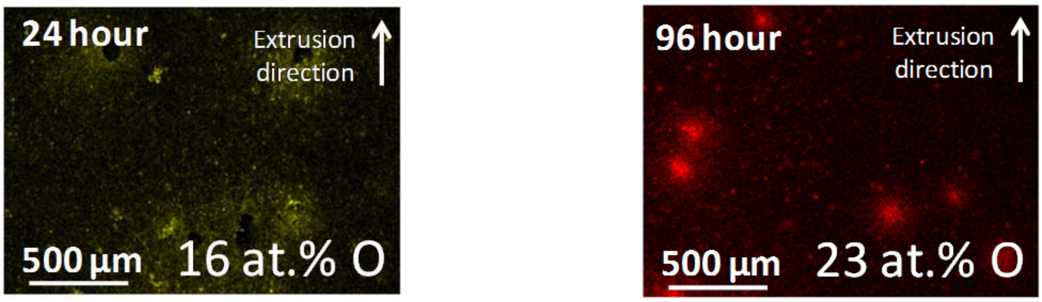

Figure 5-34: EDS maps showing the increase in O concentration with increasing immersion time on SF1.

EDS of the corrosion product showed that with increasing immersion time the concentration of O increased whilst a reduction in Al was observed. The ratio of Al:O in the corrosion product changed from ~ 10:9 to ~ 1:3 after 96 hrs, with the final Al and O concentrations being 25 at.% and 69 at.% respectively. The only other element that showed an increase was Cl^-, which had a maximum after 96 hrs at 4 at.% from the breakdown of the NaCl solution. Fe and Mn concentrations were also seen to reduce to negligible (< 1 at.%) values after 24 hrs of immersion. Mg concentrations showed a reduction with time, reducing from ~ 4 at.% to ~ 2 at.% between 24 and 96 hrs, but this is to be expected due to the sacrificial nature of Mg when alloyed alongside Al [26], [60], [63], [80].

The V_f of IMCs within SF1 was very low and they were also very fine in size. Figure 5-35 shows example EDS maps of IMCs within SF1. EDS showed that they were Al-Mg-Si and Al-Mg-Si-Fe in composition. Galvanic corrosion around the IMCs was seen to take place, possibly due to Mg dissolving from the particles. After 96 hrs some of the IMCs had no Mg remaining (confirmed via EDS) and their O concentration had increased. After 24 hrs the Mg concentration of the IMCs had reduced from ~ 13 at.% to 5 at.% [19], [27], [60–64]. Even though Mg is still present within the IMCs the charge of the IMCs changed and they became highly cathodic from the Fe and Si concentrations [26], [60], [63], [80].

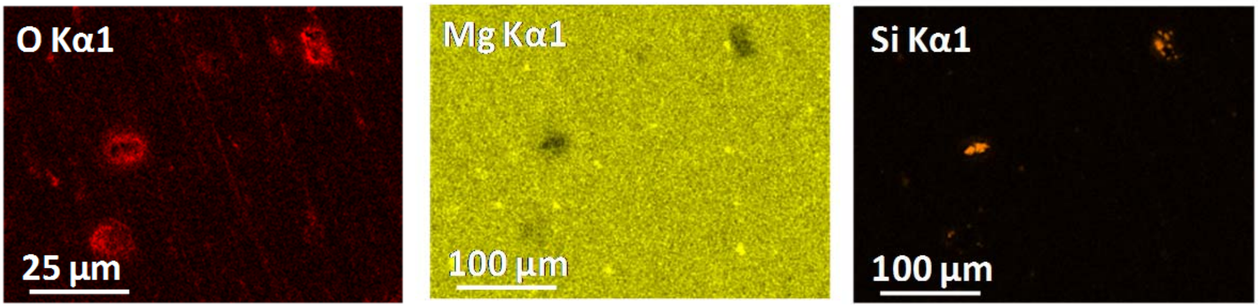

Figure 5-35: EDS maps showing the cathodic nature of the Si rich IMCs within SF1.

Cross sectioning of SF1 did not reveal any information for either the 24 hour of 96 hour immersion samples. Due to the low V_f of pitting corrosion sites on the surface a coarse cross sectioning which was unable to examine any of the pitting corrosion sites.

5.2.3 Spray formed Al-Mg-Li-Cu-Zn (SF2)

Figure 5-36 a and b show the OCP over the initial 6 and 96 hour immersion period respectively. SF2 shows a large reduction in OCP over the 96 hour immersion period similar to that of SF1. This large change in OCP could be associated to the spray forming procedure with both SF alloys showing substantial reductions in OCP. Figure 5-36 a shows that the OCP had reduced by 120 mV from -752±13 mV to -872±28 mV after 6 hrs and Table 5-8 shows the change in OCP over the 96 hour immersion period. The standard deviation for SF2 was on average ~ 44 mV and the maximum was 83 mV. This large variation has been attributed to the width of the Cu and Zn rich region, with each specimen having a different width. EBSD revealed that at different depths after mechanical polishing the Cu and Zn rich region will alter in thickness. This thickness affects the corrosion rate of the samples and thus leads to fluctuations in the standard deviation. Overall the OCP suggests that SF2 has a poor corrosion resistance due to a 312 mV reduction in OCP over a 96 hour immersion period.

Table 5-8: OCP of SF2 over the 96 hour immersion period in 3.5 wt.% NaCl.

Time (hrs)	**0**	**24**	**48**	**72**	**96**
OCP (mV)	-752±13	-882±49	-947±72	-1041±30	-1064±20

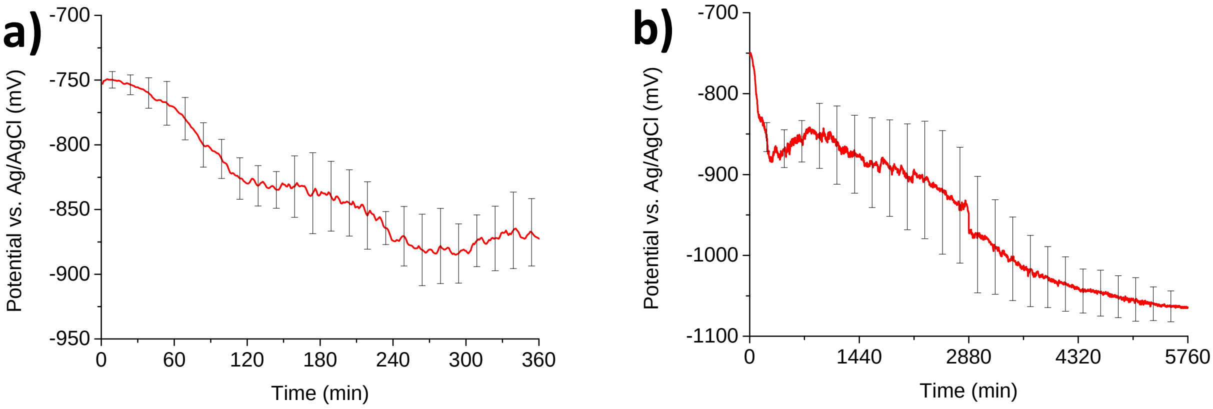

Figure 5-36: Graphs showing the OCP of SF2 following immersion in 3.5 wt.% NaCl for a) 6 hrs. b) 96 hrs.

Figure 5-37 a, b, c and d show the surface after 24, 48, 72 and 96 hrs of immersion respectively. EDS revealed that the Cu and Zn rich region had a lower Mg concentration to that of the surrounding matrix as well as increased Cu and Zn levels. Local alkalisation of the Cu and Zn rich region took place and a large galvanic cell was formed between the Cu and Zn rich region and the surrounding matrix. With increasing time galvanic corrosion formed on the periphery of the Cu and Zn rich region and there was more corrosion products on the Cu and Zn rich region. Examination of the OCP data suggests that a significant level of corrosion should have taken place on SF2, however, observations of the surface do not replicate this with few sites of established pitting corrosion being observed. The difference in OCP, however, could be related to the galvanic cell that has formed and in essence the OCP was not measuring a single cell system it was measuring a dual phase system (Cu and Zn rich, Mg reduced compared to the denuded region).

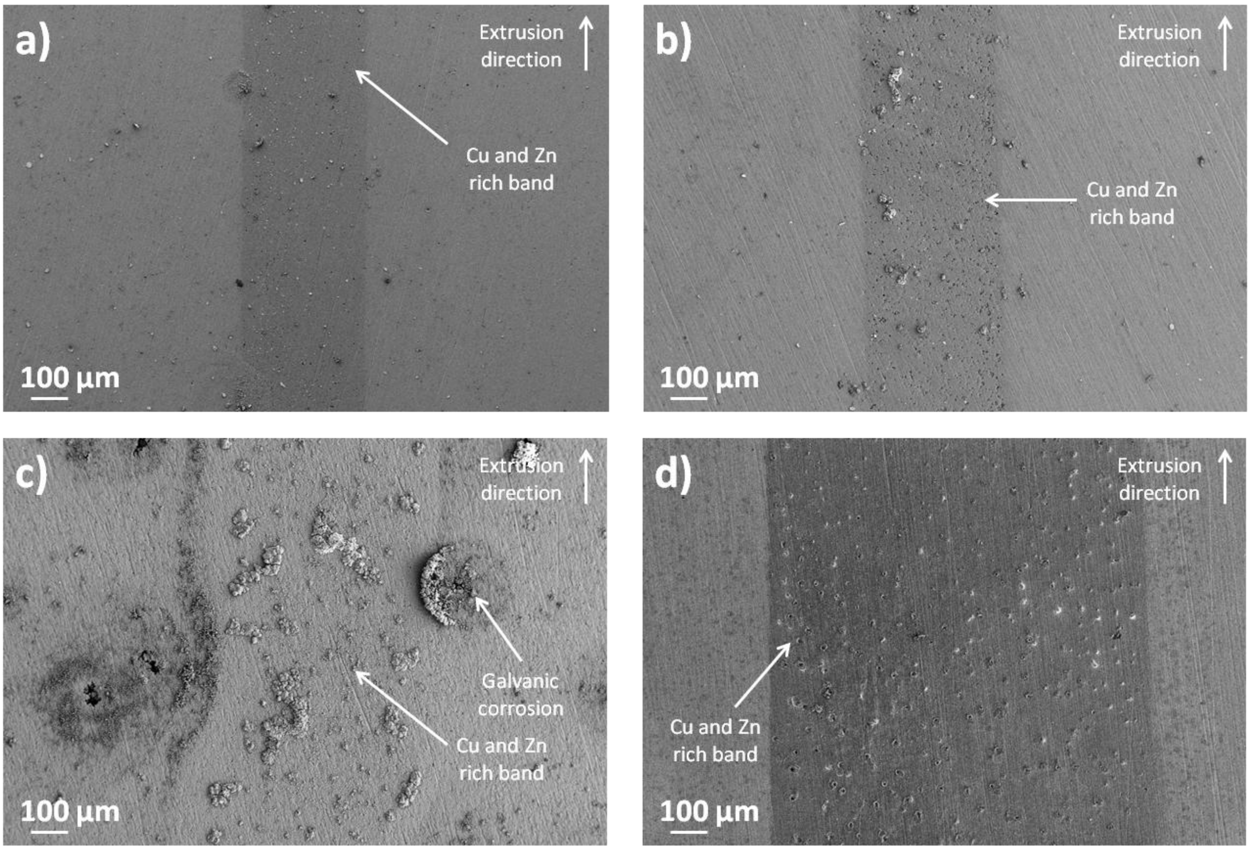

Figure 5-37: SEM micrographs of SF2 immersed in 3.5 wt.% NaCl for a) 24 hrs. b) 48 hrs. c) 72 hrs. d) 96 hrs.

Figure 5-38 a and b show the Cu and Zn rich region demonstrating preferential attack due to the galvanic cell that forms between it and the surrounding matrix. Figure 5-38 a shows the Cu and Zn rich region shows the most corrosion. Corrosion can be seen on the Cu and Zn denuded region, with the number of sites being less but the size was increased compared to the surrounding area. Figure 5-38 b shows a circular corrosion ring forming on the periphery of the Cu and Zn rich region, which can be seen to be the start of galvanic corrosion on the periphery. Even though the Cu and Zn rich region is the cathode in this reaction, corrosion probably takes place due to the presence of Cu rich phases [24], [80], [84], [152]. Figure 5-38 b shows galvanic corrosion, which EDS showed that the corrosion site is high in O, whereas the immediate circular region around it is reduced in O. Due to the galvanic nature of the Cu and Zn rich region, this means that the surrounding material is forced to be anodic. Even though Figure 5-38 b only shows a semi-circular corrosion product, other pits showed the formation of an entire circular corrosion ring, even though galvanic corrosion is not as extensive as the pitting corrosion away from the Cu and Zn rich region. Figure 5-38 c and d shows extensive pitting corrosion forming on the Cu and Zn denuded region. Their size, however, can be related to the galvanic nature of SF2, in that since the Cu and Zn rich region is cathodic, the surrounding matrix is forced to be anodic and thus will accelerate the corrosion at these regions [26], [61], [62], [84], [96].

Figure 5-38 c and d that the pits are highly elongated, with the pit in Figure 5-38 c being ~ 300 µm wide and in length, whereas the largest pit seen in Figure 5-38 d is ~ 100 µm wide and ~ 600 µm in length. Most of the corrosion in the Cu and Zn denuded regions did not appear to progress very deep into the specimens, however, those identified in Figure 5-38 c and d progressed further than most. This is to be expected; since galvanic corrosion is highly associated with the periphery thus develops in depth more than width. Examination of the pits revealed faceted pitting corrosion had developed.

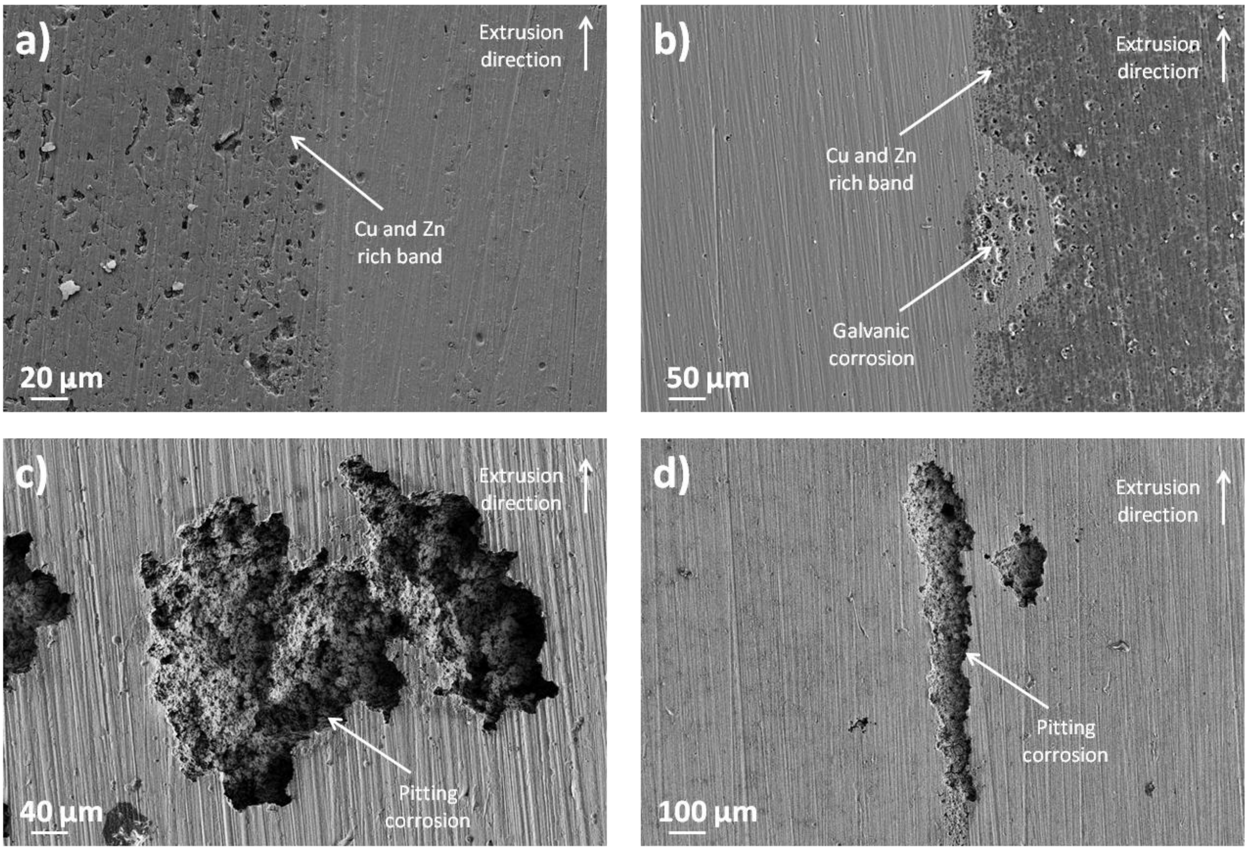

Figure 5-38: SEM micrographs of SF2 showing evidence of a) galvanic corrosion around cathodic IMCs in the Cu and Zn rich region. b) pitting corrosion at the periphery of the Cu and Zn rich region. c) hemispherical pitting corrosion of the Cu and Zn denuded region. d) hemispherical pitting corrosion of the Cu and Zn denuded region.

Figure 5-39 shows a distinct increase in O on the Cu and Zn rich region from ~ 18 at.% to 52 at.% after 96 hrs. The corrosion products form in circular regions on the edges of the Cu and Zn rich region. Dome shaped corrosion products have been seen to be associated with pitting corrosion, in that the corrosion lies beneath the dome. The cathodic nature of the Cu and Zn rich region is highlighted by the change in O concentration. O concentrations of 18 at.% and 52 at.% compared to 8 at.% and 5 at.% for 24 and 96 hrs on the Cu and Zn rich / Cu and Zn denuded regions respectively.

The ratio of Al:O on the Cu and Zn rich region changed from ~ 4:1 to ~ 13:10 after 96 hrs of immersion, however, the ratio of Al:O changed from ~ 11:1 to ~ 9:5 after 96 hrs of immersion. The concentration of Al and O on the Cu and Zn denuded region was relatively consistent over the 96 hrs of immersion with the average Al and O content being 85 at.% and 8 at.% respectively, whereas on the Cu and Zn rich region the Al concentration reduces from 76 at.% to 43 at.% hrs after 96 hrs. This shows that even though the Cu and Zn rich region is acting as the cathode it is also undergoing corrosion itself. The Mg content on the Cu and Zn rich region reduced with time (~ 1 at.% per 24 hrs) from an initial 6 at.%, however, on the Cu and Zn denuded region the Mg concentration was not affected. Cu, Fe and Mn concentrations for both regions were not seen to be affected with increasing immersion time. Once again analysis of the O and Al concentrations does not agree with the results seen by OCP in that over the initial 48 hrs of immersion the visual and chemical analysis suggests a low level of corrosion, however, the OCP shows that a large reduction takes place over this same time period.

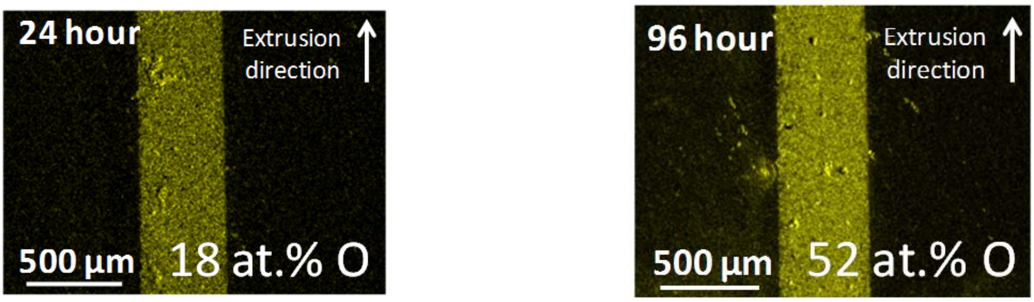

Figure 5-39: EDS maps showing the increase in O concentration with increasing immersion time on the Cu and Zn rich region of SF2.

EDS of the corrosion product on the Cu and Zn rich region showed that with increasing immersion time the concentration of O increased. After 24 hrs the O concentration was 48 at.% rising to 56 at.% after 96 hrs. In comparison the Cu and Zn denuded regions showed an O concentration of 8 at.% after 24 hrs and 3 at.% after 96 hrs. Due to the very small changes in O concentrations on the Cu and Zn denuded region, the Al concentration was not seen to change, staying at ~ 85 at.% over the entire 96 hour immersion period. Mg concentrations were seen to reduce, through sacrificial dissolution, but the concentrations were different between the Cu and Zn denuded and Cu and Zn rich regions [19], [27], [60–64]. On the Cu and Zn rich region the Mg concentration reduced from 6 to 4 at.% between 24 and 96 hrs, whereas on the Cu and Zn denuded region the Mg concentration did not appear to show any change, with all being ~ 3 at.%. This correlates with the EDS which showed that the Cu and Zn rich region had a reduced Mg concentration than the Cu and Zn denuded region. On the Cu and Zn rich region, the Cu and Zn concentrations were seen to reduce, but since they were < 1 at.% after 24 hrs these results are negligible.

The V_f of IMCs within SF2 was very low and they were also very fine in size. The Cu and Zn rich region did, however, show Cu rich phases. The IMCs of the Cu and Zn denuded region were Al-Mg-Si and Al-Mg-Si-Fe. Similar to SF1, galvanic corrosion around the IMCs took place, demonstrating that the Mg was quickly dissolved. After 96 hrs some of the IMCs had no Mg measured and their O concentration increased. After 24 hrs the average Mg concentration of the IMCs reduced from ~ 13 at.% to 3 at.%. Even though Mg was present within the IMCs the charge of the IMCs changed and they became highly cathodic from the Fe and Si concentrations [25], [26], [60], [63], [80]. This also demonstrates the accelerating factor of the cathodic Cu and Zn rich region which has caused an accelerated dissolution of the less noble to Al phases within the Cu and Zn denuded region.

Figure 5-40 a and b show cross section of SF2 after 24 hrs in immersion. Evidence of galvanic corrosion around IMCs of the Cu and Zn rich region is shown in Figure 5-40 a. This galvanic corrosion formed small pitting corrosion sites < 5 µm in depth in the Cu and Zn rich region. In the Cu and Zn denuded region limited pitting corrosion was observed. Galvanic corrosion at the periphery of the Cu and Zn rich region was seen, as shown in Figure 5-40 b. After 24 hrs this galvanic corrosion was seen to be < 20 μm in depth. This suggests that SF2 had a high corrosion resistance, due to the finite amount of corrosion that takes place, however, due to the dual cell (Cu and Zn rich region vs. denuded region) that operates it cannot be concluded as to whether SF2 is good or bad for corrosion resistance. With no IGC being observed, this suggests that SF2 is absent of anodic and / or cathodic phases, which have a tendency to precipitate to the GB.

The 96 hour immersed sample did not reveal any further information and no corrosion sites were observed following cross sectioning. If we assume that the rate of corrosion is constant we can say that the Cu and Zn rich region could develop pits that are < 20 μm deep and the galvanic corrosion at the periphery could be < 80 μm after 96 hrs of immersion, however, since the rate of Al and O changes are not constant this can only be used as an estimate.

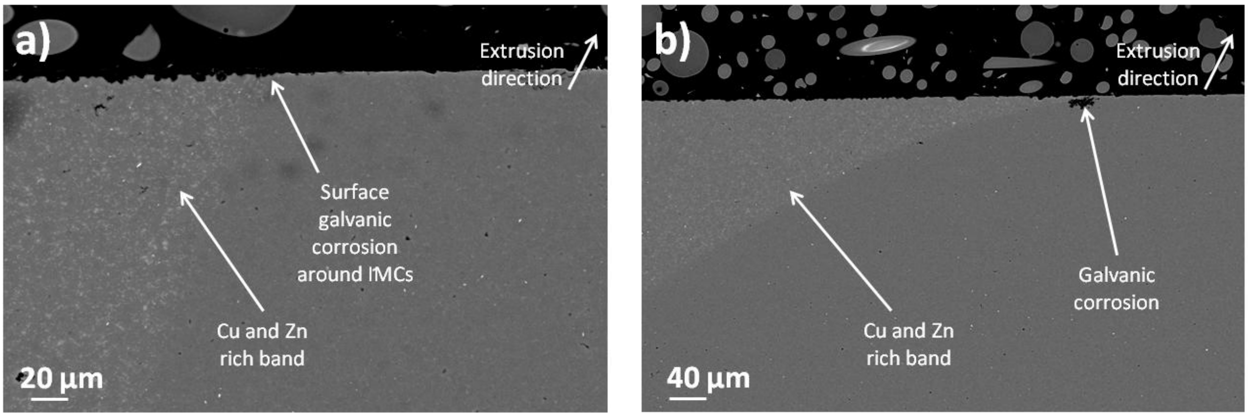

Figure 5-40: Cross-sectional SEM micrographs of SF2 after 24 hrs of immersion in 3.5 wt.% NaCl showing evidence of a) shallow faceted pitting corrosion. b) deep galvanic corrosion at the periphery of the Cu and Zn rich region.

5.2.4 Comparison of Al-Mg alloys following immersion testing

OCP as shown in Figure 5-41 shows that Mg1 had an entirely different profile compared to SF1 and SF2. The SF alloys had similar OCP trends, which was inconsistent given the substantial chemical difference between them especially the Cu and Zn rich region. Both showed a lot of similarities, however, with regards to grain size, IMC density and distribution. SF2 showed the more noble OCP as Cu is a highly noble element and should cause an anodic shift in the OCP of the specimen [12]. After 96 hrs both showed similar OCPs suggesting that over prolonged immersion they had similar corrosion resistances. One item to note is that the trend of SF1 appeared to be stabilising with time, whereas SF2 shows a continual reduction, which suggests that if the tests were prolonged, SF2 would have continued to generate more corrosion [12]. If these trends continued SF1 would become the more noble, suggesting a higher corrosion resistance [12], [156–158]. Mg1 in comparison shows a very stable OCP which is more noble than either, suggesting that it actually would have the superior corrosion out of the Al-Mg alloys [12], [156–158].

Table 5-9 shows the change in OCP for each of the Al-Mg alloys from the initial OCP through to after 96 hrs of immersion. After 6 hrs the OCP of Mg1 had reduced by ~ 7 mV, whereas SF1 and SF2 had reduced by ~ 140 mV and ~ 120 mV respectively. Literature [12] therefore would suggest that the SF alloys have a large amount of corrosion taking place and even over the entire 96 hour immersion period. Over 96 hrs the OCP of Mg1 reduced by a ~ 14 mV compared to 291 mV and 312 mV for SF1 and SF2 respectively.

Table 5-9: OCP of Mg1, SF1 and SF2 over the 96 hour immersion period in 3.5 wt.% NaCl.

Time (hrs) / Alloy OCP (mV)	0	24	48	72	96
Mg1	-714±1	-708±5	-711±8	-716±6	-728±1
SF1	-758±5	-924±66	-1057±16	-1055±24	-1049±1
SF2	-752±13	-882±49	-947±72	-1041±30	-1064±20

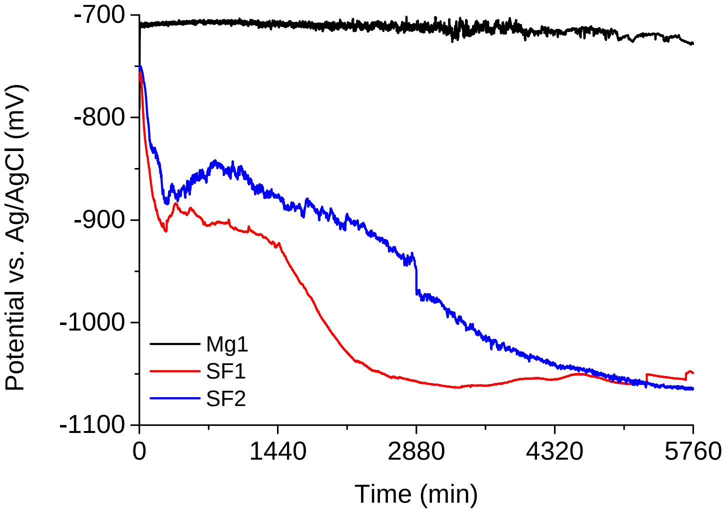

Figure 5-41: Graph showing the OCP of Mg1, SF1 and SF2 over a 96 hour immersion in 3.5 wt.% NaCl.

Each of the Al-Mg alloys corroded in different ways. Mg1 showed localised pitting and uniform attack over the entire surface, which was expected due to the sacrificial nature of the less noble Mg to Al [19], [27], [60–64]. However, SF1 showed localised pitting corrosion and SF2 showed localised pitting as well as galvanic corrosion around the Cu and Zn rich region. Since SF1 and Mg1 corroded in different ways, it has to be concluded that the spray forming and / or the Li additions affected the corrosion resistance. SF1 had a fine grain structure, whereas Mg1 had a coarse grain structure and as such OCP data suggests that the larger grain size has a similar corrosion resistance, which goes against theory of fine grain structures being superior for corrosion [71], [72], [74]. The largest corroded region on Mg1 was seen to be > 500 µm in length and > 300 µm in width, whereas the localised pits on SF1 were shown to be Ø = 120 µm after 96 hrs of immersion. Closer inspection showed that IMCs were associated with pitting corrosion, in particular those that contained Fe, Mn and Si as they are more noble than the Al matrix [19], [27], [60–64]. Mg1 showed faceted and hemispherical pitting, whereas SF1 only showed hemispherical pitting which is associated with localised alkalisation [19], [39], [63], [80], [86], [91].

Inspection of the Cu and Zn rich region on SF2 shows that galvanic corrosion started to develop and after 72 hrs evidence of corrosion beneath circular corrosion products could be seen. The corrosion products were Ø = 200 µm and the corrosion was Ø = ~ 100 µm. Inspection of SF2 away from the Cu and Zn rich region showed the formation of substantial pitting corrosion sites, an example being seen in Figure 5-38 d at ~ 100 µm wide and ~ 600 µm in length. This shows that accelerated corrosion that takes place on the anodic part of SF2 since the Cu and Zn rich region will act as a cathode. In theory the Cu and Zn denuded matrix of SF2 should have corroded at a similar rate to that of SF1, however, due to the cathodic effect of the welded region (Cu and Zn rich), this is not the case. Small shallow pits formed on the surface of the Cu and Zn rich region, which cross sectioning showed were ~ 5 µm in depth.

With increasing immersion time the Al and O concentrations on the surface reduced and increased respectively on all of the Al-Mg alloys. Table 5-10 shows the change in Al and O concentrations with increasing immersion time on the surface and within the corrosion products. Mg1 and SF1 showed similar levels of corrosion product on their surface, however, the Cu and Zn rich region on SF2 showed a high degree of oxidation which is associated with the cathodic nature of the Cu. Mg1 and SF1 showed a 6 and 7 at.% increase in O respectively, after 96 hrs. The Cu and Zn denuded region of SF2 showed a reduction in O from 8 to 5 at.%, however, on the Cu and Zn rich region the O concentrations increased by 34 at.%. The corrosion products show that on all of the Al-Mg alloys the trends were comparable with Al reducing and O concentrations increasing with immersion time.

Table 5-10: Change in Al and O concentration for Mg1, SF1 and SF2 on the surface and in the corrosion product over the 96 hour immersion period in 3.5 wt.% NaCl.

at.%	Surface				Corrosion Product			
	24 hrs		96 hrs		24 hrs		96 hrs	
	Al	O	Al	O	Al	O	Al	O
Mg1	74	18	62	24	34	63	20	78
SF1	79	16	74	23	50	46	25	69
SF2 Cu and Zn rich	76	18	43	52	50	48	40	56
SF2 Cu and Zn denuded	86	8	88	5	86	8	88	5

The IMCs in the Al-Mg alloys showed that the Mg was anodic and sacrificial [19], [27], [60–64]. This was until the polarity of the IMC changed once the anodic elements had been dissolved. Once this developed galvanic corrosion surrounding the IMCs took place. If the IMCs contained elements that were more noble they would also generate galvanic corrosion. It was shown that the Fe, Mn and Si elements were cathodic and as such were the elements responsible for generating the galvanic corrosion within the Al-Mg alloys [26], [60], [63], [80].

With SF1 and SF2 having such low volumes of pitting corrosion, cross sectioning was unable to locate these sites for further examination. On all of the Al-Mg alloys, IMCs were associated with pitting corrosion, however, on SF2 the Cu and Zn rich region also showed pitting corrosion. Similarities that were observed are that all of the corrosion appeared to be faceted in morphology; however, Mg1 did show evidence of hemispherical pitting on the surface also. Hemispherical pitting is associated with localised alkalisation of the surface surrounding cathodic IMCs [26], [35], [39], [60], [63]. Mg1 showed uniform attack over the surface which was seen to be ~ 20 µm deep and the deepest pit was 30 µm.

After 96 hrs the same corrosion depths were observed, which suggests that only the number of pit sites increased with time. No comparison could be made to SF1 and on SF2 the Cu and Zn rich region meant that galvanic corrosion was the main corrosion observed. No IGC was seen, which was unexpected due to the Cu and Zn rich region. However, galvanic corrosion at the periphery of the Cu and Zn rich region progressed to 20 µm after 24 hrs.

Since no corrosion depth information was acquired for SF1 it is difficult to conclude which of the Al-Mg alloys had the best corrosion resistance. SF2 developed a large galvanic cell which caused corrosion of the anodic matrix. SF1 developed localised pitting corrosion compared to the uniform corrosion seen on Mg1; however, the corrosion depth on Mg1 was less than that of SF1. The uniform corrosion of Mg1 shows that it is highly anodic and the Mg content is acting as a sacrificial anode [19], [27], [60–64]. Corrosion resistance has been measured with regards to the amount of oxidation measured and the depth and number of corrosion sites. Since no depth information was available for SF1 it cannot be concluded whether the Li and / or spray forming improved the corrosion resistance. *Moore et al.* [28], [93], [94], however, also showed that spray forming offered negligible improvement to the corrosion resistance of Al alloys.

Chapter 6: Potentiodynamic Polarisation

Potentiodynamic polarisation has been conducted to obtain an understanding of the corrosion mechanisms of a range of Al-Mg and Al-Cu alloys with different grain sizes by driving the system electrochemically in the anodic direction within a corrosive electrolyte. Degreased surfaces and MG surfaces as explained in Chapter 2 were investigated. Potentiodynamic polarisation curves are plotted as potential (V) against $\log_{10}$ of the current density (A/cm^2). From these polarisation curves the pitting potentials (E_{pit}), charge passed and variation in free corrosion potential / OCP (E_{corr}) have been investigated. The analysis also gives an understanding of how the underlying microstructure, IMC distributions, chemistry and electrolyte influence the resulting corrosion performance.

E_{pit} is defined as the potential where a significant increase in current density is observed [89], therefore using the polarisation curves in this thesis this definition is used to determine the individual pitting potentials per specimen per alloy. Using E_{pit}-E_{corr} an estimate of the pitting corrosion resistance of a material can be determined. This value typically gives an indication of how much potentiodynamic polarisation is required to allow stable pit growth and as such this value is an indication of the size of the metastable pitting region. This is where pits are active and then passivate, and undergo this cycling procedure until the E_{pit} is reached at which the pit can no longer passivate and stable pits develop [61], [70].

Prior to polarisation a 5 min OCP measurement was taken on every sample to allow the system to come to relative stability. These results will be discussed prior to the polarisation curves.

Throughout this analysis, for ease degreased specimens will be abbreviated to DEG and MG specimens will be abbreviated to MG, for example AA2024-T3 degreased will be described as Cu1-DEG. Due to the high level of corrosion associated with potentiodynamic polarisation, analysis of corrosion products and changes to IMC chemistry have not taken place. Chapters 4 and 5, however, have covered this in detail.

6.1 Potentiodynamic polarisation of Al-Cu alloys

6.1.1 AA2024-T3 (Cu1)

OCP was recorded prior to potentiodynamic polarisation and Figure 6-1 shows the difference between Cu1-DEG and Cu1-MG. EBSD showed that Cu1-DEG had a coarser grain structure to that of Cu1-MG, therefore a difference in polarisation resistance was expected. OCP showed that Cu1-MG had a more noble starting potential of ~ -630 mV compared to ~ -660 mV of Cu1-DEG. Both show similar trends with reductions in OCP before increasing. Cu1-DEG specimens showed a gradual increase to ~ -590 mV where it stabilised, whereas Cu1-MG showed a trough over the initial 50 s of immersion before stabilising at ~ -610 mV. *Vargel* [12] stated that an increase in potential signifies passivation whilst a reduction is corrosion taking place, this trough could therefore be the breakdown of an air formed, surface passive layer. Table 6-1 shows the E_{corr} of 5 specimens recorded for Cu1, indicating the average and standard deviation of Cu1. It can be seen that both Cu1-DEG and Cu1-MG specimens showed a high degree of reproducibility. The final OCP values of each show that Cu1-DEG is more noble than Cu1-MG, however, Cu1-DEG increased its OCP by ~ 80 mV to -592±2 mV and Cu1-MG increased its OCP by ~ 10 mV to -614±7 mV over the 5 min immersion period.

When compared to the results seen for Section 5.1.1, which examined the same electrolyte, no difference in OCP was observed. Since the Immersion testing results examined MG specimens only, this is all that can be discussed. On average the results in Section 5.1.1 shows that the OCP after 5 min's was -600±45 mV, compared to -614±7 mV for the polarisation OCP, however, the error had reduced significantly showing that Cu1 had very good reproducibility.

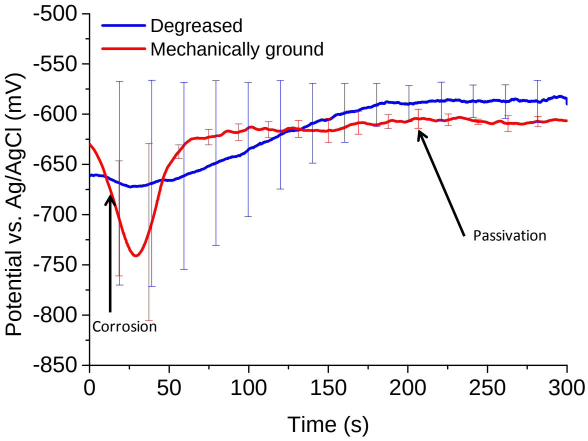

Figure 6-1: Graph showing the change in OCP of Cu1 following 5 min immersion prior to potentiodynamic polarisation in a 3.5 wt.% NaCl.

Examination of the polarisation plots shown in Figure 6-2 a and b show that Cu1-DEG and Cu1-MG specimens performed in a very similar manner. Table 6-1 shows the E_{corr} and E_{pit} values taken from Figure 6-1 and Figure 6-2. E_{pit} values were seen to have a smaller difference than the E_{corr} values, with Cu1-DEG having an E_{pit} of -582±5 mV compared to -587±6 mV of Cu1-MG. Other authors [26], [160], [161] demonstrated E_{pit} values at ~-600 mV vs. Ag/AgCl for AA2024. Cu has a significant impact on the OCP of Al alloys due to it being highly noble compared to Al [12], [27], [28]. The profile of the polarisation curves, showed the absence of a metastable pitting region, which is related to the equilibrium potential of the system being very close to that at which stable pits will form. E_{pit} and E_{corr} are therefore very similar potentials, which can be characteristic of Al-Cu alloys [28]. This highlights the poor corrosion resistance of Al-Cu alloys by the amount of time these specimens spend above their respective E_{pit} during these experiments. Typically a noble E_{pit} is a sign that the system has a high corrosion resistance, however, with Al-Cu systems this is not the case [12], [156–158]. As such E_{pit} values can only be used as an indication of corrosion resistance, E_{pit} alone cannot tell the user whether a system has a good or bad corrosion resistance. When you have the E_{corr} value also, this allows for a quantifiable measure of corrosion resistance by finding the difference between them.

Table 6-1: Table showing the difference in E_{pit}, E_{corr}, E_{pit} - E_{corr} and charges passed on Cu1-DEG and Cu1-MG following potentiodynamic polarisation in a 3.5 wt.% NaCl.

Specimen Number	Cu1-DEG				Cu1-MG			
	E_{pit} (mV)	E_{corr} (mV)	E_{pit} - E_{corr} (mV)	Charge (C)	E_{pit} (mV)	E_{corr} (mV)	E_{pit} - E_{corr} (mV)	Charge (C)
1	-578	-591	13	22	-587	-617	30	20
2	-580	-593	13	25	-582	-606	24	22
3	-590	-595	5	22	-591	-619	28	24
4	-580	-589	9	21	-594	-620	26	18
5	-582	-594	12	22	-581	-606	25	19
Average	-582	-592	10	22	-587	-614	27	21
Standard deviation	5	2	3	1	6	7	3	4

Frankel et al. [85] examined AA2024 and stated that a double breakdown potential was observed. These related to IGC and pitting corrosion respectively and formed at ~ -595 mV and ~ -565 mV vs. Ag/AgCl. *Meng et al.* [36] also observed a double breakdown potential on 7XXX series Al alloys with Cu additions, suggesting it was associated with Cu. This author tried to replicate the results by *Frankel et al.* [85], however, no double breakdown potential was observed. The value of E_{pit} in this thesis, however, are shown to be similar to values quoted in the literature [36], [73], [84], [85], [154], [155].

Table 6-1 shows the charge passed on each of the specimens and an average, as well as the calculated pitting corrosion resistance via E_{pit}-E_{corr}. Cu1-DEG had an average E_{pit}-E_{corr} of 10±3 mV compared to 27±3 mV for Cu1-MG, suggesting that the latter had a marginally higher pitting corrosion resistance. The amount of charge that passes shows that both systems had very similar values, which is to be expected due to their similar grain size characteristics. Overall the standard deviations for Cu1 are all very low proving that Cu1 had a reproducible corrosion resistance.

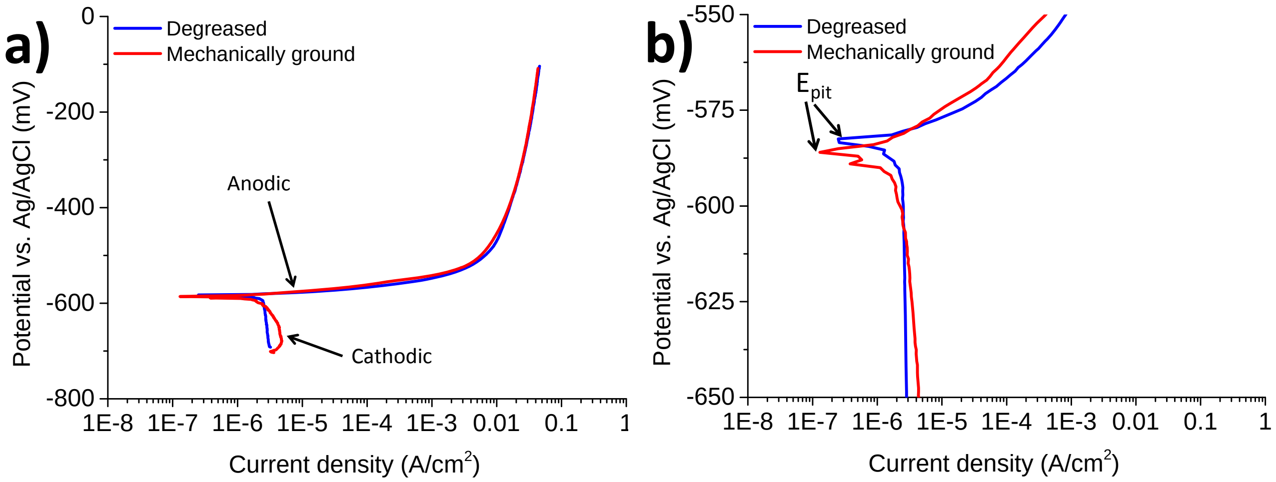

Figure 6-2 a) Graph showing the potentiodynamic polarisation response of Cu1-DEG and Cu1-MG in 3.5 wt.% NaCl. b) Graph showing an enlarged region of the potentiodynamic polarisation response of Cu1-DEG and Cu1-MG in 3.5 wt.% NaCl, highlighting the E_{corr} and E_{pit} regions.

Visual observations of the Cu1 surfaces following polarisation reveals a difference in the corrosion resistance of Cu1-DEG and Cu1-MG. Figure 6-3 a and b show micrographs of Cu1-DEG and Figure 6-3 c shows a micrograph of Cu1-MG after potentiodynamic polarisation. Figure 6-3 a shows the corner edge of a Cu1-DEG specimen, highlighting that edge effects can cause large amounts of corrosion to initiate. Large volumes of H_2 bubbles appear to have got trapped at the edges of the samples. These bubbles formed from the redox reaction around cathodic particles, which causes local alkalisation to occur increasing the local pH [19], [39], [63], [86]. Figure 6-3 b shows an example micrograph taken from a more central region on a Cu1-DEG specimen, showing that pitting corrosion does still take place in the central regions but the number of pits are reduced significantly, but all are of a similar size at over 100 µm. In contrast the pits seen on Cu1-MG are much smaller, but there is a higher V_f of them, as shown in Figure 6-3 c. The largest pit on Cu1-DEG was ~ 300 µm by 200 µm, whereas on Cu1-MG the largest was ~ 150 µm by 200 µm. The vast majority of the pits, however, were ~ 50 µm by 50 µm on Cu1-MG. These results agree with the electrochemical data, in that Cu1-MG shows a higher corrosion resistance to Cu1-DEG.

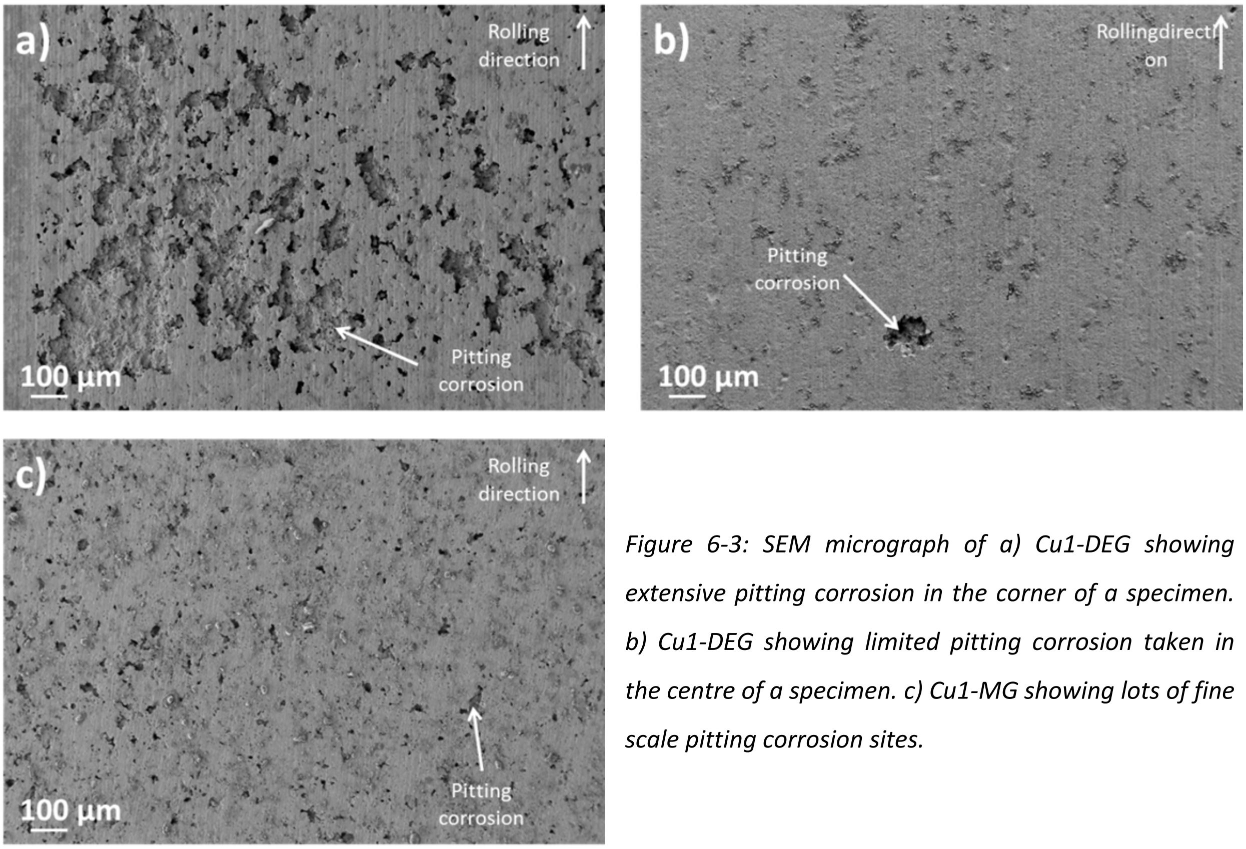

Figure 6-3: SEM micrograph of a) Cu1-DEG showing extensive pitting corrosion in the corner of a specimen. b) Cu1-DEG showing limited pitting corrosion taken in the centre of a specimen. c) Cu1-MG showing lots of fine scale pitting corrosion sites.

Closer inspection of the pits revealed that faceted pitting corrosion occurred, as shown in Figure 6-4 a, b, c and d. Figure 6-4 b shows a link between the IGC and faceted pitting corrosion and Figure 6-4 c, shows some IMCs within a matrix of IGC and faceted pitting corrosion, demonstrating the link between corrosion and cathodic IMCs [26], [60–64], [80]. Figure 6-4 c shows dark spherical spots along GB regions, which are related to the dissolution of the Al matrix around the cathodic θ type phases, as such what can be seen in Figure 6-4 c is a potential IGC initiation site. *Birbilis and Buchheit* [26] showed that the pitting potential of the θ type phase is -652 mV vs. SCE and as such it can be concluded that the θ type phase will have been active as soon as the E_{pit} was reached. Figure 6-4 d shows a grain undergoing dissolution, suggesting that corrosion dissolves certain grains in a specific order. This could be selective grain dissolution [31], [32], [115], [116], which is observed in Al-Cu-Li alloys, however, this may demonstrate that it is also a feature of Al-Cu 'base' alloys. Authors have shown that this can be related to grain stored energy, orientation, mis-orientation, particle density and chemistry [13], [75]. Figure 6-4 e shows more evidence of IMC impact on corrosion, with dark banding around IMCs being seen which is the dissolution of the Al matrix due to galvanic corrosion being initiated by cathodic elements [26], [60–63], [80], [84]. Figure 6-4 f shows evidence of IMCs being present at GB regions and within the matrix, demonstrating that IMCs can be associated with both pitting corrosion and IGC.

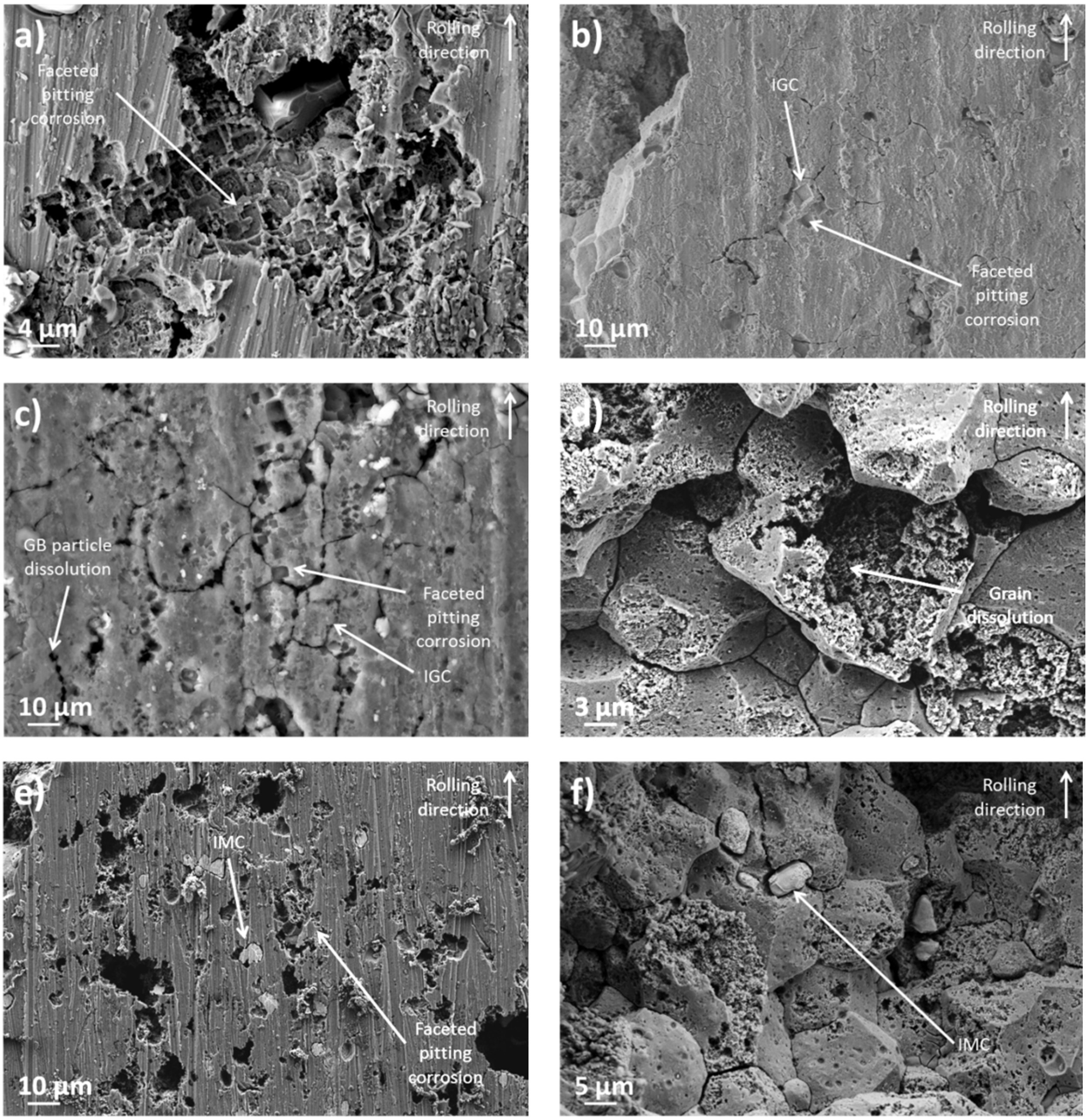

Figure 6-4: SEM micrographs of a) Cu1-DEG showing faceted pitting corrosion. b) Cu1-DEG showing the link between IGC and faceted pitting corrosion. c) Cu1-DEG showing dissolution around precipitates on the GBs. d) Cu1-MG showing faceted corrosion of an individual grain, suggesting selective grain dissolution. e) Cu1-MG showing the cathodic nature of some IMCs. f) Cu1-MG showing the presence of IMCs within the grain and on GBs.

Figure 6-5 a and b indicate the extrusion and transverse direction respective, for Cu1-DEG. Each shows evidence of IGC and pitting corrosion taking place, with the IGC progressing further into the specimens than the pits [102], [124]. *Knight et al.* [124] showed that on AA2024 IGC progressed to a self-limiting depth which was deeper than that of pitting corrosion. One aspect which was seen to be located with both the IGC and pitting corrosion was Cu rich IMCs, which can be seen in Figure 6-5 a and b. From potentiodynamic polarisation it can be difficult to identify the initiating point of IGC, in that it could start from precipitates as shown in Figure 6-4 c or from an IMC. However, Cu1-DEG had shown strong evidence that IGC can initiate from any cathodic particle regardless of size if it is located next to or on a GB. IGC was seen to progress to an average depth of 40 µm; however, some IGC was seen to progress to 60 µm. Most of the pitting corrosion progressed into the specimen further than they grew in width, like those seen in Figure 6-5 d. However, some pits were seen to develop sub-surface cavities as shown in Figure 6-5 a. A variation in pit depth was seen over Cu1-DEG surface, with some being ~ 10 µm in depth, like that seen in Figure 6-5 b, however, some were more substantial in depth reaching ~ 40 µm. The pit openings ranged from 10 to 60 µm in width, showing a high amount of inconsistency. Overall the majority of the surface had undergone pitting and IGC, forming a weakened friable layer.

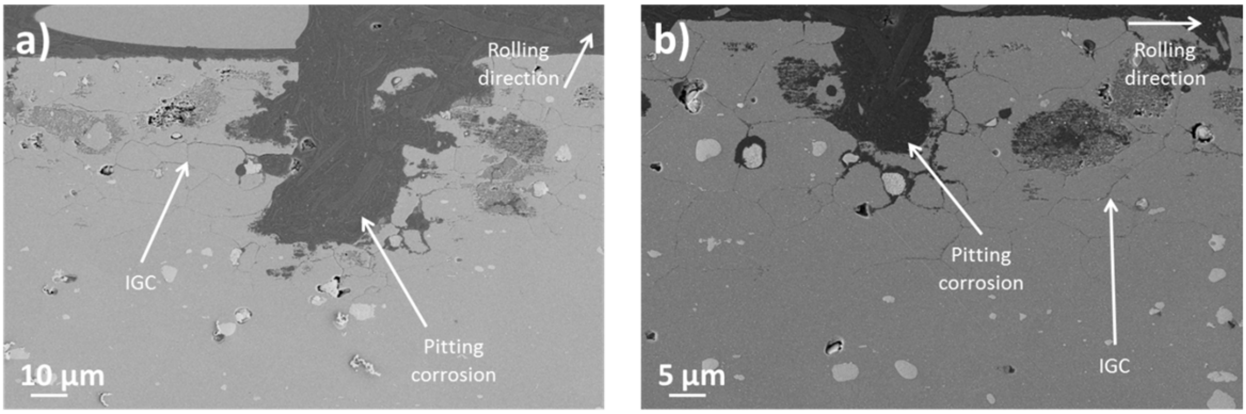

Figure 6-5: Cross-sectional SEM micrographs of Cu1-DEG after potentiodynamic polarisation in 3.5 wt.% NaCl showing a) sub-surface corrosion, IGC and corrosion associated with IMCs. b) pitting corrosion, IGC and their association with IMCs.

Figure 6-6 a and b observes the extrusion and transverse direction of cross-sectioned Cu1-MG. Analysis shows that the corrosion on Cu1-MG progressed to similar depths as Cu1-DEG and developed both IGC and pitting corrosion. This was not unexpected since the grains within the recrystallised grain structure were a similar size to those in the bulk of the specimen. Some regions showed higher amounts of corrosion, but the maximum depth of corrosion was seen to be ~ 70 µm for IGC and ~ 60 µm for pitting corrosion, once again showing that IGC progresses further than pitting corrosion [102], [124]. Pit openings were also a similar sizes, but like Cu1-DEG a lot of variation took place, ranging from 10 µm to 60 µm. Differences were expected between Cu1-DEG and Cu1-MG since both showed similar E_{pit} values and charges, which typically signifies that the same amount of corrosion could be taking place and the cross-sections in Figure 6-5 and Figure 6-6 reinforce this. It can, however, be said that both formed weakened, friable layers on the surface of the specimens. Overall, both had very similar corrosion resistances; however, the depth of attack was marginally deeper on Cu1-MG as such these results have to be taken lightly. However, the electrochemical data and surface overviews show that Cu1-DEG had larger areas being corroded. As such Cu1-MG had a marginally improved corrosion resistance overall. This shows that electrochemical predictions were accurate in predicting that Cu1-DEG would develop more corrosion.

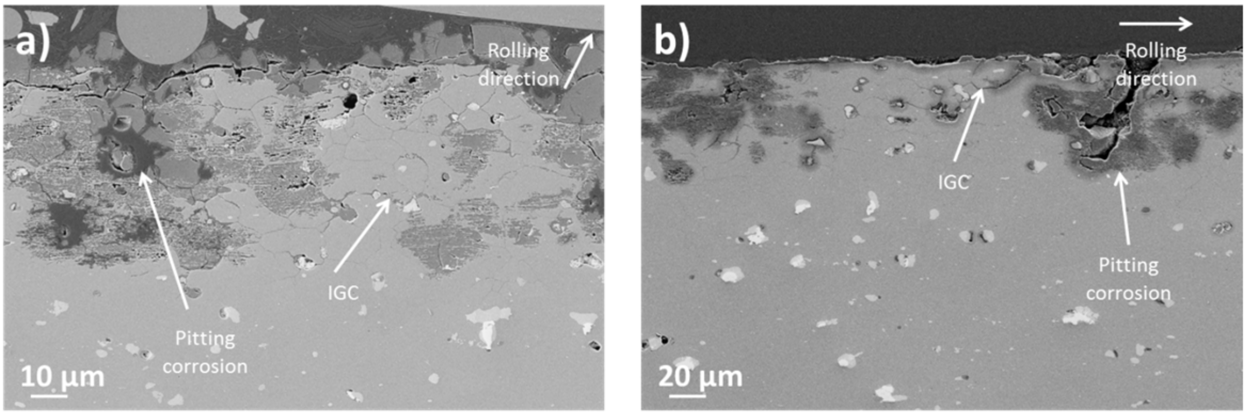

Figure 6-6: Cross-sectional SEM micrographs of Cu1-MG after potentiodynamic polarisation in 3.5 wt.% NaCl showing a) extensive pitting corrosion and IGC. b) pitting corrosion and IGC.

6.1.2 AA2099-T8E77 extrusion (Cu2)

Figure 6-7 shows the difference in the 5 min OCP prior to polarisation, between Cu2-DEG and Cu2-MG. EBSD showed a ~ 100 µm coarse recrystallised grain structure at the surface of the Cu2-DEG specimens, whereas for Cu2-MG the coarse grain structure was removed and the underlying finer grain structure was examined. This allowed a direct comparison between coarse and fine grain structures, to see which offered the higher corrosion resistance. At the start of immersion, Cu2-DEG had a less noble potential, however, after 60 s both showed a similar OCP. Cu2-MG shows that its OCP reduces with increasing time, however, it stabilised within 5 min's of immersion as does Cu2-DEG. After 5 min's Cu2-MG had a less noble OCP to Cu2-DEG and a 10 mV difference is noted. Both do, however, show the same trend in that both reduce in OCP with increasing immersion time, which is an indication of corrosion taking place. Cu2-DEG was seen to reduce by ~ 15 mV to -635±5 mV and Cu2-MG reduced by ~ 40 mV to -644±7 mV, which could be related to the higher density of GB particles in Cu2-MG [71], [72]. A bigger difference between the grain structures was, however, expected since there is a substantial difference in grain size. Table 6-2 shows the E_{corr} of 5 specimens recorded for Cu2, indicating the average and standard deviation.

When compared to the results seen for Section 5.1.2, no notable difference was observed. On average the OCP in Section 5.1.2, after 5 min's of immersion was -645±7 mV, which is very similar to the polarisation OCP at -644±7 mV. *Proton et al.* [115] examined the OCP of a NHT Al-Cu-Li alloy and showed that it had an OCP of ~ -620 mV vs. SCE, whereas a HT specimen showed an OCP of -730 mV vs. SCE. This shows that the OCP values obtained in this work are similar to those of *Proton et al.* [115].

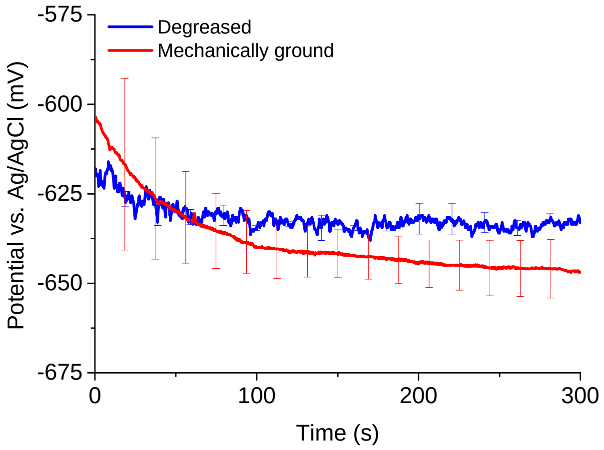

Figure 6-7: Graph showing the change in OCP of Cu2 following 5 min immersion in 3.5 wt.% NaCl prior to potentiodynamic polarisation.

The polarisation plots shown in Figure 6-8 a and b show Cu2-DEG and Cu2-MG performed in a very similar manner, in that once they reached their respective E_{corr} values, an increase in current density was observed, resulting in the E_{pit} being achieved. This is characteristic of Al-Cu alloys and had been shown to take place in literature [93]. Similar to Cu1, no metastable pitting region was observed. Table 6-2 shows the E_{corr} and E_{pit} values taken from Figure 6-7 and Figure 6-8. E_{pit} values were similar to the E_{corr}, with Cu2-DEG having an E_{pit} of -621±3 mV compared to -612±2 mV for Cu2-MG. This shift in the anodic direction could be associated with the cathodic particle rich GBs, creating a demand for current causing an imbalance in the equilibrium state [71], [72]. Literature mentions that a noble E_{pit} is a sign that the system has a high corrosion resistance, however, this is not the case on Al-Cu alloys, but for Cu2 it appears as if this may be true [12], [156–158].

Table 6-2: Table showing the difference in E_{pit}, E_{corr}, E_{pit} - E_{corr} and charges passed on Cu2-DEG and Cu2-MG following potentiodynamic polarisation in a 3.5 wt.% NaCl.

Specimen Number	**Cu2-DEG**				**Cu2-MG**			
	E_{pit} (mV)	**E_{corr} (mV)**	**E_{pit} - E_{corr} (mV)**	**Charge (C)**	**E_{pit} (mV)**	**E_{corr} (mV)**	**E_{pit} - E_{corr} (mV)**	**Charge (C)**
1	-621	-641	20	24	-610	-638	28	17
2	-624	-633	9	24	-611	-638	27	20
3	-624	-639	15	25	-610	-653	43	13
4	-619	-633	23	24	-613	-644	31	16
5	-618	-630	20	25	-615	-649	34	14
Average	-621	-635	14	24	-612	-644	33	16
Standard Deviation	3	5	4	1	2	7	6	3

E_{pit}-E_{corr} showed that Cu2-DEG had an average pitting corrosion resistance of 14±4 mV compared to 33±6 mV for Cu2-MG, suggesting that the latter had the higher pitting corrosion resistance even though it was more noble. Cu2-DEG had a higher charge pass at 24±1 C compared to 16±3 C for Cu2-MG. This is not unexpected, with theory suggesting a higher corrosion resistance for finer grain structures [71], [72], [74], thus those with lower charges have a higher corrosion resistance. Overall the standard deviations for Cu2 are all very low, proving that Cu2 had a reproducible corrosion resistance, which is a common association with Al-Cu alloys. Theory agrees with the information in Table 6-2 and as such these results show that Cu2-MG had a higher corrosion resistance than Cu2-DEG. This increase in potential is more than likely to be associated with the increased number of active sites, with regards to the increase in grains and GBs under attack at any given point [71], [72].

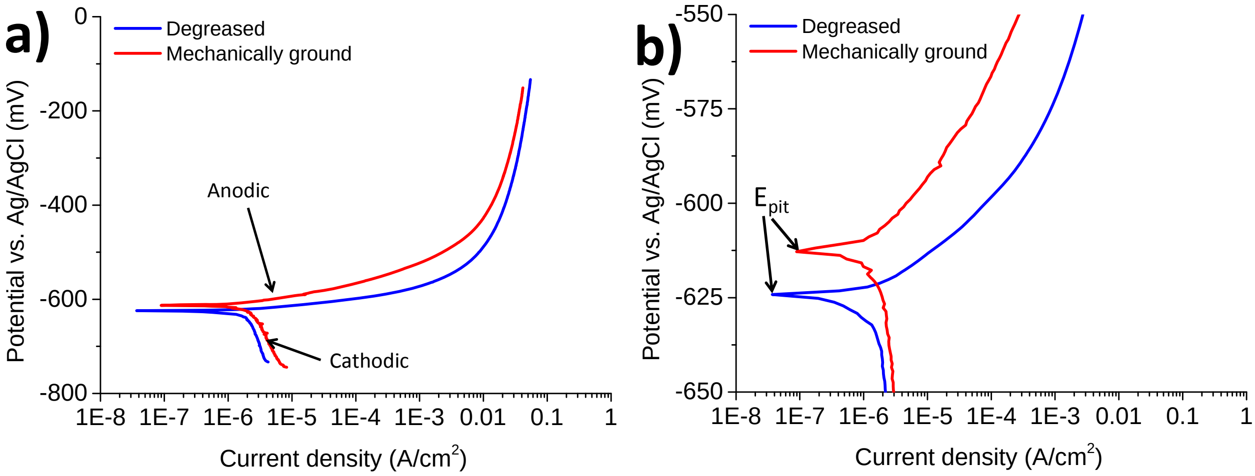

Figure 6-8 a) Graph showing the potentiodynamic polarisation response of Cu2-DEG and Cu2-MG in 3.5 wt.% NaCl. b) Graph showing an enlarged region of the potentiodynamic polarisation response of Cu2-DEG and Cu2-MG in 3.5 wt.% NaCl, highlighting the E_{corr} *and* E_{pit} *regions.*

Visual observations of Cu2 following potentiodynamic polarisation reveals a difference in the corrosion resistance for Cu2-DEG and Cu2-MG. Figure 6-9 a and b show micrographs of Cu2-DEG and Figure 6-9 c and d show micrographs of Cu2-MG after potentiodynamic polarisation. Cu2-DEG exhibits large corrosion sites across the sample surface (Figure 6-9 a), but this does not take place across the entire surface, as shown in Figure 6-9 b. The coarse structure of Cu2-DEG suggests that it is undergoing highly accelerated corrosion and in particular selective grain dissolution which had been mentioned in literature to take place on Al-Cu-Li alloys, primarily through the dissolution of the T type phases [31], [32], [162]. Li is less noble than Al and *Li et al.* [32] showed that the T_1 phase had a potential of -1076 mV vs. SCE compared to -0.855 mV vs. SCE for Al. High concentrations of T type phase within the matrix and at GBs allows potential differences to form, which develop galvanic corrosion at the GB forming IGC or between neighbouring grains forming selective grain dissolution. Selective grain dissolution can also be attributed to grain stored energy and grain mis-orientation, thus a definitive conclusion would require further investigation.

Cu2-MG shows more corrosion sites developing; however, they are smaller and more likely to be pitting corrosion than those observed on Cu2-DEG. The corrosion that forms on Cu2-MG was also uniformly distributed over the surface, compared to the selected regions observed on Cu2-DEG. This suggests that selective grain dissolution is associated with coarse grain structures. Some of the corrosion sites on Cu2-DEG were > 600 µm in length and 200 µm wide. Some corrosion sites were elongated, supporting the theory of selective grain dissolution of the elongated coarse recrystallised grains. *Pasang et al.* [44] even stated that elongated grain structures had increased susceptibility to IGC. Some pits were spherical in nature, similar to those seen on Cu2-MG in Figure 6-9 c and d. The main corrosion site shown in Figure 6-9 a is ~ 1 mm in length and in places close to 500 µm wide, which shows that Cu2-DEG had a poor corrosion resistance. In comparison the pits seen on Cu2-MG had an Ø = 100 - 200 µm for the most, however, some were seen to be in excess of Ø = 400 µm, which also shows that Cu2-MG had a poor corrosion resistance. When related to the electrochemical response, the visual observations tend to agree, in that Cu2-DEG actually had the lower corrosion resistance due to the formation of very substantial pits.

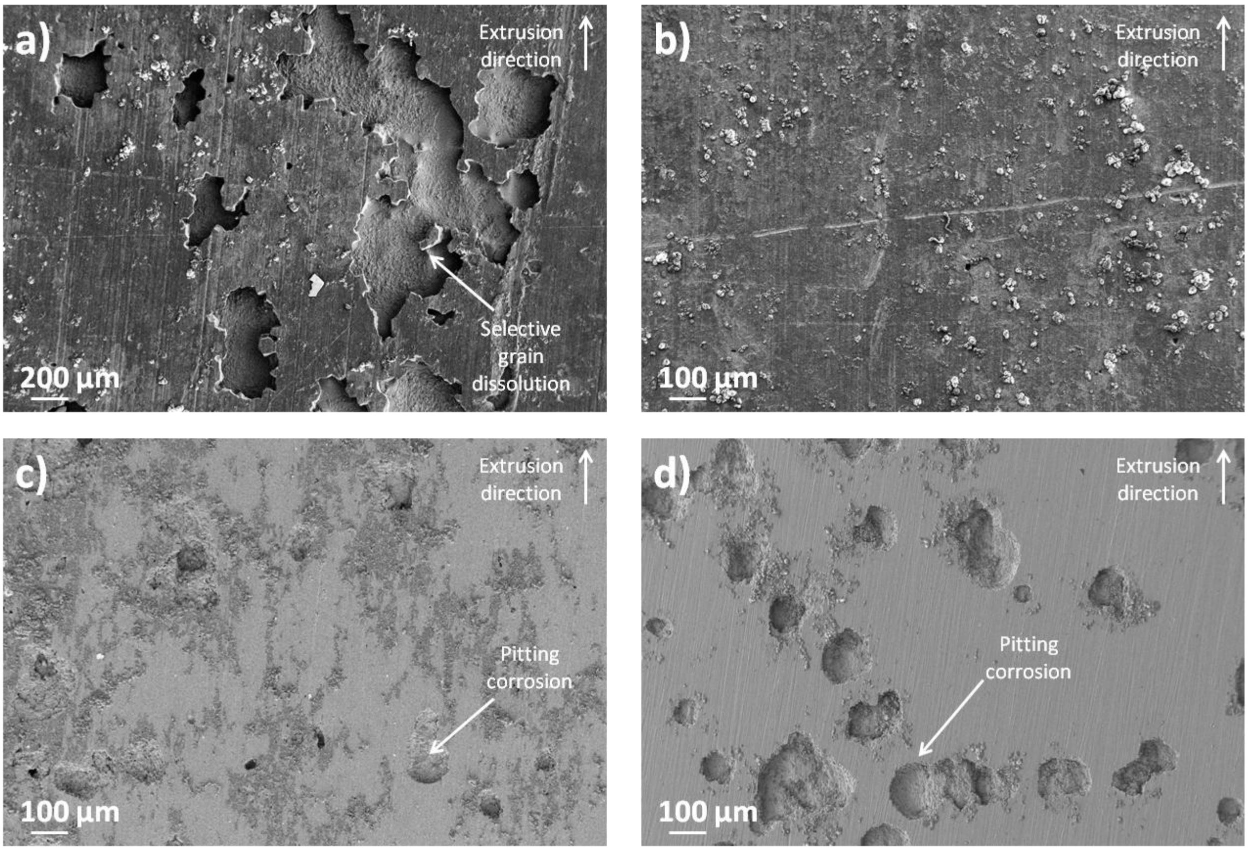

Figure 6-9: SEM micrographs following potentiodynamic polarisation in 3.5 wt.% NaCl of a) Cu2-DEG showing large scale selective grain dissolution. b) Cu2-DEG showing regions of limited corrosion. c) Cu2-MG showing lots of surface oxidation and pitting corrosion. d) Cu2-MG showing lots of spherical pitting corrosion sites.

Figure 6-10 a shows for Cu2-DEG, dissolution of the coarse grains and a region where the underlying fine grain structure is starting to be corroded, which gives the impression that the corrosion depth is substantial. Figure 6-10 b shows corrosion sites from Cu2-MG, highlighting the highly corrosive nature of Cu2 irrespective of grain size [71], [72], [74]. Figure 6-10 c reveals, sites where cathodic precipitates have caused dissolution of the Al matrix at the GB forming IGC, which is outlined by what EDS showed to be corrosion products along GBs. Figure 6-10 d shows dissolution around fine scale precipitates in Cu2-MG and it highlights where a particle on a GB has caused dissolution, which could lead to IGC propagation. Regions where multiple pits joined together were observed, highlighting their close proximity, however, the matrix was also shown to be raised. The latter is believed to be caused by the creation of corrosion products beneath the surface, increasing the level of stresses within the material which lead to a break in the surface. This gives the impression that sub-surface corrosion may be forming as this pit is small in comparison to the majority observed on Cu2-MG and Cu2-DEG. The coarse grain structure of Cu2-DEG has a reduced corrosion resistance, agreeing with literature [71], [72], [74], due to the high dissolution rate compared to the fine grain structure of Cu2-MG.

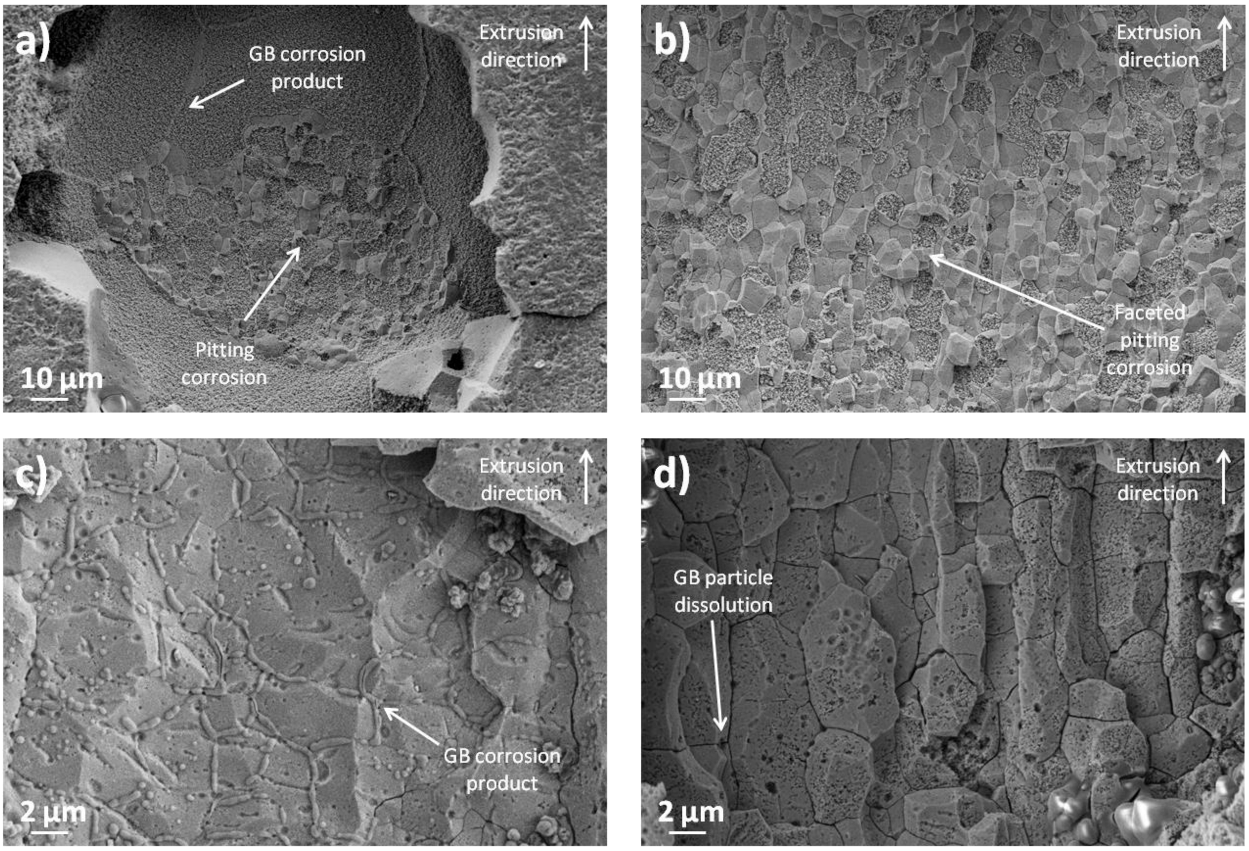

Figure 6-10: SEM micrographs of a) Cu2-DEG showing corrosion through the coarse recrystallised grain structure into the underlying fine structure. b) Cu2-MG showing selective grain dissolution. c) Cu2-DEG showing the formation of corrosion products on the GBs from cathodic reactions. d) Cu2-MG showing an IGC initiation site from a cathodic precipitate on the GB.

Figure 6-11 a and b observe the extrusion direction and Figure 6-11 c and d show the transverse direction for Cu2-DEG, with evidence of IGC and selective grain dissolution. The IGC is seen to progress down the GBs of the coarse grain structure in Figure 6-11 a and b. Once the IGC progresses past the coarse recrystallised layer, it branches out following the underlying fine grain structure. This is one of the reasons why coarse grain structures have poor corrosion resistances, especially when they are prone to IGC, as it allows a very easy path, deep into the sample, which causes sub-surface corrosion cavities to form [23], [46], [113], [115], [116]. *Luo et al.* [13], [75] showed that grains that had high levels of stored energy were susceptible to IGC, which means that grains that have high dislocation densities can be prone to IGC. FEGTEM revealed concentrations of both θ and T type phases along the GBs, which are known to promote IGC [31], [32], [114], [163]. It is also evident that selective grain dissolution is taking place, as shown in Figure 6-11 b, c and d.

Figure 6-11 b and d show selective grain dissolution taking place, where certain coarse grains are completely dissolved. The corrosion pits follow the GBs deep into the sample, confirming that this corrosion is specific to the corroding grain. Literature states that the tip of a proceeding pit is acidic, and as such, corrosion propagation will accelerate [91]. Once the corrosion reaches the underlying fine grain structure it starts to grow primarily in the lateral direction, forming shoe-like morphologies. This shows that there is something specific about those coarse grains that have been corroded, making them more anodic than their neighbours. Literature has concluded, that in Al-Cu-Li alloys, it is primarily due to the concentration of T_1 phases within the anodic grains [31], [32], [46], [113–116]. This selective grain dissolution could also be related to the amount of stored energy / dislocation density within the coarse recrystallised layer [13], [75]. IGC is the initiating stage for corrosion, with IGC dissolving the regions around the GBs, allowing for the corrosion to propagate in a very uniform manner. Observations of the surface suggest a high corrosion resistance for Cu2, however, cross-sectioning reveals that more corrosion progresses sub-surface but also that there is a high degree of IGC that cannot be identified from surface observations. For Cu2-DEG a large range in corrosion cavity sizes was recorded ranging from 20 µm to > 600 µm. The vast majority were seen to be over 100 µm and a few were over 400 µm, highlighting the very poor corrosion resistance of the coarse grain structure as a whole not just its high GB dissolution rate. With regard to corrosion depth the maximum observed was 82 µm, however, the average depth was ~ 65 µm.

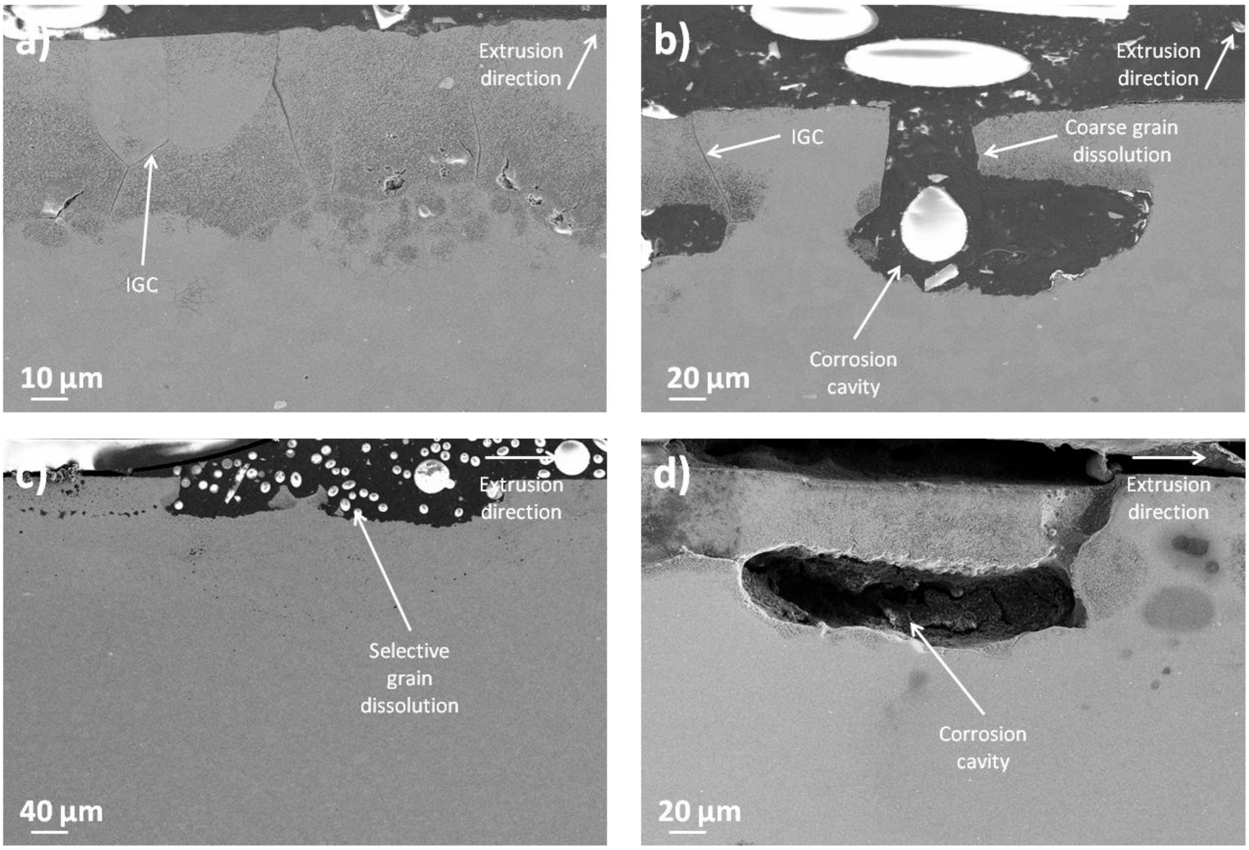

Figure 6-11: Cross-sectional SEM micrographs of Cu2-DEG after potentiodynamic polarisation in 3.5 wt.% NaCl showing a) IGC propagation and corrosion of the coarse recrystallised grain structure. b) selective dissolution of the coarse recrystallised grain structure that develops a shoe shape once it reaches the fine underlying grain structure. c) surface selective grain dissolution. d) sub-surface corrosion cavity from selective grain dissolution.

Figure 6-12 a and b observe the extrusion and transverse direction respective, of cross-sectioned Cu2-MG. On Cu2-DEG, coarse grains underwent selective grain dissolution and IGC, before branching out into the underlying fine grain structure. IGC and pitting were still observed on Cu2-MG, however, the IGC progressed further. This was also observed on Cu1 and literature, however, this may be a phenomenon related to Al-Cu alloys in general [124]. In most cases, the IGC progressed a further distance equal to the pit depth, with some pits being ~ 35 µm and the IGC being ~ 70 µm deep, as demonstrated in Figure 6-12 a. No evidence of sub-surface progression was observed on Cu2-MG, whereas Cu2-DEG showed sub-surface cavity formation. This suggests that sub-surface corrosion was associated primarily with the coarse recrystallised grain structure, showing that they are detrimental to corrosion [71], [72], [74]. The size of the pit openings ranged from 25 µm to 400 µm, which are less than that of Cu2-DEG, especially with most being ~ 100 µm. The maximum pit depth was 56 µm, but the average was 35 µm. IGC progressed further with the average depth being ~ 65 µm and the maximum being 82 µm. This shows that Cu2-MG had a higher resistance to corrosion than Cu2-DEG, however, more IGC does progress on Cu2-MG due to the finer grain structure being exposed. This therefore demonstrates that the fine grain structure of Cu2 had improved corrosion resistance than the coarse recrystallised grain structure of Cu2-DEG agreeing with literature [71], [72], [74].

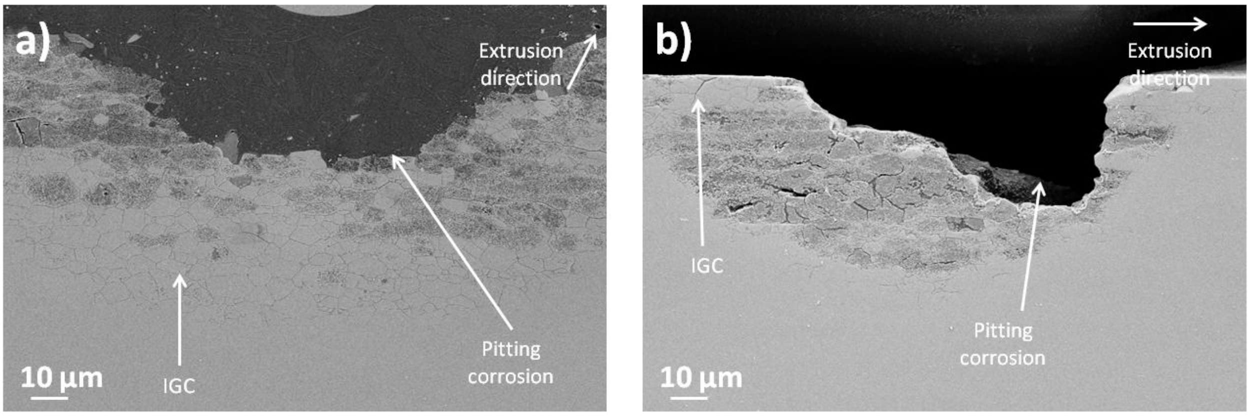

Figure 6-12: Cross-sectional SEM micrographs of Cu2-MG after potentiodynamic polarisation in 3.5 wt.% NaCl showing a) pitting corrosion and IGC. b) pitting corrosion and IGC.

It might be suggested that it is difficult to say whether Cu2-DEG or Cu2-MG presents the superior corrosion resistance, with electrochemical results being relatively similar, but a major difference in the corrosion morphologies is being observed. The presence of selective grain dissolution means that the coarse grain structure of Cu2-DEG was prone to large scale dissolution; however, IGC did not progress as deep due to the low density of GBs. This author, however, has concluded that the coarse grain structure of Cu2-DEG is more detrimental due to the much higher dissolution rate, which agrees with literature [71], [72], [74].

6.1.3 AA2099-T8E77 plate (Cu3)

Figure 6-13 shows the OCP difference between Cu3-DEG and Cu3-MG. EBSD showed that a ~ 150 µm coarse recrystallised grain structure was present on the surface of Cu3-DEG. A difference of ~ 20 mV was noted between Cu3-DEG and Cu3-MG, with Cu3-DEG being more noble with an OCP of ~ -650 mV, compared to ~ -670 mV for Cu3-MG after a 5 min immersion. Both do, however, show the same trend in that both reduced by ~ 20 mV, which is an indication of corrosion taking place [12]. Table 6-3 shows the E_{corr} of 5 specimens recorded for Cu3-DEG and Cu3-MG, indicating the average and standard deviation. It can be seen that both have similar levels of reproducibility.

When compared against the results seen for Section 5.1.3, a marginal difference is observed. On average an OCP of -670±5 mV after 5 min's was recorded, which was similar to that seen for the polarisation OCP at -672±1 mV. This shows that the OCP values obtained in this work are similar in nature to those of *Proton et al.* [115].

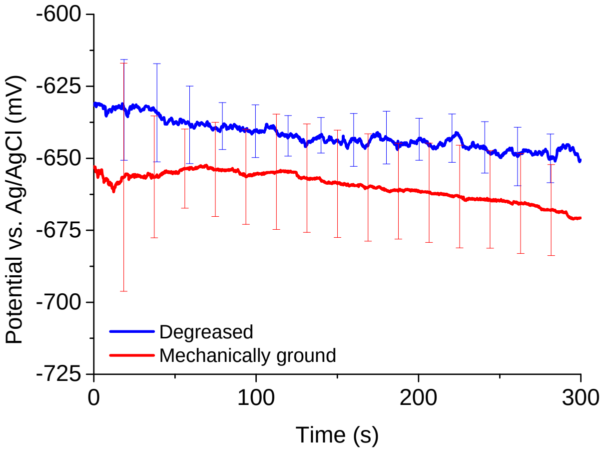

Figure 6-13: Graph showing the change in OCP of Cu3 following 5 min immersion prior to potentiodynamic polarisation in 3.5 wt.% NaCl.

Polarisation plots shown in Figure 6-14 a and b show Cu3-DEG and Cu3-MG performed in a very similar manner. Similar to both Cu1 and Cu2, no metastable pitting region was observed. Table 6-3 shows the E_{corr} and E_{pit} values taken from Figure 6-13 and Figure 6-14. The E_{pit} values, were seen to have similar differences to the E_{corr} values, with Cu3-DEG having an E_{pit} of -621±17 mV compared to -627±8 mV for Cu3-MG. This suggests that the recrystallised grains had a similar chemistry as the grain size on the outer was smaller than those in the bulk. In the bulk highly elongated grains were observed, but also smaller grains as such the number of GB was higher on Cu3-MG than Cu3-DEG.

Table 6-3: Table showing the difference in E_{pit}, E_{corr}, E_{pit} - E_{corr} and charges passed on Cu3-DEG and Cu3-MG following potentiodynamic polarisation in 3.5 wt.% NaCl.

Specimen Number	**Cu3-DEG**				**Cu3-MG**			
	E_{pit} (mV)	**E_{corr} (mV)**	**E_{pit} - E_{corr} (mV)**	**Charge (C)**	**E_{pit} (mV)**	**E_{corr} (mV)**	**E_{pit} - E_{corr} (mV)**	**Charge (C)**
1	-622	-665	43	8	-621	-672	51	12
2	-608	-643	35	10	-638	-671	33	13
3	-607	-645	38	9	-629	-672	43	10
4	-649	-661	12	13	-618	-673	55	14
5	-621	-639	18	10	-631	-673	42	12
Average	-621	-651	29	10	-627	-672	45	12
Standard deviation	17	12	13	2	8	1	9	2

E_{pit}-E_{corr} showed that Cu3-DEG had an average pitting corrosion resistance of 29±13 mV compared to 45±9 mV for Cu3-MG, suggesting that the latter had the higher pitting corrosion resistance. Examination of the different E_{pit}-E_{corr} values shows that the main reason for the difference between Cu3-DEG and Cu3-MG is the cathodic shift in the E_{corr} value of Cu3-MG. Examination of the charge passing on each of the different specimens, shows that both are very similar. Cu3-DEG showed 10±2 C passed, compared to ~ 12±2 C for Cu3-MG thus suggesting more corrosion initiated on Cu3-MG. This could be related to what *Pasang et al.* [44] showed with regards to elongated grain structures having increased susceptibility to IGC, thus demanding a higher current. But it could also be related to selective grain dissolution associated with the T type phases in Al-Cu-Li alloys and / or grain stored energy, grain mis-orientation etc. [13], [31], [32], [46], [75], [113–116]. Figure 6-14 a demonstrates that Cu3-MG had a higher demand for current and as such explains the higher charge passing. E_{pit} values are similar for both Cu3-DEG and Cu3-MG, however, due to the more noble potential of the E_{corr} for Cu3-DEG it means a higher calculated pitting corrosion resistance.

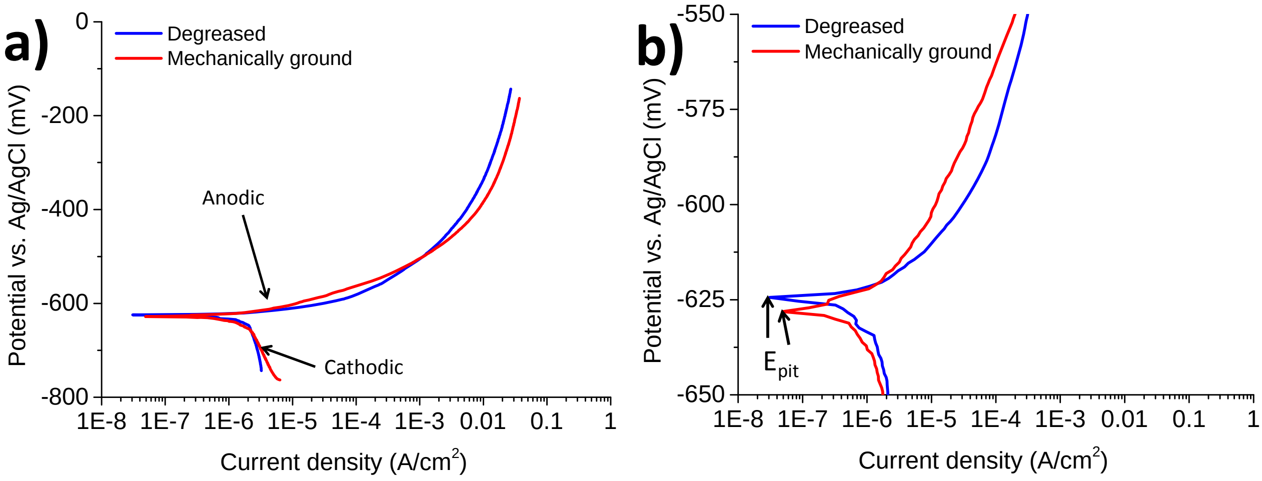

Figure 6-14 a) Graph showing the potentiodynamic polarisation response of Cu3-DEG and Cu3-MG in 3.5 wt.% NaCl. b) Graph showing an enlarged region of the potentiodynamic polarisation response of Cu3-DEG and Cu3-MG, highlighting the E_{corr} and E_{pit} regions.

Figure 6-15 a and b show micrographs of Cu3-DEG and Figure 6-15 c shows a micrograph of Cu3-MG after potentiodynamic polarisation. Figure 6-15 a and b show that the distribution of corrosion is not homogenous, with some regions showing higher levels than others. The morphology of the corrosion sites is also relatively unpredictable, with some being spherical and others being elongated. It is also evident that the size of the corrosion sites are substantial (> 100 µm), in fact Cu3-DEG showed that the vast majority were different in size, with some being ~ 200 µm wide and some > 2 mm. A variety of sizes were noted, but the vast majority were in excess of 400 µm, which suggests a very poor corrosion resistance. The concern rises from the large amount of corrosion that had taken place from a 10 C charge that had passed on Cu3-DEG. In comparison Cu3-MG shows once again substantial corrosion sites, as shown in Figure 6-15 c, but this is to be expected since the amount of charge passed was higher and the grains were larger. The presence of fine grains within Cu3-MG could also affect the corrosion resistance. Analysis of the pits on Cu3-MG showed that there was a higher density but there size, on average was a lot smaller than those observed on Cu3-DEG. They ranged from 60 µm up to a maximum of 350 µm and were primarily spherical / oval in morphology. When related to the electrochemical data, the visual results disagree with what was seen, in that Cu3-MG had the higher corrosion resistance, even though on average more charge passed during potentiodynamic polarisation. The visual results disagree with theory that a fine grain structure has a higher corrosion resistance [71], [72], [74]. However, this could be that the region examined in EBSD, showed multiple grains at the surface, whereas in reality the majority of the surface grains were coarser than those on Cu3-MG.

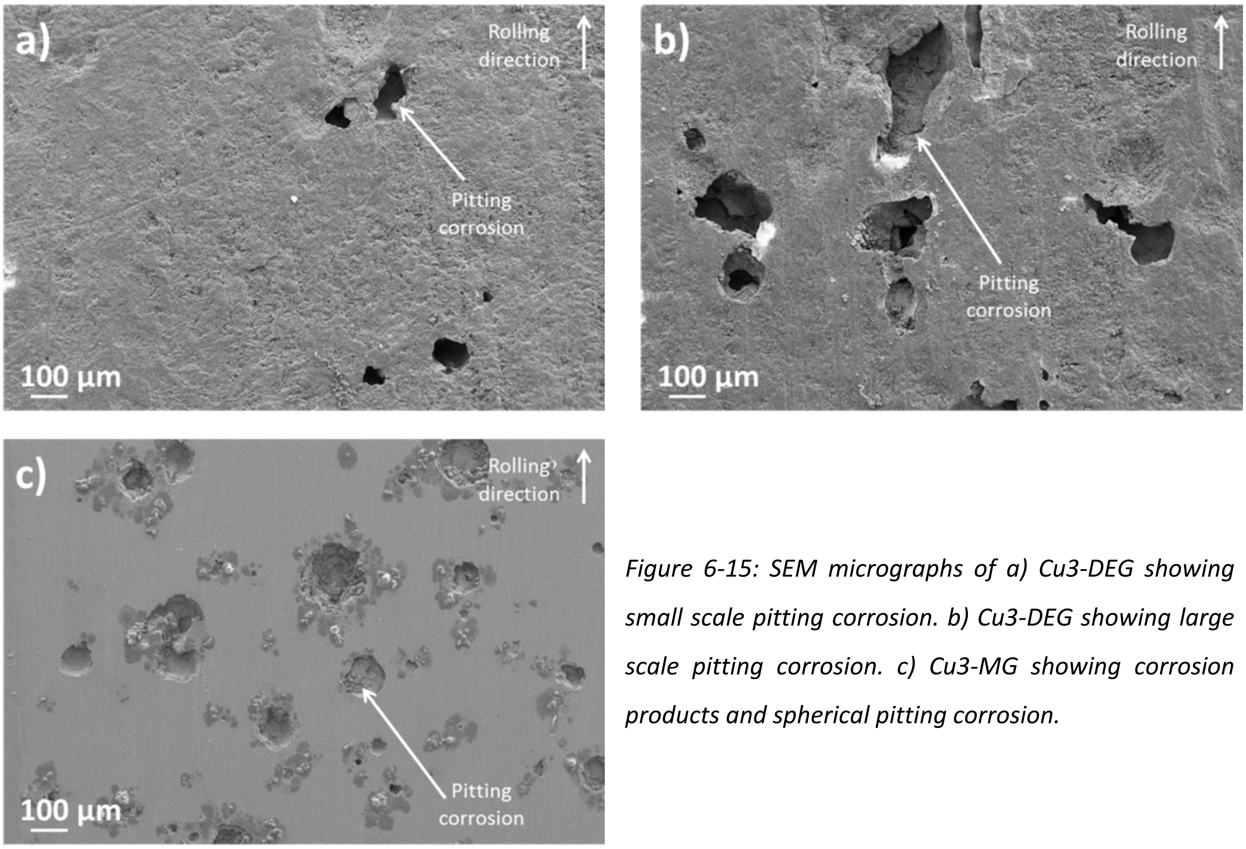

Figure 6-15: SEM micrographs of a) Cu3-DEG showing small scale pitting corrosion. b) Cu3-DEG showing large scale pitting corrosion. c) Cu3-MG showing corrosion products and spherical pitting corrosion.

Figure 6-16 a shows the size that some of the corrosion sites grew to on Cu3-DEG, suggesting selective grain dissolution. It has been noted in literature [46], [113], [115], [116] that selective grain dissolution can take place in Al-Cu-Li alloys, however, even though the corrosion sites are expansive on both Cu3-DEG and Cu3-MG, the corrosion had not shown any strong evidence of selective grain dissolution from the observations taken to this point. Closer inspection revealed that some of the corrosion was aligned with the grain structure as shown in Figure 6-16 b. This alignment wasn't just seen at low magnifications, it was also seen within the corrosion cavities themselves. Since the V_f of IMCs within Cu3-DEG is low, it suggests that most of the corrosion is being initiated by fine scale precipitates and dispersoids, like the θ type, T type and $Al_{20}Cu_2Mn_3$ phases [31], [32], [46], [113–116]. The T_1 phase had been observed in literature to be detrimental to the corrosion resistance and even support selective grain dissolution, however, literature also demonstrates that grain stored energy, grain mis-orientation etc. can be associated [31], [75], [114], [115], [162]. Figure 6-16 c shows the formation of corrosion products on the GBs, showing that Cu3-DEG and Cu3-MG are subject to both IGC and pitting corrosion, however, selective grain dissolution is only prominent on Cu3-DEG. θ type particles are present on the GBs within Cu3 and as such the presence of IGC was expected [31], [113], [114]. No evidence of surface IGC was seen on Cu3-MG, but this could be associated to the coarse grain size, limiting the frequency of GB sites.

These sites were seen to be primarily spherical in nature, which could suggest a H_2 bubble had broken out from beneath the surface during corrosion [19].

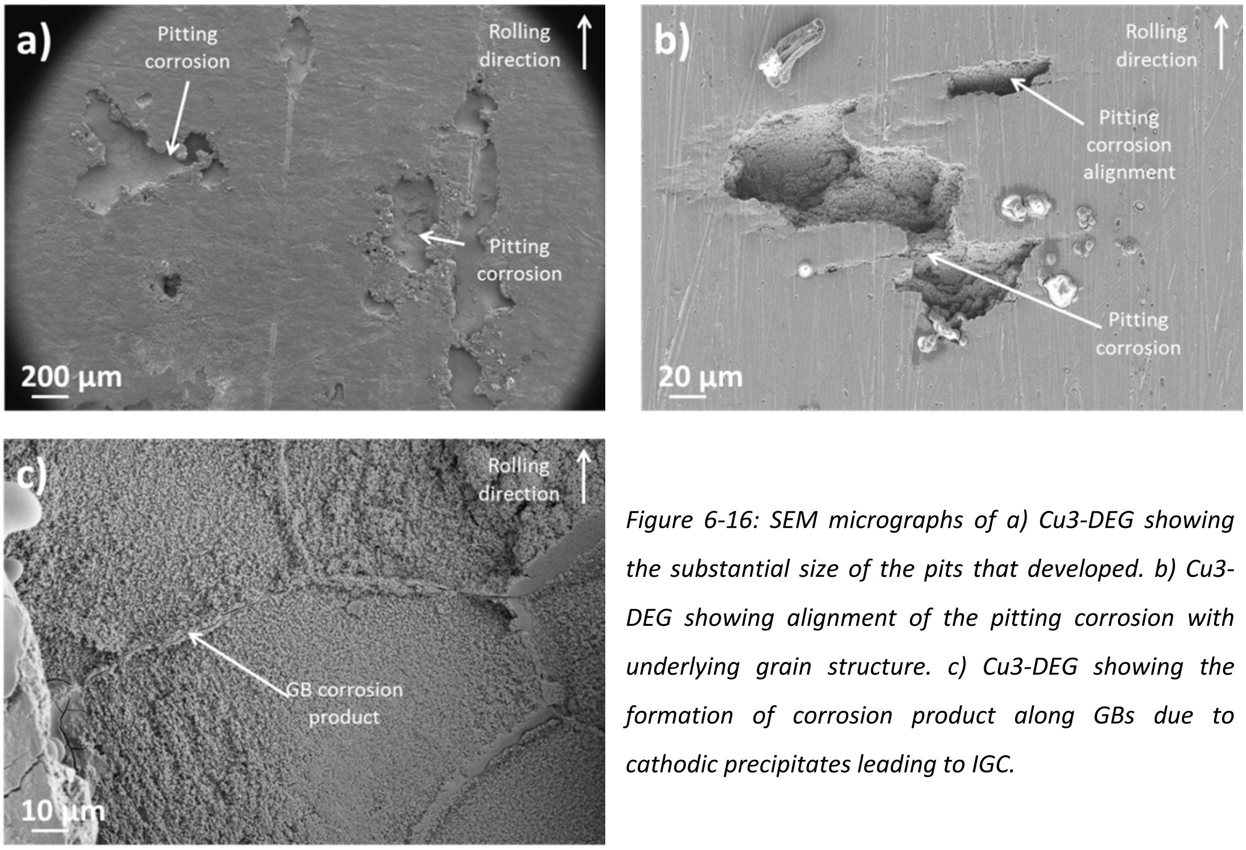

Figure 6-16: SEM micrographs of a) Cu3-DEG showing the substantial size of the pits that developed. b) Cu3-DEG showing alignment of the pitting corrosion with underlying grain structure. c) Cu3-DEG showing the formation of corrosion product along GBs due to cathodic precipitates leading to IGC.

Figure 6-17 a and b observe the extrusion direction and Figure 6-17 c and d show the transverse direction for Cu3-DEG. IGC was seen to progress down the GBs of the coarse recrystallised layer as shown in Figure 6-17 a and c. Corrosion is then observed to progress from the IGC, thus removal of the IGC could increase the corrosion resistance of Cu3-DEG. Cu2 also produced a similar phenomenon on the GB of the recrystallised layer and it was said that it was related to the amount of stored energy / dislocation density [13], [75]. *Henon et al.* [4] showed that by altering the heat treatment of an Al-Cu-Li alloy, they were able to control the susceptibility to IGC. This allowed the detrimental phases to be removed from the GBs, however, this then increases the sensitivity to pitting corrosion / selective grain dissolution [102]. IGC is present due to the θ type phases, so by altering heat treatment methods, the θ type phases could be dissolved back into solid solution. Corrosion sites ranged in size from ~ 100 µm to > 1 mm in length and progressed into the samples by ~ 80 µm, with the maximum pit depth being 87 µm. Some small surface corrosion sites were also observed that reached to ~ 20 µm depth.

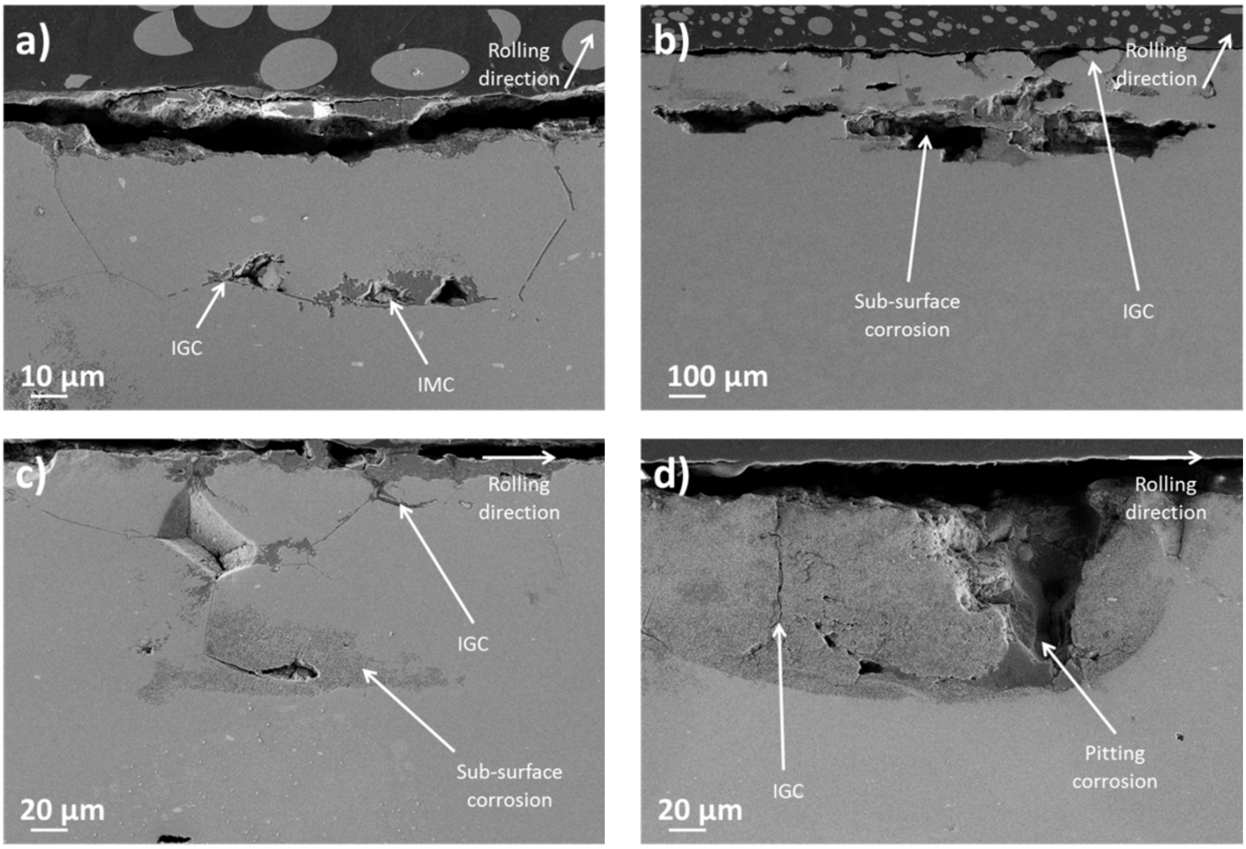

Figure 6-17: Cross-sectional SEM micrographs of Cu3-DEG after potentiodynamic polarisation in 3.5 wt.% NaCl showing a) sub-surface corrosion developing from IGC. b) extensive sub-surface corrosion sites. c) IGC and sub-surface corrosion. d) IGC and surface corrosion in the form of selective grain dissolution.

The sub-surface corrosion observed in Figure 6-17 b was 1.2 mm in length and was 230 µm beneath the surface, which shows that on Cu3-DEG sub-surface corrosion was a major concern and that any surface attack does not give a true representation of the total amount of corrosion progressing. A number of these sub-surface cavities were observed and the shallowest was 100 µm beneath the surface. This suggests a relationship between sub-surface corrosion and the coarse underlying grain structure, possibly selective grain dissolution. Overall the IGC propagated to a similar depth as the other forms of corrosion. The surface was observed to have undergone significant amounts of corrosion and even sites which appear to show no visible evidence of corrosion are likely to have undergone IGC, which subsequently develops sub-surface cavities. Since the sub-surface corrosion was more severe than that observed on the surface the question relating to whether coarse grains offer a higher or lower corrosion resistance can be answered. The cross-sectional information on Cu3-DEG show that the coarse elongated grains are being selectively dissolved sub-surface, causing a highly active and poorly corrosion resistant material, showing that coarse grains are detrimental for corrosion [71], [72], [74].

Figure 6-18 a and b show the extrusion and transverse direction respective, of Cu3-MG after cross-sectioning. Cu3-MG showed that IGC, selective grain dissolution and pitting corrosion was observed. The pits that form on Cu3-MG are subject to selective grain dissolution [31], [32], [46], [113–116], which gives the impression that the grains beneath the recrystallised layer have large amounts of stored energy / dislocation density [13], [75]. This had been characterised by the corrosion morphology, with dissolution of entire grains before progressing into other areas and can be seen in Figure 6-18 a and b. It is also likely that IGC will be forming on the GBs, which is why the outlined grains undergoing selective grain dissolution are so defined. The size of the pits were smaller than those on Cu3-DEG but were more frequent. The largest pit was 230 µm wide and 40 µm deep, however, the pits progressed on average to a depth of 35 µm, with the deepest pit reaching 96 µm. Sub-surface corrosion was observed on Cu3-MG as shown in Figure 6-18 b, which demonstrates that it was not a feature associated with the recrystallised layer. Both Cu2 and Cu3 have, however, shown that the larger the grain structure the lower the corrosion resistance [71], [72], [74].

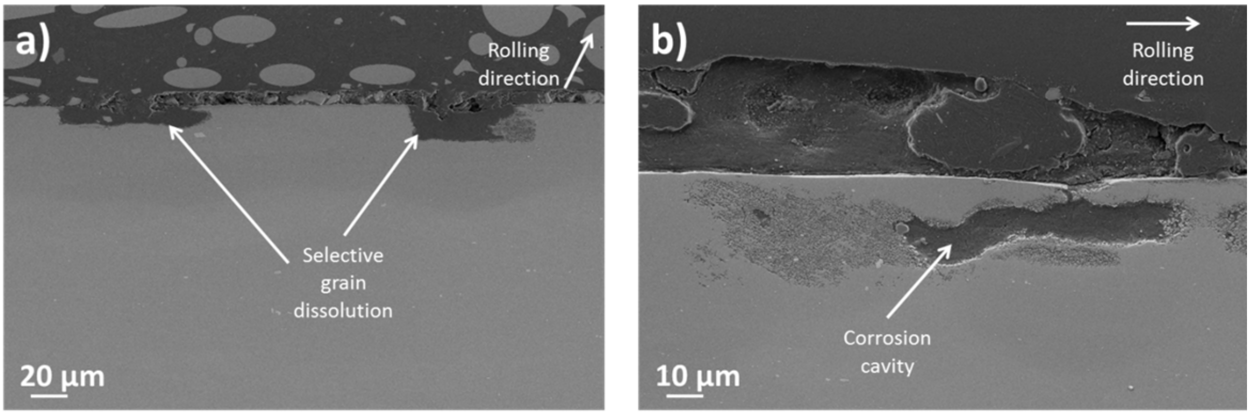

Figure 6-18: Cross-sectional SEM micrographs of Cu3-MG after potentiodynamic polarisation in 3.5 wt.% NaCl showing a) selective grain dissolution on the surface. b) sub-surface corrosion, likely in the form of selective grain dissolution.

6.1.4 Comparison of Al-Cu vs. Al-Cu-Li

Even though Cu1 is the only non-Li containing Al-Cu alloy there should be a lot of similarities between each of the Al-Cu alloys examined. IMCs and precipitates were shown to be of similar chemistry and since they were all within Al-Cu base alloys inherit some of the common issues associated with Al-Cu alloys. These include susceptibility to corrosion, especially IGC due to the cathodic nature of Cu compared to Al [30–32]. The main differences that arise are related to the alloying additions with the Al-Cu-Li being absent of Mg and containing a lower Cu content compared to Cu1. The reduction in Cu content can improve corrosion resistance as there is likely to be less Cu rich phases and SEM analysis revealed a lower V_f of IMCs and precipitates within Cu2 and Cu3 compared to Cu1. In Cu1, the main problematic phase was the Al-Cu-Mg IMCs, which shows that Mg in Al-Cu systems promotes detrimental phase evolution [17], [18], [26], [35], [60–64], [80], [84]. S phase precipitates were not identified in this thesis, but a number of authors have shown that it was more detrimental than the θ type phase as it is more noble [30–32]. Since Mg is less noble than Al it acts as an anode and thus selectively dissolves in preference to the Al. Li, is also less noble than Al and thus the large V_f of T type phases within Cu2 and Cu3 can have a similar impact to the S phase, however, literature has shown that the T_1 phase can develop selective grain dissolution [31], [32], [46], [113–116].

Cu1 had a very fine grain structure, whereas Cu3 had a very coarse grain structure. Cu2 had a fine grain structure beneath a coarse recrystallised region, which meant a detailed examination of the impact of grain size on corrosion could take place. The θ type phase was seen to be present on the GBs in all of the Al-Cu alloys, showing they could all develop IGC. The T type phase was seen in both Cu2 and Cu3 to be uniformly distributed within the matrix, but Cu2 also showed T type phases at the GBs, suggesting Cu2 had increased sensitivity to IGC.

Figure 6-19 shows the comparison in OCP for the Al-Cu alloys, for which it can be seen that Cu1 in general was more noble than both of the Al-Cu-Li alloys, suggesting that the Al-Cu-Li alloys had the higher corrosion resistance, which goes against what literature believes [2], [4], [44], [48]. Table 6-4 shows the change in OCP over the 5 min immersion period prior to polarisation, as well as the E_{pit}, E_{corr}, E_{pit}-E_{corr} and charges for each of the Cu1, Cu2 and Cu3 alloys in the DEG and MG conditions. The trend for Cu1 was different to Cu2 and Cu3, with passivation taking place, whereas the Al-Cu-Li alloys showed a reduction, which suggests corrosion taking place. This increase was not unexpected for Cu1, due to the large amount of corrosion product being formed from the galvanic cells generated around IMCs. However, on Cu2 and Cu3 the reduced V_f of IMCs meant that no significant amounts of corrosion product formed. Comparison with Section 5.1 showed that the results were similar and also a number of results correlated well with literature [26], [115], [160], [161].

Table 6-4: Comparison of the changes in OCP, E_{pit}, E_{corr}, E_{pit}-E_{corr}, charge and average pit depth for Cu1, Cu2 and Cu3 in the DEG and MG condition.

	Cu1-DEG	**Cu1-MG**	**Cu2-DEG**	**Cu2-MG**	**Cu3-DEG**	**Cu3-MG**
OCP after 5 min's (mV)	-592±2	-614±7	-635±5	-644±7	-651±12	-672±1
E_{pit} (mV)	-582±5	-587±6	-621±3	-612±2	-621±17	-627±8
E_{corr} (mV)	-592±2	-614±7	-635±5	-644±7	-651±12	-672±1
E_{pit}-E_{corr} (mV)	10±3	27±3	14±4	33±6	29±13	45±9
Charge (C)	21±2	21±2	24±1	16±3	10±2	12±2
Average pit depth (µm)	40	40	65	35	80	35

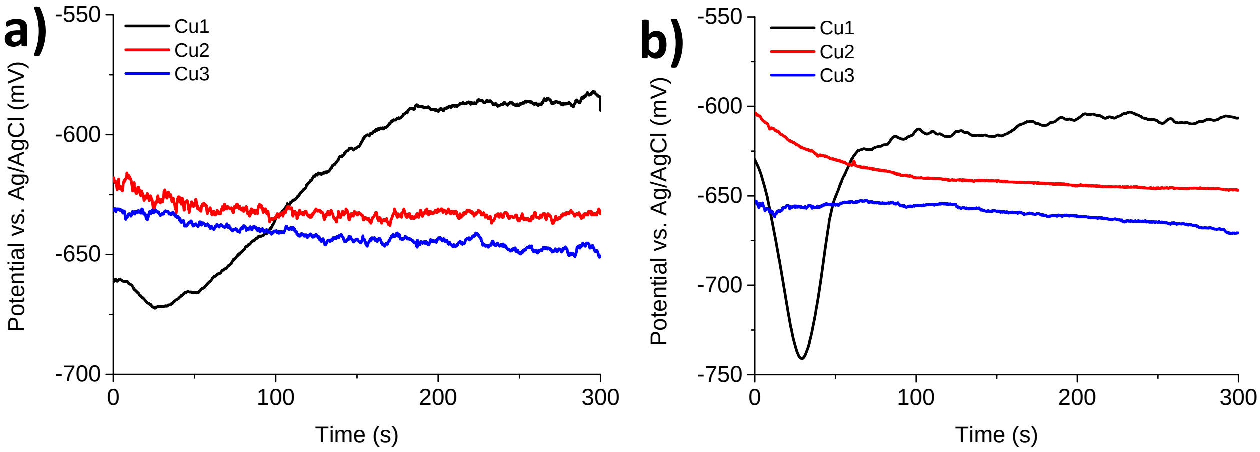

Figure 6-19: Graphs showing the comparison of Cu1, Cu2 and Cu3, over the 5 min of immersion prior to potentiodynamic polarisation in 3.5 wt.% NaCl in the a) DEG and b) MG surface condition.

The values shown in Table 6-4 demonstrates that Cu1 had a more noble E_{pit} than either of the Al-Cu-Li systems. This is, however, not unexpected due to the higher V_f of cathodic phases within Cu1 causing the higher nobility of the E_{corr} and E_{pit} values [12], [30–32]. This does not, however, mean that the Al-Cu-Li alloys have a higher corrosion resistance, as E_{pit} / E_{corr} alone cannot tell the user whether corrosion is initiating / propagating [12], [156–158]. It is notable that the data for Cu1 and Cu2 is similar, suggesting a high level of reproducibility in fine grain specimens. No metastable pitting regions were observed on any of the Al-Cu alloys as shown in Figure 6-20, however, this is characteristic of Al-Cu alloys [28]. There was a marginal difference in E_{pit} between DEG and MG specimens on all of the Al-Cu alloys, suggesting grain size has limited impact on E_{pit}. Figure 6-21 shows the difference in E_{pit} for Cu1, Cu2 and Cu3 in the DEG and MG condition, highlighting changes associated with grain size and Li additions.

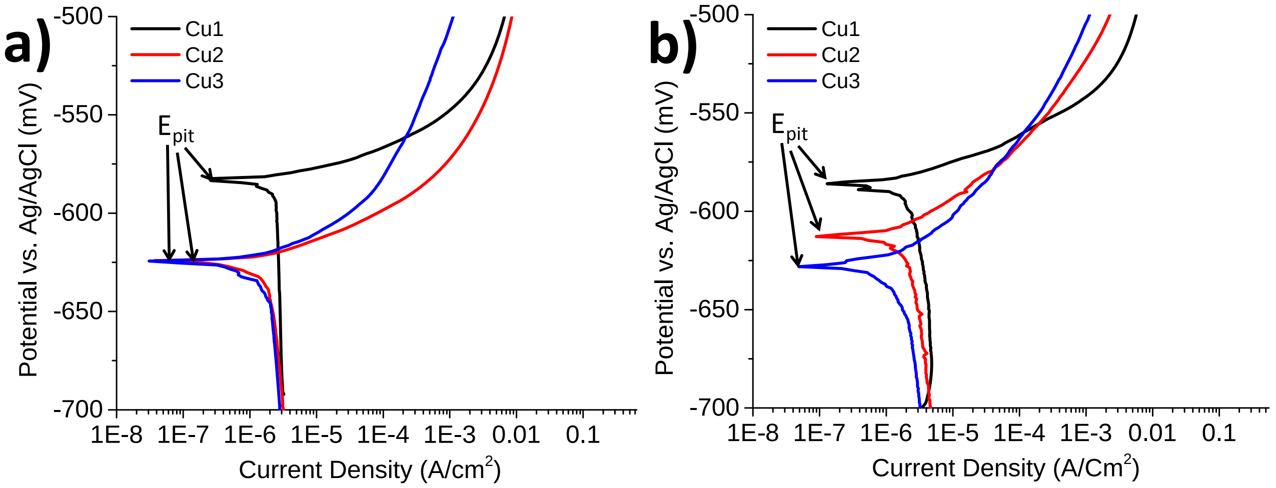

Figure 6-20: Graphs showing the comparison of the potentiodynamic polarisation response for Cu1, Cu2 and Cu3, after a 5 min of immersion in 3.5 wt.% NaCl in the a) DEG and b) MG surface condition.

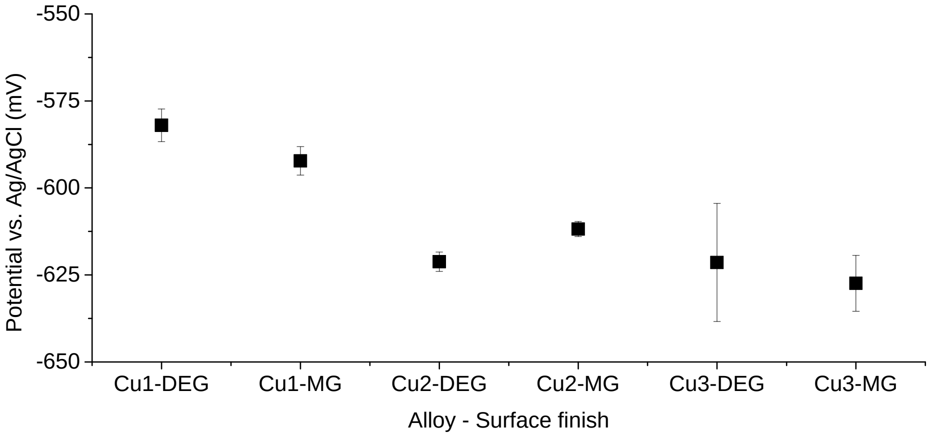

Figure 6-21: Graph showing the comparison of the difference in E_{pit} values for Cu1, Cu2 and Cu3, in the DEG and MG surface condition following potentiodynamic polarisation in 3.5 wt.% NaCl.

Table 6-4 shows that Cu1-MG had a higher E_{pit}-E_{corr} value than Cu1-DEG, suggesting a higher pitting corrosion resistance for a fine grain structure, agreeing with literature [71], [72], [74]. This follows the same trend as the Al-Cu-Li alloys in that the MG specimens showed the higher E_{pit}-E_{corr} values, once again suggesting a higher pitting corrosion resistance of finer grain structures, as shown in Figure 6-22. The exception was Cu3, in that Cu3-MG had a more elongated and larger grain size to Cu3-DEG. Al-Cu-Li are noted in literature to have a poor corrosion resistance [2], [4], [44], [48], however, this thesis had shown that the E_{pit}-E_{corr} values of the Al-Cu-Li alloys are higher than the Al-Cu system (see Table 6-4), suggesting an improved pitting corrosion resistance.

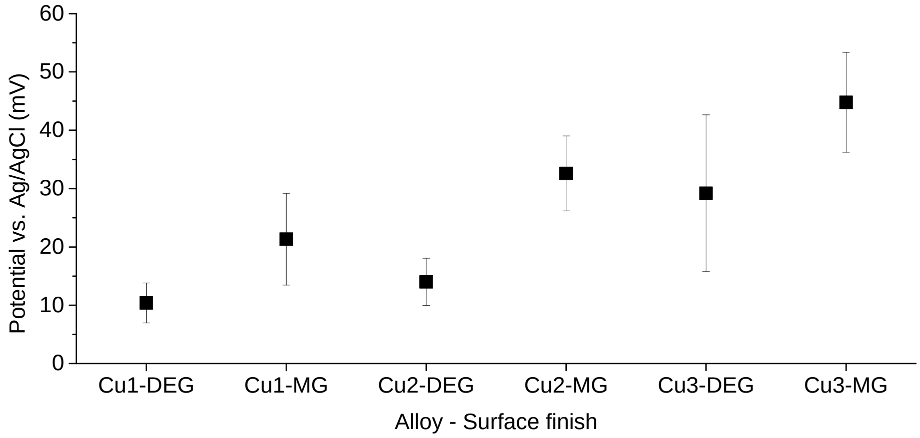

Figure 6-22: Graph showing the comparison of E_{pit}-E_{corr} values for Cu1, Cu2 and Cu3, in the DEG and MG surface condition following potentiodynamic polarisation in 3.5 wt.% NaCl.

Examination of the charge also shows that Cu1 had some of the highest charges passing; whereas Cu3 showed the lowest charges (see Table 6-4). The comparison of charges passed on the Al-Cu alloys can be seen in Figure 6-23, which demonstrates that the Al-Cu-Li systems were similar if not more improved than the Al-Cu alloy with regards to corrosion resistance which tends to disagree with literature [2], [4], [44], [48]. The high level of charge on Cu1 and Cu2 could be associated with the high V_f of cathodic phases on the GBs, creating a demand for current.

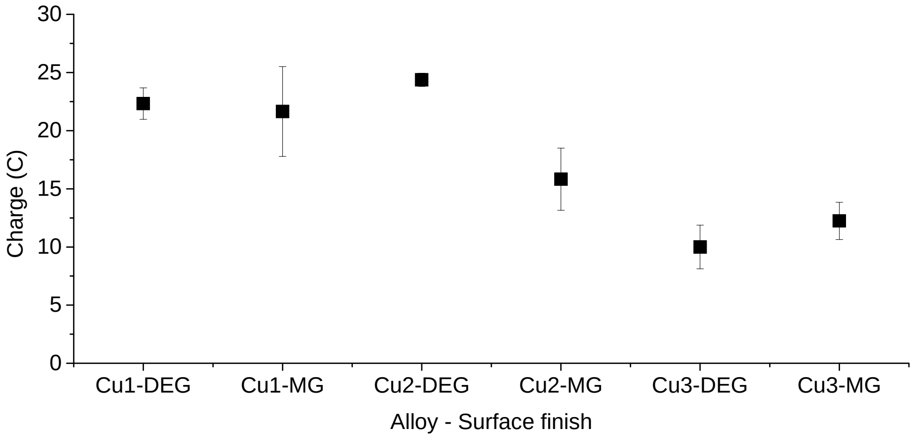

Figure 6-23: Graph showing the comparison of the amount of charge passed on Cu1, Cu2 and Cu3, in the DEG and MG surface condition following potentiodynamic polarisation in 3.5 wt.% NaCl.

When compared against one another there is limited evidence supporting whether grain size has a positive or negative impact on corrosion resistance. E_{pit} was not affected by grain size and the E_{corr} was seen to be less noble for the fine grain sized samples. For E_{pit}-E_{corr} values which are good indications of pitting corrosion resistance, all Al-Cu alloys showed that the fine grain size offered an increased difference [71], [72], [74]. However, only Cu2 showed a significant change in charge when the coarse recrystallised grain structure was removed, whereas Cu1 and Cu3 stayed at similar values.

IGC and pitting corrosion were seen on all of the Al-Cu alloys. It can be theorised that selective grain dissolution took place on Cu1, however, due to the fine grain size it meant that the overall impact of this phenomenon was reduced in comparison to the Al-Cu-Li alloys. The selective grain dissolution on Cu2 and Cu3 was associated with the highly anodic T type phases, causing changes to individual grain potentials, thus ensuring that a galvanic cell was created, leading to the preferential dissolution of the grains with higher Li concentrations [75], [115]. This author also believes that stored energy / dislocation density has a role to play in the selective nature of the corrosion. This is because all of the grains contain T type phases, therefore there must be an additional feature causing the selective grain dissolution [13], [75]. The IGC was also seen to be associated with the T and θ type phases in the Al-Cu-Li alloys and just the θ type phases in Cu1. Cu1 developed a high volume of 100 µm wide pits, whereas on Cu2 and Cu3, most of the corrosion developed sub-surface, which in some cases progressed over 1 mm in length. The surface pits were also seen to be much bigger than those on Cu1, with most being in excess of 100 µm and some > 500 µm.

All of the DEG, Al-Cu-Li specimens showed very large pits and selective grain dissolution forming in low quantities in comparison to the MG specimens, showing that the recrystallised grains had a reduced corrosion resistance, which agrees with the E_{pit}-E_{corr} predictions. The recrystallised grains of the Al-Cu-Li alloys had a heightened sensitivity to IGC, with cross-sectioning revealing that IGC led to sub-surface cavity formation. This sub-surface corrosion was seen on the MG specimens also, but it was on a smaller scale. Some of the cavities observed on Cu3-DEG were > 1.2 mm in length and were over 200 µm beneath the surface as shown in Figure 6-17 b, showing that the coarse grains had a reduced corrosion resistance.

Cross-sectioning showed that IGC progressed further into the specimens than pitting corrosion. *Knight et al.* [124] examined an AA2024 alloy and showed that IGC progresses further than pitting corrosion also. Table 6-4 shows that the maximum pit depths were deeper on Cu2 and Cu3 than Cu1 in the DEG condition, however, in the MG condition Cu1 showed the deepest pits forming. The issue with Cu1, was that some pits would be seen at ~ 10 µm in depth, but an adjacent pit would be 60 µm deep and as such care must be taken in concluding these findings. The combination of sub-surface cavities on Cu2 and Cu3, suggests that the Li containing Al-Cu alloys were more susceptible to corrosion, thus agreeing with some authors [2], [4], [44], [48] but disagreeing with others [3], [5]. Both Cu2 and Cu3 showed evidence of shoe-like corrosion taking place, where the surface recrystallised grains were selectively dissolved and the resulting corrosion site once it reached the underlying grain structure progressed in a lateral direction, an example of which can be seen in Figure 6-11 b and d.

The conclusion is that Al-Cu-Li alloys show increased E_{pit}-E_{corr} values, but visual inspection shows they develop higher amounts of corrosion, primarily though sub-surface cavity formation and selective grain dissolution. As such it can be said that Li additions appear to reduce the corrosion resistance of Al-Cu alloys and that grain size does not appear to have as big an impact on corrosion as literature suggests [71], [72], [74].

6.2 Potentiodynamic polarisation of Al-Mg alloys

6.2.1 AA5083-T3510 (Mg1)

Figure 6-24 shows the difference between Mg1-DEG and Mg1-MG over a 5 min immersion prior to potentiodynamic polarisation. EBSD of Mg1-DEG revealed a 200 µm deep recrystallised elongated grain layer, whereas for Mg1-MG this layer was removed and a less coarse grain structure was examined. A difference of ~ 140 mV was noted between Mg1-DEG and Mg1-MG, with Mg1-DEG being more noble with an OCP of ~ -680±18 mV compared to ~ -816±8 mV for Mg1-MG after the same time period. Both show different OCP trends, with Mg1-DEG showing a reduction in OCP with immersion time, compared to an increase in OCP for Mg1-MG and as such appear to be tending towards one another. *Aballe et al.* [80] examined AA5083 and showed that over prolonged immersion, the OCP converged to ~ -740 mV vs. SCE. Passivation is not unexpected for Al-Mg alloys due to Mg being less noble than Al, thus the Al undergoes a reduction reaction (cathode), whilst the Mg oxidises (anode) [19].

When compared against the results seen from Section 5.2.1, a difference is also observed. Since the immersion testing results examined MG specimens only, this is all that can be discussed. On average the OCP after 5 min's of immersion was -723±27 mV, which is ~ 90 mV more noble than that recorded for the polarisation OCP. This 90 mV difference was not a concern, as the trend of all the specimens examined in Section 5.2.1 was that they all tended towards a potential of -720 mV. *Aballe et al.* [70], [80], [98] and *Moore et al.* [28], [93] also showed that AA5083 had a high degree of fluctuation in its E_{corr} value, however, its E_{pit} was seen to be relatively constant. *Moore et al.* [28], [93] examined superplastic AA5083 that was supplied in the as-rolled condition, thus the microstructure of the material would be different to Mg1. The surface preparation of *Moore et al.* [28], [93] samples were mechanically polished to 800 grit SiC, compared to 1200 grit of this work and *Aballe et al.* [98] showed that the degree of polishing influences the OCP of Al alloys.

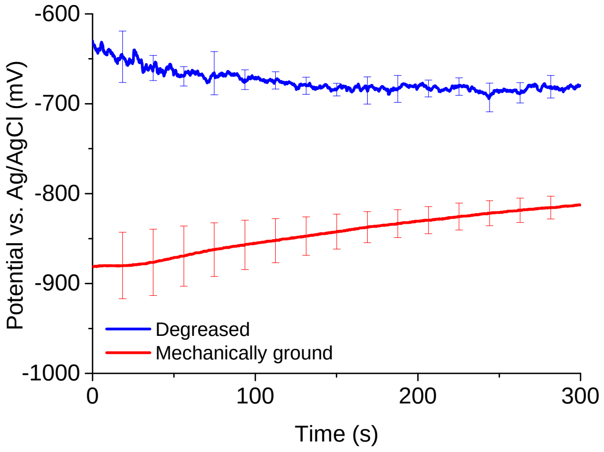

Figure 6-24: Graph showing the change in OCP of Mg1 following 5 min immersion prior to potentiodynamic polarisation in 3.5 wt.% NaCl.

Table 6-5 shows the E_{corr}, E_{pit}, E_{pit}-E_{corr} and charge passed from 5 specimens of Mg1, indicating the average and standard deviation. Literature states that the more noble the E_{pit} in 5XXX series Al alloys the higher the corrosion resistance [12], [156–158]. Figure 6-25 a and b show the potentiodynamic polarisation response of Mg1-DEG and Mg1-MG and that they performed in a different manner. A 30 mV difference in E_{pit} was observed, with Mg1-DEG specimens having a more noble E_{pit} of -655±10 mV compared to -685±5 mV of Mg1-MG. *Moore et al.* [28], [93] showed that AA5083 had an E_{pit} of ~ -711 mV vs. Ag/AgCl which shows a difference of ~ 25 mV between the results in this thesis and those examined by *Moore et al.* [28], [93]. The results in this work are, however, comparable to those in literature. *Aballe et al.* [80], showed an average E_{pit} of ~ -675 mV vs. Ag/AgCl and as such shows a higher association with those results in this thesis to those by *Moore et al.* [28], [93].

Table 6-5: Table showing the difference in E_{pit}, E_{corr}, E_{pit} - E_{corr} and charges passed on Mg1-DEG and Mg1-MG following potentiodynamic polarisation in 3.5 wt.% NaCl.

Specimen Number	**Mg1-DEG**				**Mg1-MG**			
	E_{pit} (mV)	**E_{corr} (mV)**	**E_{pit} - E_{corr} (mV)**	**Charge (C)**	**E_{pit} (mV)**	**E_{corr} (mV)**	**E_{pit} - E_{corr} (mV)**	**Charge (C)**
1	-662	-673	11	24	-679	-819	140	10
2	-668	-710	42	15	-681	-809	128	15
3	-648	-681	33	20	-690	-815	125	18
4	-655	-669	14	21	-689	-812	123	17
5	-644	-666	22	18	-684	-829	145	10
Average	-655	-680	24	19	-685	-816	132	14
Standard deviation	10	18	13	4	5	8	10	4

Using E_{pit}-E_{corr} it can be seen that Mg1-DEG had an average pitting corrosion resistance of 24±13 mV compared to 132±10 mV for the Mg1-MG specimens, suggesting the latter had the higher corrosion resistance. This confirms that E_{pit} alone cannot accurately predict the corrosion resistance [12], [156–158]. *Moore et al.* [28], [93] showed E_{pit}-E_{corr} for AA5083 was ~ 80 mV, however, there was a difference in the E_{pit} values obtained in their work. Mg1-MG showed metastable pitting corrosion, whilst Mg1-DEG did not. Mg1-DEG showed a profile similar to those that are characteristic of Al-Cu alloys in that the E_{pit}

and E_{corr} are of a similar potential [28]. The polarisation curves seen in this thesis also relate well to literature [28], [70], [80], [93], [98]. Both Mg1 samples had similar charges, with Mg1-DEG passing 19±4 C compared to 14±4 C for Mg1-MG. Overall the electrochemical data suggests that Mg1-MG had the higher corrosion resistance.

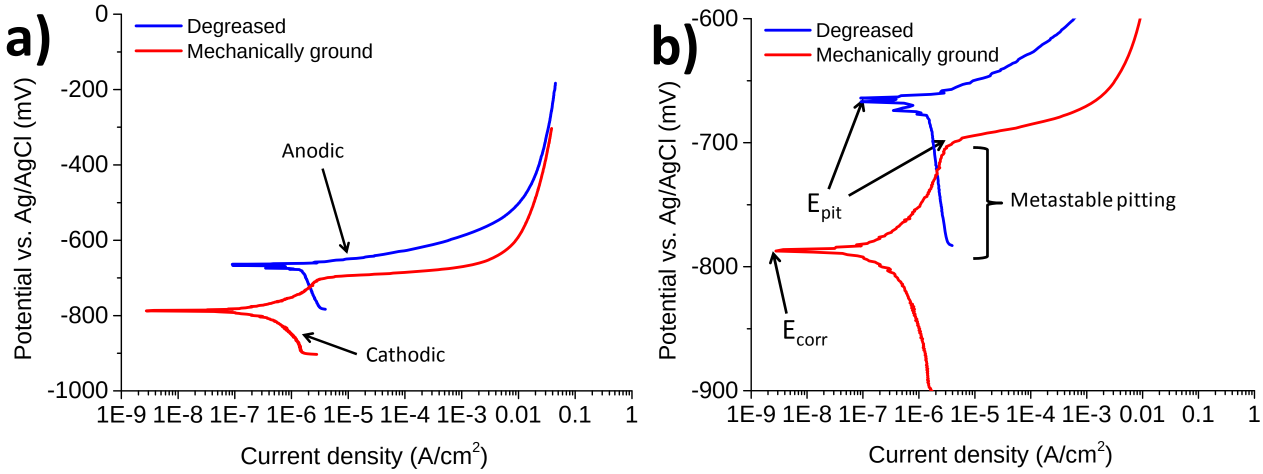

Figure 6-25 a) Graph showing the potentiodynamic polarisation response of Mg1-DEG and Mg1-MG in 3.5 wt.% NaCl. b) Graph showing an enlarged region of the potentiodynamic polarisation response of Mg1-DEG and Mg1-MG in 3.5 wt.% NaCl, highlighting the E_{corr} and E_{pit} regions.

Figure 6-26 a and b show micrographs of Mg1-DEG and Mg1-MG respective after potentiodynamic polarisation. Figure 6-26 a shows a large V_f of pitting corrosion develops and in particular it is linear in morphology. This is not unexpected since Mg1 was extruded, thus should show elongated grains. Linear pitting corrosion did not take place across the entire sample surface, with localised pitting sites also being observed. Figure 6-26 a shows that the width of the pitting corrosion was ~ 100 µm and there are few sites that are in excess of this. It can, however, be seen that most are longer, some being mm's in length. It is, however, understood that the reason for the continuous nature of the pitting corrosion is associated with numerous pitting corrosion sites joining together. Mg1-DEG has also shown a correlation between grain orientation and corrosion. In contrast the pits on Mg1-MG appear shallower. Comparison of the electrochemical and visual results, suggests that Mg1-MG had the higher corrosion resistance. Even though larger areas have been corroded on Mg1-MG, the progression of the corrosion is reduced compared to Mg1-DEG.

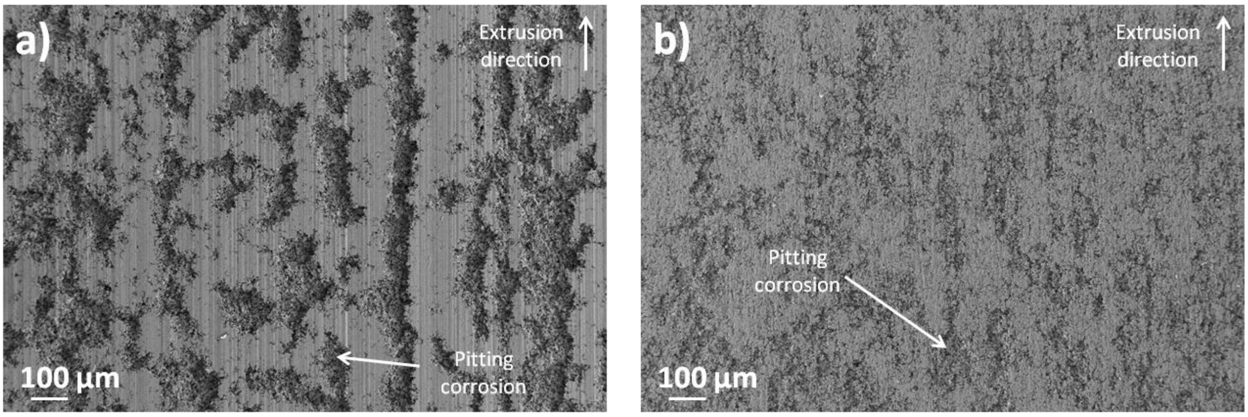

Figure 6-26: SEM micrographs following potentiodynamic polarisation in 3.5 wt.% NaCl of a) Mg1-DEG showing linear pitting corrosion. b) Mg1-MG showing uniform pitting corrosion.

Mg1-DEG and Mg1-MG developed faceted pitting corrosion, as shown in Figure 6-27 a, b and c, showing that there was no change in the corrosion morphology between the surface conditions. A number of authors [28], [60], [70], [80], [86], [93] have also observed faceted pitting corrosion behaviour on AA5083. Figure 6-27 a shows a fine scale faceted pitting corrosion network, from which growth of surface oxidation had formed. This also highlights the branching nature of the faceted pitting corrosion on Mg1, as it can be seen that pitting corrosion filaments start to join to other pitting corrosion sites. These filament structures could be as *Moore et al.* [93] described as 'tunnelling'. They were described as narrow, one-dimensional, square features that are formed when pits re-passivate. The reason they develop is to maintain the anodic reaction and, as such, develop thin pitting corrosion sites.

Figure 6-27 b shows a pitting corrosion site from an Mg1-DEG specimen, showing faceted corrosion filaments around the edges of the pit itself. This reinforces the theory that these pits eventually grow and join with surrounding pits. Figure 6-27 c shows faceted pitting corrosion from Mg1-MG, which was uniform in depth over the surface, however, some localised pits were also observed. Figure 6-27 d shows evidence of galvanic corrosion taking place around cathodic Fe and Mn rich IMCs [26], [35], [39], [60], [63]. These sites are the main initiation points for pitting corrosion. This agrees with what had been observed on Mg1-MG with corrosion taking place all over the specimen surface but not progressing far in depth, which is related to the sacrificial nature of the Mg.

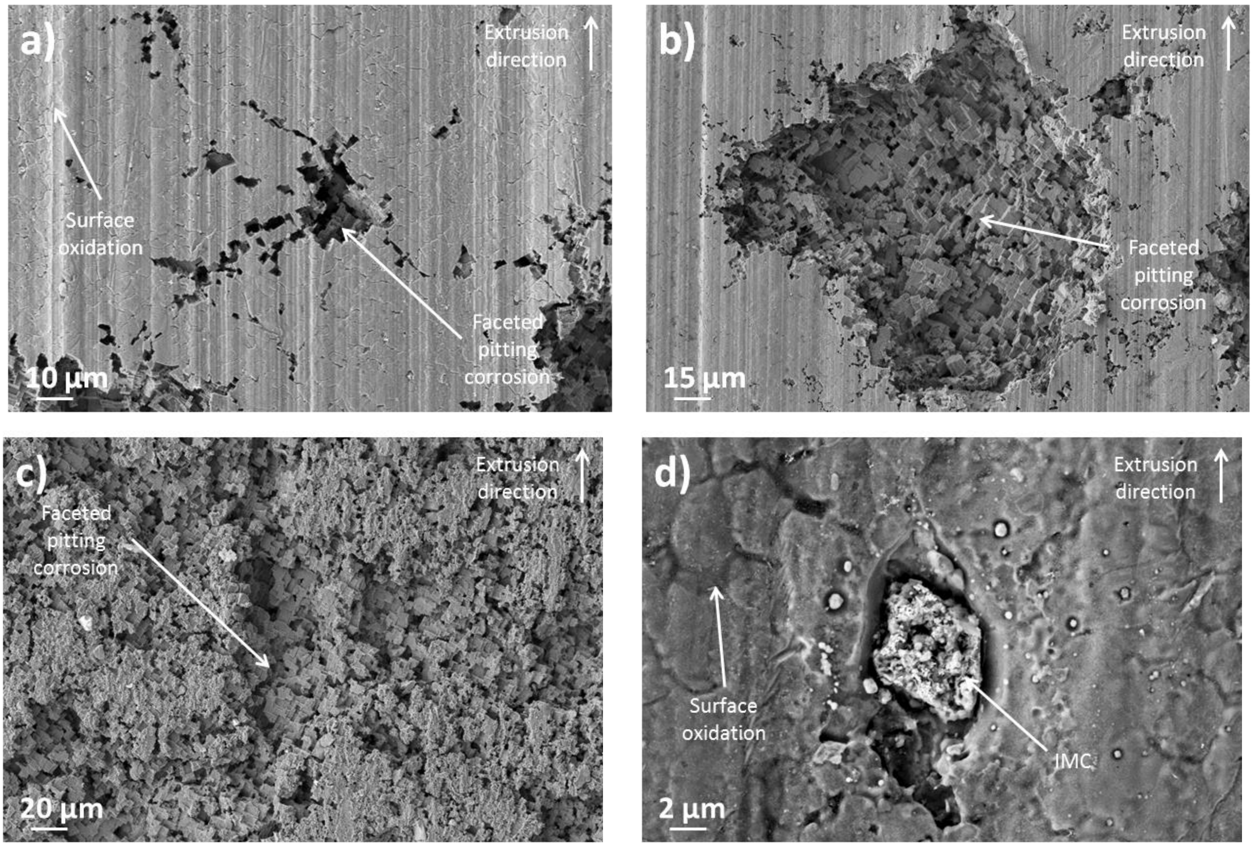

Figure 6-27: SEM micrographs of a) Mg1-DEG showing faceted pitting corrosion filaments. b) Mg1-DEG showing faceted pitting corrosion. c) Mg1-MG showing faceted pitting corrosion across the entire surface, with isolated pit sites. d) Mg1-MG showing evidence of surface oxidation and galvanic corrosion around Fe and Mn rich IMCs.

Figure 6-28 a and b observe the extrusion and transverse directions respectively, for cross-sectioned Mg1-DEG. Each shows evidence of faceted pitting corrosion taking place over a range of depths; however, there was no difference in corrosion depth between the extrusion and transverse direction. There was, however, a large difference in the size of the pits themselves, related to the size of the grain structure. The average pit depth was ~ 40 µm, but none were seen to be greater than 50 µm. The width of the pits was seen to fluctuate, but this was linked with numerous pits joining together. The smallest pit width was ~ 30 µm, but some were seen to be in excess of 300 µm, which was 3 individual pit sites joined together. On average, the vast majority of the pit sites were between 50 and 80 µm in width. Figure 6-28 a shows the typical cross-section of Mg1-DEG, with numerous pitting corrosion sites being seen to be isolated from one another. However, as shown previously some of the pits formed close to one another and eventually merged into larger, singular corrosion sites. Figure 6-28 b shows evidence of faceted pitting corrosion progressing around the side of a IMCs, which EDS showed to be Fe and Mn rich. Figure 6-28 b also shows the formation of a crystalline corrosion product, around the edge of the pitting corrosion site.

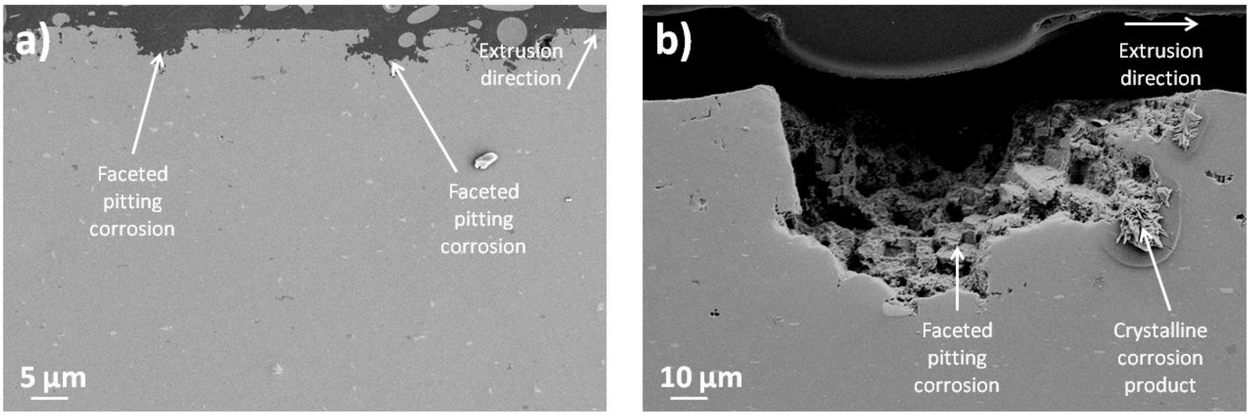

Figure 6-28: Cross-sectional SEM micrographs of Mg1-DEG after potentiodynamic polarisation in 3.5 wt.% NaCl showing a) faceted surface pitting corrosion. b) faceted pitting corrosion and crystalline corrosion products.

Figure 6-29 a and b observe the extrusion and transverse directions respectively, of cross-sectioned Mg1-MG. Observations of the surface showed that both Mg1-DEG and Mg1-MG corroded in a different manner, in that pit widths on Mg1-MG were difficult to identified due to the fact that most of the surface had undergone some form of corrosion. The average pitting corrosion depth on Mg1-MG was ~ 30 µm and the maximum pit depth was seen to be 39 µm. These results agree with the electrochemical analysis in that Mg1-MG had a higher corrosion resistance than Mg1-DEG and that elongated, coarse recrystallised grain structures have a reduced corrosion resistance [71], [72], [74].

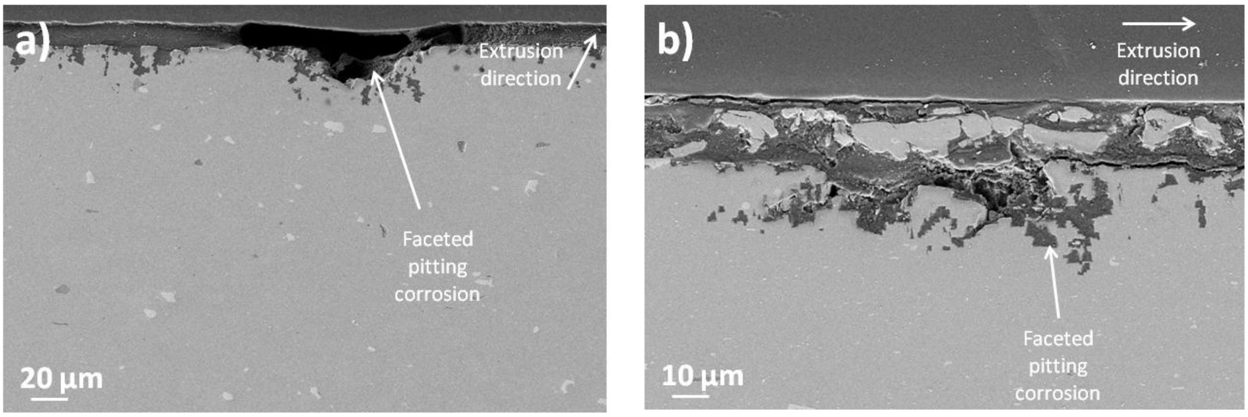

Figure 6-29: Cross-sectional SEM micrographs of Mg1-MG after potentiodynamic polarisation in 3.5 wt.% NaCl showing a) faceted surface pitting corrosion. b) surface faceted pitting corrosion.

6.2.2 Spray formed Al-Mg-Li (SF1)

Figure 6-30 shows the difference between SF1-DEG and SF1-MG over a 5 min immersion prior to potentiodynamic polarisation. EBSD revealed that both SF1-DEG and SF1-MG had very fine grain structures, so a major difference in corrosion resistance was not expected. However, Figure 6-30 demonstrates a difference between the specimens was observed. SF1-DEG and SF1-MG showed similar trends, but were offset by ~ 80 mV, with SF1-DEG being more noble. Even though both had similar grain sizes, the grains on the surface were ~ 2 µm^2 compared to ~ 4 µm^2 in the bulk [71], [72], [74]. SF1-DEG shows an increase before reducing to a final OCP of -953±26 mV compared to -1019±48 mV of SF1-MG. The overall profiles of SF1-DEG and SF1-MG were similar and indicated passivation.

When compared to the results seen in Section 5.2.2 a difference was observed, in that the average OCP for the Immersion testing specimens was -762±8 mV after 5 min compared to -1019±48 mV for the polarisation specimens. This large fluctuation shows the heterogeneous nature of SF1, which was also observed in literature. *Moore et al.* [28], [93] showed that the E_{corr} of SF1 was -838±72 mV vs. SCE after a 2 hour immersion period. The results in this thesis, are different to those seen by *Moore et al.* [28], [93], however, due to the heterogeneous nature of the E_{corr} values, a more informative comparison would be to compare the E_{pit} values. As mentioned previously the surface preparation of *Moore et al.* [28], [93] samples were mechanically polished to a 800 grit SiC, compared to 1200 grit of this work.

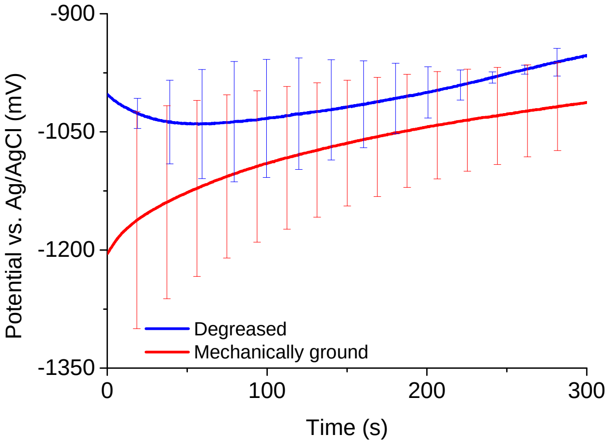

Figure 6-30: Graph showing the change in OCP of SF1 following 5 min immersion prior to potentiodynamic polarisation in 3.5 wt.% NaCl.

Table 6-6 shows the E_{corr}, E_{pit}, E_{pit}-E_{corr} and charge passed from 5 specimens of SF1, indicating the average and standard deviation. Figure 6-31 a and b show SF1-DEG and SF1-MG had different polarisation profiles. The E_{pit} of SF1-DEG was -694±6 mV and the E_{pit} of SF1-MG was -769±4 mV, showing that SF1-DEG was once again more noble, agreeing with theory that more noble E_{pit} values offer increased corrosion resistances [12], [156–158]. *Moore et al.* [28], [93] examined SF1 and showed that its E_{pit} was ~ -715±19 mV vs. Ag/AgCl, so when compared to the results in this thesis even though the E_{corr} values were entirely different, both showed that SF1 had a stable E_{pit}.

Table 6-6: Table showing the difference in E_{pit}, E_{corr}, E_{pit} - E_{corr} and charges passed on SF1-DEG and SF1-MG.

Specimen Number	**SF1-DEG**				**SF1-MG**			
	E_{pit} (mV)	**E_{corr} (mV)**	**E_{pit} - E_{corr} (mV)**	**Charge (C)**	**E_{pit} (mV)**	**E_{corr} (mV)**	**E_{pit} - E_{corr} (mV)**	**Charge (C)**
1	-694	-984	290	20	-766	-1036	269	13
2	-700	-932	232	17	-764	-1053	289	7
3	-699	-925	226	7	-772	-1037	265	5
4	-686	-974	288	6	-768	-1026	258	6
5	-689	-951	262	7	-773	-1042	269	8
Average	-694	-953	260	12	-769	-1019	270	8
Standard deviation	6	26	30	6	4	48	12	3

Using E_{pit}-E_{corr}, SF1-DEG was seen to have a pitting corrosion resistance of 260±30 mV compared to 270±12 mV for SF1-MG, suggesting that the SF1-DEG had the lower pitting corrosion resistance. These are, however, very similar to each other, suggesting that they have a comparable corrosion resistances. Due to the large fluctuations in E_{corr}, however, some specimens spent less time above their respective E_{pit} causing large amounts of deviation. The E_{pit}-E_{corr} values were also in excess of those seen by *Moore et al.* [28], [93], who reported E_{pit}-E_{corr} values of ~ 78±72 mV. The reason for this difference is related to the unpredictable nature of the E_{corr}. Both SF1-DEG and SF1-MG show characteristic metastable pitting corrosion regions and as such it can be said no stable pit growth took place in these regions offering a large E_{pit}-E_{corr} value [61], [87]. Analysis of the charges that passed, showed that SF1-MG had the lowest at 8±3 C, with the DEG specimen showing a higher charge at 12±6 C. Overall the calculated results of E_{pit}-E_{corr} and charge suggest that SF1-MG had the higher corrosion resistance, thus the larger of the grain structures having a higher corrosion resistance [71], [72], [74]. However, due to both systems having a very fine grain structure a comparison between them cannot be made with regards to coarse and fine grain structures and which offers the higher corrosion resistance.

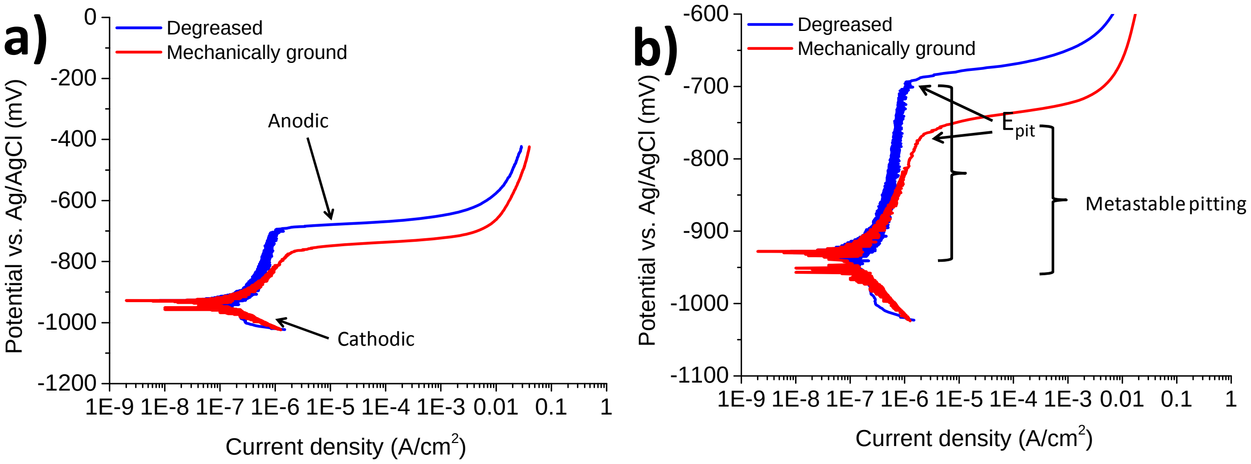

Figure 6-31 a) Graph showing the potentiodynamic polarisation response of SF1-DEG and SF1-MG in 3.5 wt.% NaCl. b) Graph showing an enlarged region of the potentiodynamic polarisation response of SF1-DEG and SF1-MG in 3.5 wt.% NaCl, highlighting the E_{corr} and E_{pit} regions.

Visual observations of SF1 following polarisation shows that both SF1-DEG and SF1-MG had a very similar corrosion resistance. Figure 6-32 a and b show micrographs of SF1-DEG and Figure 6-32 c and d show micrographs of SF1-MG after potentiodynamic polarisation. Figure 6-32 a shows the development of corrosion patches on SF1-DEG, but with time these would grow to cover the entire specimen surface. Figure 6-32 b shows that on the periphery of all SF1 specimens localised pitting corrosion develops, which extents along the entire edge and corner regions. In contrast it can be seen that SF1-MG develops corrosion across the entire specimen surface as shown in Figure 6-32 c and it can be seen in Figure 6-32 d that any pits that do form are very small, but the V_f of these pits is high.

EBSD showed that SF1 had a very fine equiaxed grain structure and due to the high level of corrosion that had developed it is difficult to identify whether IGC was also taking place. FEGTEM has been suggested as further work and would clarify whether any highly anodic phases like Al_3MgLi or the β phase have formed during the spray forming process [130], [134]. Some sites, showed potential evidence of IGC but nothing was definitive on either SF1-DEG or SF1-MG. Large pit sites were noted on

SF1-DEG, with some being > 100 µm wide and ~ 500 µm in length. Some were recorded as being greater in size, however, these were multiple joined pits. In comparison the largest pits seen on SF1-MG were Ø = ~ 40 µm, but as mentioned these were spread along the periphery of the specimen in a distinct pattern, with ~ 50 µm between the edge of the next pit. Visual inspection suggests that SF1-DEG had less corrosion sites than SF1-MG but they progressed deeper into the specimens, thus SF1-DEG has a reduced corrosion resistance. This agrees with the electrochemical data that shows that SF1-MG had the higher corrosion resistance. The question of which offers the higher corrosion resistance; lots of small corrosion sites or a few large pits? Needs to be answered.

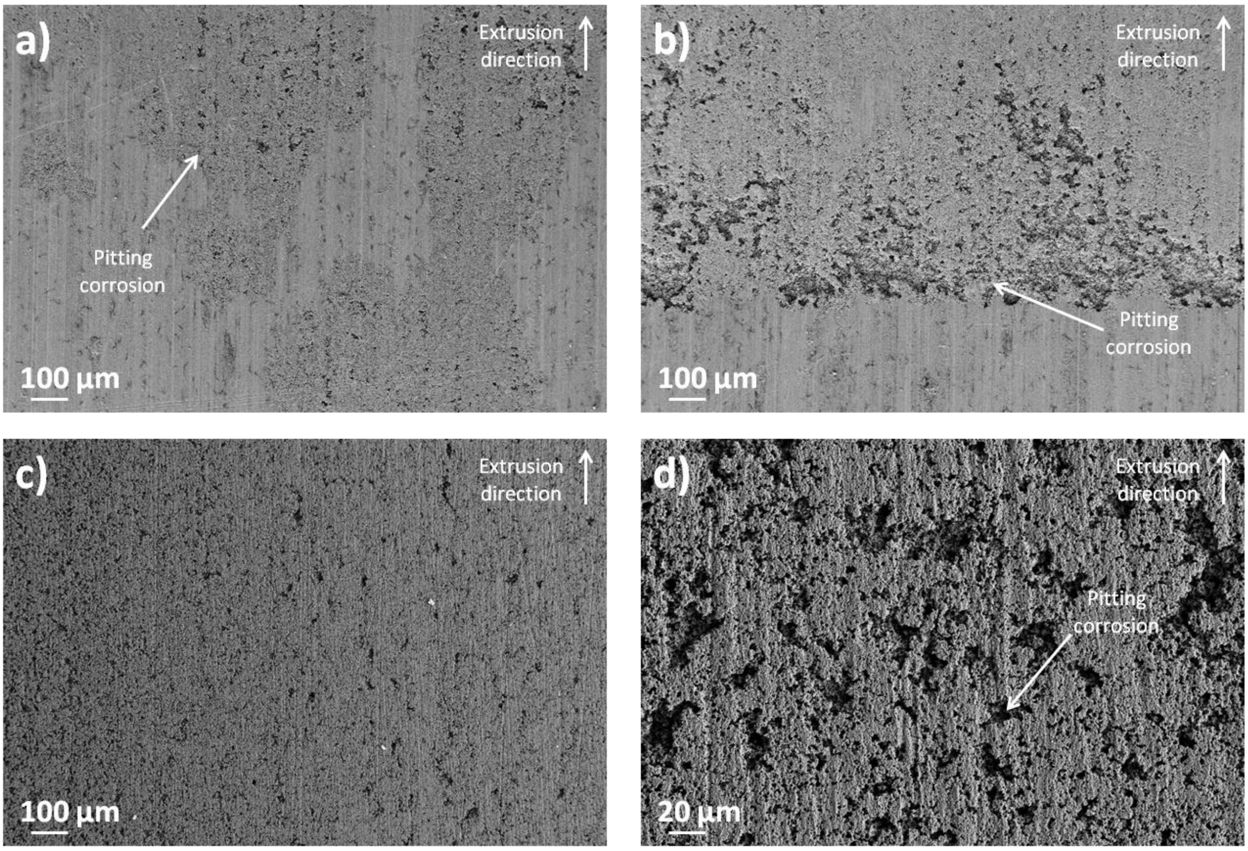

Figure 6-32: SEM micrographs of a) SF1-DEG showing uniform pitting corrosion developing in patches. b) SF1-DEG showing accelerated corrosion at the edge of the specimens. c) SF1-MG showing uniform pitting corrosion. d) SF1-MG showing a higher magnification micrograph of the uniform pitting corrosion.

SF1-DEG develops large scale pits following potentiodynamic polarisation as shown in Figure 6-33 a and closer inspection of these pits reveals that they are faceted in morphology. SF1-MG revealed faceted pitting corrosion taking place as shown in Figure 6-33 b. Figure 6-33 c shows the regular pattern of pits that developed around the edges of SF1-MG specimens after potentiodynamic polarisation and Figure 6-33 d shows a micrograph detailing the typical corrosion seen over the surface of SF1-MG. Since little pitting corrosion was observed on SF1-MG, except for the edge pitting, it can be said that SF1-MG showed a relatively high corrosion resistance. The IMCs were identified to be actively undergoing galvanic corrosion and EDS showed that they were Fe rich, suggesting their cathodic nature [60], [63]. IMCs are known to be associated with pitting corrosion, however, due to the very low V_f within SF1, it has to be concluded that from the extent of the corrosion, the pitting is being initiated from fine scale precipitates instead of the coarse second phase IMCs [26], [60], [63], [64], [80], [84]. No evidence of IGC was seen, thus at this stage SF1 was only susceptible to pitting corrosion and galvanic corrosion around cathodic IMCs.

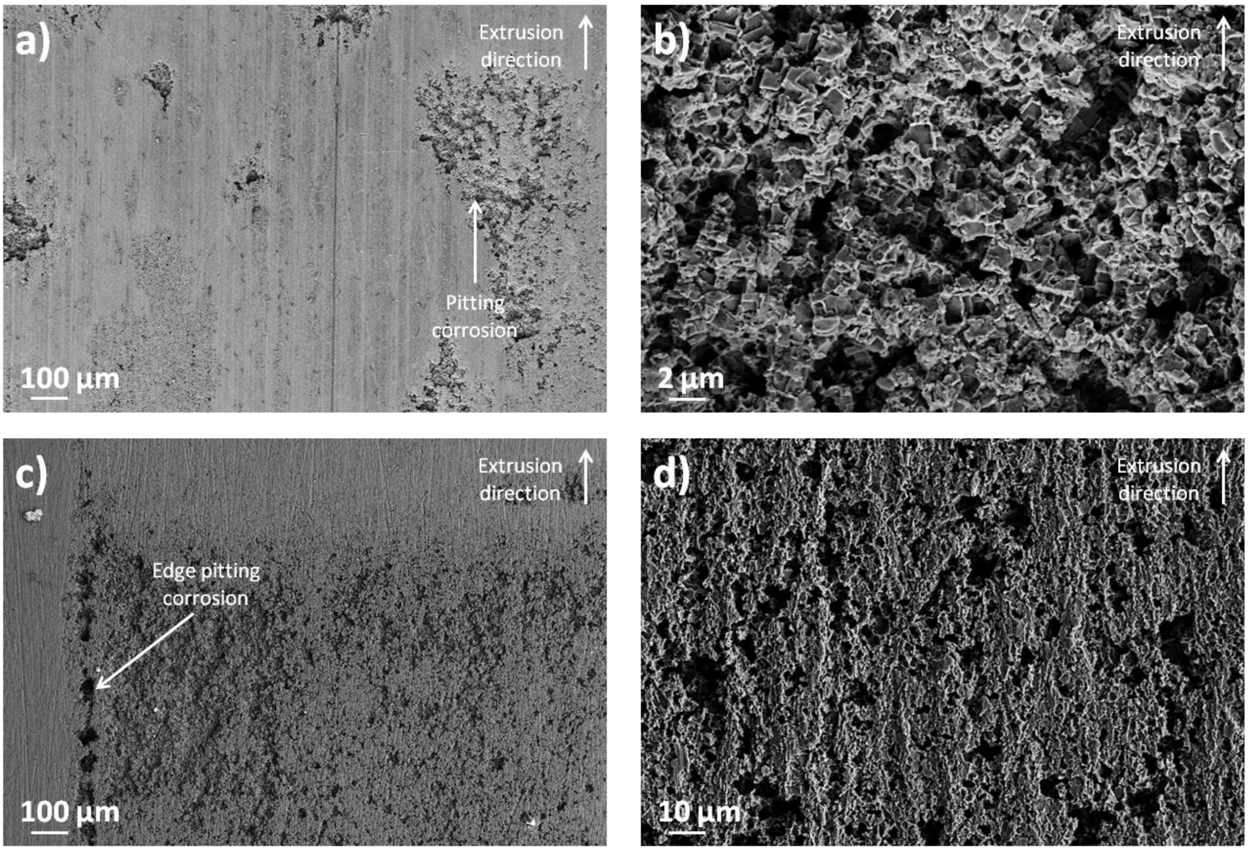

Figure 6-33: SEM micrographs following potentiodynamic polarisation in 3.5 wt.% NaCl of a) SF1-DEG showing the development of large scale pits. b) SF1-MG showing faceted pitting corrosion. c) SF1-MG showing the edge pitting corrosion patterns observed. d) SF1-MG showing a higher magnification examination of the surface.

Figure 6-34 a and b observe the extrusion and transverse direction respective, for cross-sectioned SF1-DEG. Each sample shows evidence of substantial pitting corrosion, but as previously mentioned SF1-DEG formed much larger pits. Cross-sectioning showed that the width of the pits fluctuated, with some being ~ 20 µm and others ~ 300 µm in width. The depth of the pits was also seen to fluctuate with some being ~ 30 µm and others > 70 µm. This fluctuation is not surprising based on the surface observations of SF1-DEG, with some regions showing very little corrosion, whereas others showed extensive attack. In most cases the progression of corrosion into the specimens was uniform, however, in some cases pitting progressed more substantially sub-surface. Once again no evidence of IGC could be seen via cross-sectioning and it can therefore be concluded that no IGC forms on SF1-DEG. It must be noted, however, that a transfer of electrolyte must be taking place from the surface to the sub-surface corroded regions and this can take place via IGC.

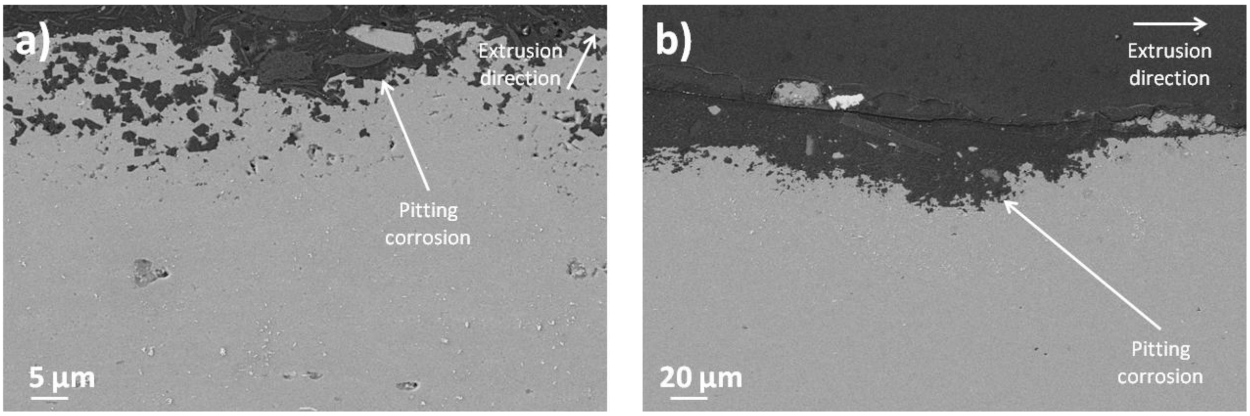

Figure 6-34: Cross-sectional SEM micrographs of SF1-DEG after potentiodynamic polarisation in 3.5 wt.% NaCl showing a) surface faceted pitting corrosion. b) surface faceted pitting corrosion.

Figure 6-35 a and b observe the extrusion and transverse directions respectively, for cross-sectioned SF1-MG. Examination showed that both SF1-DEG and SF1-MG developed faceted pitting corrosion and on SF1-MG there was evidence of what appeared to be IGC as shown in Figure 6-35 a. The pitting corrosion covered the vast majority of the specimen surface; especially more than that of SF1-DEG. With regards to pit opening sizes, it was difficult to distinguish with the majority of the surface undergoing uniform corrosion. This also made examination of the pit depth difficult, however, it had been shown that, on average, the pit depth was ~ 25 µm, which is less than that observed on SF1-DEG and as such agrees with electrochemical data that SF1-MG had the higher corrosion resistance.

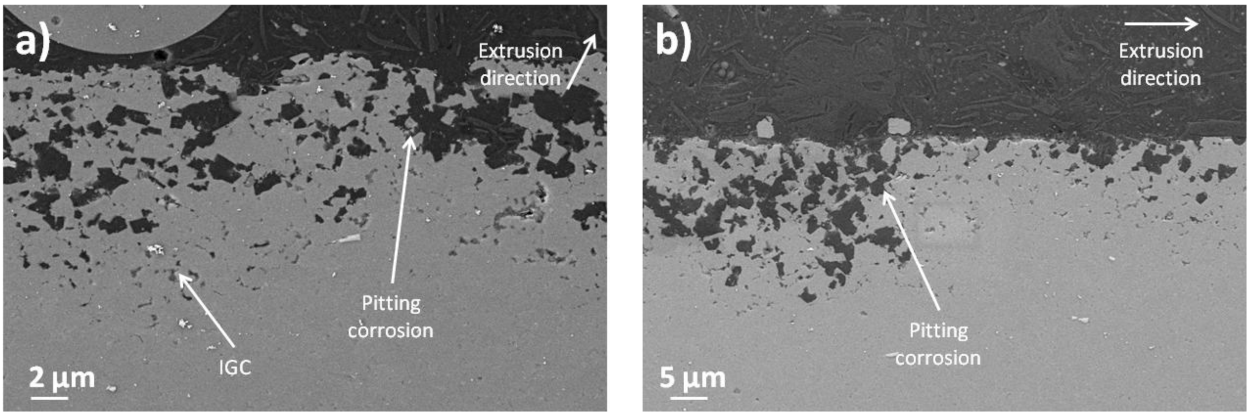

Figure 6-35: Cross-sectional SEM micrographs of SF1-MG after potentiodynamic polarisation in 3.5 wt.% NaCl showing a) faceted pitting corrosion and IGC. b) faceted pitting corrosion.

6.2.3 Spray formed Al-Mg-Li-Cu-Zn (SF2)

Figure 6-36 shows the difference between SF2-DEG and SF2-MG over the 5 min immersion period prior to potentiodynamic polarisation. SF2-DEG and SF2-MG had very fine grain structures, so a difference in corrosion resistance was not expected. However, EDS revealed that a Cu and Zn rich region was present. This can cause a galvanic cell to form with the surrounding material and as such affect the electrochemical response. Both specimens had the Cu and Zn rich region present, however, it was much wider, but shallower on SF2-DEG. Figure 6-36 shows that SF2-MG passivated, which is to be expected as the Cu and Zn rich region will promote dissolution of the Al matrix whilst also promoting O reduction [63]. This also tends to suggest that SF2-MG will have a higher corrosion resistance. SF2-DEG which had the larger Cu and Zn rich region on the surface, shows a more noble OCP, due to more of the surface containing cathodic phases [26], [35], [60], [63], [80], [84]. SF2-DEG was more noble at the offset of immersion, but after 5 min's SF2-MG was more noble. This agrees with predictions that SF2-DEG would have the lower corrosion resistance due to the coverage of the Cu and Zn rich region. SF2-DEG shows large fluctuations in OCP, which is associated with the high level of galvanic corrosion taking place. SF2-DEG shows a slight increase at the offset before reducing to a final OCP of -802±30 mV compared to -783±1 mV of SF2-MG. Care must be taken in the examination of these results as the OCP of SF1 and the results seen by *Moore et al.* [28], [93] show that SF alloys tend to have a low level of E_{corr} reproducibility.

When compared to the results seen in Section 5.2.3 a small difference was observed, in that the average OCP for the immersion testing specimens was -749±7 mV after 5 min compared to -783±1 mV for the polarisation specimens, showing that both systems had good reproducibility.

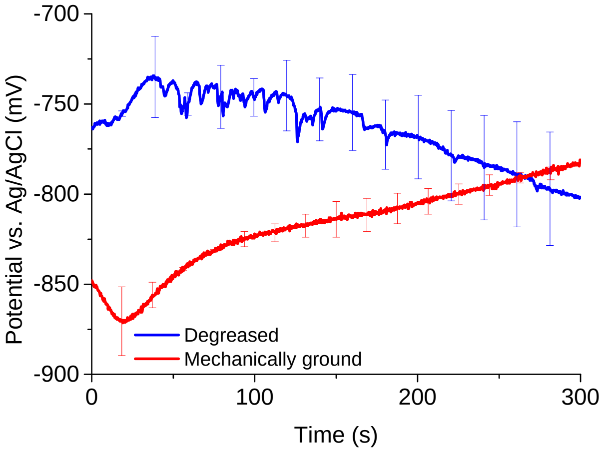

Figure 6-36: Graph showing the change in OCP of SF2 following 5 min immersion prior to potentiodynamic polarisation in 3.5 wt.% NaCl.

Table 6-7 shows the E_{corr}, E_{pit}, E_{pit}-E_{corr} and charge passed from 5 specimens of SF2, indicating the average and standard deviation. Examination of the polarisation plots shown in Figure 6-37 a and b show SF2-DEG and SF2-MG performed in a very different manner. SF2-DEG had an E_{pit} of -698±11 mV compared to -741±10 mV of SF2-MG, which once again shows that SF2-DEG had a more noble E_{pit}. This shows that similar to SF1, that a more noble E_{pit} suggests an increased corrosion resistance, however, E_{pit} alone cannot be used to determine the corrosion resistance [12], [156–158].

Table 6-7: Table showing the difference in E_{pit}, Ecorr, E_{pit} - E_{corr} and charges passed on SF2-DEG and SF2-MG following potentiodynamic polarisation in 3.5 wt.% NaCl.

Specimen Number	SF2-DEG				SF2-MG			
	E_{pit} (mV)	E_{corr} (mV)	E_{pit} - E_{corr} (mV)	Charge (C)	E_{pit} (mV)	E_{corr} (mV)	E_{pit} - E_{corr} (mV)	Charge (C)
1	-682	-832	150	10	-730	-783	53	22
2	-711	-769	58	14	-749	-783	34	28
3	-699	-815	116	6	-730	-783	53	22
4	-693	-772	79	11	-749	-781	32	28
5	-706	-823	117	6	-745	-782	37	24
Average	-698	-802	104	10	-741	-783	42	25
Standard deviation	11	30	36	4	10	1	10	3

SF2-DEG specimen had an average E_{pit}-E_{corr} of 104±36 mV compared to 42±10 mV for SF2-MG, suggesting that the latter had the lower pitting corrosion resistance. Even though both showed metastable pitting corrosion, SF2-DEG showed a much larger metastable region and as such should visually have less corrosion present. Both also showed a double breakdown potential, which appear as separate E_{corr} points. This double breakdown is more pronounced on SF2-DEG, which shows that it is associated with the size of the Cu and Zn rich region. *Frankel et al.* [85] examined a double breakdown potential on an AA2024 alloy and concluded that pitting and IGC had their own breakdown potentials, which may be an indication that pitting and IGC will be observed on SF2[19]. Another possible conclusion for the double breakdown potential is due to unstable passivation behaviour caused by a variation in which cathodic process is most dominant; H^+ evolution, O reduction or metal cation reduction [164].

After reaching its E_{pit}, SF2-DEG shows a gradual increase in potential with increasing current density. Since this increase is gradual it means that the specimens spend less time in the anodic region where large amounts of charge flow meaning that the charge that passes on SF2-DEG is less than that on SF2-MG at 10±4 C compared to 25±3 C respectively. Electrochemical results show that SF2-DEG had the higher corrosion resistance, which is expected due to the large Cu and Zn rich region acting as the cathode, in comparison to that of SF2-MG, where large amounts of dissolution are predicted to initiate.

---

[19] E_{pit}-E_{corr} values have been calculated from the more anodic breakdown point.

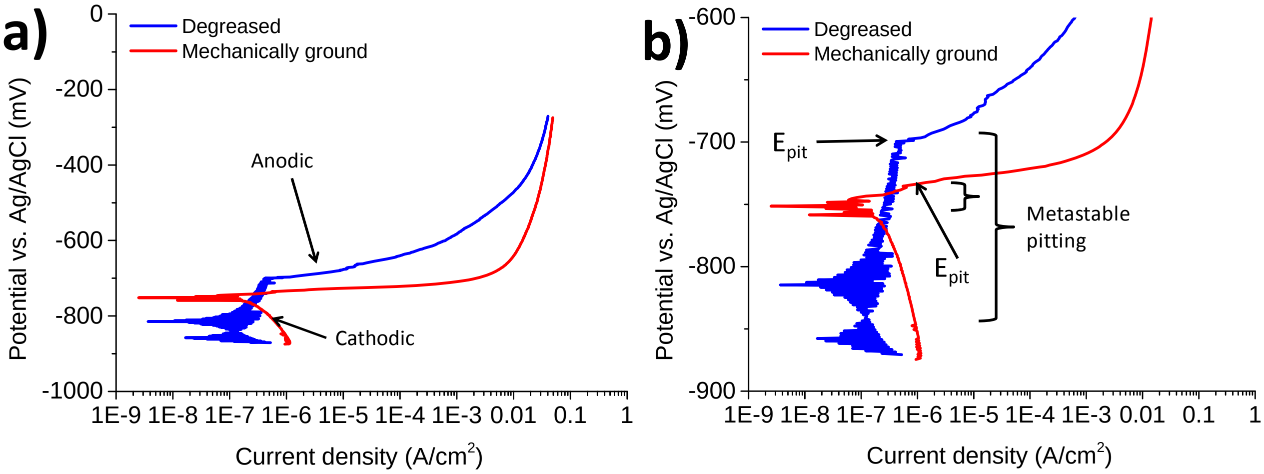

Figure 6-37 a) Graph showing the potentiodynamic polarisation response of SF2-DEG and SF2-MG in 3.5 wt.% NaCl. b) Graph showing an enlarged region of the potentiodynamic polarisation response of SF2-DEG and SF2-MG in 3.5 wt.% NaCl, highlighting the E_{corr} and E_{pit} regions.

Figure 6-38 a and b show micrographs of SF2-DEG and Figure 6-38 c and d show micrographs of SF2-MG after potentiodynamic polarisation. It can be seen in Figure 6-38 a and b that pitting corrosion develops and that the corrosion sites are very substantial in size. Some pits were so large they could not be measured by FEGSEM as they extended beyond the field of view. Some of the pits that were measured were > 1.5 mm in length and ~ 200 µm wide, but not all were this size, with some seen to be ~ 70 µm wide and 20 µm in length. Overall the pits ranged from < 100 µm in size up to 2 mm in length, as well as appearing to have substantial depth. This was expected, as with the Cu and Zn rich region acting as the cathode, the Cu / Zn denuded region is forced to be the anode. This means that galvanic corrosion develops and leads to highly accelerated dissolution of the anodic material[28]. In comparison SF2-MG shows that the Cu and Zn rich region had very little corrosion on it due to the galvanic cell that forms between it and the surrounding matrix, as shown in Figure 6-38 c. Some specimens showed that the Cu and Zn rich region eventually underwent corrosion, but this only took place at the edges of the samples and it is more likely to be an edge effect, due to the build-up of H_2 bubbles [128]. The denuded region undergoes a relatively uniform dissolution across the entire surface on SF2-MG, which is to be expected. Because of this no individual pits were seen to develop, which gives the impression that SF2-MG had a poor corrosion resistance compared to SF2-DEG.

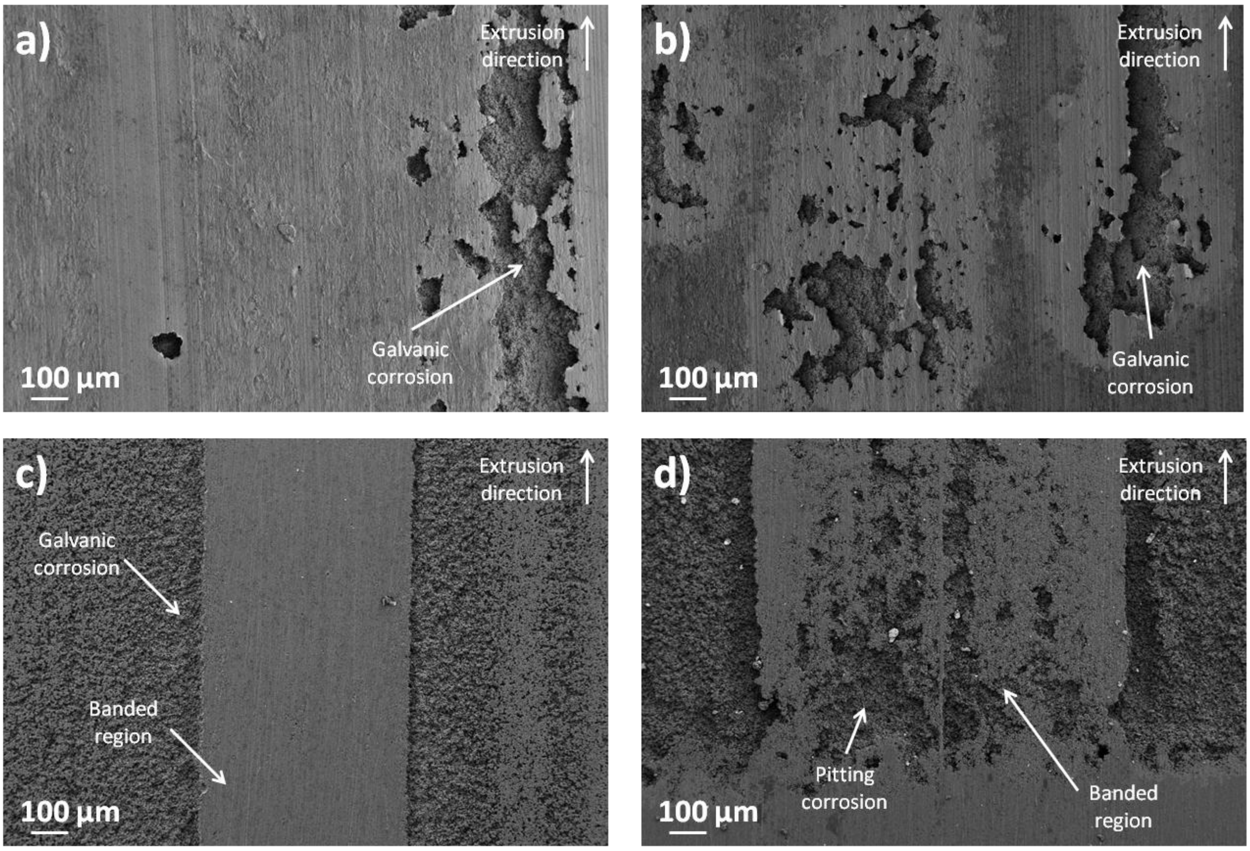

Figure 6-38: SEM micrographs after potentiodynamic polarisation in 3.5 wt.% NaCl of a) SF2-DEG showing galvanic corrosion. b) SF2-DEG galvanic corrosion. c) SF2-MG showing galvanic corrosion of the matrix surrounding the Cu rich Cu and Zn rich region. d) SF2-MG showing galvanic corrosion of the matrix surrounding the Cu and Zn rich region and corrosion of this region at the sample periphery.

Figure 6-39 a and b show that faceted pitting corrosion on SF2-DEG and SF2-MG developed. An interesting feature on SF2-DEG is that in some locations it looks like IGC, however, closer inspection reveals that it is fine scale faceted filament corrosion, similar to the tunnelling phenomenon observed by *Moore et al.* [28], [93]. EDS revealed that the IMCs within SF2 were very fine and very sparsely distributed throughout the matrix as such their impact on pitting corrosion was expected to be less than that of fine scale precipitates. As such it is assumed that the corrosion had been generated mainly from the high Mg (anodic to Al) concentration within the Al matrix alongside the Cu and Zn (cathodic to Al) region [12]. Some IMC sites undergoing galvanic corrosion were located, as shown in Figure 6-39 c, from which EDS showed that the IMCs were Fe rich. The edge regions on both SF2-DEG and SF2-MG showed accelerated dissolution with larger pits forming. Figure 6-39 d shows an edge from SF2-MG, demonstrating spherical pits that form around the periphery, which were all distributed homogenously and were ~ Ø = 50 µm. The spherical nature and location of these pits, suggests that they have been formed via H_2 evolution, resulting in accelerated corrosion at the edges [128]. Localised regions where the surface had risen up were created by stresses produced beneath the surface from the generation of corrosion products.

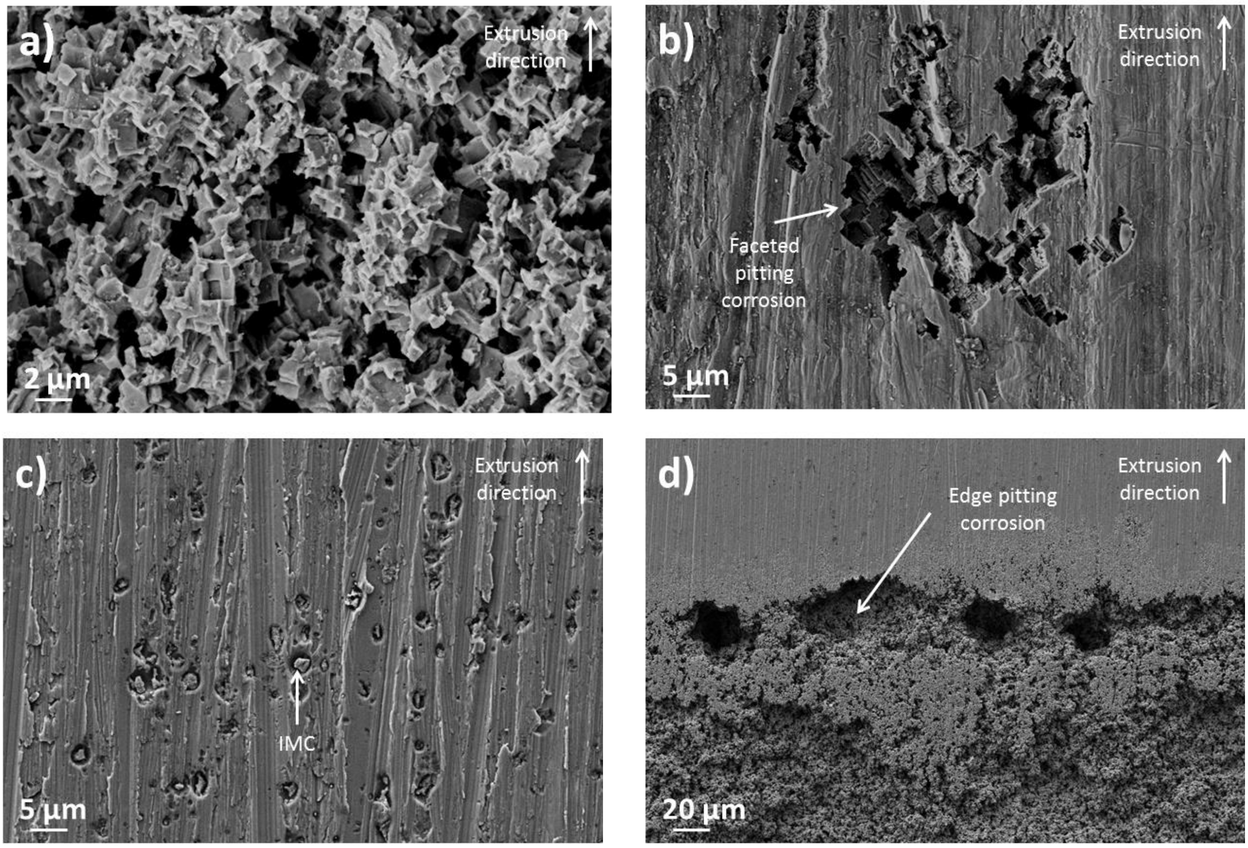

Figure 6-39: SEM micrographs following potentiodynamic polarisation in 3.5 wt.% NaCl of a) SF2-DEG showing faceted pitting corrosion. b) SF2-DEG showing faceted pitting corrosion. c) SF2-DEG showing galvanic corrosion around IMCs. d) SF2-MG showing the formation of edge pitting corrosion, homogeneously distributed around the periphery.

Figure 6-40 a and b observe the extrusion direction and Figure 6-40 c and d show the transverse direction for SF2-DEG. Primarily only faceted pitting corrosion was observed, however, some IGC was seen to take place within the Cu and Zn rich region. Figure 6-40 a shows the Cu and Zn rich region and how pitting corrosion and IGC are seen to develop on the surface and on the periphery of the Cu and Zn rich region respectively. Pitting corrosion was also seen to form across the entire surface and appeared to progress to similar depths. EBSD showed that the Cu and Zn rich region was wide at the surface, but varied in depth. The Cu and Zn rich region did not encompass the entire area that was exposed to solution, which may explain the double breakdown potential of SF2-DEG. The pits that formed on the Cu and Zn rich region were seen to progress about 30 µm, and the pits that formed in the denuded were much deeper at ~ 75 µm, highlighting the galvanic impact of the Cu and Zn rich region, also showed that galvanic corrosion had initiated. Figure 6-40 c and d also show that sub-surface corrosion takes place. This is of concern as sub-surface corrosion cannot be observed visually and thus in service inspections would not reveal the true amount of corrosion. Figure 6-40 c and d are taken from within the Cu and Zn rich region and show a large V_f of IMCs, which were not observed previously in Section 3.2.3Section. EDS showed that the IMCs were Cu and Fe rich and thus further accelerated the galvanic corrosion effect.

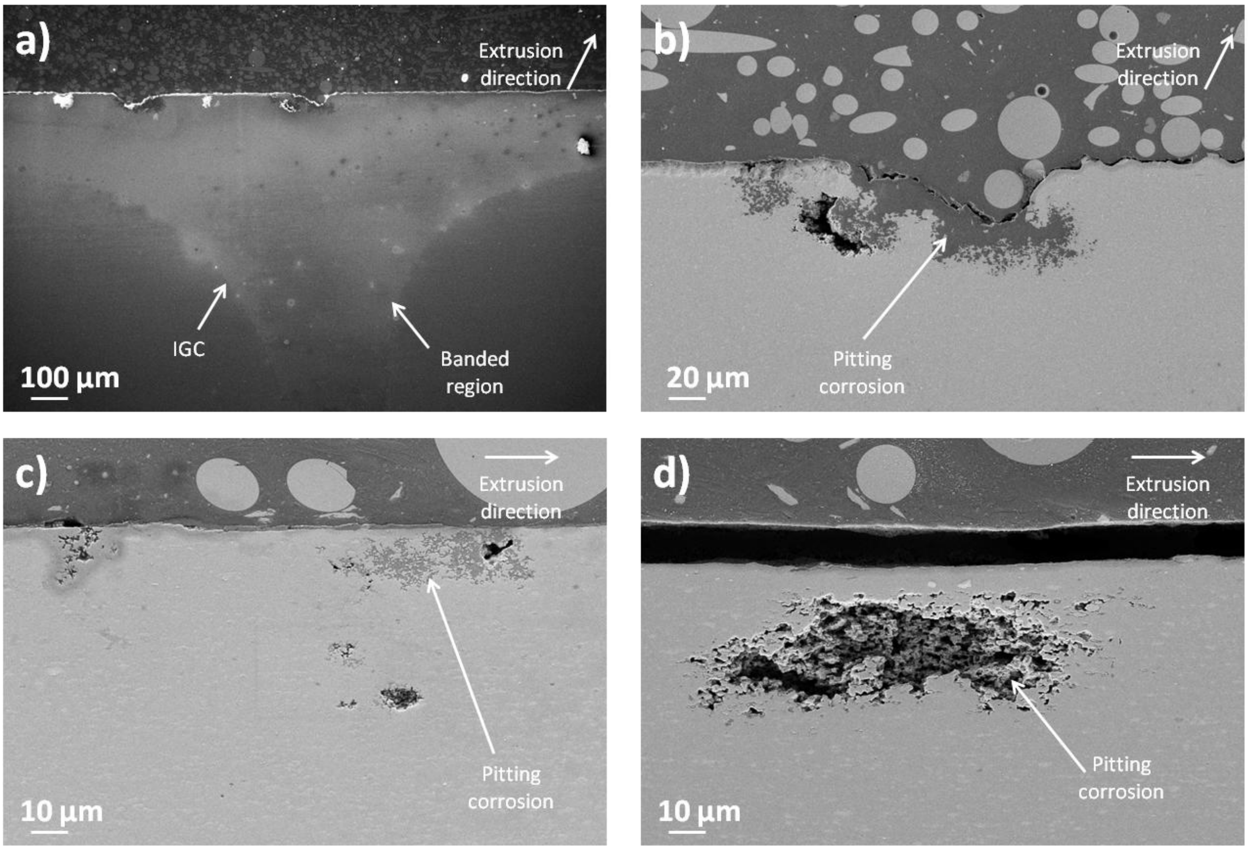

Figure 6-40: Cross-sectional SEM micrographs of SF2-DEG after potentiodynamic polarisation in 3.5 wt.% NaCl showing a) IGC along the periphery of the Cu and Zn rich region and surface pitting corrosion. b) surface pitting corrosion off the Cu and Zn rich region. c) pitting corrosion on the surface of the Cu and Zn rich region. d) sub-surface pitting corrosion on the Cu and Zn rich region.

Cross-sectioning of SF2-MG shown in Figure 6-41 a and b observes the extrusion direction and Figure 6-41 c and d show the transverse direction. After SF2-MG was MG there was a divide between the Cu and Zn rich region and the surrounding matrix. This enabled a substantial galvanic cell to form between the two components. In comparison the Cu and Zn rich region was not as wide as that on SF2-DEG, however, it progressed much deeper into the specimen. Galvanic corrosion can be observed, due to the fact that the pitting corrosion at the periphery is much deeper than the rest of the matrix, as shown in Figure 6-41 a. Figure 6-41 b shows this periphery region and it can be seen that the pit at the periphery is 68 µm deep. The corrosion then spreads to a relatively uniform depth over the entire surface of the denuded region as shown in Figure 6-41 a. Figure 6-41 c and d show that the corrosion is highly homogenous and had an average depth of ~ 20 µm. Cross-sectioning revealed that both systems had very poor corrosion resistances, due to the galvanic corrosion that developed, however, the corrosion depths seen on SF2-MG were shallower than those on SF2-DEG. Since uniform corrosion takes place on SF2-MG it had to be said that more material had been corroded and thus SF2-MG had the lowest corrosion resistance, which agrees with the electrochemical data.

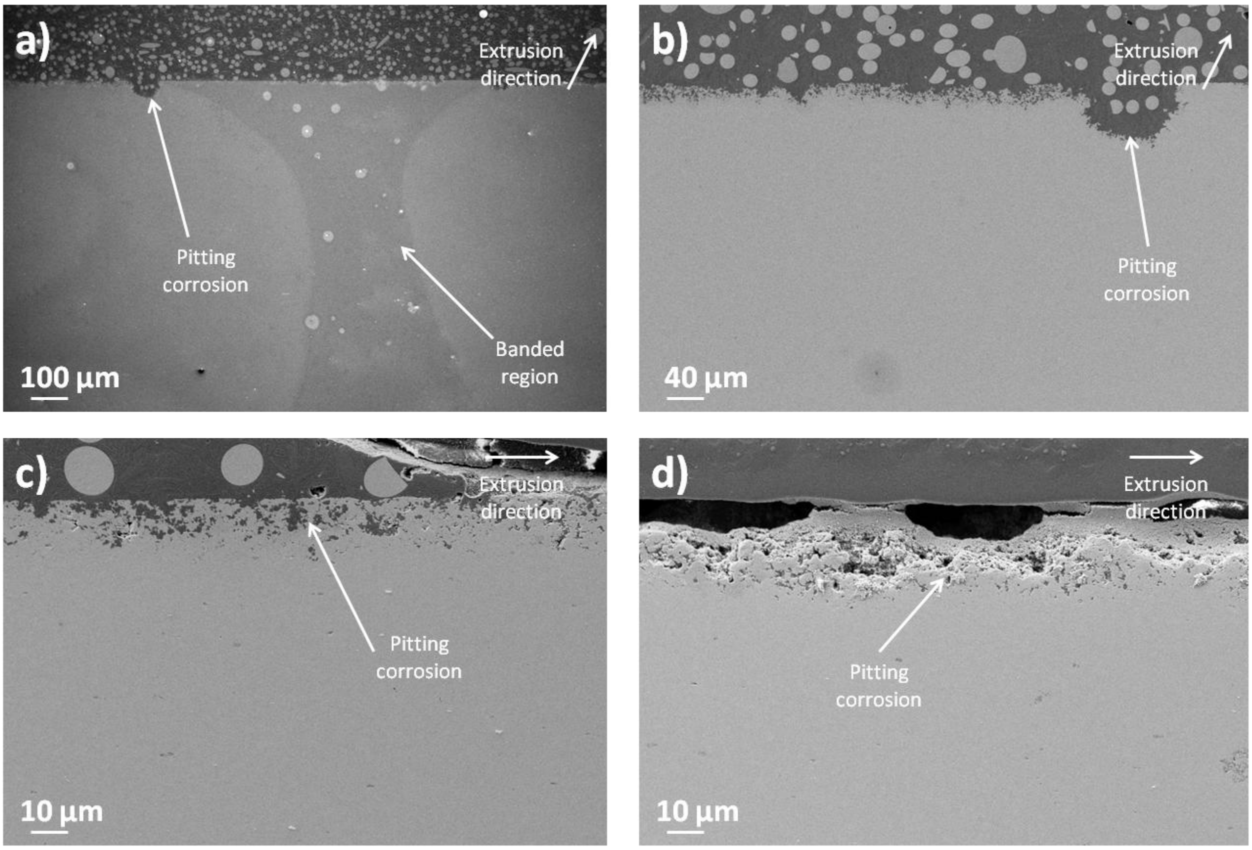

Figure 6-41: Cross-sectional SEM micrographs of SF2-MG after potentiodynamic polarisation in 3.5 wt.% NaCl showing a) galvanic corrosion at the periphery of the Cu and Zn rich region. b) galvanic corrosion at the periphery of the Cu and Zn rich region which is deeper than the uniform corrosion over the rest of the denuded region. c) uniform pitting corrosion depth on the denuded region. d) uniform pitting corrosion on the denuded region.

6.2.4 Comparison of Al-Mg vs. Spray formed Al-Mg-Li alloys

Comparison of the Al-Mg alloys, shows different corrosion rates for Al-Mg (Mg1) compared to both of the SF alloys (SF1 and SF2). Comparison of Mg1 and SF1 against SF2 will be difficult due to the large galvanic Cu and Zn rich region present within SF2. Both are, however, SF and an understanding of how they perform is of interest in this thesis, as such this section will make a direct comparison of Mg1 against both SF1 and SF2.

Mg1 is a non-Li containing Al-Mg alloy that had a very coarse grain structure, whereas SF1 and SF2 are SF and have very fine grain structures and are Li containing. OCP showed that Mg1 had the more noble OCP of all 3 Al-Mg alloys as shown in Table 6-8. This was unexpected as SF2 contained Cu which is a highly noble element. All showed high levels of standard deviation, suggesting that Al-Mg alloys are not very reproducible. In the MG condition, SF2 had the more noble potential, followed by Mg1 and SF1 respectively. It was expected that SF2 would have a very noble OCP due to the Cu additions, however, the difference between Mg1 and SF2 in the MG state was small. SF1 had the least noble OCP in both the DEG and MG condition, which gives the impression of increased corrosion resistance, however, the error for SF1 was also the highest. The error on Mg1 and SF2 reduced when the recrystallised grains were removed, however, for SF1 the standard deviation increased. This was, however, shown in literature by *Moore et al.* [28], [93]. A comparison of all of the OCP values can be seen in Figure 6-42 and it suggests that Mg1 had the highest corrosion resistance in the DEG and MG condition. This is because since SF2 contains Cu, theory that relates to the more noble E_{pit} being a higher corrosion resistance is no longer valid [12], [156–158].

Table 6-8: Comparison of the changes in OCP, E_{pit}, E_{corr}, E_{pit}-E_{corr}, charge and average pit depth for Mg1, SF1 and SF2 in the DEG and MG condition.

	Mg1-DEG	**Mg1-MG**	**SF1-DEG**	**SF1-MG**	**SF2-DEG**	**SF2-MG**
OCP after 5 min's (mV)	-680±18	-816±8	-953±26	-1019±48	-802±30	-783±1
E_{pit} (mV)	-655±10	-685±5	-694±6	-769±4	-698±11	-741±10
E_{corr} (mV)	-680±18	-816±8	-953±26	-1019±48	-802±30	-783±1
E_{pit}-E_{corr} (mV)	24±13	132±10	260±30	270±12	104±36	42±10
Charge (C)	19±4	14±4	12±6	8±3	10±4	25±3
Average pit depth (µm)	40	30	50	25	75	70

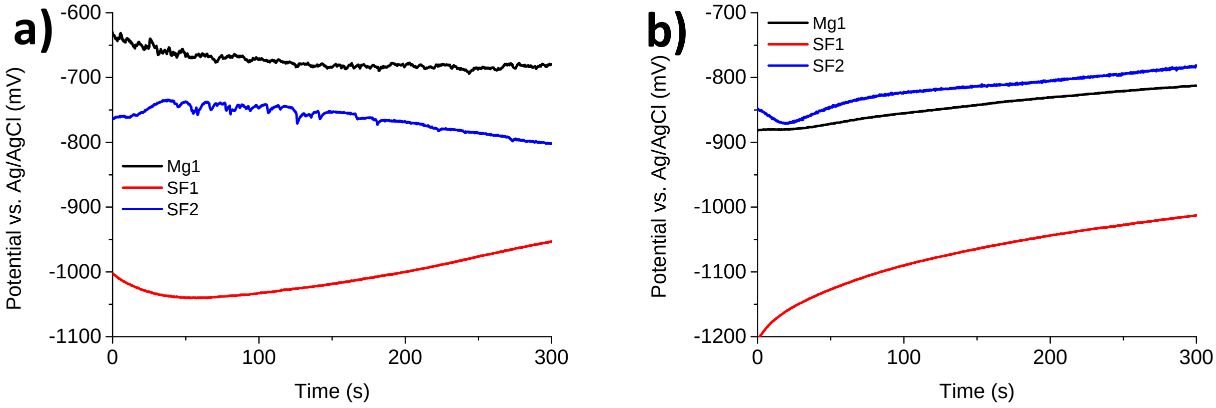

Figure 6-42: Comparison of Mg1, SF1 and SF2, over the 5 min of immersion prior to potentiodynamic polarisation in 3.5 wt.% NaCl in the a) DEG and b) MG surface condition.

Table 6-8 demonstrates that Mg1 had the most noble E_{pit} in the DEG condition and SF1 and SF2 had very similar E_{pit} values. Both SF alloys showed metastable pitting corrosion, which is an indication of good corrosion resistance, whereas Mg1 did not. This suggests that the SF alloys had the higher corrosion resistance and with them having the smaller grain structure it could be said that fine grains offered increased corrosion resistance [71], [72], [74]. It was expected that SF2 would have the most noble E_{pit} due to the presence of Cu. It could also be said that the Li additions did not have a detrimental impact on the corrosion resistance [2], [4], [44], [48]. When the specimens were MG, Mg1 once again showed the most noble E_{pit}, however, now a metastable pitting region had developed. SF2 also showed a metastable pitting region, however, SF1 did not. Examination of the E_{pit} values showed that SF2 had the least noble E_{pit}. Overall each Al-Mg alloy shows a reduction in E_{pit} nobility by removing the recrystallised grain layer, showing that this layer does have an impact on the corrosion resistance. A comparison of all of the potentiodynamic polarisation plots can be seen in Figure 6-43. Figure 6-44 shows a comparison between all of the E_{pit} values for the Al-Mg alloys. Overall these results show that Mg1 does not agree with theory that a more noble E_{pit} offers an increased corrosion resistance, however, SF1 and SF2 do [12], [156–158]. One noteworthy point is that SF1-DEG and both SF2 specimens showed evidence of a double breakdown potential which *Frankel et al.* [85] showed on an Al-Cu alloy to be independent breakdown potentials for pitting and IGC. This suggests that SF2 and SF1-DEG would be prone to IGC, however, no characterisation of the GBs was undertaken to confirm this, but it had been suggested as further work.

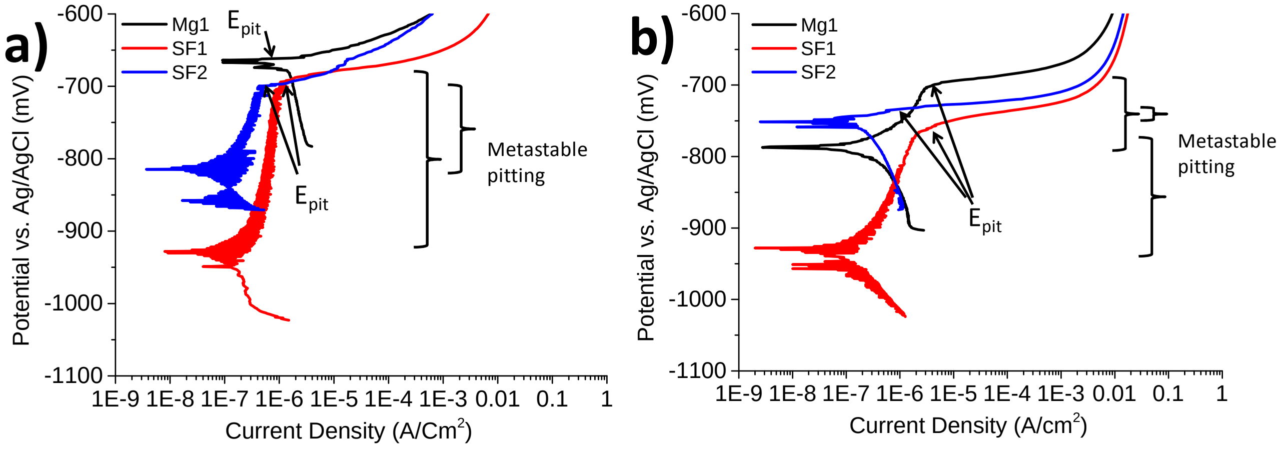

Figure 6-43: Comparison of the potentiodynamic polarisation response for Mg1, SF1 and SF2, after a 5 min of immersion in 3.5 wt.% NaCl in the a) DEG and b) MG surface condition.

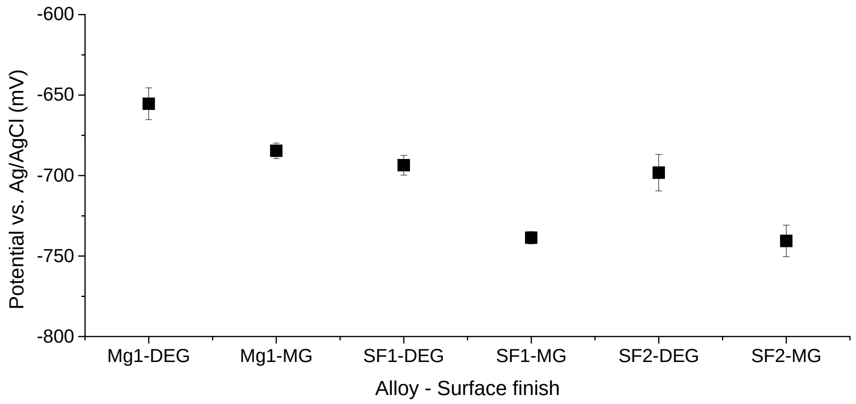

Figure 6-44: Comparison of the difference in E_{pit} values for Mg1, SF1 and SF2, in the DEG and MG surface condition following potentiodynamic polarisation in 3.5 wt.% NaCl.

E_{pit}-E_{corr} showed that Mg1 had an increase in pitting corrosion resistance between the DEG and MG condition, as shown in Table 6-8. SF1 showed a similar pitting corrosion resistance value when the recrystallised grain structure was removed. SF2 showed a reduction from the DEG to MG condition, which is believed to be related to the width of the Cu and Zn rich region, with SF2-MG having a thinner region, thus developing a larger anodic region where dissolution occurs. These results had a direct impact on the amount of charge that developed with both SF1 and SF2 having lower charges passed than Mg1 in the DEG condition, however, when MG SF1 had the lowest charge, followed by Mg1 and SF2 respectively, as shown in Table 6-8. This shows that the E_{pit}-E_{corr} values give a good indication of the pitting corrosion resistance. Overall this shows that SF1 had a higher theoretical corrosion resistance to that of Mg1, however, SF2 could be argued to have a similar corrosion resistance to Mg1. This shows that spray forming / reducing the grain size and alloying Li could improve the corrosion resistance of Al-

Mg alloys. *Moore et al.* [28] showed that spray forming did not appear to impact on the corrosion resistance. The results in this thesis, do, however, suggest that spray forming has an impact on the corrosion resistance. A comparison of the E_{pit}-E_{corr} and charges for the Al-Mg alloys can be seen in Figure 6-45 and Figure 6-46 respectively.

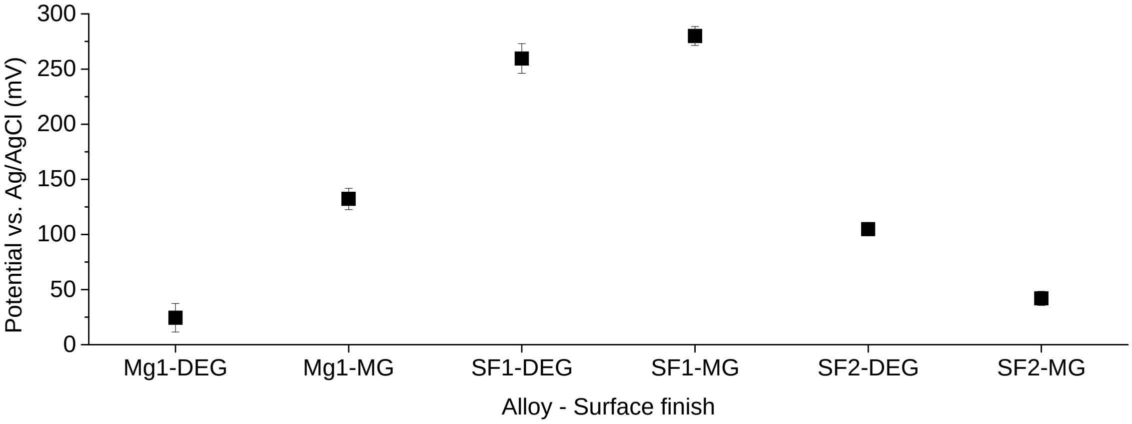

Figure 6-45: Comparison of the difference in E_{pit}-E_{corr} values for Mg1, SF1 and SF2, in the DEG and MG surface condition following potentiodynamic polarisation in 3.5 wt.% NaCl.

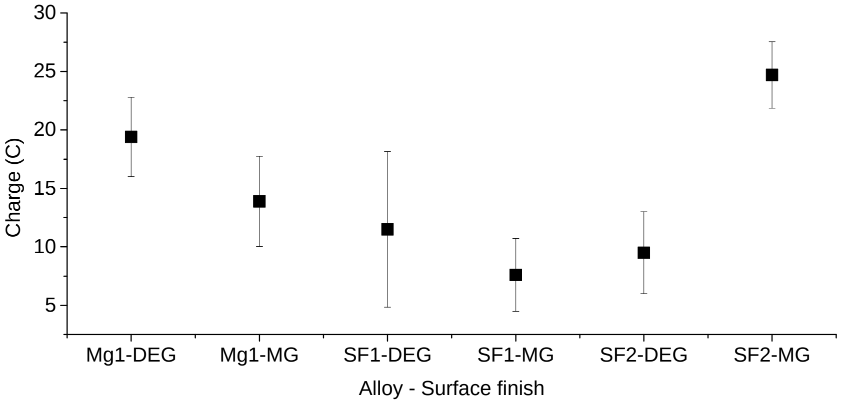

Figure 6-46: Comparison of the amount of charge passed on Mg1, SF1 and SF2, in the DEG and MG surface condition following potentiodynamic polarisation in 3.5 wt.% NaCl.

Comparing Mg1 and SF1 directly it can be seen that trends start to appear. SF2 was not considered, because of the direct impact of the Cu and Zn rich region. It can be seen that by reducing the grain size the E_{corr} and E_{pit} values become less noble, the E_{pit}-E_{corr} values are seen to increase and the charges reduce. This gives a good indication that reducing the grain size had a positive impact on the corrosion resistance. It also suggests that Li does not seem to affect the corrosion resistance.

Visual observations showed that all Al-Mg systems developed faceted pitting corrosion and all of the DEG specimens show large pits developing. In comparison on the MG samples it appeared as if the entire surfaces were undergoing uniform dissolution. Cathodic rich particles were identified within the matrix to be associated with pitting corrosion also [26], [60–64], [80]. It was not expected that IGC would be observed, however, SF1 and SF2 showed what appeared to be IGC, however, further investigations are needed to confirm this. No IGC was seen on Mg1, but it was not expected, however, in SF1 and SF2, highly anodic Mg and Li rich phases could develop on the GBs [25], [35], [39]. SF2 could also form highly cathodic Cu rich particles, so IGC could take place on the SF alloys [26], [60], [63]. One issue with SF1, is due to the large fluctuations in E_{corr} it meant that most of the samples examined did not spend a lot of time above their E_{pit} and as such very little corrosion was observed, which may explain the low charges that pass and the high E_{pit}-E_{corr} values.

Cross-sectioning showed that the pitting corrosion progressed further on the DEG samples of Mg1 and SF1, whereas the MG, Mg1 and SF1 samples showed corrosion that did not progress as deep (see Table 6-8). This shows that in the DEG condition, the fine grain structure was detrimental, but when the recrystallised grains were removed the corrosion depth was less than that of the coarse Mg1 grains. Sub-surface corrosion also formed on SF1, which was shown in the Al-Cu alloy discussion to be associated with electrolyte transfer down GBs into the bulk of specimen, forming sub-surface cavities. In comparison SF2-DEG shows extensive pits that were over 2 mm in length in regions, but SF2-MG showed a uniform dissolution of the surface, to a considerable depth, as shown in Table 6-8. The size of these pits was due to galvanic corrosion around the Cu and Zn rich region. The uniform corrosion on SF2-MG was seen to progress to ~ 20 µm. Overall it shows that SF2-MG had the shallowest pit depths at ~ 20 µm, however, since this covered the entire surface and galvanic corrosion formed pits that were ~ 70 µm in depth, as well as potential IGC, this showed that SF2 had a very poor corrosion resistance. Comparison of Mg1 and SF1, however, show that they performed in very similar manners. The electrochemical data suggested that SF1 would have a much higher corrosion resistance; however, the differences are minimal.

It can therefore be concluded that from the information available spray forming and Li additions do not appear to improve or reduce the corrosion of an Al-Mg alloy. Confirmation of potential GB segregation in the SF alloys could change this conclusion, especially if the existence of IGC is identified.

Chapter 7: Concluding Discussion

A number of questions were posed within the Aims & Objectives of this work following the literature survey, see Section 1.8. This section will look to address these questions by using results from literature and results from this present work.

7.1 Does Li impact on the corrosion resistance of Al alloys?

On the Al-Cu series alloys a question was proposed;

Which offers a higher corrosion resistance, lots of small corrosion sites or a few large corrosion sites?

This question directly relates to whether Li offers an increase in corrosion resistance. Literature has a varied opinion with some authors [3], [5] saying that Li can improve the corrosion resistance and others stating that it reduces it [2], [4], [44], [48]. In this study it has been found that Al-Cu-Li systems form pits and IGC just like other Al-Cu systems, however, the size of the corrosion sites and their volume was different. In that the Al-Cu system examined in this thesis, developed numerous small, shallow pits along with deep IGC, whereas the Al-Cu-Li systems developed very few extremely large corrosion sites from selective grain dissolution and pitting corrosion, as well as shallower IGC. This selective grain dissolution meant large amounts of matrix were dissolved due to differences in grain polarity. This difference, in literature is associated with the highly anodic Li containing T type phases and / or grain stored energy [13], [31], [32], [75], [115], [116]. It did not matter which corrosion experiment results were used, the formation of corrosion on each of the Al-Cu alloys was similar.

Atmospheric corrosion showed that Cu1 developed shallow pitting corrosion but a large amount of IGC, whereas Cu2 and Cu3 formed deeper pits but less or no IGC. Selective grain dissolution, especially in Cu3, was, however, an issue. A friable weakened layer formed on Cu1, compared to large scale localised corrosion on Cu2 and Cu3. They also produced wider and deeper corrosion sites than Cu1. The pits / corrosion cavities from selective grain dissolution on Cu2 and Cu3 following immersion were seen to also form substantial sub-surface cavities, but in comparison to Cu1, the corrosion was deeper. Hence the question of which is better, lots of small pits or a number of extreme pits that are potentially sub-surface. Following atmospheric exposure it was found that less corrosion propagated on SF1 and SF2 than Mg1. IGC was observed, however, on SF1 and SF2.

Electrochemical analysis showed that for immersion testing, Cu2 and Cu3 had very similar OCP trends and potentials; however, Cu2 was more noble. Cu1, however, showed a more noble starting OCP but its value fell significantly with time. The more noble the OCP the higher the corrosion resistance, according to literature [12], [116], [157], [158]. However, in Al-Cu alloys this statement is not entirely accurate as Al-Cu alloys are highly noble yet they develop large amounts of corrosion. Reductions in OCP signify corrosion taking place, which suggests that Cu1 underwent more corrosion than Cu2 and Cu3. After 48 hr's, Cu2 and Cu3 were now more noble than Cu1 and now according to literature, had a higher corrosion resistance [12], [156–158]. SF1 and SF2 had very similar OCP trends and potentials; however, Mg1 was more noble. Mg1 showed a slight reduction in OCP, however, SF1 and SF2 showed significant reductions. This suggests Mg1 had the higher corrosion resistance, throughout the entire period of exposure.

Following potentiodynamic polarisation the E_{pit} for Cu1 was more noble than either of Cu2 or Cu3. A more noble E_{pit} is a sign that the system has a high corrosion resistance, however, with Al-Cu systems this is not the case [12], [156–158]. As such E_{pit} values alone cannot tell whether a system has a good or bad corrosion resistance. None of the Al-Cu alloys showed metastable pitting corrosion, but this is typical of Al-Cu alloys [28]. The Al-Cu-Li alloys even showed similar to higher E_{pit}-E_{corr} values compared to Cu1 and similar to lower charges passing. Following immersion testing and potentiodynamic polarisation the electrochemical results suggest that Al-Cu-Li alloys have a higher corrosion resistance to Al-Cu alloys. The E_{pit} for Mg1 was more noble than either of SF1 or SF2. All showed evidence of metastable pitting after the surface grains were removed, however, prior to this only Mg1 did not show metastable pitting. In each case when the surface grains were removed the E_{pit} became less noble and on Mg1 and SF1 the E_{pit}-E_{corr} values increased alongside reductions in charge. In comparison, SF1 showed the highest E_{pit}-E_{corr} values and lowest charges, suggesting that Li additions improve the corrosion resistance of Al-Mg alloys.

Since Al-Mg alloys have an inherent high corrosion resistance, the impact of Li was harder to identify, especially if it offers an improvement to corrosion resistance. The Li containing Al-Mg alloys were also SF which generates very fine grain structures. No Li was identified during characterisation; however, FEGTEM analysis was not completed and is a recommended area for further work. If Li was identified it would could confirm its association to the IGC that was observed, however, with the information that is present at this stage it has to be assumed that the IGC seen on the SF alloys is related to solute segregation from the spray forming process. β phase should not be observed in SF2, as the Cu and Zn were added to restrict its precipitation to the GBs. However, Al_3MgLi phases could be present in both SF1 and SF2 that could propagate IGC. If the IGC is associated to Li additions, the difference in corrosion resistance is minimal between SF1 and Mg1 and it could be argued that SF1 offers a higher corrosion resistance. A number of factors have to be considered, however, with Mg1 having a very coarse grain structure, which is associated with reduced corrosion resistances and SF1 having a very fine structure, it is difficult to make any firm conclusions. No conclusions can be made regarding SF2 due to the Cu and Zn rich region that creates a large galvanic cell within the area of investigation.

Overall it suggests that Al-Cu-Li alloys have a reduced corrosion resistance to that of Al-Cu systems (even though electrochemical experiments may suggest otherwise). This is primarily through the formation of selective grain dissolution that can propagate sub-surface. They showed less IGC, however, the overall amount of matrix dissolved through corrosion was higher. Once again even though SF1 suggested improved corrosion resistance following electrochemical results, the presence of both IGC and pitting corrosion concludes that Al-Mg-Li alloys had a lower corrosion resistance to the non-Li containing Al-Mg alloy.

7.2 Does spray forming improve corrosion resistance?

Spray forming can refine the microstructure with a dispersion of fine particles along with low levels of internal solute partitioning. Typically thermo-mechanical and / or heat treatments are, however, required to improve the mechanical properties which can subsequently alter the grain size. The main disadvantage is that systems can include porosity, which, in order to be removed, must undergo further heat treatments [28], [51], [130], [131], [133], [165]. This has, however, been shown to promote GB segregation depending on the heat treatment cycles [28], [51], [130], [131], [133], [165]. FEGSEM showed that both SF1 and SF2 had porosity within the structure, demonstrating that further heat treatments were required to optimise their properties, see Figures 3-21 and 3-24.

SF2 cannot be used as a conclusive tool, due to the formation of the Cu and Zn rich region, however, SF1 can be used to give an indication of corrosion resistance. The formation of this Cu and Zn rich region shows that SF alloys may be highly sensitive to thermo-mechanical processing. In the three corrosion environments examined; atmospheric, immersion and potentiodynamic polarisation, many similarities have been found with respect to the corrosion resistances of SF alloys. All experiments showed evidence of pitting corrosion, possible IGC and very similar electrochemical responses.

As previously mentioned following atmospheric exposure it was found that that corrosion progressed less on SF1 and SF2 than Mg1. IGC was observed, however, on SF1 and SF2, this could be related to solute segregation of highly anodic Mg and Li rich phases [25], [35], [39], [134]. Overall this suggests that the SF alloys over a longer immersion time had the propensity to corrode more severely through more corrosion mechanisms.

Immersion testing showed that the SF alloys had a lot of similarities with regards to electrochemical response. SF2 was more noble due to the Cu additions; however, after 96 hr's both had very similar OCP values. Mg1 had a higher starting OCP to both SF1 and SF2 respectively. Overall Mg1 reduced by 14 mV compared to 291 mV and 312 mV for SF1 and SF2 respectively. Mg1 developed faceted and hemispherical pitting corrosion whereas SF1 and SF2 only developed hemispherical pitting. Mg1 underwent entire surface dissolution and localised pitting, whereas only localised pitting corrosion developed on SF1 and SF2. No corrosion depth could be measured on the SF alloys and as such no firm conclusions could be made, however, it can be theorised that the SF alloys had a reduced corrosion resistance compared to Mg1. This can be associated with EDS measurements that showed the reduction in Mg concentration within the matrix and IMCs through sacrificial dissolution. It can also be said that with the reductions in OCP, more corrosion is taking place on the SF alloys compared to Mg1.

Potentiodynamic polarisation showed that SF1 and SF2 had very similar E_{pit} values, which were less noble than Mg1. A more noble E_{pit} is a sign that the system has a high corrosion resistance, as such this offers more evidence to the fact that the SF alloys had a reduced corrosion resistance compared to Mg1 [12], [156–158]. A number of authors [28], [93], [130], [131], [135], [136] have shown that SF Al alloys can lead to a reduction in the E_{pit} by ~ 200 mV. However, if we compare the E_{pit} of SF1 and SF2 to that of Mg1 it can be said that there was < 100 mV difference. Both SF1 and SF2 developed metastable pitting corrosion which Mg1 did not in the degreased surface condition, suggesting a higher corrosion resistance for the SF alloys. When mechanically ground, SF1 no longer developed a metastable pitting region, whereas Mg1 and SF2 did. This meant that the calculated E_{pit}-E_{corr} values were different, with Mg1 increasing, SF1 staying similar and SF2 reducing for the degreased and mechanically ground surface condition respectively. If we discount SF2 due to the Cu and Zn rich region it has to be said that SF1 showed a much higher corrosion resistance to Mg1 with regards to E_{pit}-E_{corr}. Examination of the charge passed also showed lower charges for SF1 compared to Mg1, which directly related to the E_{pit}-E_{corr} values, as in the higher the charge the lower the E_{pit}-E_{corr}.

Following potentiodynamic polarisation it was shown that the pitting corrosion penetrated deeper in the degreased condition, whereas after being mechanically ground these values reduced. This shows that overall, negligible difference between Mg1 and SF1 could be identified. However, since SF1 showed possible IGC it may be said that Mg1 had the higher corrosion resistance which raises the question:

Which is more detrimental IGC or pitting corrosion?

Moore et al. [28], [94] examined Al-Mg and Al-Cu series SF alloys which were both Li containing and found that spray forming did not offer any improvement to the corrosion resistance over non-SF alloys. This is similar to that which has been observed in this thesis, with Mg1 and SF1 in particular having very similar corrosion resistances. A number of authors [28], [93], [130], [131], [135] stated that spray forming increased the corrosion resistance of Al alloys, by increasing the potential at which pitting occurs, however, this thesis and the work shown by *Moore et al.* [28], [94] have shown that visually no significant difference in corrosion resistance has been observed. With regards to E_{pit} it was shown that the E_{pit} values of the SF alloys were less than that of Mg1, thus disagreeing with literature.

This work has been able to show that spray forming had a substantial impact on the electrochemical response (OCP and E_{pit} in particular) of Al alloys. Following atmospheric exposure the SF alloys showed improvements, however, after immersion testing they showed reductions in the corrosion resistance compared to Mg1. Following potentiodynamic polarisation it showed very similar if not improved corrosion resistances to Mg1. This shows that the SF alloys were highly unpredictable and in some cases suggested improved corrosion resistances and in others reductions. Unfortunately it is unknown at this stage whether the differences are purely related to the spray forming process or other elemental additions such as Li to the matrix.

7.3 Does a coarse grain structure show a higher corrosion resistance?

GBs have distinct properties relative to the bulk material in terms of atomic coordination, reactivity and diffusion rates. The proportions of atoms that lie at inter-crystalline regions as a total of the surface area are significant as the grain size decreases. It is therefore not unreasonable to expect regions with high GB densities to exhibit different electrochemical responses to those with lower GB densities. As such it can be expected that a difference in corrosion resistance would be expected between a coarse grain structure and a fine grain structure. Literature has shown that grain size has a significant impact on corrosion, with a number of authors stating that improvements to corrosion can be made by refining the grain structure of Al alloys. *Handel et al.* [78] examined a 6XXX series Al alloy and showed that pitting corrosion progressed to ~ 20 µm on a coarse grain structure (> 500 µm grain diameter) compared to 5 µm on a fine grain structure (< 10 µm grain diameter). Other authors have, however, suggested that the increase in grain size can be detrimental due to the increases in stored energy within the grains and at the GB which can promote accelerated corrosion [13], [46], [75], [113–116].

The Al-Cu-Li alloys were shown to be prone to selective grain dissolution due to the presence of T type phases and / or grain stored energy as reported in the literature [13], [31], [32], [46], [75], [113–116]. The results in this thesis have shown it to be highly detrimental to have large grains in Al-Cu-Li alloys. Potentiodynamic polarisation revealed that the coarse grains on Cu2 were entirely dissolved before the corrosion progressed sub-surface forming extensive corrosion cavities. When these coarse grains were removed from Cu2 via mechanical polishing no evidence of selective grain dissolution was seen. With the grains being a lot smaller it meant less matrix was dissolved.

Atmospheric exposure showed that Cu1 developed large amounts of IGC, which is associated with the θ type phases that cause micro-galvanic cells to form around the GBs, causing large networks to form [26], [63], [75], [80], [84], [85]. Cu3 had a coarse grain structure and the maximum depth of IGC was higher, however, the amount was less due to the reduced GB density. This highlights that fine grains can be detrimental as they allow for an easy path to follow when IGC initiates. Cu2, despite having a fine grain structure did not reveal any IGC (this does not mean that it did not occur), even though it had anodic and cathodic phases along the GBs. In comparison it was shown that the fine grain structures of SF1 and SF2, showed reduced pitting corrosion depth, reinforcing the theory of improved corrosion resistance for fine grain structures. There was, however, evidence of IGC formation, which overall tends to suggest that they had a reduced corrosion resistance.

Immersion testing showed that with the Al-Cu alloys the coarser the grain structure the deeper the pitting corrosion but the shallower the IGC. This shows that coarse grains are more susceptible to pitting corrosion, whereas a fine grain structure can promote accelerated IGC. Immersion testing also showed that the fine grain structures had the more noble OCPs in the Al-Cu alloys, suggesting a reduced corrosion resistance. In comparison, the OCP of the SF alloys was less noble than the coarse Mg1, suggesting fine grain structures / SF alloys have reduced corrosion resistances. Potentiodynamic polarisation of the Al-Cu alloys indicated that the E_{pit}-E_{corr} values increased with reducing grain size. The charges passed also showed a trend in that for the Al-Cu-Li alloys the finer the grain size the lower the charge passed thus the higher the pitting corrosion resistance, however, this was not true for Cu1 which showed the highest charge [71], [72], [74].

For the Al-Mg alloys it can be seen that by reducing the grain size the E_{pit}-E_{corr} values increased and the charges reduced, except on SF1 where the charge increased. This gives a good indication that reducing the grain size increased the corrosion resistance. It was shown after potentiodynamic polarisation that the pitting corrosion depth of SF1 was less than that of Mg1, however, the difference was only 5 µm, suggesting that grain size does not impact Al-Mg alloys as much as other Al alloys. This could, however, be related to the Li additions and / or the spray forming process, which have been discussed above. Overall it was shown that by removing the surface grains of the Al-Mg alloys their respective E_{pit} values became less noble.

This shows that a fine grain size can improve the corrosion resistance of Al alloys, however, not all Al alloy series will respond in the same manner. Reducing the grain size of Al-Mg alloys has been shown to be beneficial; however, reducing the grain size of the Al-Cu alloys can be detrimental. This is because in the Al-Cu alloys segregation of anodic / cathodic phases was seen on the GBs which cause IGC as the finer the grain size the easier path propagation for IGC.

To conclude a fine grain size in general is good for improving the corrosion resistance, however, this is dependent on the segregation on the GBs. In the Al-Mg alloys no segregation was observed. Coarse grains can reduce the volume of IGC; however, typically the depth will be deeper than a fine grain structure.

7.4 How does atmospheric corrosion affect the corrosion of Al alloys?

Atmospheric corrosion is a global concern for its impact on the service life of components For which the main factors that affect atmospheric corrosion include temperature, moisture, rainfall, solar radiation, wind, weathering etc.

Atmospheric corrosion offers a more complex approach in the understanding of how Al alloys corrode when compared to electrochemical techniques where the constituents of the experiments are known. The latter can therefore control the chemistry of the environment, but the question this then raises is; how realistic are electrochemical tests? Especially if exposure to atmospheric conditions shows that impurities within the atmosphere combined with the weather conditions play a major role in the local corrosion chemistries. *Vilche et al.* [129] stated that electrochemical testing of corrosion products is important to see whether they act as passive layers and protect the exposed surface and as such this area has been considered for further work.

The main issue that does arise with atmospheric corrosion is that it is not reproducible and is highly unpredictable. The atmosphere has been shown to be a mixture of dry air, H_2O vapour and gases such as SOx, NOx, Cl^- ions, CO_2, H_2O_2, HCl^-, O_3, O, H_2S, and NaCl particulates, leading to the unpredictable nature of atmospheric corrosion [125]. *Wang et al.* [121] stated that atmospheric exposure, unlike any electrochemical testing method is not a controlled system, meaning it can change from day to day even from hour to hour. *Vilche et al.* [129] also showed that on replicated samples uneven pollutant deposits caused discrepancies in their findings and this was also the case in this thesis, with significant changes in surface chemistries. Month to month changes in surface concentrations were expected, but there were no significant trends that could be identified.

Atmospheric exposure allowed elements and compounds to accumulate on the surface of the specimens over time. Due to the thin film nature of the corrosion, specific compounds could be dissolved into any surface moisture and thus be deposited onto the surface within the corrosion products [122]. EDS identified concentrations of N, Na, O, C, S, Si and Cl^- were present throughout the exposure time on both Al-Cu and Al-Mg series alloys, however, the concentrations of these were not seen to increase. XPS identified that organic matrix material, carbonaceous pollutants, SO_4^{2-}, Al_2O_3, OH^- and in some locations, PO_4^{3-} were the main contaminants.

Vera et al. [122] also utilised XRD to examine the contamination on the surface of AA6201. They also used EDS from which they identified that the main contaminants that were present at industrial locations were Na, Si, S, Cl^-, K and Ca, thus agreeing with many of the results seen in this thesis. XRD was also conducted in this thesis, however, the results were inconclusive and it was assumed that there were not enough corrosion products to be able to distinguish from the Al matrix.

The influence of atmospheric exposure has been said to be characterised in terms of the RH, TOW and exposure time and as such can be split into three categories: dry, wet and damp. Dry oxidation takes place when a surface has a negative free energy, damp films are created at certain critical humidity levels (adsorption of H_2O molecules) and wet is associated with dew, rain, ocean spray etc.

Thin film electrolytes form on metallic surfaces at specific RH levels. When a thin film is present, a balance between the anodic and cathodic regions is created, causing anodic dissolution and cathodic reduction of O to take place. O is readily supplied from the atmosphere to these thin films of H_2O. The H_2O then reacts with the electrons generated from the breakdown of the Al anode, forming $Al(OH)_3$ / AlO(OH) corrosion products. When H_2O is split, the H^+ flows into a pit, creating a highly acidic region over time, which can draw in other contaminant elements in such as Cl^- and at a certain pH, H_2 bubbles could form [19]. With atmospheric exposure the likelihood is that these reactions did not last long, before potentially being diluted by rainfall or the H_2O being evaporated, hence why most of the corrosion sites were not very well established [119]. In can therefore be concluded that the composition of the thin film electrolyte is fundamentally what determines the rate of corrosion.

Knight et al. [124], showed that with increasing humidity the corrosion depth on AA2024 increased. *Wang et al.* [121] found that the Mg ions within AA2024 played a significant role in the corrosion, in the form of an anodic reactant. Analysis of atmospheric conditions in the present work, showed an average RH[20] of 80 % over the entire 12 month exposure, so it can be said that thin film formation was a major contributor to corrosion. The lowest RH recorded was 73 % as such no comparison can be made to a low RH environment to see whether RH had an impact on corrosion depth. The maximum RH was 88 % and was recorded on the 6 month specimens, which shows that high RH levels do have an impact on corrosion, with most of the Al alloys in this thesis observing changes in deposited contamination, primarily in the form of carbonaceous Al products and SO_4^{2-} after 6 months of exposure.

Increased exposure to H_2O can have a 'washing' effect, in that it can remove corrosion products, thus reducing the overall amount of corrosion that takes place as it can also remove any corrosion stimulators and dilute the pH of established corrosion regions. *Mendoza et al.* [119] showed that thick layers of H_2O act as a sink for SO_2 but act as barriers for NO_2, which can in some cases, be detrimental, as it has been shown that on some metallic systems such as Al, NO_2 can actually act as a corrosion inhibitor. The results in this thesis, showed that the TOW changed over the 12 months of exposure, with the specimens examined after 1 month having been exposed to 30 mm of rainfall, compared to 152 mm of rainfall on the 6 month samples. Theory suggests increased TOW should cause an increase in corrosion and corrosion products [67], for which this thesis has shown considerable evidence towards increased corrosion with TOW and RH. This was primarily observed by monitoring the increased pollutant levels on all of the 6 month specimens, with increased levels of S, Si, Cl^-, N and C being recorded. Literature [119] has shown that increased concentrations of pollutants, especially those mentioned, can lead to increased corrosion taking place. Visually no substantial difference in corrosion could be observed, however, due to the slow nature of atmospheric corrosion this is to be expected for a short term exposure.

Other aspects that could affect corrosion, like air pressure, air temperature etc. does not appear to have any impact, using the results in this thesis. In principle these parameters should affect corrosion resistance, with the likes of air pressure and wind speed governing whether pollutants are blown far afield or not. One aspect that could have been changed relates to the time of exposure, the results identified do show that atmospheric corrosion can be observed, but its relation to RH, TOW, air temperature etc. are difficult to conclude. As such the best option would be to increase the time of exposure and this has been suggested for further work.

This thesis and preceding literature shows how unpredictable atmospheric corrosion is, in that trends cannot really be identified. With regards to examining the impact of RH, air temperature, air pressure etc. laboratory examinations are required, because under atmospheric conditions there are too many

---

[20] Relative Humidity measurements obtained from the Loughborough University, Department of Geography

uncontrollable parameters that can affect the results. As such a number of experiments have been suggested as further work.

Chapter 8: Conclusions

8.1 Al-Cu alloys

8.1.1 AA2024-T3 (Cu1)

Cu1 has a large V_f of IMCs of which there were four main types; Al-Cu-Fe-Mn (Cu-rich and Cu-depleted), Al-Cu-Mg and Al-Cu-Mg-Fe-Mn particles. The main precipitates identified were; Al-Cu-Fe-Mn, Al-Cu-Mg [S type phase (Al-Cu-Mg)], Al-Cu-Mn and Al-Cu particles (θ type phase). EBSD revealed a fine, equiaxed grain structure where a recrystallised grain layer was seen at the surface. On each of the three corrosion tests it was shown that Cu1 developed similar corrosion mechanisms, with spherical pits developing, enveloped by corrosion product domes. Faceted pitting and IGC were seen to develop and in all cases IGC progressed deeper than pitting corrosion which ultimately meant that Cu1 developed a weakened friable layer on its surface. Atmospheric corrosion showed large amounts of corrosion product formed on the surface within a short exposure period, highlighting the high activity of Cu1. Immersion testing showed that the OCP reduced with increasing immersion time, indicating corrosion. After calculation of the E_{pit}-E_{corr} values it was seen to be greater for the mechanically ground system, however, both passed a similar charge. Overall this suggested that the fine grain structure offered the higher corrosion resistance.

8.1.2 AA2099-T8E77 extrusion (Cu2)

Cu2 has a low V_f of IMCs of which there were two main types; Al-Cu-Fe-Mn and Al-Cu-Mn particles. The main precipitates identified were; Al-Cu-Zr and Al-Mn-Cu-Fe-Zr. There was, however, a range of fine scale dispersoids present of which extensive levels of T type phases within the grains and on GBs were seen. θ type phases were also seen to form on the GBs and a large V_f of Al_3Zr particles were seen to be distributed throughout the matrix. EBSD showed a fine, equiaxed grain structure with banding of specific grain orientations on the normal direction. EBSD also revealed a coarse recrystallised grain layer at the surface region. Faceted corrosion and IGC were seen to develop, with large scale cavities forming on and below the surface. The coarse recrystallised structure developed selective grain dissolution which accelerated through the specimen at a high rate. The number of corrosion sites that developed were not very substantial, however, there size was. After calculation of the E_{pit}-E_{corr} values it was seen to be greater for the mechanically ground system and the charge was also seen to be lower. Overall this showed that the fine grain structures offered the highest corrosion resistance.

8.1.3 AA2099-T8E77 plate (Cu3)

Cu3 has a low V_f of IMCs throughout the matrix, of which the two main types were; Al-Cu-Mn-Fe and Al-Fe-Mn-Cu particles. The main precipitates identified were; Al-Cu-Zr and Al-Cu-Mn-Fe-Zr particles. There was also a high V_f of T type phases within the grain structure but not at GB locations; extensive θ type phase were also seen on the GBs. EBSD showed a coarse grain structure on all directions and a thick recrystallised grains layer was seen at the surface. Faceted corrosion and IGC were seen to develop and in most cases the corrosion was identified as selective grain dissolution. All grains developed selective grain dissolution, however, this phenomenon was more pronounced on recrystallised grains. The number of corrosion sites that developed were not very substantial, however, there size was. After calculation of the E_{pit}-E_{corr} values it was seen to be greater for the mechanically ground system, however, the charge was seen to be higher. Overall this tentatively suggested an improved corrosion resistance of the finer grain structure as the increased charge could be associated with other surface activity.

8.2 Al-Mg alloys

8.2.1 AA5083-T3510 (Mg1)

Mg1 has a large V_f of IMCs of which there were three main types; Al-Fe-Mn-Mg-Si, Al-Mg-Si and Al-Mn-Si. The main precipitates identified were; Al-Mg-Mn-Fe-Cr-Ti. EBSD revealed a coarse recrystallised grain structure in all three directions, but some fine grain regions were observed throughout the matrix. A distinct elongation of the grain structure was also observed in the extrusion direction. A coarse recrystallised grain layer was also seen at the surface. On each of the corrosion tests it was shown that faceted and hemispherical corrosion developed. The attack was relatively uniform over the entire surface; however, there were instances of localised pitting corrosion. Depth of attack was also seen on all tests to be relatively shallow when compared against the other Al alloys in this thesis. Only Mg1-MG showed a characteristic metastable pitting region, which meant that after calculating the E_{pit}-E_{corr} values it was seen to be greater for the mechanically ground system. Similarly the charge was lower for the mechanically ground system. Overall this suggested an improved corrosion resistance when the recrystallised grains were removed.

8.2.2 Spray formed Al-Mg-Li (SF1)

SF1 has a low V_f of IMCs, of which there were two main types; Al-Mg-Si and Al-Mg-Si-Fe. EBSD revealed a very fine, equiaxed grain structure, where no coarse recrystallised grains were seen at the surface. Faceted and / or hemispherical pitting corrosion formed and what appeared to be IGC was observed, however, no conclusive evidence was acquired. Potentiodynamic polarisation revealed characteristic metastable pitting regions, which meant after the calculation of the E_{pit}-E_{corr} values they were marginally higher for the mechanically ground surface condition, however, both systems had very similar values. However, the mechanically ground samples also showed a higher charge being passed. SF1-DEG developed a high V_f of small and large scale pits whereas SF1-MG showed more uniform dissolution of the entire surface with localised pits developing, following potentiodynamic polarisation. On the immersion and atmospheric samples, evidence of localised pits and IGC were also observed. Overall this suggested an improved corrosion resistance when the surface grains were removed.

8.2.3 Spray formed Al-Mg-Li-Cu-Zn (SF2)

SF2 has a low V_f of IMCs, of which there were two main types; Al-Mg-Si and Al-Mg-Fe-Si. A weld region was observed which had reduced Mg and increased Cu and Zn concentrations to the surrounding matrix. EBSD revealed a very fine, equiaxed grain structure in all three directions. Examination of the Cu and Zn rich region showed that it had the same grain size and as such the only difference to it and the surrounding matrix was its chemical composition. No coarse recrystallised grain layer was observed at the surface. On each of the three corrosion tests faceted corrosion was observed. Faceted and / or hemispherical pitting corrosion formed and what appeared to be IGC was also seen, however, no conclusive evidence was acquired. Potentiodynamic polarisation revealed characteristic metastable pitting regions, which meant after the calculation of the E_{pit}-E_{corr} values they were slightly higher for the degreased surface condition. However, the degreased samples showed the higher charge being passed. Galvanic corrosion around the Cu and Zn rich region was seen to take place, with deep pits forming at the periphery. IGC was also observed only within the Cu and Zn rich region, suggesting some form of Cu segregation effects. On the immersion and atmospheric samples, evidence of localised pits and IGC were also observed. Overall this suggested an improved corrosion resistance when the surface grains were not removed.

8.3 Conclusive statements

- Particles more noble than Al causes initiation sites for corrosion (Fe, Mn, Cu).
- Particles less noble than Al are sacrificially dissolved (Mg, Li).
- θ and T type phases are detrimental to corrosion by forming IGC.
- Multi-component particles like T and S type phases undergo selective dissolution of their anodic component before creating highly cathodic regions accelerating the rate of corrosion.
- Li additions to Al alloys cause changes to the corrosion mechanisms and have been shown to lead to the formation of selective grain dissolution in Al-Cu-Li systems.
- Grain size does impact the corrosion resistance, with fine grains being shown to have a higher corrosion resistance.
- Coarse recrystallised grain structures at the periphery of materials can be detrimental in Al-Cu-Li alloys due to selective grain dissolution.
- All Al alloys investigated in this thesis showed carbonates of Al, $Al_2(SO_4)_3$, NO_x, SO_x and NaCl compounds formed on the surface following 12 months atmospheric exposure in a rural environment.
- SF does not show any substantial improvement to corrosion resistance of Al-Mg alloys.
- Al-Cu alloys show no metastable pitting corrosion region following potentiodynamic polarisation.
- Grain size does not appear to affect E_{pit} on Al-Cu alloys.
- E_{pit} alone cannot be used to give an estimate of corrosion resistance.
- Surface observations alone do not offer enough information to conclude the corrosion resistance of an Al alloy.

Further Work

If more time were available further areas of research would have been examined. In particular these include investigations that would enhance on the current conclusions of this work and areas for which the research should progress to.

Characterisation of the SF alloys using FEGTEM would be beneficial to conclude whether IGC forms. Diffraction analysis of all of the Al alloys would also conclude which phases are present. Utilisation of an EELS system could help to identify the Li containing phases as well as analysis of dislocation densities.

Further analysis of atmospheric exposure conditions by repeating the experiments for a longer exposure period (> 2 years) would allow for a direct comparison of current data and expand on theories to date. XRD and Fourier Transform Infra-Red spectroscopy of the corrosion products should allow for phase identification. Weight loss measurements would be another area that would add to this research especially in helping to identify whether Li additions were detrimental to corrosion of Al-Cu alloys. Laboratory based, atmospheric experiments by conducting electrochemical tests on atmospherically exposed specimens and investigate the impact of changing RH has been shown in literature to demonstrate differences in corrosion resistance and thus would be a useful area of understanding.

Due to the selective grain dissolution of the Al-Cu-Li alloys further research into how this propagates is required. In particular this should involve EBSD analysis of corrosion sites, before and after attack, to observe the grain orientations; mis-orientation indices and stored energy to see if any have a correlation to corrosion.

With the advances in composite structures and their increasing use within the automotive and aerospace industry, the corrosion response of composites when galvanically connected to a metallic system should be a major area of research. With Al-Cu-Li alloys also seeing an increase in use in the aerospace industry a study as to the galvanic corrosion response between these Li containing Al alloys and composite structures, primarily carbon fibre reinforced polymers should be investigated.

Analysis of the corrosion has been examined in depth in this thesis, however, examination of changes to the mechanical properties would add considerable amounts of information to give a more accurate conclusion as to which Al alloys offered the highest corrosion resistance.

All of these areas will enhance the scientific community especially with regards to the Al-Li alloys as there are a finite number to no publications in circulation that examine atmospheric exposure and galvanic corrosion of Al-Li alloys at the time of writing this thesis.

References

[1] J. C. Williams and E. a Starke, “Progress in Structural Materials for Aerospace Systems,” *Acta Materialia*, vol. 51, no. 19, pp. 5775–5799, Nov. 2003.

[2] C. Giummarra, B. Thomas, and R. Rioja, “New Aluminium Lithium Alloys for Aerospace Applications,” in *Proceedings of the Light Metals Technology Conference*, Saint-Sauveur, Quebec, Canada, 2007.

[3] Aircraft Committee on New Materials for Advanced Civil, *New Materials for Next-Generation Commercial Transports*. National Academics Press, 1996.

[4] C. Henon and S. Rouault, “Comparison of corrosion performance and mechanisms of Al-Cu alloys with and without Li additions.,” in *ICAA13: 13th International Conference on Aluminum Alloys*, Pittsburgh, Pennsylvania, USA, 2013.

[5] P. Niskanen, T. Sanders, J. Rinker, and M. Marek, “Corrosion of Aluminium Alloys containing Lithium,” *Corrosion Science*, vol. 22, no. 4, pp. 283 – 304, 1982.

[6] Z. Huang and M. Loretto, “Influence of Lithium additions on precipitation and Age Hardening of 7075 alloy,” *Materials Science and Technology*, vol. 9, pp. 967–980, 1993.

[7] V. John, *Introduction to Engineering Materials*, Third Edit. Palrgave Macmillan, 2003.

[8] M. University of Liverpool, European Aluminium Association, “AluMatter: Alloying and Property Examples.” [Online]. Available: http://aluminium.matter.org.uk/content/html/eng/default.asp?catid=214&pageid=2144417047. [Accessed: 06-Feb-2016].

[9] M. University of Liverpool, European Aluminium Association, “AluMatter: Common Minors, Traces & Unwanted Elements.” [Online]. Available: http://aluminium.matter.org.uk/content/html/eng/default.asp?catid=214&pageid=2144417054. [Accessed: 06-Feb-2016].

[10] F. Mazzolani, *Aluminium Alloy Structure*, Second Edi. E & FN Spon, 1995.

[11] M. University of Liverpool, European Aluminium Association, “AluMatter: Classification of the Wrought Alloy Series.” [Online]. Available: http://aluminium.matter.org.uk/content/html/eng/default.asp?catid=214&pageid=2144417045. [Accessed: 06-Feb-2016].

[12] C. Vargel, *Corrosion of Aluminium*. Elsevier Science, 2004.

[13] C. Luo, “Role of Microstructure on Corrosion Control of AA2024-T3 Aluminium Alloy,” Manchester University, 2011.

[14] I. Polmear, “Aluminium Alloys – A Century of Age Hardening,” *Materials Forum*, vol. 28, pp. 1–14, 2004.

[15] K. Kurt, A. Dursun, B. Dilsizo, G. Anger, and M. Ürgen, “Comparison of the Corrosion Behaviors of Twin-Roll Cast and DC Cast AA 6016 and AA6082 for Automotive Applications,” *The Minerals, Metals and Materials Society*, 2006.

[16] W. Fang, L. Jinshan, H. Rui, and K. Hongchao, “Influence of 1.0 wt % Li on Precipitates in Al-Zn-Mg-Cu Alloy,” *Chinese Journal of Aeronautics*, vol. 21, no. 6, pp. 565–570, 2008.

[17] L. Li, T. Zhou, H. Li, C. Chen, B. Xiong, and L. Shi, “Effect of additional elements on aging behaviour of Al-Zn-Mg-Cu alloys by spray forming,” *Transactions of Nonferrous Metals Society of China*, vol. 16, no. 3, pp. 532–538, Jun. 2006.

[18] D. Cao, L. Wu, Y. Sun, G. Wang, and Y. Lv, “Electrochemical behavior of Mg – Li , Mg – Li – Al and Mg – Li – Al – Ce in sodium chloride solution,” *Journal of Power Sources*, vol. 177, no. 2, pp. 624–630, 2008.

[19] G. Frankel, “Pitting Corrosion of Metals: A Review of the Critical Factors,” *J. Electrochem. Soc.*, vol. 145, no. 6, pp. 2186–2198, 1998.

[20] J. Kruger, “Electrochemistry of Corrosion,” 2001. [Online]. Available: http://knowledge.electrochem.org/encycl/art-c02-corrosion.htm. [Accessed: 06-Feb-2016].

[21] D. Apelian, “Aluminium Cast Alloys: Enabling Tools for Improved Performance,” 2009. [Online]. Available: http://www.diecasting.org/research/wwr/WWR_AluminiumCastAlloys.pdf. [Accessed: 21-May-2012].

[22] P. C. King, I. S. Cole, P. a. Corrigan, A. E. Hughes, T. H. Muster, and S. Thomas, “FIB / SEM study of AA2024 corrosion under a seawater drop : Part I,” *Corrosion Science*, vol. 53, no. 3, pp. 1086–1096, Mar. 2011.

[23] Y. Ma, “Effect of Microstructure on corrosion resistance and anodising behaviour of AA 2099-T8 aluminium alloy,” Manchester University, 2010.

[24] R. Buchheit, R. Grant, P. Hlava, B. Mckenzie, and G. Zender, “Local Dissolution Phenomena Associated With S Phase (Al 2 CuMg) Particles in Aluminum Alloy 2024-T3,” *Journal of Electrochemical Society*, vol. 144, no. 8, pp. 2621–2628, 1997.

[25] W. Da Ren, J. Li, Z. Zheng, and W. Chen, “Localized corrosion mechanism associated with precipitates containing Mg in Al alloys,” *Transactions of Nonferrous Metals Society of China*, vol. 17, pp. 727–732, 2007.

[26] N. Birbilis and R. G. Buchheit, “Electrochemical Characteristics of Intermetallic Phases in Aluminum Alloys An Experimental Survey and Discussion,” *Journal of The Electrochemical Society*, vol. 152, no. 4, pp. 140–151, 2005.

[27] S. Adhikari and K. Hebert, “Factors controlling the time evolution of the corrosion potential of Aluminum in alkaline solutions,” *Corrosion Science*, vol. 50, no. 5, pp. 1414–1421, 2008.

[28] K. Moore, J. Sykes, S. Hogg, and P. Grant, “Pitting corrosion of spray formed Al – Li – Mg alloys,” *Corrosion Science*, vol. 50, no. 11, pp. 3221–3226, 2008.

[29] L. Lacroix, C. Blanc, N. Pébère, G. Thompson, B. Tribollet, and V. Vivier, “Simulating the galvanic coupling between S-Al2CuMg phase particles and the matrix of 2024 aerospace aluminium alloy,” *Corrosion Science*, vol. 64, pp. 213–221, Nov. 2012.

[30] W. R. and Z. Z. J. Li, W. Chen, X. Zhao, “Corrosion behavior of 2195 and 1420 A1-Li alloys in neutral 3.5% NaCl solution under tensile stress,” *Transactions of Nonferrous Metals Society of China*, vol. 16, pp. 1171–1177, 2006.

[31] J. Li, C. Li, Z. Peng, W. Chen, and Z. Zheng, “Corrosion mechanism associated with T1 and T2 precipitates of Al–Cu–Li alloys in NaCl solution,” *Journal of Alloys and Compounds*, vol. 460, no. 1–2, pp. 688–693, Jul. 2008.

[32] J. Li, Z. Zheng, W. Ren, W. Chen, X. Zhao, and S. Li, “Simulation on function mechanism of T 1 (Al2CuLi) precipitate in localized corrosion of Al-Cu-Li alloys,” *Transactions of Nonferrous Metals Society of China*, vol. 16, no. 50401012, pp. 1268–1273, 2006.

[33] Y. J. Gu, A. Wahab, Z. Huang, Y. G. Zhang, and C. Q. Chen, “The structure transformation in an Al–Li–Zn–Mg–Cu–Zr alloy,” *Materials Science and Engineering A*, vol. 316, pp. 39–45, 2001.

[34] G. Svenningsen, J. Lein, A. Bjørgum, J. Nordlien, Y. Yu, and K. Nisancioglu, “Effect of low copper content and heat treatment on intergranular corrosion of model AlMgSi alloys,” *Corrosion Science*, vol. 48, no. 1, pp. 226–242, Jan. 2006.

[35] K. Blommedal, “Corrosion Development in Welded AA6082 Alloys,” 2013.

[36] Q. Meng and G. Frankel, “Effect of Cu Content on Corrosion Behavior of 7xxx Series Aluminum Alloys,” *Journal of The Electrochemical Society*, vol. 151, no. 5, pp. B271 – B283, 2004.

[37] I. Polmear, *Light Alloys: Metallurgy of the Light Metals*, Second Edi. Edward Arnold Publishing, 1989.

[38] R. Goswami, G. Spanos, P. Pao, and R. Holtz, “Precipitation behavior of the beta phase in Al-5083,” *Materials Science & Engineering A*, 2009.

[39] H. Ezuber, A. El-Houd, and F. El-Shawesh, “A study on the corrosion behavior of Aluminum Alloys in seawater,” *Materials and Design*, vol. 29, pp. 801–805, 2008.

[40] Z. Du, T. Zhou, C. Chen, P. Liu, and B. Dong, “Quantitative analysis of precipitation in an Al – Zn – Mg – Cu – Li alloy,” *Materials Characterization*, vol. 55, no. 1, pp. 75–82, 2005.

[41] A. Joshi, “Lithium Aluminium Alloys – The New Generation Aerospace Alloys Junior Research Fellow Commercial Al-Li Alloys Physical Properties of Al-Li alloys Property.”

[42] P. Bai, T. Zhou, P. Liu, Y. Zhang, and C. Chen, “Effects of lithium addition on precipitation in Li-containing Al – Zn – Mg – Cu alloy,” *Materials Letters*, vol. 58, pp. 3084–3087, 2004.

[43] D. Liu and D. Williams, “Accurate Quantification of Lithium in Aluminium-Lithium Alloys with Electron Energy-Loss Spectrometry,” *Mathematical and Physical Sciences*, vol. 425, no. 1868, pp. 91–111.

[44] T. Pasang, N. Symonds, S. Moutsos, R. Wanhill, and S. Lynch, “Low-energy intergranular fracture in Al–Li alloys,” *Engineering Failure Analysis*, vol. 22, pp. 166–178, Jun. 2012.

[45] N. Below, D. Eskin, and A. Aksenov, *Multicomponent Phase Diagrams: Applications for Commercial Aluminium Alloys*. Elsevier, 2005.

[46] Y. Ma, X. Zhou, G. Thompson, T. Hashimoto, P. Thomson, and M. Fowles, “Distribution of Intermetallics in an AA 2099-T8 Aluminium Alloy extrusion,” *Materials Chemistry and Physics*, vol. 126, no. 1–2, pp. 46–53, Mar. 2011.

[47] P. Taylor, H. Djaaboube, D. Physique, U. Mentouri, R. Ain, and E. Bey, “TEM diffraction study of Al 2 CuMg (S ′ / S) precipitation in an Al – Li – Cu – Mg (Zr) alloy,” *Taylor & Francis*, no. October, pp. 37–41, 2012.

[48] C. Zhang, X. Huang, M. Zhang, L. Gao, and R. Wu, “Electrochemical characterization of the corrosion of a Mg–Li Alloy,” *Materials Letters*, vol. 62, no. 14, pp. 2177–2180, May 2008.

[49] F. King, *Aluminium and its Alloys*. Chichester: Ellis Horwood, 1987.

[50] F. Meng, Z. Chai, J. Li, H. Bian, and Y. Wang, “Small-angle X-ray scattering study of the d 0 phase growth kinetic in 1420 Al – Li alloy,” *Materials Characterization*, vol. 47, pp. 43–46, 2001.

[51] S. Hogg, I. Palmer, L. Thomas, and P. Grant, “Processing , microstructure and property aspects of a spraycast Al – Mg – Li – Zr alloy,” *Acta Materialia*, vol. 55, pp. 1885–1894, 2007.

[52] B. Wei, C. Chen, Z. Huang, and Y. Zhang, “Aging behavior of Li containing Al–Zn–Mg–Cu alloys,” *Materials Science and Engineering A*, vol. 280, pp. 161–167, 2000.

[53] L. Ye, X. Zhang, D. Zheng, S. Liu, and J. Tang, “Superplastic behavior of an Al–Mg– Li alloy,” *Journal of Alloys and Compounds*, vol. 487, pp. 109–115, 2009.

[54] C. Wolverton, “Solute–vacancy binding in aluminum,” *Acta Materialia*, vol. 55, no. 17, pp. 5867–5872, Oct. 2007.

[55] M. Carroll, P. Gouma, G. Daehn, and M. Mills, “Effects of minor Cu additions on a Zn-modified Al-5083 alloy,” *Materials Science and Engineering A*, vol. 321, pp. 425–428, 2001.

[56] K. Dinsdale, B. Noble, and S. J. Harris, “Development of Mechanical Properties in AI-Li-Zn-Mg-Cu Alloys,” *Materials Science and Engineering*, vol. 104, pp. 75–84, 1988.

[57] D. M. and P. G. R. Buchheit, “Grain boundary corrosion and stress corrosion cracking studies of al-li-cu alloy AF/C458,” pp. 2–10.

[58] M. Carroll, P. Gouma, M. Mills, G. Daehn, and B. Dunbar, “Effects of Zn additions on the grain boundary precipitation and corrosion of Al-5083,” *Scripta Materialia*, vol. 42, no. 4, pp. 335–340, 2000.

[59] P. Kobe, M. MIlls, K. Unocic, and G. Daehn, “Grain Boundary Precipitate Modification for Improved Intergranular Corrosion Resistance,” *Materials Science Forum*, vol. 519–521, pp. 327–332, 2006.

[60] R. Ambat, A. Davenport, G. Scamans, and A. Afseth, “Effect of iron-containing intermetallic particles on the corrosion behaviour of aluminium,” *Corrosion Science*, vol. 48, no. 11, pp. 3455–3471, 2006.

[61] Z. Szklarska-Smialowska, “Insight into the pitting corrosion behaviour of aluminium alloys,” *Corrosion Science*, vol. 33, no. 8, pp. 1193–1202, 1992.

[62] Z. Szklarska-Smialowska, “Pitting corrosion of Aluminum,” *Corrosion Science*, vol. 41, pp. 1743–1767, 1999.

[63] K. Yasakau, M. Zheludkevich, S. Lamaka, and M. Ferreira, “Role of intermetallic phases in localized corrosion of AA5083,” *Electrochimica Acta*, vol. 52, pp. 7651–7659, 2007.

[64] J. Chang and T. Chuang, “The Degradation of Corrosion Resistance for Al 5083 Alloy after Thermal and Superplastic Forming Processes,” *Journal of Materials Engineering and Performance*, vol. 9, no. February, pp. 253–260, 2000.

[65] P. Cavaliere, E. Cerri, and P. Leo, “A Study of the Response of a Zr-modified 2014 Aluminium Alloy Subjected to Fatigue Loading,” *Materials Forum*, vol. 28, pp. 172–177, 2004.

[66] N. J and J. D, “Influence of Zr addition on the microstructure evolution and thermal stability of Al – Mg – Mn alloy processed by ECAP at elevated temperature,” *Materials Science and Engineering A*, vol. 453, pp. 552–557, 2007.

[67] S. Syed, “Atmospheric corrosion of materials,” vol. 11, no. 1, pp. 1–24, 2006.

[68] G. Svenningsen, “Corrosion of Aluminium Alloys,” 1992. [Online]. Available: http://www.sintef.no/static/mt/norlight/seminars/norlight2003/postere/gaute svenningsen.pdf. [Accessed: 14-May-2012].

[69] B. Strohmeier, “An ESCA Method for Determining the Oxide Thickness on Aluminum Alloys,” *Surface and Interface Analysis*, vol. 15, pp. 51–56, 1990.

[70] A. Aballe, M. Bethencourt, F. Botana, M. Cano, and M. Marcos, “Localized alkaline corrosion of alloy AA5083 in neutral 3.5% NaCl solution,” *Corrosion Science*, vol. 43, no. 9, pp. 1657–1674, Sep. 2001.

[71] K. Ralston, D. Fabijanic, and N. Birbilis, “Effect of grain size on corrosion of high purity aluminium,” *Electrochimica Acta*, vol. 56, no. 4, pp. 1729–1736, Jan. 2011.

[72] K. Ralston, N. Birbilis, and C. Davies, “Revealing the relationship between grain size and corrosion rate of metals,” *Scripta Materialia*, vol. 63, no. 12, pp. 1201–1204, Dec. 2010.

[73] J. Brunner, N. Birbilis, K. Ralston, and S. Virtanen, “Impact of ultrafine-grained microstructure on the corrosion of aluminium alloy AA2024,” *Corrosion Science*, vol. 57, pp. 209–214, Apr. 2012.

[74] S. Gollapudi, “Grain size distribution effects on the corrosion behaviour of materials,” *Corrosion Science*, vol. 62, pp. 90–94, Sep. 2012.

[75] C. Luo, X. Zhou, G. Thompson, and A. Hughes, “Observations of intergranular corrosion in AA2024-T351: The influence of grain stored energy,” *Corrosion Science*, vol. 61, pp. 35–44, Aug. 2012.

[76] A. Davenport, Y. Yuan, R. Ambat, B. Connolly, M. Strangwood, A. Afseth, and G. Scamans, “Intergranular Corrosion and Stress Corrosion Cracking of Sensitised AA5182,” *Materials Science Forum*, vol. 519–521, pp. 641–646, 2006.

[77] S. Lillard, “Relationships Between Pitting Corrosion and Crystallographic Orientation, An Historical Perspective,” vol. 291. 2001.

[78] M. Händel, D. Nickel, and T. Lampke, “Effect of different grain sizes and textures on the corrosion behaviour of aluminum alloy AA6082,” *Materialwissenschaft und Werkstofftechnik*, vol. 42, no. 7, pp. 606–611, Jul. 2011.

[79] P. Campestrini, E. van Westing, H. van Rooijen, and J. de Wit, “Relation between microstructural aspects of AA2024 and its corrosion behaviour investigated using AFM scanning potential technique,” *Corrosion Science*, vol. 42, no. 11, pp. 1853–1861, Nov. 2000.

[80] A. Aballe, M. Bethencourt, and F. Botana, “Influence of the cathodic intermetallics distribution on the reproducibility of the electrochemical measurements on AA5083 alloy in NaCl solutions,” *Corrosion*, vol. 45, no. 1, pp. 161–180, 2003.

[81] N. Alexopoulos, C. Dalakouras, P. Skarvelis, and S. Kourkoulis, “Accelerated corrosion exposure in ultra thin sheets of 2024 aircraft aluminium alloy for GLARE applications,” *Corrosion Science*, vol. 55, pp. 289–300, Feb. 2012.

[82] Y. Cheng, Z. Zhang, F. Cao, J. Li, J. Zhang, J. Wang, and C. Cao, “A study of the corrosion of aluminum alloy 2024-T3 under thin electrolyte layers,” *Corrosion Science*, vol. 46, no. 7, pp. 1649–1667, Jul. 2004.

[83] J. Idrac, G. Mankowski, G. Thompson, P. Skeldon, Y. Kihn, and C. Blanc, “Galvanic corrosion of aluminium – copper model alloys,” *Electrochimica Acta*, vol. 52, pp. 7626–7633, 2007.

[84] A. Boag, A. Hughes, A. Glenn, T. Muster, and D. McCulloch, “Corrosion of AA2024-T3 Part I: Localised corrosion of isolated IM particles,” *Corrosion Science*, vol. 53, no. 1, pp. 17–26, Jan. 2011.

[85] W. Zhang and G. Frankel, “Transitions between pitting and intergranular corrosion in AA2024,” *Electrochimica Acta*, vol. 48, pp. 1193–1210, 2003.

[86] A. Trueman, “Determining the probability of stable pit initiation on aluminium alloys using potentiostatic electrochemical measurements,” *Corrosion Science*, vol. 47, no. 9, pp. 2240–2256, 2005.

[87] S. Pride, J. Scully, and J. Hudson, “Metastable Pitting of Aluminum and Criteria for the Transition to Stable Pit Growth,” *Journal of Electrochemical Society*, vol. 141, no. 11, pp. 3028–3040, 1994.

[88] H. Leckie, “A contribution to the Applicability of Critical Pitting Potentials,” *Journal of Electrochemical Society*, vol. 117, no. 9, pp. 1152–1154, 1970.

[89] A. Broli and H. Holtan, “Use of Potentiokinetic methods for the determination of characteristic potentials for pitting corrosion of aluminium in a deaerated solution of 3 % NaCl,” *Corrosion Science*, vol. 13, pp. 237–246, 1973.

[90] “Pourbaix Diagrams.” [Online]. Available: http://neural.bioengineering.gmu.edu/subpages/ece590s08/Pourbaix.pdf. [Accessed: 23-Apr-2012].

[91] P. Natishan, E. McCafferty, and G. Hubler, “The Effect of pH of Zero Charge on the Pitting Potential,” *Journal of Electrochemical Society*, vol. 133, no. 5, pp. 1061–1062, 1986.

[92] R. Newman, “Local chemistry considerations in the tunneling corrosion of aluminium,” *Corrosion Science*, vol. 37, no. 3, pp. 527–533, 1995.

[93] K. Moore, “Pitting Corrosion of Spray Formed Aluminium Aerospace Alloys,” Oxford University, 2007.

[94] K. Moore, J. Sykes, and P. Grant, “An electrochemical study of repassivation of aluminium alloys with SEM examination of the pit interiors using resin replicas,” *Corrosion Science*, vol. 50, no. 11, pp. 3233–3240, 2008.

[95] D. Battocchi, J. He, G. Bierwagen, and D. Tallman, “Emulation and study of the corrosion behavior of Al alloy 2024-T3 using a wire beam electrode (WBE) in conjunction with scanning vibrating electrode technique (SVET),” *Corrosion Science*, vol. 47, no. 5, pp. 1165–1176, May 2005.

[96] C. Liao and R. Wei, “Galvanic coupling of model alloys to aluminum — a foundation for understanding particle-induced pitting in aluminum alloys,” *Electrochimica Acta*, vol. 45, pp. 881–888, 1999.

[97] G. Williams, A. Coleman, H. McMurray, and N. Mcmurray, “Inhibition of Aluminium Alloy AA2024-T3 pitting corrosion by copper complexing compounds,” *Electrochimica Acta*, vol. 55, no. 20, pp. 5947–5958, Aug. 2010.

[98] A. Aballe, M. Bethencourt, and F. Botana, “Influence of the degree of polishing of alloy AA 5083 on its behaviour against localised alkaline corrosion,” *Corrosion Science*, vol. 46, pp. 1909–1920, 2004.

[99] K. Deshpande, “Validated numerical modelling of galvanic corrosion for couples : Magnesium alloy (AE44)– mild steel and AE44 – aluminium alloy (AA6063) in brine solution,” *Corrosion Science*, vol. 52, no. 9, pp. 2819–2826, Sep. 2010.

[100] K. Deshpande, “Experimental investigation of galvanic corrosion: Comparison between SVET and immersion techniques,” *Corrosion Science*, vol. 52, no. 9, pp. 2819–2826, Sep. 2010.

[101] R. Revie, *Corrosion and corrosion control: An introduction to corrosion science and engineering*. New Jersey: John Wiley & Sons, 2008.

[102] E. Ghali, *Corrosion resistance of Aluminium and Magnesium Alloys: Understanding, performance and testing*. Canada: John Wiley & Sons, 2010.

[103] C. Panagopoulos, E. Georgiou, and A. Gavras, “Corrosion and wear of 6082 aluminum alloy,” *Tribology International*, vol. 42, no. 6, pp. 886–889, Jun. 2009.

[104] S. Agarwal, P. Krajewski, and C. Briant, “Texture Development and Dynamic Recrystallization in AA5083 During Superplastic Forming at Various Strain Rates,” *Strain*.

[105] U. Agarwala, *New Methods for Corrosion testing of Aluminium Alloys*. Philadelphia, USA: American Society for Testing and Materials, 1992.

[106] L. Tan and T. Allen, “Effect of thermomechanical treatment on the corrosion of AA5083,” *Corrosion Science*, vol. 52, no. 2, pp. 548–554, 2010.

[107] S. Jain, M. Lim, J. Hudson, and J. Scully, “Spreading of intergranular corrosion on the surface of sensitized Al-4.4Mg alloys: A general finding,” *Corrosion Science*, vol. 59, pp. 136–147, Jun. 2012.

[108] M. Larsen, “Effect of composition and thermomechanical processing on the intergranular corrosion of AA6000 Aluminium Alloys,” 2010.

[109] G. Svenningsen, M. Larsen, J. Nordlien, and K. Nisancioglu, “Effect of thermomechanical history on intergranular corrosion of extruded AlMgSi(Cu) model alloy,” *Corrosion Science*, vol. 48, no. 12, pp. 3969–3987, Dec. 2006.

[110] D.Lloyd and S. Esmaeili, “The role of copper in the precipitation kinetics of 6000 series Al alloys,” *Materials Science Forum*, vol. 519–521, pp. 169–176, 2006.

[111] G. Svenningsen and M. Hurlen, “Effect of high temperature heat treatment on intergranular corrosion of AlMgSi (Cu) model alloy,” *Corrosion*, vol. 48, pp. 258–272, 2006.

[112] G. Svenningsen, M. Larsen, J. Nordlien, K. Nisancioglu, and J. Walmsley, “Effect of artificial aging on intergranular corrosion of extruded AlMgSi alloy with small Cu content,” *Corrosion Science*, vol. 48, no. 6, pp. 1528–1543, Jun. 2006.

[113] A. Williams, “Microstructural Analysis of Aluminium Alloy 2096 as a Function of Heat Treatment,” The University of Birmingham, United Kingdom, 2010.

[114] T. Dorin, A. Deschamps, F. De Geuser, W. Lefebvre, and C. Sigli, “Quantitative description of the T 1 formation kinetics in an Al–Cu–Li alloy using differential scanning calorimetry, small-angle X-ray scattering and transmission electron microscopy,” *Philosophical Magazine*, vol. 94, no. 10, pp. 1012–1030, Feb. 2014.

[115] V. Proton, J. Alexis, E. Andrieu, J. Delfosse, A. Deschamps, F. De Geuser, M. Lafont, and C. Blanc, “The influence of artificial ageing on the corrosion behaviour of a 2050 aluminium–copper–lithium alloy,” *Corrosion Science*, vol. 80, pp. 494–502, Mar. 2014.

[116] Y. Xu, X. Wang, Z. Yan, and J. Li, “Corrosion Properties of Light-weight and High-strength 2195 Al-Li Alloy,” *Chinese Journal of Aeronautics*, vol. 24, no. 5, pp. 681–686, Oct. 2011.

[117] Y. Liu, Z. Wang, and W. Ke, “Study on influence of native oxide and corrosion products on atmospheric corrosion of pure Al,” *Corrosion Science*, vol. 80, pp. 169–176, Mar. 2014.

[118] F. Hernández, J. Santana, R. Souto, S. González, and J. Morales, “Characterization of the Atmospheric Corrosion of Aluminum in Archipelagic Subtropical Environments,” vol. 6, pp. 6567–6580, 2011.

[119] A. Mendoza and F. Corvo, “Outdoor and indoor atmospheric corrosion of non-ferrous metals,” *Corrosion Science*, vol. 42, no. 7, pp. 1123–1147, Jul. 2000.

[120] D. Blücher, *Carbon Dioxide: The Unknown Factor in the Atmospheric Corrosion of Light Metals A Laboratory Study*. 2005.

[121] B. Wang, Z. Wang, W. Han, and W. Ke, “Atmospheric corrosion of aluminium alloy 2024-T3 exposed to salt lake environment in Western China,” *Science*, vol. 59, pp. 63–70, 2012.

[122] R. Vera, D. Delgado, and B. Rosales, “Effect of atmospheric pollutants on the corrosion of high power electrical conductors: Part 1. Aluminium and AA6201 alloy,” *Corrosion Science*, vol. 48, no. 10, pp. 2882–2900, Oct. 2006.

[123] A.Radharkrishnan and B.Ganesh, “Estimation of Microbiologically Influenced Corrosion of Aluminium Alloy in Natural Aqueous Environment,” *Nature and Science*, vol. 4, no. 3, pp. 1–4, 2006.

[124] S. Knight, M. Salagaras, and A. Trueman, “The study of intergranular corrosion in aircraft aluminium alloys using X-ray tomography,” *Corrosion Science*, vol. 53, no. 2, pp. 727–734, Feb. 2011.

[125] Z. Dan, I. Muto, and N. Hara, “Constant Dew Point Corrosion Tests for Metals,” 2014.

[126] S. Sun, Q. Zheng, D. Li, and J. Wen, “Long-term atmospheric corrosion behaviour of aluminium alloys 2024 and 7075 in urban, coastal and industrial environments,” *Corrosion Science*, vol. 51, no. 4, pp. 719–727, Apr. 2009.

[127] H. Townsend, *Outdoor Atmospheric Corrosion, Issue 1421*. Philadelphia, USA: American Society for Testing and Materials, 2002.

[128] W. Zhen-yao, MA.Tang, H. Wei, and Y. Guo-cai, “Corrosion behavior on aluminum alloy LY 12 in simulated atmospheric corrosion process,” *Metals, Nonferrous*, no. 50499331, 2007.

[129] J. Vilche, F. Varela, E. Codaro, and B. Rosales, “A survey corrosion: of Argentinean Atmospheric Aluminium and Zinc Samples,” vol. 37, no. 6, pp. 941–961, 1995.

[130] P. Grant, “Spray Forming,” *Progress in Materials Science*, vol. 39, pp. 497 – 545, 1995.

[131] K. Raju, S. Ojha, and A. Harsha, “Spray forming of aluminium alloys and its composites: an overview,” *Journal of Materials Science*, vol. 43, no. 8, pp. 2509–2521, Feb. 2008.

[132] S. Dai, J. Delphanque, and E. Lavernia, “Grain growth in reactive spray deposited 5083 alloys,” *Scripta Materialia*, vol. 40, no. 2, pp. 145–151, 1999.

[133] J. Mi, P. Grant, U. Fritsching, O. Belkessam, I. Garmendia, and A. Landaberea, “Multiphysics modelling of the spray forming process,” *Materials Science and Engineering A*, vol. 477, pp. 2–8, 2008.

[134] K. Mingard, B. Cantor, I. Palmer, I. Hughes, P. Alexander, T. C. Willis, and J. White, “Macro-segregation in Aluminium Alloys sprayformed billets,” *Acta Metallurgica*, vol. 48, pp. 2435–2449, 2000.

[135] Z. Wang and P. Prangnell, “Microstructure refinement and mechanical properties of severely deformed Al – Mg – Li alloys,” *Materials Science and Engineering*, vol. 328, pp. 87–97, 2002.

[136] G. Frankel, M. Russak, C. Jahnes, M. Mirzamaani, and V. Brusic, “Pitting of Sputtered Aluminum Alloy Thin Films,” *Journal of The Electrochemical Society*, vol. 136, no. 4, pp. 1243–1244, 1989.

[137] MetPrep, “MetPrep consumables.” [Online]. Available: http://www.metprep.co.uk/hot-mounting-compounds/ . [Accessed: 30-Jan-2016].

[138] A. Scientific, “Lacomit varnish and remover.” [Online]. Available: http://www.agarscientific.com/lacomit-varnish-and-remover.html. [Accessed: 30-Jan-2016].

[139] ALCOA, “Alloy 2099-T83 and 2099-T8E67 Extrusions,” 2005. [Online]. Available: http://www.alcoa.com/adip/catalog/pdf/Alloy2099TechSheet.pdf. [Accessed: 21-Jan-2013].

[140] ALCOA, “Alloy 2024 Sheet and Plate,” 2005. [Online]. Available: http://www.alcoa.com/mill_products/catalog/pdf/alloy2024techsheet.pdf. [Accessed: 21-Jan-2013].

[141] Basi, “BASI Reference Electrodes.” [Online]. Available: http://www.basinc.com/products/ec/ref.php. [Accessed: 30-Jan-2016].

[142] N. L. Sukiman, X. Zhou, N. Birbilis, A. E. Hughes, J. M. C. Mol, S. J. Garcia, and G. E. Thompson, *Aluminium Alloys - New Trends in Fabrication and Applications*. 2012, p. Chapter 2.

[143] S. Ltd, “Struers Ltd: Consumables.” [Online]. Available: http://www.struers.co.uk/default.asp?top_id=3&doc_id=282. [Accessed: 30-Jan-2016].

[144] Leco, “Leco Consumables.” [Online]. Available: http://www.leco.com/#. [Accessed: 30-Jan-2016].

[145] J. J. Bozzola and L. D. Russell, *Electron Microscopy: Principles and Techniques for Biologists*. Jones & Bartlett Learning, 1999.

[146] D. Henry, “Electron-Sample Interactions.” [Online]. Available: http://serc.carleton.edu/research_education/geochemsheets/electroninteractions.html. [Accessed: 27-Feb-2016].

[147] B. department Smith College, “Scanning Electron Microscope: Machine Variables.” [Online]. Available: http://131.229.88.77/microscopy/semvar.html. [Accessed: 27-Feb-2016].

[148] O. Instruments, “Representation of Grains and Grain Boundaries.” [Online]. Available: http://www.ebsd.com/ebsd-analysis/types-of-ebsd-experiment/representation-of-grains-and-grain-boundaries. [Accessed: 27-Feb-2016].

[149] J. F. Mongillo, *Nanotechnology 101*. ABC-CLIO, 2007.

[150] N. P. Laboratory, “Introduction to XPS – X-Ray Photoelectron Spectroscopy,” 2012. [Online]. Available: http://www.npl.co.uk/science-technology/surface-and-nanoanalysis/surface-and-nanoanalysis-basics/introduction-to-xps-x-ray-photoelectron-spectroscopy. [Accessed: 27-Feb-2016].

[151] R. Hodgkins, “Loughborough University, Meteorological data 2013-2014.” Loughborough University, Geography Department, Loughborough, Leicestershire.

[152] S. C. Wang and M. J. Starink, “Precipitates and intermetallic phases in precipitation hardening Al–Cu–Mg–(Li) based alloys,” *International Materials Reviews*, vol. 50, no. 4, pp. 193–215, Aug. 2005.

[153] I. C. Hsiao and J. C. Huang, “DEVELOPMENT OF LOW TEMPERATURE SUPERPLASTICITY IN COMMERCIAL 5083 Al-Mg ALLOYS,” *Acta Metallurgica*, vol. 40, no. 6, pp. 697–703, 1999.

[154] A. Glenn, T. Muster, C. Luo, X. Zhou, G. Thompson, A. Boag, and A. Hughes, “Corrosion of AA2024-T3 Part III: Propagation,” *Corrosion Science*, vol. 53, no. 1, pp. 40–50, Jan. 2011.

[155] E. Hughes, A. Boag, A. Glenn, D. McCulloch, T. Muster, C. Ryan, C. Luo, X. Zhou, G. Thompson, and A. Hughes, “Corrosion of AA2024-T3 Part II: Co-operative corrosion,” *Corrosion Science*, vol. 53, no. 1, pp. 40–50, Jan. 2011.

[156] X. Zhang, *Corrosion and Electrochemistry of Zinc*. New York: Springer Science and Business Media, 1996.

[157] J. Davis, *Corrosion of Aluminium and Aluminium Alloys*, Second Edi. ASM International, 1999.

[158] Scully, Silverman, and Kendig, *Electrochemical Impedance: Analysis and Interpretation*. Philadelphia, USA: American Society for Testing and Materials, 1993.

[159] P. Roberge, E. Halliop, D. Lenard, and and J. Moores, “Electrochemical characterisation of the corrosion resistance of Aluminium-lithium alloys,” *Corrosion Science*, vol. 35, no. 1–4, pp. 213–221, 1993.

[160] N. Sukiman, X. Zhou, N. Birbilis, A. Hughes, J. Mol, S. Garcia, and G. Thompson, “Durability and Corrosion of Aluminium and Its Alloys : Overview , Property Space , Techniques and Developments,” 2011.

[161] S. Pathak, S. Mendon, M. Blanton, and J. Rawlins, “Magnesium-Based Sacrificial Anode Cathodic Protection Coatings (Mg-Rich Primers) for Aluminum Alloys,” *Metals*, vol. 2, no. 4, pp. 353–376, Sep. 2012.

[162] T. Dorin, A. Deschamps, F. De Geuser, and C. Sigli, “Quantification and modelling of the microstructure/strength relationship by tailoring the morphological parameters of the T1 phase in an Al–Cu–Li alloy,” *Acta Materialia*, vol. 75, pp. 134–146, Aug. 2014.

[163] X. Zhou, C. Luo, T. Hashimoto, a. E. Hughes, and G. E. Thompson, “Study of localized corrosion in AA2024 aluminium alloy using electron tomography,” *Corrosion Science*, vol. 58, pp. 299–306, May 2012.

[164] A. W. Batchelor, N. L. Loh, and M. Chandrasekaran, *Materials Degradation and Its Control by Surface Engineering*. World Scientific, 2011.

[165] S. Hogg, J. Mi, K. Nilsen, E. Liotti, and P. Grant, “Microstructure and property development in spray formed and extruded Al-Mg-Li-Zr alloys for aerospace and autosport applications,” *Matt.-wiss.u.Werkstofftech*, no. 7, pp. 562–567, 2010.

[166] N. E. Prasad, A. Gokhale, and R. J. . Wanhill, *Aluminium-Lithium Alloys: Processing, Properties and Applications*. Butterworth-Heinemann, 2013.

[167] T. Materia, “Aluminum - Lithium Alloys,” 2002. [Online]. Available: http://www.totalmateria.com/Article58.htm. [Accessed: 30-Jan-2016].

[168] W. Masteton, C. Hurley, and E. Neth, *Chemistry: Principles and Reactions*, Seventh Ed. 2009.

[169] ISO, “ISO 9223: Corrosion of metals and alloys -- Corrosivity of atmospheres -- Classification, determination and estimation,” 2012. [Online]. Available: http://www.iso.org/iso/iso_catalogue/catalogue_tc/catalogue_detail.htm?csnumber=53499. [Accessed: 30-Jan-2016].

[170] ASTM International, “ASTM G85-11: Standard Practice for Modified Salt Spray (Fog) Testing,” 2011. [Online]. Available: http://www.astm.org/Standards/G85.htm. [Accessed: 30-Jan-2016].

[171] S. International, “J2334_200312: Laboratory Cyclic Corrosion Test,” 2003. [Online]. Available: http://standards.sae.org/j2334_200312/. [Accessed: 30-Jan-2016].

Appendix

This appendix shows the change in chemical composition of sheet AA2024-T3, extruded and plate AA2099-T8E77 as well as extruded AA5083-T3510 and extruded SF Al-Mg-Li and Al-Mg-Li-Cu-Zn following atmospheric exposure for 12 months, recorded via XPS.

AA2024-T3 sheet

Table 1: Chemical change over 12 month atmospheric exposure for sheet AA2024-T3

Month	Al2p Oxide	Al2p Metal	C1s	Cl2p	Cu2p3	F1s	N1s	O1s	Si2p	S2p	Na1s	Mg1s
0	27.00	18.49	7.51	0.00	0.99	0.00	0.00	37.4	0.00	0.00	0.00	8.29
1	20.81	2.92	16.28	0.52	0.64	0.57	0.58	55.18	0.00	2.31	0.00	0.00
2	19.35	1.55	20.44	1.15	0.52	0.45	0.45	53.91	0.06	1.98	0.11	0.00
3	20.55	0.14	20.68	0.24	0.17	0.00	0.69	54.72	0.11	2.70	0.00	0.00
6	20.59	0.12	19.54	0.38	0.13	0.19	0.68	55.42	0.23	2.72	0.00	0.00
12	18.68	0.00	24.37	0.37	0.13	0.20	0.72	50.75	1.62	3.14	0.00	0.00

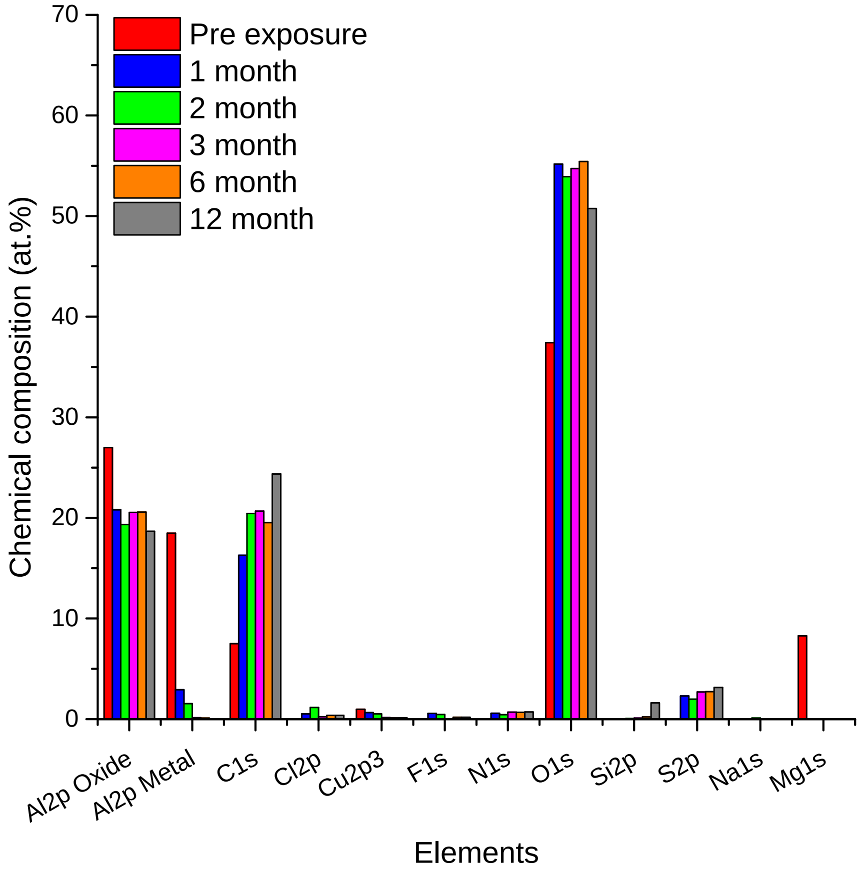

Figure 1: Chemical change over 12 month atmospheric exposure for sheet AA2024-T3

AA2099-T8E77 extrusion

Table 2: Chemical change over 12 month atmospheric exposure for extruded AA2099-T8E77

Month	Al2p Oxide	Al2p Metal	C1s	Cl2p	Cu2p3	F1s	N1s	O1s	Si2p	S2p	Na1s	Mg1s
0	20.00	39.00	16.00	0.00	1.00	0.00	0.00	25.00	0.00	0.00	0.00	1.00
1	8.79	3.16	29.17	0.41	0.08	0.68	0.78	55.71	0.00	1.21	0.00	0.00
2	19.08	3.16	24.17	1.36	0.00	0.89	1.09	51.10	0.00	1.65	0.64	0.00
3	22.07	2.89	18.64	0.48	0.00	0.65	0.67	52.47	0.76	1.36	0.00	0.00
6	13.00	0.14	26.28	2.30	0.00	1.34	1.21	44.82	3.00	3.33	3.54	0.00

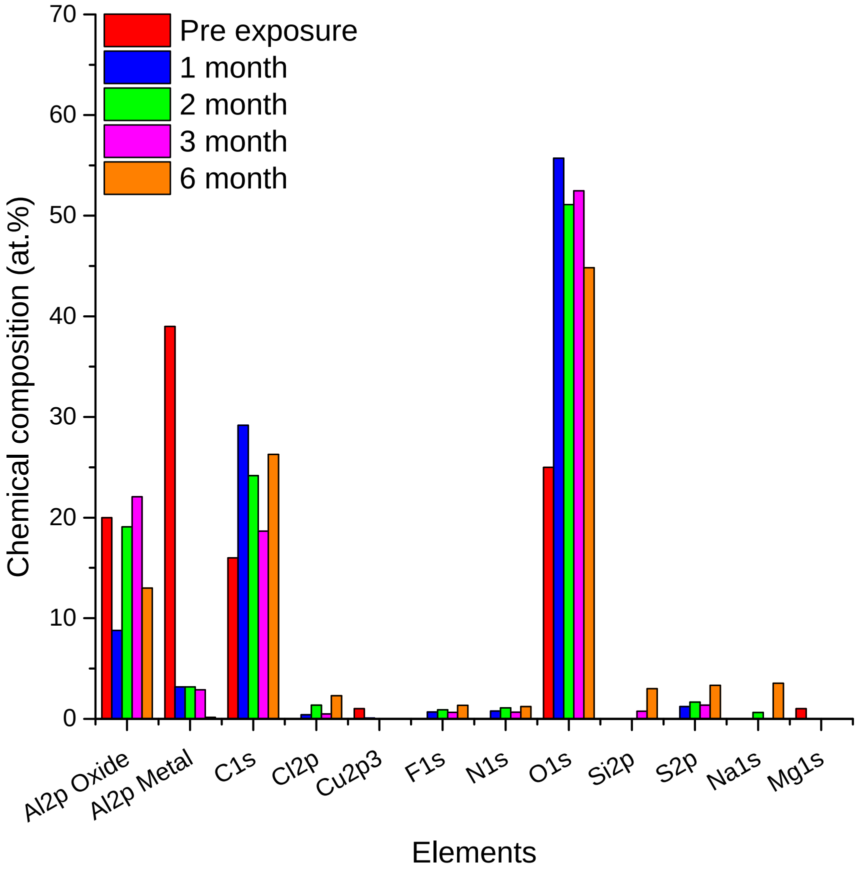

Figure 2: Chemical change over 12 month atmospheric exposure for extruded AA2099-T8E77

AA2099-T8E77 plate

Table 3: Chemical change over 12 month atmospheric exposure for plate AA2099-T8E77

Month	Al2p Oxide	Al2p Metal	C1s	Cl2p	Cu2p3	F1s	N1s	O1s	Si2p	S2p	Na1s	Mg1s
0	20.00	38.62	15.83	0.00	1.00	0.00	0.00	25.00	0.00	0.00	0.00	1.00
1	21.83	4.81	19.90	0.26	0.00	1.18	0.94	50.23	0.00	0.85	0.00	0.00
2	18.98	2.09	21.37	1.72	0.00	0.75	0.90	51.17	0.83	1.79	0.40	0.00
3	19.83	3.74	20.37	0.34	0.00	0.47	0.86	51.87	0.58	1.65	0.31	0.00
6	13.01	0.01	26.28	2.30	0.00	1.34	1.21	44.82	3.00	3.33	3.54	0.00
12	12.91	0.09	33.65	0.06	0.00	0.17	1.23	44.50	4.83	1.19	0.00	0.00

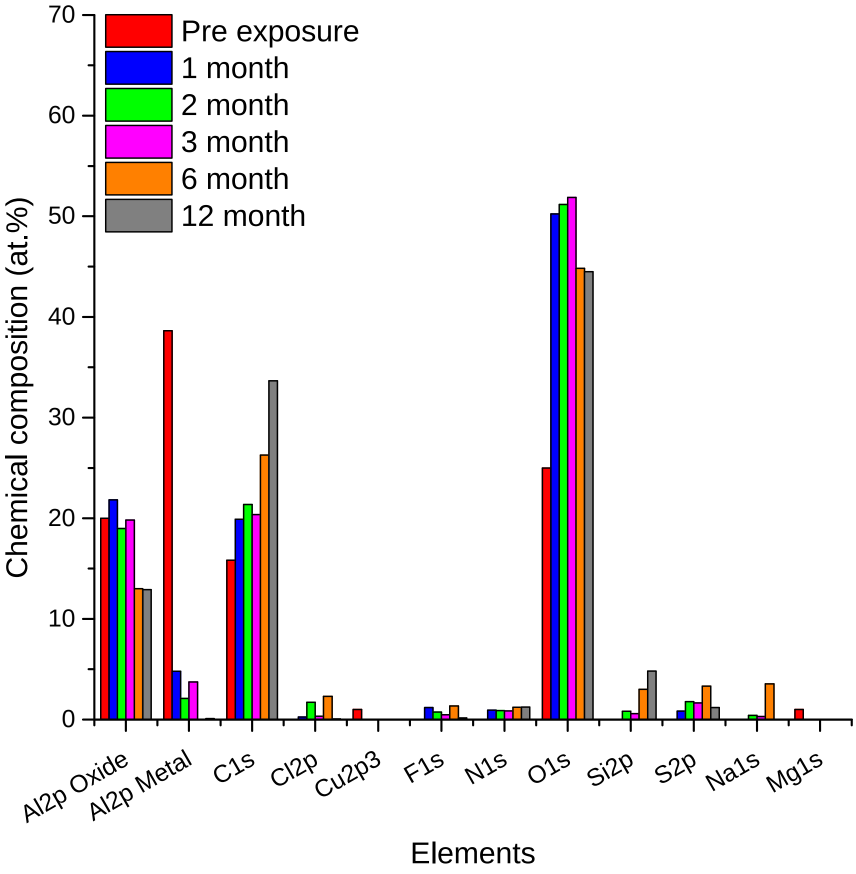

Figure 3: Chemical change over 12 month atmospheric exposure for plate AA2099-T8E77

AA5083-T3510 extrusion

Table 4: Chemical change over 12 month atmospheric exposure for extruded AA5083-T3510

Month	Al2p Oxide	Al2p Metal	C1s	Cl2p	Cu2p3	F1s	N1s	O1s	Si2p	S2p	Na1s	Mg1s
0	17.98	38.48	9.09	0.00	0.00	0.00	0.00	28.67	0.00	0.00	0.00	4.65
1	22.32	2.51	20.96	0.74	0.00	0.75	0.81	51.06	0.00	0.85	0.00	0.00
2	20.06	2.60	22.08	1.87	0.00	0.91	1.46	49.78	0.00	1.16	0.00	0.00
3	20.80	2.81	20.14	0.54	0.00	0.60	0.75	51.73	1.26	1.31	0.00	0.00
6	12.69	0.00	34.79	0.67	0.00	0.99	1.47	41.18	4.42	1.85	0.36	0.00
12	14.76	0.00	33.35	0.28	0.00	0.39	1.22	43.58	4.02	1.33	0.00	0.02

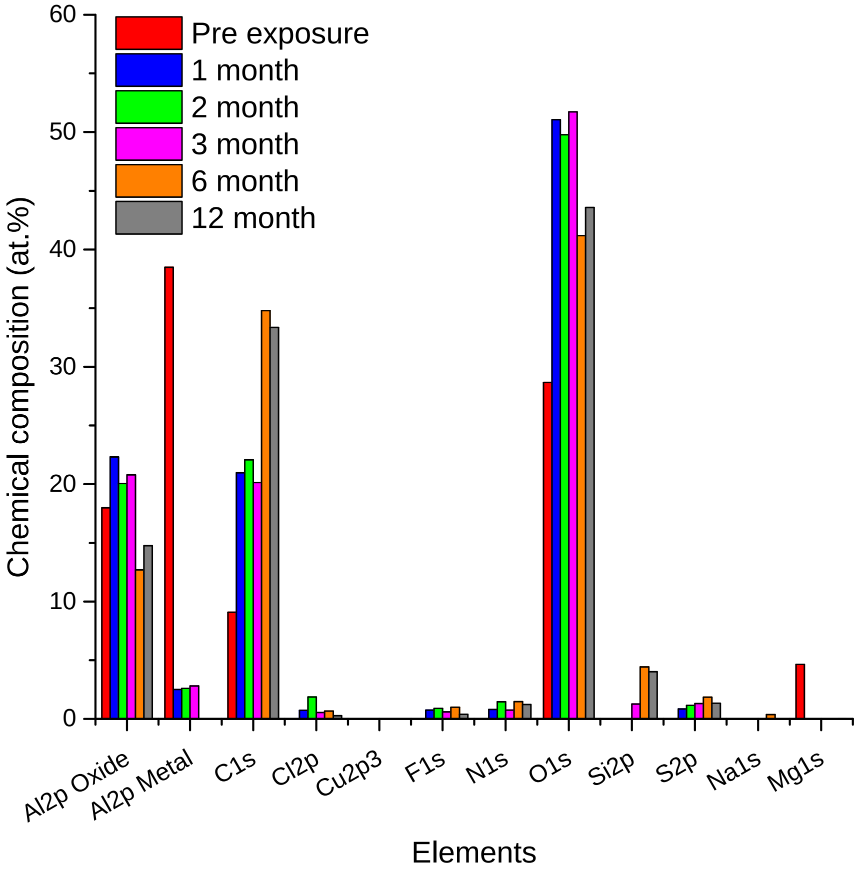

Figure 4: Chemical change over 12 month atmospheric exposure for extruded AA5083-T3510

Spray formed, Al-Mg-Li extrusion

Table 5: Chemical change over 12 month atmospheric exposure for extruded, SF Al-Mg-Li

Month	Al2p Oxide	Al2p Metal	C1s	Cl2p	Cu2p3	F1s	N1s	O1s	Si2p	S2p	Na1s	Mg1s
0	9.00	32.00	7.00	0.00	0.00	0.00	0.00	40.00	0.00	0.20	0.00	12.00
1	19.26	2.55	22.81	0.39	0.00	1.14	1.99	50.89	0.00	0.96	0.00	0.00
2	19.70	2.18	20.07	2.15	0.00	1.12	0.79	51.13	1.20	0.96	0.48	0.00
3	15.57	1.65	29.67	0.83	0.05	0.39	1.70	46.11	1.21	1.32	1.17	0.00
6	14.91	0.72	33.51	0.79	0.00	0.67	1.13	44.34	2.34	1.04	0.56	0.00
12	12.94	0.00	30.19	0.28	0.00	9.04	1.03	39.64	4.88	0.99	0.00	0.00

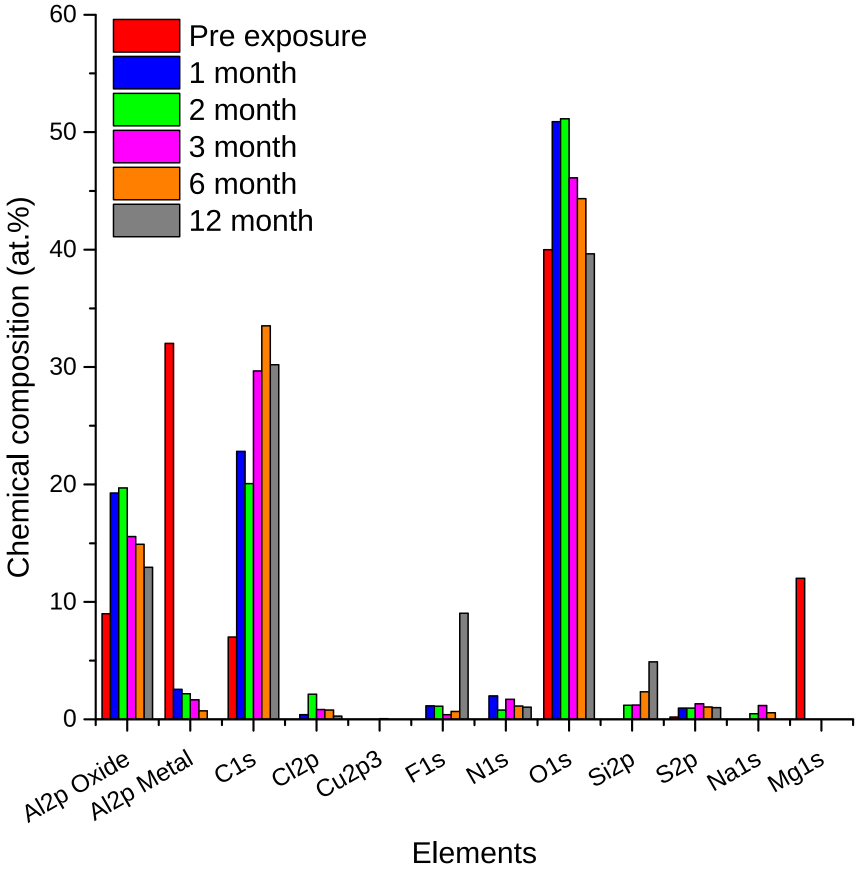

Figure 5: Chemical change over 12 month atmospheric exposure for extruded, SF Al-Mg-Li –Cu-Zn

Spray formed, Al-Mg-Li-Cu-Zn extrusion

Table 6: Chemical change over 12 month atmospheric exposure for extruded, SF Al-Mg-Li–Cu-Zn

Month	Al2p Oxide	Al2p Metal	C1s	Cl2p	Cu2p3	F1s	N1s	O1s	Si2p	S2p	Na1s	Mg1s
0	7.00	24.00	10.00	0.00	0.00	0.00	0.00	40.00	0.00	0.00	0.00	15.00
1	22.05	2.04	19.68	0.71	0.00	0.85	0.50	53.31	0.00	0.86	0.00	0.00
2	19.38	2.30	21.99	1.52	0.00	1.15	0.69	51.22	0.00	1.07	0.47	0.05
3	17.09	4.19	25.43	0.31	0.02	0.61	0.91	48.60	1.01	1.02	0.59	0.00
6	13.40	0.20	33.79	0.38	0.00	0.92	1.38	42.34	3.64	2.39	0.25	0.00
12	14.76	0.00	33.35	0.28	0.00	0.39	1.22	43.58	4.02	1.33	0.00	0.00

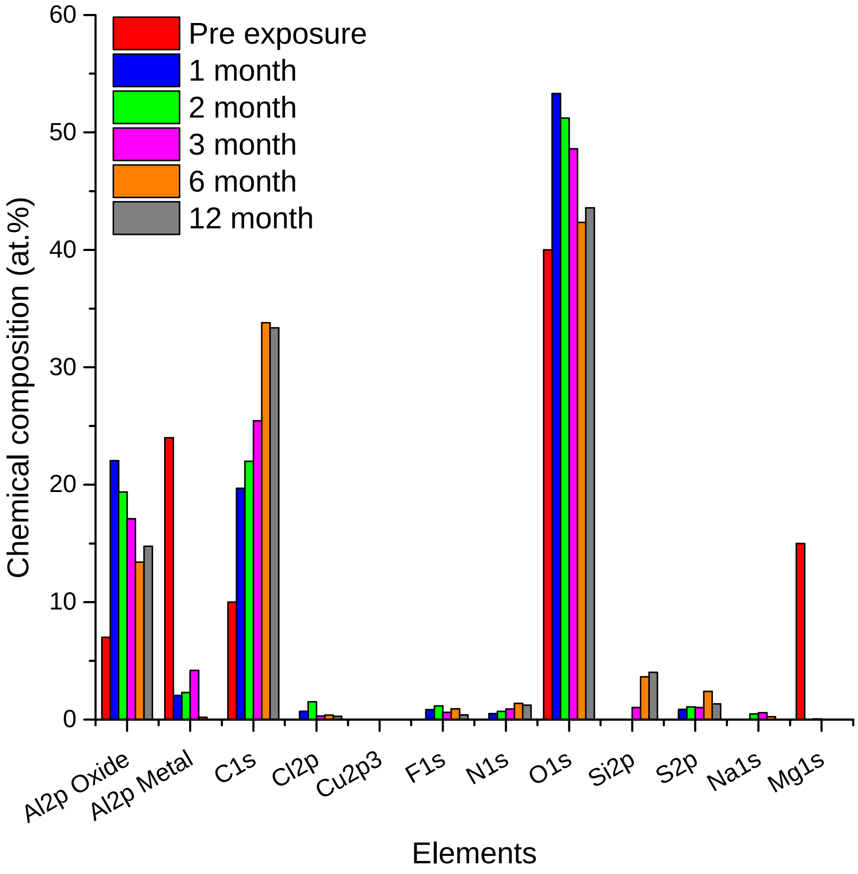

Figure 6: Chemical change over 12 month atmospheric exposure for extruded, SF Al-Mg-Li –Cu-Zn